



Jimenez-Garcia, Antonio (2018) Development of predictive methods for tiltrotor flows. PhD thesis.

<http://theses.gla.ac.uk/8603/>

Copyright and moral rights for this work are retained by the author

A copy can be downloaded for personal non-commercial research or study, without prior permission or charge

This work cannot be reproduced or quoted extensively from without first obtaining permission in writing from the author

The content must not be changed in any way or sold commercially in any format or medium without the formal permission of the author

When referring to this work, full bibliographic details including the author, title, awarding institution and date of the thesis must be given

Enlighten:Theses  
<http://theses.gla.ac.uk/>  
theses@ gla.ac.uk



University  
of Glasgow

**Development of Predictive Methods for  
Tiltrotor Flows**  
by  
**Antonio Jimenez-Garcia**

A thesis submitted in partial  
fulfillment of the requirements for  
the degree of Doctor of Philosophy  
University of Glasgow  
School of Engineering  
July 2017

© 2017  
Antonio Jimenez-Garcia



# Declaration

I hereby declare that this dissertation is a record of work carried out in the School of Engineering at the University of Liverpool during the period from January 2014 to August 2015, and at the University of Glasgow during the period from September 2015 to July 2017. The dissertation is original in content except where otherwise indicated.

July 2017

.....  
(Antonio Jimenez-Garcia)

# Abstract

This thesis presents evidence on the ability of grid-based, Computational Fluid Dynamics methods based on the Unsteady Reynolds Averaged Navier-Stokes equations to accurately predict axial flight performance of rotors with modest computer resources. Three well-studied blades, the B0-105, S-76, and PSP main rotor blades, are used and results are compared with experimental data. Likewise, performance analyses of the JORP propeller and XV-15 tiltrotor blades are carried out, respectively, aiming to validate the employed CFD method for such relevant flows.

Validation of the HMB3 CFD solver for complete tiltrotors is also presented. The aim is to assess the capability of the present CFD method in predicting tiltrotor airloads at different flight configurations. In this regard, three representative cases of the ERICA tiltrotor were selected, corresponding to aeroplane, transition corridor, and helicopter modes, covering most modes of tiltrotor flight.

Aerodynamic optimisation of tiltrotor blades with high-fidelity computational fluid dynamics coupled with a discrete adjoint method is also carried out. This work shows how the main blade shape parameters influence the optimal performance of the tiltrotor in helicopter and aeroplane modes, and how a compromise blade shape can increase the overall tiltrotor performance.

Finally, the implementation and validation of an efficient, high-order, finite-volume scheme (up to 4th-order of spatial accuracy) in the HMB3 CFD solver is presented. The scheme shows a higher level of accuracy if compared with the standard-MUSCL, and 4th-order accuracy was achieved on Cartesian grids. Furthermore, a significantly high spectral resolution (dispersion and dissipation) of the new scheme is observed. Two-and three-dimensional test cases were considered to demonstrate the new formulation. Results of the steady flow around the 7AD, S-76, JORP propeller, and XV-15 blades showed a better preservation of the vorticity and higher resolution of the vortical structures compared with the standard MUSCL solution. The method was also demonstrated for three-dimensional unsteady flows using overset and moving grid computations for the UH-60A rotor in forward flight and the ERICA tiltrotor in aeroplane mode. For medium grids, the new high-order scheme adds CPU and memory overheads of 22% and 23%, respectively. The parallel performance of the scheme is fair but can be further improved.

# Publications

## Journal Articles

- Jimenez-Garcia, A., and Barakos, G.N., “CFD Analysis of Hover Performance of Rotors at Full-and Model-Scale Conditions”, *The Aeronautical Journal*, Vol. 120, No. 1231, 2016, pp. 1386-1424, doi: 10.1017/aer.2016.58.
- Jimenez-Garcia, A., and Barakos, G.N., “Accurate Predictions of Rotor Hover Performance at Low and High Disc Loadings”, *Journal of Aircraft*, Advance Online Publication, 2017, doi: 10.2514/1.C034144.
- Jimenez-Garcia, A., and Barakos, G.N., “Numerical Simulations on the ERICA Tiltrotor”, *Aerospace Science and Technology*, Vol. 64, 2017, pp. 171-191, doi: 10.1016/j.ast.2017.01.023.
- Jimenez-Garcia, A., Barakos, G.N., and Gates, S., “Tiltrotor CFD Part I - Validation”, *The Aeronautical Journal*, Vol. 121, No. 1239, 2017, pp. 577-610, doi: 10.1017/aer.2017.17.
- Jimenez-Garcia, A., Biava, M., Barakos, G.N., Gates, S., Baverstock, K., and Mullen, P., “Tiltrotor CFD Part II - Aerodynamic Optimisation of Tiltrotor Blades”, *The Aeronautical Journal*, Vol. 121, No. 1239, 2017, pp. 611-636, doi: 10.1017/aer.2017.21.
- Jimenez-Garcia, A., and Barakos, G.N., “Assessment of a High-Order MUSCL Method for Rotor Flows”, *International Journal for Numerical Methods in Fluids*, Under Review.

## Publications in Conference Proceedings

- Jimenez-Garcia, A., and Barakos, G.N., “Hover Predictions on the S-76 Rotor Using HMB2”, *Proceedings of the 53rd Aerospace Sciences Meeting*, Kissimmee, Florida, USA, AIAA-2015-1712, 2015, doi: 10.2514/6.2015-1712.
- Jimenez-Garcia, A., and Barakos, G.N., “Numerical Simulation of the ERICA Tiltrotor Using HMB2”, *Proceedings of the 41st European Rotorcraft Forum*, Munich, Germany, ERF-2015-42, 2015, pp. 1-15.
- Jimenez-Garcia, A., and Barakos, G.N., “Hover Predictions of the S-76 Rotor Using HMB2 - Model to Full Scale”, *Proceedings of the 54th Aerospace Sciences Meeting*, San Diego, California, USA, AIAA-2016-0299, 2016, doi: 10.2514/6.2016-0299.

- Jimenez-Garcia, A., and Barakos, G.N., “CFD Simulations of the ERICA Tiltrotor Using HMB2”, *Proceedings of the 54th Aerospace Sciences Meeting*, San Diego, California, USA, AIAA-2016-0329, 2016, doi: 10.2514/6.2016-0329.
- Jimenez-Garcia, A., and Barakos, G.N., “Aerodynamic Study of Tiltrotor Blades”, *Proceedings of the 42nd European Rotorcraft Forum*, Lille, France, ERF-2016-56, 2016, pp. 1-16.
- Jimenez-Garcia, A., Colonia, S., and Barakos, G.N., “Accurate Predictions of Hovering Rotor Flows Using CFD”, *Proceedings of the 55th Aerospace Sciences Meeting*, Grapevine, Texas, USA, AIAA-2017-1666, 2017, doi: 10.2514/6.2017-1666.
- Jimenez-Garcia, A., and Barakos, G.N., “Implementation of High-Order Methods in the HMB CFD Solver”, *Proceedings of the 73rd American Helicopter Society Annual Forum*, AHS, Fort Worth, Texas, USA, 2017.
- Jimenez-Garcia, A., and Barakos, G.N., “Numerical Simulations of Rotors Using High Fidelity Methods”, *Proceedings of the 35th Applied Aerodynamics Conference*, Denver, Colorado, USA, AIAA-2017-3053, 2017, doi: 10.2514/6.2017-3053.
- Jimenez-Garcia, A., and Barakos, G.N., “Towards High-Order Methods for Rotorcraft Applications”, *Proceedings of the 43rd European Rotorcraft Forum*, Milan, Italy, ERF-2017-516, 2017, pp. 1-16.
- Jimenez-Garcia, A., and Barakos, G.N., “Numerical Simulations on the PSP Rotor Using HMB3”, *Proceedings of the 56th Aerospace Sciences Meeting*, Kissimmee, Florida, USA, 2018, Abstract Accepted.

## Other Conferences/Symposia

- Jimenez-Garcia, A., and Barakos, G.N., “Numerical Simulations of Helicopters and Tiltrotors using the HMB2 Solver”, *1st U.K. Vertical Lift Network (VLN) Technical Workshop*, Oakmere, Cheshire, U.K, 2015.
- Jimenez-Garcia, A., and Barakos, G.N., “Aerodynamic and Optimisation Study of Tiltrotor Blades”, *2nd U.K. Vertical Lift Network (VLN) Technical Workshop*, Pott Shrigley, Cheshire, U.K, 2016.
- Jimenez-Garcia, A., and Barakos, G.N., “CFD Simulations on the ERICA Tiltrotor using HMB3”, *2nd International Scientific Conference Science of the Future*, Kazan, Russia, 2016.
- Jimenez-Garcia, A., and Barakos, G.N., “A High-Order Method for Rotorcraft Flow”, *3rd U.K. Vertical Lift Network (VLN) Technical Workshop*, Pott Shrigley, Cheshire, U.K, 2017.

## Technical Reports

- Jimenez-Garcia, A., “D4.1a HMB Validation I”, *HiperTilt Project - Technology Strategy Board (TSB)*, January 2014.
- Jimenez-Garcia, A., “D4.1b HMB Validation II”, *HiperTilt Project - Technology Strategy Board (TSB)*, April 2015.
- Jimenez-Garcia, A., “D4.5 Aeroacoustic Method”, *HiperTilt Project - Technology Strategy Board (TSB)*, June 2015.
- Jimenez-Garcia, A., “D4.6 Aeroelasticity Study using HMB2”, *HiperTilt Project - Technology Strategy Board (TSB)*, July 2015.
- Jimenez-Garcia, A., “High-Order Schemes with HMB3”, *Technical Note TN16-008*, CFD Laboratory, University of Glasgow, May 2016.
- Jimenez-Garcia, A., “D5.1 CFD Simulations on the ERICA Tiltrotor using HMB2”, *HiperTilt Project - Technology Strategy Board (TSB)*, June 2016.

## Placements

- Leonardo Helicopters, Aerodynamics Department, Lysander Rd, Yeovil BA20 2YB, 12–15 January 2015. ”Integration of the BENP and HMB Solvers”
- Leonardo Helicopters, Aerodynamics Department, Lysander Rd, Yeovil BA20 2YB, 11–15 May 2015. ”Computing Tiltrotor Cases using the HMB Solver”

# Acknowledgements

First and foremost, I would like to thank my supervisor Professor George Barakos for his constant guidance, support, encouragement, and technical knowledge throughout this work. His contagious enthusiasm and passion for Computational Fluid Dynamics kept me highly motivated and made this thesis a reality. I am also very grateful to Dr. Mark Woodgate and Dr. Massimo Biava for sharing their tremendous expertise and experience in numerical methods and for the numerous discussions we had on high-order and adjoint methods. Special thanks for Dr. Rene Steijl, who advised me and shared his knowledge on rotorcraft flows at all moments. I would like also to extend my gratitude to all members of the CFD lab for creating a family-supportive work environment and making me feel at home. The time spent with Dr. Nick Tantaroudas, Dr. Vasilis Pastrikakis, Dr. Simone Colonia, Dr. Vladimir Leble, Jur Mourits, and many others, is of great value.

The financial support of the HiperTilt Project of the U.K. Technology Strategy Board (TSB) and Leonardo Helicopters under Contract Nr. 101370 is gratefully acknowledged. Many thanks should go to Alessandro Scandroglio, Dr. Florent Dehaeze, Stuart Gates, Karl Baverstock, and Paul Mullen of Leonardo Helicopters for their contributions to the acoustic and optimisation work and for hosting me during my placements in the Acoustic and Aerodynamics Departments.

The use of the clusters Chadwick of the University of Liverpool and the EPSRC funded ARCHIE-WeSt High Performance Computer ([www.archie-west.ac.uk](http://www.archie-west.ac.uk)), EPSRC grant no. EP/K000586/1 is gratefully acknowledged.

In addition, I would like to thank to all members of Scottish International Youth Charity Organisation, and its football branch for being my second family and providing an unconditional support in every aspect beyond sports. A very special thank you goes to my housemate, football manager, and friend Abdul Duane Lawal. The support and friendship of Francisco Suarez, Juan Pablo Paez, Miguel Ballesteros, Juan Molina and Manuel Jesus Algarin must be fully recognised and appreciated. *Gracias Amigos.*

Most importantly, I would like to thank my parents Antonio and Rosa, my brothers Juan Miguel and Eduardo and my fiance Sonia for their endless love and patience during these years and for supporting me in every hard situation. *Vuestro amor y comprensión en estos años ha sido la luz que me ha guiado cada día. Papá, Mamá, Juan Miguel, Eduardo y Sonia, os quiero con todo mi corazón. Gracias por creer en mi.*

# Contents

<b>1</b>	<b>Introduction</b>	<b>1</b>
1.1	Motivation . . . . .	1
1.2	Literature Survey . . . . .	3
1.2.1	Validation Data Related to Helicopter Rotors . . . . .	3
	Modelling Rotors . . . . .	3
	CFD Efforts . . . . .	9
	S-76 Rotor . . . . .	10
1.2.2	Validation Data Related to Propellers . . . . .	16
1.2.3	Validation Data Related to Tiltrotors . . . . .	18
1.2.4	Aerodynamic Optimisation of Tiltrotor Blades . . . . .	27
1.2.5	Validation Data for Aeroacoustics . . . . .	29
1.2.6	High-Order Discretisation Methods for CFD . . . . .	32
1.3	Summary of Findings . . . . .	34
1.4	Objectives of the Thesis . . . . .	35
1.5	Outline of the Thesis . . . . .	35
<b>2</b>	<b>HMB3 Solver</b>	<b>37</b>
2.1	CFD Method . . . . .	37
2.2	Variable Extrapolation-MUSCL Approach . . . . .	38
2.3	Turbulence Modelling . . . . .	40
2.3.1	The Reynolds-Averaging . . . . .	41
	Time Averaging . . . . .	42
2.3.2	RANS and URANS . . . . .	42
2.3.3	Turbulence Models . . . . .	44
	$k-\omega$ and SST Model . . . . .	45
	$k-\omega$ SST- $\gamma$ Model . . . . .	45
	$\gamma$ - $Re_{\theta_t}$ Model . . . . .	46
	Transition Criteria . . . . .	46
2.4	Aerodynamic Models . . . . .	47
2.5	Overset Grid Method . . . . .	50
2.6	Optimisation Framework . . . . .	51
2.7	Visualisation of Vortical Flows . . . . .	53
<b>3</b>	<b>Aeroacoustic Method</b>	<b>55</b>
3.1	Helicopter Ffowcs Williams-Hawkings . . . . .	55
3.2	BENP Acoustics . . . . .	59

3.2.1	Aeroacoustic File for the S-76 Rotor Blade in Hover . . . . .	68
3.2.2	Aeroacoustic File for the AW-139 Rotor Blade in Forward Flight . . . . .	70
<b>4</b>	<b>High-Order Method</b>	<b>79</b>
4.1	High-order Formulation . . . . .	79
4.2	Green-Gauss Formulation . . . . .	81
4.3	Memory Overhead . . . . .	82
4.4	Order of Accuracy in 1D . . . . .	84
4.5	Implementation Details . . . . .	85
4.6	Fourier Analysis . . . . .	85
4.7	Vortex Transported by Uniform flow . . . . .	87
<b>5</b>	<b>Validation of HMB for Helicopter Blades in Hover</b>	<b>91</b>
5.1	B0-105 Main Rotor . . . . .	91
5.1.1	B0-105 Rotor Mesh . . . . .	92
5.1.2	Test Conditions and Computations . . . . .	93
5.1.3	Results and Discussion . . . . .	94
	Estimation of Transition Onset . . . . .	94
	Integrated Blade Loads . . . . .	96
5.2	S-76 Main Rotor . . . . .	100
5.2.1	S-76 Rotor Mesh . . . . .	101
5.2.2	Test Conditions and Computations . . . . .	104
5.2.3	Swept-Taper Tip (Blade-Tip Mach Number of 0.65) . . . . .	106
	Mesh Convergence . . . . .	106
	Integrated Blade Loads . . . . .	108
	Sectional Blade Loads . . . . .	110
	Surface Pressure Predictions . . . . .	110
	Trajectory and Size of the Tip Vortex . . . . .	112
5.2.4	Swept-Taper Tip (Blade-Tip Mach Numbers of 0.60 and 0.55) . . . . .	118
5.2.5	Rectangular Tip (Blade-Tip Mach Numbers of 0.65 and 0.6) . . . . .	118
5.2.6	Anhedral Tip (Blade-Tip Mach Numbers of 0.65 and 0.60) . . . . .	121
5.2.7	Effect of the Tip Shape . . . . .	121
5.2.8	Hovering Endurance . . . . .	123
5.2.9	Aeroacoustic Study . . . . .	124
5.3	Full-Scale S-76 Rotor Blade . . . . .	128
5.3.1	Aeroelastic Analysis of the S-76 Rotor . . . . .	128
	Structural Model . . . . .	128
	Analysis of Elastic Blade Results . . . . .	131
5.3.2	Comparison Between Full and Model-Scale Rotors . . . . .	132
5.3.3	Tip Vortex Trajectory . . . . .	134
5.3.4	Aeroacoustic Study . . . . .	134
5.4	PSP Main Rotor . . . . .	137
5.4.1	PSP Rotor Mesh . . . . .	138
5.4.2	Test Conditions and Computations . . . . .	138
5.4.3	Blade-Tip Mach Number of 0.585 . . . . .	141
	Integrated Blade Loads . . . . .	141



	Surface Pressure Predictions . . . . .	143
5.4.4	Blade-Tip Mach Number of 0.65 . . . . .	143
	Integrated Blade Loads . . . . .	143
	Sectional Blade Loads . . . . .	146
	Surface Pressure Predictions . . . . .	146
	Tip Vortex Trajectory . . . . .	150
5.5	Summary of Findings . . . . .	153
<b>6</b>	<b>Validation of HMB for Propeller Blades</b>	<b>154</b>
6.1	Rotor Mesh . . . . .	156
6.2	Test Conditions and Computations . . . . .	158
6.3	Results and Discussion . . . . .	159
<b>7</b>	<b>Validation of HMB for Tiltrotor Blades</b>	<b>163</b>
7.1	Aerodynamic and Aeroacoustic Study . . . . .	163
7.1.1	XV-15 Rotor Geometry . . . . .	163
7.1.2	XV-15 Rotor Mesh . . . . .	164
7.1.3	Test Conditions and Computations . . . . .	167
7.1.4	Helicopter Mode . . . . .	168
	Surface Pressure Predictions . . . . .	170
	Sectional Blade Loads . . . . .	172
	Aeroacoustic Analysis . . . . .	173
7.1.5	Aeroplane Mode . . . . .	174
	Sectional Blade Loads . . . . .	175
	Surface Pressure Predictions . . . . .	175
	Flowfield Details . . . . .	175
7.2	Effect of the Turbulence Model . . . . .	180
7.3	Summary of Findings . . . . .	184
<b>8</b>	<b>Validation of HMB for Complete Tiltrotors</b>	<b>185</b>
8.1	Aerodynamic Models . . . . .	185
8.2	ERICA Tiltrotor Mesh . . . . .	186
8.3	Test Conditions and Computations . . . . .	192
8.4	Results and Discussion . . . . .	194
8.4.1	Aeroplane Mode AC1 . . . . .	195
	Surface Pressure Predictions . . . . .	195
	Load Distributions . . . . .	206
	Flowfield Details . . . . .	207
8.4.2	Transition Corridor CC4 . . . . .	210
	Surface Pressure Predictions . . . . .	210
	Flowfield and Aerodynamic Comparison Between AC1 and CC4 . . . . .	217
8.4.3	Helicopter Mode HC3 . . . . .	217
	Surface Pressure Predictions . . . . .	217
8.5	Summary of Findings . . . . .	222

<b>9</b>	<b>Aerodynamic Optimisation of Tiltrotor Blades</b>	<b>228</b>
9.1	Introduction . . . . .	228
9.2	Optimisation Framework . . . . .	231
9.2.1	Objective and Constraint Functions . . . . .	231
9.2.2	Optimisation Tools Chain . . . . .	232
9.2.3	Parametrisation Technique . . . . .	235
9.3	Results and Discussion . . . . .	237
9.3.1	Ideal Twist Using Blade Element Theory . . . . .	237
9.3.2	XV-15 Blade Mesh . . . . .	240
9.3.3	Design Cases . . . . .	240
9.3.4	Helicopter Mode . . . . .	242
9.3.5	Aeroplane Mode . . . . .	247
9.3.6	Multi-Point Optimisation . . . . .	251
9.4	Summary of Findings . . . . .	255
<b>10</b>	<b>Validation of High-Order Methods in the HMB CFD Solver</b>	<b>257</b>
10.1	Blade-Vortex Interaction . . . . .	257
10.2	Turbulent Flow over the RAE2822 Aerofoil . . . . .	260
10.3	7AD Helicopter Blade . . . . .	261
10.4	S-76 Helicopter Blade . . . . .	268
10.4.1	CPU and Memory Overheads . . . . .	272
10.5	JORP Propeller Blade . . . . .	273
10.5.1	CPU and Memory Overheads . . . . .	275
10.6	XV-15 Tiltrotor Blade . . . . .	278
10.6.1	CPU and Memory Overheads . . . . .	283
10.7	UH-60A Rotor in Forward Flight . . . . .	286
10.7.1	CPU and Memory Overheads . . . . .	289
10.8	Complete Tiltrotor Computation . . . . .	293
10.8.1	CPU and Memory Overheads . . . . .	296
10.9	Summary of Findings . . . . .	300
<b>11</b>	<b>Conclusions and Future Work</b>	<b>301</b>
11.1	Summary and Conclusions . . . . .	301
11.2	Future Work . . . . .	304
	<b>References</b>	<b>305</b>
<b>A</b>	<b>Matlab Program for the Theoretical Noise</b>	<b>326</b>

# List of Figures

1.1	(a) XV-15 (b) V-22 Osprey and (c) AW609 tiltrotors. . . . .	2
1.2	Schematic of the three-dimensional wake structures of a rotor in hover. Adapted from [16]. . . . .	5
1.3	Schematic of the actuator disk concept in hover. . . . .	6
1.4	Comparison of the wake geometry for a 2-bladed, untwisted and untapered rotor with NACA 230-12 sections at blade pitch angle of 12 degrees. Adapted from [21].	8
1.5	Tip shapes of the 1/4.71 model-scale S-76 rotor. Adopted from Balch and Lombardi [33]. . . . .	12
1.6	Model test cell hover facility with the BMTR for the 1/4.71 model-scale S-76 rotor [33]. . . . .	12
1.7	Aerofoil trailing edge of the S-76 rotor blade generated by Prof. Sankar and Barakos [42]. Adopted from [43]. . . . .	13
1.8	Pressure Tapped Propeller (PTP) model in the transonic wind tunnel of the Aircraft Research Association [72]. . . . .	18
1.9	The TILTAERO half-span 40% Mach-scaled model in the DNW-LLF wind tunnel (left) and aeroacoustic test set-up in the 8×6m 3/4 open test section (right) [80]. . .	20
1.10	Full-scale XV-15 rotor on the rotor test apparatus in the 80-ft by 120-ft wind tunnel at NASA Ames [87]. . . . .	22
1.11	ERICA tiltrotor in the S1MA ONERA (left) and DNW-LLF (right) wind tunnels [93].	23
1.12	Sketch of the BVI noise, showing the noise directivity of this source of noise [137].	31
1.13	Schematic of the directivity of the source of rotor noise [137]. . . . .	31
2.1	Reynolds decomposition in averaged and fluctuation part. . . . .	42
2.2	Set-up of the transition corridor (left) and helicopter mode (right) configurations with the rotor actuator disk. . . . .	50
2.3	Flow chart of the optimisation process. . . . .	52
3.1	Illustration of the trajectory of a source point $\eta$ relative to an fixed observed [208].	56
3.2	Distributions of radial sections along the spanwise direction of the S-76 rotor blade with 60% taper-35° degrees swept tip. . . . .	58
3.3	Leonardo Helicopters aeroacoustic computational chain. CAMRAD/JA [213] is a tool used to evaluate a required trim state, ADPANEL [103] and HMB are used as aerodynamic solvers, BENP is the main acoustic solver, and HELENA [214] is used to propagate the acoustic sphere to the locations of the microphones. More details of these solvers can be found in [215, 6]. . . . .	60

3.4	Geometry (left) and surface mesh distribution (right) of the sphere acoustic located at $r/R=1.1$ for the S-76 rotor blade. The complete surface mesh contains 21,400 nodes distribute along 19,968 panels. . . . .	67
3.5	Order in which various utilities are used to generate the geometric file of the acoustic solver BENP referred to as BENP1. . . . .	67
3.6	Fluctuation of pressure in Pa (top) and sound pressure level in dB (bottom) of the acoustic pressure sphere located at $r/R=1.1$ from the centre of the rotor. . . . .	69
3.7	Fluctuation of pressure in Pa for the AW-139 rotor blade at azimuth blade $\Psi = -10^\circ$ . IDM=Inverse Distance Method; LM=Linear Method. . . . .	71
3.8	Fluctuation of pressure in Pa for the AW-139 rotor blade at azimuth blade $\Psi = 0^\circ$ . IDM=Inverse Distance Method; LM=Linear Method. . . . .	72
3.9	Fluctuation of pressure in Pa for the AW-139 rotor blade at azimuth blade $\Psi = 10^\circ$ . IDM=Inverse Distance Method; LM=Linear Method. . . . .	73
3.10	Fluctuation of pressure in Pa for the AW-139 rotor blade at azimuth blade $\Psi = 20^\circ$ . IDM=Inverse Distance Method; LM=Linear Method. . . . .	74
3.11	Fluctuation of pressure in Pa for the AW-139 rotor blade at azimuth blade $\Psi = 30^\circ$ . IDM=Inverse Distance Method; LM=Linear Method. . . . .	75
3.12	Fluctuation of pressure in Pa for the AW-139 rotor blade at azimuth blade $\Psi = 40^\circ$ . IDM=Inverse Distance Method; LM=Linear Method. . . . .	76
3.13	Fluctuation of pressure in Pa for the AW-139 rotor blade at azimuth blade $\Psi = 50^\circ$ . IDM=Inverse Distance Method; LM=Linear Method. . . . .	77
3.14	Fluctuation of pressure in Pa for the AW-139 rotor blade at azimuth blade $\Psi = 60^\circ$ . IDM=Inverse Distance Method; LM=Linear Method. . . . .	78
4.1	Illustration of the domain discretisation. . . . .	80
4.2	Illustration of stencil for Green-Gauss gradient calculation for cell-centre discretisation on 2D. . . . .	83
4.3	Sketch of stencil for distance calculation for left and right states in $j$ planes on 2D. . . . .	84
4.4	Fourier analysis for MUSCL-2 and MUSCL-4 schemes. . . . .	86
4.5	Error convergences rate of MUSCL-2 (2nd-order upwind), MUSCL-3 (3rd-order upwind), and MUSCL-4 (4th-order upwind) schemes for vortex transport problem. . . . .	88
4.6	Pressure contours for isentropic vortex convection after travelling two times the computational domain. Solutions were obtained on $64 \times 64$ equi-spaced Cartesian grids. . . . .	89
4.7	Comparison of cross-sectional pressure contours computed by several schemes on a $128 \times 128$ equi-spaced Cartesian grid. . . . .	90
5.1	Computational domain and boundary conditions employed (left) and detailed view of the B0-105 rotor mesh topology (right). . . . .	93
5.2	(I) Overview of the transition onset on the upper blade surface, showing estimates of transition criteria compared with experimental data, (II) close-view of the transition onset, and (III) comparison of predicted transition locations along the rotor radius. . . . .	95

5.3	(I) Overview of the transition onset on the lower blade surface, showing estimates of transition criteria compared with experimental data, (II) close-view of the transition onset, and (III) comparison of predicted transition locations along the rotor radius. . . . .	96
5.4	$C_f$ profile comparisons between the $k-\omega$ SST [191] and the $\gamma\text{-Re}_{\theta_t}$ [47, 48] turbulence models at radial stations $r/R = 0.69, 0.75, 0.82, 0.87, 0.92$ , and $0.97$ . . . . .	97
5.5	$C_p$ profile comparisons between the $k-\omega$ SST [191] and the $\gamma\text{-Re}_{\theta_t}$ [47, 48] turbulence models at radial stations $r/R = 0.69, 0.75, 0.82, 0.87, 0.92$ , and $0.97$ . . . . .	98
5.6	Comparisons of blade sectional thrust coefficient (top) and torque coefficient (bottom) for the B0-105 rotor between the $k-\omega$ SST [191] and the $\gamma\text{-Re}_{\theta_t}$ [47, 48] turbulence models. . . . .	99
5.7	Geometry of the S-76 model rotor with 60% taper-35° swept tip, (I) SC-1095-R8 aerofoil, (II) SC-1095 aerofoil, (III) planform of the S-76 rotor, and (IV) twist and thickness distributions [37]. . . . .	102
5.8	Planform of the S-76 model rotor with 60% taper-35° swept-20° anhedral tip, and geometric details of the flat/rounded tip-caps. . . . .	103
5.9	Planform of the S-76 model rotor with 60% taper-35° swept-16.23° anhedral tip. . . . .	104
5.10	Computational domain and boundary conditions employed (top) and detailed view of the S-76 rotor mesh (bottom). . . . .	105
5.11	Effect of the mesh density on the FoM as a function of the $C_T/\sigma$ for the S-76 model rotor with 60% taper-35° swept tip. . . . .	107
5.12	Figure of merit versus blade loading coefficient for the S-76 model rotor with 60% taper-35° swept tip at blade-tip Mach number of 0.65. . . . .	109
5.13	Blade sectional thrust coefficient (top) and torque coefficient (bottom) for the S-76 model rotor with 60% taper-35° swept tip at blade-tip Mach number of 0.65. . . . .	111
5.14	Surface pressure coefficient for the S-76 model rotor with 60% taper-35° swept tip at blade-tip Mach number of 0.65. Critical $C_p^* = \frac{2}{\gamma(M_{\text{tip}} \frac{r}{R})^2} \left[ \left( \frac{2+(\gamma-1)(M_{\text{tip}} \frac{r}{R})^2}{\gamma+1} \right)^{\frac{\gamma}{\gamma-1}} - 1 \right]$ . . . . .	113
5.15	Contours of Mach number on a plane extracted at $r/R = 0.975$ (top) and radial location where the local flow becomes first supersonic as function of $\theta_{75}$ (bottom). . . . .	114
5.16	Comparison between the computed tip vortex displacements and the prescribed wake-models (top) and effect of the collective on the radial and vertical displacements of the tip vortices (bottom). . . . .	115
5.17	Vortex core size versus wake age (in degrees) at blade pitch angles $\theta_{75}$ of 5.0°, 7.0°, and 9.0°. . . . .	116
5.18	Wake visualisation of the S-76 model-scale in hover using the $\tilde{Q}$ criterion for over-set grids II (top) and III (bottom) of Table 5.6. . . . .	117
5.19	Figure of merit versus blade loading coefficient for the S-76 model rotor with 60% taper-35° swept tip at blade-tip Mach numbers of 0.6 (top) and 0.55 (bottom). . . . .	119
5.20	Figure of merit versus blade loading coefficient for the S-76 model rotor with rectangular tip at blade-tip Mach numbers of 0.65 (top) and 0.60 (bottom). . . . .	120
5.21	Figure of merit versus blade loading coefficient for the S-76 model rotor with 60% taper-35° swept-20° anhedral tip at blade-tip Mach numbers of 0.65 (top) and 0.60 (bottom). . . . .	122
5.22	Effect of the blade-tip shape on the figure of merit for the S-76 model rotor at blade-tip Mach number of 0.65. . . . .	123

5.23	Comparison of theoretical and numerical thickness, loading, and total noise distributions at the rotor-disk plane for the 1/4.71 scale S-76 rotor with rectangular, swept-taper, and anhedral tip configurations. . . . .	126
5.24	Total noise for the 1/4.71 scale S-76 rotor blade with rectangular, swept-taper, and anhedral tip configurations, as function of the radial distance at the rotor-disk plane (top) and total noise as a function of the radial distance for a set of microphones located 45° downward of the rotor-disk plane (bottom). . . . .	127
5.25	Structural model of the full-scale S-76 rotor blade, showing the distribution of the 17 elements of the CBEAM type through the spanwise of the blade. . . . .	129
5.26	Sectional area and linear mass distribution (top) and chordwise, flapwise, and torsional area moments of inertia (bottom) for the S-76 rotor blade with 60% taper-35° swept tip [36]. . . . .	130
5.27	Effect of the rigid/elastic blades (top) and Reynolds number (bottom) on the figure of merit for the S-76 rotor blade with 60% taper-35° swept tip. . . . .	133
5.28	Comparison of the radial displacements of the tip vortices as functions of the wake age (in degrees), with the prescribed wake-model of Landgrebe [19] and experimental data of Swanson [41] for two blade loading coefficients (a) $C_T/\sigma = 0.065$ and (b) $C_T/\sigma = 0.080$ . This case corresponds to the full-scale S-76 rotor with 60% taper-35° degrees swept tip and $M_{tip} = 0.605$ . . . . .	135
5.29	(a) Total noise for the full-scale S-76 rotor blade with swept-taper tip configuration, as function of the radial distance at the rotor-disk plane and (b) total noise as a function of the radial distance for a set of microphones located 45 degrees downward and upward of the rotor-disk plane. $M_{tip} = 0.60$ and $C_T/\sigma = 0.057$ were used as hovering conditions. . . . .	136
5.30	Computational domain and boundary conditions employed (top) and topology of the PSP rotor mesh (bottom). . . . .	139
5.31	Integrated blade loads for the PSP model rotor at blade-tip Mach number of 0.585. Comparisons with published CFD data using FUN3D [245] (green lines) and Star CCM+ [246] (red triangle symbols). Experimental data [242] (opened square symbols) is also shown. . . . .	142
5.32	$C_p$ profile comparisons between experimental data using the PSP technique (dashed line) and pressure tap (square symbols) [239, 240] and CFD (solid line) at radial station $r/R = 0.93$ . . . . .	144
5.33	$C_p$ profile comparisons between experimental data using the PSP technique (dashed line) and pressure tap (square symbols) [239, 240] and CFD (solid line) at radial station $r/R = 0.99$ . . . . .	145
5.34	Integrated blade loads for the PSP model rotor at blade-tip Mach number of 0.65. Comparison with published CFD data using OVERFLOW [248] (red triangle symbols) is also shown. . . . .	147
5.35	Blade sectional thrust coefficient (top) and torque coefficient (bottom) for the PSP model rotor at blade-tip Mach number of 0.65 and $\theta_{75} = 6^\circ, 9^\circ$ , and $12^\circ$ . . . . .	148
5.36	$C_p$ profile as function of the blade pitch angle for the PSP model rotor at blade-tip Mach number of 0.65. Radial stations considered: $r/R = 0.75, 0.85, 0.95$ , and 0.975. Critical $C_p^* = \frac{2}{\gamma(M_{tip} \frac{r}{R})^2} \left[ \left( \frac{2 + (\gamma - 1)(M_{tip} \frac{r}{R})^2}{\gamma + 1} \right)^{\frac{\gamma}{\gamma - 1}} - 1 \right]$ . . . . .	149

5.37	Comparison between the radial (top) and vertical (bottom) tip vortex displacements and the prescribed wake-models of Kocurek and Tangler [20] (solid lines) and Landgrebe [19] (dashed lines). This case corresponds to the PSP model rotor at blade-tip Mach number of 0.65 and $\theta_{75} = 11^\circ$ . . . . .	151
5.38	(a) Visualisation of the flowfield of the PSP rotor using the $\tilde{Q}$ -criterion and (b) contours of vorticity magnitude at $y = 0$ . Blade-tip Mach number is 0.65 and blade pitch angle $11^\circ$ . . . . .	152
6.1	Pressure Tapped Propeller (PTP) model in the transonic wind tunnel of the Aircraft Research Association [72]. . . . .	154
6.2	(a) Front and (b) iso-views of the propeller rotor with unswept tip (baseline), and geometric details of the spinner. . . . .	155
6.3	Twist and chord distributions for the JORP propeller blade. . . . .	156
6.4	Computational domain and boundary conditions employed for the propeller blade. . . . .	157
6.5	(a) Overview and (b) close-view of the C-H topology employed for the propeller blade. . . . .	157
6.6	Residual of the flow solution as function of the number of iterations. . . . .	159
6.7	$C_p$ profile comparisons between experimental data [72] and HMB3 at radial stations $r/R = 0.351, 0.423$ , and $0.495$ . Contours of Mach number is also shown in the figures. . . . .	160
6.8	$C_p$ profile comparisons between experimental data [72] and HMB3 at radial stations $r/R = 0.6, 0.7$ , and $0.8$ . Contours of Mach number is also shown in the figures. . . . .	161
6.9	$C_p$ profile comparisons between experimental data [72] and HMB3 at radial stations $r/R = 0.85, 0.9$ , and $0.95$ . Contours of Mach number is also shown in the figures. . . . .	162
7.1	Planform of the XV-15 rotor blade (top) and twist and chord distributions [250] (bottom). . . . .	165
7.2	Computational domain and boundary conditions employed (top) and detailed view of the XV-15 rotor mesh (bottom). . . . .	166
7.3	Effect of the mesh density on the figure of merit (top) and torque coefficient (bottom) for the full-scale XV-15 rotor. . . . .	169
7.4	Comparison of predicted surface pressure coefficient between HMB3 using the coarse grid and OVERFLOW2 from Kaul <i>et al.</i> [95]. . . . .	171
7.5	Blade sectional thrust coefficient (top) and torque coefficient (bottom) for the full-scale XV-15 rotor in helicopter mode. . . . .	172
7.6	Total noise in dB as function of the normalised radial distance $r/R$ at the tip-path-plane of the full-scale XV-15 rotor. . . . .	174
7.7	Propulsive propeller efficiency and torque coefficient as function of the thrust coefficient for the XV-15 rotor blade in propeller mode configuration. . . . .	176
7.8	Blade sectional thrust coefficient (top) and torque coefficient (bottom) for the full-scale XV-15 rotor in aeroplane mode. . . . .	177
7.9	Contours of surface pressure coefficient on the XV-15 rotor blade. . . . .	178
7.10	Wake visualisation of the propeller wake using $\tilde{Q}$ -criterion shaded by contours of $C_p$ at blade pitch angle of $\theta_{75} = 26^\circ$ (top) and $\theta_{75} = 28.8^\circ$ (bottom). . . . .	179

7.11	Comparison between the computed skin friction coefficient using fully turbulent and transitional solutions with the experimental data of Wadcock <i>et al.</i> [88]. Conditions employed: $M_{\text{tip}} = 0.69$ , $Re = 4.95 \times 10^6$ , and $\theta_{75} = 3^\circ$ . . . . .	181
7.12	Comparison between the computed skin friction coefficient using fully turbulent and transitional solutions with the experimental data of Wadcock <i>et al.</i> [88]. Conditions employed: $M_{\text{tip}} = 0.69$ , $Re = 4.95 \times 10^6$ , and $\theta_{75} = 10^\circ$ . . . . .	182
7.13	Surface skin friction coefficient for the fully turbulent and transition cases. . . . .	183
8.1	Set-up of the transition corridor (top) and helicopter mode (bottom) configurations with the rotor actuator disk. . . . .	187
8.2	ERICA's nacelle structured mesh domain, topology, and surface mesh detail. . . . .	189
8.3	ERICA's fuselage structured mesh domain, topology, and surface mesh detail. . . . .	190
8.4	Details of the multi-block overset arrangement of the ERICA tiltrotor in aeroplane mode configuration. Blue line=background component; purple line=fuselage component; green line=nacelle component; grey line=blade component. . . . .	191
8.5	Trimmed test conditions for the ERICA tiltrotor reported by Bruin <i>et al.</i> [251]. AC1 (Aeroplane configuration), CC4 (Transition Corridor), and HC3 (Helicopter configuration) were selected for numerical computations. . . . .	193
8.6	Cross-sections selected for comparisons between CFD and experiments [92, 91] on the fixed and tiltable wings, and fuselage of the ERICA tiltrotor for the aeroplane mode configuration. . . . .	196
8.7	$C_p$ profile comparisons between CFD and experiments [92, 91] on the fixed and tiltable wings of the ERICA tiltrotor for the aeroplane mode configuration AC1 (sections SYM-TOP, FW-A, FW-B, and FW-C). . . . .	199
8.8	$C_p$ profile comparisons between CFD and experiments [92, 91] on the fixed and tiltable wings of the ERICA tiltrotor for the aeroplane mode configuration AC1 (sections FW-D, TW-A, TW-B, and TW-C). . . . .	200
8.9	$C_p$ profile comparisons between CFD and experiments [92, 91] on the fixed and tiltable wings of the ERICA tiltrotor for the aeroplane mode configuration AC1. Results correspond to half or complete aircraft geometries with or without rotor (sections SYM-TOP, FW-C, FW-D, and TW-A). . . . .	201
8.10	$C_p$ profile comparisons between CFD and experiments [92, 91] on the fixed and tiltable wings of the ERICA tiltrotor for the aeroplane mode configuration AC1. Results correspond to half or complete aircraft geometries with or without rotor (sections TW-B and TW-C). . . . .	202
8.11	$C_p$ profile comparisons between CFD and experiments [92, 91] on the nacelle of the ERICA tiltrotor for the aeroplane mode configuration AC1. . . . .	203
8.12	$C_p$ profile comparisons between CFD and experiments [92, 91] on the fuselage of the ERICA tiltrotor for the aeroplane mode configuration AC1 (sections FU-A, FU-B, FU-C, and FU-D). . . . .	204
8.13	$C_p$ profile comparisons between CFD and experiments [92, 91] on the fuselage of the ERICA tiltrotor for the aeroplane mode configuration AC1 (sections FU-E, FU-F, FU-G, and FU-H). . . . .	205
8.14	$C_p$ profile comparisons between CFD and experiments [92, 91] on the bottom part of the fuselage of the ERICA tiltrotor for the aeroplane mode configuration AC1. . . . .	206



8.15	History of the lift and drag coefficients in the tiltable wing, nacelle, and fuselage and fixed wing of the ERICA tiltrotor. . . . .	208
8.16	Wake-visualisation of the ERICA tiltrotor in aeroplane mode configuration using $\tilde{Q}$ -criterion ( $\tilde{Q}=0.075$ ) shaded by contour of Mach numbers. Results with the FRB (top) and URAD (bottom). . . . .	209
8.17	Detailed view of the refined mesh employed for the aeroplane mode configuration with the fully resolved blade. . . . .	210
8.18	Cross-sections selected for comparisons between CFD and experiments [92, 91] on the fixed and tiltable wings, and fuselage of the ERICA tiltrotor for the transition corridor configuration. . . . .	211
8.19	$C_P$ profile comparisons between CFD and experiments [92, 91] on the fixed and tiltable wings of the ERICA tiltrotor for the transition corridor configuration (sections SYM-TOP, FW-A, FW-B, and FW-C). . . . .	213
8.20	$C_P$ profile comparisons between CFD and experiments [92, 91] on the fixed and tiltable wings of the ERICA tiltrotor for the transition corridor configuration (sections FW-D, TW-A, TW-B, and TW-C). . . . .	214
8.21	$C_P$ profile comparisons between CFD and experiments [92, 91] on the fuselage of the ERICA tiltrotor for the transition corridor configuration (sections FU-A, FU-B, FU-C, and FU-D). . . . .	215
8.22	$C_P$ profile comparisons between CFD and experiments [92, 91] on the fuselage of the ERICA tiltrotor for the transition corridor configuration (sections FU-E, FU-F, FU-G, and FU-H). . . . .	216
8.23	Wake-visualisation of the ERICA tiltrotor in transition corridor configuration using $\tilde{Q}$ -criterion ( $\tilde{Q}=0.075$ ) shaded by contour of Mach numbers. Results with the FRB (top) and URAD (bottom). . . . .	218
8.24	$C_P$ profile comparisons between CFD and experiments [91] on the fixed and tiltable wings of the ERICA tiltrotor for the aeroplane and transition corridor configurations (sections SYM-TOP, FW-A, FW-B, and FW-C). . . . .	219
8.25	$C_P$ profile comparisons between CFD and experiments [91] on the fixed and tiltable wings of the ERICA tiltrotor for the aeroplane and transition corridor configurations (sections FW-D, TW-A, TW-B, and TW-C). . . . .	220
8.26	Cross-sections selected for comparisons between CFD and experiment [91] on the fixed and tiltable wings, and fuselage of the ERICA tiltrotor for the helicopter configuration. . . . .	221
8.27	$C_P$ profile comparisons between CFD and experiment [91] on the fixed and tiltable wings of the ERICA tiltrotor for the helicopter configuration (stations SYM-TOP, FW-A, FW-B, and FW-C). . . . .	224
8.28	$C_P$ profile comparisons between CFD and experiment [91] on the fixed and tiltable wings of the ERICA tiltrotor for the helicopter configuration (sections FW-D, TW-A, TW-B, and TW-C). . . . .	225
8.29	$C_P$ profile comparisons between CFD and experiment [91] on the fuselage of the ERICA tiltrotor for the helicopter configuration (stations FU-A, FU-B, FU-C, and FU-D). . . . .	226
8.30	$C_P$ profile comparisons between CFD and experiment [91] on the fuselage of the ERICA tiltrotor for the helicopter configuration (stations FU-E, FU-F, FU-G, FU-H). . . . .	227

9.1	Flow chart of the optimisation process. Steps of the method are shown in brackets ().	234
9.2	Schematic view of the twist, chord, and sweep parametrisation for the XV-15 tiltrotor blade. . . . .	236
9.3	Modified “ideal” twist distributions for minimum power with a linear inboard approximation. . . . .	238
9.4	The conflicting tiltrotor blade twist requirements for efficient operation in two distinct flight modes and comparison with two successful tiltrotor blade designs [253, 250]. . . . .	239
9.5	Plot of baseline, ideal, and optimal blade twist distributions. . . . .	244
9.6	$C_t/C_q$ curve for the baseline blade and optimal design case HM2. . . . .	244
9.7	Vorticity contours of the blade-tip vortex for baseline blade and design case HM2 .	245
9.8	Comparison between ideal, baseline, and optimal induced velocity distribution. . .	245
9.9	Contours of Mach number at blade section $r/R = 0.95$ for the baseline blade (top) and design case HM2 (bottom). . . . .	246
9.10	Figure of merit of the baseline and optimal designs HM1 and HM2. . . . .	246
9.11	Plot of baseline and optimal blade twist distributions. . . . .	247
9.12	Comparison of (a) twist, (b) chord, (c) sweep distributions, and (d) blade shape between baseline and design case AM2. . . . .	249
9.13	Blade sectional thrust coefficient (top) and torque coefficient (bottom) for the baseline blade and design cases AM1 and AM2. . . . .	250
9.14	Contours of Mach number at blade section $r/R = 0.95$ for the baseline blade and design case HM2. . . . .	251
9.15	Comparison of baseline and optimal blades twist distributions for the multi-point cases (top) and for the single-point cases (bottom). . . . .	253
9.16	Comparison of (a) twist, (b) chord, (c) sweep distributions, and (d) blade shape between baseline and design cases HM3, AM2, and MP3. . . . .	254
9.17	Improvements of the optimal design cases HM, AM, and MP for $\eta$ (x-axis) and FoM (y-axis). . . . .	255
10.1	Computational domain and multi-block topology of the 2D grid used for the simulation of the head-on BVI, NACA-0012 aerofoil. . . . .	259
10.2	Influence of the high spatial accurately numerical schemes on the time history of the surface pressure coefficient. Head-on BVI problem, NACA-0012 aerofoil, inviscid calculations, $M_\infty=0.5$ , Scully-model with $\hat{\Gamma} = -0.283$ and $R_c = 0.018$ . . . .	262
10.3	(a) Contours of pressure and (b) $C_P$ profile comparison between CFD and experiments [261] around the RAE2822 aerofoil. Red and black lines correspond to MUSCL-2 and MUSCL-4 solutions, respectively. . . . .	263
10.4	$C_P$ profile comparisons between experiment [263] and MUSCL-2 and MUSCL-4 schemes for the full-scale 7AD rotor. . . . .	265
10.5	Wake flowfield for the 7AD rotor using $\tilde{Q}$ -criterion ( $\tilde{Q} = 0.05$ ) obtained with MUSCL-2 (top) and MUSCL-4 (bottom) schemes. . . . .	266
10.6	Vorticity field of the 7AD hovering rotor using MUSCL-2 (top) and MUSCL-4 (bottom) schemes. . . . .	267
10.7	Computational domain and boundary conditions employed (top) and detailed view of the body-fitted S-76 rotor mesh (bottom). . . . .	270

10.8	Effect of the MUSCL-2 and MUSCL-4 schemes on the figure of merit (top) and torque coefficient (bottom) for the 1/4.71 scale S-76 rotor blade. . . . .	271
10.9	Residual of the flow solution of the JORP propeller blade as function of the number of iterations for the MUSCL-2 and MUSCL-4 schemes. . . . .	275
10.10	$C_P$ profile comparisons between experimental data [72] and MUSCL-2 and MUSCL-4 schemes for the JORP propeller blade at radial stations $r/R = 0.6$ (left) and 0.9 (right). . . . .	276
10.11	Wake flowfield for the JORP propeller blade using $\tilde{Q}$ -criterion ( $\tilde{Q} = 0.1$ ) obtained with MUSCL-2 (top) and MUSCL-4 (bottom) schemes. . . . .	277
10.12	Computational domain and boundary conditions employed (top) and detailed view of the body-fitted XV-15 rotor mesh (bottom). . . . .	279
10.13	Residual of the flow solution of the XV-15 tiltrotor blade (coarse mesh) as function of the number of iterations for the MUSCL-2 and MUSCL-4 schemes. . . . .	280
10.14	Effect of the MUSCL-2 and MUSCL-4 schemes on the figure of merit (top) and torque coefficient (bottom) for the full-scale XV-15 rotor. . . . .	282
10.15	Wake flowfield for the full-scale XV-15 rotor using $\tilde{Q}$ -criterion ( $\tilde{Q}=0.05$ ). Results with the MUSCL-2 (top) and MUSCL-4 (bottom) schemes. Vortex A has wake age of $\Psi=30^\circ$ . . . . .	284
10.16	Vorticity of the vortex cores as function of the wake age in degrees obtained with the MUSCL-2 and MUSCL-4 schemes on the coarse grid. . . . .	285
10.17	Comparison between the radial (left) and vertical (right) tip vortex displacements computed with the MUSCL-2 and MUSCL-4 schemes. . . . .	285
10.18	Comparison between experimental data and predictions using MUSCL-2 and MUSCL-4 schemes for the UH-60A blade normal force and pitching moment (mean removed) at advance ratio ( $\mu=0.368$ ) at three radial stations. . . . .	288
10.19	Vorticity contours at the plane $x/R=0.5$ of the blade 1 ( $\Psi=0$ ) for the MUSCL-2 and MUSCL-4 schemes. . . . .	291
10.20	Vorticity contours at the plane $x/R=1$ of the blade 1 ( $\Psi=0$ ) for the MUSCL-2 and MUSCL-4 schemes. . . . .	291
10.21	Wake-visualisation of the UH-60A rotor in forward flight using $\tilde{Q}$ -criterion ( $\tilde{Q}=0.0007$ ). Results with the MUSCL-2 (top) and MUSCL-4 (bottom) schemes. . . . .	292
10.22	Vorticity contours at the plane $x/R=2$ of the blade 1 ( $\Psi=0$ ) for the MUSCL-2 and MUSCL-4 schemes. . . . .	292
10.23	Details of the multi-block overset arrangement of the ERICA tiltrotor in aeroplane mode configuration. Blue line=background component; purple line=fuselage component; green line=nacelle component; grey line=blade component. . . . .	294
10.24	$C_P$ profile comparisons between CFD and experiments [92, 91] on the fixed and tiltable wings of the ERICA tiltrotor for the aeroplane mode configuration AC1. . . . .	297
10.25	$C_P$ profile comparisons between CFD and experiments [92, 91] on the fuselage of the ERICA tiltrotor for the aeroplane mode configuration AC1. . . . .	298
10.26	Wake-visualisation of the ERICA tiltrotor in aeroplane mode configuration using $\tilde{Q}$ -criterion ( $\tilde{Q}=0.007$ ) shaded by contour of Mach numbers. Results with the MUSCL-2 (top) and MUSCL-4 (bottom) schemes. . . . .	299

# List of Tables

1.1	Keywords and number of hits from each database. . . . .	3
1.2	Key works on prescribed wake models. . . . .	8
1.3	Key works on free-wake models. . . . .	9
1.4	Rotor characteristics of the 1/4.71 scale S-76 rotor blade [33]. . . . .	11
1.5	Rotor characteristics of the S-76 full model rotor blade [36]. . . . .	11
1.6	Computations of the 1/4.71 scale S-76 rotor blade. . . . .	17
1.7	Flight conditions employed for the simulation of a half-span 40% Mach-scaled tiltrotor model [78]. . . . .	19
1.8	Flight conditions simulated in the DNW-LLF wind tunnel for the half-span 40% Mach-scaled model based [80]. . . . .	20
1.9	Flight conditions simulated for the TILTAERO half-span model [79]. . . . .	21
1.10	Work related to CFD on the XV-15 tiltrotor blades. . . . .	25
1.11	Component mesh size (given as million nodes [93]) for the 1:5 scale-model ERICA tiltrotor. . . . .	26
2.1	Different types of $k$ - $\omega$ turbulence models. . . . .	45
3.1	Geometric file of the acoustic solver BENP refers to as BENP1. . . . .	61
3.2	Motion file of the acoustic solver BENP refers to as BENP2 - continued. . . . .	61
3.3	Motion file of the acoustic solver BENP refers to as BENP2 - concluded. . . . .	62
3.4	Aeroelastic file of the acoustic solver BENP refers to as BENP3. . . . .	63
3.5	Aerodynamic file of the acoustic solver BENP refers to as BENP4 - continued. . . . .	63
3.6	Aerodynamic file of the acoustic solver BENP refers to as BENP4 - continued. . . . .	64
3.7	Aerodynamic file of the acoustic solver BENP refers to as BENP4 - concluded. . . . .	65
3.8	Convert grid from IcemCFD to HMB format using the <i>hexa2hmb</i> utility. . . . .	66
3.9	Test conditions for the AW-139 main rotor in forward flight. . . . .	70
4.1	Spatial accuracy of the MUSCL-scheme as function of the $k_1$ parameter. The values are only valid for regular grids. . . . .	80
5.1	Geometric properties of the B0-105 rotor [223]. . . . .	92
5.2	Meshing parameters for the B0-105 rotor using a matched grid with sharp trailing edge. . . . .	93
5.3	Test conditions of the B0-105 rotor [223]. . . . .	94
5.4	Transition position at several radial stations of the B0-105 rotor blade [223]. . . . .	94
5.5	Geometric properties of the 1/4.71 scale S-76 rotor [33]. . . . .	100
5.6	Meshing parameters for the S-76 mesh rotor blade. . . . .	101
5.7	Computational cases for the 1/4.71 scale S-76 rotor. . . . .	106

5.8	Effect of the mesh density on the $C_T/\sigma$ , $C_Q/\sigma$ , and FoM using the coarse and the medium chimera grids. . . . .	108
5.9	Comparison between experimental data [33, 34] and CFD predictions for the 1/4.71 scale S-76 rotor at blade-tip Mach number of 0.65. . . . .	109
5.10	Effect of the tip shape on the hovering endurance (in hours) for the 1/4.71 scale S-76 main rotor at blade-tip Mach number of 0.65. . . . .	124
5.11	Performance on the 1/4.71 scale S-76 rotor with rectangular, swept-taper, and anhedral shape tips at $C_T/\sigma = 0.06$ and $M_{\text{tip}} = 0.65$ . The medium chimera grid was used (grid II on Table 5.6) for this study. . . . .	125
5.12	Thickness, loading, and total noise for a microphone located $45^\circ$ downward of the rotor-disk plane ( $r/R = 3$ ) for the S-76 rotor blade with rectangular, swept-tapered, and anhedral tip configurations. . . . .	128
5.13	Eigenfrequencies of the full-scale S-76 rotor blade at nominal speed $\Omega = 296$ rpm, using NASTRAN. Comparison with the DYMORE IV and RCAS codes [236] is also shown. . . . .	130
5.14	Geometric properties of the PSP rotor [241]. . . . .	138
5.15	Meshing parameters for the PSP rotor mesh. . . . .	138
5.16	Computational cases for the PSP rotor. . . . .	140
6.1	Geometric properties of the unswept propeller blade (baseline) [72]. . . . .	155
6.2	Meshing parameters for the propeller rotor blade. . . . .	158
6.3	Flow conditions for the propeller blade. . . . .	158
7.1	Radial location of the XV-15 rotor blade aerofoils [84]. . . . .	164
7.2	Geometric properties of the full-scale XV-15 rotor [87]. . . . .	164
7.3	Meshing parameters for the XV-15 rotor mesh. . . . .	167
7.4	Flow conditions for the full-scale XV-15 tiltrotor blade. . . . .	167
7.5	Predicted and experimental peak FoM for the full-scale XV-15 rotor. . . . .	170
7.6	Predicted and experimental [88] figure of merit at blade pitch angle of $10^\circ$ . . . . .	170
7.7	Effect of the collective pitch angle on the thrust coefficient, FoM, and total noise in SPL for the full-scale XV-15 rotor. . . . .	173
7.8	Comparison of predicted $C_T$ , $C_Q$ , and FoM at $3^\circ$ and $10^\circ$ collective angles between the fully-turbulent $k-\omega$ SST and transitional $k-\omega$ SST- $\gamma$ . Conditions employed: $M_{\text{tip}} = 0.69$ and $Re = 4.95 \times 10^6$ . . . . .	184
8.1	ERICA model-scale component mesh sizes, given as million of nodes. . . . .	188
8.2	Test conditions for the selected cases [251, 252]. . . . .	192
8.3	Computational cases for the 1:5 model-scale ERICA tiltrotor. . . . .	194
8.4	Nomenclature of the stations selected for $C_P$ profile comparisons. . . . .	195
8.5	Averaged lift and drag coefficient comparisons between CFD and experiments [92, 91] for the ERICA tiltrotor. . . . .	207
9.1	Design variables along with their baseline and boundary values employed to describe the variation of the blade twist, chord, and sweep distributions. . . . .	236
9.2	Meshing parameters for the XV-15 mesh rotor blade. . . . .	240
9.3	Design cases considered in the aerodynamic optimisation study. . . . .	241
9.4	Results of single-point design cases for the helicopter mode. . . . .	242

9.5	Results of single-point design cases for the aeroplane mode. . . . .	248
9.6	Results of single and multi-point design cases. . . . .	252
10.1	List of test cases used in the validation of high-order methods. . . . .	258
10.2	Predictions and experimental suction peak $C_p$ for the full-scale 7AD rotor. . . . .	264
10.3	Geometric properties of the 1/4.71 scale S-76 rotor [33]. . . . .	268
10.4	Mesh size in million cells for the S-76 rotor mesh. . . . .	269
10.5	Computational run-time for the S-76 rotor blade with MUSCL-2 and MUSCL-4 schemes on the coarse and medium meshes. . . . .	273
10.6	Mesh size in million cells for the JORP rotor mesh. . . . .	274
10.7	Flow conditions for the propeller blade. . . . .	274
10.8	Computational run-time for the JORP propeller blade with MUSCL-2 and MUSCL-4 schemes. . . . .	276
10.9	Geometric properties of the full-scale XV-15 rotor [87]. . . . .	278
10.10	Mesh size in million cells for the XV-15 rotor mesh. . . . .	280
10.11	Predicted and experimental [88, 98] figure of merit at blade pitch angle of $10^\circ$ . . . .	281
10.12	Computational run-time for the XV-15 tiltrotor blade with MUSCL-2 and MUSCL-4 schemes on the coarse mesh. . . . .	286
10.13	Geometric properties of the UH-60A rotor [33, 265, 266]. . . . .	286
10.14	Trim state for the UH-60A forward flight case using MUSCL-2 and MUSCL-4 schemes. . . . .	287
10.15	Comparison of core maximum vorticity for the UH-60A forward flight case using MUSCL-2 and MUSCL-4 schemes. . . . .	289
10.16	Computational run-time for the UH-60A rotor in forward flight with MUSCL-2 and MUSCL-4 schemes on the same mesh. . . . .	290
10.17	ERICA model-scale component mesh sizes, given as million nodes. . . . .	293
10.18	Test conditions for the aeroplane mode AC1 [251, 252]. . . . .	295
10.19	Nomenclature of the stations selected for $C_p$ profile comparisons. . . . .	295
10.20	Computational run-time for the ERICA tiltrotor with MUSCL-2 and MUSCL-4 schemes on the same mesh. . . . .	300

# Nomenclature

## Latin symbols

$a$	lift slope coefficient
$a_\infty$	freestream speed of sound
$A$	rotor-disk area
$AR$	blade aspect ratio, $R/c_{\text{ref}}$
$A_\varepsilon$	aerofoil cross sectional area
$B$	tip-loss factor
$c$	blade chord
$c_e$	equivalent blade chord, $c_e = 3 \int_0^R c(r/R) (r/R)^2 d(r/R)$
$c_p$	heat capacity at constant pressure
$c_{\text{ref}}$	reference blade chord
$C_q$	blade sectional torque coefficient, $C_q = \frac{dq/dr}{1/2\rho_\infty cR(\Omega r)^2}$
$C_t$	blade sectional thrust coefficient, $C_t = \frac{dt/dr}{1/2\rho_\infty c(\Omega r)^2}$
$C_D$	drag coefficient, $\frac{D}{1/2\rho_\infty V_\infty^2 S_{\text{ref}}}$
$C_{D0}$	overall profile drag coefficient
$C_L$	lift coefficient, $\frac{L}{1/2\rho_\infty V_\infty^2 S_{\text{ref}}}$
$C_P$	blade sectional pressure coefficient, $C_P = \frac{P - P_\infty}{1/2\rho_\infty(\Omega r)^2}$
$C_P^*$	critical pressure coefficient
$C_Q$	rotor torque coefficient, $C_Q = \frac{Q}{\rho_\infty(\Omega R)^2 \pi R^3}$
$\bar{C}_Q$	baseline rotor torque coefficient
$C_Q/\sigma$	blade torque coefficient, torque coefficient divided by rotor solidity
$C_T$	rotor thrust coefficient, $C_T = \frac{T}{\rho_\infty(\Omega R)^2 \pi R^2}$
$\bar{C}_T$	baseline rotor thrust coefficient
$C_T/\sigma$	blade loading coefficient, thrust coefficient divided by rotor solidity
$D$	drag measured by main balance
$E$	hovering endurance
$E$	total energy
$f$	integration surface to evaluate thickness and loading noise
FoM	figure of merit, $\text{FoM} = \frac{C_T^{3/2}}{\sqrt{2}C_Q}$

$F_\varepsilon$	aerofoil shape factor, $F_\varepsilon = A_\varepsilon/S_{\text{rot}}$
$F_H$	distance factor for the thickness noise, $F_H = R/r_H$
$g, h$	constraint functions
$\mathbf{G}_i$	inviscid fluxes
$\mathbf{G}_v$	viscous fluxes
$H$	total enthalpy
$I$	cost function
$I_c$	chordwise stiffness
$I_f$	beamwise stiffness
$J$	torsional stiffness
$k$	turbulent kinetic energy
$k_1, k_2$	MUSCL-4 scheme parameters
$k_i$	induced power factor
$K_{m,n}$	binomial coefficient
$L$	lift measured by main balance
$L_{\text{ref}}$	reference length
$L_M$	loading factor
$M_{\text{tip}}$	blade-tip Mach number, $M_{\text{tip}} = \frac{V_{\text{tip}}}{a_\infty}$
$M_r$	Mach number of the source in the radiation direction
$\mathbf{n}$	outward pointing unit normal vector
$N_b$	number of blades
$P$	pressure or rotor power
$Pr$	Prandtl number
$Pr_t$	turbulent Prandtl number
$P'_L$	loading noise
$P'_T$	thickness noise
$P_\infty$	freestream pressure
$q_j$	heat flux vector
$Q$	rotor torque
$\tilde{Q}$	$Q$ -criterion
$R$	rotor radius
$\text{Re}$	Reynolds number, $\text{Re} = V_{\text{ref}}c_{\text{ref}}/\nu_\infty$
$\text{Re}_{\theta_t}$	momentum thickness Reynolds number
$\mathbf{R}$	flow equation residual vector
$R_c$	vortex core radius
$r$	radial coordinate along the blade span
$\hat{r}$	normalised radial coordinate along the blade span, $\hat{r} = r/R$
$\vec{\mathbf{r}}_{fj}$	vector of distance between the cell face $j + 1/2$ and the cell-centre volume $j$
$\vec{\mathbf{r}}_{fj+1}$	vector of distance between the cell face $j + 1/2$ and the cell-centre volume $j + 1$
$r_H$	distance from an acoustic probe to the rotor hub
$S_{\text{ref}}$	reference area
$S_{\text{rot}}$	rotor-disk area



$S_{ij}$	symmetric part of the velocity gradient
$t$	blade sectional aerofoil thickness
$T$	rotor thrust
$T_M$	thickness factor
$u$	velocity in x direction
$v$	velocity in y direction
$v_n$	local normal velocity of the source surface
$v_i$	induced velocity
$V$	cell volume
$V_{\text{ref}}$	reference velocity
$V_{\text{tip}}$	blade-tip speed, $V_{\text{tip}} = \Omega R$
$V_{\infty}$	freestream velocity
$w$	weight factor in multi-point objective function or velocity in z direction
$\mathbf{W}$	vector of conservative variables
$X _S$	point vector
$(\cdot)''$	fluctuating quantity
$\hat{(\cdot)}$	Favre average
$\overline{(\cdot)}$	time-average mean
$(\cdot)$	dimensionless variable

## Greek symbols

$\alpha$	design variables
$\beta$	coning angle
$\gamma$	specific heat ratio, intermittency factor or Lock number
$\hat{\Gamma}$	non-dimensionalised vortex strength
$\delta$	angle of the vortex cylinder slope
$\delta_{ij}$	Kronecker delta function
$\delta_{\text{FU}}$	fuselage angle of attack
$\delta_{\text{NAC}}$	nacelle angle of attack
$\delta_{\text{TW}}$	tiltable wing angle of attack
$\Delta P$	jump of pressure across the disk plane
$\Delta P^*$	non-dimensional $\Delta P$ across the disk plane
$\varepsilon$	turbulent energy dissipation rate
$\eta$	propeller propulsive efficiency, $\eta = \frac{C_T V_{\infty}}{C_Q V_{\text{tip}}}$ or Lagrangian variable of a point on the moving surface $f=0$
$\theta$	local angle between the normal to the surface and the radiation direction at the emission time
$\theta_{75}$	blade pitch angle at $r/R = 0.75$
$\Theta$	local blade twist angle
$\Theta_{\text{twist}}^{\text{IP}}$	local ideal blade twist angle
$\Theta_{\text{nom}}$	nominal twist
$\lambda_i$	downwash, $\lambda_i = \frac{v_i}{V_{\text{tip}}}$
$\lambda$	adjoint variables
$\mu$	advance ratio or dynamic viscosity
$\mu_t$	dynamic eddy-viscosity

$v_\infty$	freestream kinematic viscosity
$\xi$	vorticity
$\rho_\infty$	freestream density
$\rho$	density
$\sigma$	rotor solidity, $\sigma = \frac{N_b c_{\text{ref}} R}{\pi R^2}$
$\sigma_{ij}$	viscous stress tensor
$\tau_{ij}$	Reynolds stress tensor
$\tau$	retarded time
$\Phi$	limiter function
$\Psi$	azimuth angle
$\omega$	specific dissipation frequency of turbulence
$\Omega$	rotor rotational speed
$\Omega_{ij}$	antisymmetric part of the velocity gradient

## Subscripts

am	aeroplane mode
hm	helicopter mode
$i, j, k$	mesh cell indices
mp	multi-point
nac	nacelle
nom	nominal value
ref	reference value
ret	retarded time
$S$	aerodynamic surface
tilt	tiltable wing
tip	blade-tip value
$\infty$	freestream value

## Superscripts

IP	induced power
L	left side
R	right side
*	sonic condition

## Acronyms

AC	Aeroplane Configuration
ADD	Aviation Development Directorate
ADT	Actuator Disk Theory
ADYN	Advanced European tiltrotor DYnamics and Noise
AIAA	American Institute of Aeronautics and Astronautics
ALE	Arbitrary Lagrangian Eulerian
ANN	Artificial Neural Network
AHD	Airbus Helicopters Deutschland

AoA	Angle of Attack
ARA	Aircraft Research Association
ATB	Advanced Technology Blade
BEM	Boundary Element Method
BET	Blade Element Theory
BEMT	Blade Element Momentum Theory
BILU	Block Incomplete Lower-Upper
BMTR	Basic Model Test Ring
BVI	Blade-Vortex Interaction
BVWT	Boeing Vertical Wind Tunnel
BWI	Blade-Wake Interaction
CAA	Computational AeroAcoustics
CAMRAD	Comprehensive Analytical Model of Rotorcraft Aerodynamics and Dynamics
CC	Corridor Configuration
CHARM	Comprehensive Hierarchical Aeromechanics Rotorcraft Model
CFD	Computational Fluid Dynamics
CFL	Courant-Friedrichs-Lewy condition
CPU	Central Processing Unit
CREATE	Computational Research and Engineering Acquisition Tools and Environments
CRWENO	Compact-Reconstruction Weighted Essentially Non-Oscillatory
CSD	Computational Structural Dynamics
CVC	Constant Vorticity Contour
DAP	Dowty Aerospace Propellers
DART	Development of an Advanced Rotor for Tiltrotor
DES	Detached Eddy Simulation
DDES	Delay Detached Eddy Simulation
DLR	German Aerospace Centre
DNW-LLF	German-Dutch Wind Tunnels Large Low-Speed Facility
DoD	Department of Defense
DRP	Dispersion-Relation-Preserving
ELSA	Ensemble Logiciel pour la Simulation en Aerodynamique
EHPIC	Evaluation of Hover Performance using Influence Coefficients
EIPM	Extended linear Interior Penalty function Method
ENO	Essentially Non-Oscillatory
ERICA	Enhanced Rotorcraft Innovation Concept Achievement
EU	European Union
FD	Finite Difference
FGMRES-DR	Flexible Generalised Minimum Residual with Deflated Restarting
FRB	Fully Resolved Blade
FV	Finite Volume
FW-H	Ffowcs Williams-Hawkings
F-WM	Free-Wake Method
GA	Genetic Algorithm
GCG	Generalised Conjugate Gradient
HC	Helicopter Configuration
HELIOS	HELicopter Overset Simulations

HFWH	Helicopter Ffowcs Williams-Hawkings
HMB	Helicopter Multi-Block Solver
HSI	High-Speed Impulsive
IDM	Inverse Distance Method
IDW	Inverse Distance Weighting
IGE	In-Ground Effect
IPF	Induced Power Factor
ISA	International Standard Atmosphere
KAIST	Korea Advanced Institute of Science and Technology
LBL-VS	Laminar Boundary Layer-Vortex Shedding
LCTM	Local Correlation-based Transition Model
LES	Large Eddy Simulation
LM	Linear Method
LS	Lifting Surface
MUSCL	Monotone Upstream-Centred Schemes for Conservation Laws
NACA	National Advisory Committee for Aeronautics
NASA	National Aeronautics and Space Administration
NFAC	NASA Ames National Full-Scale Aerodynamics Complex
NICETRIP	Novel Innovative Competitive Effective Tilt Rotor Integrated Project
NLR	Netherlands Aerospace Centre
NSGA	Non-dominated Sorting Genetic Algorithm
NTRS	NASA Technical Report Server
NURAD	Non-Uniform Rotor Actuator Disk
PIV	Particle Image Velocimetry
OARF	Outdoor Aeronautical Research Facility
OGE	Out-of-Ground Effect
ONERA	Office National d'Etudes et de Recherches Aerospatiales
OVERFLOW	OVERset grid FLOW
OVERTURNS	OVERset Transonic Unsteady Rotor Navier-Stokes
RK	Runge-Kutta
PoliMi	Politecnico di Milano
PSP	Pressure Sensitive Paint
PTP	Pressure Tapped Propeller
RBAR	Rigid BAR
ROBIN	ROtor BOdy Interaction
ROSITA	ROtorcraft Software ITAlly
RTC	Rotor Test Cell
SA	Spalart-Allmaras
SAMA	Surrogate-Assisted Memetic Algorithm
SAS	Scale Adaptive Simulation
SDM	Stall Delay Model
SFC	Specific Fuel Consumption
SLSQP	Least-Square Sequential Quadratic Programming
SPL	Sound Pressure Level
SST	Shear-Stress Transport
ST	Swept-Taper
STA	Swept-Taper-Anhedral

STVD	Symmetric Total Variation Diminishing
TBL	Turbulence Boundary Layer
TILTAERO	TILTrotor interactional AEROdynamics
TRAM	Tilt-Rotor Aeroacoustics Model
TSB	Technology Strategy Board
TVD	Total Variation Diminishing
TW	Tiltable Wing
TWT	Transonic Wind Tunnel
UofG	University of Glasgow
URAD	Uniform Rotor Actuator Disk
(U)RANS	(Unsteady) Reynolds Averaged Navier-Stokes
UTRC	United Technology Research Center
VLN	Vertical Lift Network
VTM	Vorticity Transport Model
V/STOL	Vertical and/or Short Take-off and Landing
WoK	Web of Knowledge
WENO	Weighted Essentially Non-Oscillatory
WSL	Wake Shear Layers

# Chapter 1

## Introduction

### 1.1 Motivation

Over the past 50 years, the scientific community has attempted to answer some complex questions about the design of tiltrotor aircraft. This new type of vehicle is seen as an alternative to helicopters, and is designed to combine vertical take-off/landing capability with high speed cruise. This leads to many compromises in the design, since tiltrotor blades have to operate efficiently in hover and propeller modes. In addition, interactional aerodynamics can be very important for tiltrotor aircraft, and should be studied and researched to improve their safety and performance. Not much data for tiltrotors is currently available, and so far, only two tiltrotor aircraft have been successfully built, the XV-15 and the Bell Boeing V-22 Osprey. Until recently, no European manufactures were involved in tiltrotor design. In 1998, AugustaWestland and Bell Helicopters formed a partnership to develop a new civil tiltrotor aircraft. The first prototype was BA609, and it evolved into AW609. Figure 1.1 shows the XV-15, V-22 Osprey, and AW609 tiltrotors.

This work employs CFD for the study of tiltrotors and where possible wind tunnel data is used for validation.



(a) XV-15 tiltrotor.



(b) V-22 Osprey tiltrotor.



(c) AW609 tiltrotor.

Figure 1.1: (a) XV-15 (b) V-22 Osprey and (c) AW609 tiltrotors.

## 1.2 Literature Survey

This section presents the literature survey carried out for this dissertation. The objective of the literature survey is to find publications related to CFD for tiltrotor aircraft, as well as, wind tunnel data for validation of CFD methods. First, the mechanism of the literature survey is presented with four databases used, including the Web of Knowledge (WoK) [1], Scopus [2], National Aeronautics and Space Administration (NASA) Technical Report Server (NTRS) [3], and the American Institute of Aeronautics and Astronautics (AIAA) [4]. Table 1.1 shows the keywords used for the survey, as well the number of findings from each database. Large numbers of papers on aerodynamics, aeroacoustics, and turbulence models were found. On the other hand, the tiltrotor keywords resulted in a limited number of works.

Table 1.1: Keywords and number of hits from each database.

Keywords	Number of hits			
	WoK [1]	Scopus [2]	NTRS [3]	AIAA [4]
Aerodynamics	39,448	20,985	17,313	79,279
Aerodynamic interactions	567	3,192	3,842	21,647
Aero-acoustics	1,024	223	1,981	4,299
Turbulence model	15,754	16,278	6,004	41,749
Turbulence model and CFD	2,855	1,315	1,509	14,009
Tiltrotor	173	215	278	603
Tiltrotor and wind tunnel	27	10	150	365
Tiltrotor and CFD	9	-	90	211
Tiltrotor XV-15	3	1	84	158
Tiltrotor V-22	31	20	103	124
Tiltrotor BA609	3	7	17	20
Tiltrotor AW609	-	3	4	5

### 1.2.1 Validation Data Related to Helicopter Rotors

#### Modelling Rotors

Tremendous effort and significant progress have been made in accurately predicting the efficiency of hovering rotors using Computational Fluid Dynamics (CFD) [5, 6, 7, 8, 9]. For helicopters in hover, the Figure of Merit (FoM) is used as an indicator of the rotor efficiency, because it represents



the ratio between the ideal absorbed power in hovering predicted by the momentum theory and the actual absorbed power [10]:

$$\text{FoM} = \frac{\text{Ideal power required to hover}}{\text{Actual power required to hover}} < 1. \quad (1.1)$$

The hover condition is a very important design point due to its high power consumption. Moreover, the prediction of the FoM within 0.1 counts (1 count of FoM is 0.01) along with the strength and position of the vortex core is still a challenge [11]. As an example, an averaged error of 2.4% in FoM was reported by Yamauchi *et al.* [12] when CFD predictions of NASA were compared with measured data.

The flowfield around a rotor in hover is dominated by helical vortex filaments that trail from each of the blade tips, and by wake sheets trailed behind the trailing edge of the blade [10]. Both vortex wake systems interact with the blades and remain beneath the rotor-disk plane, resulting in significant changes to the angle of attack (AoA) seen by the rotor sections. The schematic of Figure 1.2 shows the three-dimensional wake structure generated by a single rotor blade, based on smoke visualisation [13]. In these experiments, Gray [13, 14] observed that due to the induced downwash generated by the distribution of loads over the blade, the trailing edge Wake Shear Layers (WSL) convect downward faster than the tip-vortex structures.

To ensure realistic predictions of the wake-induced effects, and consequently accurate numerical prediction of the FoM, the radial and vertical displacements, and the size of the vortex core ( $\sim 0.0025 R$ ) [15] should be resolved, at least for the first and second wake blade passages [9]. In this regard, various methodologies and approaches have been developed to account for the rotor wake and therefore provide a more realist representation of hovering rotor flows. The simplest model is based on one-dimensional momentum theory known as Actuator Disk Theory (ADT) developed by W. Froude in 1878, and can predict rotor performance in hover and climb. It accounts for the conservation of mass, momentum, and energy, without consideration of the details of the flow around the blades. It also has a number of simplifying assumptions:

- The rotor is modelled as an actuator disk, adding momentum and energy to the flow equations.

- One-dimensional, incompressible, steady, and inviscid flow.
- No velocity jump across the rotor-disk plane.
- No swirl flow effects.

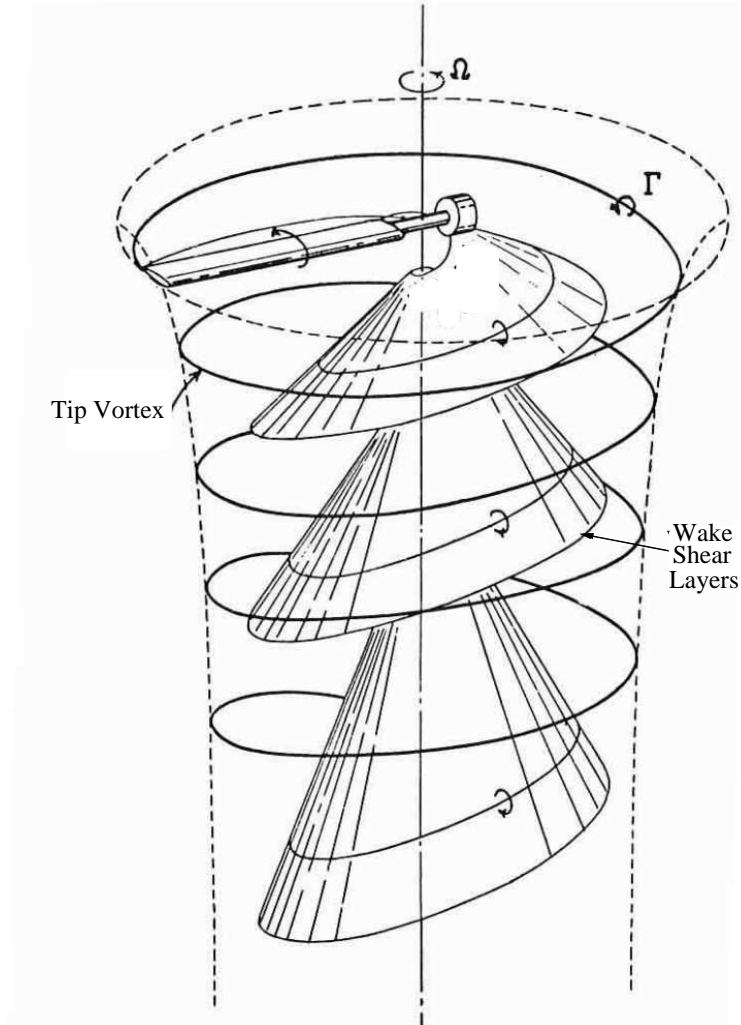


Figure 1.2: Schematic of the three-dimensional wake structures of a rotor in hover. Adapted from [16].

Figure 1.3 shows a schematic of the actuator disk concept in hover, where a fluid particle is convected downstream and generating a rotor thrust  $T = \frac{1}{2}\rho V_2^2 A$  across the rotor-disk plane of area  $A$ . The far wake velocity  $V_2$  is twice the induced velocity at the rotor-disk plane, so the stream tube contracts. This theory gives an expression for induced velocity  $v_i = \sqrt{\frac{T}{2\rho A}}$  at the rotor-disk plane and ideal power  $P = T v_i = T \sqrt{\frac{T}{2\rho A}}$  consumed by a rotor. This methodology is sufficient to size a

rotor (e.g. rotor-disk area, radius of the rotor) when empty and gross weight are known. However, this theory cannot be used during the design process of rotor since it does not account for number of blades, aerofoil characteristics, blade twist distribution and planform of the blade.

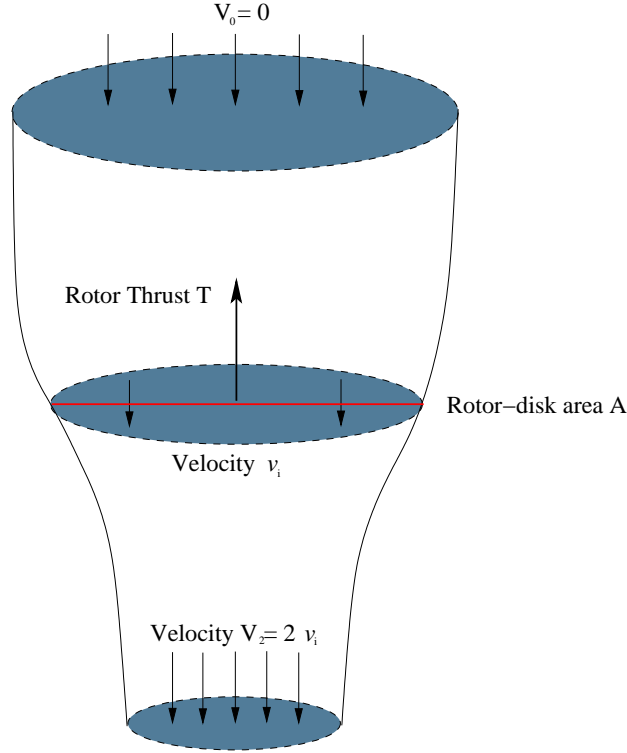


Figure 1.3: Schematic of the actuator disk concept in hover.

Blade Element Theory (BET) [17] represents a more advanced approach and overcomes some of the drawbacks of ADT. The rotor plane is divided into a number of strips  $dr$ , with each behaving in a 2D way independently of the rest. Moreover, the lift generated by each strip and the power consumed can be computed using 2D aerodynamics. If we define the ideal blade twist as the one providing uniform induced flow over the disk (independent of  $r$ ), the total thrust and rotor power can be obtained integrating along the blade:

$$T = N_b \int_0^R 4\pi\rho v_i^2 r dr, \quad (1.2)$$

$$P = \underbrace{N_b \int_0^R \Omega r dD}_{\text{Profile power}} + \underbrace{N_b \int_0^R v_i dL}_{\text{Induced power}}. \quad (1.3)$$

where  $N_b$  is the number of blades,  $\Omega$  is the rotor rotational speed,  $R$  is the rotor radius, and  $dD$  and  $dL$  are the sectional drag and lift forces. The first and second terms of the rotor power are the profile and induced power, respectively. Assuming constant chord  $c$ , constant drag coefficient  $C_{D0}$ , and uniform induced velocity  $v_i$ , the rotor power is written:

$$P = \underbrace{\frac{1}{8}\rho(\Omega R)^3 N_b c R C_{D0}}_{\text{Profile power}} + \underbrace{\frac{T^{3/2}}{\sqrt{2\rho\pi R^2}}}_{\text{Induced power}}. \quad (1.4)$$

It is seen that profile power is controlled by the blade-tip speed  $\Omega R$ , blade area  $N_b c R$ , and drag coefficient  $C_{D0}$ . The induced power, however, is dominated by the rotor-disk area  $\pi R^2$ . To account for tip effects, the predicted power needs to be corrected for these losses with a factor  $k_i$  known as a Induced Power Factor (IPF). The expression for the FoM according to BET, then is given in Equation 1.5:

$$\text{FoM} = \frac{\text{Ideal power}}{\text{Profile power} + \text{Induced power}} = \frac{P_{\text{ideal}}}{P_0 + k_i P_{\text{ideal}}} = \frac{\frac{C_T^{3/2}}{\sqrt{2}}}{\sigma \frac{C_{D0}}{8} + k_i \frac{C_T^{3/2}}{\sqrt{2}}}. \quad (1.5)$$

where  $P_0 = \sigma \frac{C_{D0}}{8}$  and  $k_i \frac{C_T^{3/2}}{\sqrt{2}}$  represent the profile and induced drag coefficients, respectively. The rotor solidity is represented by  $\sigma = \frac{N_b c R}{\pi R^2}$  and is the total blade area over the rotor-disk area. In the literature, typical values of induced power factor  $k_i$  fall in the range of [1.1 - 1.15] [17] and for the profile drag, a coefficient of  $C_{D0} = 0.01$  [18] is used. This method does not account for non-ideal flow, viscous losses, and swirl flow loss effects. Hence, the vortex wake of the rotor is not accurately represented in this basic model either.

Prescribed and free-wake approaches include a detailed vortex wake with root and tip vortices. Prescribed wake models use empirical and analytical approximations based on experimental studies for the circulation, size and position of the vortical structures of the wakes. Then, the Biot-Savart law is used to calculate the induced velocity field at any point of interest. Key works on prescribed wake models are summarised in Table 1.2.

Figure 1.4 shows a comparison of the wake geometry for a two-bladed, untwisted and untapered rotor with NACA 230-12 sections between prescribed-wake models [19, 20] and CFD results extracted from [21]. It can be seen that good agreement is found when using the prescribed models.

However, this technique is limited to rotors with similar planform and features such as the rotors used in the cited experiments.

Table 1.2: Key works on prescribed wake models.

Author	Year	Theme	Technique Used
Gray [13]	1955	Rotor wake geometry	Smoke flow visualisation
Jenney <i>et al.</i> [22]	1968	Rotor wake geometry	Smoke flow visualisation
Landgrebe [19]	1972	Rotor wake geometry	Smoke flow visualisation
Kocurek and Tangler [20]	1977	Rotor wake geometry	Schlieren flow visualisation
Egolf and Landgrebe [23]	1983	Wake geometry in forward flight	Fourier series of a wake shape

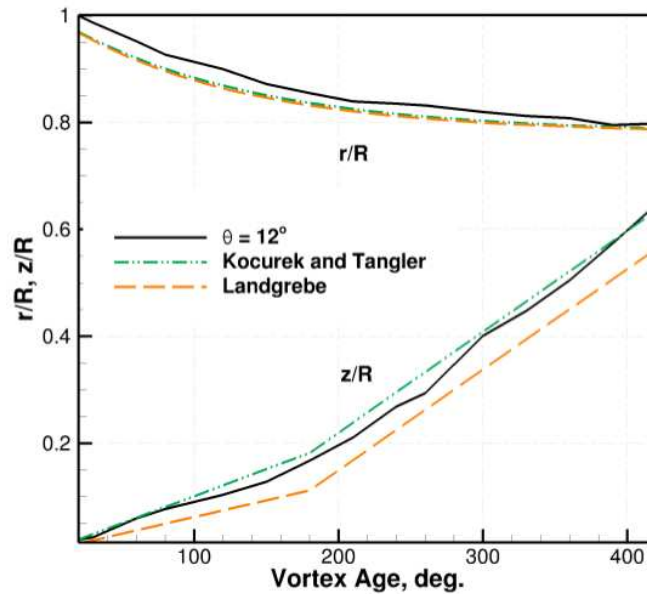


Figure 1.4: Comparison of the wake geometry for a 2-bladed, untwisted and untapered rotor with NACA 230-12 sections at blade pitch angle of 12 degrees. Adapted from [21].

Free wake models were initially developed by Landgrebe [24], Clark and Leiper [25], Scully [26] and later by Bliss *et al.* [27], Quackenbush *et al.* [28], and others. They use empirical relations for the strength and core size of the vortices, but better models for their positions. Prescribed wake models produce results with less computing power, but are restricted to set wake geometries. Free-wake models require larger computing power, but they can adapt to the environment they are in. Key works on free-wake models are summarised in Table 1.3.

Table 1.3: Key works on free-wake models.

Author	Year	Theme	Technique Used
Landgrebe [24]	1969	Distorted rotor wake	Biot-Savart law
Clark and Leiper [25]	1970	Distorted rotor wake	Iterative procedure
Scully [26]	1975	Rotor wake geometry	Lifting-surface theory
Bliss <i>et al.</i> [27]	1987	Accuracy of the model	Curved vortex elements
Quackenbush <i>et al.</i> [28]	1989	Rotor wake geometry	Influence coefficients

## CFD Efforts

High fidelity approaches based on numerical simulation of the Navier-Stokes equations are being gradually employed partly due to the availability of low-cost parallel computer clusters, reducing the high computational time associated with these approaches. Strawn *et al.* [29] highlights the CFD research and development over the past 30-years on rotorcraft. One interesting aspect of CFD is that it can provide engineers with integrated loads on the blades as well as the details of the flowfield around any rotor. On the other hand, traditional design methods stem from the classic aerodynamic approach that separates contributions to the blade drag in profile, induced, and wave components. CFD can provide the pressure or viscous contributions instead. It would, however be instructive if with appropriate post-processing of the CFD data, engineers could obtain quantities like wave drag or profile drag. This issue is addressed by Verley [30] who proposed a set of integrations on closed surfaces of the CFD solution as the way to compute the drag contributions. For example, integrating along a surface that surrounds a shock wave can lead to the wave drag. Examples were presented for well-known helicopter rotor cases like the ONERA (Office National d'Etudes et de Recherches Aérospatiales) 7AD case.

Recently, the AIAA Applied Aerodynamics Rotor Simulations Working Group [31] was established in 2014 and comprised members across Research Centres, Academia, Industries, Universities, and Departments of Defense (DoD) with the following aims:

- Evaluate the current state-of-the-art prediction performance in hover using different CFD solvers and methods for the same blade geometry.
- Assessment of the level of accuracy of current CFD solvers in computing FoM.

- Study fundamental physics of the rotor wake system.
- Identify and address wake instability issue observed in the results of some CFD solvers [32].

The S-76 rotor blade was selected for assessment because of its public availability and data sets with various tip shapes [33, 34]. Moreover, the effects of the blade-tip Mach number, and of the model vs. full-scale [35, 36] Reynolds numbers  $Re$ , could be evaluated.

### **S-76 Rotor**

During the 1980s, a comprehensive experimental study of four model-scale rotors (UH-60A, S-76, High Solidity, and H-34) was conducted by Balch *et al.* [37, 38], in hover. The study was born out of the need for the characterisation of the aerodynamic interference associated with main and tail rotors, and fuselage, with the aim to improve hovering performance. Further work by Balch and Lombardi [33, 34] compared advanced tip designs, in hover, for the UH-60A and S-76 rotor blade geometries. The S-76 rotor blade was 1/4.71 scale of the full-size, meanwhile in Balch [37, 38] a 1/5 scale was used. The effect of using different tip configurations (rectangular, swept, tapered, swept-tapered, and swept-tapered with anhedral, see Figure 1.5) on the performance of the rotors was experimentally investigated in-ground effect (IGE) and out-of-ground effect (OGE) conditions. This study was conducted at the Sikorsky model hover test facility using the Basic Model Test Ring (BMTR) as shown in Figure 1.6, and was divided in two phases. Firstly, the isolated main rotor was investigated using all tip configurations. The second phase focused on four cases, with two tips each, tested on two main rotors, operating with tractor and pusher tail rotors.

At the same time, during the development phase of the S-76 rotor system in 1980, a full-scale S-76 helicopter rotor was tested in the NASA Ames 40- by 80- foot wind tunnel by Johnson [39]. Airloads and noise generated by four tip rotor geometries (rectangular, tapered, swept, and swept-tapered) were measured over a low to medium advance ratio range from 0.075 to 0.40. Three years later, Jepson [40] carried out flight model-scale tests (1/5 scale) and full-scale test. Wind tunnel data was acquired in the United Technology Research Center's (UTRC) 18 foot large subsonic wind tunnel and NASA Ames 40- by 80- foot wind tunnel for model and full-scale, respectively.

In all these works, no data was acquired for full-scale rotors in hover. An additional wind tunnel test was conducted by Shinoda [35, 36] in 1993, where the main goal was to measure the performance and noise characteristics of the full-scale rotor inside the 0 - 100 knots velocity range. For this study, the NASA Ames 80- by 120- foot wind tunnel was employed, where hover and forward flight rotor performance data was recorded for a range of rotor shaft angles and thrust coefficients. Flow visualisation studies of the rotor wake for the full-scale S-76 helicopter rotor in hover, low-speed forward flight, and descent operating conditions were also carried out by Swanson [41] using the shadowgraph flow visualisation technique. Their study was conducted using the same hover facility, and the radial position of the wake geometry was measured. The main characteristics of the model and full-scale rotor blades are summarised in Tables 1.4 and 1.5.

Table 1.4: Rotor characteristics of the 1/4.71 scale S-76 rotor blade [33].

Parameter	Value
Number of blades, $N_b$	4
Rotor radius, $R$	56.04 inches
Rotor blade chord, $c_{\text{ref}}$	3.1 inches
Aspect ratio, $R/c_{\text{ref}}$	18.07
Rotor solidity, $\sigma$	0.0704
Non-linear twist, $\Theta$	-10°

Table 1.5: Rotor characteristics of the S-76 full model rotor blade [36].

Parameter	Value
Number of blades, $N_b$	4
Rotor radius, $R$	264 inches
Rotor blade chord, $c_{\text{ref}}$	15.5 inches
Aspect ratio, $R/c_{\text{ref}}$	17.03
Rotor solidity, $\sigma$	0.0748
Non-linear twist, $\Theta$	-10°
Flapping hinge offset	3.70% $R$
Lock No., $\gamma$	11.6

Several authors have used this experimental data to validate computational methods and explore the capability of CFD solvers. The first AIAA Applied Aerodynamics Rotor Simulations Working Group session in 2014 focussed on the 1/4.71 scale S-76 rotor blade with 60% taper-35° degrees swept tip (see Figure 1.5). A blade-tip Mach number of 0.65 was selected for comparison



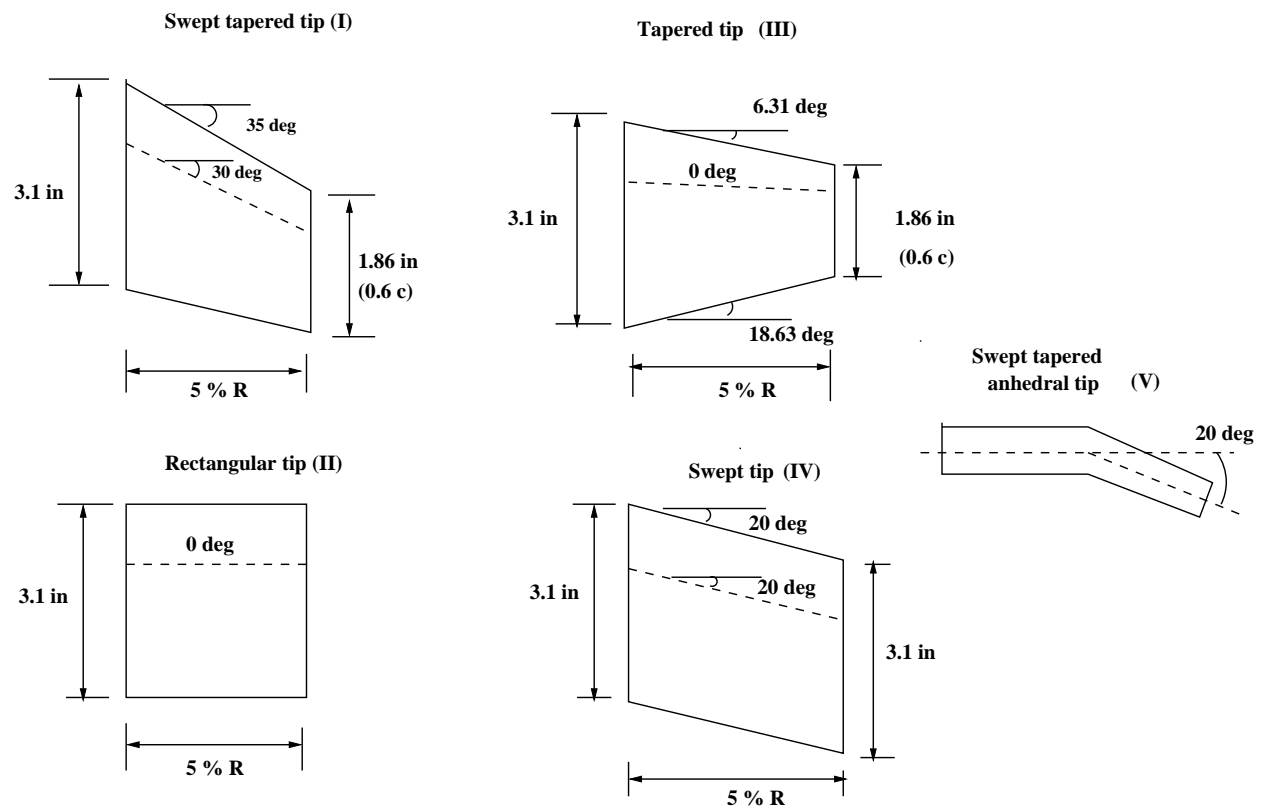


Figure 1.5: Tip shapes of the 1/4.71 model-scale S-76 rotor. Adopted from Balch and Lombardi [33].

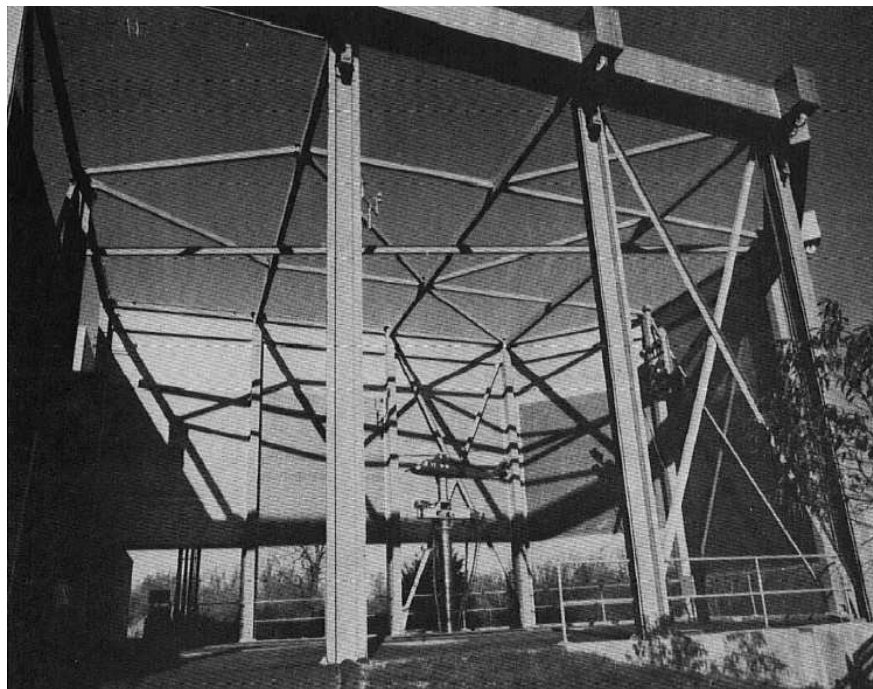


Figure 1.6: Model test cell hover facility with the BMTR for the 1/4.71 model-scale S-76 rotor [33].

with experimental data. Hariharan *et al.* [31] provided the S-76 geometry to all the participants including; Korea Advanced Institute of Science and Technology (KAIST), University of Glasgow, University of Toledo, University of Maryland, Army Aeroflight Dynamics Directorate, Boeing Philadelphia, Boeing Mesa, Sikorsky, and Georgia Tech. Two different blade surface grids were provided to all participants through the rotor simulation working group share-point facility [42]. The first planforms were modelled by Prof. Sankar and this team and contain a sharp blunt trailing edge. Prof. George Barakos and his team generated the second set with a modified blunt trailing edge (see Figure 1.7). The sensitivity of the FoM with both surface grids was assessed [43], showing good agreement between them.

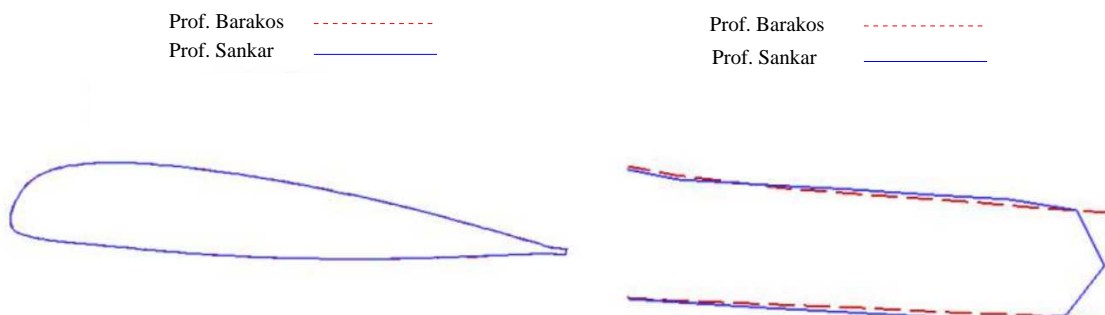


Figure 1.7: Aerofoil trailing edge of the S-76 rotor blade generated by Prof. Sankar and Barakos [42]. Adopted from [43].

Jung *et al.* [44] used an unstructured mixed mesh method to compute the 1/4.71 scale S-76 rotor with a swept-tapered tip at a blade-tip Mach number of 0.65. It includes tetrahedral/prismatic mesh in the near-body region and adaptive Cartesian mesh in the off-body region where a 7th-order accurate Weighted Essentially Non-Oscillatory (WENO) scheme was applied. Results reported an underestimated FoM by about 12% to 22% which may be inaccurate for design purposes. Likewise, Sheng *et al.* [45] used the same tip shape with the unstructured Navier-Stokes CFD solver U<sup>2</sup>NCLE [46]. The effect of transition models such as the Local Correlation-based Transition Models (LCTM) by Langtry [47, 48], as well as the Stall Delay Model (SDM) coupled with the Delayed Detached Eddy Simulation (DDES) [49] were investigated. Baeder *et al.* [50] used the OVERset Transonic Unsteady Rotor Navier-Stokes (OVERTURNS) solver [51], and performed simulations for the 1/5 scale S-76 rotor with swept-tapered tip at blade-tip Mach num-

ber of 0.65 for a range of blade pitch angles from  $0^\circ$ - $15^\circ$ . At high collective settings, separated flow was found outboard on the blade, which was due to shock-induced stall. Jain and Potsdam [52] evaluated the performance of the S-76 model-scale rotor with a swept-tapered tip using the HPCMP CREATE<sup>TM</sup>-AV HELIcopter Overset Simulations (HELIOS) CFD solver [53], where FoM was predicted within 1 count. The structured curvilinear OVERset grid FLOW solver (OVERFLOW) [54] and Cartesian SAMARC (without viscous terms) solvers were used at the near and off-body regions, respectively, with a 6th-order central differences scheme and 6th-order dissipation term. A high resolution mesh was used near the rotor wake region of 400 million nodes, and simulations captured up to the third blade passing where braid instability problems were also observed [52]. Further work of Jain [55] showed negligible effects on FoM of a hub model and of blade coning, for the S-76 model rotor.

Unsteady simulations of the 1/4.71 scale S-76 rotor blade with swept-tapered tips were performed by Tadghighi [56] using the NSU3D unstructured module of HELIOS. Under-predicted FoM within two or three counts was found for a range of blade pitch angles from  $4^\circ$  to  $10^\circ$  and both blade-tip Mach numbers 0.60 and 0.65. Likewise, the same rotor blade was assessed using the OVERFLOW structured module of HELIOS by Narducci [57]. Unlike Jain and Potsdam [52], 2nd and 5th-order schemes were employed near the blade and in the off-body regions, respectively. The results obtained with the structured grid method were consistent with unstructured mesh results by Tadghighi [56], showing also an underpredicted FoM. Sensitivities of the FoM to the blade-tip Mach number and tip shape were also captured.

An alternative method to grid-based Navier-Stokes solvers is the hybrid Navier-Stokes / Lagrangian approach used in the GT-Hybrid flow solver [58]. Marpu *et al.* [59] computed performance predictions on the same rotor blade, and results showed an under-predicted FoM mainly due to the over-predicted torque coefficient. Kim *et al.* [43] extended this work to rectangular and anhedral tip shapes, showing an under-predicted FoM for the full range of blade collective angles. However, due to its computer efficiency, the method may be used as a first step in rotor design or for exploring design trends.

Three comprehensive rotorcraft analysis methods such as the Evaluation of Hover Performance using Influence Coefficients (EHPIC) [28], the Comprehensive Hierarchical Aeromechanics Rotorcraft Model (CHARM) [60], and the Vorticity Transport Model (VTM) [61] were employed by Whitehouse *et al.* [62] to assess the sensitivity of the FoM of the 1/4.71 S-76 model-scale to rotor tip shapes. The methods captured very well the trends of the FoM and the torque coefficient  $C_Q$  as functions of the thrust coefficient  $C_T$  for all shapes. However, these methods need accurate aerofoil look-up tables, and thus cannot predict absolute values of FoM without experimental or CFD data being made available. Further studies by Inthra *et al.* [63] using the commercial CFD software ANSYS FLUENT [64] and evaluated the differences of steady vs. unsteady computations in the performance of scale S-76 rotor blade. Rectangular, swept-taper, and swept-taper-anhedral tips were selected for computations at a blade-tip Mach number of 0.65. A better preserved wake was observed for the unsteady solution but the FoM predictions showed minimal differences. Moreover, different turbulence models were assessed with the anhedral tip, where the DES (Detached Eddy Simulation) model was found to be the best. Liu *et al.* [65] showed the benefits of using high order CFD schemes for the S-76 model-scale. The TURNS solver [66] was used with a Symmetric Total Variation Diminishing (STVD) scheme. A blade-tip Mach number of 0.65 was used. Fluxes at cell-centre faces were decomposed into a symmetric part (up to eighth order accurate) plus an upwind-biased numerical viscosity term computed either with the third-order Monotone Upstream-centred Schemes for Conservation Laws (MUSCL) or the fifth-order WENO schemes. A more detailed description of the scheme and its implementation can be found in [67]. Computations for the aforementioned tip shapes and at three blade-tip Mach numbers using a free-wake model with wake relaxation factor and constrained downwash velocity, loosely coupled with a Navier-Stokes solver (UT-GENCAS [68]), were carried out by Min *et al.* [69]. Both approaches were able to predict the changes in the FoM with the tip shape for the swept-taper and anhedral designs. However, free-wake model results for the swept-tapered case did not show any performance improvement when compared with the rectangular tip. The effect of the blade-tip Mach number was captured by both methods.

Abras [70] used the same model-scale rotor to compare the CFD solvers HPCMP CREATE<sup>TM</sup>, AV HELIOS and FUN3D. It was shown that a Cartesian off-body grid preserved better the rotor wake if it was not dissipated by the near-body grid. Overall, the HELIOS computations provided better predictions of FoM than FUN3D mainly due to the reduced dissipation and higher spatial accuracy employed in the region of the rotor wake. Table 1.6 summarises the works on the model-scale S-76 rotor blade. Details of the solvers employed, tip shapes, turbulence models, and flow conditions are given.

By contrast, few complete studies on numerical simulations of the full-scale S-76 were found in the literature. Wachspress [71] evaluated the full-scale S-76 in hover, using the CHARM solver, which employs a vortex lattice lifting surface model to determine airloads coupled with a constant vorticity contour free-wake model. Comparisons with the experimental data of Shinoda [35] showed good agreement for all the range of thrust coefficients.

### **1.2.2 Validation Data Related to Propellers**

To evaluate propeller aerodynamics, experiments were carried out in the 8×7ft Transonic Wind Tunnel (TWT) of the Aircraft Research Association (ARA) (see Figure 1.8) under contract by Dowty Aerospace Propellers (DAP) [72]. The model referred to as the Pressure Tapped Propeller (PTP) consisted of a single row of six blades with spinner, at cruise and climb conditions. Two modern high speed designs of blades were tested, one with unswept and another with moderately swept planform. The diameter of the blade was chosen as 3ft (0.914 m) to provide high disk loading and to make the best use of the acoustic qualities of the transonic tunnel. Aerofoils from the ARA-D/A family were used for both blades. An Euler code called JamProp developed at the ARA, was used to predict pressure distributions along the blade radius. Both blade sets have been calculated and compared against the PTP test data at three different Mach numbers. Good agreement between CFD and test data was reported. Noise polar for unswept blade and swept blades were also studied for different Mach number. This data is used here for validation since surface pressure coefficient on the blades is available. This is not the case for most other propeller tests.

Table 1.6: Computations of the 1/4.71 scale S-76 rotor blade.

Author Organisation	Code	Structured/ Unstructured	Steady/ Unsteady	Periodic Plane	Tip Geometry	Turbulence Model	Finest Grid Deployed
<b>Jung <i>et al.</i> [44]</b> KAIST	KAIST	Unstr	Unsteady	NO	ST(f)	SA rcc	6.3 M nodes near-body 6.9 M nodes off-body
<b>Sheng <i>et al.</i> [45]</b> University of Toledo	U <sup>2</sup> NCLE	Unstr	Unsteady	YES	ST(f)	SA DDES LCTM/SDM	44.9 M
<b>Baeder <i>et al.</i> [50]</b> University of Maryland	OVERTURNS	Str	Steady	YES	ST(f)	SA	a
<b>Jain <i>et al.</i> [52]</b> US Army	HELIOS	OVERFLOW Str near-body SAMARC Str off-body	Unsteady	NO	ST(f)	SA rcc	48 M near-body 400 M off-body
<b>Narducci [57]</b> The Boeing Company, Philadelphia	HELIOS	OVERFLOW Str near-body SAMARC Str off-body	Unsteady	NO	ST(f)	SA rcc	20.8 M near-body 42.6 M off-body
<b>Tadghighi [56]</b> The Boeing Company, Mesa	HELIOS	NSU3D Unstr near-body SAMARC Str off-body	Unsteady	NO	ST(f)	SA	8.4 M near-body 18.1 M off-body
<b>Marpu <i>et al.</i> [59]</b> Georgia Tech	GT-Hybrid	Str near-body Lagrangian off-body	Unsteady	YES	ST(f)	SA	1.7 M near-body
<b>Kim <i>et al.</i> [43]</b> Georgia Tech	GT-Hybrid	Str near-body Lagrangian off-body	Unsteady	YES	ST(f), R(f) STA(f)	SA	1.7 M near-body
<b>Whitehouse <i>et al.</i> [62]</b> Continuum Dynamics, Inc.	EHPIC	LS and F-WM	Steady	YES	R(f),ST(f),STA(f)	-	-
	CHARM	LS and CVC F-WM	a	a	R(f),ST(f),STA(f)	-	-
	VTM	LS and CFD-based wake	Unsteady	a	R(f),ST(f),STA(f)	-	41 spanwise panels
<b>Inthra <i>et al.</i> [63]</b> University of Tennessee	FLUENT	Str	Unsteady Steady	YES	ST(f), R(f) STA(f)	$k$ - $\epsilon$ , $k$ - $\omega$ SST, transition $k$ - $\omega$ SST SAS, DES, LES	a
<b>Liu <i>et al.</i> [65]</b> Georgia Tech	URNS	Str	Steady	YES	ST(f)	SA	0.2 M
<b>Min <i>et al.</i> [69]</b> UTRC	UT-GENCAS	Str near-body Lagrangian off-body	Unsteady	YES	ST(f), R(f) STA(f)	SA rcc	12 M near-body
<b>Jain [55]</b> US Army	OVERFLOW/NSU3D	Structured Unstructured	Unsteady	NO	R(r),ST(r) STA(f)	SA rcc $k$ - $\omega$ SST	448 M
<b>Abras and Hariharan [70]</b> NAVAIR and HPCMP CREATE-AV	NSU3D FUN3D	Unstructured	Unsteady	NO	ST(f)	SA, SA rcc	40.1 M

f=flat tip-caps; r=rounded tip-caps; rcc=rotation curvature correction; CVC=Constant Vorticity Contour; DES=Detached Eddy Simulation; F-WM=Free-Wake Method; LCTM=Local Correlation-based Transition Model; LES=Large Eddy Simulation; LS=Lifting Surface; M=million cells (four blades); R=Rectangular; SA=Spalart-Allmaras; SAS=Scale Adaptive Simulation; SDM=Stall Delay Model; SST=Shear-Stress Transport; ST=Swept-Taper; STA=Swept-Taper-Anhedral;  $k$ =Turbulent kinetic energy;  $\epsilon$ =Turbulent energy dissipation rate;  $\omega$ =Specific dissipation frequency of turbulence; "a"=Not specified in the literature

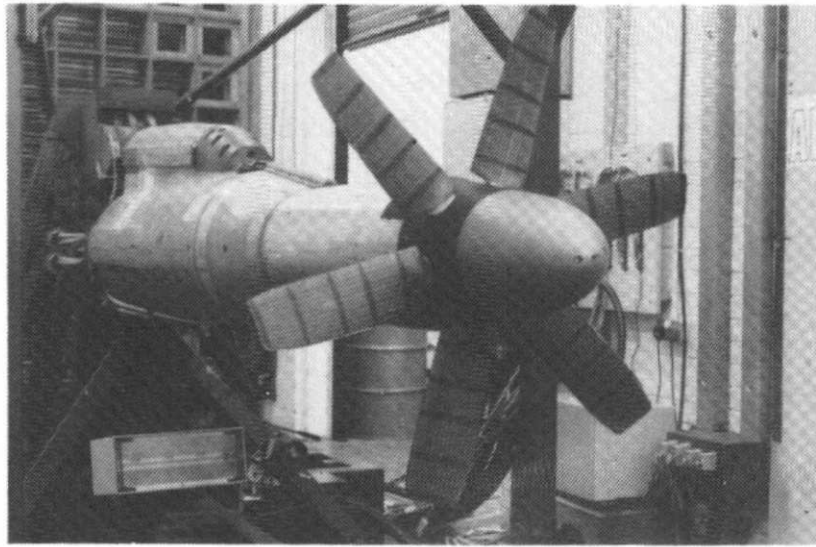


Figure 1.8: Pressure Tapped Propeller (PTP) model in the transonic wind tunnel of the Aircraft Research Association [72].

### 1.2.3 Validation Data Related to Tiltrotors

Tiltrotor is a flying vehicle that combines the Vertical and/or Short Take-Off and Landing (V/S-TOL) capability of helicopters with the high speed cruise of turbo-prop aircraft. For the first time, this aircraft configuration was successfully demonstrated with the Bell XV-3 in 1955 [73]. In the late 1960s and early 1970s, a major program was jointly launched by the NASA Ames Research Center and Bell Helicopters to develop the XV-15 tiltrotor. Data from this aircraft was used to support the development of a new generation of tiltrotors like the Bell-Boeing V-22 Osprey and the AW609.

Tiltrotor blades must be designed to efficiently operate in helicopter and aeroplane modes, resulting in a compromise blade design with high twist and solidity, along with smaller rotor radius. Hence, the aerodynamic interaction between the rotor and the wings seems to be one of the most important aerodynamic phenomena to affect the design of tiltrotor blades and the overall performance of the aircraft. In this regard, experimental studies carried out by Felker and Light [74] and numerical simulations performed by Potsdam and Strawn [75] investigated the rotor/wing aerodynamic interactions in helicopter mode. To mitigate the strong aerodynamic interaction between the

rotor and the wing of tiltrotor aircraft and to reduce the downward force acting on the wings in hover [76], a new design was proposed where a small outboard part of the wing can be partially rotated. This configuration is known as tiltwing.

Most studies related to tiltrotors have been conducted in the United States. Following these, several research and development projects were launched in Europe to provide more insight into tiltrotor aircraft. DART [77] (Development of an Advanced Rotor for Tiltrotor) aimed to improve rotor hub designs; TILTAERO [78, 79] (TILTrotor interactional AEROdynamics) to study the interactional aerodynamics; and ADYN [80] (Advanced European tiltrotor DYNamics and Noise) to investigate rotor dynamics, performance, and level of noise on tiltrotors. All these projects have provided notable contribution to the tiltrotor knowledge-base. In this context, a blind-test activity of the TILTAERO project was carried out by Visingardi [78]. A half-span 40% Mach-scaled model tiltrotor was simulated using the Boundary Element Methodology (BEM) (which assumes that the flow is incompressible and inviscid) as well as unsteady and steady Reynolds Averaged Navier-Stokes (RANS) solvers. The rotor was modelled using a non-uniform actuator disk. Table 1.7 summarises the simulated cases. Results reported a large region of strong unsteadiness on the wing of the aircraft. However, a weak rotor/wing aerodynamic interaction was observed in aeroplane mode.

Table 1.7: Flight conditions employed for the simulation of a half-span 40% Mach-scaled tiltrotor model [78].

Test case	Nacelle	Fixed wing	Tiltable wing	$M_{tip}$	$M_{\infty}$
Transition corridor 1	59.95°	2.95°	3.64°	0.63	0.212
Transition corridor 2	84.84°	2.84°	29.48°	0.63	0.098
Aeroplane mode	0.3°	3.3°	3.3°	0.63	0.212

Likewise, Decours [80] evaluated tiltrotor aerodynamic interactions using CFD and experimental data. Experiments were performed in the 8×6m 3/4 open test section of the DNW-LLF (German-Dutch Wind Tunnels Large Low-Speed Facility) wind tunnel, on a half-span 40% Mach-scaled model (see Figure 1.9), which was based on the advanced European tiltrotor concept ERICA (Enhanced Rotorcraft Innovation Concept Achievement) proposed by AGUSTA [81]. A comparison between the TILTAERO and ADYN blades was carried out using CFD, and experimental data



was available. Six different test points were reported, which cover helicopter hover mode, cruise flight, and conversion corridor. Table 1.8 shows six different cases, where different nacelle tilt angle, fixed wing and tiltable wing AoA were studied. Regarding numerical simulations, a steady approach was considered where the rotors were modelled with an actuator disk. Comparison between predicted and experimental surface pressure coefficient and normal force along the wingspan showed good agreement for all cases. Flow visualisation with streamlines around the wing-nacelle junction showed loss of lift due to separation on the outer wing during the conversion phase.

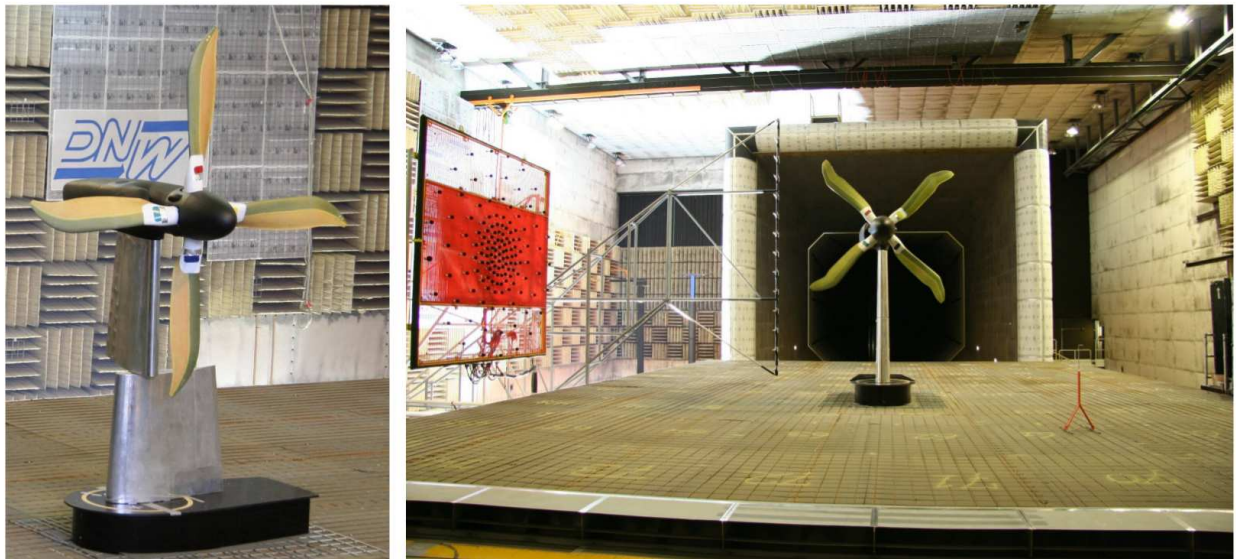


Figure 1.9: The TILTAERO half-span 40% Mach-scaled model in the DNW-LLF wind tunnel (left) and aeroacoustic test set-up in the  $8 \times 6\text{m}$   $3/4$  open test section (right) [80].

Table 1.8: Flight conditions simulated in the DNW-LLF wind tunnel for the half-span 40% Mach-scaled model based [80].

Test case	Nacelle	Fixed wing	Tiltable wing	$V_\infty$ (m/s)
Helicopter mode	$87^\circ$	$0^\circ$	$80^\circ$	0
Transition corridor 1	$84.8^\circ$	$2.8^\circ$	$29.5^\circ$	26.3
Transition corridor 2	$74.9^\circ$	$3^\circ$	$10.7^\circ$	42.88
Transition corridor 3	$60^\circ$	$3^\circ$	$3.7^\circ$	57.1
Transition corridor 4	$45^\circ$	$3^\circ$	$3.2^\circ$	63.3
Aeroplane mode	$0.3^\circ$	$3.3^\circ$	$3.3^\circ$	57.04

Numerical simulations of the interactional aerodynamics of the TILTAERO half-span model were also conducted by Beaumier [79]. The main purpose of his study was to capture the aerodynamic interactions of the rotor-wing using CFD and validate the obtained performance against the experimental data taken from the DNW-LLF wind-tunnel. A set of six test cases were chosen covering hover to cruise, including the conversion flight, in low speed flight conditions for all cases. Table 1.9 shows the six flight conditions simulated. A steady approach was used to model the rotor, using an actuator-disk approach. In general, good agreement between CFD and experiments was obtained, for hovering, aeroplane, and transition corridor cases. Further studies were carried out to understand the origin of flow separation on the outer wing at low speed flight conditions. It has been shown that this separation is due to nacelle-wing interaction.

Table 1.9: Flight conditions simulated for the TILTAERO half-span model [79].

Test case	Nacelle	$M_\infty/M_{tip}$
Helicopter mode	$87^\circ$	0
Transition corridor 1	$82^\circ$	0.078
Transition corridor 2	$71.9^\circ$	0.127
Transition corridor 3	$57^\circ$	0.169
Transition corridor 4	$42^\circ$	0.187
Aeroplane mode	$-3^\circ$	0.17

Very few wind tunnel data is available for model and full-scale tiltrotors. At the early stages of the XV-15 program, the NASA 40- by 80- foot wind tunnel was used to measure integrated rotor loads in helicopter [82], aeroplane, and transition corridor modes [83]. However, force and moment measurements did not exclude the contribution from the rest of the airframe. The NASA-Ames Outdoor Aeronautical Research Facility (OARF) was also used by Felker *et al.* [84] with the XV-15 rotor, and by Bartie *et al.* [85] with the XV-15 Advanced Technology Blade (ATB). The hover and forward flight tests began in the late 90s with the work of Light [86] in the 80-ft by 120-ft wind tunnel at NASA Ames, but only few conditions were tested. To fill this gap, Betzina [87] in 2002 undertook an extensive campaign of experiments on the full-scale XV-15 rotor in the 80-ft by 120-ft wind tunnel at NASA Ames (see Figure 1.10), where the experiments were corrected for hub and tare effects. For all sets of experiments cited, neither surface pressure

nor skin friction coefficients were measured. In this regard, Wadcock *et al.* [88] measured the skin friction coefficient on a hovering full-scale XV-15 tiltrotor in the 80-ft by 120-ft wind tunnel at NASA Ames. At low thrust, a region of laminar flow was encountered over a significant fraction of the blade chord, while at high disk loading conditions, the laminar to turbulent transition region on the upper blade surface moved towards the blade leading edge with a fully turbulent boundary layer encountered outboard. This set of experiments can be used to validate and improve flow transition models for tiltrotors.



Figure 1.10: Full-scale XV-15 rotor on the rotor test apparatus in the 80-ft by 120-ft wind tunnel at NASA Ames [87].

Unlike conventional tiltrotor configurations, tiltwing aircraft have not been widely studied. To fill this gap, the research project NICETRIP [89] (Novel Innovative Competitive Effective Tilt Rotor Integrated Project) was funded by the European Union (EU) to develop a database covering aerodynamic interactional phenomena and other technology aspects of tiltwing vehicles. A 1:5 motorised model-scale tiltrotor was designed and manufactured under the name of ERICA [90] and experiments were undertaken using the 9.5×9.5m DNW-LLF and the 8m S1MA ONERA

wind tunnels (see Figure 1.11). The tests covered the full flight envelope from helicopter mode, where the nacelles were tilted 90 degrees relative to the aircraft axis, to aeroplane mode, for a range of AoA and freestream Mach numbers ( $M_\infty$ ). Helicopter and transition conversion configurations were studied at low speed ( $M_\infty$  0 to 0.168) in the DNW-LLF wind tunnel [91] due to its larger test section, and to minimise wake reingestion in the test chamber. By contrast, the high speed tests ( $M_\infty$  0.168 to 0.55) were conducted in the test section no.2 (45m<sup>2</sup>) of the S1MA ONERA wind tunnel [92].



Figure 1.11: ERICA tiltrotor in the S1MA ONERA (left) and DNW-LLF (right) wind tunnels [93].

Concerning numerical simulations of tiltrotors, only a few complete studies are found in the literature. For the XV-15 tiltrotor blade, Kaul *et al.* [94, 95, 96] studied the effect of inflow boundary conditions and turbulent models on the hovering XV-15 rotor blade, using the OVERFLOW2 CFD solver. Results with the Spalart-Allmaras (SA) model [97] in its DES formulation revealed lack of agreement with the experiments of Wadcock *et al.* [88] in the laminar-turbulent transitional region. Likewise, Yoon *et al.* [98] investigated the effect of the employed turbulence model on the hover performance, and skin friction coefficients of the XV-15 rotor blade at a blade pitch angle of 10°. It was found that the  $k-\omega$  Shear-Stress Transport (SST) with DDES turbulence model predicted the FoM closer to experiment than the SA-DDES one-equation model. However, minimal differences between these fully-turbulent models were observed in the predictions of skin friction coefficient, which did not reproduce well the flowfield measured during experiments [88]. Sheng *et al.* [99, 100] used the U<sup>2</sup>NCLE and HELIOS CFD solvers to assess the effect of transition mod-

els on hover FoM for the XV-15 blade. Despite the use of a very large grid of 145 million nodes for the whole rotor, results at  $10^\circ$  collective showed an over-predicted FoM with a discrepancy of more than 3%. It was shown that the transitional flow modelling did not have a significant impact on the predicted FoM mainly due to the small laminar-turbulent transition region encountered on the XV-15 blades.

A detailed performance analysis of the hover and propeller modes of the XV-15 blades was performed by Gates [101] using the Helicopter Multi-Block (HMB) CFD solver. Good agreement with published experimental data was reported, even though a medium grid size (9.6 million cells per blade) was employed for computations. Furthermore, the effect of the hub spinner on the propeller performance at moderate advance ratios was highlighted. Likewise, Massaro *et al.* [102] performed numerical simulations on the XV-15 tiltrotor in helicopter and aeroplane modes with two aerodynamic solvers; the structured finite-volume HMB CFD solver and the ADPANEL solver which is a full-unstructured panel code coupled with a time-stepping non-linear free-wake vortex model [103]. Both codes matched very well the experimental data for both configurations, despite small discrepancies observed when the rotor was close to stall condition in hover. Performance analysis of the full-scale XV-15 tiltrotor blades in aeroplane, transition corridor, and helicopter modes were evaluated with the solver RotCFD [104] by Koning *et al.* [105], where the rotor was modelled with an actuator disk. Two-dimensional aerofoil data and the Corrigan stall delay model [106] were employed. Results with the Comprehensive Analytical Model of Rotorcraft Aerodynamics and Dynamics (CAMRAD) II solver [107] with a free-wake model and Corrigan stall delay model carried out by Johnson [108] were also reported. Comparisons with the experimental data of Felker *et al.* [84] in the OARF tunnel and Bell Helicopter [82] in the NASA Ames National Full-Scale Aerodynamics Complex facility (NFAC) revealed an acceptable agreement at low and medium disk loadings. At high loading however, discrepancies arose mainly due to the assumption of incompressible flow. Table 1.10 summarises published papers related to CFD studies of the XV-15 tiltrotor blades.

Table 1.10: Work related to CFD on the XV-15 tiltrotor blades.

Author	Code	Structured Unstructured	St/ Uns	Turbulence Model	Finest Grid Deployed	Modes
Kaul <i>et al.</i> [94]	OVERFLOW2.2c	Str	Uns	SA-fv3 [109]	45 M	Hel
Kaul <i>et al.</i> [95]	OVERFLOW2.2c	Str	Uns	SA-DES,SST-DES	45 M	Hel
Yoon <i>et al.</i> [98]	OVERFLOW	Str	Uns	SA-DES,SST-DES	286.9 M	Hel
Sheng <i>et al.</i> [99, 100]	U <sup>2</sup> NCLE	Unstr	Uns	SA-LCTM	23.6 M	Hel
	HELIOS	Unstr NSU3D near-body	St	SA	11.8 M	Hel
		Str SAMARC off-body	St	-	133 M	
Gates [101]	HMB2	Str	St	$k-\omega$ SST	9.6 M	Hel, Aer
Massaro <i>et al.</i> [102]	HMB2	Str	St	$k-\omega$ SST	a	Hel, Aer
	ADPANEL	Unstr	Uns	-	a	Hel, Aer
Koning <i>et al.</i> [105]	RotCFD	Str	Uns	$k-\varepsilon$	2 M	Hel, Aer, TC

Aer=Aeroplane; Hel=Helicopter; M=million cells/nodes; St=Steady; Str=Structured; Uns=Unsteady; Unstr=Unstructured;  $\varepsilon$ =Turbulent energy dissipation rate;  $k$ =Turbulent kinetic energy;  $\omega$ =Specific dissipation frequency of turbulence; DES=Detached Eddy Simulation; LCTM=Local Correlation-based Transition Model; SA=Spalart-Allmaras; SST=Shear-Stress Transport; TC=Transition Corridor;

<sup>a</sup>Not specified in the literature

Further studies were also published for the V-22 tiltrotor using numerical simulations. The drag polar of the V-22 aircraft has been measured in the 20×20ft Boeing Vertical Wind Tunnel (BVWT) [110] and the results were compared against CFD predictions from the FUN3D and OVERFLOW CFD codes [111]. Neither CFD nor experiments considered the effect of the rotors. The experiments concerned a model of the V-22 of 0.15 scale and provided integrated lift, drag, and moment data. In general, the authors state that good agreement between CFD and experiments was obtained but further studies were recommended to ensure mesh independent results can be obtained.

In 2014, a validation study for the 1:5 model-scale ERICA tiltrotor was carried out by Decours *et al.* [93], using the state-of-the-art helicopter structured finite-volume CFD solvers in Europe (ELSA [112], ROSITA [113], and FLOWer [114]). Two flight configurations, corresponding to minimum speed and highly loaded aeroplane and transition corridor modes, were simulated using different CFD tools, methodologies, turbulence models, and grids, with the aim to characterise the aerodynamic interactional phenomena on the ERICA tiltrotor. Concerning the aeroplane mode configuration, experiments predicted a local separation at the top of the fuselage near the centre-line and the fixed wing junction. Not all CFD solvers were able to well reproduce this, though a fair agreement has been obtained between CFD and experiments. Table 1.11 summarises the published works related to CFD on the 1:5 model-scale ERICA tiltrotor and compares the mesh size used for CFD computations.

Table 1.11: Component mesh size (given as million nodes [93]) for the 1:5 scale-model ERICA tiltrotor.

Components	ONERA	PoliMi	AHD	DLR
	ELSA [112]	ROSITA [113]	FLOWer [114]	FLOWer [114]
Fuselage and fixed wing	5.8	5.6	18.6	36.7
Tilttable wing	2.0	2.0	1.7	0.7
Nacelle	3.8	3.8	5.7	10.4
Rotor blades (x4)	4.0	4.0	-	5.4
Actuator disk	-	-	0.4	-
Model support	0.8	0.8	2.3	0.3
Wind tunnel	9.8	9.8	10.8	0.5
<b>Total</b>	<b>26.2</b>	<b>26</b>	<b>39.5</b>	<b>54</b>

AHD=Airbus Helicopters Deutschland; DLR=German Aerospace Centre; ELSA=Ensemble Logiciel pour la Simulation en Aerodynamique; ONERA=Office National d'Etudes et de Recherches Aerospatiales; PoliMi=Politecnico di Milano; ROSITA=ROtorcraft Software ITALy.

### 1.2.4 Aerodynamic Optimisation of Tiltrotor Blades

The aerodynamic design of tiltrotor blades is a challenging task, requiring the best compromise in performance between hover and propeller modes [115, 116]. In hover, the blade aerodynamics is characterised by strong interaction with the rotor wake, resulting in a significant effect of the induced drag on the total drag [17]. The propeller mode on the other hand, is dominated by strong compressibility effects, especially at high advance ratio, resulting in a prominent contribution of the profile and wave drag components [117]. As a consequence, to accurately capture the effect of the blade shape on rotor performance, the use of high-fidelity flow models is required.

Aerodynamic optimisation needs large computational resources, since each design point requires the solution of a set of partial differential equations. The choice of the optimisation algorithm is therefore crucial. Broadly speaking, the optimisation algorithms can be classified as gradient-based or gradient-free methods. Gradient-based methods usually require a limited number of flow evaluations [118], and this makes them particularly attractive for complex aerodynamic optimisation problems. They need, however, the computation of flow derivatives with respect to the design variables, which can be a very expensive task, unless adjoint methods are used. Also, gradient-based methods are local in nature, and they do not guarantee to find the global optimum. On the other hand, gradient-free methods are simpler to implement, because they do not require flow derivatives, and some of them are guaranteed to find the global optimum. Nevertheless, they typically need two to three orders of magnitude more objective function evaluations than gradient-based methods [119]. Gradient-free methods are therefore effective only when coupled with very efficient or reduced-order methods, for which the evaluation of the flow solution is cheap. It may also be stated that gradient-free methods are more appropriate to the preliminary design of the aircraft, while gradient-based methods, coupled with high-fidelity flow models, may be used at more advanced stages of the design process.

Gradient-based methods have been widely employed for optimisation of rotors in hover, as in the work of Walsh *et al.* [120], Zibi *et al.* [121], and more recently in Le Pape *et al.* [122], Choi *et al.* [123] and Dumont *et al.* [124]. These works demonstrated the efficiency of gradient-based



optimisation methods for blade design, but also highlighted the dependency of the final design on the initial design point. This was due to the behaviour of gradient-based algorithms, that may fail to find the global optimum and converge to a local extremum of the objective function. Several authors tried to overcome this drawback, developing strategies to select the best starting point in the design space [125, 126]. Application of gradient-free methods can be found in the work of Imiela [127], who optimised the ONERA 7A model rotor blade and compared results from both gradient and gradient-free methods, and in Johnson *et al.* [128], where the UH60-A rotor peak normal and torque loads were reduced using a Genetic Algorithm (GA) and a reduced-order model based on Artificial Neural Networks (ANN).

For the optimisation of propeller blades, Cho *et al.* [129] used the Extended linear Interior Penalty function Method (EIPM) in conjunction with panel and vortex lattice methods to find the optimal blade twist and chord distributions. Coupled aeroacoustic and aerodynamic optimisation of propeller blades was instead carried out by Marinus *et al.* [130] using a gradient-free method, where aerofoil shapes, twist and chord distributions were simultaneously optimised at multiple operating conditions.

Tiltrotor blades must be designed to be efficient both in helicopter and aeroplane modes. This makes their design particularly challenging, because the aerodynamic characteristics of helicopter rotor and propeller blades are significantly different, and the optimal values of the main shape parameters (*e.g.* twist and chord distributions, sweep, anhedral, etc.) can be different in these two cases. It follows that the blade design requires the solution of a multi-objective optimisation problem, where the objective functions are suitable measures of the performance at selected flight conditions in both helicopter and aeroplane modes. A multi-objective optimisation of the ERATO blade in conjunction with a gradient based-optimiser was put forward by Leon *et al.* [131], seeking to maximise the FoM in hover and minimise the rotor power in forward flight. Wilke [132] applied single and multi-objective techniques for the variable-fidelity optimisation of a helicopter rotor. Single optimisations of hover and forward flight blades showed a detrimental performance when used in the opposite flight condition. However, the shape obtained with the multi-objective optimisation technique was a compromised design of both antagonistic objectives. To reduce compu-

tational cost, the multi-objective optimisation can be reduced to a single-objective optimisation by considering the weighted sum of the objective functions at each flight condition. Higher weights are assigned to the flight conditions that cover the most part of a typical tiltrotor mission. This strategy is usually referred to as “multi-point” optimisation.

An application of multi-objective optimisation to the design of a generic tiltrotor blade is reported in Droandi *et al.* [133], where a Non-dominated Sorting Genetic Algorithm II (NSGA-II) was used in conjunction to a Blade Element Momentum Theory (BEMT) solver. The BEMT solver allowed for a quick evaluation of the flow solution at each design point, but the model could not account for the effect of all the blade shape parameters, such as the sweep angle, which requires a higher-fidelity flow modelling. The aerodynamic optimisation of the XV-15 rotor blades was investigated by Massaro *et al.* [102] using a Surrogate-Assisted Memetic Algorithm (SAMA), combined with a panel method for the blade aerodynamics. Aerofoil shapes, twist and chord distributions, and anhedral and sweep angles were considered for the maximisation of the FoM and the propeller propulsive efficiency  $\eta$ . They showed that a compromise solution can be selected from the Pareto front, which has 3.2% higher FoM in hover and 6.5% higher  $\eta$  in aeroplane mode with respect to the XV-15 baseline blade. Multi-point optimisation based on a gradient method was carried out by Jones *et al.* [115] for the Tilt-Rotor Aeroacoustics Model (TRAM) [134]. They employed the unstructured FUN3D flow solver [135, 136] coupled with a discrete adjoint solver to determine the optimal aerofoil shapes, twist and taper.

### 1.2.5 Validation Data for Aeroacoustics

For helicopter main rotors, significant progress has been made in understanding the noise-generation mechanisms and noise prediction methods. In fact, high levels of noise are generated in descending or landing, due to the interaction of the rotor blades with their generated vortices. This is known as Blade-Vortex Interaction noise (BVI) [137]. The main physical sources of rotor noise can be classified in discrete-frequency and broadband, according to their frequency content. The rotor acoustics depends on geometric features and the operating environment of the helicopter rotor.

Furthermore, different mechanisms contribute to the aerodynamic sources of noise.

A classification of the discrete-frequency noise (tonal noise) is first presented, and is divided into the following determinist components [137]:

- **Thickness noise** is mainly due to the displacement of the fluid in the flowfield by the thickness of the blades. It is a function of the dynamic pressure, geometry of the rotor blade, and the acoustic properties of air [138, 139].
- **Loading noise** is due to the unsteadiness of the pressure and viscous stresses in the flowfield caused by the rotor-blade surface motion.
- **BVI noise** is caused by interaction of the rotor blades with the tip vortex generated from preceding blades (see Figure 1.12).
- **High-Speed Impulsive (HSI) noise** is caused by compressibility effects associated with the high-speed of the blade. The effect of the HSI becomes particularly intense at high-speed flight.

Likewise, a classification of the broadband noise consists of the non-determinist loading noise and is presented here [137]:

- **Turbulence ingestion noise** is due to the turbulence ingested into the rotor, mainly generated by natural atmospheric turbulence or from blade wakes.
- **Blade-Wake Interaction (BWI) noise** is due to the interaction of the rotor blades with the sheet of turbulence generated from preceding blades.
- **Blade self-noise** is generated by several mechanisms related to the blade itself, namely trailing edge noise associated to the turbulence boundary layer or separated flow interaction, laminar boundary layer-vortex shedding, and blade tip noise.

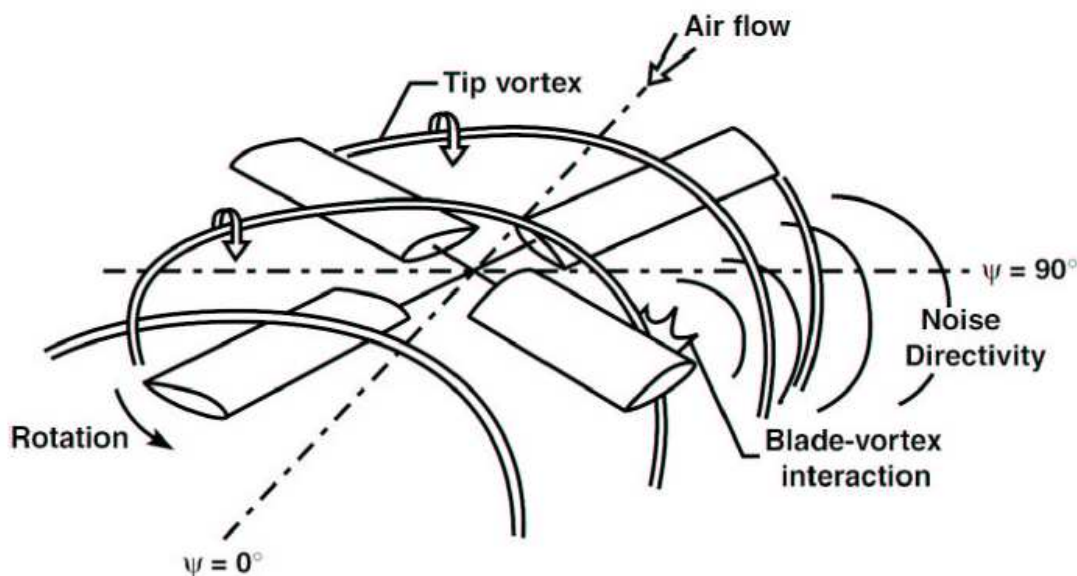


Figure 1.12: Sketch of the BVI noise, showing the noise directivity of this source of noise [137].

A schematic of the directionality of each type of rotor noise is shown in Figure 1.13. It is seen that loading and broadband noise sources tend to propagate downwards of the rotor-disk, whereas thickness and high-speed impulsive noise are mainly propagated near the rotor-disk plane. BVI noise tend to propagate at 45 degrees relative to the plane of the rotor.

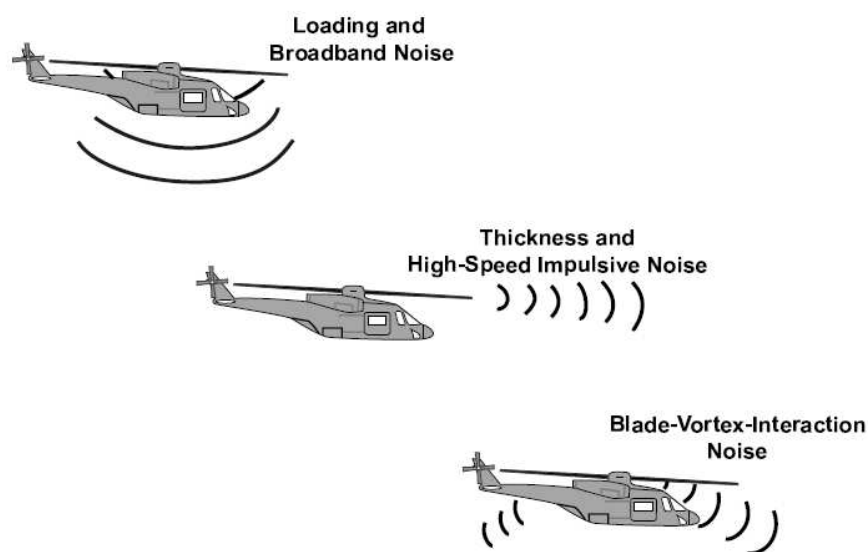


Figure 1.13: Schematic of the directivity of the source of rotor noise [137].

The thickness and loading noise sources for rotor blades were first studied in the late 1930's. The first articles were focused on propellers because of their popularity at the time. Gutin [140] was the first to establish a theoretical noise prediction for rotating propellers based on aerodynamic principles. Moreover, comparisons of his theoretical results of the propeller noise directivity with experimental data were acceptable. Works related with thickness noise predictions were addressed by Deming [138, 139], who analysed the effect of blade thickness on the propeller noise using a symmetric section at zero blade angle. A complete theoretical study on the noise generated by propellers in forward flight was conducted by Garrick and Watkins [141]. Their work extended Gutin's theory, which was limited to predict the fundamental and the first harmonics at a distance far away from the rotor-disk (several diameters of the rotor).

By the 1960's, the first theoretical noise prediction studies for helicopters were published by Lowson [142] and Wright [143]. The theory of Lowson was based on the work of Lighthill [144], deriving the equations of the sound fields for the case of singularities under an arbitrary motion. An extensive review on the helicopter rotor noise prediction work, at the NASA Langley Research Center, was made by Brentner [137]. This article focused on the modelling of aerodynamically generated sound of helicopter rotors and computational developments were complete by 1994.

Two computational methods for transonic rotor noise for helicopters in hover and forward flight were reported by Brentner [145], who used the Ffowcs Williams-Hawkings (FW-H) equation including the quadrupole term, and a rotating Kirchhoff formulation. Both methods need a CFD solution as input to predict the level of noise near and farfield. Experimental data for hover and forward flight were available so that both methods were compared against them. Good agreement was found for all cases tested. Moreover, an extensive study of the effect of the CFD grid resolution and the location of the integration surface/volume was also conducted.

### **1.2.6 High-Order Discretisation Methods for CFD**

In recent years, significant progress has been made in accurately predicting rotorcraft flows using Computational Fluid Dynamics [146]. It has also been established in Computational Aero-

Acoustics (CAA), that CFD methods need to provide higher spatial and temporal resolution accuracy to deliver the spectral resolution required for acoustic flow quantities [147]. Indeed, their potential in delivering higher accuracy at reasonable computational cost compared to low order methods, makes them suitable for aerodynamic applications [148].

A numerical method is  $K$ -order accurate if the solution error  $e$  is proportional to the mesh size  $h$  to the power  $K$ . If  $K$  is greater or equal than three, the method is considered "high-order". The reason of this criterion ( $K \geq 3$ ) is due to the effect that most CFD solvers used in the aerospace community are second-order accurate. Given the same CPU time, high-order methods may achieve higher level of accuracy than low-order methods. In addition, since first and second-order methods are dissipative, high-order methods are needed to accurately predict vortex dominated flows problems (e.g. vortex wake of a helicopter rotor in hover [9]). However, high-order schemes are less robust and are slower to converge to steady-state solutions than low-order methods, and present higher memory requirements especially when implicit time stepping techniques are required.

Several types of high-order methods have been developed during the past three decades to cope with a wide range of problems. Spectral methods firstly introduced by Orszag [149] and first-order schemes (Godunov's scheme [150]) represent the most and least accurate methods, respectively. A first classification covers high-order schemes developed either for structured [151, 152] or unstructured meshes [153, 154, 155, 156]. The formulation of those methods in Finite-Difference (FD) [157, 158] or Finite-Volume (FV) [159, 160] frameworks is also a means of classification. A more complete classification is given by Ekaterinaris [161] in his review paper.

Numerous studies in high-order methods have been formulated in the FD framework [157] and it is well known that FD schemes have advantages in developing high-order spatial discretisation methods [161]. However, they can only be applied on smooth, structured, and curvilinear meshes. In this regard, Tam *et al.* [157] developed a high-order Dispersion-Relation-Preserving (DRP) finite difference scheme. The high-order derivatives were computed in the wave number and frequency space (using Fourier transform) which led to preserve the dispersion relation of the scheme. Visbal *et al.* [158] applied high-order methods (up to 6th-order accurate) on a structured curvilinear mesh using implicit and compact finite-difference schemes. The method was observed

to be robust through the use of a spatial filtering strategy (low-pass Pade-type non-dispersive filter) that smoothed the solution.

By contrast, FV formulations are a more popular choice for the discretisation of the fluid flow equations. Their main advantage is that the resulting discretisation satisfies the conservation of mass, momentum, and energy. Despite these methods being robust, they are typically restricted to second-order accuracy in space [162].

In gas dynamics it is common to find problems that involve shocks and other discontinuities or high gradient regions in the solution, making it difficult to develop stable and robust high-order methods. To address this issue, Essentially Non-Oscillatory (ENO) [163, 164, 165] and WENO [152] schemes were designed and applied to complex flows. In 1994, the first WENO scheme was designed by Liu *et al.* [152] and was third-order accurate in a finite-volume framework. Two years later, Jiang *et al.* [166] extended the WENO schemes to multi-space dimensions using third and fifth order finite differences, whilst Balsara *et al.* [167] developed higher-order finite difference schemes (up to 11th-order accurate). A substantial effort was also made to construct compact central WENO schemes [168, 169]. Along with the WENO scheme, a Compact-Reconstruction Weighted Essentially Non-Oscillatory Scheme (CRWENO) was introduced by Ghosh [170] (up to 5th-order accurate) using the finite-volume method. A more detailed review of ENO and WENO schemes can be found in the work of Shu [171].

### 1.3 Summary of Findings

The survey shows that not much information related to tiltrotor can be found. Experimental data were carried out for the XV-15 tiltrotor in hover and propeller configuration by Betzina [87], and additionally, skin friction measurements on a hovering full scale XV-15 tiltrotor were carried out by Wadcock [88] using an oil-film interferometric skin friction technique. An extensive experimental study in hover was conducted by Balch [33] who showed the role of advanced geometry tip configurations in the performance of isolated S-76 helicopter rotor. Performing evaluations of propeller aerocoustics design were carried out by Dowty Aerospace Propellers [72], where cruise and

climb conditions were tested. Finally, some works about tiltrotor CFD were added into literature-survey, highlighting the contributions of the profile, induced, and wave components of drag on the rotor blades.

### 1.4 Objectives of the Thesis

The objectives of the present research project are listed below.

1. Implementation of an efficient, high-order, finite-volume scheme in the HMB CFD solver.
2. To use the B0-105, S-76, and PSP test data in hover to validate the CFD solver.
3. To use the JORP propeller data to validate the CFD solver.
4. To validate the CFD solver for tiltrotor blades using the XV-15.
5. Assess the capability of the present CFD method in predicting airloads on a complete tiltrotor at different flight configurations.
6. To perform aerodynamic optimisation of tiltrotor blades with high-fidelity computational fluid dynamics, where the required high-fidelity flow gradients were computed using a discrete adjoint solver.

### 1.5 Outline of the Thesis

The structure of the thesis is presented here.

Chapter 1 presents the motivation and background of this work. The literature survey covers works related to validation data for helicopters, propellers, and tiltrotors. Works on aerodynamic optimisation and aeroacoustics of tiltrotor blades are also presented and high-order methods and their application to rotorcraft flows are finally shown.



Chapter 2 describes the CFD solver used for computations (HMB3) along with its main features such as the overset grid method, the optimisation framework, and the gradient-based optimiser.

Chapter 3 is devoted to aeroacoustic methods; the acoustic solver BENP of the Leonardo Helicopters aerocoustics computational chain was integrated with the HMB3 solver, and a description of the inputs required is first presented. The in-house acoustic code Helicopter Ffowcs Williams-Hawkings (HFWH) is also presented.

Chapter 4 presents the implementation of an efficient, high-order, finite-volume scheme (up to 4th-order of spatial accuracy) in the HMB3 CFD solver. Theoretical and numerical analyses of the truncation error are also included.

Chapter 5 presents evidence on the ability of modern CFD methods to accurately predict hover performance of rotors with modest computer resources. Three well-studied blades, the B0-105, S-76 and PSP main rotor blades, are used and results are compared with experimental data. Likewise, chapters 6 and 7 present performance analyses of the JORP propeller and XV-15 tiltrotor blades, respectively, aiming to validate the employed CFD method for such relevant flows.

Validation of HMB for complete tiltrotors is shown in chapter 8. The aim of this section is to assess the capability of the present CFD method in predicting airloads on tiltrotors at different flight configurations. In this regard, three representative flight configurations of the ERICA were selected, corresponding to aeroplane, transition corridor, and helicopter modes, covering most modes of tiltrotor flight.

Aerodynamic optimisation of tiltrotor blades with high-fidelity computational fluid dynamics is carried out in chapter 9. This section shows how the main blade shape parameters influence the optimal performance of the tiltrotor in helicopter and aeroplane modes, and how a compromise blade shape can increase the overall tiltrotor performance.

Chapter 10 demonstrates the underlying high-order method through a wide variety of problems, including two- and three-dimensional test cases. Conclusions and future work are drawn in chapter 11.

# Chapter 2

## HMB3 Solver

### 2.1 CFD Method

The HMB [172, 173, 174, 6] is used as the CFD solver for the present work. It solves the Unsteady Reynolds Averaged Navier-Stokes (URANS) equations in integral form using the arbitrary Lagrangian Eulerian (ALE) formulation, first proposed by Hirt *et al.* [175], for the time-dependent domains with moving boundaries:

$$\frac{d}{dt} \int_{V(t)} \mathbf{W} dV + \int_{\partial V(t)} (\mathbf{G}_i(\mathbf{W}) - \mathbf{G}_v(\mathbf{W})) \mathbf{n} dS = \mathbf{S}_{\text{source}}, \quad (2.1)$$

where  $V(t)$  is the time dependent control volume,  $\partial V(t)$  its boundary,  $\mathbf{W}$  is the vector of conserved variables  $[\rho, \rho u, \rho v, \rho w, \rho E]^T$ , where the variables  $\rho, u, v, w, P$  and  $E$  have their usual meaning of density, three components of velocity, pressure, and total energy, respectively.  $\mathbf{G}_i$  and  $\mathbf{G}_v$  are the inviscid and viscous fluxes, including the effects of the time dependent domain, and  $\mathbf{n}$  is the outward pointing unit normal vector. For forward flying rotor simulations, a moving grid approach is used and the source term is set to  $\mathbf{S}_{\text{source}} = 0$ . Regarding hovering rotor simulations, the grid is fixed and a source term  $\mathbf{S}_{\text{source}} = [0, -\rho \boldsymbol{\omega} \times \mathbf{u}_h, 0]^T$  is added to compensate for the inertial effects of the rotation, where  $\boldsymbol{\omega}$  and  $\mathbf{u}_h$  are the rotational vector and local velocity field in the rotor-fixed frame of reference, respectively [6].

The Navier-Stokes equations are discretised using a cell-centred finite volume approach on a

multi-block grid. The spatial discretisation of these equations leads to a set of ordinary differential equations in time,

$$\frac{d}{dt}(\mathbf{W}_{i,j,k} V_{i,j,k}) = -\mathbf{R}_{i,j,k}(\mathbf{W}_{i,j,k}), \quad (2.2)$$

where  $i, j, k$  represent spatial components,  $\mathbf{R}$  is the flux residual vectors, and  $V$  is the volume of the cell. To evaluate the convective fluxes, Osher's [176] and Roe's [177] approximate Riemann solvers are used in HMB, while the viscous terms are discretised using a second order central differencing spatial discretisation. The Monotone Upstream-centred Schemes for Conservation Laws (MUSCL) developed by van Leer [178] is used to provide second order accuracy in space. HMB uses the alternative form of the van Albada limiter [179] activated in regions where large gradients are encountered, mainly due to shock waves, avoiding the non-physical spurious oscillations. An implicit, dual-time stepping method is employed to performed the temporal integration [6]. The solution is marching in the pseudo-time to achieve fast convergence, using a first-order backward difference. The linearised system of the Navier-Stokes equations is solved using the Generalised Conjugate Gradient (GCG) method with a Block Incomplete Lower-Upper (BILU) factorisation as a pre-conditioner [180]. Multi-block structured meshes are used for HMB, which allow easy sharing of the calculation load in parallel computing. Structured multi-block hexa meshes are generated using ICEM-Hexa<sup>TM</sup>.

## 2.2 Variable Extrapolation-MUSCL Approach

Second-order spatial accuracy for the convective flux of the Navier-Stokes equations can be achieved using upwind schemes. This process is based on the Godunov's first-order scheme [150] developed for the Lagrangean equations of ideal compressible flow, and followed by van Leer [181]. The Monotone Upstream-centred Scheme for Conservation Laws is referred to in the literature as the MUSCL approach, and was developed by van Leer [178]. This scheme builds on a first-order, Total Variation Diminishing (TVD) scheme for a second-order spatial accuracy. Instead of replacing the original state quantities by piecewise constant functions, MUSCL uses a linear function. These linear distributions make possible to attain second-order accuracy. The state quantities at the

interfaces can be obtained from an extrapolation of the neighbouring cells. To illustrate this idea, the extrapolation values at the right face of  $j + 1/2$  within cell  $j + 1$  is shown, where an uniform spacing in one dimension is used. The superscripts L and R refer to the left and right sides at the considered interface,

$$\mathbf{F}_{j+1/2}^L = \mathbf{F}_j + \Phi(r_j) \left[ \frac{k_1}{2} (\mathbf{F}_{j+1} - \mathbf{F}_j) + (1 - k_1) \vec{\nabla} \mathbf{F}_j \bullet \vec{\mathbf{r}}_{f_j} \right]. \quad (2.3)$$

$$\mathbf{F}_{j+1/2}^R = \mathbf{F}_{j+1} - \Phi(r_{j+1}) \left[ \frac{k_1}{2} (\mathbf{F}_{j+1} - \mathbf{F}_j) + (1 - k_1) \vec{\nabla} \mathbf{F}_{j+1} \bullet \vec{\mathbf{r}}_{f_{j+1}} \right]. \quad (2.4)$$

In Eqns. 2.3 and 2.4, the vectors  $\vec{\mathbf{r}}_{f_j}$  and  $\vec{\mathbf{r}}_{f_{j+1}}$  represent the distances between the cell-centre face  $j + 1/2$  and the cell-centre volumes  $j$ , and  $j + 1$ , respectively. The parameter  $k_1$  is used to provide different spatial accuracy and properties of the MUSCL-scheme. The value of  $k_1$  in the standard HMB is set up to zero which corresponds a linear interpolation at the interface against an upstream and a downstream cell, providing a 2nd-order upwind scheme.

To reconstruct the gradients  $\vec{\nabla} \mathbf{F}_j$  and  $\vec{\nabla} \mathbf{F}_{j+1}$  at cell-centre volumes  $j$  and  $j + 1$ , HMB uses a second-order finite difference approximation:

$$\vec{\nabla} \mathbf{F}_j \bullet \vec{\mathbf{r}}_{f_j} = \frac{1}{4} (\mathbf{F}_{j+1} - \mathbf{F}_{j-1}). \quad (2.5)$$

$$\vec{\nabla} \mathbf{F}_{j+1} \bullet \vec{\mathbf{r}}_{f_{j+1}} = \frac{1}{4} (\mathbf{F}_{j+2} - \mathbf{F}_j). \quad (2.6)$$

This formulation is less expensive than Green-Gauss or Least Squares methods [182], and it does not require to exchange data for parallel executions. So, this presents a compromise between accuracy and computational time. However, this approximation can not be used with high-order schemes, as discussed in chapter 4.

The limiter function is represented as  $\Phi(r)$ , and  $r_j = \frac{\mathbf{F}_j - \mathbf{F}_{j-1}}{\mathbf{F}_{j+1} - \mathbf{F}_j}$  and  $r_{j+1} = \frac{\mathbf{F}_{j+1} - \mathbf{F}_j}{\mathbf{F}_{j+2} - \mathbf{F}_{j+1}}$  are the ratio of successive gradients. This scheme has the properties of monotonicity, so does not produce non-physical solutions, such as expansion shocks which correspond to a negative entropy variation. In addition, the entropy condition is satisfied in the sense of Lax [183]. Introducing the

limiter function  $\Phi(r_j)$ , first and high-order schemes can be combined. In fact, if  $\Phi(r_j) = 0$  the first-order is activated but if  $\Phi(r_j) = 1$  a higher-order scheme is activated, which is at least second-order of accuracy. The HMB solver uses the alternative form of the van Albada limiter [179] namely,

$$\Phi(r) = \frac{2r}{r^2 + 1}. \quad (2.7)$$

Indeed, this limiter is activated in regions where large gradients are found due to shock waves and thin boundary layers, avoiding non-physical spurious oscillations. It is interesting to note that this limiter function is not second order TVD because this limiter cannot guarantee the following inequality for any  $r \in (1, 2)$ ,

$$1 \leq \Phi(r) \leq r. \quad (2.8)$$

The advantages of using this limiter function is that is differentiable for any value of  $r$ .

## 2.3 Turbulence Modelling

Understanding of turbulent flow behaviour has brought out an enormous interest in many fields of science. In aerospace, most fluid flows are turbulent, so their study and understanding are required. Despite the widespread development of computers in the last decade, which has allowed to boost the number of works in turbulence models, we do not understand in entire detail the turbulent flow behaviour. The Navier-Stokes equations, which were introduced in the early 19<sup>th</sup> Century by Navier and Stokes, present a few exact solutions due mainly to their non-linearity and variety of boundary conditions. The result of this complexity implied the introduction of simplifications and assumptions. The first investigation of transition from laminar to turbulent flow was carried out by Osborne Reynolds [184], injecting a dye streak into flow through a pipe. Further studies led him identify one of the most famous dimensionless parameter in turbulence, the Reynolds number  $Re$ , which expresses the relative importance of inertial and viscous forces [184]. Two physical phenomena are associated with turbulence. The first is the turbulence diffusion, which is

the transport of mass, momentum or heat from a system due to the chaotic time-dependent motion of fluid [185]. The second is the dissipation of the turbulent kinetic energy, which is dissipated by viscous forces at the Kolmogorov scale [186]. It seems likely that a turbulent flow can be characterised by the following features: chaotic motion, non-repeatability, large range of length and time scales, diffusion and dissipation, three dimensionality and rotationality [185]. A wide range of length and time scales are also important features of the turbulent flows. In fact, three sets of scales in turbulent flows are always present. The integral length scale, which is the largest and is associated to the highest energy structures, the Taylor length scales and Kolmogorov length scale, which is the smallest scales of the turbulence.

The work presented by Reynolds [184] in 1894, led to set the base of the decomposition of flow variables in mean and fluctuating parts. This description of the flow underlines a second idea, the use of statistics description of the turbulent flow. Most of the current turbulent models are based on these concepts.

### 2.3.1 The Reynolds-Averaging

In presenting different turbulent models, it is important to begin with key concepts, such as the Reynolds decomposition and averaging. The Reynolds decomposition of  $u(x, t)$ , separates the averaged and the fluctuating or random parts, of a signal obtained from a turbulent flowfield. These quantities can be expressed as,

$$u(x, t) = \bar{u}(x) + u'(x, t), \quad (2.9)$$

where  $\bar{u}(x)$  and  $u'(x, t)$  are averaged and fluctuating parts, respectively. Figure 2.1 shows the temporal behaviour of these quantities. It is clear from Figure 2.1 that the averaged part represents a steady quantity, while that the fluctuation part represents a random with mean zero.

As it has been mentioned, this decomposition is used to rewrite the Navier-Stokes equations introducing this formulation. This process has to be followed by the adoption of an averaging method. This entire formulation is widely known as Reynolds average.

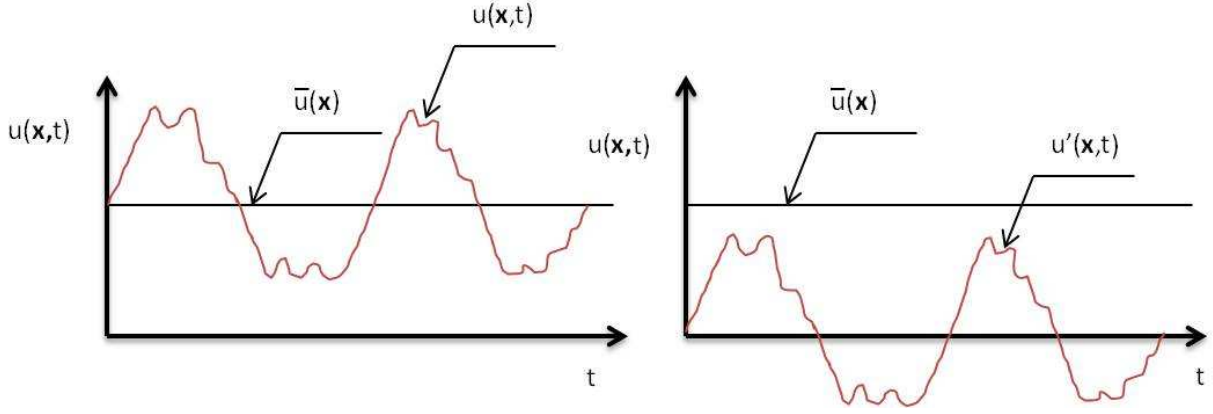


Figure 2.1: Reynolds decomposition in averaged and fluctuation part.

### Time Averaging

Let  $u(x, t)$  be an integrate function with respect to  $t$ , for  $t \rightarrow \infty$ . The time average of  $u$  is defined as,

$$\bar{u}(x) = \lim_{T \rightarrow \infty} \frac{1}{T} \int_0^T u(x, t) dt \quad (2.10)$$

This method is widely employed for statistically stationary turbulent flow where it is clear that the average can not be a function of the time, and  $T$  needs to be long enough relative to the maximum period of the assumed fluctuations. In fact, a compromise time step should be chosen, being large enough for the average of turbulent fluctuations to be zero, and small enough to resolve unsteadiness of the mean flow. For rotorcraft unsteady flows, the time step is often chosen as a time that is required for a rotor to cover an azimuth angle of  $0.25^\circ - 1^\circ$  [6, 187]. This range is also used throughout this work.

### 2.3.2 RANS and URANS

In this work the averaged Navier-Stokes equations were used. In a turbulent flow, the fields of density, velocity, pressure, and temperature vary randomly in time. Reynolds approach involves separating the flow quantities into stationary and random parts. The quantities are then presented as a sum of the mean flow value and the fluctuating part. The Reynolds-Averaged Navier-Stokes Equations can be derived employing the Reynolds decomposition and averaging mass, momentum,

and energy equations. The compressible Reynolds-Averaged Navier-Stokes equations (also known as the Favre-Averaged Navier-Stokes Equations) [188] can be written as follows:

$$\frac{\partial \bar{\rho}}{\partial t} + \frac{\partial}{\partial x_j}(\bar{\rho} \hat{u}_j) = 0. \quad (2.11)$$

$$\frac{\partial(\bar{\rho} \hat{u}_i)}{\partial t} + \frac{\partial}{\partial x_j}(\bar{\rho} \hat{u}_i \hat{u}_j) = -\frac{\partial \bar{P}}{\partial x_i} + \frac{\partial \bar{\sigma}_{ij}}{\partial x_j} + \frac{\partial \tau_{ij}}{\partial x_j}. \quad (2.12)$$

$$\frac{\partial(\bar{\rho} \hat{E})}{\partial t} + \frac{\partial}{\partial x_j}(\bar{\rho} \hat{u}_j \hat{H}) = \frac{\partial}{\partial x_j}(\bar{\sigma}_{ij} \hat{u}_i + \overline{\sigma_{ij} u_i''}) - \frac{\partial}{\partial x_j}(\bar{q}_j + c_p \overline{\rho u_j'' T''} - \hat{u}_i \tau_{ij} + \frac{1}{2} \overline{\rho u_i'' u_i'' u_j''}). \quad (2.13)$$

where  $\hat{H} = \hat{E} + \frac{\bar{P}}{\bar{\rho}}$  is the total enthalpy,  $\bar{q}_j = -\overline{k_T \partial T / \partial x_j} \approx -\frac{c_p \hat{\mu}}{Pr} \frac{\partial \hat{T}}{\partial x_j}$  is the heat flux vector, and the viscous stress tensor is:

$$\bar{\sigma}_{ij} \approx 2\hat{\mu} \left( \hat{S}_{ij} - \frac{1}{3} \frac{\partial \hat{u}_k}{\partial x_k} \delta_{ij} \right). \quad (2.14)$$

The Reynolds stress tensor is defined as  $\tau_{ij} = -\overline{\rho u_i'' u_j''}$ , defined in tensor notation. The term  $c_p$  represents the heat capacity at constant pressure, and  $Pr$  is the Prandtl number (around 0.72 for air). The overbar represents the conventional time-average mean. The hat represents the Favre or density-weighted average defined as:  $\hat{f} = \frac{\bar{\rho f}}{\bar{\rho}}$  where  $f = \bar{f} + f' = \hat{f} + f''$ . The Sutherland's Law is used here to relate the dynamic viscosity  $\hat{\mu}$  with the temperature of an ideal gas [189]:

$$\hat{\mu} = \mu_0 \left( \frac{\hat{T}}{T_0} \right)^{3/2} \left( \frac{T_0 + S}{\hat{T} + S} \right), \quad (2.15)$$

where  $\mu_0 = 1.716 \times 10^{-5}$  kg/(ms),  $T_0 = 273.15$  K, and  $S = 110.4$  K. Finally, the equation of state is written as:

$$\bar{P} = (\gamma - 1) \left( \bar{\rho} \hat{E} - \frac{1}{2} \bar{\rho} (\hat{u}^2 + \hat{v}^2 + \hat{w}^2) - \bar{\rho} k \right), \quad (2.16)$$

where  $\gamma$  is the heat capacity ratio and is often taken as 1.4 for air and  $k$  is the local turbulent kinetic energy  $k = [(\hat{u}_i'')^2 + (\hat{v}_i'')^2 + (\hat{w}_i'')^2]/2$ . We noted that there are more unknowns variables than equations. In fact, this is addressed via turbulence models. This problem is known in the literature



as the *turbulence closure problem* [185]. So the following terms need to be modelled:

$$\begin{aligned}
 & \tau_{ij}, \\
 & \overline{c_p \rho u_j'' T''}, \\
 & \overline{\sigma_{ij} u_i''}, \\
 & \frac{1}{2} \overline{\rho u_i'' u_i'' u_j''}.
 \end{aligned} \tag{2.17}$$

Note that most turbulence models use the Boussinesq eddy viscosity hypothesis, which states that the Reynolds stress tensor  $\tau_{ij}$  can be calculated as a product of the mean strain rate tensor  $\hat{S}_{ij}$  and the dynamic eddy viscosity  $\hat{\mu}_t$ .

$$\tau_{ij} = 2\hat{\mu}_t \left( \hat{S}_{ij} - \frac{1}{3} \frac{\partial \hat{u}_k}{\partial x_k} \delta_{ij} \right) - \frac{2}{3} \bar{\rho} k \delta_{ij}, \tag{2.18}$$

where  $\hat{S}_{ij} = (\partial \hat{u}_i / \partial x_j + \partial \hat{u}_j / \partial x_i) / 2$ , and  $\hat{\mu}_t$  is the eddy viscosity obtained by the turbulence model.

Likewise, a Reynolds analogy is used to model the turbulent heat flux:

$$\overline{c_p \rho u_j'' T''} \approx - \frac{c_p \hat{\mu}_t}{Pr_t} \frac{\partial \hat{T}}{\partial x_j}, \tag{2.19}$$

where  $Pr_t$  is the turbulent Prandtl number and often taken to be constant (around 0.9 for air).

Finally, the molecular diffusion and turbulent transport in the energy equation are often modelled together, for example:

$$\overline{\sigma_{ij} u_i''} - \frac{1}{2} \overline{\rho u_i'' u_i'' u_j''} \approx \left( \hat{\mu} + \frac{\hat{\mu}_t}{\sigma_k} \frac{\partial k}{\partial x_j} \right) \tag{2.20}$$

where  $\sigma_k$  is a coefficient associated with the turbulence model.

### 2.3.3 Turbulence Models

Various turbulence models are available in HMB, including several one-equation, two-equation, three-equation, and four-equation turbulence models. Furthermore, Large Eddy Simulation (LES), DES, and DDES are also available.

Two-equation turbulence models are the most popular type. Two transport equations are used for the calculation of the turbulence properties of the flow. Commonly, the turbulent kinetic energy  $k$ , is chosen as a transported variable. The second transported variable depends on the

employed two-equation model, and is used to estimate the turbulence scales. The most common two-equation models involve the turbulent energy dissipation rate  $\varepsilon$ , providing the rate at which the turbulent energy is dissipated by viscous effects at the Kolmogorov scale and the specific dissipation frequency  $\omega$  or any variable that determines the scale of the turbulence  $l$ . So, the eddy viscosity  $\hat{\mu}_t$  has to be calculated from the two transported equations.

### ***k*- $\omega$ and SST Model**

In 1988, Wilcox [190] developed the *k*- $\omega$  turbulence model, which has become very popular. This model uses as second extra transported variable the specific dissipation frequency  $\omega$ , which is function of the scale of the turbulence. The eddy viscosity is obtained by,

$$\hat{\mu}_t = \rho \frac{k}{\omega}. \quad (2.21)$$

In 1994, Menter [191] proposed the hybridation of the *k*- $\omega$  turbulence model and the *k*- $\varepsilon$  turbulence model. The aim was to combine the robust and accurate formulation of the *k*- $\omega$  model near the wall with the lack of sensitivity to free-stream values of the *k*- $\varepsilon$  model far away from the wall it. Table 2.1 lists the four versions of the *k*- $\omega$  models. A detailed description of the *k*- $\omega$  and *k*- $\omega$  SST models can be found in [190, 192, 191].

Table 2.1: Different types of *k*- $\omega$  turbulence models.

Model	Year
Wilcox [190]	1988
Wilcox [192]	1994
Menter [191] (baseline model)	1994
Menter [191] (SST model)	1994

### ***k*- $\omega$ SST- $\gamma$ Model**

It is well known that the fully-turbulent *k*- $\omega$  SST model predicts the transition onset further upstream than nature, requiring the use of transition models. In this regard, Menter *et al.* [193] developed a model for the prediction of laminar-turbulent transitional flows, involving two transport equations for the intermittency factor  $\gamma$  and the momentum thickness Reynolds number  $Re_{\theta_l}$ .

The intermittency factor  $\gamma$  is used to trigger and control the transition onset location, and it varies between 0 (laminar flow) to 1 (fully-turbulent flow). In 2015, a new one-equation local correlation-based transition model  $\gamma$  was proposed by Menter *et al.* [194], where the  $\text{Re}_{\theta_t}$  equation was avoided.

The form of the transport equation for the intermittency factor  $\gamma$  reads as:

$$\frac{\partial(\bar{\rho}\hat{\gamma})}{\partial t} + \frac{\partial(\bar{\rho}\hat{u}_j\hat{\gamma})}{\partial x_j} = P_\gamma - E_\gamma + \frac{\partial}{\partial x_j} \left[ \left( \hat{\mu} + \frac{\hat{\mu}_t}{\sigma_\gamma} \right) \frac{\partial \hat{\gamma}}{\partial x_j} \right], \quad (2.22)$$

where  $P_\gamma$  and  $E_\gamma$  represent the production and dissipation sources, respectively. A more detailed description of the  $\gamma$  equation can be found in [194].

### $\gamma$ - $\text{Re}_{\theta_t}$ Model

Transition turbulence models are also available in HMB through  $\gamma$ - $\text{Re}_{\theta_t}$  model developed in 2006 by Menter *et al.* [193]. Based on two transport equations: the equation for the intermittency factor  $\gamma$  and for the transition momentum thickness Reynolds number,  $\text{Re}_{\theta_t}$ . The intermittency factor  $\gamma$  is used to trigger and control the transition onset and varies between 0 (laminar flow) to 1 (fully turbulent flow). The momentum thickness Reynolds number is used to avoid non-local flow variables. This set of transport equations are written as:

$$\frac{\partial(\bar{\rho}\hat{\gamma})}{\partial t} + \frac{\partial\bar{\rho}\hat{u}_j\hat{\gamma}}{\partial x_j} = P_{\gamma 1} + P_{\gamma 2} + \frac{\partial}{\partial x_j} \left[ \left( \hat{\mu} + \frac{\hat{\mu}_t}{\sigma_\gamma} \right) \frac{\partial \hat{\gamma}}{\partial x_j} \right]. \quad (2.23)$$

$$\frac{\partial(\bar{\rho}\hat{R}e_{\theta_t})}{\partial t} + \frac{\partial(\bar{\rho}\hat{u}_j\hat{R}e_{\theta_t})}{\partial x_j} = P_{\theta_t} + \frac{\partial}{\partial x_j} \left[ \sigma_{\theta_t}(\hat{\mu} + \hat{\mu}_t) \frac{\partial \hat{R}e_{\theta_t}}{\partial x_j} \right]. \quad (2.24)$$

The production terms for intermittency  $\gamma$  and transition momentum thickness Reynolds number,  $\hat{R}e_{\theta_t}$  are given by  $P_{\gamma 1}$ ,  $P_{\gamma 2}$ , and  $P_{\theta_t}$  and can be found in [193].

### Transition Criteria

Transition criteria like the ones of Michel [195] and Cebeci-Smith [196] are also available in HMB solver. Both criteria are based on empirical correlations to estimate the location of the transition onset. Freestream turbulence intensity, transition Reynolds number, and momentum thickness

Reynolds number are used as parameters for these models. In 1951 [195] and 1952 [197], Michel developed a method based on measurements of two-dimensional, incompressible flows over flat plates with a weak pressure gradient. For the version one and two, the transition onset occurs when:

$$\hat{Re}_{\theta t, \text{tr}} = 2.9 Re_{x, \text{tr}}^{0.4}, \quad (2.25)$$

$$\hat{Re}_{\theta t, \text{tr}} = 1.174 Re_{x, \text{tr}}^{0.46}, \quad (2.26)$$

where  $\hat{Re}_{\theta t, \text{tr}}$  is the Reynolds number based on momentum thickness and  $Re_{x, \text{tr}}$  is the Reynolds number, based on the distance measured from the stagnation point. In fact, the transition point is estimated when,

$$Re_{\theta} \geq Re_{\text{Michel}}. \quad (2.27)$$

An improvement of Michel's criterion was proposed by Cebeci and Smith some years later. It states that the transition takes place where:

$$\hat{Re}_{\theta t, \text{tr}} = 1.174 \left( 1 + \frac{22,400}{Re_{x, \text{tr}}} \right) Re_{x, \text{tr}}^{0.46}, \quad (2.28)$$

which is applicable a wider range of local length Reynolds number,

$$1 \times 10^5 \leq Re_x \leq 4 \times 10^7. \quad (2.29)$$

## 2.4 Aerodynamic Models

For this work, two aerodynamic methods are employed to model rotor blades. The higher fidelity method includes the geometry of the blades in the computational domain and it will be referred to as Fully Resolved Blade (FRB). This methodology provides a full representation of the wake and detailed information of the source of unsteadiness of the flow. Furthermore, the boundary layers on the blades are resolved so the method provides the best estimate loads. The other aerodynamic model presented here is the Actuator Disk (AD) [10], which simulates the effect of the rotor blades by creating a pressure jump across an infinitesimally thin disk.

The actuator disk models employed in this work are now described. The first model is a Uniform Rotor Actuator Disk (URAD) while the second model allows for variable loading as function of the rotor radius and is named as Non-Uniform Rotor Actuator Disk (NURAD).

As previously introduced, the actuator disk simulates the effect of the rotor blades by creating a pressure difference on a single plane. For the case of uniform rotor actuator disk, the pressure jump in dimensionless form is:

$$\Delta P^* = \frac{T}{\rho_\infty V_\infty^2 S_{\text{rot}}}, \quad (2.30)$$

where the thrust coefficient is defined as  $C_T = \frac{T}{\rho_\infty V_{\text{tip}}^2 S_{\text{rot}}}$  with  $V_{\text{tip}}$  and  $S_{\text{rot}}$  being the blade-tip speed and the rotor-disk area, respectively.

The non-uniform rotor actuator disk calculates the jump of pressure across the disk plane based on Shaidakov's method [198]. This approach results in a non-uniform pressure distribution and as a function of radial position along the blade ( $r$ ) and blade azimuth  $\Psi$ . The model is based on the following equation:

$$\Delta P^* = P_0 + P_{1S} \sin(\Psi) + P_{2C} \cos(2\Psi), \quad (2.31)$$

where the coefficients  $P_0$ ,  $P_{1S}$  and  $P_{2C}$  depend on rotor radius and solidity, rotor attitude, advance ratio, thrust coefficient, lift coefficient slope and free-stream velocity. The model enables to account for blade tip offload and rotor reverse flow region. Its advantage is its efficiency and the ability to provide results with no iterative methods. Application examples of Shaidakov's model can be found in [199]. The model originates from the theory of an ideal lifting rotor in incompressible flow and it has been tuned for realism using flight tests data. A brief description of the model in its first approximation is given below.

In an incompressible flow, the pressure jump can be written as:

$$\Delta P = \rho_\infty \gamma \left[ \frac{\gamma \text{sign}(\delta)}{2} + V_\infty \cos(\alpha_\infty - \alpha + \delta) \right], \quad (2.32)$$

where  $\delta$  is the angle of the vortex cylinder slope,  $(\alpha_\infty - \alpha)$  is the actual incidence of the rotor inflow and  $\gamma$  is the distribution of the circulation on disk, which is decomposed in an average

component  $\gamma_0$  and a part dependent on the azimuth angle  $\gamma_\Psi$ , i.e.  $\gamma = \gamma_0 + \gamma_\Psi$ . The average blade loading distribution is written as:

$$\gamma_0 = m_1 r^2 (2 - r^2 - r^4), \quad (2.33)$$

while the azimuthal component of the circulation has the form

$$\gamma_\Psi = m_2 \mu_i \gamma_0 \left( \frac{1}{r} - \frac{25}{13} r \right) \sin(\Psi), \quad (2.34)$$

where  $\mu_i$  is the rotor advance ratio computed using both free-stream and induced velocities:  $\mu_i = (V_\infty + \overline{V}_{\text{ind}})/V_{\text{tip}}$ .

The average induced velocity is here estimated as follows:

$$\overline{V}_{\text{ind}} = \frac{1}{4} V_\infty \left[ -\cos(\alpha_\infty - \alpha + \delta) + \sqrt{\cos^2(\alpha_\infty - \alpha + \delta) + \text{sign}(\delta) \frac{C_T}{\mu^2}} \right] \tan(\delta^*), \quad (2.35)$$

where the angle  $\delta^*$  is defined as  $\delta^* = \left( \frac{\pi}{4} - \frac{|\delta|}{2} \right)$ . The coefficients of the model  $m_1$  and  $m_2$  have been calibrated using test data to give realistic results. In particular, they are determined by the formulas:

$$\begin{cases} m_1 = 1.989 V_\infty \left[ -\cos(\alpha_\infty - \alpha + \delta) + \sqrt{\cos^2(\alpha_\infty - \alpha + \delta) + 1.27 \frac{C_T}{\mu^2}} \right], \\ m_2 = \frac{8 \mu_i [1 + \tan^2(\delta^*)] + a \sigma \tan(\delta^*)}{[1 + \tan^2(\delta^*)][4 \mu_i + a \sigma \tan(\delta^*)]}, \end{cases} \quad (2.36)$$

where  $a$  is the lift coefficient slope and  $\sigma$  is the rotor solidity.

Figure 2.2 shows an overview of the relative position of the actuator disk for the ERICA tiltrotor for the transition corridor (left) and for the helicopter mode configurations (right).

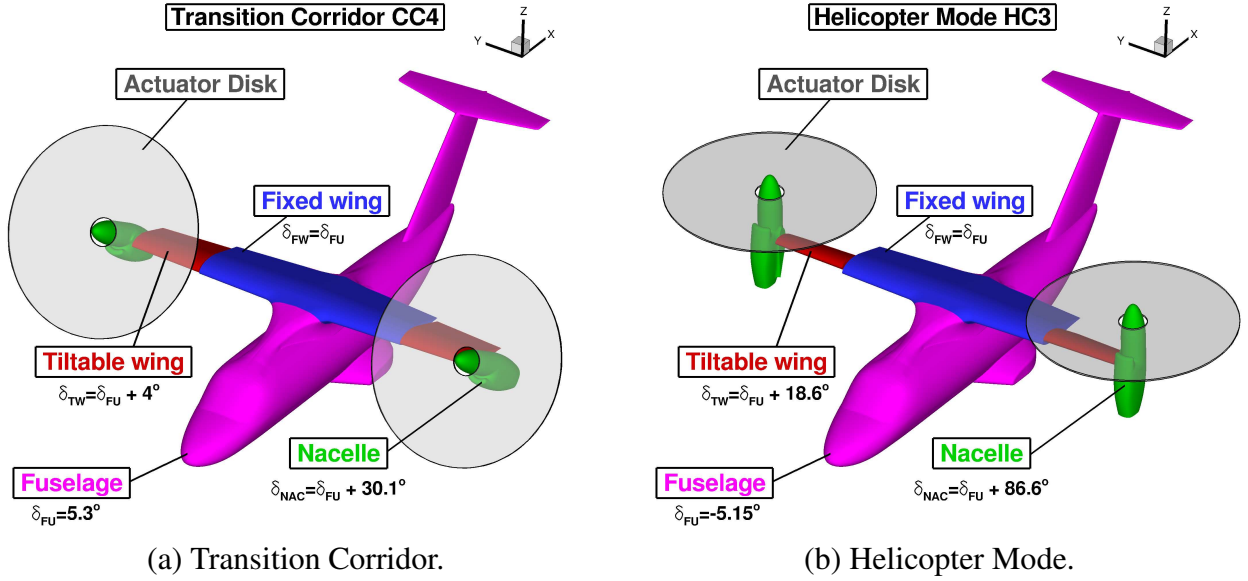


Figure 2.2: Set-up of the transition corridor (left) and helicopter mode (right) configurations with the rotor actuator disk.

## 2.5 Overset Grid Method

Overset grid and sliding plane methods are available in HMB [174, 200] to allow the relative motion between different mesh components. Both methods have been widely employed for isolated rotor blades, such as the UH-60A by Dehaeze *et al.* [201], S-76 by Jimenez *et al.* [202], XV-15 by Gates [101], and complete helicopter configurations [174]. For the present work, an overset grid method is employed to explore its capabilities with helicopter, propeller, and tiltrotor configurations.

The overset grid method, also referred to as chimera method, is based on structured composite grids with hexahedral elements, consisting of independently generated, overlapping non-matching sub-domains. A hierarchical approach is employed allowing to interpolate the solution variables based on an user-specified hierarchy of sub-domains. The interpolation between composite grids depends on a localisation procedure, that includes a localisation pre-processing and a chimera search which aim is to minimise the number of searches due to potential mesh overlap. Three methods are available to control the interpolation needed for the chimera solution; zero order single-neighbour, inverse distance, and variable-distribution reconstruction-based interpola-

tion. Further information about the implementation of the overset grid method in HMB can be found in [200].

## 2.6 Optimisation Framework

The employed optimisation framework is based on the Least-Square Sequential Quadratic Programming (SLSQP) algorithm, coupled with the HMB3 CFD solver and to a discrete adjoint method with full accounting of the Menter's  $k-\omega$  turbulence model coupling terms. The linear system for the adjoint variable is solved using a Flexible Generalised Minimum Residual solver with Deflated Restarting (FGMRES-DR) nested with GMRES-DR as a preconditioner [203].

An economic way to obtain the flow gradients with CFD is the adjoint method, which reduces the cost function derivatives evaluation to about the cost of the base flow solution, regardless of the number of design variables [204]. The underlying idea is to write explicitly the cost function  $I$  in terms of the flow variables  $\mathbf{W}$  and of the design variables  $\boldsymbol{\alpha}$ , that is,  $I = I(\mathbf{W}(\boldsymbol{\alpha}), \boldsymbol{\alpha})$ . The flow variables are subject to satisfy the governing equations (*e.g.* the Reynolds Averaged Navier–Stokes equations) written in compact form as

$$\mathbf{R}(\mathbf{W}(\boldsymbol{\alpha}), \boldsymbol{\alpha}) = 0. \quad (2.37)$$

Formally, taking the derivative of  $I$  with respect to  $\boldsymbol{\alpha}$  we obtain:

$$\frac{dI}{d\boldsymbol{\alpha}} = \frac{\partial I}{\partial \boldsymbol{\alpha}} + \frac{\partial I}{\partial \mathbf{W}} \frac{\partial \mathbf{W}}{\partial \boldsymbol{\alpha}}. \quad (2.38)$$

By introducing the adjoint variable  $\boldsymbol{\lambda}$  as the solution of the following linear system:

$$\left( \frac{\partial \mathbf{R}}{\partial \mathbf{W}} \right)^T \boldsymbol{\lambda} = - \left( \frac{\partial I}{\partial \mathbf{W}} \right)^T, \quad (2.39)$$

equation (2.38) can be rewritten as:

$$\frac{dI}{d\boldsymbol{\alpha}} = \frac{\partial I}{\partial \boldsymbol{\alpha}} + \boldsymbol{\lambda}^T \frac{\partial \mathbf{R}}{\partial \boldsymbol{\alpha}}, \quad (2.40)$$

which is known as the *dual* form of the sensitivity equation. The computation of the derivatives of the functional  $I$  is reduced to the solution of the linear sensitivity problem (2.39)-(2.40). The



computational cost scales with the number of outputs, since the right-hand side of the linear system (2.39) depends on  $I$ , but it is independent of the input parameters. The linear system (2.39) is usually hard to compute, since the Jacobian matrix  $\partial \mathbf{R} / \partial \mathbf{W}$  is characterised by a high stiffness, and the solution time can be comparable to that of the base flow.

The HMB3 flow solver uses two methods for solving the linear system (2.39). The first is an implicit, fixed-point iteration scheme [204], while the second is a nested FGMRES-DR/GMRES-DR Krylov-subspace method [203]. Both adjoint solvers can be interfaced to a gradient based optimiser to efficiently solve a design problem, which amounts in minimising an objective function  $I$  (*e.g.* drag, power, etc.), possibly subject to constraints (*e.g.* fixed lift, fixed thrust, etc.). In the current implementation, the optimisation problem is solved using a Least-Square Sequential Quadratic Programming (SLSQP) algorithm [205].

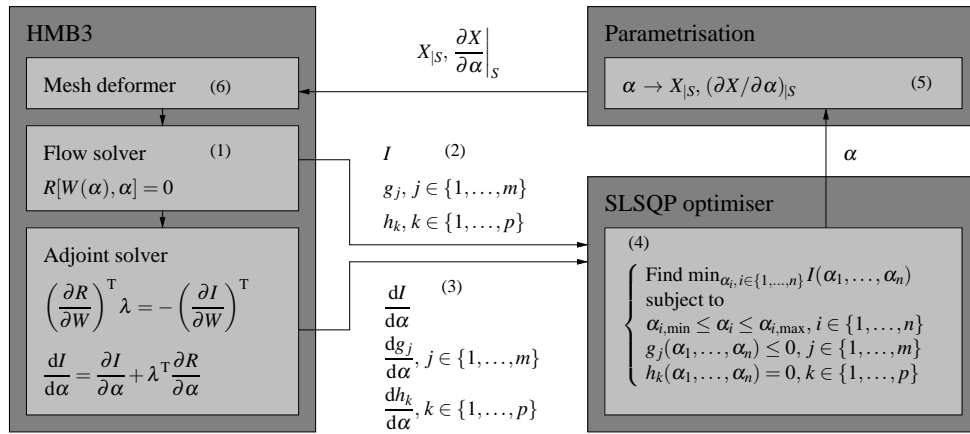


Figure 2.3: Flow chart of the optimisation process.

The design optimisation procedure is described in Figure 2.3, and can be summarised as follows.

- 1 The flow around the aerodynamic surface  $S$  to be optimised (*e.g.* aerofoil, blade, etc.) is solved. For the first iteration, this solution represents the baseline flow solution.
- 2 The objective function  $I$  and the constraints  $g_j, j \in \{1, \dots, m\}, h_k, k \in \{1, \dots, p\}$ , are evaluated from the flow solution.

- 3 The adjoint problem is solved to compute the gradients  $dI/d\alpha$ ,  $dg_j/d\alpha$ ,  $j \in \{1, \dots, m\}$ ,  $dh_k/d\alpha$ ,  $k \in \{1, \dots, p\}$ .
- 4 The cost functional, the constraints and their gradients are fed to the gradient based optimiser, which produces a new set of design variables  $\alpha$ , corresponding to a design candidate in the search direction.
- 5 Based on the new values of the design variables  $\alpha$ , the point vector  $X|_S$  describing the surface  $S$  is updated, as well as the derivatives of these points with respect to the design variables  $(\partial X/\partial \alpha)|_S$ .
- 6 A mesh deformation algorithm, based on Inverse Distance Weighting (IDW) [203], computes the new volume mesh points positions  $X$ , and the derivatives  $\partial X/\partial \alpha$ . A new surface  $S$  is generated to close the cycle.

Steps 1–6 are repeated for several design cycles until convergence criteria are met. These criteria include checks on the objective function gradient module, and checks on the variation of the design variables and of the objective function between successive cycles of the optimisation process.

## 2.7 Visualisation of Vortical Flows

This section briefly presents the method used to visualise vortex cores. In fact, vortex cores are widely related to the generation of vorticity. This variable is a mathematical definition, it is not a physical property of the flow. By contrast, many phenomena, such as the formation and motion of vortex rings, are more easily understood in term of vorticity rather than pressure or velocity.

Visualisation of vortex cores, shed vorticity, and flow direction are visualised using iso-surfaces of  $Q$  criteria [206]. The quantity  $Q$  is defined as follows:

$$Q = \frac{1}{2}(\hat{\Omega}_{ij}\hat{\Omega}_{ij} - \hat{S}_{ij}\hat{S}_{ij}), \quad (2.41)$$

where  $\hat{\Omega}_{ij}$  and  $\hat{S}_{ij}$  are the antisymmetric and symmetric part of the velocity gradient, respectively:

$$\hat{\Omega}_{ij} = \frac{1}{2} \left( \frac{\partial \hat{u}_i}{\partial x_j} - \frac{\partial \hat{u}_j}{\partial x_i} \right), \quad \hat{S}_{ij} = \frac{1}{2} \left( \frac{\partial \hat{u}_i}{\partial x_j} + \frac{\partial \hat{u}_j}{\partial x_i} \right). \quad (2.42)$$

The quantity  $Q$  has the dimensions of a velocity squared divided by a length squared, and it is therefore nondimensionalised in HMB as follows:

$$\tilde{Q} = Q \left( \frac{L_{\text{ref}}}{V_{\text{ref}}} \right)^2. \quad (2.43)$$

# Chapter 3

## Aeroacoustic Method

This chapter describes the in-house acoustic code Helicopter Ffowcs Williams-Hawkings (HFWH), and the integration of the acoustic solver BENP of Leonardo Helicopters with the HMB CFD solver. The HFWH solver is used to assess the effect of the tip shapes on the noise levels radiated by the S-76 helicopter and XV-15 tiltrotor blades in chapters 5 and 7, respectively. Comparison with theory in terms of thickness and loading noise predictions at the rotor-disk plane is also shown in these chapters. Thus, both terms are presented here. A description of the inputs required by the acoustic solver BENP is also presented. The process carried out to build the acoustic pressure sphere from a HMB CFD solution, and the input needed by BENP are presented. Two cases corresponding to the S-76 rotor blade in hover and the AW-139 rotor blade in forward flight are provided as examples. In the case of the AW-139, a comparison between HMB and other numerical tools in terms of fluctuation of pressure on the acoustic pressure sphere located at  $r/R=1.1$  was carried out.

### 3.1 Helicopter Ffowcs Williams-Hawkings

The Helicopter Ffowcs Williams-Hawkings tool is described here. It is used to predict farfield noise of rotors. This method solves the Farassat 1A formulation (also known as retarded-time formulation) of the original FW-H equation [207], which is mathematically represented by the

well-known integral equation;

$$P'(\mathbf{x}, t) = \underbrace{\frac{1}{4\pi} \frac{\partial}{\partial t} \int_{f=0} \left[ \frac{\rho_\infty v_n}{r(1-M_r)} \right]_{\text{ret}} dS}_{\text{thickness noise}} + \underbrace{\frac{1}{4\pi a_\infty} \frac{\partial}{\partial t} \int_{f=0} \left[ \frac{P \cos(\theta)}{r(1-M_r)} \right]_{\text{ret}} dS + \frac{1}{4\pi} \int_{f=0} \left[ \frac{P \cos(\theta)}{r^2(1-M_r)} \right]_{\text{ret}} dS}_{\text{loading noise}}. \quad (3.1)$$

The first and second terms on the right-hand of Eqn. 3.1 are integrated over the surface  $f=0$ , which is a function that describes the source surface. The local normal velocity of the source surface is  $v_n$ ,  $M_r = M_i \hat{r}_i$  is the Mach number of the source in the radiation direction;  $r$  is the distance between observer and source defined as  $r = |\mathbf{x} - \mathbf{y}|$ ,  $P$  denotes the surface pressure, and the subscript  $\text{ret}$  denotes the retarded time  $\tau$ , which is determined as follows:

$$|\mathbf{x} - \mathbf{y}(\eta, \tau)| = a_\infty(t - \tau), \quad (3.2)$$

where  $t$  is the emission time and  $\eta$  is the Lagrangian variable of a point on the moving surface  $f=0$  (see Figure 3.1).

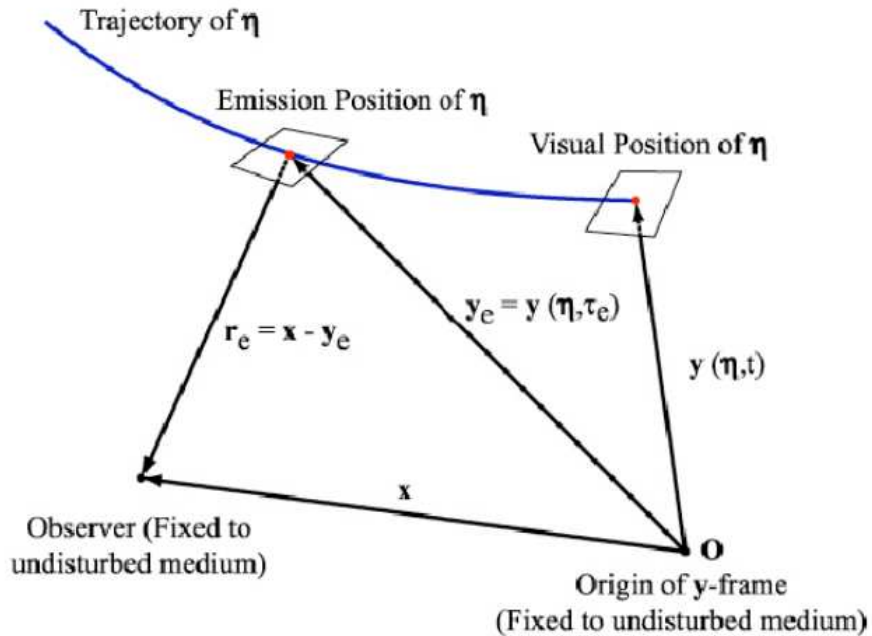


Figure 3.1: Illustration of the trajectory of a source point  $\eta$  relative to a fixed observed [208].

The first term on the right-hand, represents the noise due to the displacement of the fluid as

the body passes, which known as thickness noise. Since this term being associated with a zero spatial derivative, a monopole contribution of the radiation is found. The second term represents the noise resulting from the motion of the pressure and viscous stresses on the body surface, which is the main source of loading, blade-vortex-interaction, and broadband noise [137]. This term is associated with a dipole contribution of the radiation (one spacial derivative). If the flowfield is not transonic or supersonic, both source terms accurately predict the noise [137]. Note that the quadrupole contribution is assumed zero. However, when the flowfield becomes transonic or supersonic, this term is required to provide accurate prediction of the total noise. This source of noise accounts for the nonlinearities due to the local variation of speed of sound and fluid velocity. Note that angle  $\theta$  is defined as local angle between the normal to the surface and the radiation direction at the emission time.

For cases where the 3D term is not needed, HFWH requires as input the geometric location for radial sections of the rotor blade. Likewise, values of the pressure, density, and three components of the velocity at the centre of each panel are required. Figure 3.2 shows the surface of the S-76 rotor blade with 60% taper-35° degrees swept tip with example locations of the spanwise sections. Due to the sensitivity of the loads near the blade tip (from 95% $R$  to 100% $R$ ), clustering of the sections is required.

A comparative study of the effect of different tip configurations on the noise levels radiated by the S-76 model main rotor and XV-15 tiltrotor blades will be presented in chapters 5 and 7, respectively, using the HFWH solver.

Due to the lack of experimental data for the S-76 and XV-15 acoustics, a comparison with the theory will be conducted in terms of thickness and loading noise predictions. Both analytical solutions are based on the work of Gopalan *et al.* [209, 210] and have been successfully employed in the helicopter community [208]. The key idea was to convert the FW-H integral equations to an explicit algebraic expressions. In the case of the hover configuration and for an observer located at the rotor disk plane, the acoustic pressure due to blade thickness noise  $p'_T$ , is written in the

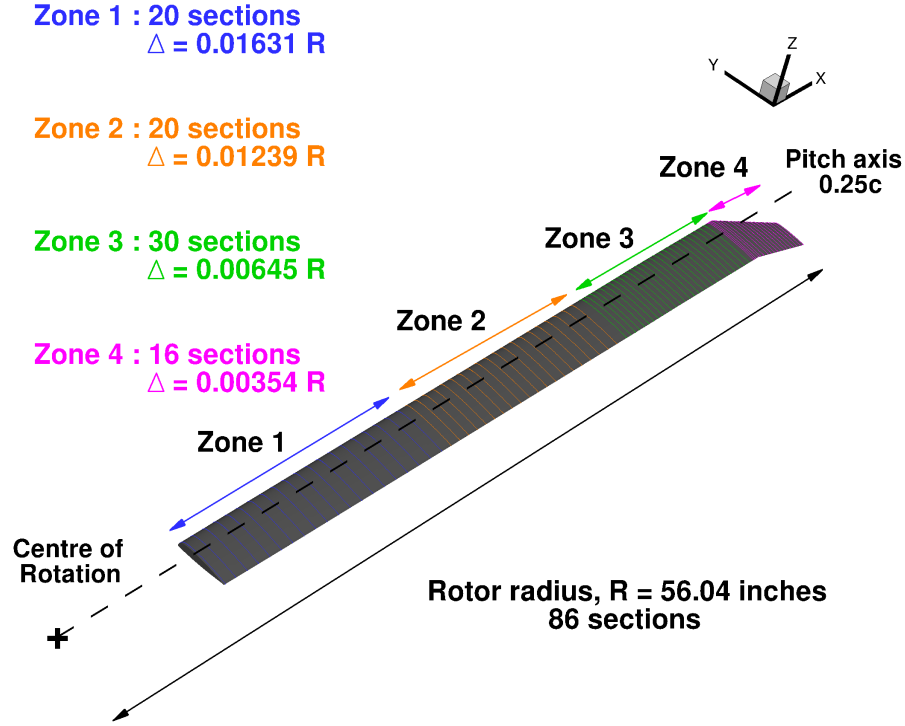


Figure 3.2: Distributions of radial sections along the spanwise direction of the S-76 rotor blade with 60% taper-35° degrees swept tip.

form [209]:

$$P'_T(\mathbf{x}, t) = \frac{\rho_\infty a_\infty^2}{2} F_H F_\epsilon T_M, \quad (3.3)$$

where  $F_H = R/r_H$  is a distance factor, where  $r_H$  is the distance from the rotor hub.  $F_\epsilon = A_\epsilon/S_{\text{rot}}$  represents the aerofoil shape factor, where  $A_\epsilon$  is the aerofoil cross sectional area and  $S_{\text{rot}}$  is the rotor disk area.  $T_M$  is the thickness factor written as:

$$T_M(\Psi) = \frac{M_{\text{tip}}^3}{12} \times \left( \frac{(M_{\text{tip}} \sin(\Psi) - 3) \sin(\Psi)}{(1 - M_{\text{tip}} \sin(\Psi))^3} + \frac{M_{\text{tip}} \cos^2(\Psi)}{10(1 - M_{\text{tip}} \sin(\Psi))^4} \times \right. \\ \left. \left( 50 + 39M_{\text{tip}}^2 - 45M_{\text{tip}} \sin(\Psi) - 11M_{\text{tip}}^2 \sin^2(\Psi) + 12M_{\text{tip}}^3 \sin(\Psi) - 18M_{\text{tip}}^3 \sin^3(\Psi) \right) \right). \quad (3.4)$$

where  $\Psi$  is the local azimuth angle. It is interesting to say that the theoretical thickness noise mainly depends on geometric parameters of the blade. Hence, the effect of the tip shape cannot be assessed by this theory.

Likewise, the acoustic pressure due to the theoretical blade loading for an observer located

at the rotor disk plane can be written as [209]:

$$P'_L(\mathbf{x}, t) = \frac{\rho_\infty a_\infty^2}{2} F_H F_T L_M, \quad (3.5)$$

where  $F_T = \frac{1}{60\sqrt{2}N_b} \left( \frac{T}{\rho_\infty a_\infty^2 A} \right)^{3/2}$ , and  $L_M$  is the loading factor:

$$L_M(\Psi) = \cos(\Psi) (1 - M_{\text{tip}} \sin(\Psi))^{-3} \times \left( 60 + 30M_{\text{tip}}^2 \cos^2(\Psi) - 120M_{\text{tip}} \sin(\Psi) \right. \\ \left. - 30M_{\text{tip}}^3 \sin(\Psi) \cos^2(\Psi) + 80M_{\text{tip}}^2 \sin^2(\Psi) + 9M_{\text{tip}}^4 \sin^2(\Psi) \cos^2(\Psi) - 20M_{\text{tip}}^3 \sin^3(\Psi) \right). \quad (3.6)$$

The source code of the theoretical thickness and loading noise can be found in Appendix A.

## 3.2 BENP Acoustics

The acoustic method BENP [211] of Leonardo Helicopters (see Figure 3.3) was integrated with the HMB solver [173, 174, 6]. Until recently, the three-dimensional panel method ADPANEL [103] combined with a free-wake Constant Vorticity Contour CVC [212] approach was the aerodynamic input to BENP. BENP solves the FW-H equation [207], following Farassat's 1A formulation [137]. Because ADPANEL is only able to evaluate the unsteady pressure for each panel node on the blade surface, BENP cannot assess the quadrupole terms of the FW-H equation from ADPANEL only.

The acoustic solver BENP requires:

- Geometric location of the nodes on the acoustic surface mesh.
- Definition of the body motion and systems of references.
- Aeroelastic data of the blade.
- Aerodynamic data of the blade.
- Location of the microphones/observers.
- General parameters.



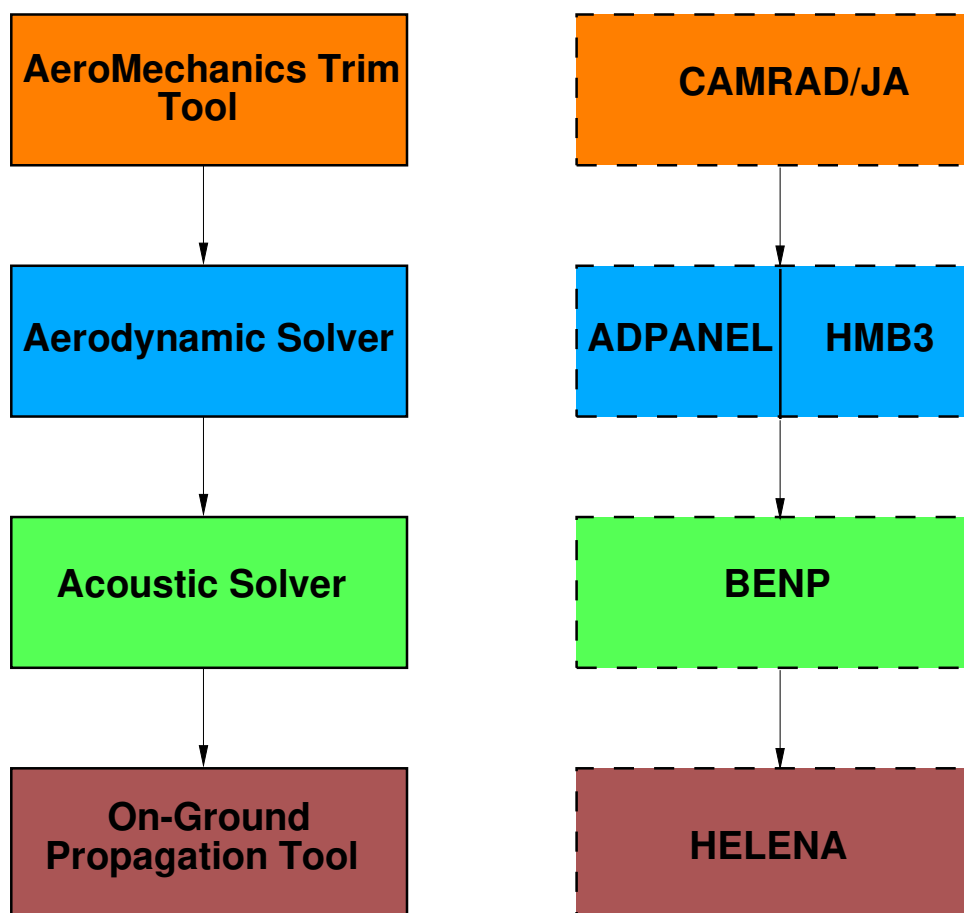


Figure 3.3: Leonardo Helicopters aeroacoustic computational chain. CAMRAD/JA [213] is a tool used to evaluate a required trim state, ADPANEL [103] and HMB are used as aerodynamic solvers, BENP is the main acoustic solver, and HELENA [214] is used to propagate the acoustic sphere to the locations of the microphones. More details of these solvers can be found in [215, 6].

The input file and variables relative to the geometric location of the nodes on the acoustic surface mesh are described in Table 3.1. This file is referred to as BENP1. The second input file describes the motion of each body, where initial position, linear velocity, and rotational frequency are defined. Tables 3.2 and 3.3 present each variable used in this file, which is referred to as BENP2. Likewise, the aeroelastic file of the acoustic solver BENP is described in Table 3.4. This file is referred to as BENP3. Finally, the aerodynamic file of the acoustic solver BENP is presented in Tables 3.5-3.7. The reference systems for the aerodynamic loads are also shown. This file is referred to as BENP4.

Table 3.1: Geometric file of the acoustic solver BENP refers to as BENP1.

NBODY	Total number of bodies
NNOD(nb)	Total nodes of body nb
NPAN(nb)	Total panels of body nb
DEFBOD(nb)	Not used (set to 0)
OPDEF(nb)	Not used (set to 0)
KGEOX(nb)	Scale factor for the X-coordinate of the nodes of the body nb
KGEOY(nb)	Scale factor for the Y-coordinate of the nodes of the body nb
KGEOZ(nb)	Scale factor for the Z-coordinate of the nodes of the body nb
X(nb,i)	X-coordinate of the $i$ -th node of the body nb in the OC system
Y(nb,i)	Y-coordinate of the $i$ -th node of the body nb in the OC system
Z(nb,i)	Z-coordinate of the $i$ -th node of the body nb in the OC system
NP(nb,i)	Numerical label of the $i$ -th panel of the body nb
TPAN(nb,i)	Type of the $i$ -th panel of the body nb 203: Surface with triangular panels with 3 nodes 204: Surface with rectangular panels with 4 nodes 206: Surface with triangular panels with 6 nodes 208: Surface with rectangular panels with 8 nodes 209: Surface with rectangular panels with 9 nodes 308: Hexahedron with 8 nodes
N1(nb,j)	Numerical label of the node of the body nb, which represents the first vertice of the panel $j$
N2(nb,j)	Numerical label of the node of the body nb, which represents the second vertice of the panel $j$
Nv(nb,j)	Numerical label of the node of the body nb, which represents the last vertice of the panel $j$

Table 3.2: Motion file of the acoustic solver BENP refers to as BENP2 - continued.

X0(nb)	Initial position of the X-coordinate of the body nb at the reference time TEMPORIF
Y0(nb)	Initial position of the Y-coordinate of the body nb at the reference time TEMPORIF
Z0(nb)	Initial position of the Z-coordinate of the body nb at the reference time TEMPORIF
VX(nb)	X-component of the linear velocity of the body nb
VY(nb)	Y-component of the linear velocity of the body nb
VZ(nb)	Z-component of the linear velocity of the body nb
TEMPORIF(nb)	Reference time (the body is at X0, Y0, Z0 position)
NFREQ(nb)	Number of harmonics for the rigid body nb
RIFROT(nb)	Reference system used if more than two harmonic oscillations of the body nb are prescribed RIFROT=0 RIFROT=1

Table 3.3: Motion file of the acoustic solver BENP refers to as BENP2 - concluded.

NF(nb)	Specifies the harmonic oscillation of the body nb
FREQ(nb,nf)	Frequency of the harmonic oscillation of the rigid body nb
TFREQR(nb)	Unit of measurement of the frequency FREQ TFREQ=1: $(2\pi f = (2\pi)/T)$ TFREQ=2: $f$ in Hz TFREQ=3: $T$ in sec
TIPROT(nb,nf)	Axis of the system (OC) of the harmonic oscillation nf of the rigid body nb
AMP0(nb,nf)	Static component of the amplitude of the harmonic oscillation of the body nb
AMP(nb,nf)	Sinusoidal component of the amplitude of the harmonic oscillation of the body nb
SFASR(nb,nf)	Phase shift of the sinusoidal component of the amplitude of the harmonic oscillation nf of the rigid body nb
TRIFR(nb,nf)	Reference time of the phase shift of the harmonic oscillation nf of the rigid body nb
XF(nb,nf)	X-coordinate of the point Q in the reference system OC, where the harmonic oscillation nf of the rigid body nb is expressed
YF(nb,nf)	Y-coordinate of the point Q in the reference system OC, where the harmonic oscillation nf of the rigid body nb is expressed.
ZF(nb,nf)	Z-coordinate of the point Q in the reference system OC, where the harmonic oscillation nf of the rigid body nb is expressed.
OMEGA(nb)	Angular velocity of the body nb around the Z-axis of the reference system OF
TFREQ(nb)	Unit of measurement for the angular velocity OMEGA TFREQ=1: $(2\pi f = (2\pi)/T)$ TFREQ=2: $f$ in Hz TFREQ=3: $T$ in sec
ALFA0(nb)	Rotation at the time TRIFALFA of the body nb around the Z-axis in the reference system (OF). Expressed in degrees
TRIFALFA(nb)	Defines the initial time at which the body nb is rotated an angle ALFA0
XALFA(nb)	X-coordinate of the point P where the body nb rotates with angular velocity OMEGA
YALFA(nb)	Y-coordinate of the point P where the body nb rotates with angular velocity OMEGA
ZALFA(nb)	Z-coordinate of the point P where the body nb rotates with angular velocity OMEGA
ROTX	Rotation (in degrees) around the X-axis of the reference system OF respect to OG
ROTY	Rotation (in degrees) around the Y-axis of the reference system OF respect to OG
ROTZ	Rotation (in degrees) around the Z-axis of the reference system OF respect to OG
SX(nb)	X-coordinate of the displacement of the body nb at the initial time with respect to the X0 data
SY(nb)	Y-coordinate of the displacement of the body nb at the initial time with respect to the Y0 data
SZ(nb)	Z-coordinate of the displacement of the body nb at the initial time with respect to the Z0 data

Table 3.4: Aeroelastic file of the acoustic solver BENP refers to as BENP3.

OPMODES(nb)	Enable/disable the elastic deformation of the body nb
NM(nb)	Specifies which of the NFREQM modes that the data follows is referred to
FREQM(nb,nm)	Frequency of the mode nm of the body nb
TFREQM(nb)	Unit of measurement for the frequency FREQM TFREQM=1: $(2\pi f = (2\pi)/T)$ TFREQM=2: $f$ in Hz TFREQM=3: $T$ in sec
AMPM(nb,nf)	Sinusoidal component of the amplitude of the mode nm
SFASM(nb,nf)	Phase shift
TSFASM(nb,nf)	Reference time of the phase shift
DX(nb,nm,nn)	X-coordinate of the node nn of the body nb due to the mode nm
DY(nb,nm,nn)	Y-coordinate of the node nn of the body nb due to the mode nm
DZ(nb,nm,nn)	Z-coordinate of the node nn of the body nb due to the mode nm

Table 3.5: Aerodynamic file of the acoustic solver BENP refers to as BENP4 - continued.

INOISE(nb)	Enable/Disable the calculation of the noise on the body nb INOISE=0, Disable the calculation of the noise on the body nb INOISE=1, Enable the calculation of the noise on the body nb
ISCATT(nb)	Enable/Disable the calculation of the scattering boundary conditions of the body nb ISCATT=0, Do not use the body nb for the calculation of the scattering boundary conditions ISCATT=1, Use the body nb for the calculation of the scattering boundary conditions
SCATT(nb)	Enable/Disable the calculation of the scattering of the body nb SCATT=0, Disable the calculation of the scattering on the body nb SCATT=1, Enable the calculation of the scattering on the body nb
AER(nb)	Enable/Disable the calculation of the aerodynamic loads on the body nb AER=0, Disable the calculation of the aerodynamic loads on the body nb AER=1, Enable the calculation of the aerodynamic loads on the body nb
AUS2(nb)	Specifies if the body nb is the wake of another body nb1 AER=0, nb is not a wake AER=1, nb is a wake
ITGMOD(nb)	Specifies the kind of integration on the panel and the definition of the aerodynamic loads ITGMOD=1, Standard integration. Aerodynamic loads are defined on the nodes of each panel ITGMOD=2, The integration is performed using the average of the aerodynamic loads in the nodes, multiplied by the area of the panel Aerodynamic loads are defined on the nodes of each panel ITGMOD=3, The integration is performed using the value at the centroid, multiplied by the area of the panel Aerodynamic loads are defined on the centroid of each panel

Table 3.6: Aerodynamic file of the acoustic solver BENP refers to as BENP4 - continued.

MODLOD(nb)	Specifies where the aerodynamic loads are defined MODLOD=0, Aerodynamic loads are defined on the centroid of each panel MODLOD=1, Aerodynamic loads are defined on the node of each panel
KTH	Scale factor for the thickness noise
KL1	Scale factor for the far field loading noise
KL2	Scale factor for the near field loading noise
KV1	Scale factor for the very near field quadrupole noise
KV2	Scale factor for the near field quadrupole noise
KV3	Scale factor for the farfield quadrupole noise
KV4	Scale factor for the quadrupole noise
KQ1	Scale factor for the surface quadrupole
KQ2	Scale factor for the surface quadrupole
KQN	Scale factor for the surface quadrupole
KQD	Scale factor for the surface quadrupole
KQT	Scale factor for the surface quadrupole
KQQ	Scale factor for the surface quadrupole
DTH	Displays the time history of the thickness noise
DL1	Displays the time history of the farfield loading noise
DL2	Displays the time history of the near field loading noise
DV1	Displays the time history of the very near field quadrupole noise
DV2	Displays the time history of the near field quadrupole noise
DV3	Displays the time history of the farfield quadrupole noise
DV4	Not used (set to 0)
DQ1	Not used (set to 0)
DQ2	Not used (set to 0)
DQN	Not used (set to 0)
DQD	Not used (set to 0)
DQT	Not used (set to 0)
DQQ	Not used (set to 0)
DLD	Displays the time history of the loading noise
DLT	Displays the time history of the thickness and loading noise
DVT	Displays the time history of the volume terms V1,V2, and V3
DSQ	Not used (set to 0)
DTT	Displays the time history of the total noise
TN(nb)	Specifies the type computation performed TN=0, Calculation of the thickness and loading noise TN=1, Calculation of the surface quadrupole TN=2, Calculation of the volume quadrupole TN=3, Calculation of the Kirchhoff formulation TN=4, Calculation of the KFWH formulation TN=101, Aerodynamic calculation (nodes of the wake) TN=102, Aerodynamic calculation (nodes of the body) TN=200, Calculation of scattering with uniform flowfield TN=211, Calculation of scattering with non uniform flowfield

Table 3.7: Aerodynamic file of the acoustic solver BENP refers to as BENP4 - concluded.

RIF	Reference system for the aerodynamic loads RIF=0, Panel reference system (OP) RIF=1, Fixed omega reference system (OF) RIF=2, Rotational omega reference system (OR) RIF=3, General reference system (OG)
FREQL(nb)	Frequency of the body nb
TFREQL(nb)	Unit of measurement for the frequency FREQ TFREQL=1: $(2\pi f = (2\pi)/T)$ TFREQL=2: $f$ in Hz TFREQL=3: $T$ in sec
SFASLOO(nb)	Phase shift of the aerodynamic loads with respect to the given time history
STOPPERIOD	If True, stops the computation if the delayed time needs aerodynamic data outside of the given time history
MODELOD	Definition of the time history for the aerodynamic loads MODELOD=0, Each node has associated a time history MODELOD=1, Each node has a pointer to a time history
COMPRESS NPNT	Not used (set to False) Number of points in the time history with frequency FREQL at which the data is given
NLOD	Pointer to time history of the node (or centroid)
SFAS	Phase shift of aerodynamic loads associated to node (or centroid) NN
NNLOD	Number of the time history defined
NL	Time history of the following aerodynamic data
TIME	Dimensionless time refers to the aerodynamic data
FX	X-component of the aerodynamic force per unit of area
FY	Y-component of the aerodynamic force per unit of area
FZ	Z-component of the aerodynamic force per unit of area
VX	X-component of the fluctuation velocity of the fluid
VY	Y-component of the fluctuation velocity of the fluid
VZ	Z-component of the fluctuation velocity of the fluid
PVAL	Pressure value
PENNE	Derivate of the pressure in the normal direction of the surface
PTIME	Temporal derivate of the pressure
RHO	Density value
DIV	Not used (set to 0)
COLAUT	If True, enables the automatic computation of the collocation point for the method CHUIF
TSTEPCOL	Defines the number of collocation points
FREQCOL	Frequency used for the determination of the optimal distance of the collocation point
TFREQCOL	Type of frequency TFREQCOL
TCOL	Type of collocation of CHIEF TCOL=11 Equation based on internal node TCOL=12 Equation based on internal node and added to the equation of the superficial node
NCOLINT	Set to 0

The process to build an acoustic sphere is presented here. A sphere is located at  $r/R=1.1$  from the origin of the S-76 rotor blade. The choice of this specific radius ( $r/R=1.1$ ) is dictated by diffusion and dispersion errors associated to the CFD numerical scheme, and the requirements of a large enough control surface to contain all noise sources. First, a surface mesh of the acoustic sphere was generated. Figure 3.4 shows the geometry and mesh of the acoustic pressure sphere for the S-76 rotor blade, which contains 21,400 nodes distributed along 19,968 panels. Note that only half of the surface mesh (Figure 3.4 b) is displayed to provide a clear view. An HMB *.grd* file is then created using the *hexa2hmb* tool (see Table 3.8).

Table 3.8: Convert grid from IcemCFD to HMB format using the *hexa2hmb* utility.

% ~hmb/bin/hexa2hmb_v6_serial_GCC_4.3.2_dd-mm-yy <mesh>
% ~hmb/bin/hexa2hmb_v6_serial_GCC_4.3.2_18-02-15 sphere

A finite element data (FEM) file is then created as output of the HMB solver, where one dummy flow step is computed. The option "Output cell centre FEM surface (0/1)" should enable in the *st.expert.output* of HMB.

Only the X,Y, and Z coordinates of the output cell centre FEM surface are stored using the datapacking point of Tecplot. This file data is structured in two levels. The highest level is a data set of one or more zones, whereas the lowest level provides the connectivity between panels. The final step was to create the geometric file of the acoustic solver BENP. This is done using a C program and an *input.dat* file where the user defines the parameters. A technical note for the HMB solver was written with the associated source codes and instructions [216].

The process to obtain the file BENP1 is shown in Figure 3.5. The files corresponding to the motion and deformation of the acoustic solver BENP called BENP2 and BENP3, respectively, are generated using a C program. The aerodynamic file needs as a main input the three components of the aerodynamic force per unit of area, the fluctuation velocities of the fluid, and the total pressure, and density values for each panel. Hover and forward flight configurations require different formulation of their variables, so the aerodynamic files are generated in a different way. For both cases, all variables are stored at the centroid of each panel (ITGMOD=3). The S-76 model main

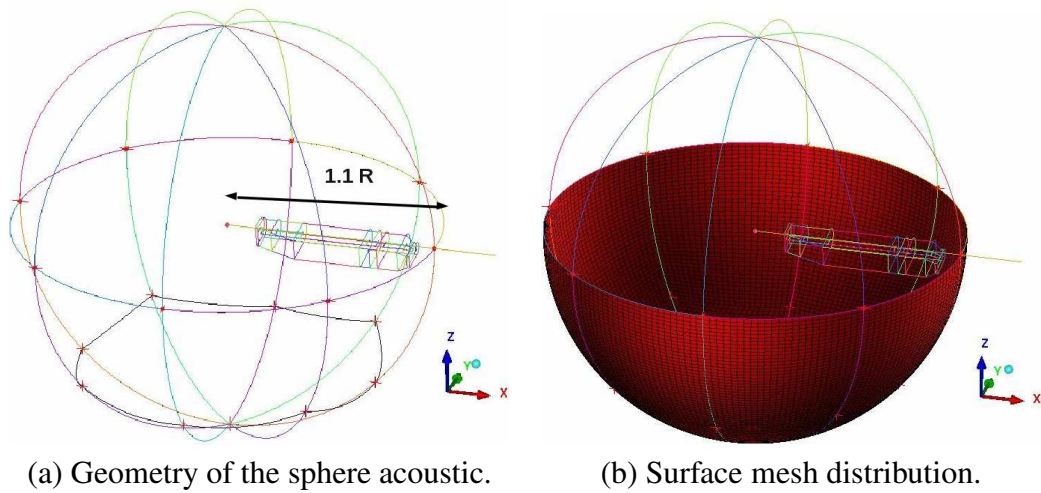


Figure 3.4: Geometry (left) and surface mesh distribution (right) of the sphere acoustic located at  $r/R=1.1$  for the S-76 rotor blade. The complete surface mesh contains 21,400 nodes distributed along 19,968 panels.

rotor blade with 60% taper-35° degrees swept-20° degrees anhedral tip in hover, and the AW-139 rotor blade in forward flight were selected to provide the two different layout examples.

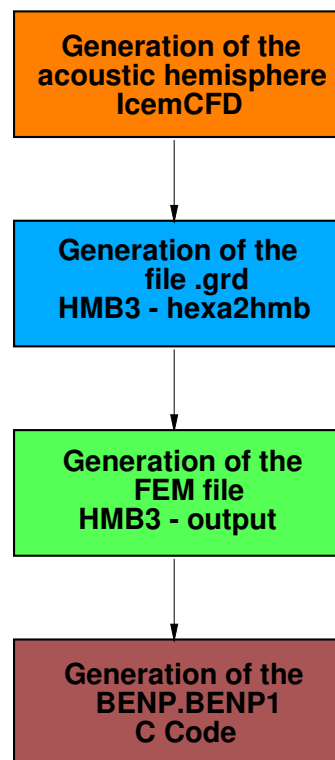


Figure 3.5: Order in which various utilities are used to generate the geometric file of the acoustic solver BENP referred to as BENP1.



### 3.2.1 Aeroacoustic File for the S-76 Rotor Blade in Hover

The S-76 model main rotor blade with anhedral tip in hover at blade-tip Mach number  $M_{\text{tip}}$  of 0.65 and blade pitch angle  $\theta_{75}$  of 7.5 degrees was taken as a baseline case. If the wake generated by the rotor is assumed periodic, hover can be formulated as a steady-state problem. Consequently, only one flow solution file is needed. The acoustic pressure sphere was interpolated through the flowfield solution. This was accomplished using a Tecplot Macro (source files can be found in Technical Report D4.5 of Technology Strategy Board (TSB)). Linear and inverse-distance methods can be selected through the variable *inter\_method* in the Tecplot Macro. For this case, an inverse-distance method was used.

Figure 3.6 shows the fluctuations of pressure in Pa and Sound Pressure Level (SPL) in dB on the acoustic pressure sphere. The SPL is a logarithmic measure of the deviation of the local pressure fluctuation from a sound reference value, defined by:

$$SPL = 10 \log \frac{P_{\text{rms}}^2}{P_{\text{ref}}^2}, \quad (3.7)$$

where  $P_{\text{ref}}$  is an international reference, considered as the minimal audible sound of human hearing ( $2 \times 10^{-5}$  Pa).  $P_{\text{rms}}$  is the root mean square of the pressure value. As consequence of the employed periodic boundary conditions, a periodic distribution of the fluctuations of pressure and of the SPL are seen in Figure 3.6. The regions of high (coloured in red) and lower (coloured in blue) pressure corresponding to the lower and upper surface of the blade are well captured by this near-acoustic approach.

Finally, the acoustic pressure file is written in a suitable format for BENP. The variables  $\rho$ ,  $u$ ,  $v$ ,  $w$ , and  $P$  are set at the centroid of each panel of the sphere. For each panel, the centroid values were computed using the nodal values. The velocity components  $u$ ,  $v$ ,  $w$  are computed in the non-inertial frame of reference, which correspond to HMB variables in dimensional form. The pressure and density are the total values in dimensional form (Pa and  $\text{kg/m}^3$ , respectively). A C program was used to complete this last step.

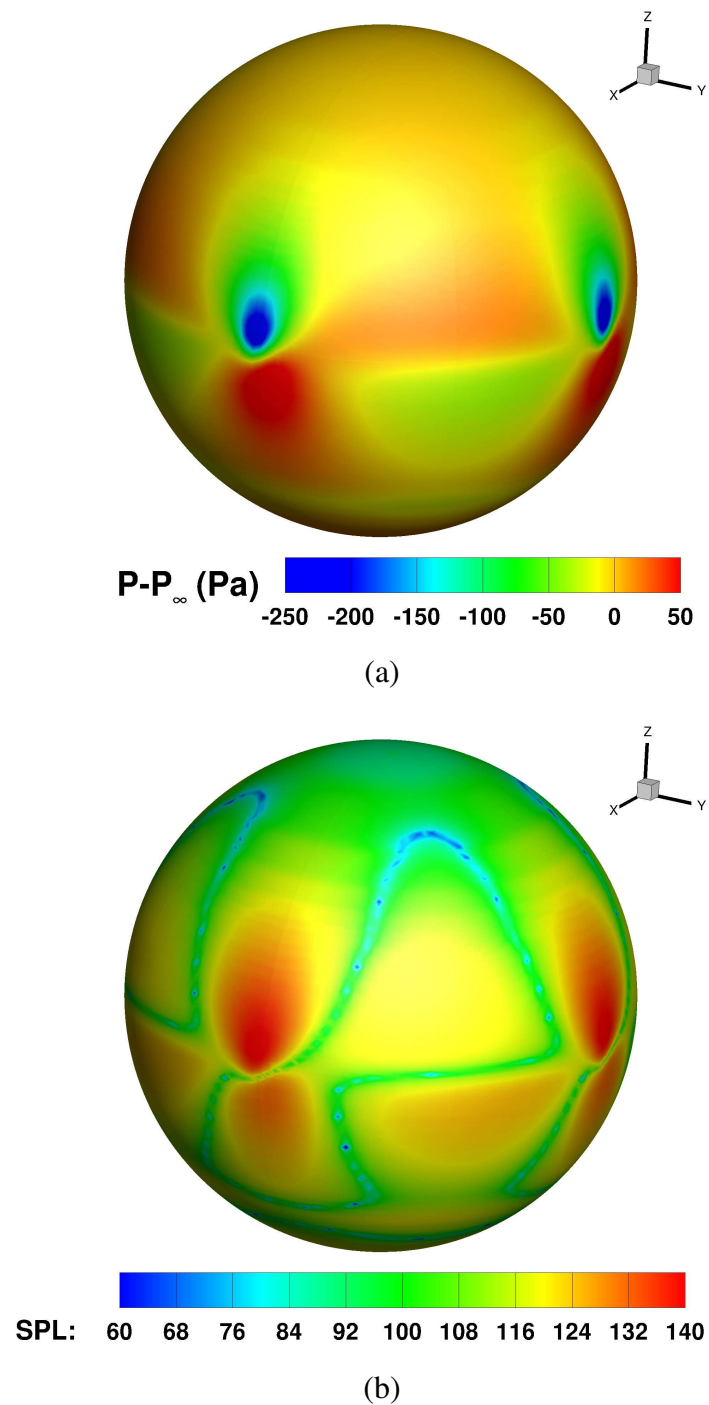


Figure 3.6: Fluctuation of pressure in Pa (top) and sound pressure level in dB (bottom) of the acoustic pressure sphere located at  $r/R=1.1$  from the centre of the rotor.

### 3.2.2 Aeroacoustic File for the AW-139 Rotor Blade in Forward Flight

The process to obtain the input files for the BENP acoustic solver is presented here for the AW-139 rotor blade in forward flight. An acoustic pressure sphere is first built near the tip blades ( $r/R=1.1$ ). Table 3.9 shows the test conditions used during this study.

Table 3.9: Test conditions for the AW-139 main rotor in forward flight.

Parameter	Value
$M_\infty$	0.1344
$Re_\infty$	$1.270 \times 10^6$
$M_{tip}$	0.6346
Blade pitch angle, $\theta_{75}$	$6.19^\circ$

Like the S-76 rotor blade, a radius of 1.1 was chosen to avoid numerical diffusion and dispersion errors. The geometric, motion, and aeroelastic files of the BENP acoustic solver for the AW-139 rotor blade were generated the same way as for the S-76 rotor blade. Due to that, the forward flight configuration is formulated as an unsteady flow problem, several flowfield solutions as a function of the blade azimuth are required during a completed rotor revolution. The acoustic pressure sphere file should be written in a suitable format for BENP. The variables  $\rho$ ,  $u$ ,  $v$ ,  $w$ , and  $P$  are stored at the centroid of each panel, and the components  $u$ ,  $v$ , and  $w$  correspond to the freestream and perturbation components of the flowfield velocity, in dimensional form. The pressure and density are the total values (reference+perturbation) in dimensional form.

Figures 3.7 - 3.14 show a comparison between the predicted fluctuation of pressure obtained with the HMB, ADPANEL, and EMAA for the AW-139 rotor blade at azimuth blades  $\Psi$  from -10 to 60 degrees. Top and bottom views are available. Regarding the HMB3 results, two interpolation methods were investigated, the Inverse Distance Method (IDM) and the Linear Method (LM). Similar behaviour was found between the three solvers, where the maximum and minimum peaks of pressure were well captured. Inverse distance formulation seems to provide better results when compared with ADPANEL and EMAA's results.

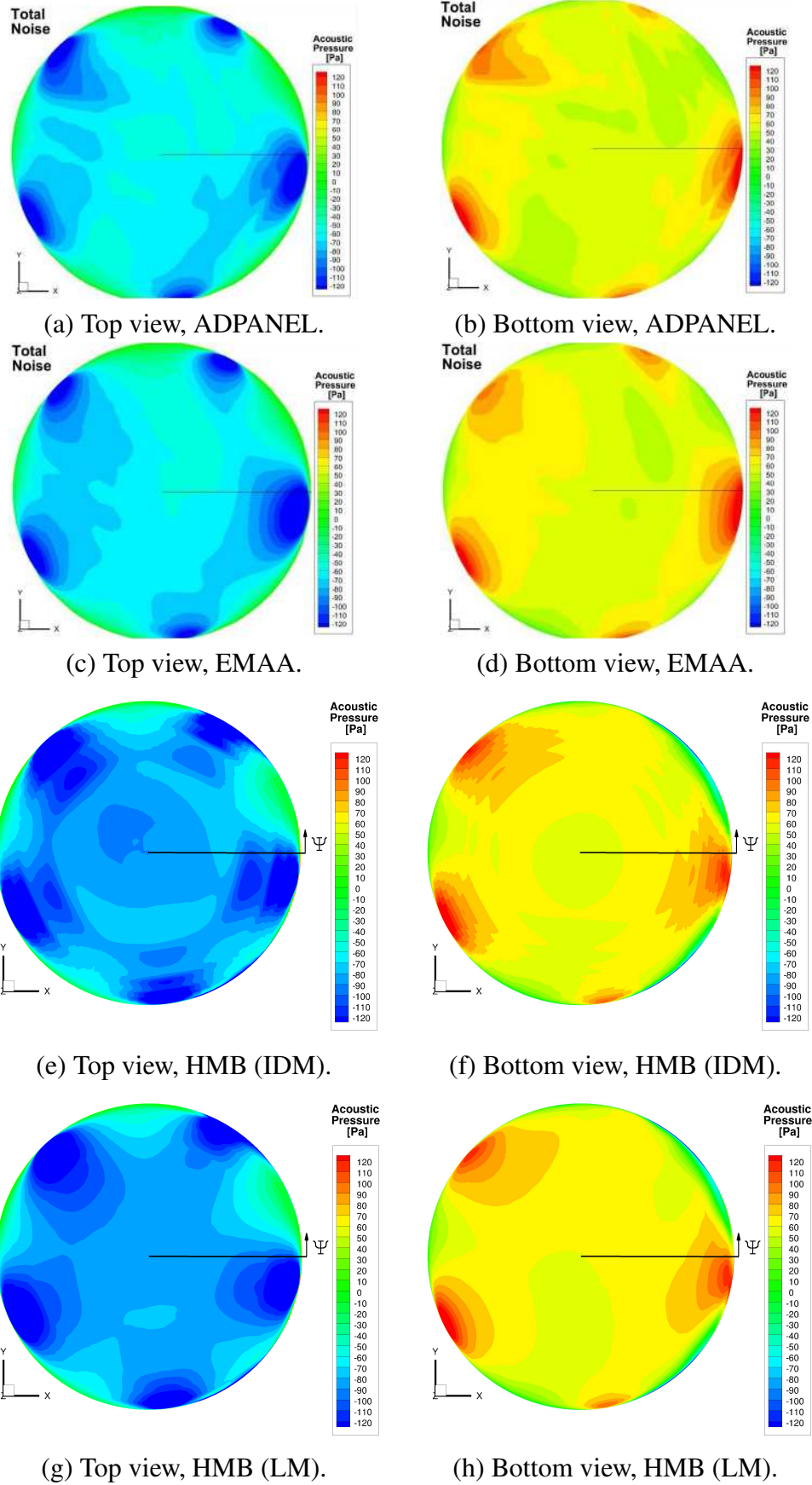


Figure 3.7: Fluctuation of pressure in Pa for the AW-139 rotor blade at azimuth blade  $\Psi = -10^\circ$ . IDM=Inverse Distance Method; LM=Linear Method.

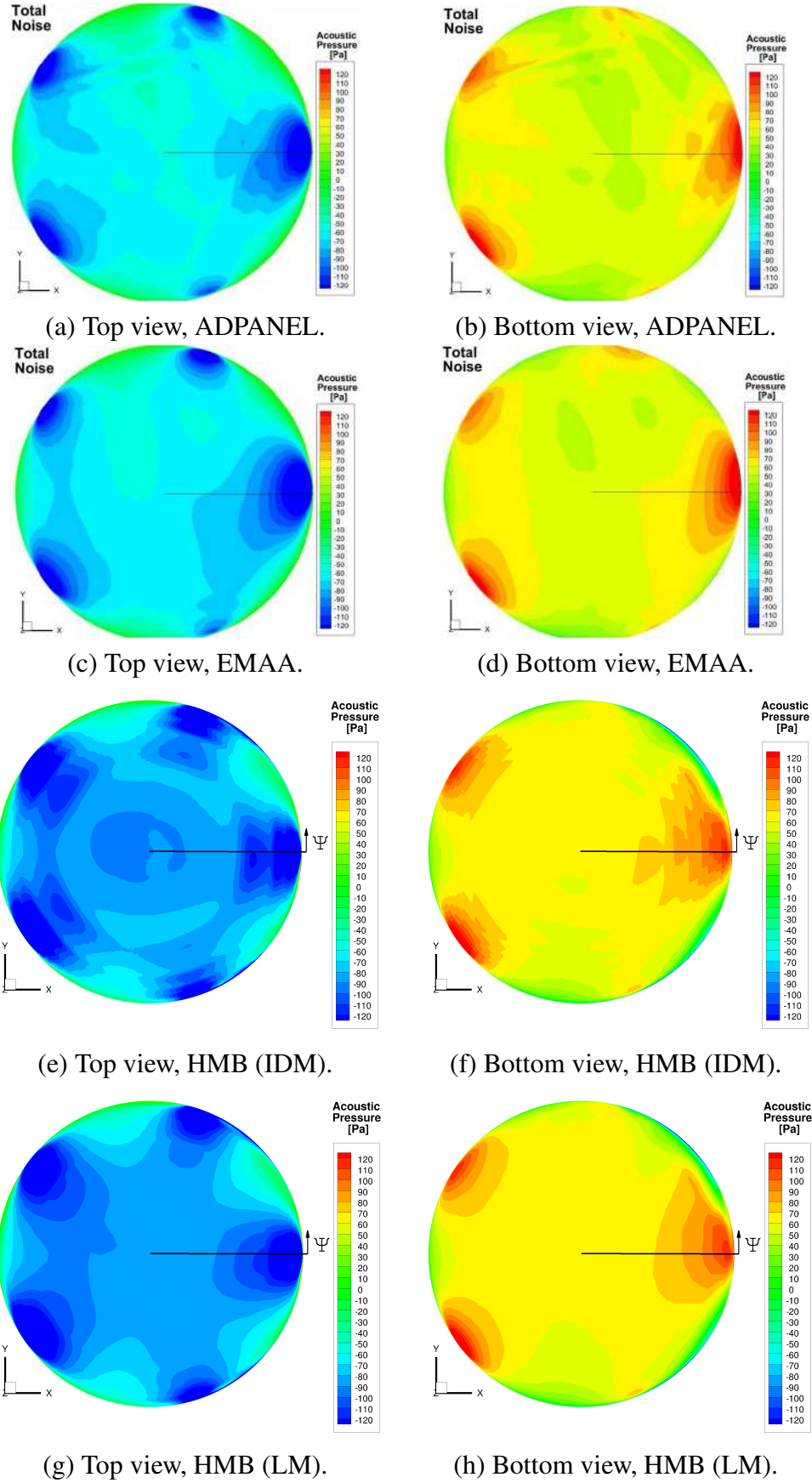


Figure 3.8: Fluctuation of pressure in Pa for the AW-139 rotor blade at azimuth blade  $\Psi = 0^\circ$ . IDM=Inverse Distance Method; LM=Linear Method.

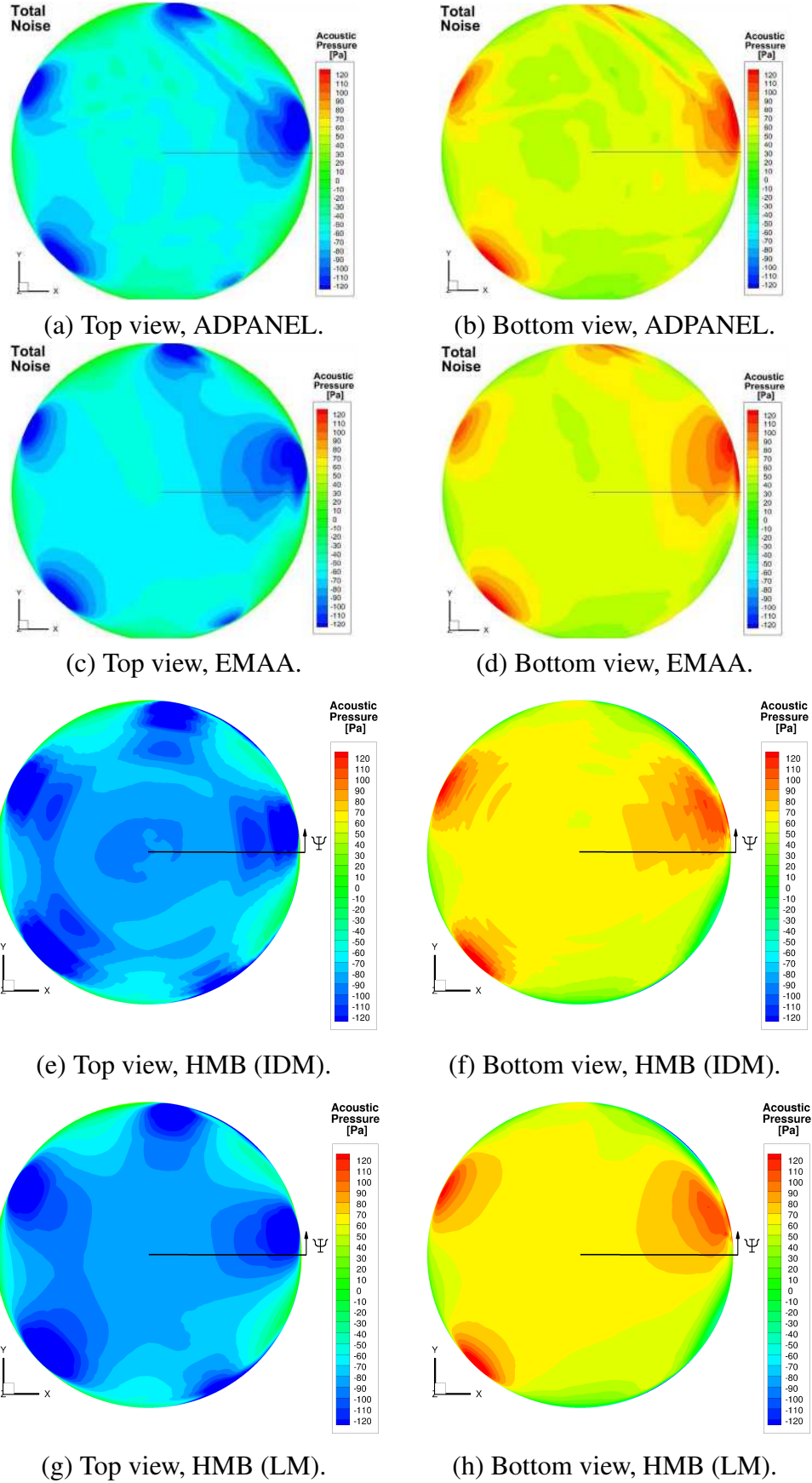


Figure 3.9: Fluctuation of pressure in Pa for the AW-139 rotor blade at azimuth blade  $\Psi = 10^\circ$ . IDM=Inverse Distance Method; LM=Linear Method.



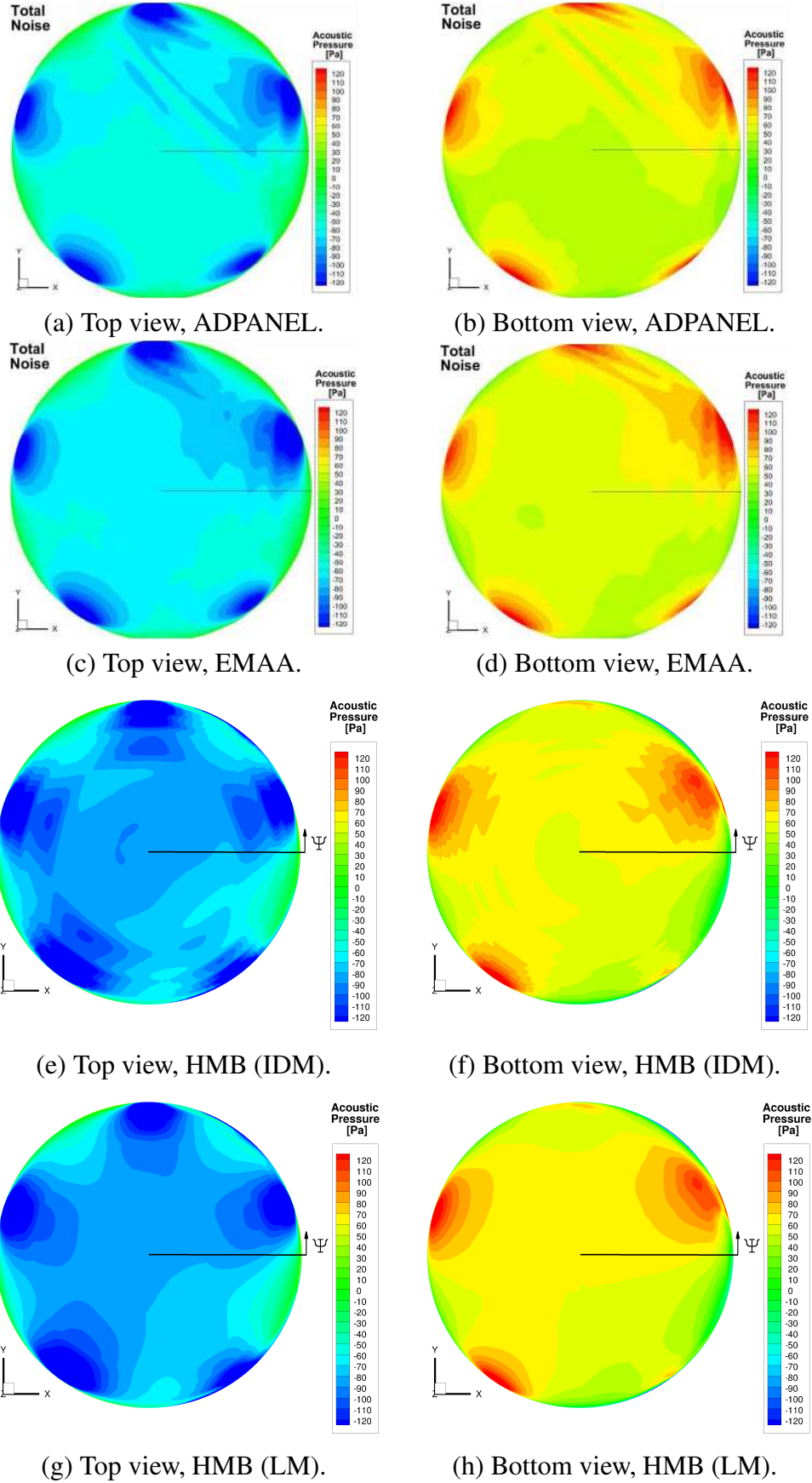


Figure 3.10: Fluctuation of pressure in Pa for the AW-139 rotor blade at azimuth blade  $\Psi = 20^\circ$ . IDM=Inverse Distance Method; LM=Linear Method.

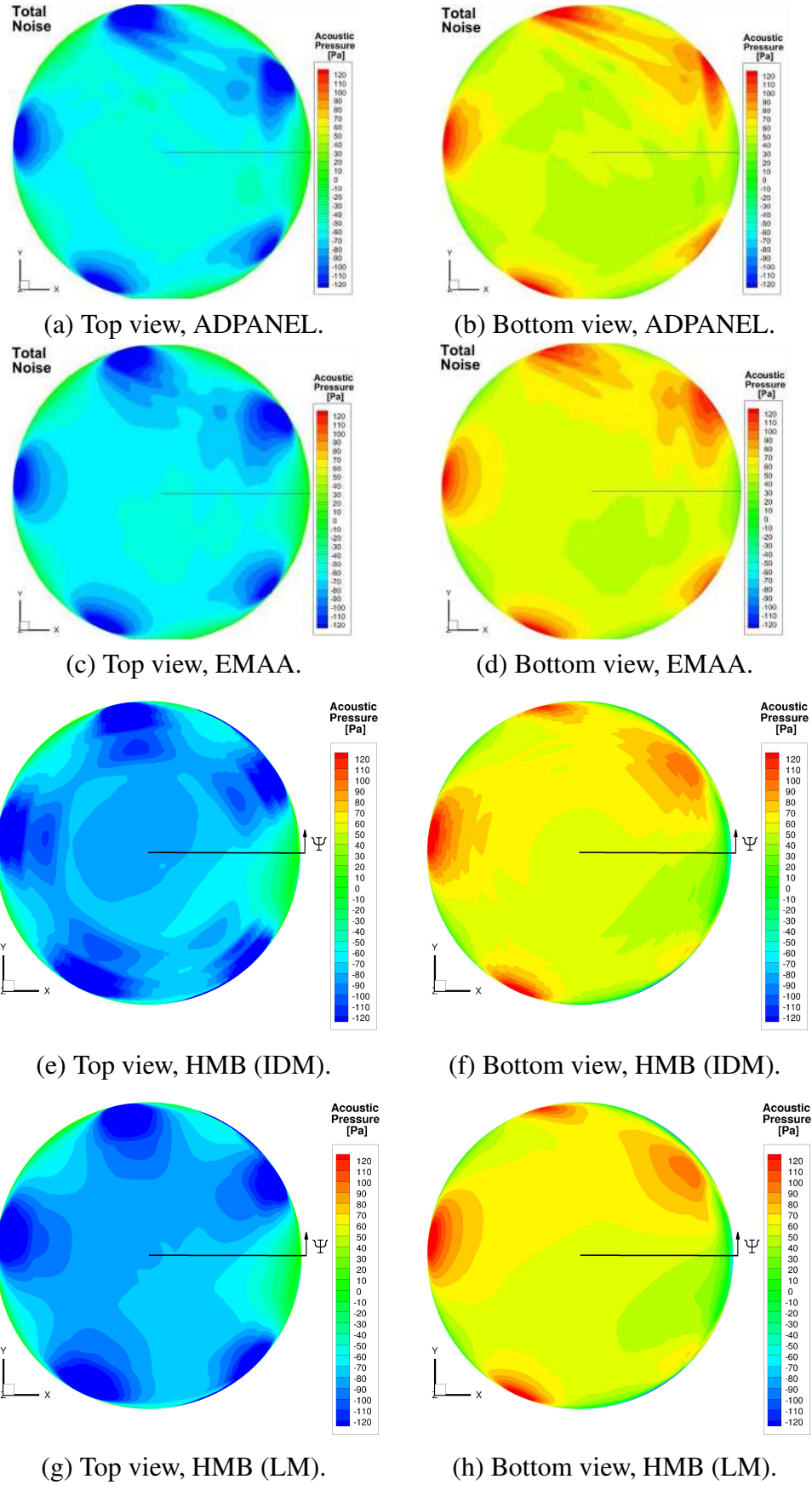


Figure 3.11: Fluctuation of pressure in Pa for the AW-139 rotor blade at azimuth blade  $\Psi = 30^\circ$ . IDM=Inverse Distance Method; LM=Linear Method.



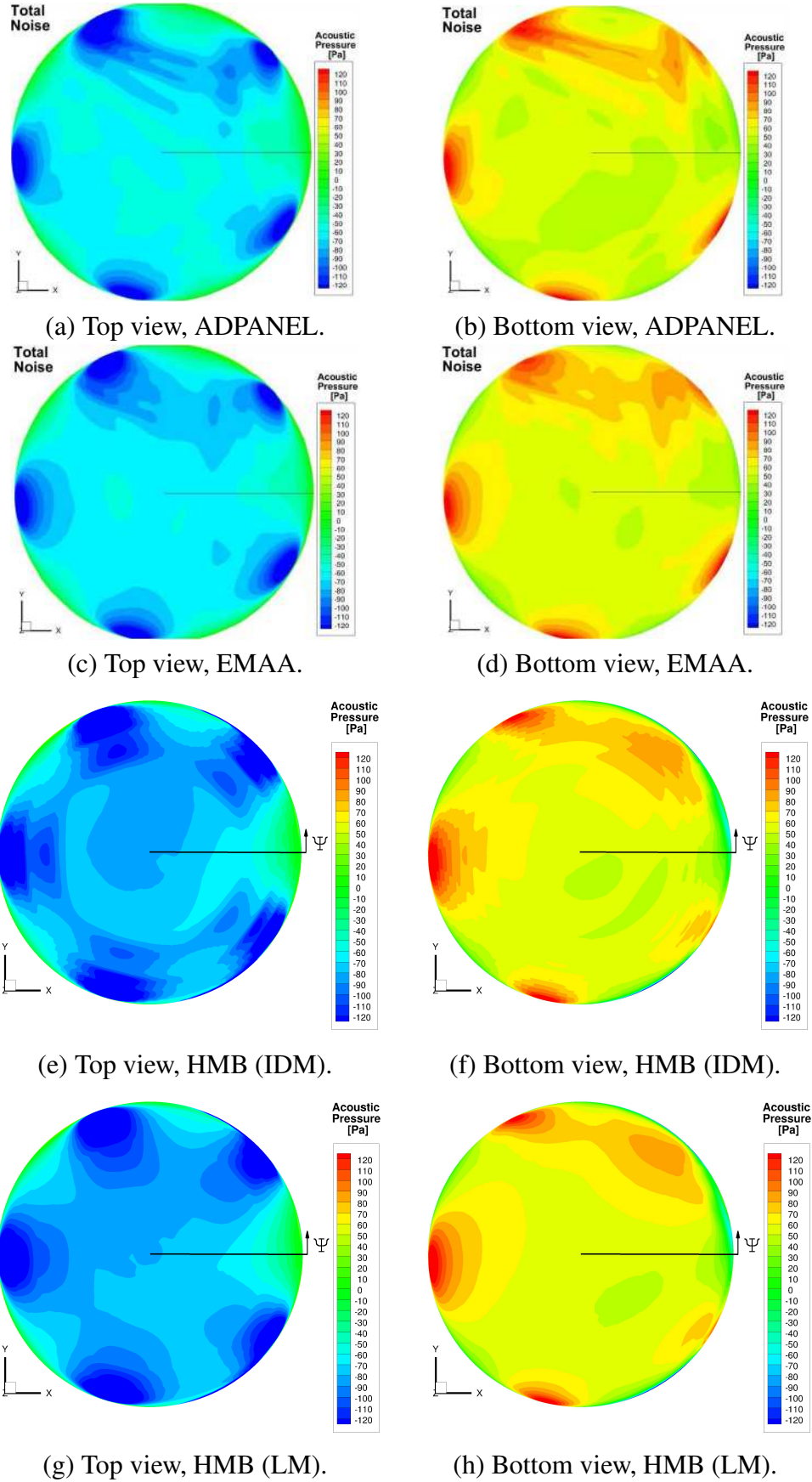


Figure 3.12: Fluctuation of pressure in Pa for the AW-139 rotor blade at azimuth blade  $\Psi = 40^\circ$ . IDM=Inverse Distance Method; LM=Linear Method.

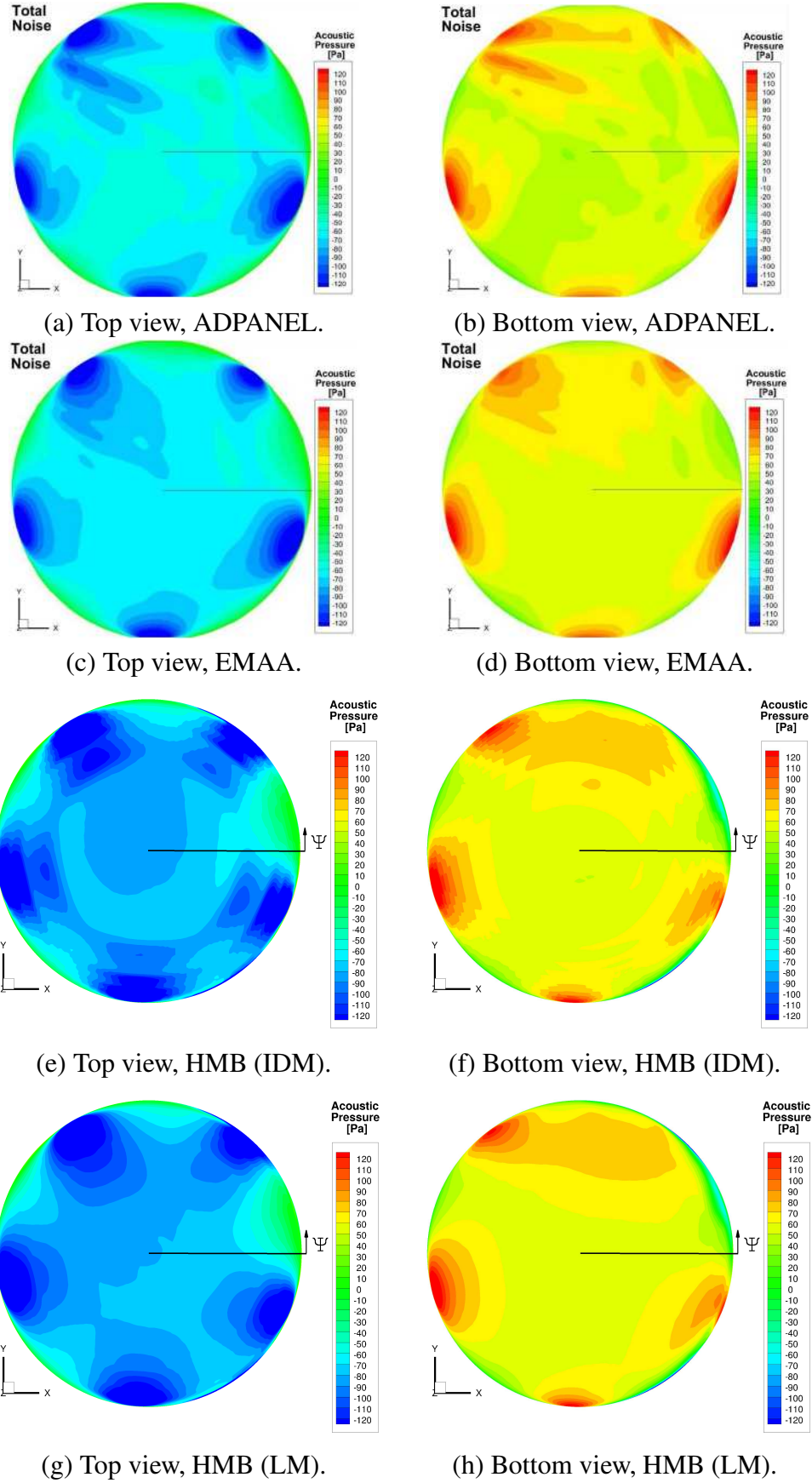


Figure 3.13: Fluctuation of pressure in Pa for the AW-139 rotor blade at azimuth blade  $\Psi = 50^\circ$ . IDM=Inverse Distance Method; LM=Linear Method.

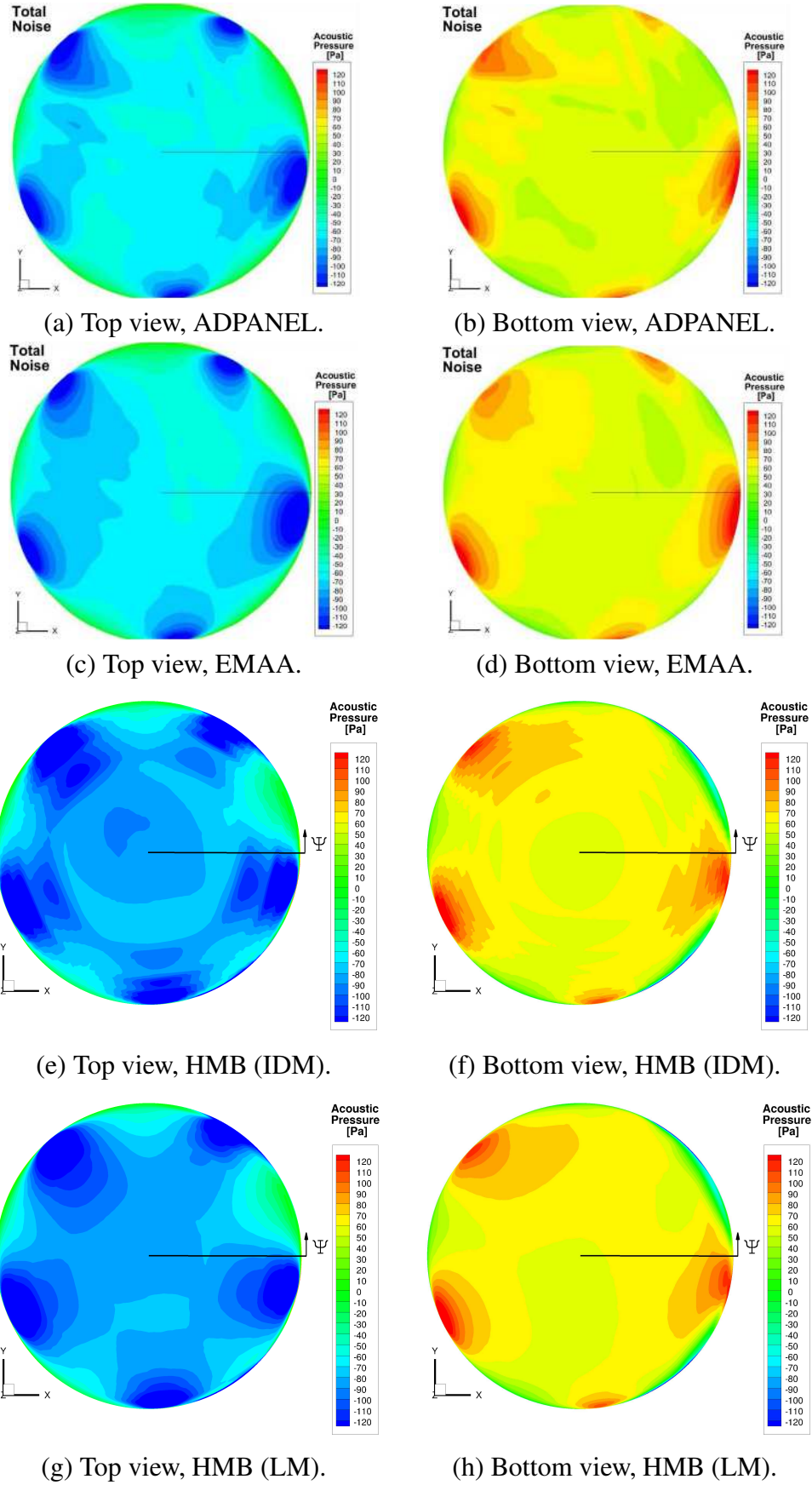


Figure 3.14: Fluctuation of pressure in Pa for the AW-139 rotor blade at azimuth blade  $\Psi = 60^\circ$ . IDM=Inverse Distance Method; LM=Linear Method.

# Chapter 4

## High-Order Method

This chapter presents a high-order method (up to 4th-order), achieved using high-order correction terms through successive differentiation [155, 156] of MUSCL. The scheme shows good scalability properties for medium density meshes (up to 10 million cells), which assure a low imbalance between the maximum and minimum computer nodes when parallel execution is needed. Spectral resolution properties (dissipation and dispersion errors) are also shown. Then, the application of the underlying scheme to the convection of an isentropic vortex is presented. Further results obtained with the new scheme for a wide variety of test cases are presented in chapter 10.

### 4.1 High-order Formulation

This section describes the formulation of the high-order correction terms. This formulation was firstly proposed by Burg [217] for unstructured finite volume codes, where third-order spatial accuracy was achieved for two-and three-dimensional problems. Yang *et al.* [155, 156] extended the scheme to fourth-order spacial accuracy. The scheme resembles the MUSCL-schemes [178], and is used here to discretise the convective part of the Navier-Stokes equations. The MUSCL implementation in HMB is represented by a one-parameter family of equations, where a third-order spatial accuracy can be achieved. For 1-dimensional problems and on uniform grids (see Figure 4.1), the extrapolation of the flow variables to both sides of a cell-face located at  $j + 1/2$  for a

MUSCL-scheme is given:

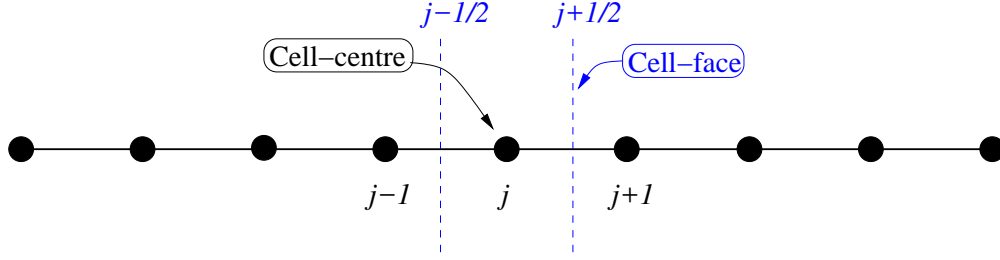


Figure 4.1: Illustration of the domain discretisation.

$$\mathbf{F}_{j+1/2}^L = \mathbf{F}_j + \left[ \frac{k_1}{2}(\mathbf{F}_{j+1} - \mathbf{F}_j) + (1 - k_1)\vec{\nabla}\mathbf{F}_j \bullet \vec{\mathbf{r}}_{f_j} \right]. \quad (4.1)$$

$$\mathbf{F}_{j+1/2}^R = \mathbf{F}_{j+1} - \left[ \frac{k_1}{2}(\mathbf{F}_{j+1} - \mathbf{F}_j) + (1 - k_1)\vec{\nabla}\mathbf{F}_{j+1} \bullet \vec{\mathbf{r}}_{f_{j+1}} \right]. \quad (4.2)$$

In Eqns. 4.1 and 4.2, the vectors  $\vec{\mathbf{r}}_{f_j}$  and  $\vec{\mathbf{r}}_{f_{j+1}}$  represent the distances between the cell face  $j + 1/2$  and the cell-centre volumes  $j$ , and  $j + 1$ , respectively. To reconstruct the gradient  $\vec{\nabla}\mathbf{F}_j$  and  $\vec{\nabla}\mathbf{F}_{j+1}$  at cell-centre volumes  $j$  and  $j + 1$ , either the Green-Gauss or the Least-Squares approaches can be used. By setting  $k_1 = 0$ , a 2nd-order upwind scheme is obtained. If  $k_1 = 1/3$ , a third order, upwind biased scheme is derived [218]. If  $k_1$  is set to 1, a 2nd-order central difference scheme is obtained. It is clear that the present MUSCL-schemes are limited to third-order accurate. Table 4.1 shows the different spatial accuracy arisen as function of the  $k_1$  MUSCL-parameter.

Table 4.1: Spatial accuracy of the MUSCL-scheme as function of the  $k_1$  parameter. The values are only valid for regular grids.

Parameter $k_1$	Comments
0	2nd-order upwind scheme
1/3	3rd-order upwind scheme
1	2nd-order central scheme

Following Yang *et al.* [155], the proposed 4th-order structured MUSCL scheme is written in

a similar fashion, where the extrapolation to both sides of the face located at  $j + 1/2$  is given as:

$$\begin{aligned}
 \mathbf{F}_{j+1/2}^L = & \overbrace{\mathbf{F}_j + \frac{k_1}{2}(\mathbf{F}_{j+1} - \mathbf{F}_j) + (1 - k_1)\vec{\nabla}\mathbf{F}_j \bullet \vec{\mathbf{r}}_{f_j}}^{\text{Standard MUSCL for the left state}} \\
 & + \underbrace{\frac{1}{2} \left[ \frac{k_2}{2} (\vec{\nabla}\mathbf{F}_{j+1} \bullet \vec{\mathbf{r}}_{f_j} - \vec{\nabla}\mathbf{F}_j \bullet \vec{\mathbf{r}}_{f_j}) + (1 - k_2)\vec{\nabla}(\vec{\nabla}\mathbf{F}_j \bullet \vec{\mathbf{r}}_{f_j}) \bullet \vec{\mathbf{r}}_{f_j} \right]}_{\text{High-order corrections for the left state}}.
 \end{aligned} \tag{4.3}$$

$$\begin{aligned}
 \mathbf{F}_{j+1/2}^R = & \overbrace{\mathbf{F}_{j+1} - \frac{k_1}{2}(\mathbf{F}_{j+1} - \mathbf{F}_j) - (1 - k_1)\vec{\nabla}\mathbf{F}_{j+1} \bullet \vec{\mathbf{r}}_{f_{j+1}}}^{\text{Standard MUSCL for the right state}} \\
 & + \underbrace{\frac{1}{2} \left[ \frac{k_2}{2} (\vec{\nabla}\mathbf{F}_{j+1} \bullet \vec{\mathbf{r}}_{f_{j+1}} - \vec{\nabla}\mathbf{F}_j \bullet \vec{\mathbf{r}}_{f_{j+1}}) + (1 - k_2)\vec{\nabla}(\vec{\nabla}\mathbf{F}_{j+1} \bullet \vec{\mathbf{r}}_{f_{j+1}}) \bullet \vec{\mathbf{r}}_{f_{j+1}} \right]}_{\text{High-order corrections for the right state}}.
 \end{aligned} \tag{4.4}$$

As can be observed, this new variable extrapolation formulation represents a two-parameter family ( $k_1$  and  $k_2$ ), and is equivalent to the standard MUSCL-scheme under certain values of  $k_1$  and  $k_2$ . As shown in Eqns. 4.3 and 4.4, the high-order correction terms have been developed using a Taylor series expansion about the centre of the face  $j + 1/2$ . The terms require knowledge of the second derivatives  $\vec{\nabla}(\vec{\nabla}\mathbf{F}_j \bullet \vec{\mathbf{r}}_{f_j})$  and  $\vec{\nabla}(\vec{\nabla}\mathbf{F}_{j+1} \bullet \vec{\mathbf{r}}_{f_{j+1}})$ . Once the first derivatives are computed, the second derivatives can be estimated by successive application of the Green-Gauss or the Least Squares methods to the first derivatives. The three normal and cross second derivatives  $(\frac{\partial^2 F}{\partial x^2}, \frac{\partial^2 F}{\partial y^2}, \frac{\partial^2 F}{\partial z^2}, \frac{\partial^2 F}{\partial x \partial y}, \frac{\partial^2 F}{\partial x \partial z}, \frac{\partial^2 F}{\partial y \partial z})$  need to be allocated in the same way like the first derivatives.

## 4.2 Green-Gauss Formulation

As discussed earlier, to reconstruct the gradient  $\vec{\nabla}\mathbf{F}_j$  and  $\vec{\nabla}\mathbf{F}_{j+1}$  at cell-centre volumes  $j$  and  $j + 1$ , either the Green-Gauss or the Least-Squares approaches can be considered. It is well known, that the least-square approach for gradient reconstruction provides higher accuracy than the Green-Gauss for most discretization techniques [182]. However, if highly stretched meshes are used, this formulation fails to provide good estimates of gradients and also presents stability issues [182]. The Green-Gauss formulation presents an alternative solution to the unweighted/weighted Least-Square methods with similar accuracy, while maintaining robustness. Therefore, this technique

is selected to reconstruct the gradient  $\vec{\nabla}\mathbf{F}_j$  and the second derivatives  $\vec{\nabla}(\vec{\nabla}\mathbf{F}_j)$  when high-order schemes are used.

The Green-Gauss formulation computes the gradient of any quantity  $\mathbf{F}_j$  by integrating around the control-volume  $V_j$  with closed boundaries  $S$ . Figure 4.2 shows the stencil for Green-Gauss gradient calculation for cell-centre discretisation in 2D. The components of the average gradients ( $\vec{\nabla}\mathbf{F}_1$ ) over the control-volume  $V_j$  can be written as:

$$\begin{aligned}\frac{\partial \mathbf{F}_1}{\partial x} &= \frac{1}{V_j} \left( \mathbf{F}_{12} \mathbf{S}_{12} \vec{n}_{12} + \mathbf{F}_{13} \mathbf{S}_{13} \vec{n}_{13} + \mathbf{F}_{14} \mathbf{S}_{14} \vec{n}_{14} + \mathbf{F}_{15} \mathbf{S}_{15} \vec{n}_{15} \right) \vec{e}_x, \\ \frac{\partial \mathbf{F}_1}{\partial y} &= \frac{1}{V_j} \left( \mathbf{F}_{12} \mathbf{S}_{12} \vec{n}_{12} + \mathbf{F}_{13} \mathbf{S}_{13} \vec{n}_{13} + \mathbf{F}_{14} \mathbf{S}_{14} \vec{n}_{14} + \mathbf{F}_{15} \mathbf{S}_{15} \vec{n}_{15} \right) \vec{e}_y.\end{aligned}\quad (4.5)$$

where  $\mathbf{F}_{12}, \mathbf{F}_{13}, \mathbf{F}_{14}$ , and  $\mathbf{F}_{15}$  are the approximation of the variable  $\mathbf{F}$  on the faces 12, 13, 14, and 15 with longitudes (2D) or surfaces (3D)  $\mathbf{S}_{12}, \mathbf{S}_{13}, \mathbf{S}_{14}$  and  $\mathbf{S}_{15}$  and unit normal vectors  $\vec{n}_{12}, \vec{n}_{13}, \vec{n}_{14}$  and  $\vec{n}_{15}$  and can be expressed as:

$$\begin{aligned}\mathbf{F}_{12} &= \frac{1}{2}(\mathbf{F}_1 + \mathbf{F}_2), & \mathbf{F}_{13} &= \frac{1}{2}(\mathbf{F}_1 + \mathbf{F}_3), \\ \mathbf{F}_{14} &= \frac{1}{2}(\mathbf{F}_1 + \mathbf{F}_4), & \mathbf{F}_{15} &= \frac{1}{2}(\mathbf{F}_1 + \mathbf{F}_5).\end{aligned}\quad (4.6)$$

Higher accuracy can be obtained using advance quadratures in space to evaluate  $\mathbf{F}$  on the faces like the fourth-order introduced by McCorquodale *et al.* [219]. However, this formulation is more expensive and it requires adding a new layer of halo cells to the standard HMB. The components of the unit vectors  $\vec{e}_x, \vec{e}_y$  are written in 2D as:  $\vec{e}_x = [1 \ 0]$  and  $\vec{e}_y = [0 \ 1]$ , respectively.

### 4.3 Memory Overhead

Eqns. 4.3 and 4.4 can be extended using Cartesian coordinates:

$$\begin{aligned}\mathbf{F}_{j+1/2}^L &= \mathbf{F}_j + \frac{k_1}{2}(\mathbf{F}_{j+1} - \mathbf{F}_j) + (1 - k_1)\vec{\nabla}\mathbf{F}_j \bullet \vec{\mathbf{r}}_{f_j} \\ &+ \frac{1}{2} \left[ \frac{k_2 \Delta x_{f_j}}{2} \left( \left( \frac{\partial \mathbf{F}}{\partial x} \right)_{j+1} - \left( \frac{\partial \mathbf{F}}{\partial x} \right)_j \right) + (1 - k_2) \Delta x_{f_j} \vec{\nabla} \left( \frac{\partial \mathbf{F}}{\partial x} \right)_j \bullet \vec{\mathbf{r}}_{f_j} \right] \\ &+ \frac{1}{2} \left[ \frac{k_2 \Delta y_{f_j}}{2} \left( \left( \frac{\partial \mathbf{F}}{\partial y} \right)_{j+1} - \left( \frac{\partial \mathbf{F}}{\partial y} \right)_j \right) + (1 - k_2) \Delta y_{f_j} \vec{\nabla} \left( \frac{\partial \mathbf{F}}{\partial y} \right)_j \bullet \vec{\mathbf{r}}_{f_j} \right] \\ &+ \frac{1}{2} \left[ \frac{k_2 \Delta z_{f_j}}{2} \left( \left( \frac{\partial \mathbf{F}}{\partial z} \right)_{j+1} - \left( \frac{\partial \mathbf{F}}{\partial z} \right)_j \right) + (1 - k_2) \Delta z_{f_j} \vec{\nabla} \left( \frac{\partial \mathbf{F}}{\partial z} \right)_j \bullet \vec{\mathbf{r}}_{f_j} \right].\end{aligned}\quad (4.7)$$

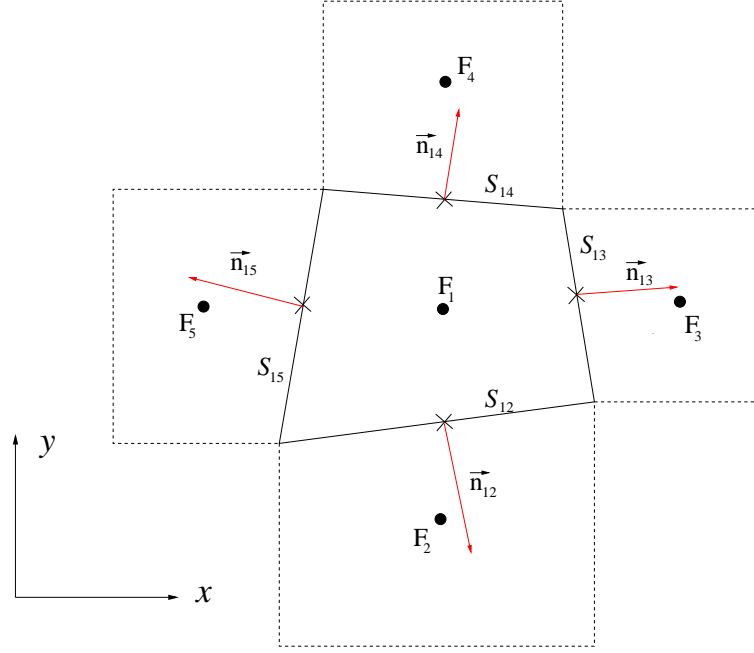


Figure 4.2: Illustration of stencil for Green-Gauss gradient calculation for cell-centre discretisation on 2D.

$$\begin{aligned}
 \mathbf{F}_{j+1/2}^R &= \mathbf{F}_{j+1} - \frac{k_1}{2}(\mathbf{F}_{j+1} - \mathbf{F}_j) - (1 - k_1)\vec{\nabla}\mathbf{F}_{j+1} \bullet \vec{\mathbf{r}}_{f_{j+1}} \\
 &+ \frac{1}{2} \left[ \frac{k_2 \Delta x_{f_{j+1}}}{2} \left( \left( \frac{\partial \mathbf{F}}{\partial x} \right)_{j+1} - \left( \frac{\partial \mathbf{F}}{\partial x} \right)_j \right) + (1 - k_2) \Delta x_{f_{j+1}} \vec{\nabla} \left( \frac{\partial \mathbf{F}}{\partial x} \right)_{j+1} \bullet \vec{\mathbf{r}}_{f_{j+1}} \right] \\
 &+ \frac{1}{2} \left[ \frac{k_2 \Delta y_{f_{j+1}}}{2} \left( \left( \frac{\partial \mathbf{F}}{\partial y} \right)_{j+1} - \left( \frac{\partial \mathbf{F}}{\partial y} \right)_j \right) + (1 - k_2) \Delta y_{f_{j+1}} \vec{\nabla} \left( \frac{\partial \mathbf{F}}{\partial y} \right)_{j+1} \bullet \vec{\mathbf{r}}_{f_{j+1}} \right] \\
 &+ \frac{1}{2} \left[ \frac{k_2 \Delta z_{f_{j+1}}}{2} \left( \left( \frac{\partial \mathbf{F}}{\partial z} \right)_{j+1} - \left( \frac{\partial \mathbf{F}}{\partial z} \right)_j \right) + (1 - k_2) \Delta z_{f_{j+1}} \vec{\nabla} \left( \frac{\partial \mathbf{F}}{\partial z} \right)_{j+1} \bullet \vec{\mathbf{r}}_{f_{j+1}} \right].
 \end{aligned} \tag{4.8}$$

These equations extrapolate the flow variables to both sides of the cell-face at  $j + 1/2$ , so first and second derivatives and the vector distances  $\vec{\mathbf{r}}_{f_j}$  and  $\vec{\mathbf{r}}_{f_{j+1}}$  need to be computed (see Figure 4.3).

For each direction and in 3D, 6 components of the vector distances are required ( $\Delta x_{f_j}, \Delta y_{f_j}, \Delta z_{f_j}, \Delta x_{f_{j+1}}, \Delta y_{f_{j+1}}, \Delta z_{f_{j+1}}$ ), so 18 components are needed.

If two equation turbulence models are used, MUSCL-4 provides a memory overhead of 23%. Its breakdown is as follows:  $3 \times 7$  and  $6 \times 7$  doubles per cell for the first and second derivatives, respectively, and 18 extra doubles for the distance vectors in 81 doubles. This value needs to be added to the 350 doubles of the standard HMB [11, 187, 220, 221], resulting in the aforementioned 23% of memory overhead.



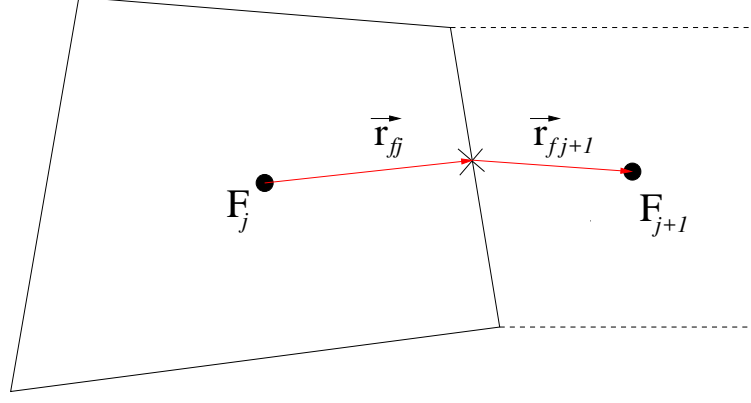


Figure 4.3: Sketch of stencil for distance calculation for left and right states in  $j$  planes on 2D.

## 4.4 Order of Accuracy in 1D

The present formulation requires optimal values of  $k_1$  and  $k_2$  to assure higher-order of accuracy. In this regard, we derive the order of accuracy of the scheme in 1D, considering the approximation of the derivative at the cell-centre as:

$$\begin{aligned}
 \int_{x-\frac{1}{2}}^{x+\frac{1}{2}} \frac{\partial \mathbf{F}}{\partial x} dx &\approx \mathbf{F}_{j+\frac{1}{2}}^L - \mathbf{F}_{j-\frac{1}{2}}^L = \frac{1+k_2}{32} \mathbf{F}_{j+2} + \frac{7+8k_1-3k_2}{32} \mathbf{F}_{j+1} + \frac{11-12k_1+k_2}{16} \mathbf{F}_j \\
 &+ \frac{-19+12k_1+k_2}{16} \mathbf{F}_{j-1} + \frac{9-8k_1-3k_2}{32} \mathbf{F}_{j-2} + \frac{-1+k_2}{32} \mathbf{F}_{j-3} \quad (4.9) \\
 &= \mathbf{F}_j' \Delta x + \frac{1+6k_1}{24} \mathbf{F}_j''' \Delta x^3 + \frac{1-2k_1+k_2}{16} \mathbf{F}_j^{(4)} \Delta x^4 + O(\Delta x^5)
 \end{aligned}$$

One can observe that this formula is at least 2nd-order accurate for all values of  $k_1$  and  $k_2$ , while if  $k_1 = -\frac{1}{6}$  and  $k_2 = -\frac{4}{3}$ , the approximation of the derivative at the cell-centre is 4th-order accurate, with no mechanism of dissipation. Moreover, a small amount of dissipation  $\delta$  can be introduced to reduce spurious oscillation and at the same time maintain the high-order accuracy when  $k_2$  is set to  $-\frac{4}{3} + \delta$ . A value of  $\delta = 1 \times 10^{-4}$  is used throughout this work, which represents a compromise value between stability and level of accuracy obtained. The effect of  $\delta$  on the solution is discussed in chapter 10.

## 4.5 Implementation Details

Some implementation details are listed here:

- Near solid bodies, the current implementation drops the order of the scheme to 2nd order using 2 cells above the surface. The mesh is quite fine near solid bodies anyway and this approximation is expected to have a small effect on the final solution.
- At chimera boundaries, the current implementation drops the order of the scheme to 2nd-order. This needs to be corrected in the near future.
- For parallel computations, the current implementation exchanges a halo of 2 cells for the first and second derivatives. The standard HMB scheme only exchanges a halo of 2 cells for the solution.
- Most of the CPU penalties of the current implementation come from additional data exchanged for parallel computations and extra effort is needed to calculate gradients with Green-Gauss's method.
- High-order derivatives are only applied to the inviscid flux, while the viscous flux remains second order.
- For most cases, there is no need to initialise the solution with a second order method due to loss of robustness.

## 4.6 Fourier Analysis

Fourier analysis is used in this section to assess the spectral properties of the proposed 4th-order scheme. If the flux function is assumed to be periodic sinusoidal function over a domain of unit length:

$$F(x) = e^{2\pi i \omega x} = e^{2\pi i \omega (j \Delta x)} \quad (4.10)$$

dissipation and dispersion errors can be quantified as functions of the grid wavenumber  $\omega \Delta x$ .

The phase error ( $\bar{\omega}\Delta x$ ) of the Fourier transformation of (Eqn. 4.9) is given as:

$$\bar{\omega}\Delta x = \frac{45 - 16k_1 - 5k_2}{32} \sin(\omega\Delta x) + \frac{-8 + 8k_1 + 4k_2}{32} \sin(2\omega\Delta x) + \frac{1 - k_2}{32} \sin(3\omega\Delta x) \quad (4.11)$$

Figure 4.4 shows the imaginary and real parts of the phase error or modified wavenumber of the derivative at the cell-centre, which are associated to dispersion and dissipation errors, respectively. The MUSCL-4 scheme ( $k_1=-1/6$  and  $k_2=-4/3$ ) is compared with the MUSCL-2 (2nd upwind scheme  $k_1=0$ ), as well as the exact solution. It is observed that the proposed high-order scheme has a significantly higher spectral resolution than the standard MUSCL-2 schemes. Therefore, a wider range of wavenumbers can be accurately resolved for the MUSCL-4 schemes. Regarding the dissipation error, the MUSCL-4 scheme shows a considerable reduction compared to MUSCL-2. Moreover, at higher wavenumbers ( $\omega\Delta x \geq 1.5$ ), the new scheme shows higher spectral resolution, which allows for capturing higher frequencies associated to the flow features (vortices, small length-scale waves).

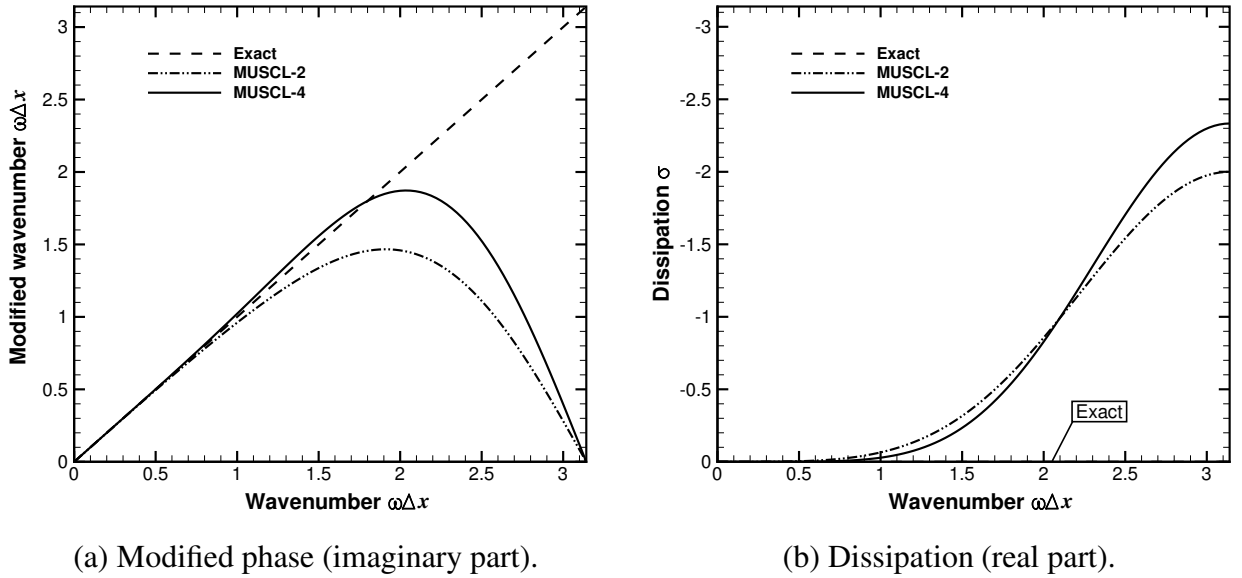


Figure 4.4: Fourier analysis for MUSCL-2 and MUSCL-4 schemes.

## 4.7 Vortex Transported by Uniform flow

The transport of a 2D isentropic vortex by a freestream flow is considered here. This problem has a well-known analytical solution [222], without numerical errors associated to dissipation and dispersion. Therefore, the capability of different numerical schemes in preserving the vortex shape and strength of the convected vortex can be evaluated. The computational domain is taken as  $[0, 10] \times [0, 10]$ , where the initial flowfield is given as:

$$\begin{aligned}\rho &= \left[ 1 - \frac{(\gamma-1)b^2}{8\gamma\pi^2} e^{1-r^2} \right]^{\frac{1}{\gamma-1}}; \quad p = \rho^\gamma \\ u &= u_\infty - \frac{b}{2\pi} e^{\frac{1-r^2}{2}} (y - y_c) \\ v &= v_\infty + \frac{b}{2\pi} e^{\frac{1-r^2}{2}} (x - x_c)\end{aligned}\tag{4.12}$$

with freestream velocity values set as  $u_\infty = 0.20, v_\infty = 0.0$ , respectively. The distance  $r$  from the vortex centre  $(x_c, y_c) = (0, 0)$  to a point  $(x, y)$  is expressed as  $r = \sqrt{(x - x_c)^2 + (y - y_c)^2}$  and  $b = 5$  is the dimensionless vortex strength. Periodic boundary conditions were applied in both directions.

To advance the solution in time, a 4th-order Runge-Kutta scheme (RK4) was employed, and selected the time-step was small enough to ensure conformity with the solution with the spatial resolution employed. Solutions were obtained on  $32 \times 32$ ,  $64 \times 64$ ,  $128 \times 128$ , and  $256 \times 256$  equispaced Cartesian grids to study the spatial accuracy of different schemes, after the vortex travels a distance of two times the computational domain. Figure 4.5 shows the  $L_\infty$  error of the convergence rate for the MUSCL-2 (2nd-order upwind), MUSCL-3 (3rd-order upwind), and MUSCL-4 (4th-order upwind) schemes. The present 4th-order upwind scheme shows 4th-order error convergence, whilst the 3rd and 2nd-order upwind schemes give a 2nd-order error convergence. Similar convergence rates were obtained by Yang *et al.* [156].

Despite that the 2nd and 3rd-order upwind schemes present similar error convergence rates, the 3rd-order upwind scheme shows a faster convergence to the solution. It is interesting to note that the solutions obtained using the 4th-order scheme have a significantly lower error than the 2nd and 3rd-order upwind schemes, showing the benefits of the higher-order method.

Figure 4.6 shows pressure contours of the isentropic vortex convection corresponding to the

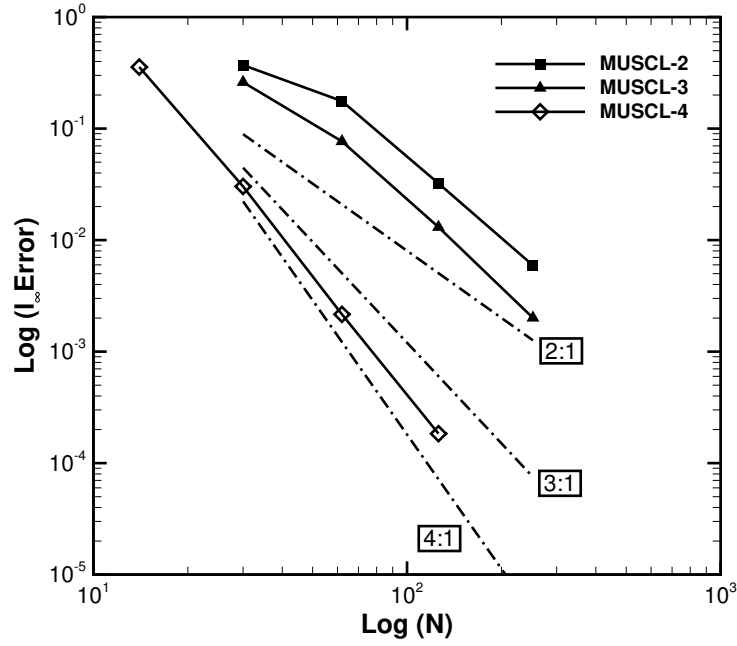
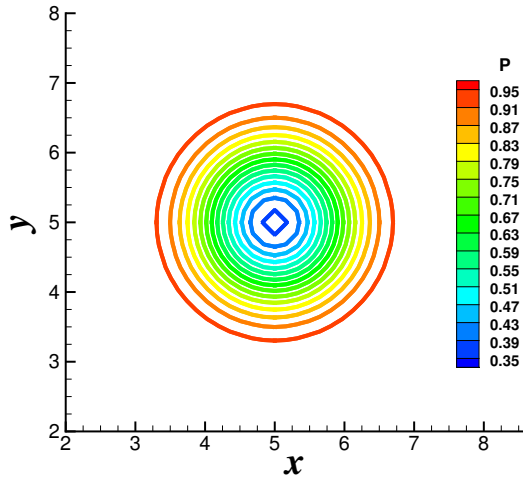
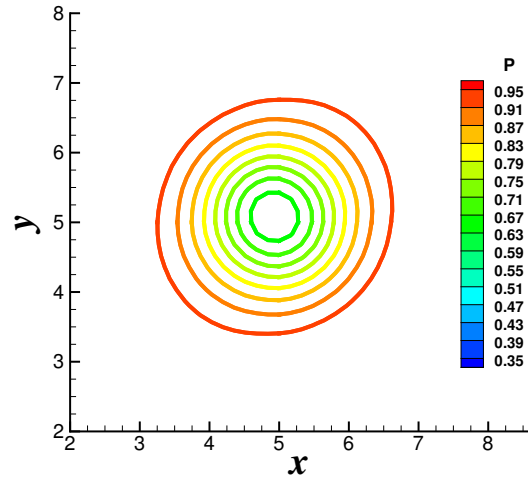


Figure 4.5: Error convergences rate of MUSCL-2 (2nd-order upwind), MUSCL-3 (3rd-order upwind), and MUSCL-4 (4th-order upwind) schemes for vortex transport problem.

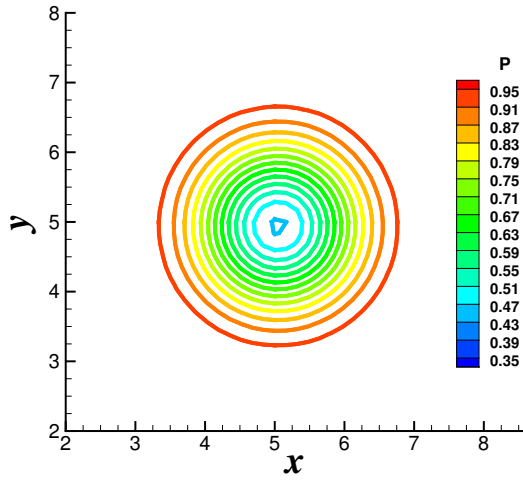
analytical and numerical solutions obtained by the MUSCL-2, MUSCL-3, and MUSCL-4 schemes on  $64 \times 64$  mesh. The solution obtained by the MUSCL-2 scheme shows significant dissipation of the vortex core and distortion of its shape. On the other hand, the MUSCL-4 scheme has the lowest dissipation error in comparison to all other schemes, which highlights the ability of this scheme in preserving the vortex shape and strength.



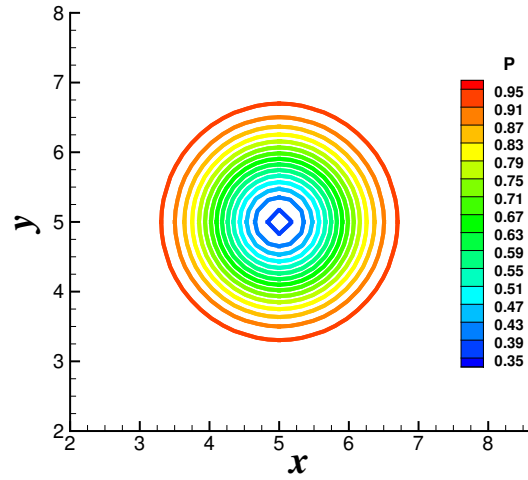
(a) Exact solution.



(b) MUSCL-2 scheme.



(c) MUSCL-3 scheme.



(d) MUSCL-4 scheme.

Figure 4.6: Pressure contours for isentropic vortex convection after travelling two times the computational domain. Solutions were obtained on  $64 \times 64$  equi-spaced Cartesian grids.

Comparison of cross-sectional pressure contours computed by several schemes is given in Figure 4.7, using an  $128 \times 128$  equi-spaced Cartesian grid. In addition to the numerical solutions obtained, the analytical solution is also included (represented by a solid line). It is seen that the MUSCL-2 scheme is not able to predict the peak of pressure mainly due to dissipation error (8.33% discrepancy with the exact solution). By contrast, solutions using MUSCL-3 and MUSCL-4, show fair agreement with the exact solution with 2.95% and 0.26% discrepancies, respectively.

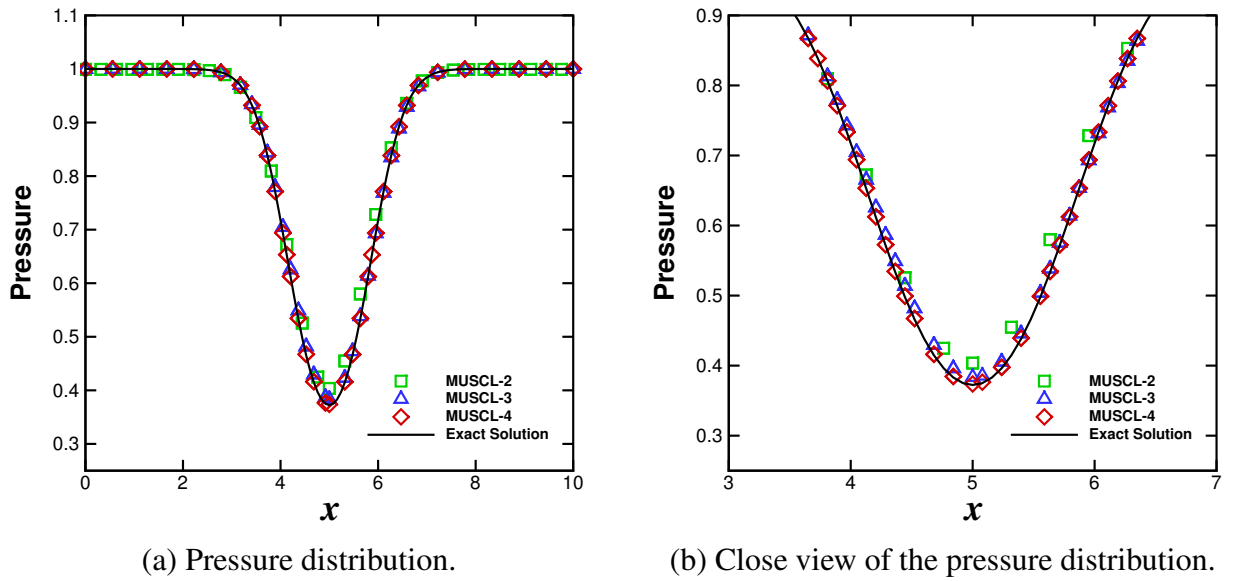


Figure 4.7: Comparison of cross-sectional pressure contours computed by several schemes on a  $128 \times 128$  equi-spaced Cartesian grid.

# Chapter 5

## Validation of HMB for Helicopter Blades in Hover

This chapter presents evidence on the ability of the HMB CFD method to accurately predict hover performance of rotors with modest computer resources. This work uses three well documented blades, the B0-105, S-76, and PSP main rotor blades. The results are compared with experiments and show that the performance is well predicted. In addition, the employed Computational Fluid Dynamics method was able to capture the effects of the tip Mach number, tip shape, blade aeroelasticity, Re number, and flow transition on the performance of the blade, as well as, on the wake structure and the rotor acoustics.

### 5.1 B0-105 Main Rotor

A comprehensive investigation of the location of the transition onset on the rotor blades of the B0-105 helicopter was attempted using the Michel [195] and Cebeci-Smith [196] empirical criteria.

---

Part of this work is published in A. Jimenez-Garcia *et al.* , CFD Analysis of Hover Performance of Rotors at Full-and Model-Scale Conditions, The Aeronautical Journal, 120 (1231), 2016, 1386–1424, doi: 10.1017/aer.2016.58 and A. Jimenez-Garcia *et al.* , Accurate Predictions of Rotor Hover Performance at Low and High Disc Loadings, Journal of Aircraft, 2017, doi: 10.2514/1.C034144.



To explore if a laminar boundary layer can be developed on a rotor under real operational flight conditions, flow visualisation of the boundary layer on the B0-105 model rotor in hover was carried out at DLR by Rohardt [223], using a sublimation technique with acenaphthene. This technique is based on the property of the acenaphthene, which sublimates at normal state conditions of pressure and temperature. The sublimation speed has a strong dependence on the heat flux and temperature inside the boundary layer. Hence, the layer of acenaphthene crystals sublimates faster in the region where a turbulent boundary layer has been developed due to the larger heat flux found in this region than in a laminar one. So, a visual inspection of the upper and lower side of the rotor blade can provide the laminar-turbulent transition location.

The main geometric properties of the B0-105 rotor are shown in Table 5.1.

Table 5.1: Geometric properties of the B0-105 rotor [223].

Parameter	Value
Number of blades, $N_b$	4
Rotor radius, $R$	4.92 m
Reference blade chord, $c_{\text{ref}}$	0.28 m
Aspect ratio, $R/c_{\text{ref}}$	17.57
Rotor solidity, $\sigma$	0.072
Non-linear twist, $\Theta$	$-8^\circ$

### 5.1.1 B0-105 Rotor Mesh

A multi-block grid with matching periodic planes was built for the B0-105 blade (see Figure 5.1). Boundaries extend to  $4R$  (top and radial) and  $6R$  (bottom) the rotor plane. Froude conditions [224] were set up to the inflow, farfield, and outflow planes (see Figure 5.1 (a)). Due to the periodicity of the flow in the azimuthal direction and assuming a steady wake, only a quarter of the domain was modelled. The hub was approximated as a cylinder extending from inflow to outflow planes with a radius of  $0.10R$ . Figure 5.1 (b) shows the B0-105 rotor mesh topology. A sharp trailing edge was used, hence justifying the use of a structured C-type mesh. Table 5.2 shows the main meshing parameters used.

Table 5.2: Meshing parameters for the B0-105 rotor using a matched grid with sharp trailing edge.

Matched grid	Meshing parameters
No. of blocks	288
No. of nodes	13,429,08
No. of cells	12,338,752
No. of nodes along the aerofoil	306
No. of nodes in azimuthal direction	153
No. of nodes in radial direction	112
Height of the first mesh layer at blade surface	$5 \times 10^{-6} c_{\text{ref}}$

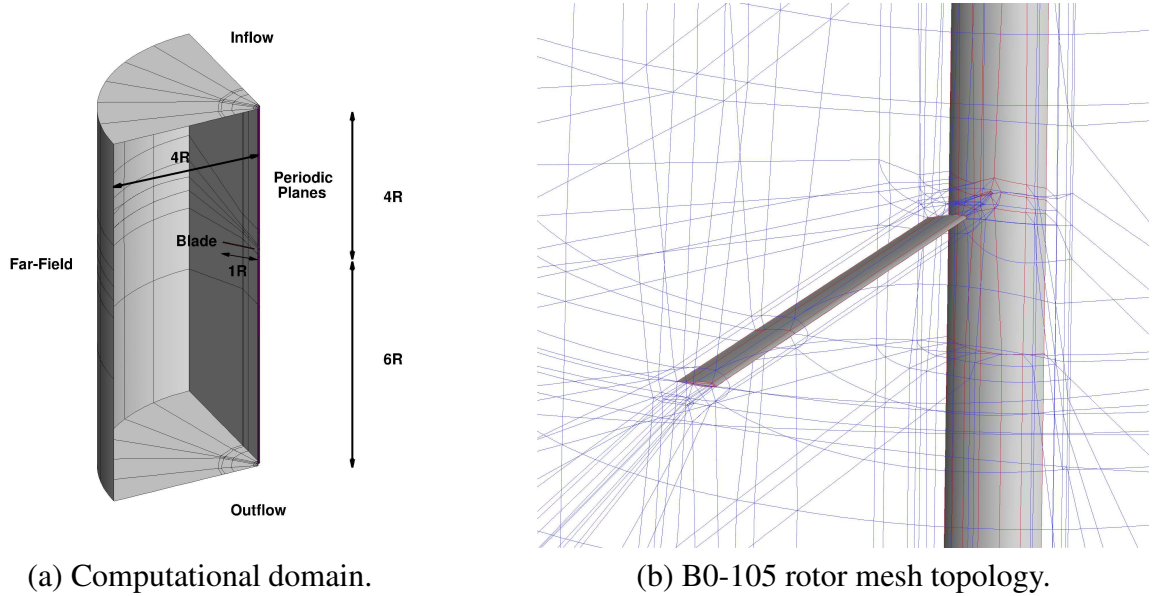


Figure 5.1: Computational domain and boundary conditions employed (left) and detailed view of the B0-105 rotor mesh topology (right).

### 5.1.2 Test Conditions and Computations

A hover condition was considered during experiments, where the blade-tip Mach number was set to 0.64, and the blade pitch angle was  $4.9^\circ$ , corresponding to a low disk loading. The Reynolds number, based on the reference blade chord of 0.28 m and on the blade-tip speed, was  $4.03 \times 10^6$ . Table 5.3 summarises the test conditions of the B0-105 rotor [223].

Seven radial stations were chosen from upper and lower surface of the rotor blade to evaluate the transition point through photographs. Table 5.4 shows the transition point at the stations as well as local Mach and Reynolds numbers from the experiments [223].

Table 5.3: Test conditions of the B0-105 rotor [223].

Parameter	Value
Blade-tip Mach number, $M_{tip}$	0.64
Reynolds number, $Re$	$4.03 \times 10^6$
RPM	425
Blade pitch angle, $\theta_{75}$	$4.9^\circ$
Coning angle, $\beta$	$2.5^\circ$

Table 5.4: Transition position at several radial stations of the B0-105 rotor blade [223].

$r/R$	$M_{local}$	$Re_{local}/10^6$	Upper Surface (transition position $x/c_{ref}$ )	Lower Surface (transition position $x/c_{ref}$ )
0.62	0.40	2.60	-	0.73
0.69	0.44	2.89	0.24	0.72
0.75	0.48	3.15	0.24	0.65
0.82	0.53	3.44	0.22	0.61
0.87	0.56	3.65	0.22	0.56
0.92	0.59	3.86	0.18	0.41
0.97	0.63	4.07	0.11	0.39

### 5.1.3 Results and Discussion

First, a fully turbulent CFD solution using the  $k-\omega$  SST turbulence model was obtained and used with the empirical transition criteria. The Michel [195] and Cebeci-Smith criteria [196] were employed to estimate the location of the transition onset. The  $\gamma-Re_{\theta_t}$  transition model was then employed, at the same test conditions, to compare with the fully turbulent CFD solution in terms of surface pressure and skin friction coefficients. Finally, an analysis of the thrust and torque coefficients of the B0-105 rotor blade is presented.

#### Estimation of Transition Onset

Figures 5.2 and 5.3 show the location of the transition onset for the fully turbulent case, using the Michel [195] and the Cebeci-Smith criteria [196] on the upper and lower blade surface along with the experimental data [223]. As observed, CFD solutions on the upper surface blade are in agreement with test data at all stations. All empirical criteria predicted the transition onset with the same level of accuracy. On the lower side, however, the fully turbulent CFD solution did not

capture the trend seen in the experiments. The computed laminar areas near the blade tip extend up to 60% chord, while for the flight data [223] this extends to 40%. This can be related to different factors. The first is the use of fully turbulent surface pressure data to predict the transition onset, which fails in extend laminar regions, as on the lower surface. Second, the part of the blade covering from  $r/R = 0.85$  to  $0.92$  is influenced by the tip vortex, which induces an area of reduced pressure near the leading edge of the blade. The earlier CFD transition onset is triggered by this change in pressure. However, the transitional flow did not affect the wake, as also reported by Heister [225].

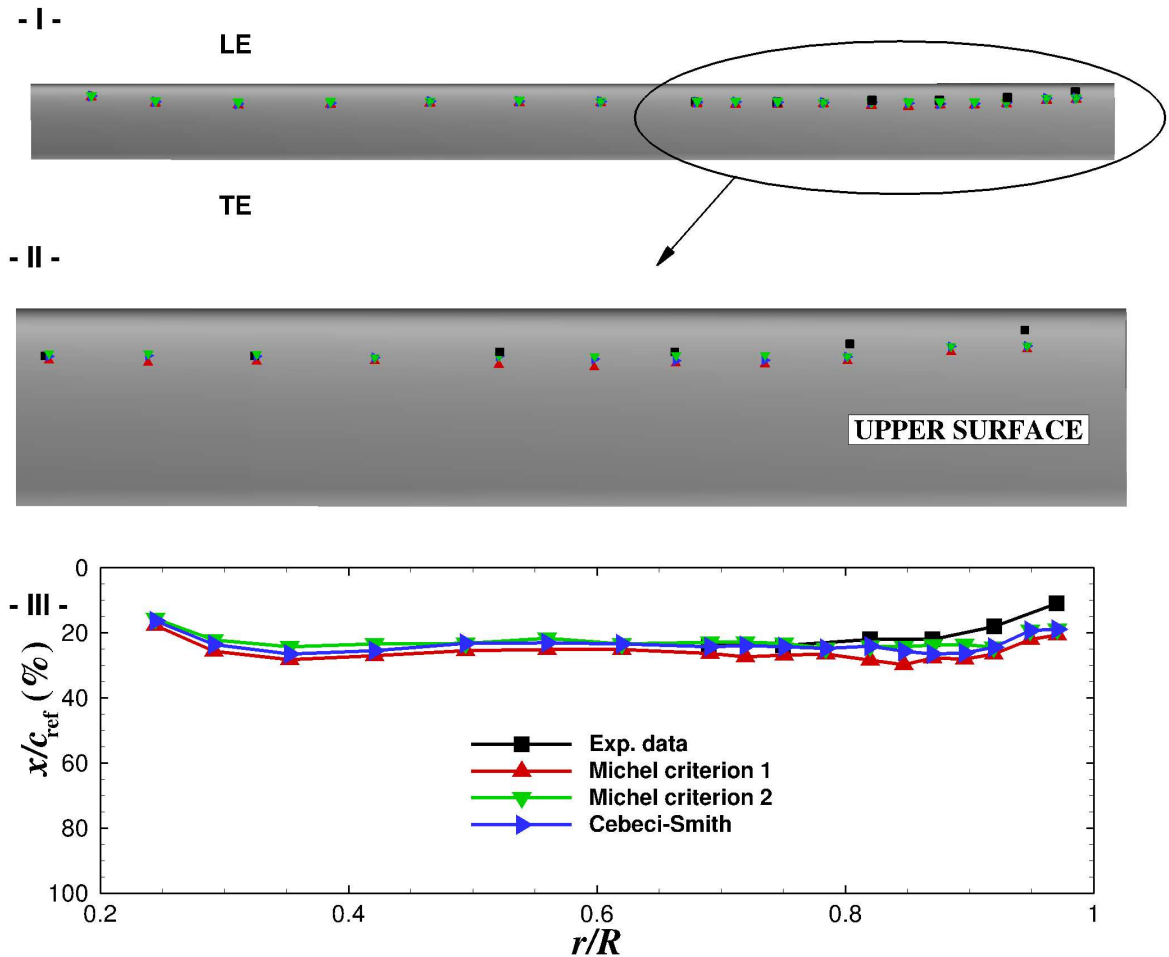


Figure 5.2: (I) Overview of the transition onset on the upper blade surface, showing estimates of transition criteria compared with experimental data, (II) close-view of the transition onset, and (III) comparison of predicted transition locations along the rotor radius.

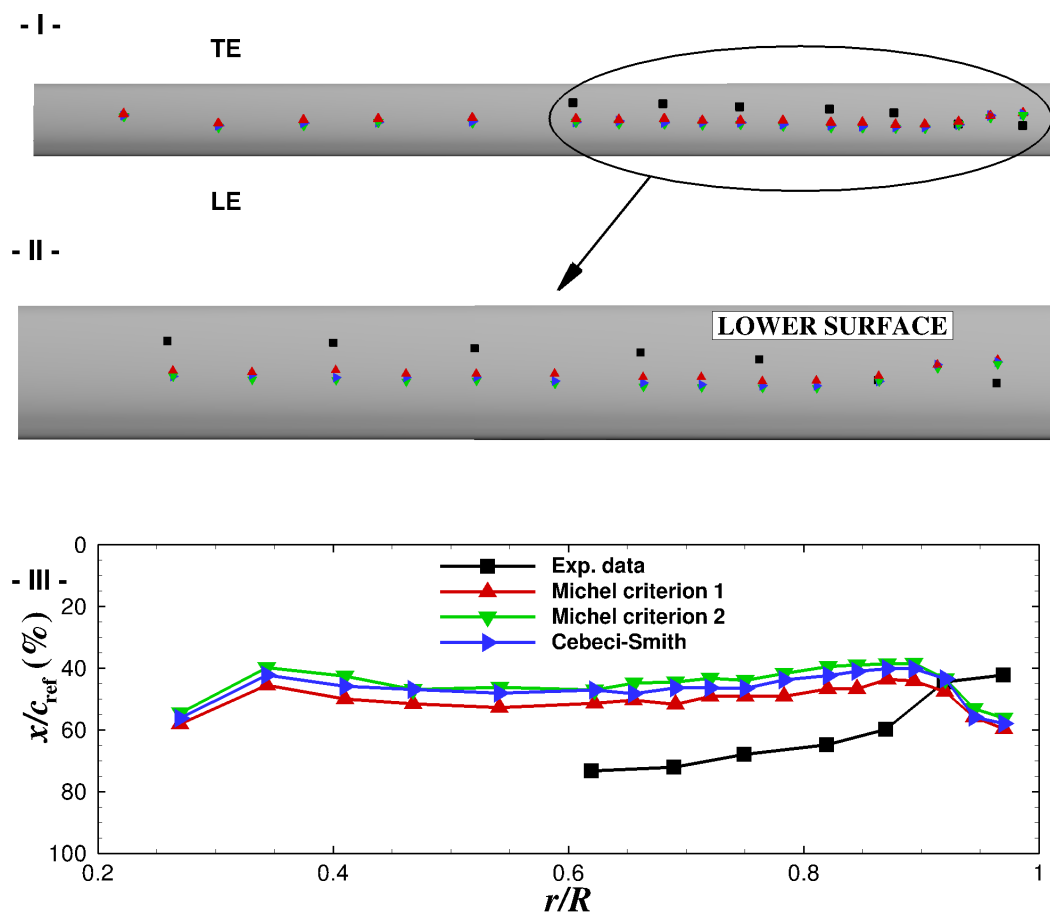


Figure 5.3: (I) Overview of the transition onset on the lower blade surface, showing estimates of transition criteria compared with experimental data, (II) close-view of the transition onset, and (III) comparison of predicted transition locations along the rotor radius.

### Integrated Blade Loads

Figure 5.5 shows the surface pressure coefficients at each radial station along the rotor blade for the  $k-\omega$  SST [191] and the  $\gamma-Re_{\theta t}$  [47, 48] turbulence models. A strong pressure gradient is found downstream the stagnation point, which becomes stronger close to the tip blade due to the increase of the local velocity. An extensive laminar region is always found on the lower surface of the blade. It is interesting to note that the highest suction peak is reached at station 7 ( $r/R = 0.97$ ) due to the passage of the tip vortex. Although skin friction distributions are different between the models (see Figure 5.4), the  $C_p$  values (see Figure 5.5) were not significantly affected by transition and turbulence model.

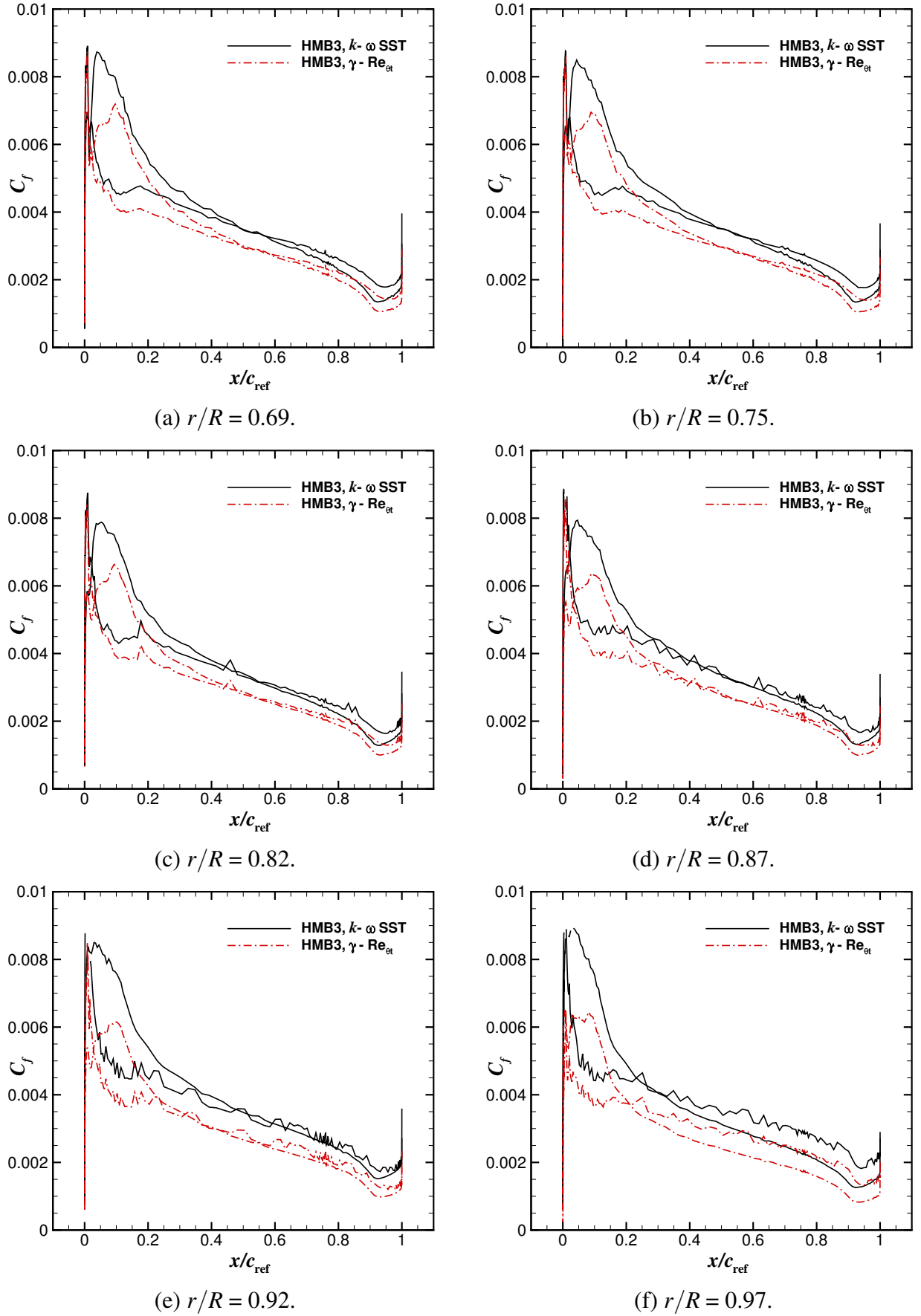


Figure 5.4:  $C_f$  profile comparisons between the  $k-\omega$  SST [191] and the  $\gamma-\text{Re}_{\theta_t}$  [47, 48] turbulence models at radial stations  $r/R = 0.69, 0.75, 0.82, 0.87, 0.92$ , and  $0.97$ .

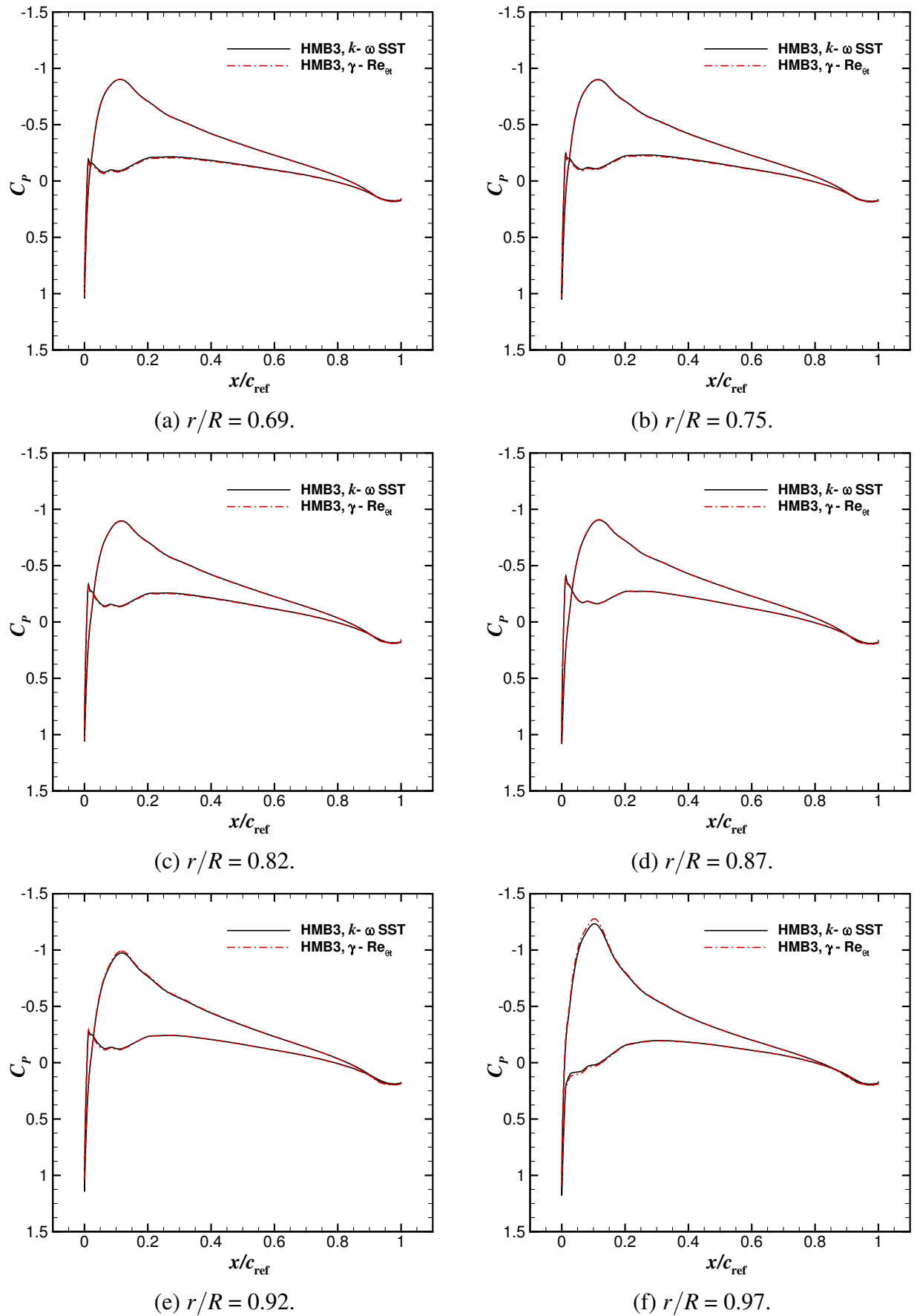
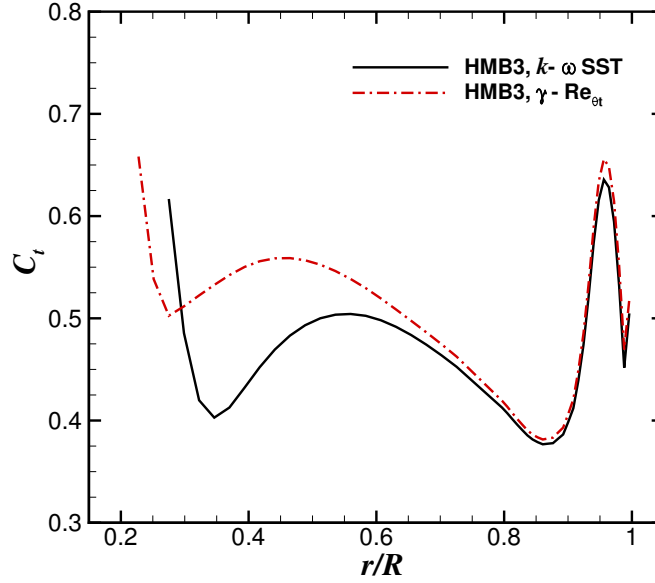
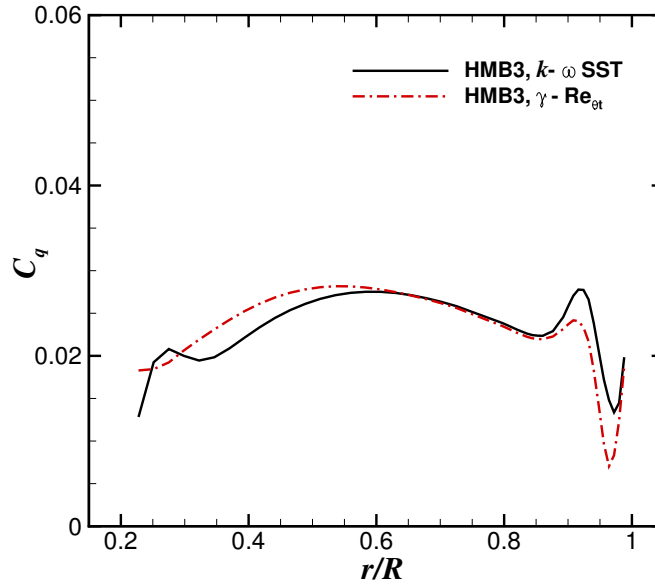


Figure 5.5:  $C_p$  profile comparisons between the  $k-\omega$  SST [191] and the  $\gamma-Re_{\theta_t}$  [47, 48] turbulence models at radial stations  $r/R = 0.69, 0.75, 0.82, 0.87, 0.92$ , and  $0.97$ .

Figure 5.6 shows the blade sectional thrust (top) and torque (bottom) coefficients. A gradual increase in loading distribution is found from 40%  $R$  to 80%  $R$  covering half of the rotor. Both coefficients are normalised with the local velocity, thus higher values of sectional thrust are seen inboard. The spanwise thrust coefficient increases steeply reaching its peak at 95%  $R$  before dropping at the tip. A similar pattern is found for the torque coefficient.



(a) Blade sectional thrust coefficient.



(b) Blade sectional torque coefficient.

Figure 5.6: Comparisons of blade sectional thrust coefficient (top) and torque coefficient (bottom) for the B0-105 rotor between the  $k-\omega$  SST [191] and the  $\gamma-Re_{\theta_t}$  [47, 48] turbulence models.



## 5.2 S-76 Main Rotor

The four-bladed S-76 model rotor, of 1/4.71 scale, and with  $-10^\circ$  of non-linear twist is now considered. To evaluate the current state-of-the-art performance prediction using different CFD solvers and methods for the same blade geometry, the AIAA Applied Aerodynamics Rotor Simulations Working Group [31, 226] was established in 2014. The 1/4.71 scale S-76 rotor blade [33, 34] was selected for assessment because of its publicly available data. The main characteristics of the model rotor blades are summarised in Table 5.5. The blade planform has been generated using eight radial stations, varying the twist  $\Theta$  along the span of blade defined with zero collective pitch at the 75%  $R$ . The SC-1013-R8 aerofoil is used from the root of the blade up to 18.9%  $R$ , the SC-1095-R8 aerofoil is used from 40%  $R$  to 80%  $R$ , and the SC-1095 aerofoil is used from 84%  $R$  to the tip. Between aerofoils, a linear transition zone is used. To increase the maximum rotor thrust, a cambered nose droop section was added to the SC-1095. Adding droop at the leading edge had two effects: it extended the SC-1095 chord, and reduced the aerofoil thickness from 9.5 to 9.4 percent. This section was designated SC-1095-R8. A detailed comparison and the aerodynamic characteristics of these aerofoils can be found in the work of Bousman [227]. The planform of the S-76 model rotor with 60% taper and  $35^\circ$  swept tip, the details on the blade radial twist, and the chord distributions are shown in Figure 5.7. Note that the thickness-to-chord ratio ( $t/c$ ) is held constant, and extends to almost 60% of the blade.

Table 5.5: Geometric properties of the 1/4.71 scale S-76 rotor [33].

Parameter	Value
Number of blades, $N_b$	4
Rotor radius, $R$	1.42 m (56.04 in)
Reference blade chord, $c_{\text{ref}}$	0.0787 m (3.1 in)
Aspect ratio, $R/c_{\text{ref}}$	18.07
Rotor solidity, $\sigma$	0.0704
Non-linear twist, $\Theta$	$-10^\circ$

The three blade tips considered for simulations were: rectangular, 60% taper- $35^\circ$  swept (baseline), and 60% taper- $35^\circ$  swept- $20^\circ$  anhedral. Flat and rounded tip-caps were also considered to study the effect of the tip vortex on the hover efficiency. Considering the rounded tip, two steps

were taken to generate a smooth tip-cap surface. First, a small part of the blade was cut off at 1/2 of the maximum  $t/c$  (which is 9.5%) of the tip aerofoil. Then, the upper and lower points of the aerofoil were revolved about each midpoint of the section. Following this procedure, the radius of the blade did not suffer a significant modification, changing from 56.04 to 56.03 inches. Figure 5.8 shows the S-76 model rotor with 60% taper-35° swept-20° anhedral with (a) flat and (b) rounded tip-caps installed. The 20 degrees of anhedral were introduced following the report of Balch and Lombardi [33] (Figure 9, page 45). Participants of the AIAA hover workshop also considered an anhedral angle of 16.23 degrees according to an internal report of Sikorsky Aircraft Corporation. In this work we follow Balch and Lombardi [33] but also computed a case with 16.23 degrees of anhedral (Figure 5.9).

### 5.2.1 S-76 Rotor Mesh

As the S-76 is a four-bladed rotor, only a quarter of the domain was meshed, assuming periodic conditions for the flow in the azimuthal direction (see Figure 5.10 (a)). If the wake generated by the rotor is assumed periodic and the blades experience limited stall, the hover configuration can be seen as a steady problem. A C-topology around the leading edge of the blade was selected, whereas an H-topology was employed at the trailing edge (see Figure 5.10 (b)). This configuration permits an optimal resolution of the boundary layer due to the orthogonality of the cells around the blade surface. Table 5.6 lists the grids employed for this study, showing the mesh size of each component.

Table 5.6: Meshing parameters for the S-76 mesh rotor blade.

Grid	Type	Background mesh size	Blade mesh size	Overall mesh size	Variation mesh size	Wall distance
I	Chimera	2 M	3 M	5 M	-	$1.0 \times 10^{-5} c_{\text{ref}}$
II	Chimera	3.5 M	4 M	7.5 M	50%	$1.0 \times 10^{-5} c_{\text{ref}}$
III	Chimera	3.5 M	26.5 M	30 M	500%	$1.0 \times 10^{-5} c_{\text{ref}}$
IV	Matched	-	-	9 M	80%	$5.0 \times 10^{-5} c_{\text{ref}}$

M=Million cells;  $c_{\text{ref}} = 3.1$  in.

The first cell normal to the blade was set to  $7.87 \times 10^{-7}$  m ( $1.0 \times 10^{-5} c_{\text{ref}}$ ) and  $3.96 \times 10^{-6}$  m

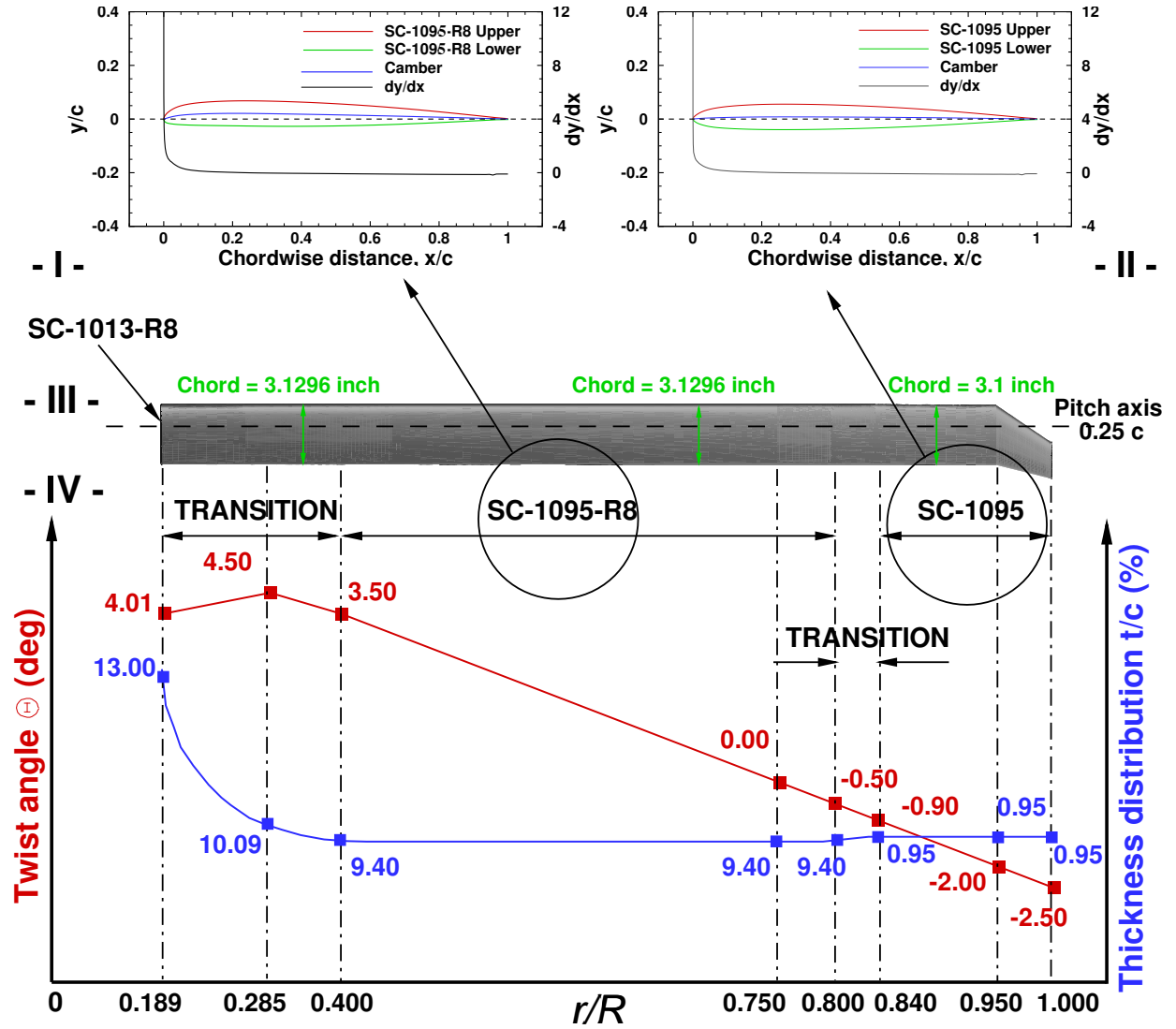
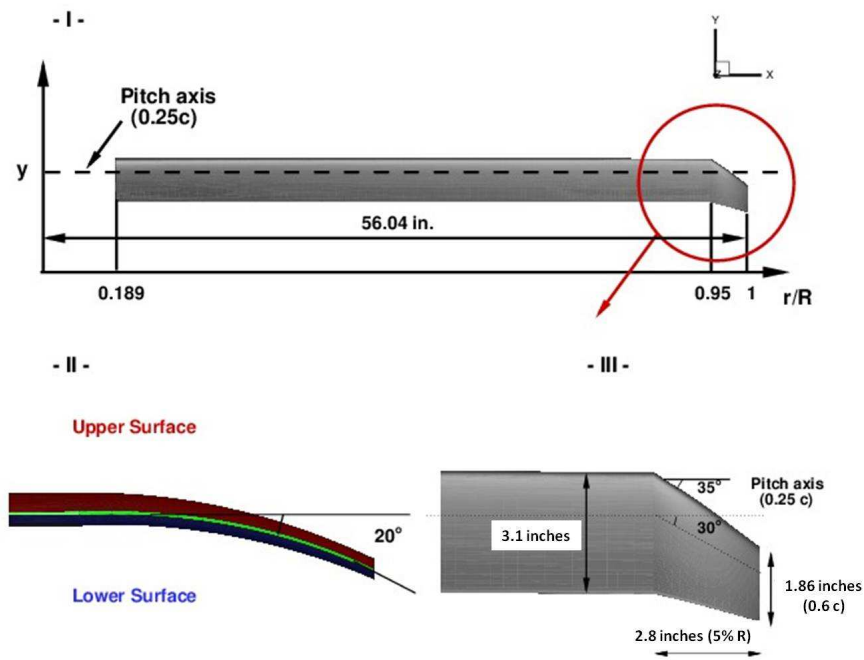
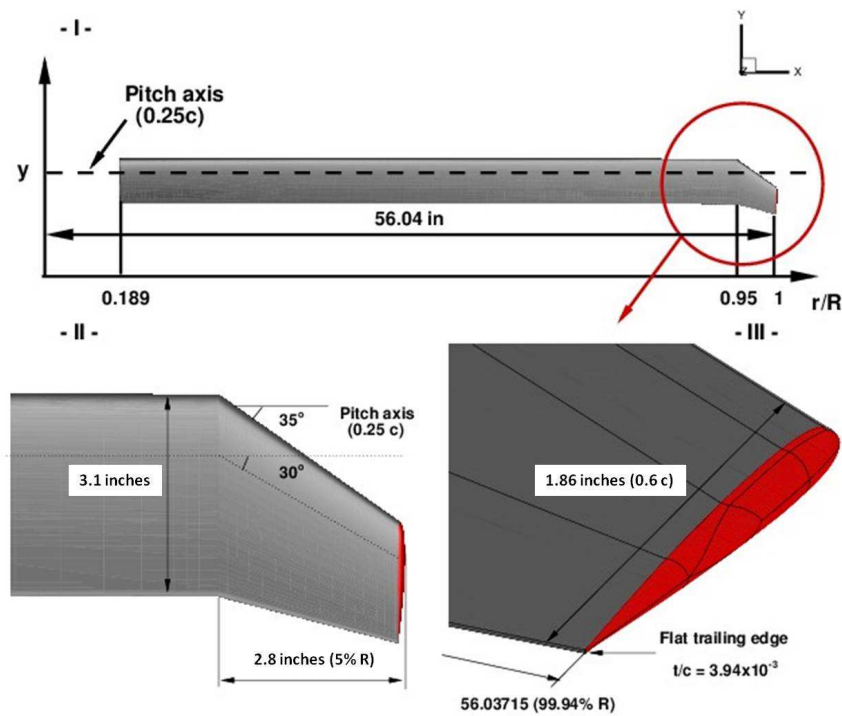


Figure 5.7: Geometry of the S-76 model rotor with 60% taper-35° swept tip, (I) SC-1095-R8 aerofoil, (II) SC-1095 aerofoil, (III) planform of the S-76 rotor, and (IV) twist and thickness distributions [37].

( $5.0 \times 10^{-5} c_{\text{ref}}$ ) for the chimera and matched grids, respectively, which assures  $y^+$  less than 1.0 everywhere on the blade for the employed  $Re$ . In the chordwise direction, between 235-238 mesh points were used, whereas in the spanwise direction 216 mesh points were used. A blunt trailing-edge was modelled using 42 mesh points. A C-H multi-block topology was used around the S-76 model rotor, combined with a background mesh using the chimera method. For all cases, the position of the farfield boundary was extended to  $3R$  (top) and  $6R$  (bottom and radial) from the rotor plane, which based on experience yields a solution independent of the boundary conditions



(a) Details of the anhedral flat tip-cap.



(b) Details of the anhedral rounded tip-cap.

Figure 5.8: Planform of the S-76 model rotor with 60% taper-35° swept-20° anhedral tip, and geometric details of the flat/rounded tip-caps.

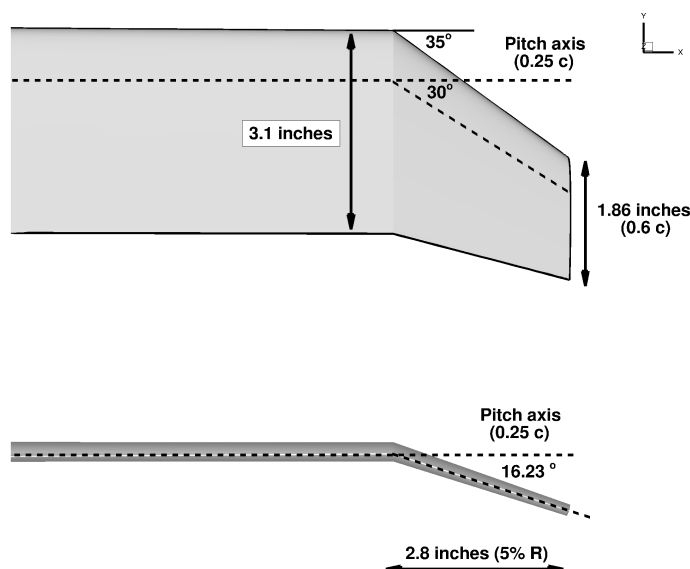
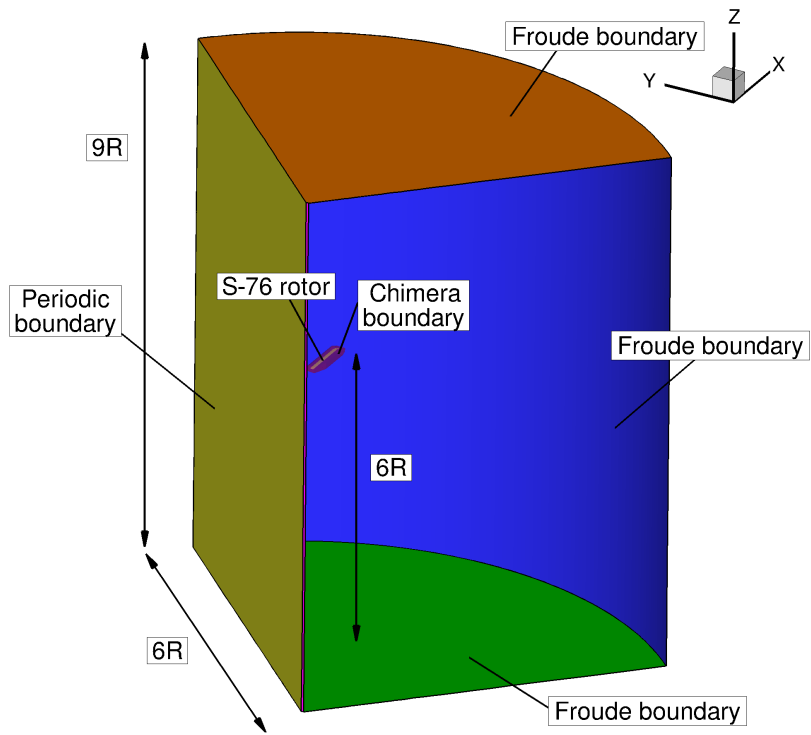


Figure 5.9: Planform of the S-76 model rotor with 60% taper-35° swept-16.23° anhedral tip.

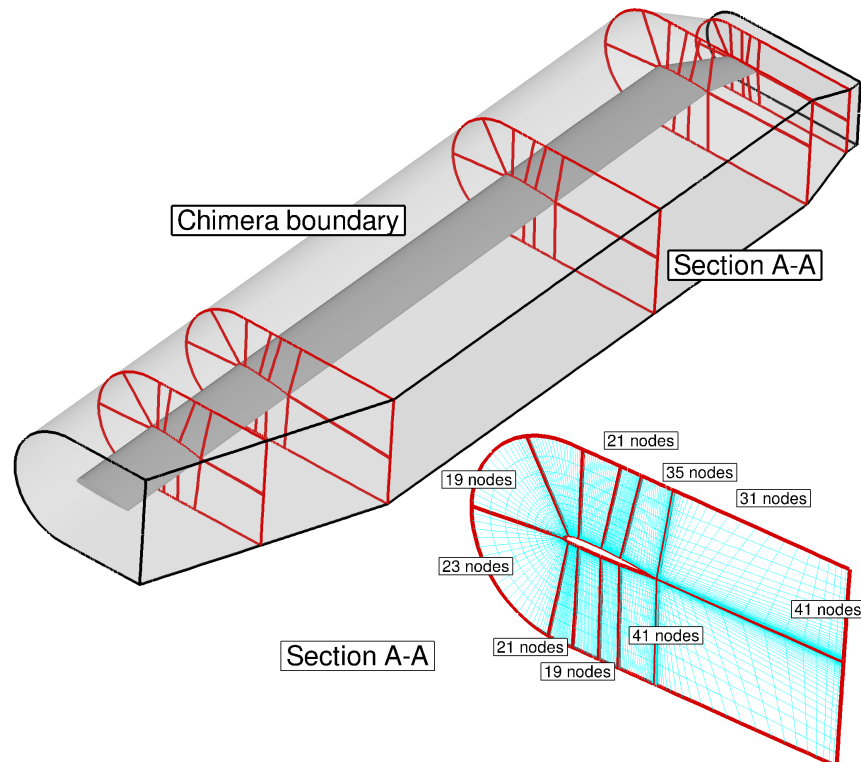
employed (Froude condition). The rotor hub was modelled as a cylinder, extending from inflow to outflow with a radius corresponding to 2.75% of the rotor radius  $R$ . If the chimera method is employed, a cylindrical mesh with nearly uniform spacing in the azimuthal direction is used as background. In the radial and vertical directions, a non-uniform spacing is used to have a finer mesh close to the wake region with a cell spacing of  $0.05c_{\text{ref}}$ , and coarser mesh towards the external boundaries.

## 5.2.2 Test Conditions and Computations

Table 5.7 summarises the employed conditions and the computations performed for each tip configuration. The blade-tip Mach number was set to 0.55, 0.60, and 0.65 and a wide range of blade pitch angles were considered, corresponding to low, medium, and high thrust. The Reynolds numbers, based on the reference blade chord of 3.1 inches and on the blade-tip speed, are  $1 \times 10^6$ ,  $1.09 \times 10^6$ , and  $1.18 \times 10^6$ , respectively. The S-76 swept-tapered tip with 16.23 degrees of anhedral, was compared with experiments for 20 degrees of anhedral at blade-tip Mach number of 0.60 and at blade pitch angle of 9.5 degrees.



(a) Computational domain.



(b) S-76 rotor mesh.

Figure 5.10: Computational domain and boundary conditions employed (top) and detailed view of the S-76 rotor mesh (bottom).

All flow solutions were computed by solving the RANS equations, coupled with Menter's  $k-\omega$  SST turbulence model [191]. The flow equations were integrated with the implicit dual-time stepping method of HMB, using a pseudo-time Courant–Friedrichs–Lewy (CFL) equal to 1.

Table 5.7: Computational cases for the 1/4.71 scale S-76 rotor.

Tip Shape	Grid employed	$M_{tip}$	$\theta_{75}$ (deg)
ST-F	I	0.65	6.5,7.5,9.5
ST-F	II	0.65	6.5,7.5,9.5
ST-RD	II	0.65	7.5
ST-F	II	0.65	4-11
ST-F	III	0.65	7
ST-F	IV	0.65	7
ST-F	II	0.60	6-9
ST-F	II	0.55	6-9
R-F	II	0.65	4-9
R-F	II	0.60	6.5,7.5,8.5,9.5
R-RD	II	0.60	7.5
STA-F	II	0.65	6.5,7.5,8.5,9.5
STA-RD	II	0.65	7.5
STA-F	II	0.60	6.5,7.5,9.5,10.5
STA-F <sup>a</sup>	II	0.60	9.5

R=Rectangular; ST=Swept-Taper; STA=Swept-Taper-Anhedral; F=flat tip-caps; RD=rounded tip-caps; a=16.23 degrees of anhedral

### 5.2.3 Swept-Taper Tip (Blade-Tip Mach Number of 0.65)

#### Mesh Convergence

The effect of the mesh density on the figure of merit as a function of the blade loading coefficient  $C_T/\sigma$  is shown in Figure 5.11, where the chimera grids I and II (see Table 5.6) were employed. Vertical lines labelled as empty (3,177 kg,  $C_T/\sigma = 0.06$ ) and maximum gross (5,307 kg,  $C_T/\sigma = 0.1$ ) weight, define the hovering range of the S-76 helicopter rotor. For the body-fitted mesh, refinements of the boundary layer and surface tip region were carried out. However, the capability to resolve the vortex structure at the background level is key for accurate predictions of the loading on the blade. Hence, half million cells were added to the new background mesh (grid II on Table 5.6). Consequently, the finest mesh (dashed lines with triangles) shows a better agreement at

low, medium, and high thrust coefficients with the test data of Balch and Lombardi [33] (opened squares). Table 5.8 reports the effect of the mesh density on  $C_T/\sigma$ ,  $C_Q/\sigma$ , and FoM for the coarse and medium chimera grids, at blade pitch angles  $\theta_{75}$  of  $6.5^\circ$ ,  $7.5^\circ$ , and  $9.5^\circ$ . Even though no thrust trimming was used, less than 1% discrepancy was found between the employed grids. This encourages the use of the 7.5 million cells mesh (grid II) to investigate the effect of the blade-tip Mach number for each tip configuration.

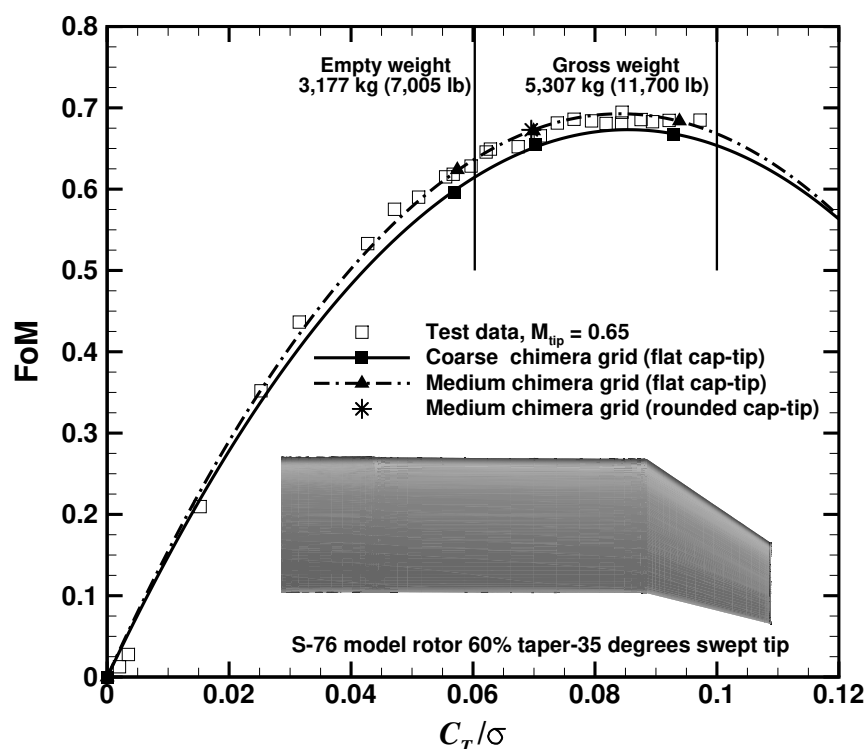


Figure 5.11: Effect of the mesh density on the FoM as a function of the  $C_T/\sigma$  for the S-76 model rotor with 60% taper-35° swept tip.

The effect of using rounded tip-caps on the hover efficiency was also investigated, where the medium chimera grid was selected for computations at blade pitch angle of  $7.5^\circ$ . Comparisons between the rounded (star symbols) and the flat tip-caps (triangle symbols) show a weak effect on the loading of the blade (Figure 5.11). If the flat tip-caps are taken as reference, differences of -0.5%, -1.0%, and 0.2% in  $C_T/\sigma$ ,  $C_Q/\sigma$ , and FoM were found when the rounded tip-caps were used.



Table 5.8: Effect of the mesh density on the  $C_T/\sigma$ ,  $C_Q/\sigma$ , and FoM using the coarse and the medium chimera grids.

Collective $\theta_{75}$ (deg)	Coarse chimera (grid I)			Medium chimera (grid II)		
	$C_T/\sigma$	$C_Q/\sigma$	FoM	$C_T/\sigma$	$C_Q/\sigma$	FoM
6.50	0.0570	0.00428	0.596	0.0574	0.00413	0.624
7.50	0.0703	0.00533	0.655	0.0699	0.00516	0.672
9.50	0.0928	0.00794	0.667	0.0939	0.00788	0.684

### Integrated Blade Loads

As shown in Figure 5.11, the performance of the S-76 with swept and tapered tip is well predicted with the medium chimera grid, of 7.5 million cells per blade. Taking this tip configuration as a baseline, the capability of the HMB solver can be explored. In this regard, performance analyses of the S-76 blade for a large range of blade pitch angles using chimera and matched multi-block grids are presented. Figure 5.12 shows the variation of the FoM with the blade loading coefficient, at eight blade pitch angles, which cover low, medium, and high thrust. Comparison with experimental data (opened squares) and momentum-based estimates of the FoM (dashed lines) are also included. For the momentum-theory curve, an induced power factor  $k_i$  of 1.1 and overall profile drag coefficient  $C_{D0}$  of 0.01 were selected, showing, as expected, a wrong tendency of the power divergence at high trust [228]. It can be seen that the CFD computations corresponding to the medium chimera grid (lines with square symbols), are in close agreement with the experimental data. Note that at low thrust, experiments and predictions show low values of the figure of merit, as consequence of the high ratio profile drag to thrust coefficient ( $\sigma C_{D0}/C_T$ ). The effect of a finer chimera grid (triangles) and a matched grid (stars) (grids III and IV on Table 5.6, respectively) on the hover performance of the S-76 rotor blade was also investigated at a blade pitch angle of  $7^\circ$ . The solution using the finest chimera grid shows a slight effect on the figure of merit with respect to the computation on the medium one. This supports the selection of the medium chimera grid to evaluate the entire range of blade pitch angles at a reduced computational cost. In addition, the effect of using a matched grid is also reported in Figure 5.12, showing a mild effect on the loads.

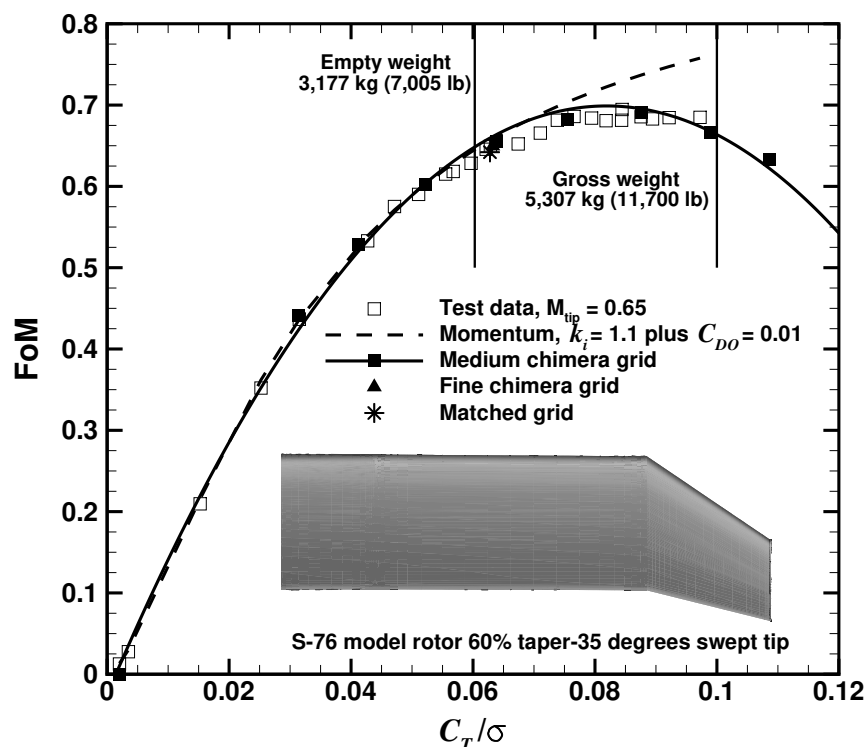


Figure 5.12: Figure of merit versus blade loading coefficient for the S-76 model rotor with 60% taper-35° swept tip at blade-tip Mach number of 0.65.

Table 5.9 summarises the S-76 (baseline) hover performance at a blade pitch angle of 7° using different grids and methods. The FoM performed by the medium chimera grid is predicted to within 0.6 counts, whereas matched and fine chimera grids predicted to within 0.7 and 0.02 counts, respectively.

Table 5.9: Comparison between experimental data [33, 34] and CFD predictions for the 1/4.71 scale S-76 rotor at blade-tip Mach number of 0.65.

Case	Grid	$C_T/\sigma$	$C_Q/\sigma$	FoM	$\Delta\text{FoM}[\%]$
Test data, $\theta_{75} = 7.1^\circ$	-	0.06285	0.004553	0.6494	-
Medium chimera grid	II	0.06381	0.004615	0.6551	0.87
Fine chimera grid	III	0.06324	0.004594	0.6496	0.02
Matched grid	IV	0.06278	0.004598	0.6420	1.14

### Sectional Blade Loads

Figure 5.13 shows the distribution of sectional thrust and torque coefficients along the rotor radius, for blade pitch angles from  $4^\circ$  to  $11^\circ$ . Both coefficients are normalised with the local velocity:

$$C_t = \frac{dt/dr}{1/2\rho_\infty c(\Omega r)^2}. \quad (5.1)$$

$$C_q = \frac{dq/dr}{1/2\rho_\infty cR(\Omega r)^2}. \quad (5.2)$$

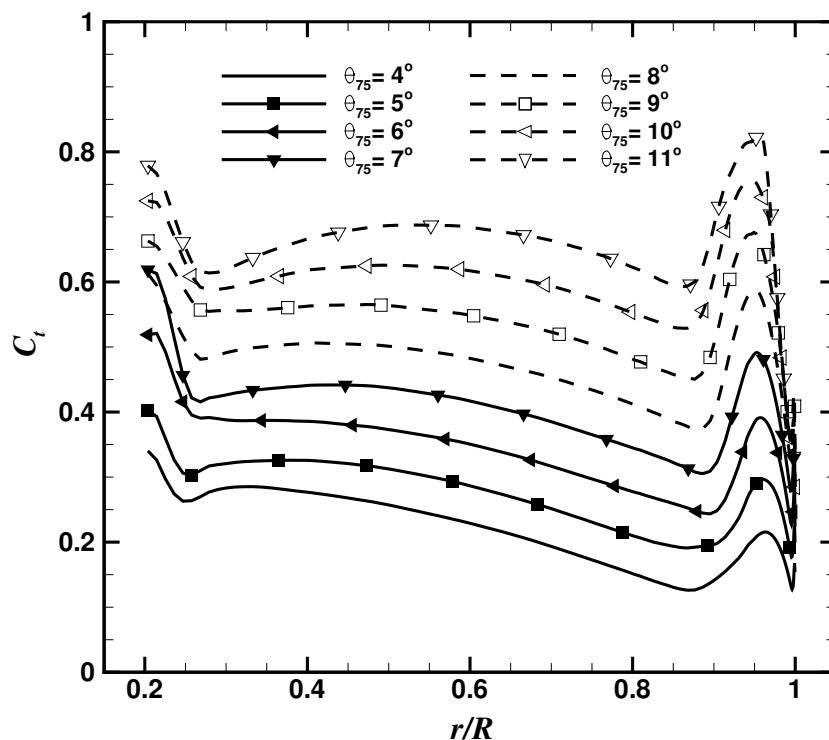
The influence of the tip vortex on the tip region (from 95%  $R$  100%  $R$ ) is visible in terms of loading and torque coefficients. As a means of comparing the effect of the thrust coefficient on the tip-loss, a tip-loss factor  $B$  is computed. Tip-loss factors  $B \approx 1 - \frac{\sqrt{C_T}}{N_b}$  for the lower and higher thrust coefficient ( $\theta_{75} = 4^\circ$  and  $11^\circ$ ) were 0.988 and 0.978, respectively.

### Surface Pressure Predictions

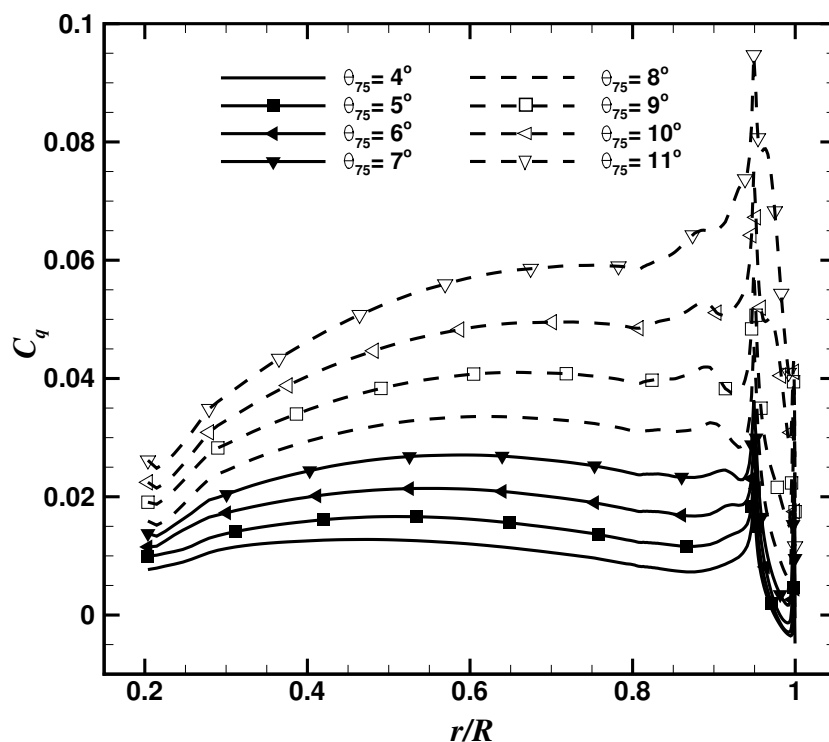
The surface pressure coefficient is analysed for four blade pitch angles at two radial stations along the S-76 blade on the medium chimera grid. It is computed based on the local velocity at each radial station:

$$C_P = \frac{P - P_\infty}{1/2\rho_\infty(\Omega r)^2}. \quad (5.3)$$

Figure 5.14 shows the surface pressure coefficient at outboard ( $r/R = 0.95$  and  $0.975$ ) blade sections, where the critical  $C_P^*$  is also given to assess the sonic region of the blade (local flow above Mach number 1). Both sections reach sonic conditions above collective angles of 7 and 5 degrees, respectively, which lead to increased drag coefficient. This zone is clearly extended further along the blade span as the collective is increased. Despite the use of the swept tip, a mild shock is found at the vicinity of the tip. Figure 5.15 (a) shows contours of Mach number on a plane extracted at  $r/R = 0.975$  for a blade collective angle of 7.0 degrees, which reveals a weak shock wave. Moreover, Figure 5.15 (b) shows for each blade collective angle the radial location where the local flow becomes supersonic.



(a) Blade sectional thrust coefficient



(b) Blade sectional torque coefficient.

Figure 5.13: Blade sectional thrust coefficient (top) and torque coefficient (bottom) for the S-76 model rotor with 60% taper-35° swept tip at blade-tip Mach number of 0.65.

### Trajectory and Size of the Tip Vortex

To ensure realistic predictions of the wake-induced effects, the radial and vertical displacements, and size of the vortex core should be resolved, at least for the first and second wake passages. Figure 5.16 (a) shows a comparison of the radial and vertical displacements of the tip vortices, as functions of the wake age (in degrees), with the prescribed wake-models of Kocurek and Tangler [20] and Landgrebe [19]. It should be mentioned that, a blade loading coefficient  $C_T/\sigma = 0.0638$  was selected, which corresponds to  $\theta_{75} = 7.0^\circ$ . Both empirical models are based on flow visualisation studies of the rotor wake flow, which is related to the geometric rotor parameters like the number of blades, aspect ratio, chord, solidity, thrust coefficient, and linear twist angle. The prediction of the trajectory is captured for up to 3-blade passages (wake age of  $270^\circ$  for a four-bladed rotor) and is in good agreement with both empirical models. The effect of the blade pitch angle ( $\theta_{75} = 5.0^\circ$ ,  $7.0^\circ$ , and  $9.0^\circ$ ) on the trajectory of the tip vortex is also investigated and it depicted in Figure 5.16 (b). Until the first passage (wake age of  $90^\circ$ ), a slow convection of the tip vortices is seen in vertical displacement ( $-z/R$ ). As result of the passage of the following blade, a linear increment of the vertical displacement of the wake is found, mainly due to the change in the downwash velocity. As the thrust coefficient is increased, a more rapid vertical displacement is seen for the tip vortices. On the other hand, the radial displacement is less sensitive to changes on the blade pitch angles, reaching asymptotic values approximately at  $r/R = 0.8$ .

Likewise, the vortex core size (based on vorticity magnitude) was computed at blade pitch angles of  $\theta_{75} = 5.0^\circ$ ,  $7.0^\circ$ , and  $9.0^\circ$ . Figure 5.17 presents the growth of the vortex core radius normalised by the equivalent blade chord ( $c_e=3.07$  inches):

$$c_e = 3 \int_0^R c(r/R) (r/R)^2 d(r/R). \quad (5.4)$$

A rapid growth of the radius of the tip vortex is seen, as function of the wake age. Up to the first passage (wake age of  $90^\circ$ ), a moderate effect of the blade pitch angles on the core size of the vortex wake is also observed, with cores reaching three times their initial values. Therefore, for the third passage (wake age of  $270^\circ$ ), the values of the core reached four times their initial value. This rapid growth it due to numerical diffusion and grid density effects.

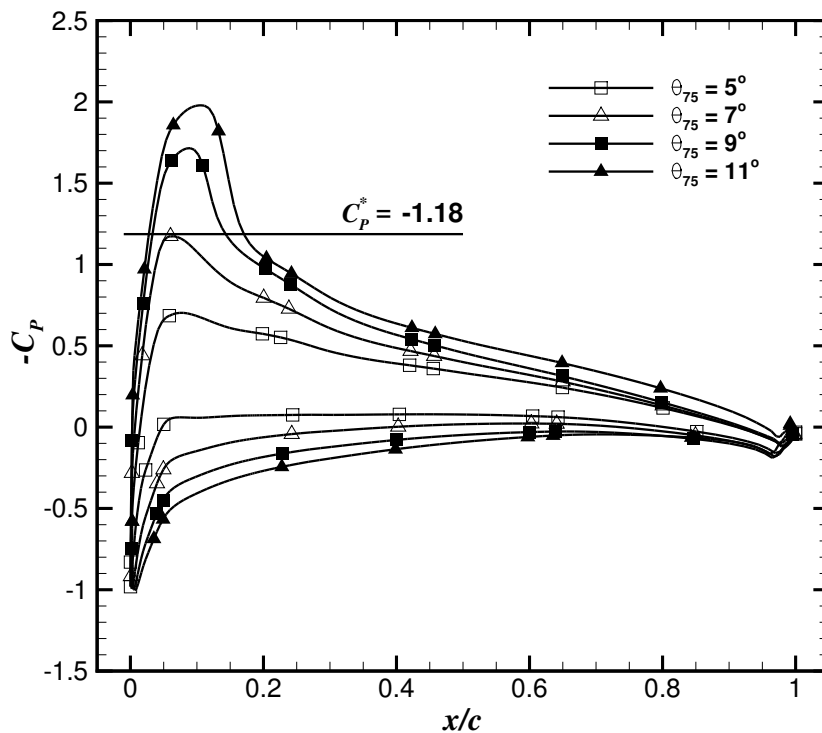
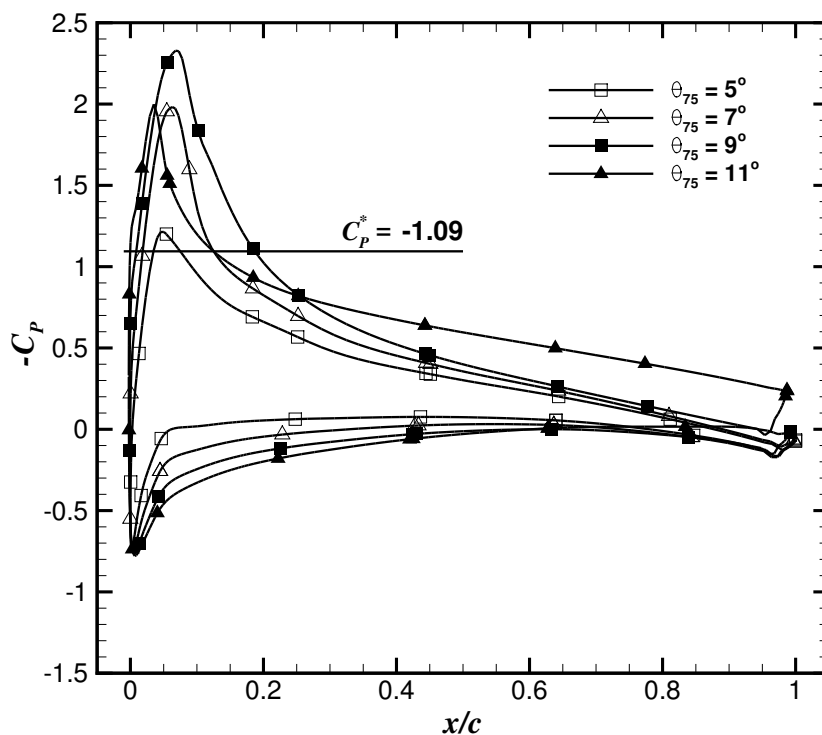
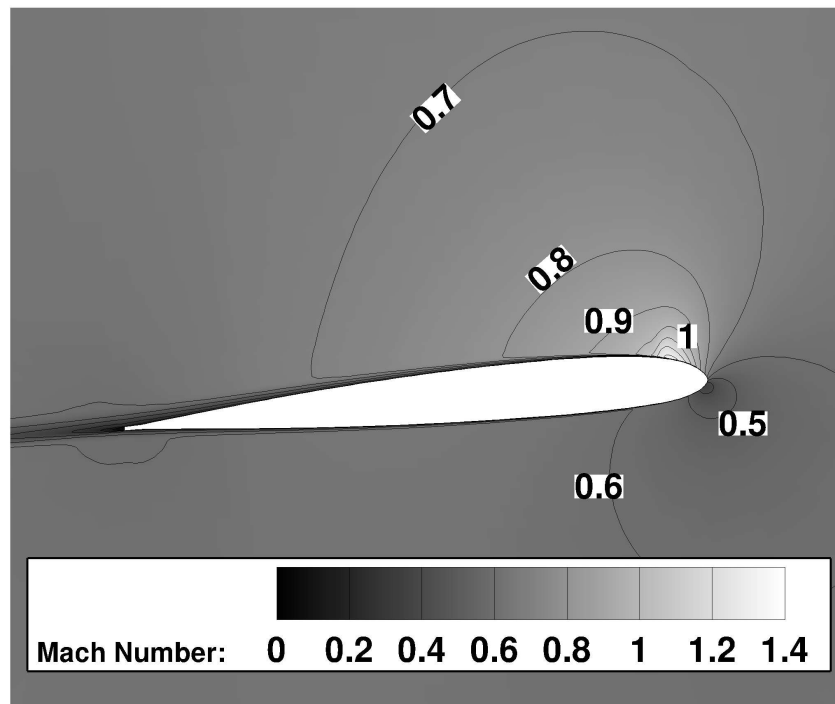
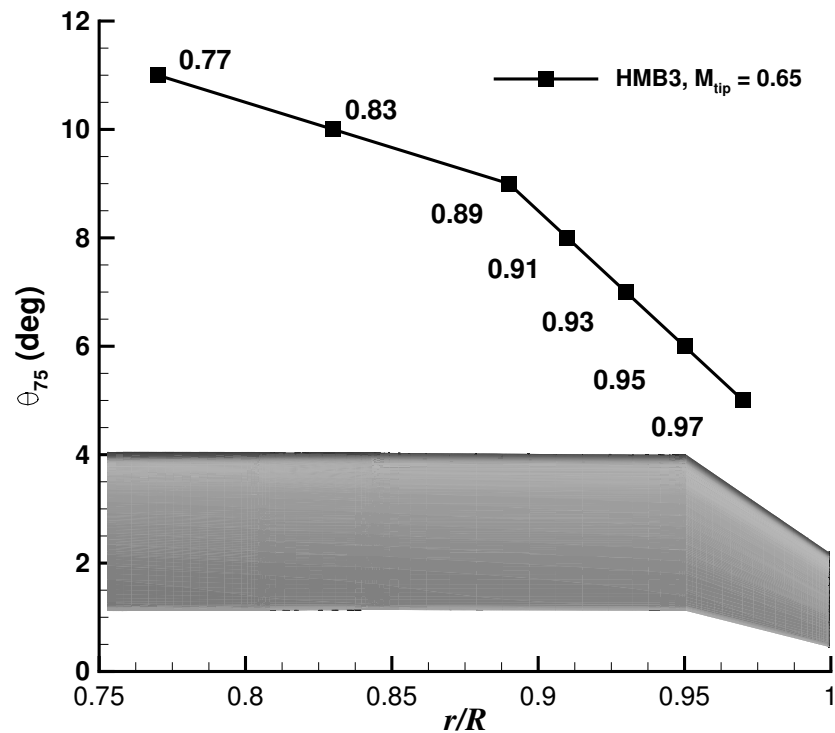

 (a)  $r/R = 0.95$ .

 (b)  $r/R = 0.975$ .

Figure 5.14: Surface pressure coefficient for the S-76 model rotor with 60% taper-35° swept tip at

blade-tip Mach number of 0.65. Critical  $C_p^* = \frac{2}{\gamma(M_{\text{tip}} \frac{r}{R})^2} \left[ \left( \frac{2 + (\gamma - 1)(M_{\text{tip}} \frac{r}{R})^2}{\gamma + 1} \right)^{\frac{\gamma}{\gamma - 1}} - 1 \right]$ .

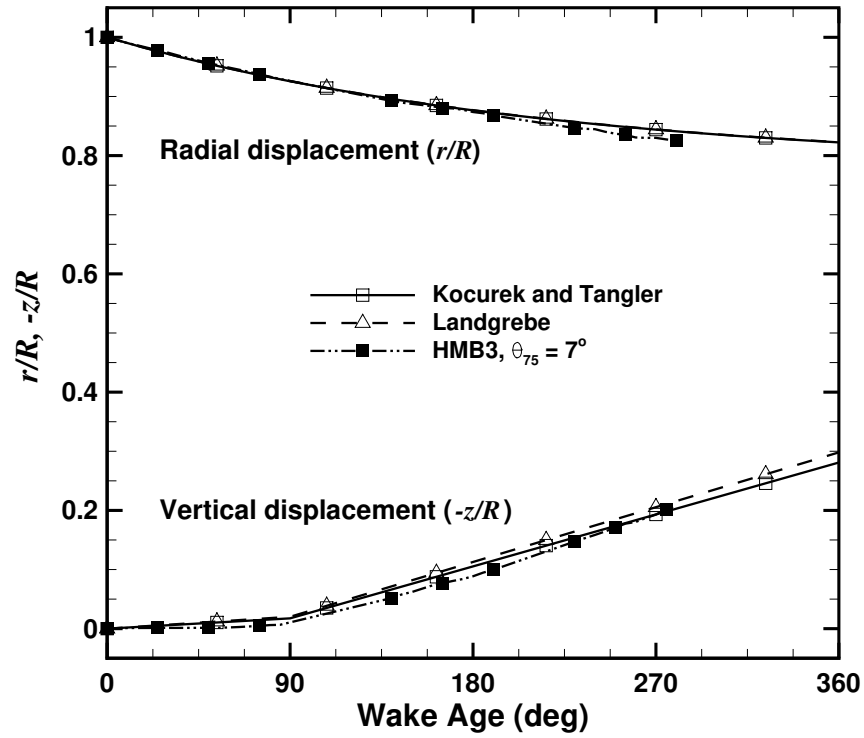


(a)

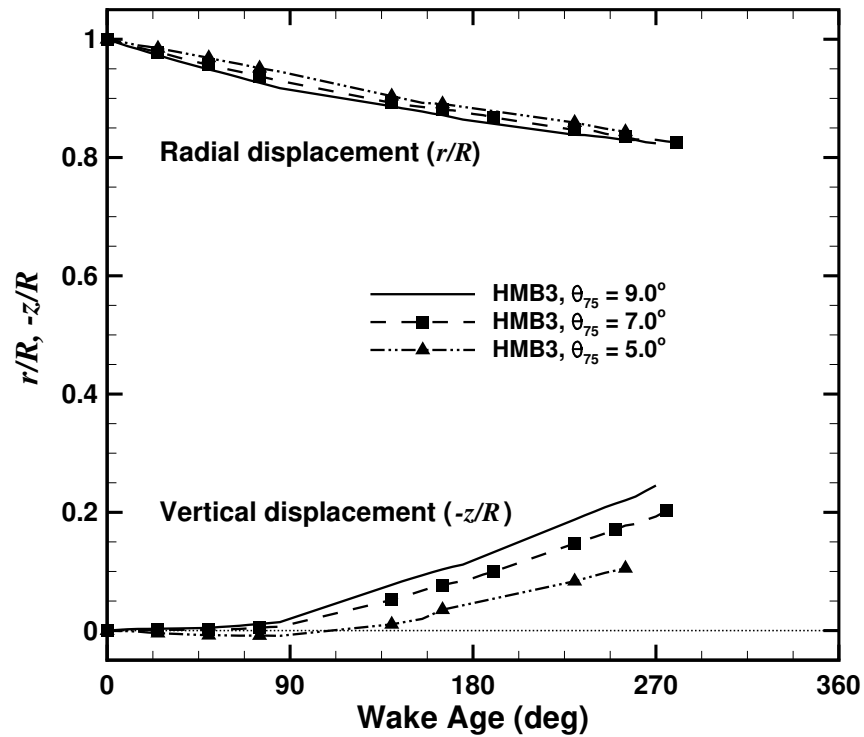


(b)

Figure 5.15: Contours of Mach number on a plane extracted at  $r/R = 0.975$  (top) and radial location where the local flow becomes first supersonic as function of  $\theta_{75}$  (bottom).



(a)



(b)

Figure 5.16: Comparison between the computed tip vortex displacements and the prescribed wake-models (top) and effect of the collective on the radial and vertical displacements of the tip vortices (bottom).



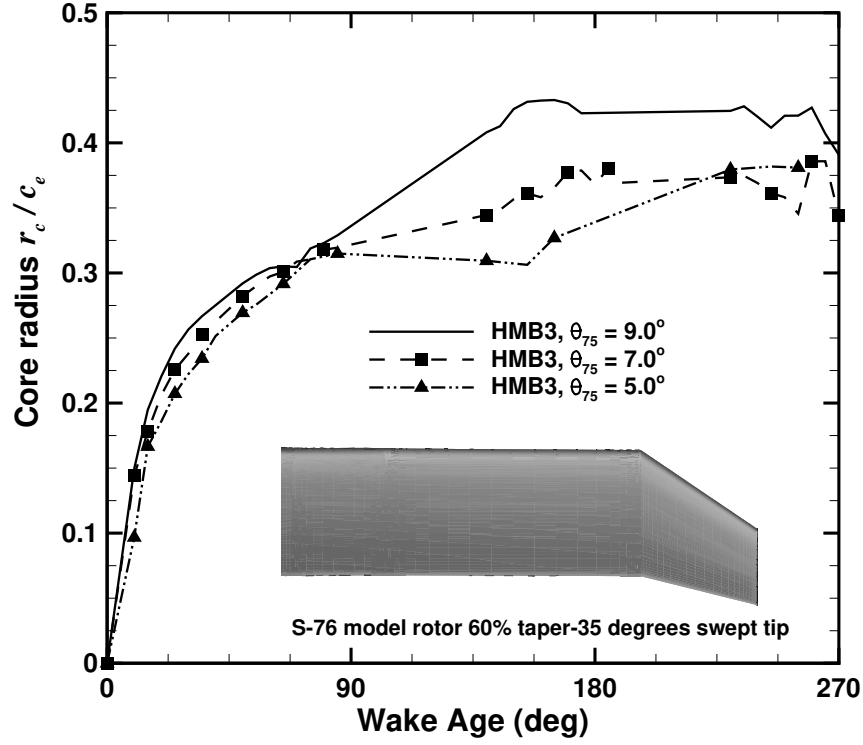


Figure 5.17: Vortex core size versus wake age (in degrees) at blade pitch angles  $\theta_{75}$  of  $5.0^\circ$ ,  $7.0^\circ$ , and  $9.0^\circ$ .

The flowfield around the S-76 blade is visualised using iso-surfaces of  $Q$  criteria [206] in Figure 5.18. The quantity  $Q$  is defined as follows:

$$Q = \frac{1}{2}(\hat{\Omega}_{ij}\hat{\Omega}_{ij} - \hat{S}_{ij}\hat{S}_{ij}), \quad (5.5)$$

where  $\hat{\Omega}_{ij}$  and  $\hat{S}_{ij}$  are the antisymmetric and symmetric parts of the velocity gradient, respectively:

$$\hat{\Omega}_{ij} = \frac{1}{2} \left( \frac{\partial \hat{u}_i}{\partial x_j} - \frac{\partial \hat{u}_j}{\partial x_i} \right), \quad \hat{S}_{ij} = \frac{1}{2} \left( \frac{\partial \hat{u}_i}{\partial x_j} + \frac{\partial \hat{u}_j}{\partial x_i} \right). \quad (5.6)$$

The quantity  $Q$  has the dimensions of a velocity squared divided by a length squared, and it is therefore nondimensionalised in HMB as follows:

$$\tilde{Q} = Q \left( \frac{L_{\text{ref}}}{V_{\text{ref}}} \right)^2. \quad (5.7)$$

The collective was set to  $7.0^\circ$  degrees. The plots reveal that the computations capture the rotor wake up to 3 and 6 blade passages for the overset grids II and III, respectively. A root vortex is also seen in both computations due to the employed mesh that has no rotor-head and hub.

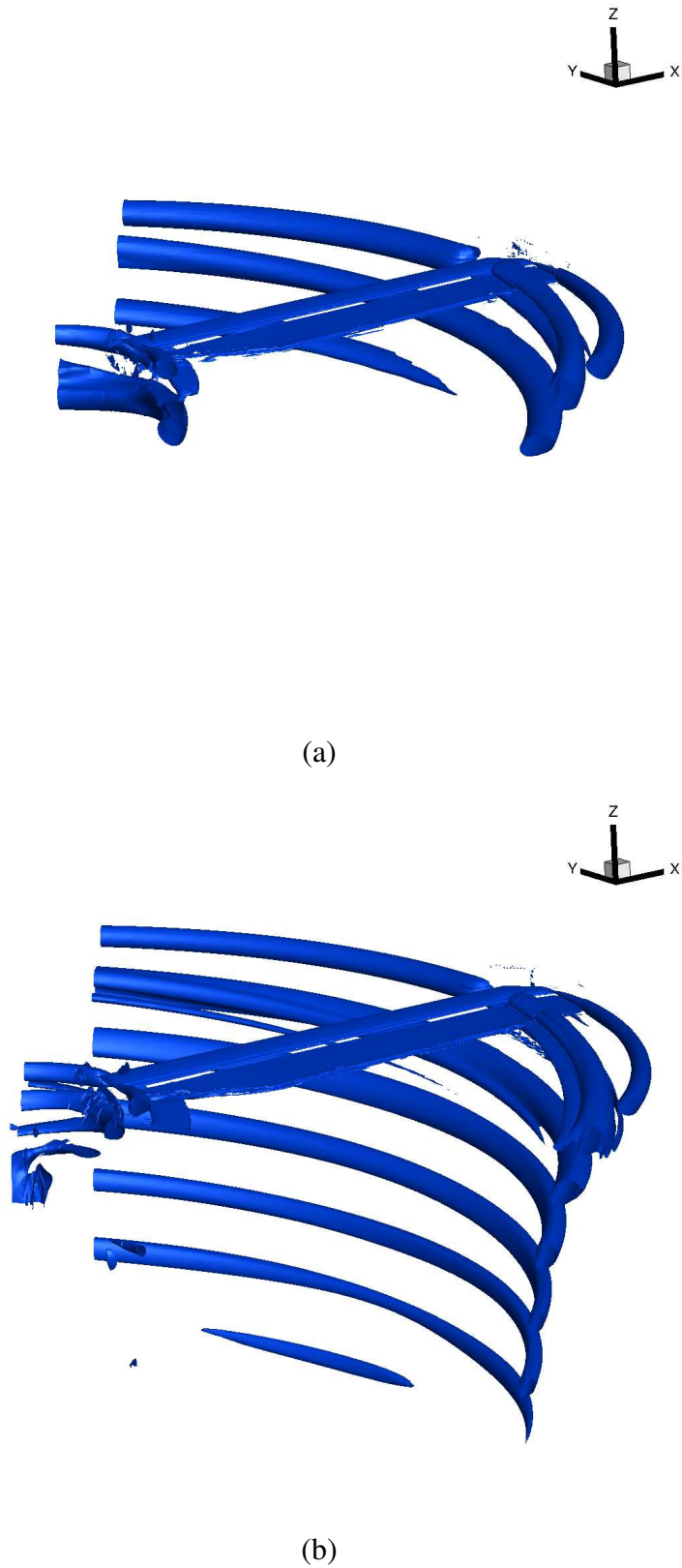


Figure 5.18: Wake visualisation of the S-76 model-scale in hover using the  $\tilde{Q}$  criterion for overset grids II (top) and III (bottom) of Table 5.6.

### 5.2.4 Swept-Taper Tip (Blade-Tip Mach Numbers of 0.60 and 0.55)

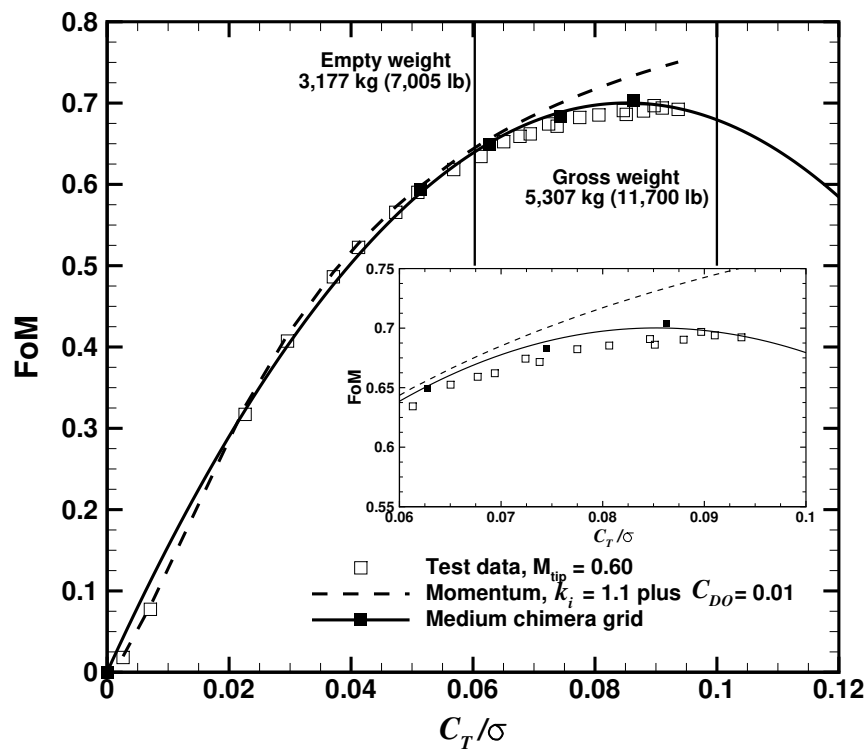
Hover predictions on the S-76 with 60% taper-35° swept flat tip at blade-tip Mach numbers of 0.55 and 0.60 were performed at four blade pitch angles (6°, 7°, 8° and 9°). For this section, integrated performance is evaluated using the available experimental data [33, 34]. The medium chimera grid was used as consequence of its good performance obtained previously at blade-tip Mach number of 0.65, and its low computational cost.

Figures 5.19 show the FoM at blade-tip Mach numbers of 0.6 (a) and 0.55 (b), respectively, as a function of the blade loading coefficient  $C_T/\sigma$ . Comparisons with the momentum-based estimation of the FoM are also given, with induced power factor  $k_i$  of 1.1 and overall profile drag coefficient  $C_{D0}$  of 0.01. It is seen that the CFD predictions slightly over-predict the values of the figure of merit at blade pitch angles of 8° and 9°. Nevertheless, the calculations show a reliable correlation to overall performance, and the tip Mach number effect is well captured.

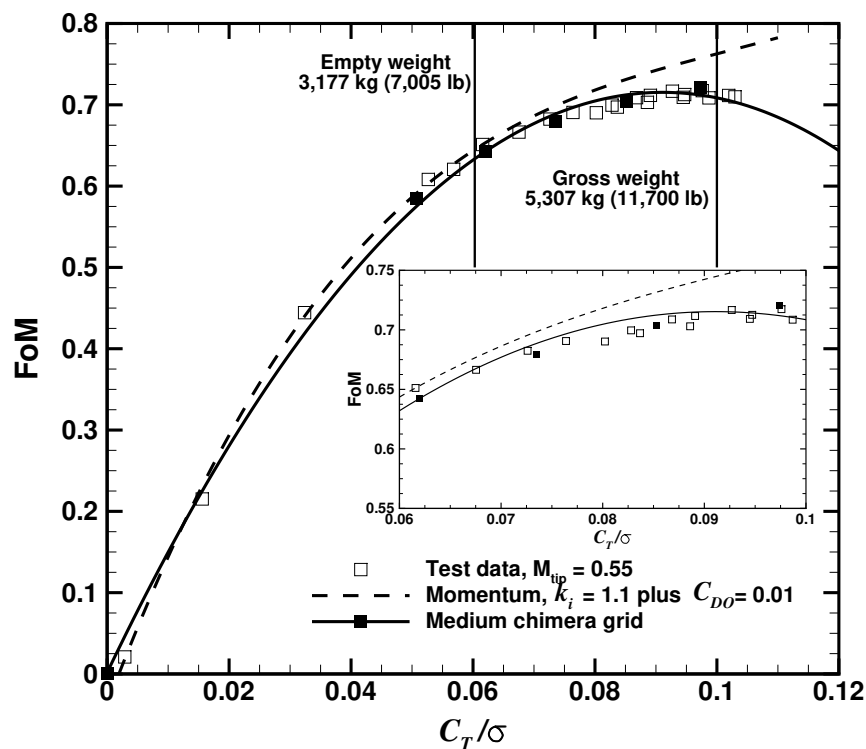
### 5.2.5 Rectangular Tip (Blade-Tip Mach Numbers of 0.65 and 0.6)

The effect of the rectangular tip on the rotor performance of the 1/4.71 scale S-76 is evaluated here. Figures 5.20 (a) and (b) show the figure of merit for blade pitch angles from 4° to 9° and 6.5°, 7.5°, 8.5°, and 9.5° at blade-tip Mach numbers of 0.65 and 0.60, respectively. Comparisons with the momentum-based estimation of the figure of merit are also given with an induced power factor  $k_i$  of 1.15 and overall profile drag coefficient  $C_{D0}$  of 0.01. Note that rectangular tips present a higher induced power factor, leading to decrease the FoM. At blade-tip Mach number of 0.65, it can be seen that CFD predictions over-predict the values of FoM at blade pitch angles of 7 and 8 degrees. However, CFD results for performance at blade-tip Mach number of 0.60 reveal good agreement with the experimental data.

The effect of using rounded tip-caps (represented with triangles in Figure 5.20 (b)) was also evaluated, showing a weak effect on the FoM. The CFD results were able to predict the trend of the rectangular tip and indicate that this shape is of lower performance than the swept-tapered one.



(a)  $M_{tip} = 0.6$ .



(b)  $M_{tip} = 0.55$ .

Figure 5.19: Figure of merit versus blade loading coefficient for the S-76 model rotor with 60% taper-35° swept tip at blade-tip Mach numbers of 0.6 (top) and 0.55 (bottom).

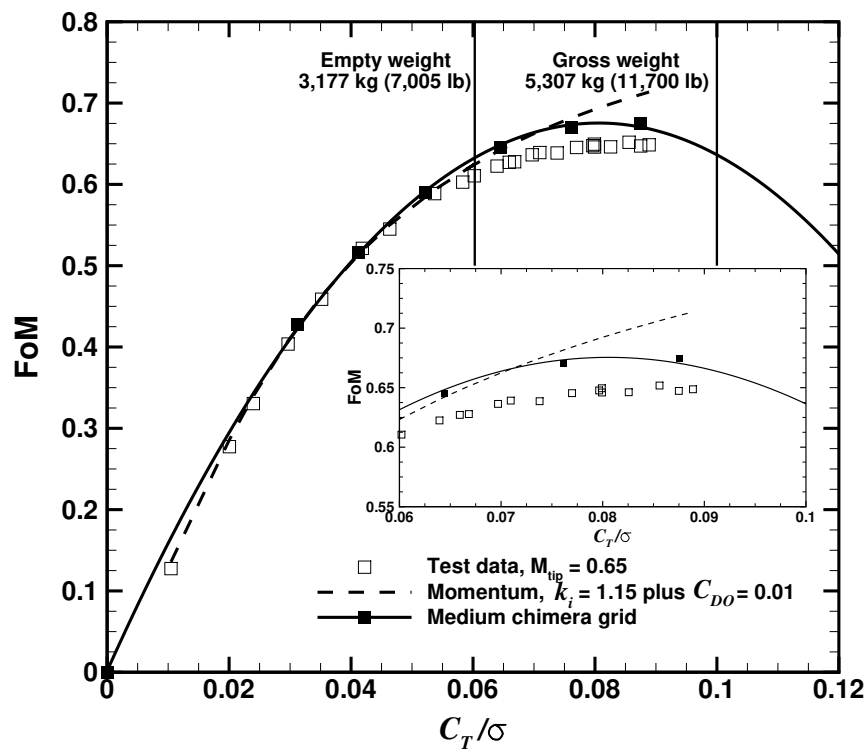
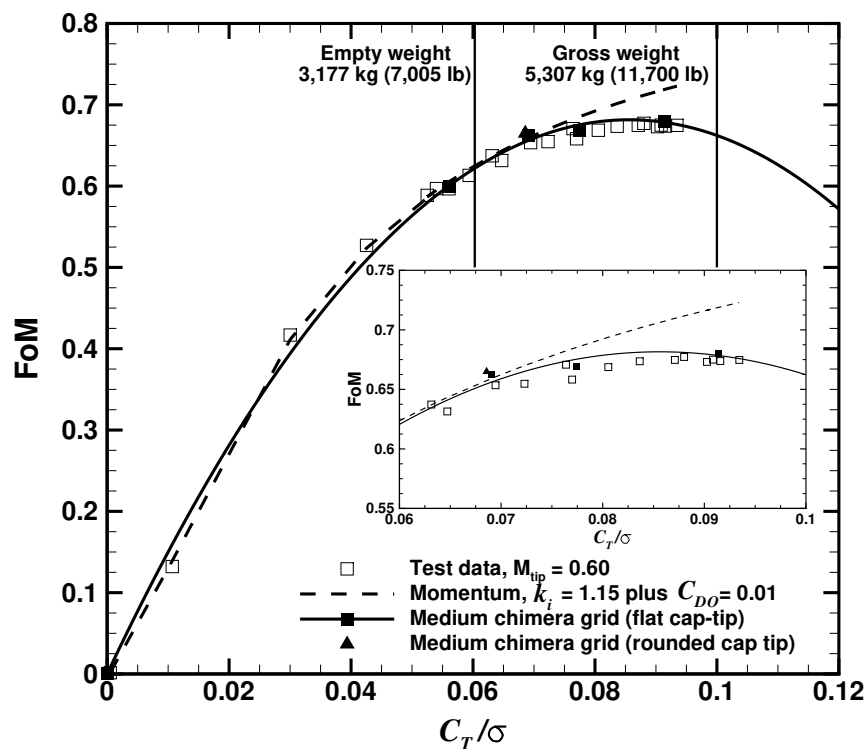

 (a)  $M_{tip} = 0.65$ .

 (b)  $M_{tip} = 0.60$ .

Figure 5.20: Figure of merit versus blade loading coefficient for the S-76 model rotor with rectangular tip at blade-tip Mach numbers of 0.65 (top) and 0.60 (bottom).

### 5.2.6 Anhedral Tip (Blade-Tip Mach Numbers of 0.65 and 0.60)

Figure of merit as function of the blade loading coefficient for the S-76 model rotor with 60% taper-35° swept-20° anhedral tip, is given in Figure 5.21 at blade-tip Mach numbers of 0.65 and 0.60. Rounded tip-caps were also computed at blade pitch angle of 7.5°. As shown for the swept-tapered tip, the effect of rounding is weak. Overall, the CFD predictions are in good agreement with the experimental data at low, medium and high thrust. The results for this tip, broadly follow the swept-tapered tip trends. The main difference is the higher figure of merit that is obtained due to the additional off-loading of the tip provided by the anhedral. This is a known effect [229] and is captured accurately by the present computations.

To assess the effect of the anhedral angle (16.23 degrees instead to 20 degrees) on the figure of merit, a comparison between both cases is shown in Figure 5.21 (b) at blade-tip Mach number of 0.6 and collective 9.5°. It is found that an anhedral of 16.23 degrees resulted in a figure of merit very close the value obtained for 20 degrees. A difference of 0.2 counts of FoM is computed with the 20 degrees anhedral giving ever so slightly higher FoM.

### 5.2.7 Effect of the Tip Shape

The effect of the tip shape on the figure of merit at blade-tip Mach number of 0.65 is depicted in Figure 5.22. Hover performance predictions are represented by solid lines for the rectangular tip, dashed lines are used for the swept-tapered tip, and dash-dotted lines for the swept-tapered tip with anhedral. Experimental data is also shown using open symbols. Considering the experimental data, the swept-tapered with anhedral and the rectangular tips represent the upper and lower bounds of the experimental figure of merit, while the swept-tapered tip is located within this band. This is in line with the HMB predictions that are in acceptable agreement with the experimental data across the range of blade thrusts, and tip shapes considered.

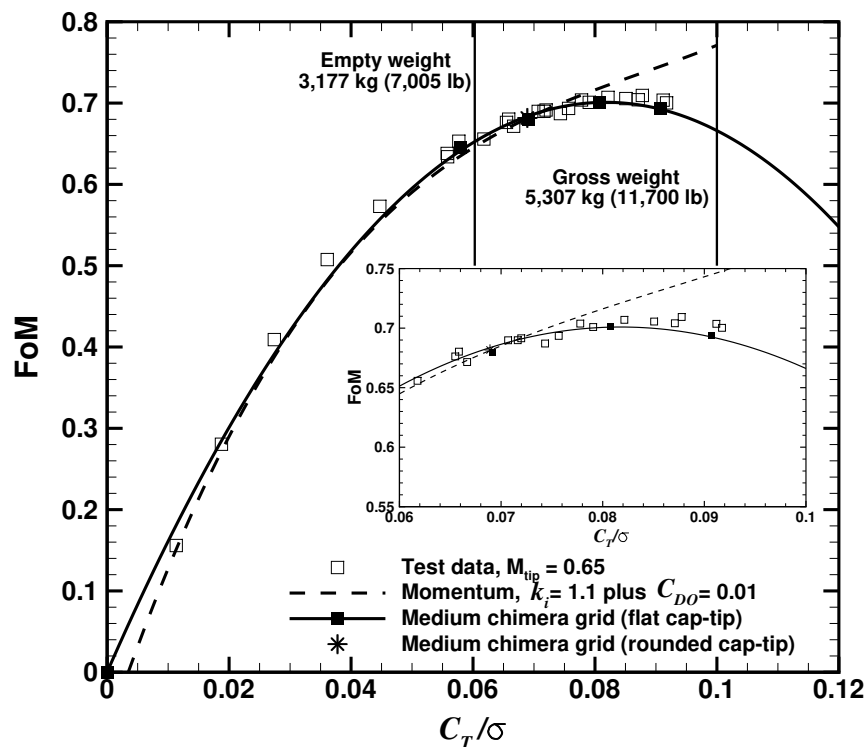
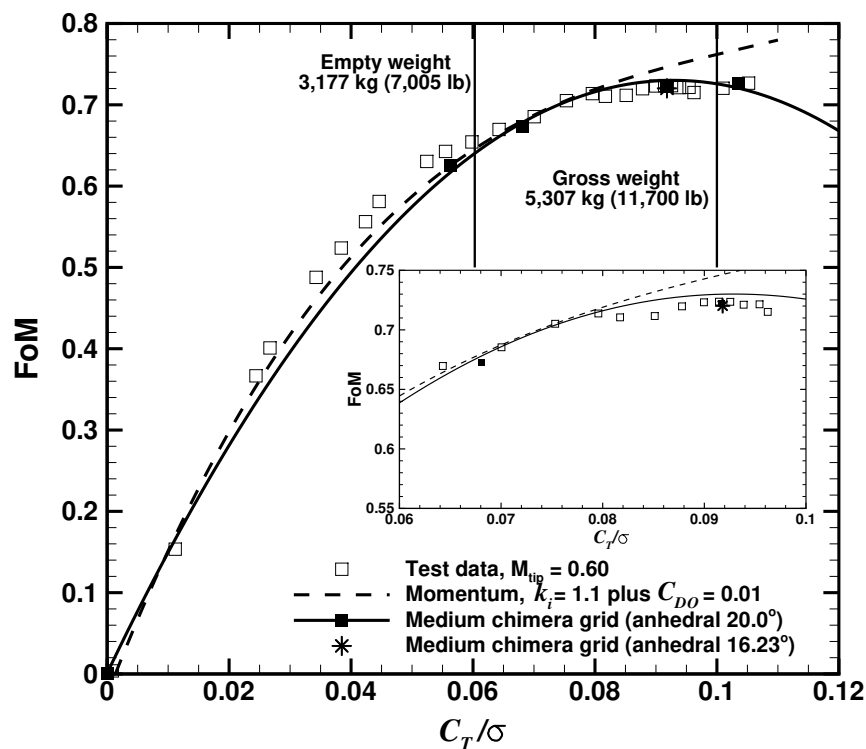

 (a)  $M_{tip} = 0.65$ .

 (b)  $M_{tip} = 0.60$ .

Figure 5.21: Figure of merit versus blade loading coefficient for the S-76 model rotor with 60% taper-35° swept-20° anhedral tip at blade-tip Mach numbers of 0.65 (top) and 0.60 (bottom).

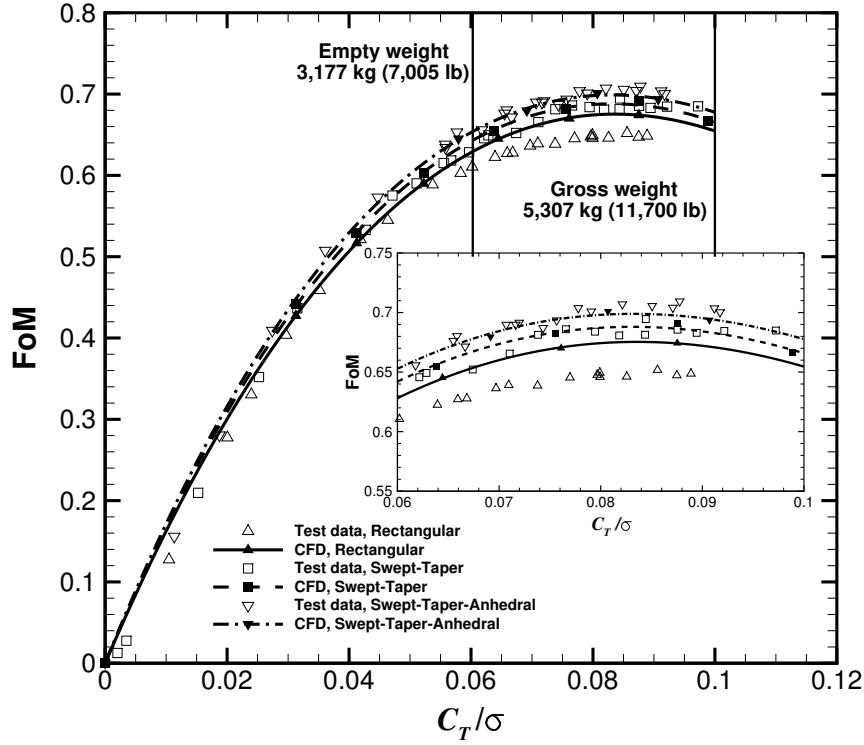


Figure 5.22: Effect of the blade-tip shape on the figure of merit for the S-76 model rotor at blade-tip Mach number of 0.65.

### 5.2.8 Hovering Endurance

As a means of comparing the effect of the tip shape on the 1/4.71 scale S-76 rotor in hover, hovering endurance has been estimated using the experimental data from Balch and Lombardi [33, 34] and CFD predictions from HMB. This parameter evaluates the performance capabilities of a helicopter in hover configuration, typically for a range of thrust coefficient from maximum takeoff gross to empty weight. Following Makofski [230], the hovering endurance of a helicopter is given by:

$$E = \frac{550}{(\text{sfc})(\Omega R)} \int_{C_{T,f}}^{C_{T,i}} \frac{1}{C_Q} dC_T. \quad (5.8)$$

where sfc is the specific fuel consumption given in (lb/(rotor hp)/hr), while the rotor rotational speed  $\Omega$  and rotor radius  $R$  have unit of rad/s and feet, respectively. For this study, the sfc is assumed to be a constant value equal to 1 and the blade-tip Mach number was set to 0.65. The initial and final thrust coefficient corresponds to empty weight 3,178 kg and maximum takeoff gross weight 5,306 kg of the modern S-76 C++ helicopter [231].



Table 5.10 compares the hovering endurance in hours for three tip configurations (rectangular, swept-taper, and anhedral) using the available experimental data from Balch and Lombardi [33, 34] and CFD predictions. According to the wind tunnel data, the rectangular tip is the worst performing blade and the swept-tapered with anhedral the best. In fact, the use of advanced tip configurations like swept-taper or anhedral has a clear benefit on the hovering endurance, delivering an extra time of 13 and 23 minutes if compared with the rectangular tip. The same trend with the shapes is captured by the present computations, which presents absolute errors of 2.57%, 0.18%, and 0.55% for the rectangular, swept-taper, and anhedral with respect to experiments. The good agreement of the endurance is a reflection of the accurate FoM predictions within 0.1 count.

Table 5.10: Effect of the tip shape on the hovering endurance (in hours) for the 1/4.71 scale S-76 main rotor at blade-tip Mach number of 0.65.

Tip Shape	CFD HMB	Wind tunnel [33, 34]
Rectangular	5 hrs and 11 mins	5 hrs and 3 mins
Swept-Taper	5 hrs and 17 mins	5 hrs and 16 mins
Anhedral	5 hrs and 25 mins	5 hrs and 26 mins

### 5.2.9 Aeroacoustic Study

The Helicopter Ffowcs Williams-Hawkings (HFWH) aeroacoustic code is used here to predict the mid and farfield noise on the 1/4.71 scale S-76 main rotor. HFWH solves the Farassat 1A formulation (also known as retarded-time formulation) of the original Ffowcs Williams-Hawkings (FWH) equation [207] and its expression was introduced in chapter 3. If the flowfield is not transonic or supersonic, thickness and loading terms are sufficient to predict the farfield noise.

A comparison of the noise levels radiated by the different tips at the rotor-disk plane of the scale S-76 main rotor blades was carried out using HFWH. A trimmed state was required for each tip, and a medium thrust coefficient  $C_T/\sigma = 0.06$  and blade-tip Mach number of 0.65 were selected as a flight conditions. Table 5.11 reports the blade pitch angle  $\theta_{75}$ , coning angle  $\beta$ , blade loading coefficient  $C_T/\sigma$ , torque coefficient normalised by the rotor solidity  $C_Q/\sigma$ , and FoM for each tip shape at the trimmed condition. The higher FoM was obtained by the anhedral tip (1.24% and

2.83% higher than the swept-taper and rectangular tips) and it is due to the additional off-loading of this tip. This is a known effect reported by Brocklehurst and Barakos [229].

Table 5.11: Performance on the 1/4.71 scale S-76 rotor with rectangular, swept-taper, and anhedral shape tips at  $C_T/\sigma = 0.06$  and  $M_{\text{tip}} = 0.65$ . The medium chimera grid was used (grid II on Table 5.6) for this study.

Tip Shape	$\theta_{75}$ (deg)	$\beta$ (deg)	$C_T/\sigma$	$C_Q/\sigma$	FoM	$\Delta\text{FoM} [\%]$
Rectangular	6.600	1.966	0.0600	0.00440	0.627	-
Swept-Taper	6.621	1.985	0.0598	0.00431	0.637	1.594
Anhedral	6.675	2.032	0.0600	0.00427	0.645	2.870

Due to the lack of experimental acoustic data for the S-76 in hover, a comparison with the theory was conducted in terms of thickness and loading noise predictions. Both analytical solutions are based on the work of Gopalan and Schmitz [209, 210], and have been successfully employed by the helicopter community [208].

Comparisons of the theoretical and numerical thickness, loading, and total noise at the rotor-disk plane are shown in Figure 5.23, as function of the observer distance  $r_H$ . The x-axis represents the observer time ( $t = \frac{\Psi + M_{\text{tip}}(\cos(\Psi) - 1)}{\Omega}$ ), where  $\Psi$  is the local azimuth angle. As expected, the effect of the tip configuration on the numerical thickness noise is negligible. It is seen that the predicted noise is in close agreement with the analytical solution, and the peaks of negative-pressure are well predicted by the HFWH.

Figure 5.24 (a) shows the total noise as a function of the radial distance at the rotor-disk plane for each tip configuration. For a radial distance  $r/R = 10$ , it is found that the swept-tapered tip is slightly louder than the anhedral with a difference of 1.83 dB. There are other regions, however, where this difference may be more significant. In this regards, a set of microphones were located  $45^\circ$  downward of the rotor-disk plane, and their level of noise is reported in Table 5.12. A reduction of the total noise by 4.53 dB is gained if the anhedral tip configuration is used. Figure 5.24 (b) shows the total noise as a function of the radial distance for those microphones. It is seen than the swept-tapered tip is louder than the anhedral tip. It is mainly due to the effect of the loading noise distribution, which is the main mechanism of noise generation in this direction.

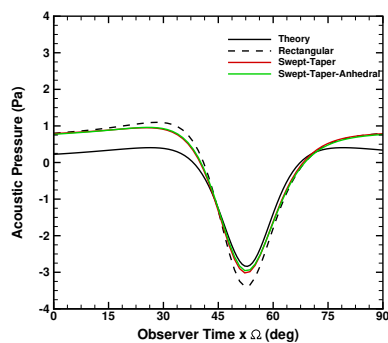
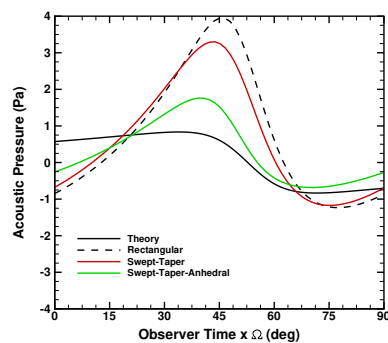
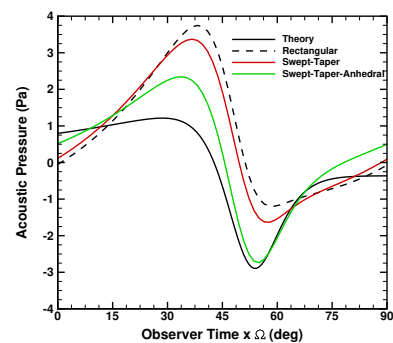
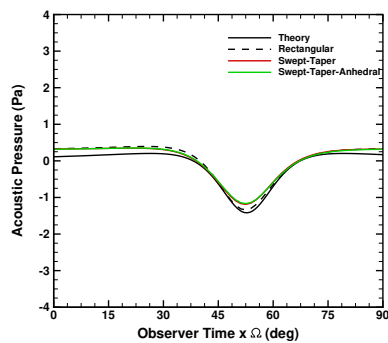
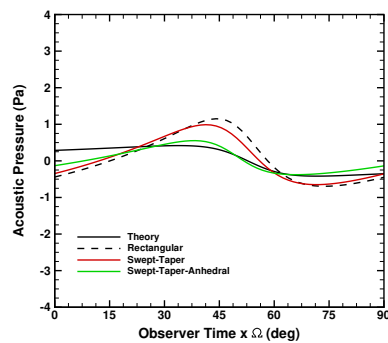
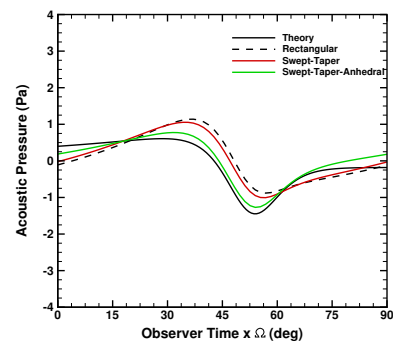
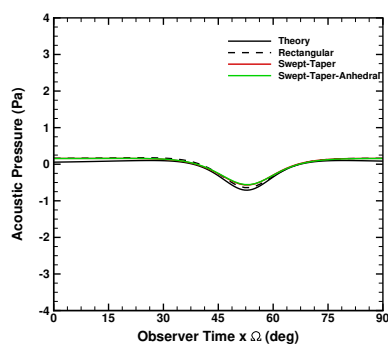
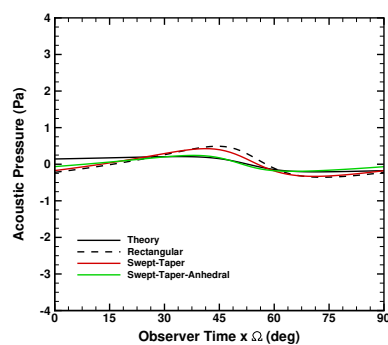
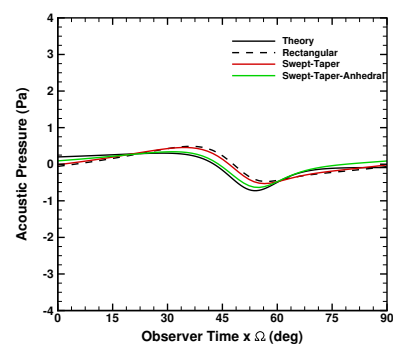
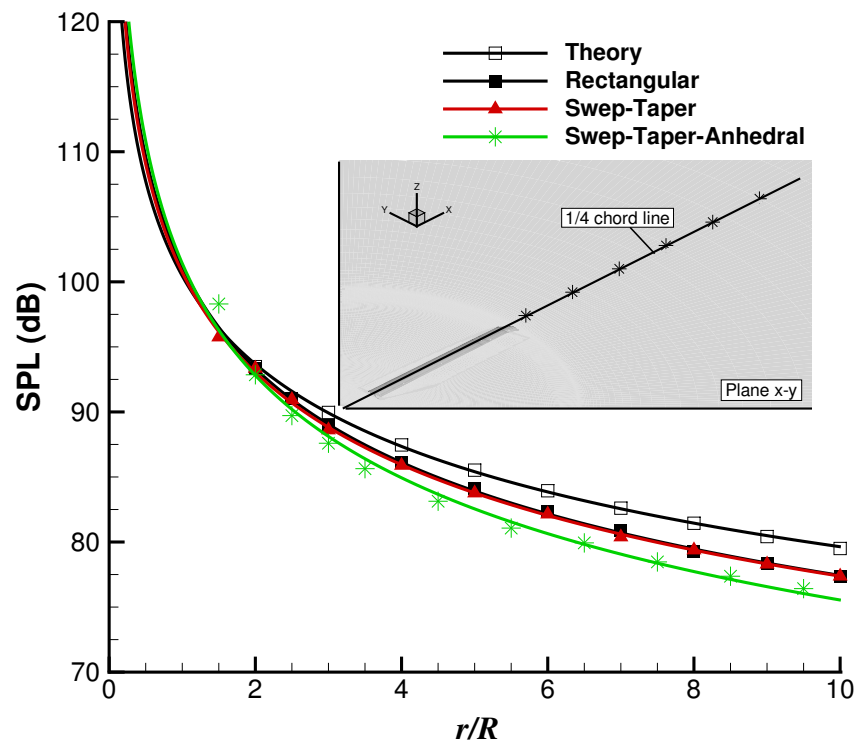
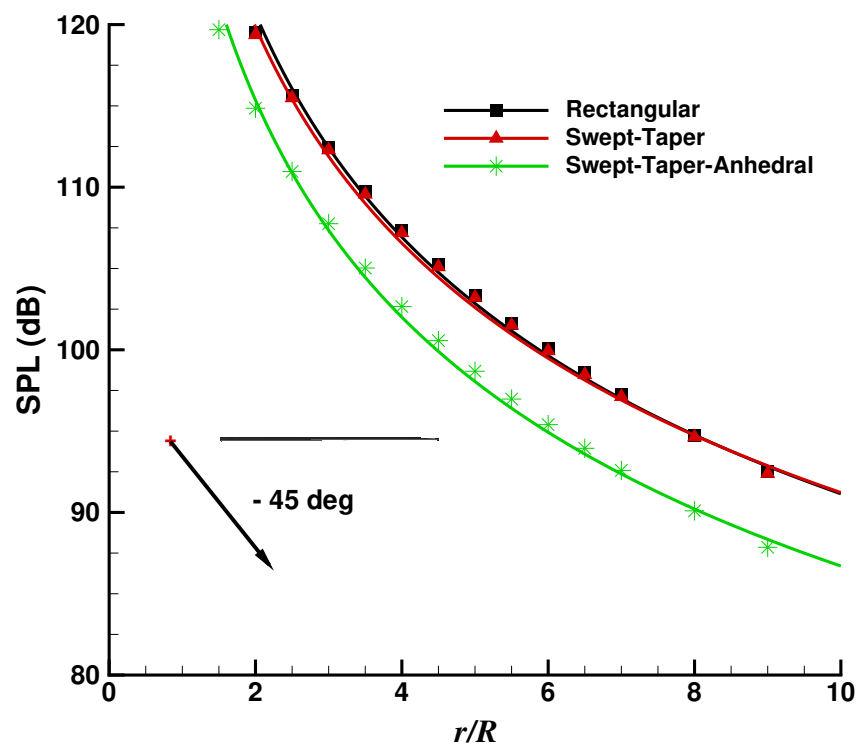

 (a)  $r/R = 2$ , Thickness noise.

 (b)  $r/R = 2$ , Loading noise.

 (c)  $r/R = 2$ , Total noise.

 (d)  $r/R = 4$ , Thickness noise.

 (e)  $r/R = 4$ , Loading noise.

 (f)  $r/R = 4$ , Total noise.

 (g)  $r/R = 8$ , Thickness noise.

 (h)  $r/R = 8$ , Loading noise.

 (i)  $r/R = 8$ , Total noise.

Figure 5.23: Comparison of theoretical and numerical thickness, loading, and total noise distributions at the rotor-disk plane for the 1/4.71 scale S-76 rotor with rectangular, swept-taper, and anhedral tip configurations.



(a)



(b)

Figure 5.24: Total noise for the 1/4.71 scale S-76 rotor blade with rectangular, swept-taper, and anhedral tip configurations, as function of the radial distance at the rotor-disk plane (top) and total noise as a function of the radial distance for a set of microphones located  $45^\circ$  downward of the rotor-disk plane (bottom).

Table 5.12: Thickness, loading, and total noise for a microphone located  $45^\circ$  downward of the rotor-disk plane ( $r/R=3$ ) for the S-76 rotor blade with rectangular, swept-tapered, and anhedral tip configurations.

Tip Shape	Thickness (dB)	Loading (dB)	Total (dB)	$\Delta$ Total [%]
Rectangular	74.09	112.42	112.43	-
Swept-Taper	73.93	112.27	112.28	0.13
Anhedral	74.26	107.88	107.91	4.02

## 5.3 Full-Scale S-76 Rotor Blade

The full-scale S-76 rotor was tested by Johnson [39] in the Ames 40- by 80- foot wind tunnel for a wide range of advance ratios from 0.075 to 0.40 and an advancing side tip Mach number  $M_{at}$  ranging from 0.640 up to 0.965. A further discussion of the rotor performance was reported by Stroub *et al.* [232], whereas blade vibratory loads and noise were investigated by Jepson *et al.* [40]. Comparison of the performance of the full-scale with the 1/5 model-scale and theoretical calculations were conducted by Balch [233]. The majority of the previous experimental studies of the full-scale S-76 did not include hover cases. To fill this gap, a major study to establish a database on the S-76 full-scale in hover was undertaken by Shinoda [35, 36]. The NASA Ames 80- by 120- foot Wind Tunnel was used as a hovering facility, where the S-76 rotor blade with 60% taper- $35^\circ$  swept tip, at tip Mach number of 0.604 was selected.

### 5.3.1 Aeroelastic Analysis of the S-76 Rotor

In this study, the static aeroelastic analysis of the S-76 full-scale rotor blade with 60% taper- $35^\circ$  swept tip is put forward as a means to quantify the effects of blade deformation and full-scale Re on performance.

#### Structural Model

A structural model of the S-76 model was generated using the available data from Johnson [39] and Jepson *et al.* [40]. In Figure 5.25 the blade is modelled using 17 elements of the CBEAM

type of NASTRAN [234]. Likewise, the Rigid BAR elements (RBAR) are also shown, which have no structural properties, and used to link the chord nodes to the leading edge with the trailing edge. The distributions along the radius of the Young's Modulus, Poisson's ratio, and torsional stiffness were not available, and the material properties of the UH-60A [235] were used instead. The structural properties of the blade are presented in Figure 5.26 which suggests that the blade suffers a reduction of the beamwise, chordwise, and torsional stiffness from the normalised radial position  $r/R = 0.75$  to the tip, corresponding to, 78.9%, 71.0%, and 86.4%, respectively. Table 5.13 shows a comparison of the eigenfrequencies obtained using NASTRAN, DYMORE IV, and RCAS by Monico [236] for the first three modes at the nominal speed of the rotor  $\Omega = 296$  rpm. Fair agreement is seen.

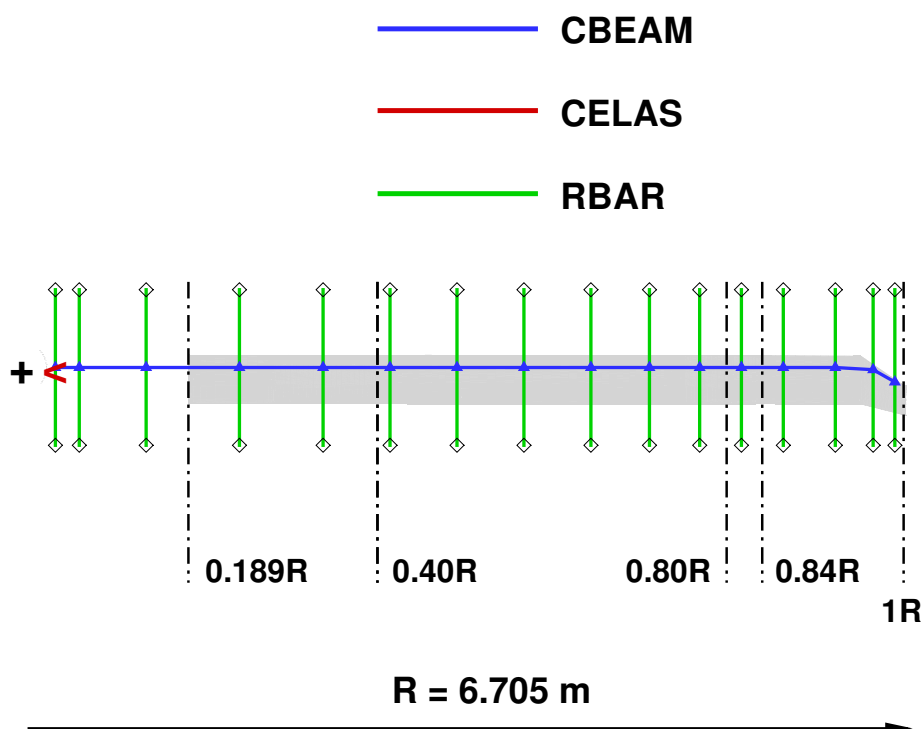
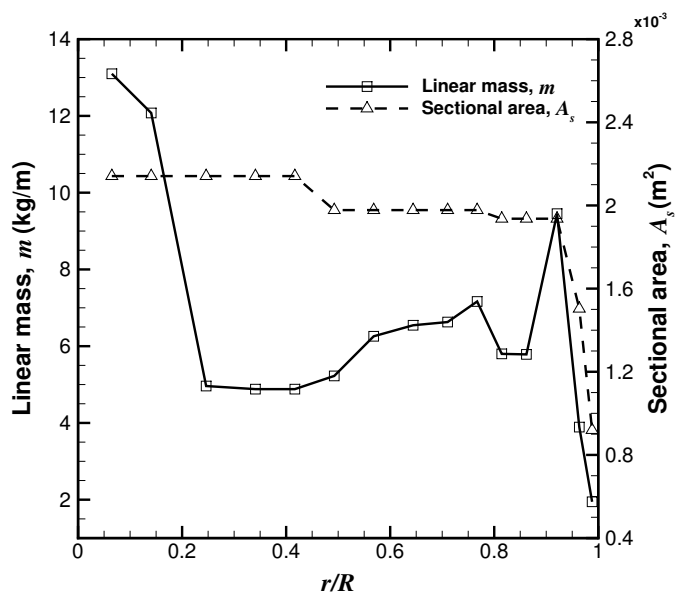
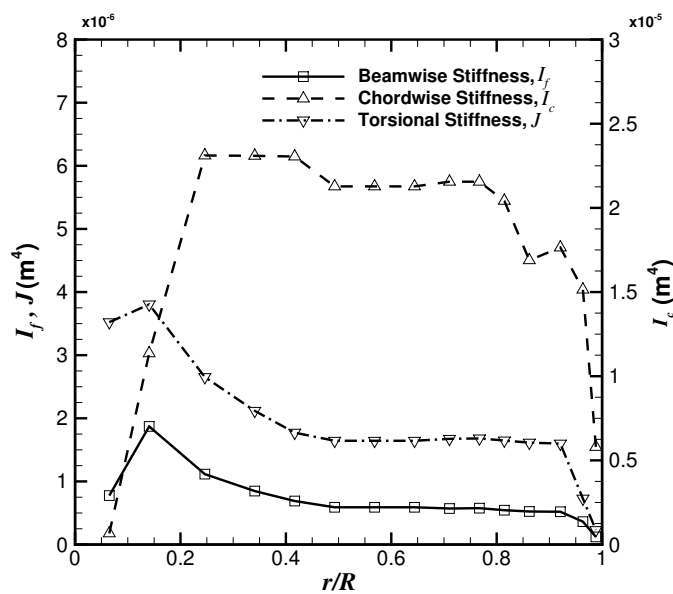


Figure 5.25: Structural model of the full-scale S-76 rotor blade, showing the distribution of the 17 elements of the CBEAM type through the spanwise of the blade.



(a)



(b)

Figure 5.26: Sectional area and linear mass distribution (top) and chordwise, flapwise, and torsional area moments of inertia (bottom) for the S-76 rotor blade with 60% taper-35° swept tip [36].

 Table 5.13: Eigenfrequencies of the full-scale S-76 rotor blade at nominal speed  $\Omega = 296$  rpm, using NASTRAN. Comparison with the DYMORE IV and RCAS codes [236] is also shown.

Code	First mode (Hz)	Second mode (Hz)	Third mode (Hz)
NASTRAN (present)	1.22	5.03	14.80
DYMORE IV	1.52	5.07	13.22
RCAS	1.19	4.88	14.03

### Analysis of Elastic Blade Results

Numerical simulations of the full-scale S-76 with a set of rigid and elastic rotor blades were performed at blade-tip Mach number of 0.605. For this hover case, the blade-tip Reynolds number was set to  $5.27 \times 10^6$ , being 4.71 times larger than the model-scale. The importance of Reynolds number is well established in fixed wing aerodynamics. By contrast, in the case of rotary wing aerodynamics, its influence is less well understood [237]. Moreover, the low Reynolds number of the model-scale may cause premature separation which does not occur at full-scale as a result of the more turbulent boundary layers on the blades. This leads to increased figure of merit for the full-scale rotor.

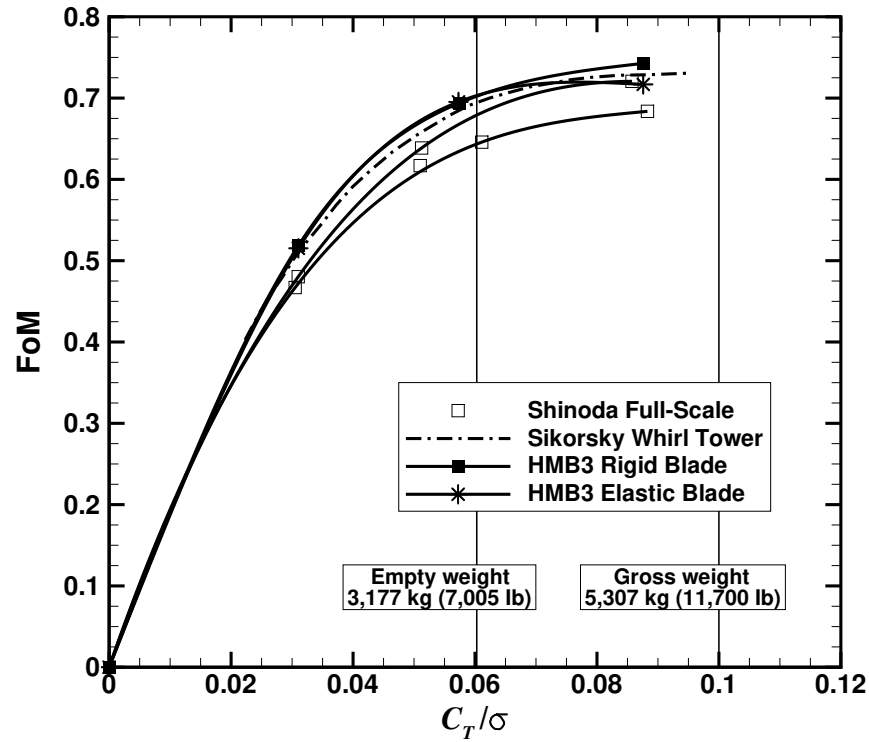
Blade pitch angles corresponding to low, medium, and high thrust coefficients were simulated. Coning angles were set according to Shinoda's report [36], with coincident flapping and lead-lag hinges located at  $0.056R$  for the model rotor. Figure 5.27 (a) presents the figure of merit as a function of the blade loading coefficient  $C_T/\sigma$  at different blade pitch angles computed with HMB. Comparisons with the experimental data of Shinoda and the Sikorsky Whirl Tower [36] are also shown. The scatter of the Shinoda data is remarkably large and two lines were best-fitted corresponding to lower and upper bounds of the test data. At low and medium thrust coefficients, the prediction of the FoM between the Sikorsky Whirl Tower and CFD with rigid blade is well captured. However, at high thrust, the FoM is slightly over-predicted. On the other hand, the FoM is over-predicted if compared with the experimental data of Shinoda. The reason for this disagreement may be partly due to the variations in experimental data between the Sikorsky Whirl Tower and wind tunnels. The reason can be due to wake reingestion as a consequence perhaps of mild in-ground effect and facility walls. These effects are difficult to control within the confines of wind tunnels or model-scale hover facilities. Considering the aeroelastic curve (lines with stars), it is found that at low and medium thrust coefficients  $C_T/\sigma = 0.031$  and  $0.057$ , the FoM does not show a significant change. In contrast, a better agreement between CFD and experimental data at high thrust is found. In fact, the drop in performance (3.48% of FoM at  $C_T/\sigma = 0.087$ ) is due to the lower twist induced by the structural properties of the blade.



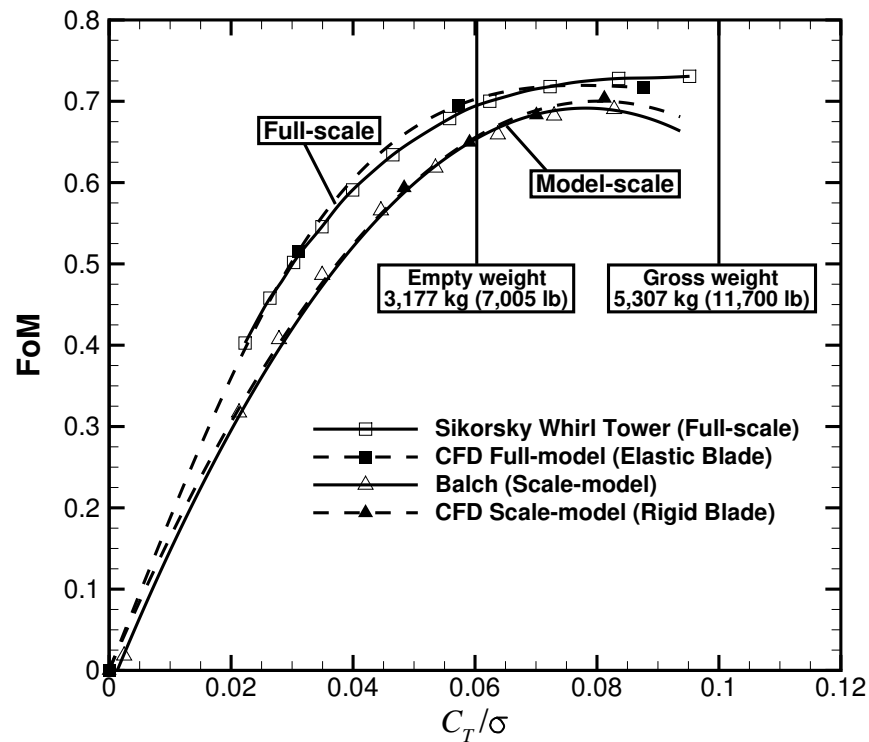
### 5.3.2 Comparison Between Full and Model-Scale Rotors

This section presents a comparison between the full and model-scale S-76 rotors in terms of figure of merit. When comparing model-scale to full-scale rotor performance data, some considerations should first be made. First, the full-scale blade-tip Mach number must be matched. Thus, the rotational velocity of the model-scale rotor would be multiplied by a geometric scale factor (4.71 for the S-76 rotor). Second, the Reynolds number is not easy to match if the full-scale blade-tip Mach number is kept constant for both rotors. This parameter is the main cause of differences between full-scale and model-scale rotor test data. Finally, the rotor blade elasticity should also be considered at high thrust to fully model the blade structural aeroelasticity effects.

Figure 5.27 (b) shows the effect of the Reynolds number on the FoM for the S-76 rotor blade with 60% taper-35° swept tip. The experimental data correspond to the Sikorsky Whirl Tower [36] for the full-scale rotor (lines with opened squares), and Balch and Lombardi [33] for the model-scale rotor (lines with opened triangles), where the blade-tip Mach number was set to 0.60. CFD results are represented by filled squares and filled triangles with dashed lines for the full-scale (elastic blades are considered) and model-scale, respectively. Analysing the experimental data, a higher FoM is observed for the full-scale rotor over the whole range of thrust coefficients. For instance, the FoM is 6.26% higher for a medium thrust coefficient ( $C_T/\sigma = 0.060$ ) and 9.66% higher for a high thrust coefficient ( $C_T/\sigma = 0.092$ ). This is consistent with experience, and justified by the decrease of the aerofoil drag coefficient for increasing Reynolds number. This is also shown for the aerofoils of the S-76 rotor blade by Yamauchi *et al.* [238]p. 30. This behaviour is also observed in the CFD results, which confirms that the present method is able to capture the Reynolds number effects (see Whitehouse *et al.* [62] page 8).



(a) Effect of the rigid/elastic blades.



(b) Effect of the Reynolds number.

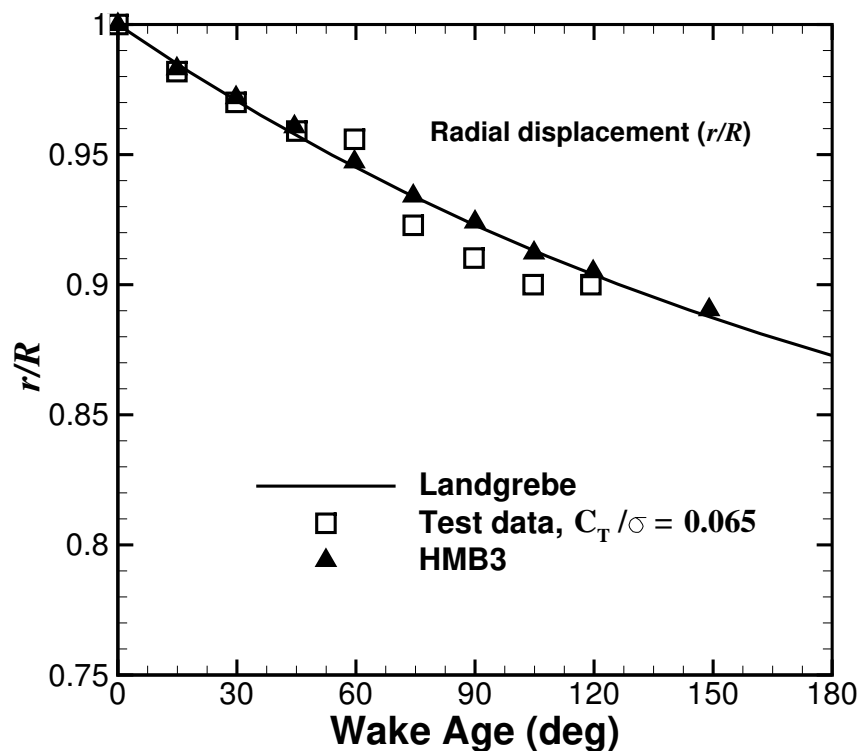
Figure 5.27: Effect of the rigid/elastic blades (top) and Reynolds number (bottom) on the figure of merit for the S-76 rotor blade with 60% taper-35° swept tip.

### 5.3.3 Tip Vortex Trajectory

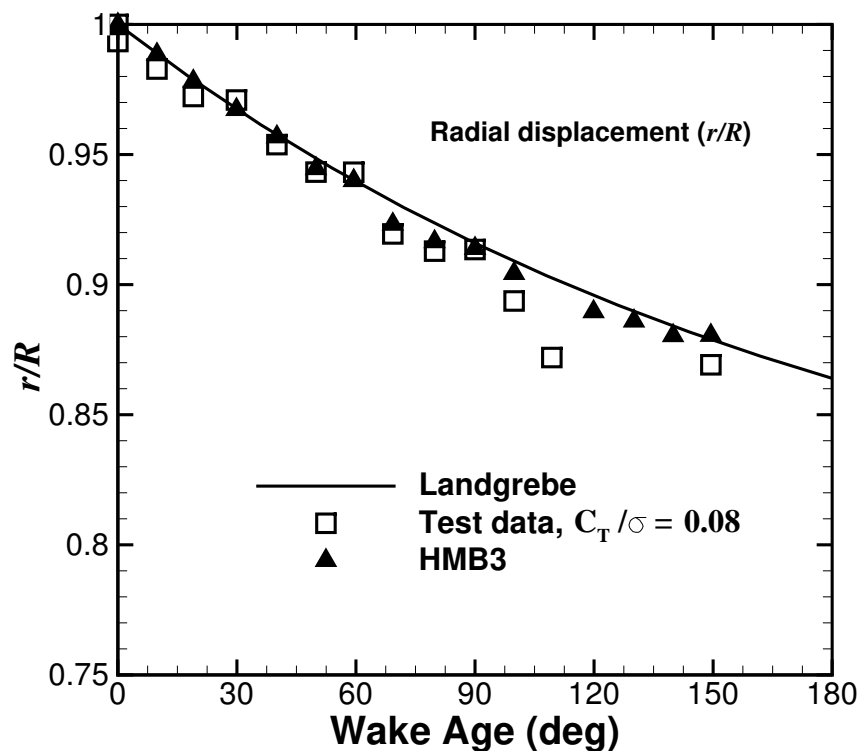
This section shows a comparison of the radial displacements of the tip vortices as a function of the vortex age (in degrees) for the full-scale S-76 with rigid blades. Comparison with the prescribed wake-model of Landgrebe [19] and experimental data carried out by Swanson [41] are also shown in Figure 5.28. The flow visualisation of the rotor wake flow was performed in the NASA Ames 80- by 120- foot wind tunnel in 1993, using a shadowgraph flow visualisation technique. Two blade pitch angles were selected for computations, corresponding to medium and high thrust,  $C_T/\sigma = 0.065$  and  $0.080$ . The prediction of the radial displacement is in good agreement with the experimental data and empirical model for both thrust coefficients. By contrast, the lack of experiments for the vertical displacement and size of the vortex core results in a deficient validation of the complete wake.

### 5.3.4 Aeroacoustic Study

Like for the 1/4.71 scale S-76 main rotor, an aeroacoustic study of the full-scale S-76 rotor blade using the HFWH code is presented here. Comparisons of the theoretical and numerical total noise for a set of microphones located at the rotor-disk plane and at 45 degrees downwards and upwards of the rotor-disk plane are shown in Figure 5.29. Despite that model-scale and full-scale rotors have different range of frequencies (higher for the model-scale), the amplitude of the sound waves should be similar for similar loads. Figure 5.29 (a) shows an excellent agreement with the theory for all radial distances. Moreover, Figure 5.29 (b) shows that the total noise has the same trend downward and upward of the rotor-disk plane.

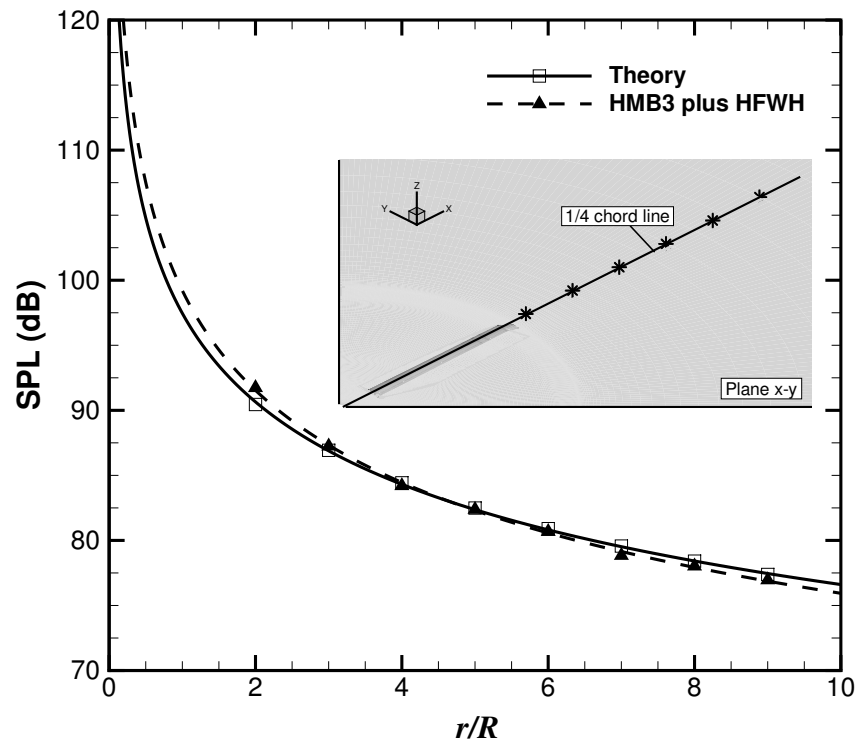


(a)

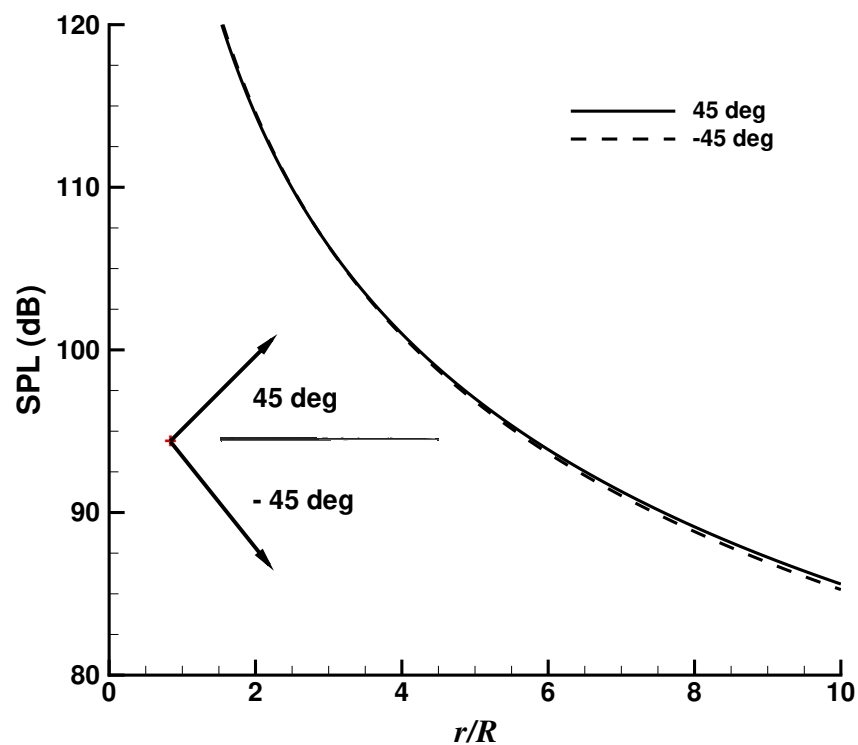


(b)

Figure 5.28: Comparison of the radial displacements of the tip vortices as functions of the wake age (in degrees), with the prescribed wake-model of Landgrebe [19] and experimental data of Swanson [41] for two blade loading coefficients (a)  $C_T/\sigma = 0.065$  and (b)  $C_T/\sigma = 0.080$ . This case corresponds to the full-scale S-76 rotor with 60% taper-35° degrees swept tip and  $M_{\text{tip}} = 0.605$ .



(a)



(b)

Figure 5.29: (a) Total noise for the full-scale S-76 rotor blade with swept-taper tip configuration, as function of the radial distance at the rotor-disk plane and (b) total noise as a function of the radial distance for a set of microphones located 45 degrees downward and upward of the rotor-disk plane.  $M_{\text{tip}} = 0.60$  and  $C_T/\sigma = 0.057$  were used as hovering conditions.

## 5.4 PSP Main Rotor

With work on the S-76 rotor blades providing encouraging results regarding the prediction of integral loads with CFD in hover, the PSP rotor [239] is now analysed.

One of the main limitation to completely validate CFD methods using the B0-105 and S-76 blades was the lack of surface pressure data. In this regard, a model-scale known as Pressure Sensitive Paint (PSP) rotor was designed jointly by NASA Langley Research Center and the U.S. Army Aviation Development Directorate (ADD) and fabricated in 2002. This blade has so far been used for experiments that compared PSP data with measurements using Kulite pressure transducers [239, 240, 241] in the Rotor Test Cell (RTC) at the NASA Langley Research Center 14×22 foot Subsonic Wind Tunnel, and is to be re-used for further tests in hover at blade-tip Mach number of 0.65 as part of a future campaign that will be conducted in the NASA Ames Full-Scale Aerodynamics Complex (NFAC) 80×120 foot Wind Tunnel.

In this work, an aerodynamic study of the PSP blades, is presented, using high-fidelity computational fluid dynamics at blade-tip Mach number of 0.585. Comparisons with experimental data available in the literature [239, 240, 242] are carried out in terms of airloads and surface pressure coefficient. To reduce the computational cost, the hover flow is solved as a steady-state problem in a noninertial reference frame. Results are presented for a range of design points, which includes medium and high thrust hover conditions. The second part of this work presents analysis of the performance of the isolated PSP at higher blade-tip Mach number of 0.65, where comparison with theory and available CFD data is also reported.

The four-bladed PSP rotor has an aspect ratio ( $R/c_{\text{ref}}$ ) of 12.2 and a nominal twist of -14 degrees. The main characteristics of the rotor blades are summarised in Table 5.14. The blade planform has been generated using three radial stations. First, the RC(4)-12 aerofoil was used up to 65%  $R$ . Then, the RC(4)-10 aerofoil from 70%  $R$  to 80%  $R$ . Finally, the RC(6)-08 aerofoil was used from 85%  $R$  to the tip. The aerodynamic characteristics of these aerofoils can be found in [243, 244].

Table 5.14: Geometric properties of the PSP rotor [241].

Parameter	Value
Number of blades, $N_b$	4
Rotor radius, $R$	1.689 m (66.50 in)
Reference blade chord, $c_{\text{ref}}$	0.138 m (5.45 in)
Aspect ratio, $R/c_{\text{ref}}$	12.2
Rotor solidity, $\sigma$	0.104
Non-linear twist, $\Theta$	-14°

### 5.4.1 PSP Rotor Mesh

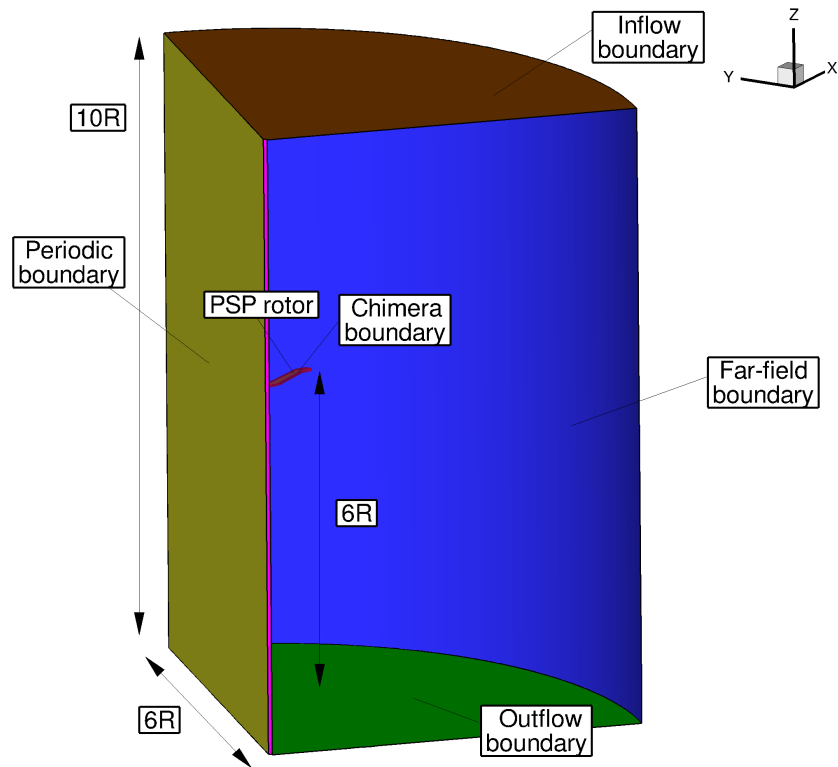
A mesh generated using the chimera technique is used for the aerodynamic study of the PSP rotor. Only a quarter of the computational domain was meshed, assuming periodic conditions for the flowfield in the azimuthal direction. A view of the computational domain along with the employed boundary conditions is given in Figure 5.30. The meshing parameters for the PSP mesh rotor blade along with the grid used are shown in Table 5.15.

Table 5.15: Meshing parameters for the PSP rotor mesh.

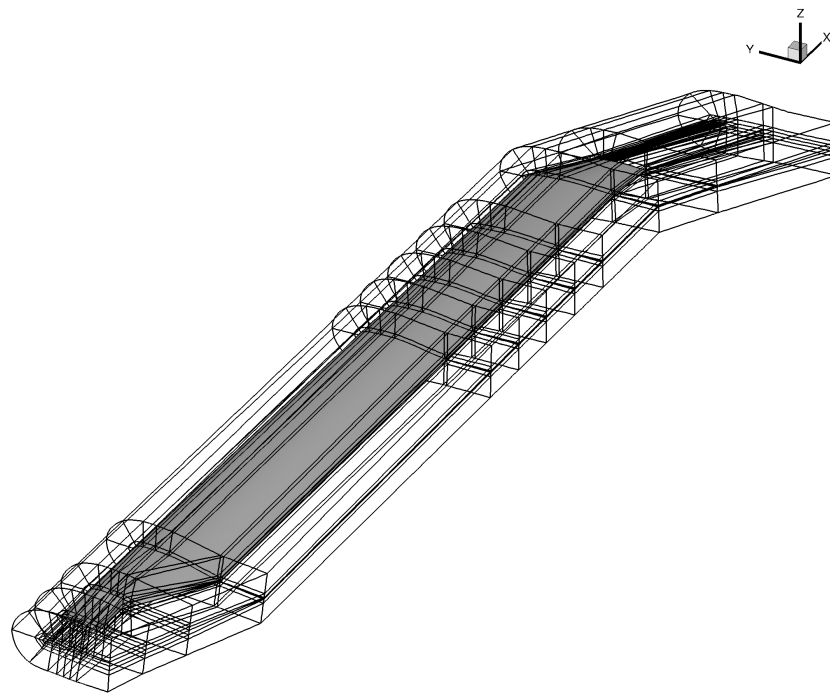
Background mesh size (cells)	7.2 million
Blade mesh size (cells)	5.2 million
Overall mesh size (cells)	12.4 million
Height of the first mesh layer at blade surface	$1.0 \times 10^{-5} c_{\text{ref}}$
Points along the span	215
Points around the aerofoil	252

### 5.4.2 Test Conditions and Computations

The PSP blade was simulated at two blade-tip Mach numbers, 0.585 and 0.65. To validate the pressure sensitive paint technique for rotor blades in hover, Wong *et al.* [239] measured  $C_p$  at two radial stations at blade-tip Mach number of 0.585 on the PSP rotor blades, which were installed on the modified Rotor Body Interaction fuselage (ROBIN Mod7). Recently, Overmeyer *et al.* [242] extended this hover test, measuring integrated blade loads for free and fixed transition and transition locations using the same conditions in the same facility (Rotor Test Cell at the NASA Langley Research Center 14×22 foot Subsonic Wind Tunnel). This hover condition is simulated here in



(a) Computational domain.



(b) PSP rotor mesh topology.

Figure 5.30: Computational domain and boundary conditions employed (top) and topology of the PSP rotor mesh (bottom).



out-of-ground effect (OGE) conditions for six blade pitch angles. The Reynolds number, based on the reference blade chord  $c_{\text{ref}}$  of 5.45 inches and on the blade-tip speed, was  $1.05 \times 10^6$ .

A future campaign of tests in hover on the PSP rotor blade is to be conducted in the NFAC 80×120 foot Wind Tunnel, where the effect of the facility on the performance and transition point will be reported. Also, visualisation of the flowfield using Particle Image Velocimetry (PIV) are being planned at higher blade-tip Mach number of 0.65. Thus, code-to-code comparisons are presented in terms of integral blade loads, surface pressure coefficients, position of the tip-vortex cores, and wake visualisation, where the blade-tip Mach number was set to 0.65. Seven collective angles were considered, covering low, medium, and high disk loadings. The Reynolds number, based on the reference blade chord of 5.45 inches and on the tip speed, was  $2.16 \times 10^6$ .

All flow solutions were computed by solving the RANS equations, coupled with Menter's  $k - \omega$  SST turbulence model [191]. The flow equations were integrated with the implicit dual-time stepping method of HMB, using a pseudo-time CFL equal to 4. Table 5.16 summarises the employed conditions and the computations performed.

Table 5.16: Computational cases for the PSP rotor.

Blade-tip Mach number 0.585			Blade-tip Mach number 0.65		
$\theta_{75}$ (deg)	$\beta$ (deg)	$C_T$	$\theta_{75}$ (deg)	$\beta$ (deg)	$C_T$
4°	0°	0.00259	6°	0°	0.00451
6.58°	1.39°	0.00503	7°	0°	0.00552
8.48°	2.44°	0.00694	8°	0°	0.00657
9.46°	3.02°	0.00797	9°	0°	0.00767
10.3°	3.5°	0.00893	10°	0°	0.00881
12°	0°	0.01059	11°	0°	0.00985
			12°	0°	0.01070

### 5.4.3 Blade-Tip Mach Number of 0.585

#### Integrated Blade Loads

Figure 5.31 shows the variation of FoM and torque coefficient with blade loading, at six blade pitch angles. Comparison with experimental data (opened squares) by Overmeyer *et al.* [242] for the fixed-transition, 5% c, upper and lower (run 156) and momentum-based estimates of the FoM (dashed lines) are also included. For the momentum-theory curve, an induced power factor  $k_i$  of 1.15 and an overall profile drag coefficient  $C_{D0}$  of 0.01 were selected. CFD simulations performed by Wong [245] and Vieira *et al.* [246] with the unstructured solver FUN3D (green lines) and the commercial software Star-CCM+ (red triangle symbols), respectively, with the S-A turbulence model [97] are also reported for direct comparisons. At low thrust  $C_T/\sigma < 0.06$ , it can be seen that all CFD computations are in close agreement with the experimental data. Note that at low thrust, FoM shows low values as consequence of the higher contribution of the profile drag, which is relatively easy to be predicted. At medium and high thrust  $0.06 < C_T/\sigma < 0.1$ , antagonist trends are observed with the use of different CFD solutions. Results with FUN3D and Star-CCM+ over-predict the values of FoM, while HMB3 shows an under-predicted FoM. As an example, at thrust coefficient of  $C_T = 0.00828$ , FUN3D, Star-CCM+, and HMB3 show a discrepancy of +2.4, +1.6, and -0.6 counts of FoM respect to the experiments. Note that the FUN3D values reported here were extracted from the paper (Wong *et al.* [245], Figure 18) which may introduce a source of discrepancy when compared. Regarding the maximum thrust coefficient measured in the wind tunnel  $C_T/\sigma < 0.096$ , HMB3 results show a maximum discrepancy of -2 counts with respect to the experiments. Jain [247] evaluated the effect of rotor installation on the FoM, and it was found that the installed-rotor FoM presents a higher values (around 1.4 counts of FoM) when compared with the isolated rotor at  $C_T/\sigma \approx 0.094$ , which perhaps is one of the source of discrepancy at high thrust between HMB3 and experiments results. Nevertheless, despite good correlation with the FoM and  $C_Q$  with the experiments, this work needs to be extended to include a mesh density study and unsteady computations in addition to the steady-state results presented here as means to gain a better insight of the PSP performance at high thrust.

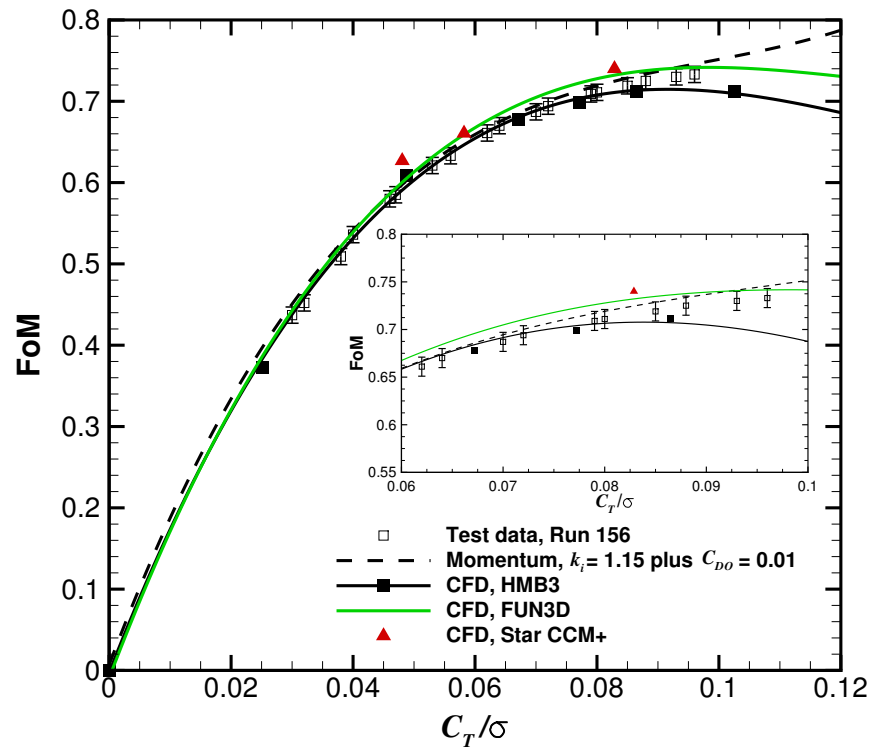
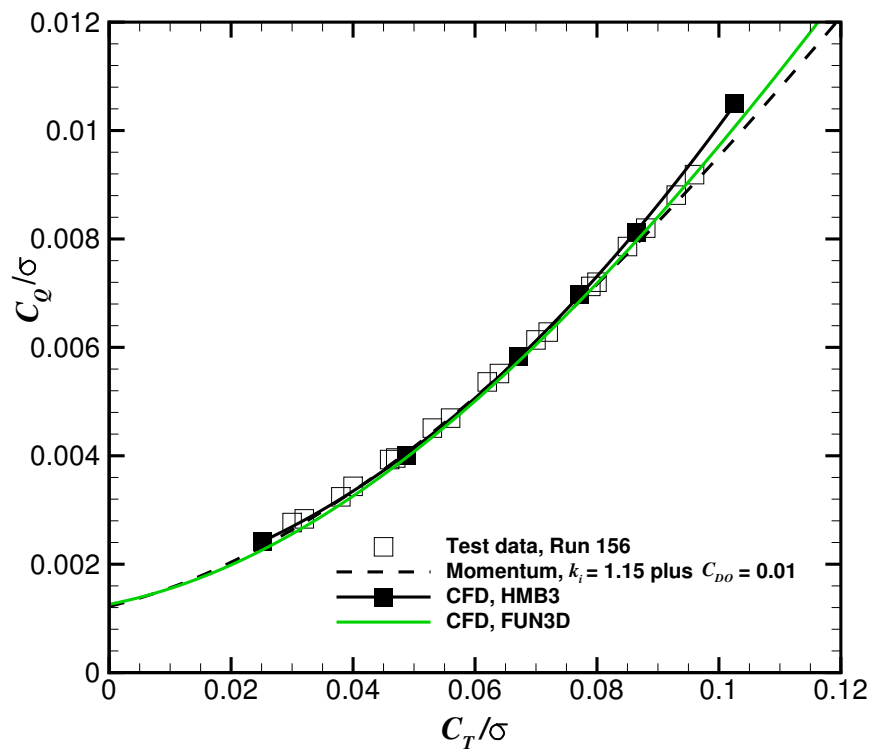

 (a)  $C_T/\sigma$  - FoM.

 (b)  $C_T/\sigma$  -  $C_Q/\sigma$ .

Figure 5.31: Integrated blade loads for the PSP model rotor at blade-tip Mach number of 0.585. Comparisons with published CFD data using FUN3D [245] (green lines) and Star CCM+ [246] (red triangle symbols). Experimental data [242] (opened square symbols) is also shown.

### Surface Pressure Predictions

Surface pressure coefficients are compared between CFD and experimental data [239, 240] at two radial stations ( $r/R= 0.93$  and  $0.99$ ) on the upper surface of the PSP blade on the medium chimera grid. It is computed based on the local velocity at each radial station:

$$C_P = \frac{P - P_\infty}{1/2\rho_\infty(\Omega r)^2}. \quad (5.9)$$

Regarding the experiments, two techniques were used to measured  $C_P$  distributions, the traditional transducers Kulite (square symbols) and the non-intrusive PSP technique (dashed lines) (see Figures 5.32 and 5.33. A reasonable agreement is seen by both techniques at both stations, and for the four thrust coefficients considered here;  $C_T= 0.005, 0.007, 0.008$ , and  $0.009$ . CFD results are able to predict the overall distribution of  $C_P$  at both stations, and the pressure at the trailing edge is also well captured. It is noticeable that discrepancies appear to be present, when sections at higher thrust are analysed. In fact, the CFD predictions reveal a slightly over-predicted  $C_P$ , even if the pressure trailing edge is well captured.

#### 5.4.4 Blade-Tip Mach Number of 0.65

Unlike the PSP blade at lower blade-tip Mach number of 0.585, no experimental data is available for this hover condition. Therefore, we compare the integrated blade loads with published CFD work by Coder [248] using the structured OVERFLOW CFD solver with the DDES turbulence model. Surface pressure coefficients, position of the tip-vortex cores, and wake visualisation are also shown for various blade pitch angles.

#### Integrated Blade Loads

A study of the performance of the PSP rotor in hover was also carried out at blade-tip Mach number of 0.65, and seven blade pitch angles were considered, from  $\theta_{75}= 6^\circ$  to  $12^\circ$  with a delta of 1 degree. Figure 5.34 shows the figure of merit and blade torque coefficient  $C_Q/\sigma$  as functions of the blade loading coefficient  $C_T/\sigma$  for the PSP blade. Momentum-based estimates of the figure of merit are

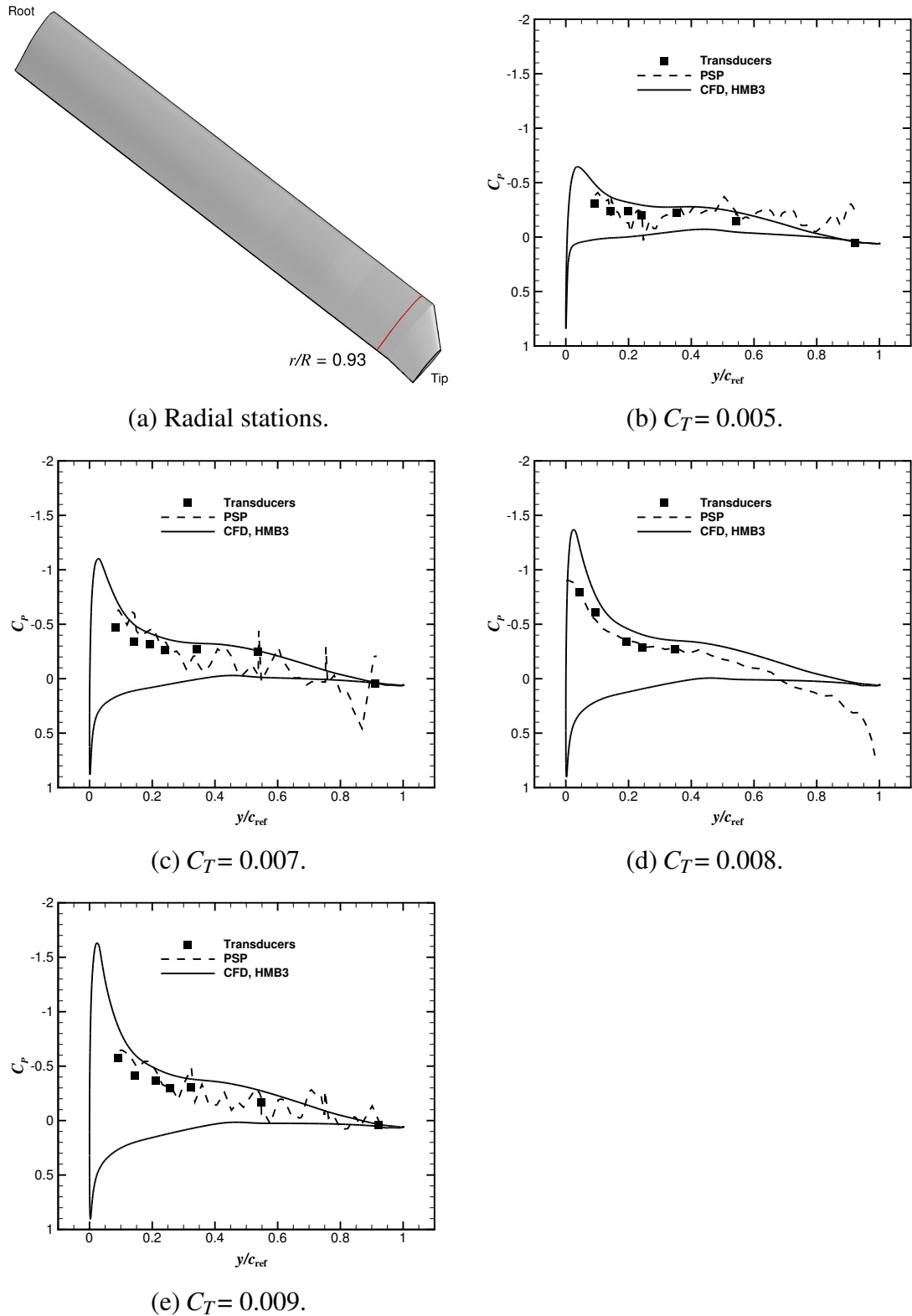


Figure 5.32:  $C_p$  profile comparisons between experimental data using the PSP technique (dashed line) and pressure tap (square symbols) [239, 240] and CFD (solid line) at radial station  $r/R = 0.93$ .

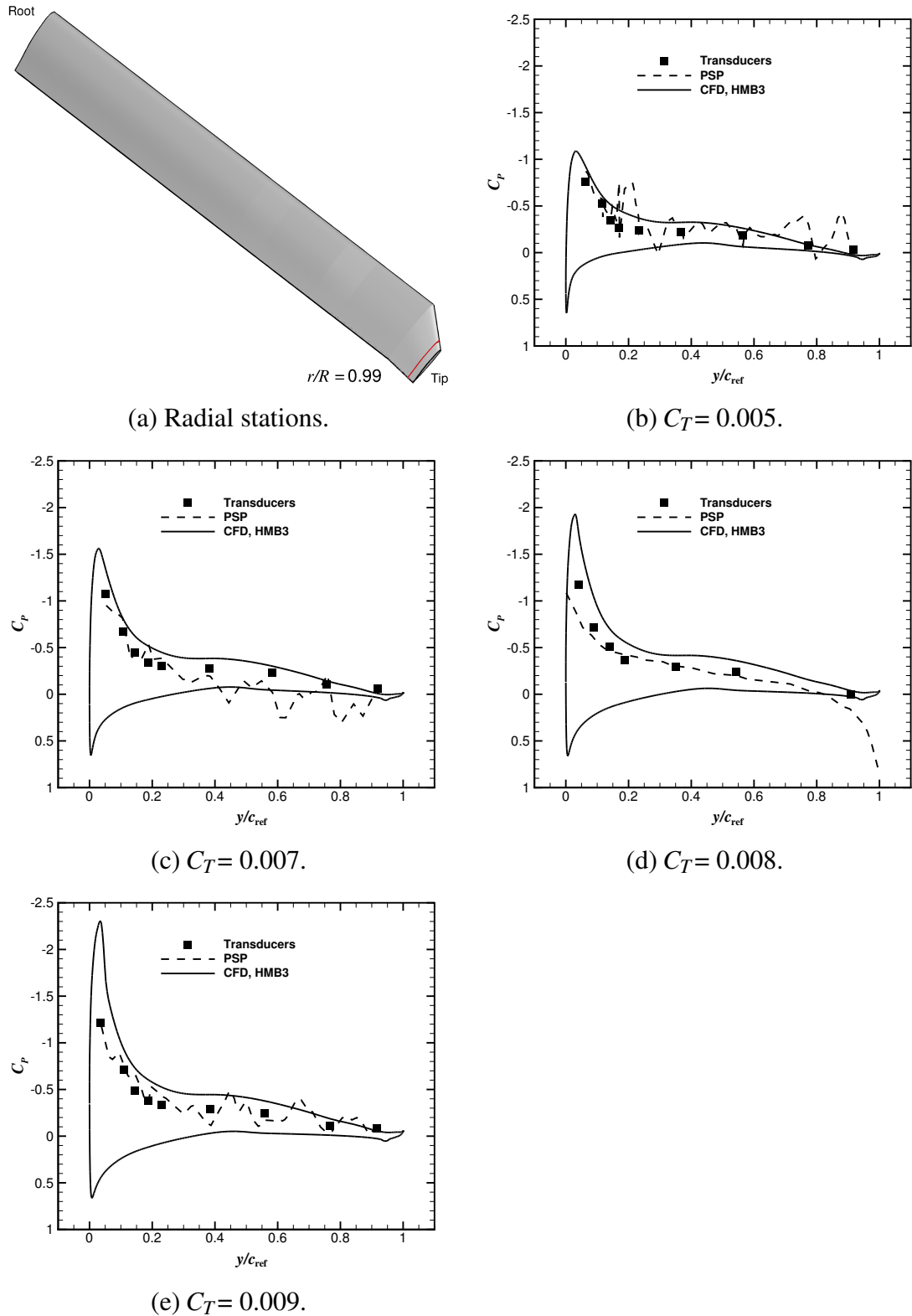


Figure 5.33:  $C_p$  profile comparisons between experimental data using the PSP technique (dashed line) and pressure tap (square symbols) [239, 240] and CFD (solid line) at radial station  $r/R = 0.99$ .

also included, where induced power factors  $k_i$  of 1.1 and 1.15, and overall profile drag coefficient  $C_{D0}$  of 0.01 were used. No experimental data is available at present for further comparisons. CFD results using the OVERFLOW CFD solver (red triangle symbols) is also shown for a code-to-code comparison. In overall, good correlation is found between both CFD results, despite that some discrepancies appear to be present at high thrust coefficient ( $C_T/\sigma > 0.1$ ) as consequence of different mesh density, turbulence models, and CFD solvers.

### Sectional Blade Loads

Figure 5.35 shows the distribution of sectional thrust and torque coefficients along the rotor radius, for blade pitch angles of  $6^\circ$ ,  $9^\circ$ , and  $12^\circ$ . Both coefficients are normalised with the local velocity:

$$C_t = \frac{dt/dr}{1/2\rho_\infty c(\Omega r)^2}. \quad (5.10)$$

$$C_q = \frac{dq/dr}{1/2\rho_\infty cR(\Omega r)^2}, \quad (5.11)$$

thus higher values of sectional thrust is seen inboard. The influence of the tip vortex on the tip region (from 95%  $R$  100%  $R$ ) is visible in terms of loading and torque coefficients, and increases as the function of the thrust (or blade pitch angle in this case).

### Surface Pressure Predictions

Four radial stations were considered ( $r/R=0.75, 0.85, 0.95$ , and  $0.975$ ), and the blade pitch angle were  $\theta_{75}=6^\circ, 9^\circ$ , and  $12^\circ$ . The surface pressure coefficient is computed based on the local velocity at each radial station:

$$C_P = \frac{P - P_\infty}{1/2\rho_\infty(\Omega r)^2}. \quad (5.12)$$

Regarding the radial station  $r/R=0.75$ , it is clear that the suction peak does not exceed the critical  $C_P^*$  values (Eq. 5.13), while the most outboard section ( $r/R=0.85, 0.95$ , and  $0.975$ ) reaches sonic conditions above  $12^\circ, 9^\circ$ , and  $6^\circ$ , respectively.

$$C_P^* = \frac{2}{\gamma(M_{\text{tip}} \frac{r}{R})^2} \left[ \left( \frac{2 + (\gamma - 1)(M_{\text{tip}} \frac{r}{R})^2}{\gamma + 1} \right)^{\frac{\gamma}{\gamma - 1}} - 1 \right]. \quad (5.13)$$

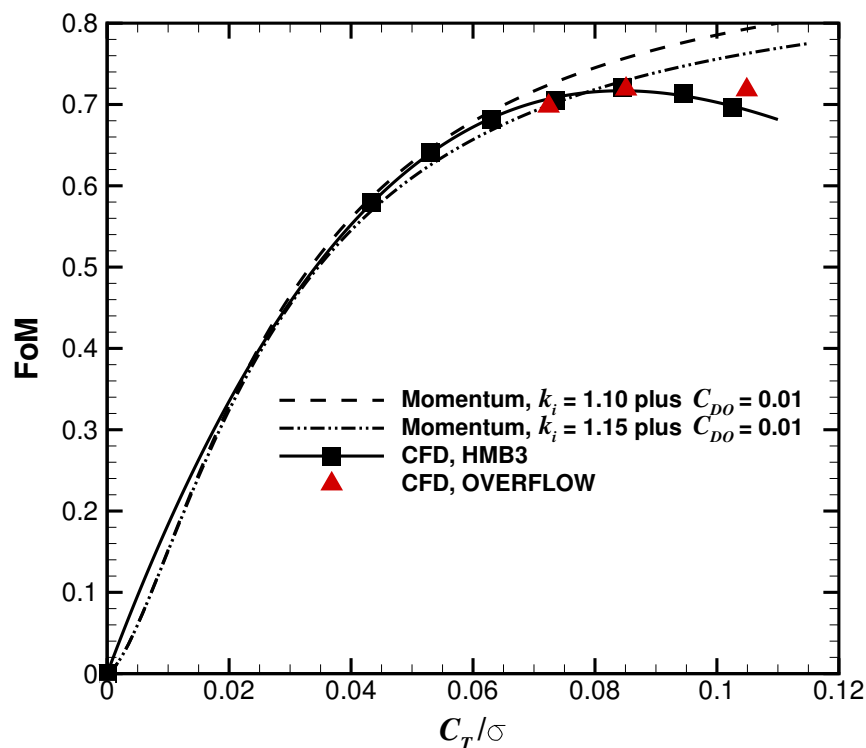
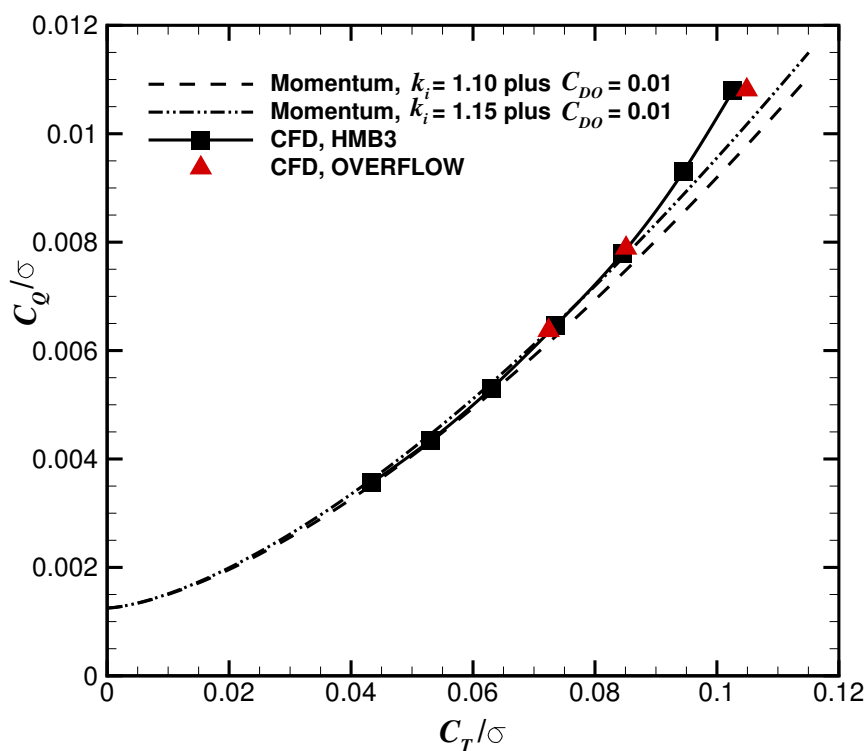
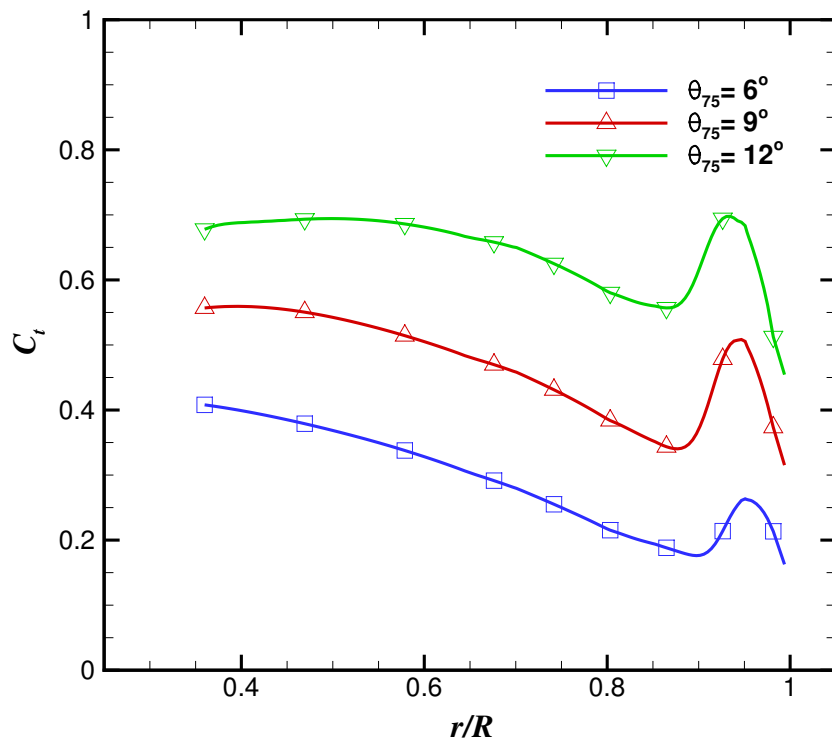
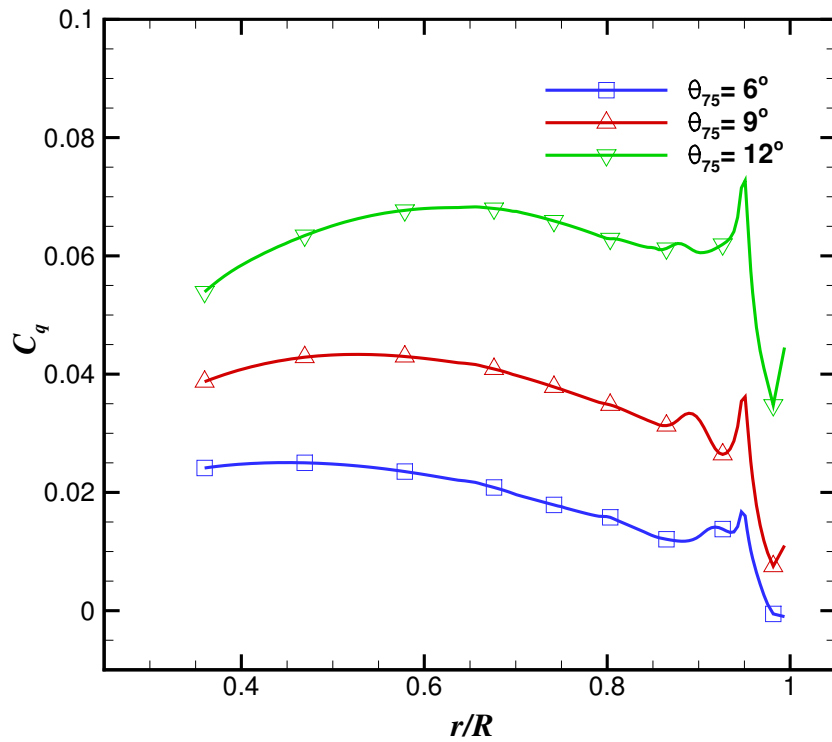

 (a)  $C_T/\sigma$  - FoM.

 (b)  $C_T/\sigma$  -  $C_Q/\sigma$ .

Figure 5.34: Integrated blade loads for the PSP model rotor at blade-tip Mach number of 0.65. Comparison with published CFD data using OVERFLOW [248] (red triangle symbols) is also shown.





(a) Blade sectional thrust coefficient.



b) Blade sectional torque coefficient.

Figure 5.35: Blade sectional thrust coefficient (top) and torque coefficient (bottom) for the PSP model rotor at blade-tip Mach number of 0.65 and  $\theta_{75} = 6^\circ$ ,  $9^\circ$ , and  $12^\circ$ .

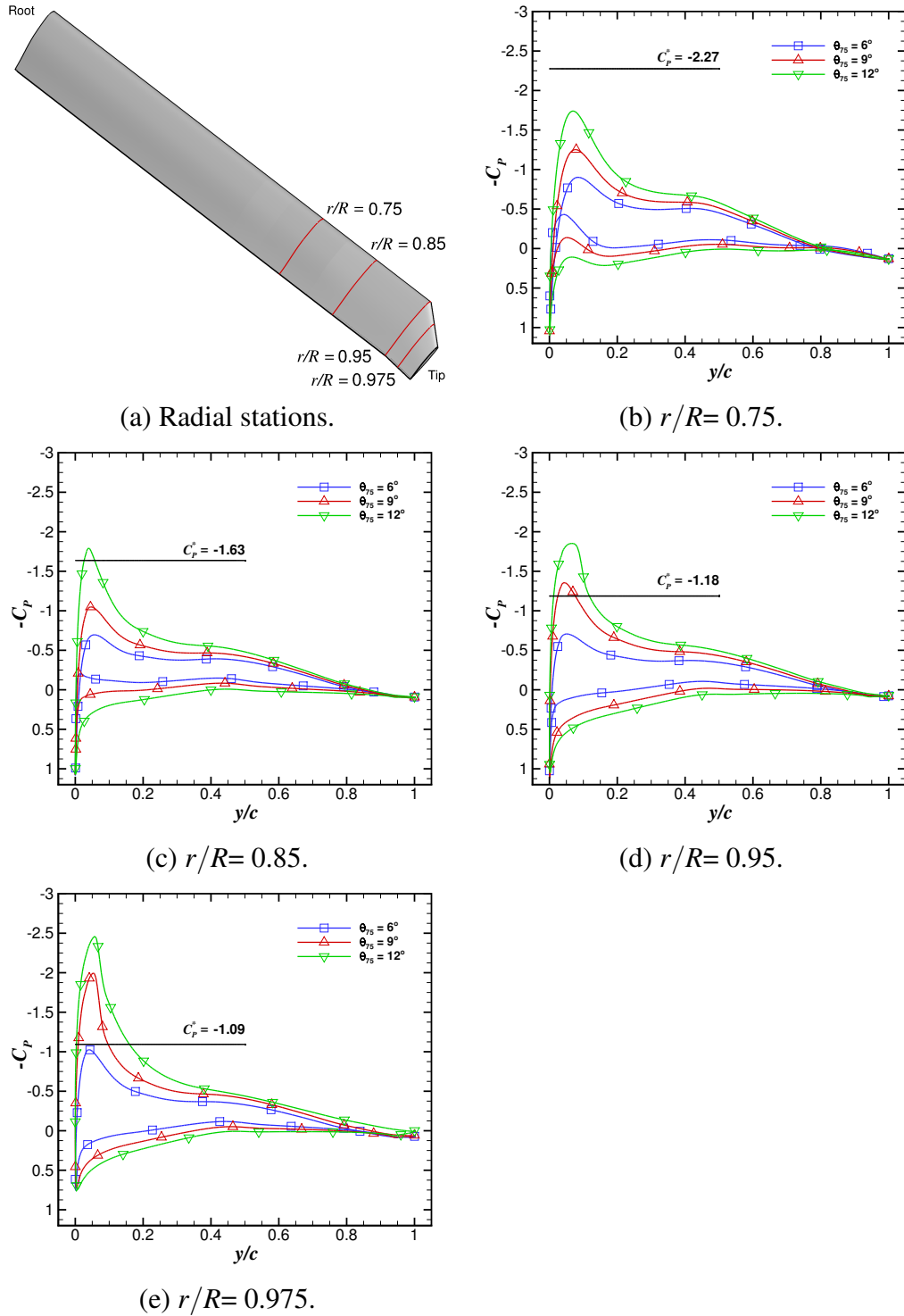


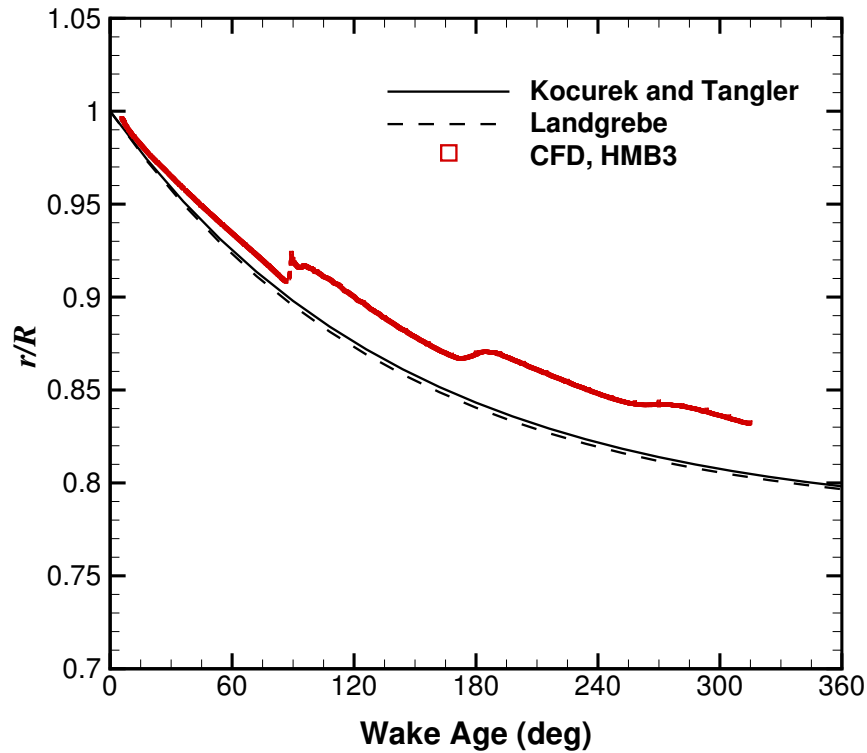
Figure 5.36:  $C_p$  profile as function of the blade pitch angle for the PSP model rotor at blade-tip Mach number of 0.65. Radial stations considered:  $r/R = 0.75, 0.85, 0.95$ , and  $0.975$ . Critical

$$C_P^* = \frac{2}{\gamma(M_{\text{tip}} \frac{r}{R})^2} \left[ \left( \frac{2 + (\gamma - 1)(M_{\text{tip}} \frac{r}{R})^2}{\gamma + 1} \right)^{\frac{\gamma}{\gamma - 1}} - 1 \right].$$

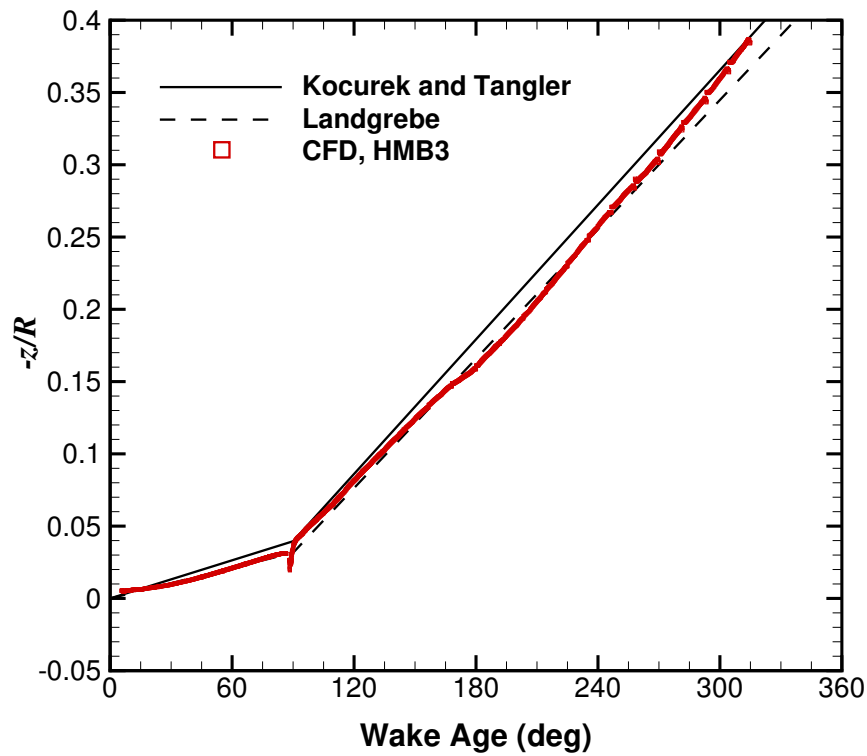
### Tip Vortex Trajectory

It is well known that to ensure realistic predictions of the wake-induced effects, the radial and vertical displacements should be resolved, at least for the first and second wake passages [17]. Figure 5.37 shows a comparison of the radial and vertical displacements of the tip vortices, as functions of the wake age (in degrees), with the prescribed wake-models of Kocurek and Tangler [20] and Landgrebe [19]. It should be mentioned that, a blade loading coefficient  $C_T/\sigma = 0.0944$  was selected, which corresponds to  $\theta_{75} = 11.0^\circ$ . The prediction of the trajectory, which is captured up to 4-blade passages (wake age of  $360^\circ$  for a four-bladed rotor) is in fair agreement with both empirical models. It is found that the radial tip vortex displacement seems to be more sensitive to the change of mesh density than the vertical one, as shown in (Figure 5.37 (a)). Nevertheless, CFD results seem to accurately predict the slow convection of the tip vortices (up to wake age of  $90^\circ$ ) seen in vertical displacement ( $-z/R$ ). This rate is drastically increased as consequence of the passage of the following blade, leading to a linear increment of the vertical displacement of the wake. These changes are well captured by the present CFD method.

Visualisation of the flowfield of the PSP rotor using the  $\tilde{Q}$ -criterion [206] is presented in Figure 5.38 (a) at blade pitch angle of  $11^\circ$ . This informative plot reveals that the computations capture the rotor wake up to four blade passages for the medium chimera grid employed. Figure 5.38 (b) shows contours of vorticity magnitude at  $y=0$ . The CFD solution obtained with the medium background grid (7.2 million cells) is able to capture the first four blade passage without a significant dissipation of the vortex core and distortion of its shape. However, the fifth blade passage suffers smearing and distortion due to the use of lower high-order spatial reconstruction and biased-scheme, respectively.

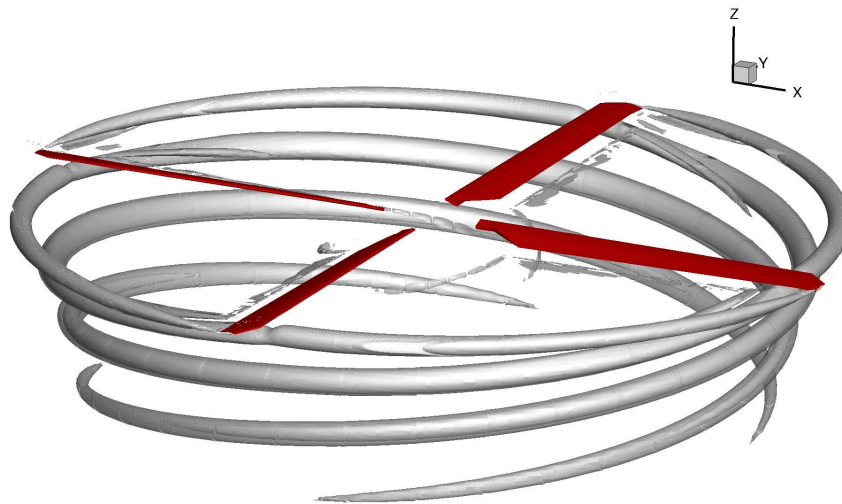


(a)

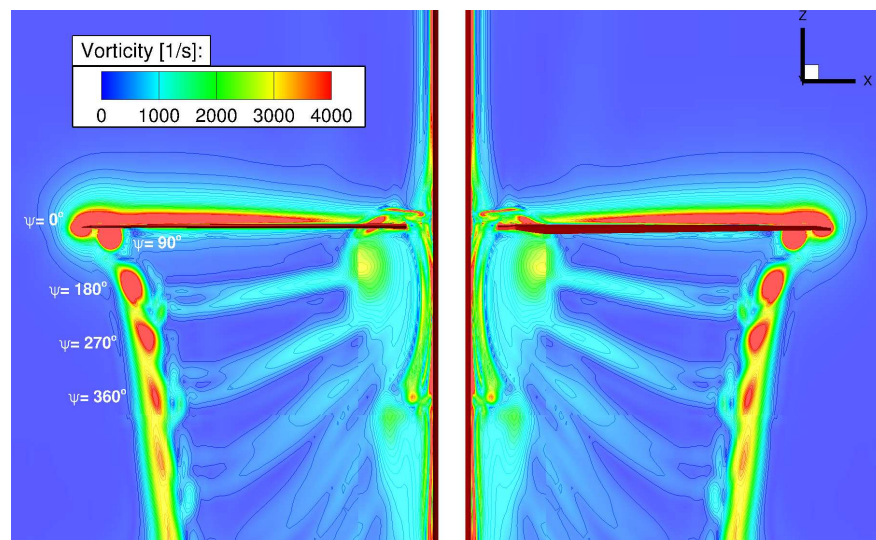


(b)

Figure 5.37: Comparison between the radial (top) and vertical (bottom) tip vortex displacements and the prescribed wake-models of Kocurek and Tangler [20] (solid lines) and Landgrebe [19] (dashed lines). This case corresponds to the PSP model rotor at blade-tip Mach number of 0.65 and  $\theta_{75} = 11^\circ$ .



(a) Rotor wake.



(b) Contours of vorticity magnitude at  $y=0$ .

Figure 5.38: (a) Visualisation of the flowfield of the PSP rotor using the  $\tilde{Q}$ -criterion and (b) contours of vorticity magnitude at  $y=0$ . Blade-tip Mach number is 0.65 and blade pitch angle  $11^\circ$ .

## 5.5 Summary of Findings

This work demonstrated the ability of the HMB solver to accurately predict the rotor hover performance at low and high disk loadings with modest computer resources. The main conclusions are:

- The effect of the tip shape and Mach number on the performance of the S-76 blade is captured by CFD within 0.1 counts of FoM for most cases, with a worst-case difference across the blade loadings and different tip shapes of 0.6 counts.
- The acoustics in hover for the S-76 blade with anhedral tip showed a reduction of the total noise by 5% if compared with the swept-taper blade.
- Aeroelastic cases showed very good agreement with whirl tower data.
- Effect of FoM on endurance is also captured and reported.
- Fully turbulent flow solutions were obtained for the PSP blade in hover. The results of CFD compare well with test data for the integrated blade load and surface pressure coefficient at blade-tip Mach number of 0.585. Regarding the PSP blade results at blade-tip Mach number of 0.65, experimental data is necessary for detailed comparisons. The agreement with the theory and published CFD works for the integrated loads is, however, encouraging.
- Overall the SST linear eddy-viscosity models, the steady-state formulation of HMB with periodic conditions, and chimera grids of about 9 million cells per blade show good consistency and accuracy when compared with experiments.
- Results obtained on a cluster of 128 cores at 3GHz were obtained at turn-around times of 24.8 hours.

## Chapter 6

# Validation of HMB for Propeller Blades

This chapter evaluates and validates the HMB3 CFD solver for propeller blade aerodynamics. As a means of evaluating propeller aeroacoustic designs and comprehensive analysis codes, Dowty Aerospace Propellers undertook the design, manufacture, and testing of a new Pressure Tapped Propeller (PTP) model in the 8×7ft transonic wind tunnel of the Aircraft Research Association (ARA) [72] (see Figure 6.1). This work provided good quality experimental blade pressure and acoustic data for modern high speed propellers, and represents a valuable data base since previous work on pressure data dated from the 1950s performed at NACA [249].

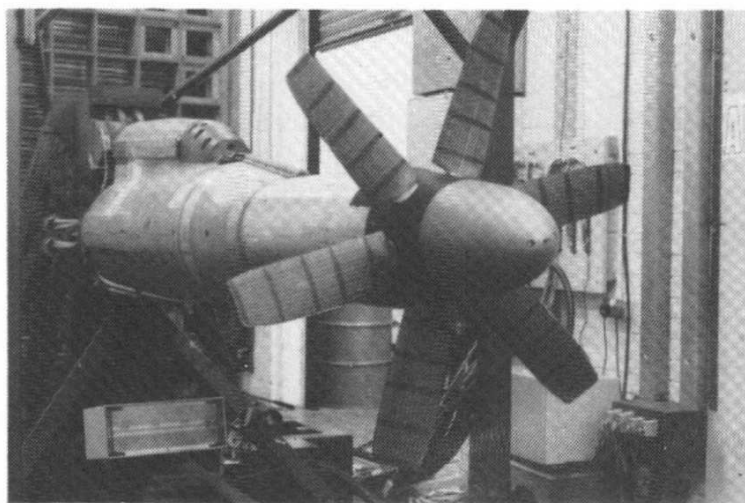


Figure 6.1: Pressure Tapped Propeller (PTP) model in the transonic wind tunnel of the Aircraft Research Association [72].

A single row of six blades were built with unswept (see Figure 6.2) and a moderate swept planforms and used in conjunction with a minimum interference spinner. The blades comprise two different aerofoils from the ARA-D/A family located at 60%  $R$  and 95%  $R$ . Those sections are a modified version of the original ARA-D family for high efficiency, especially at high speed. The rotor radius has 0.457 m and the reference chord at 70%  $R$  0.1143 m, leading to an aspect ratio of 4. Table 6.1 shows the main geometric characteristics of the unswept propeller blade (baseline), which is considered in this study and Figure 6.3 shows its twist and chord distributions. The chord distribution is reduced from its reference value of 0.1143 m to 0.089 m at the blade-tip, resulting in a moderate taper of 78%. The design of the hub system allowed to minimise radial and axial velocity gradients on the blade root.

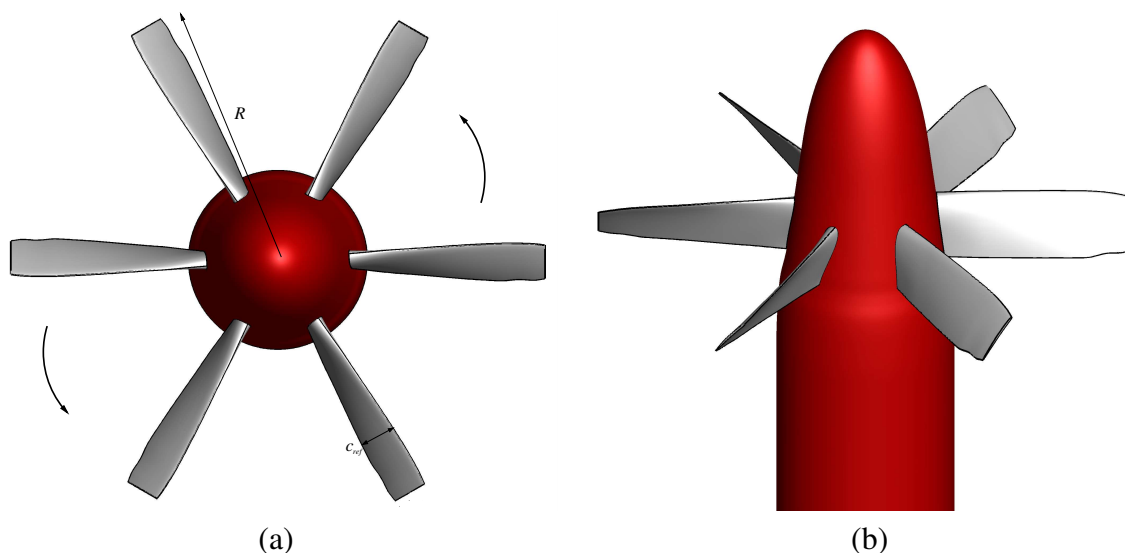


Figure 6.2: (a) Front and (b) iso-views of the propeller rotor with unswept tip (baseline), and geometric details of the spinner.

Table 6.1: Geometric properties of the unswept propeller blade (baseline) [72].

Parameter	Value
Number of blades, $N_b$	6
Rotor radius, $R$	0.457 m (17.99 in)
Reference blade chord, $c_{ref}$	0.114 m (4.48 in)
Aspect ratio, $R/c_{ref}$	4
Rotor solidity, $\sigma$	0.477
Non-linear twist, $\Theta$	-36.95°



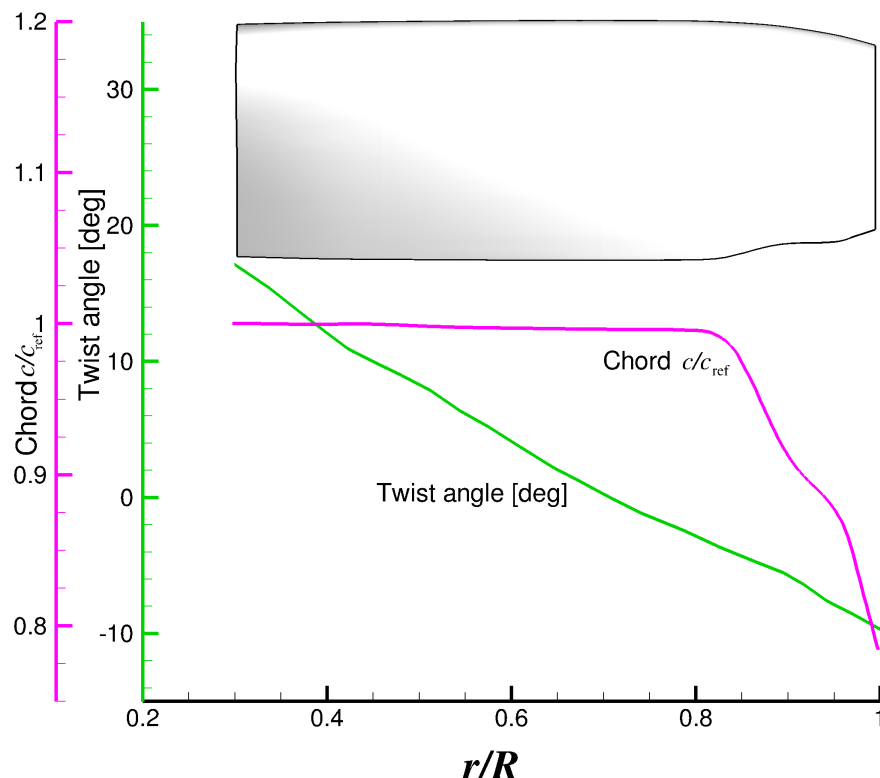


Figure 6.3: Twist and chord distributions for the JORP propeller blade.

## 6.1 Rotor Mesh

As the propeller rotor is a six-bladed rotor, only one sixth of the computational domain was meshed, assuming periodic conditions for the flow in the azimuthal direction (see Figure 6.4). The size of the computational domain and mesh were based on experience with CFD for similar cases and no mesh convergence study was conducted. Farfield boundaries were placed at 5, 10, and 20 propeller radii away from the blade hub in the radial, upstream, and downstream directions, respectively [220]. A C-topology around the leading edge of the blade was selected, whereas an H-topology was employed at the trailing edge of the blade (see Figure 6.5). The first cell normal to the blade was set to  $1.14 \times 10^{-6} \text{m}$  ( $1.0 \times 10^{-5} c_{\text{ref}}$ ), which assures  $y^+$  less than 1.0 everywhere on the blade for the employed Re. In the chordwise direction, 343 mesh points were used, whereas in the spanwise direction 127 mesh points were used. A blunt trailing-edge was modelled using 38 mesh points. Table 6.2 shows the main features about meshing parameters and point distributions of the propeller blade.

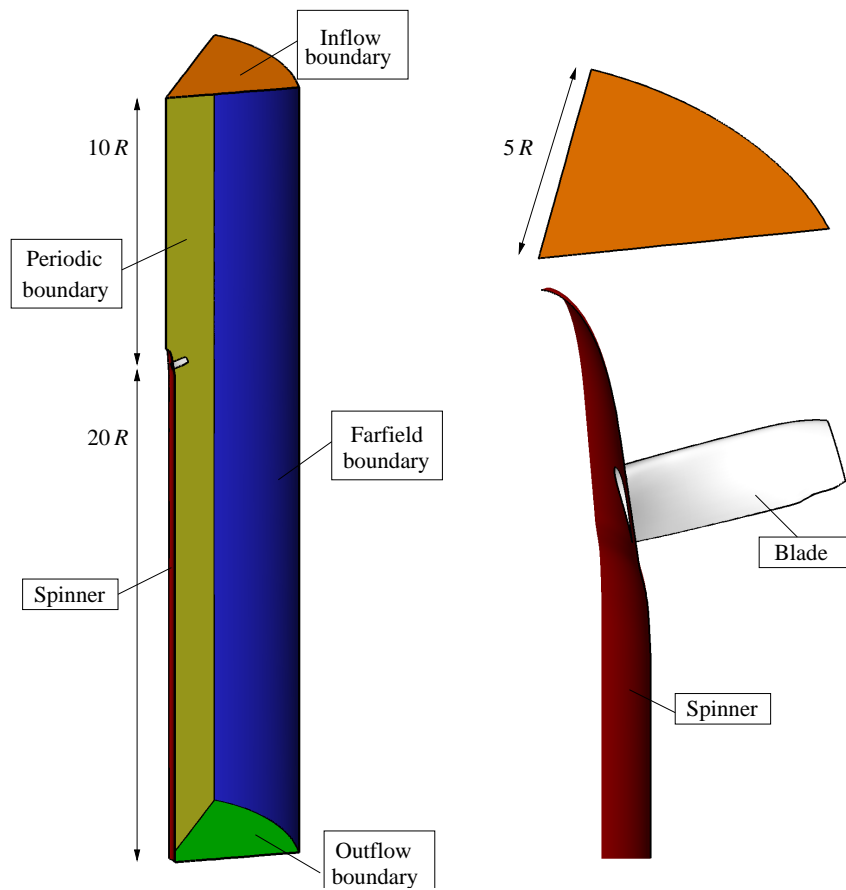


Figure 6.4: Computational domain and boundary conditions employed for the propeller blade.

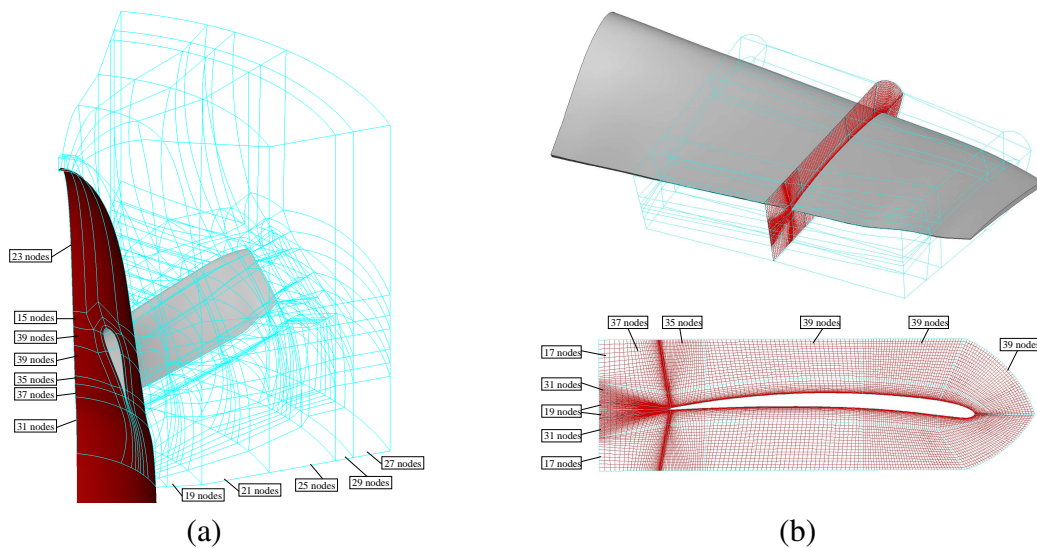


Figure 6.5: (a) Overview and (b) close-view of the C-H topology employed for the propeller blade.

Table 6.2: Meshing parameters for the propeller rotor blade.

Parameter	Value
Chordwise direction	343 mesh points
Spanwise direction	127 mesh points
Trailing edge	38 mesh points
Wall distance	$1.0 \times 10^{-5} c_{\text{ref}}$
Mesh size	8.96 million cells

## 6.2 Test Conditions and Computations

Table 6.3 shows the conditions employed for the axial flight. The cruise condition was modelled at 0 ft (ISA+0°), with a blade-tip Mach number of 0.529 and advance ratio 1.309. The Reynolds number for this case was  $1.163 \times 10^6$ , based on the reference blade chord and rotor tip speed (with no account for the advance velocity). The blade pitch angle  $\theta_{70}$  was set to 60° degrees. The blade was assumed rigid.

Table 6.3: Flow conditions for the propeller blade.

Parameter	Value
Blade-tip Mach number, $M_{\text{tip}}$	0.54
Freestream Mach number, $M_{\infty}$	0.69
Advance ratio, $\mu$	1.309
Reynolds number, Re	$1.163 \times 10^6$
Blade pitch angle, $\theta_{70}$	60°
Turbulence model	$k\text{-}\omega$ SST

All flow solutions were computed by solving the RANS equations, coupled with Menter's  $k\text{-}\omega$  SST turbulence model [191]. The flow equations were integrated with the implicit dual-time stepping method of HMB, using a pseudo-time CFL equal to 3. Typically, 15,000 iterations were necessary to drop the residual of the flow solution ( $\rho, u, v, w, P$ ) by almost 6 orders of magnitude (see Figure 6.6).

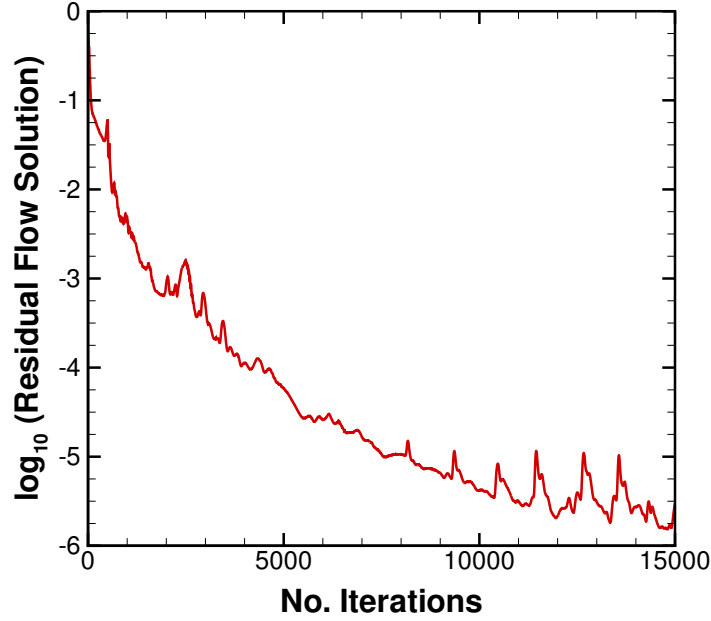


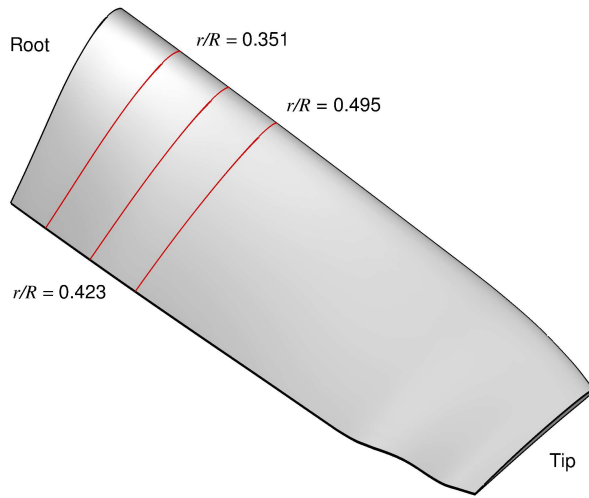
Figure 6.6: Residual of the flow solution as function of the number of iterations.

### 6.3 Results and Discussion

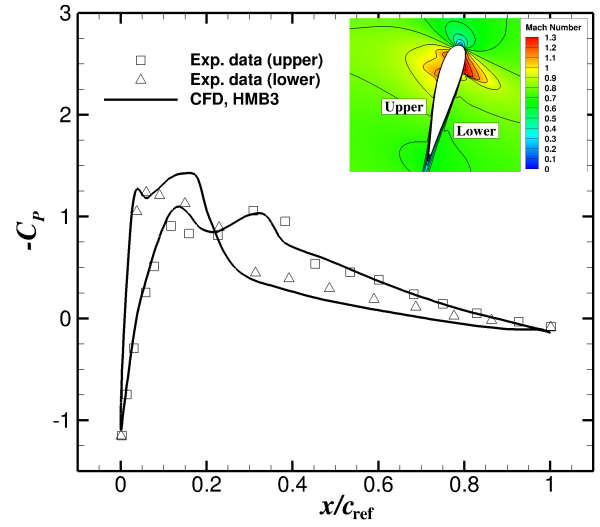
Nine radial stations along the spanwise blade (from 35%  $R$  to 95%  $R$ ) were selected for comparison, with 28 pressure taps per section. Neither blade loadings nor details of the flowfield were available from experiments. Figures 6.7-6.9 show  $C_P$  profile comparisons between experiments [72] and HMB3 at the aforementioned radial stations. The pressure coefficient is based on the local dynamic pressure and is given as:

$$C_P = \frac{P - P_\infty}{1/2 \rho_\infty V_{\text{tip}}^2} \left( \frac{M_{\text{tip}}}{M_{\text{loc}}} \right)^2 \quad (6.1)$$

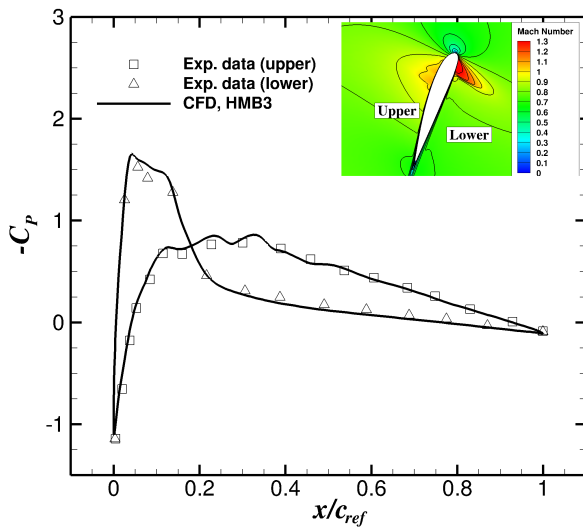
where  $M_{\text{loc}} = \sqrt{M_{\text{tip}}^2 \left( \frac{r}{R} \right)^2 + M_\infty^2}$ . Stations located near the root blade (Figures 6.7 (b), (c), and (d)) show no sign of flow separation, despite the high local angle of attack seen by these aerofoils. On the lower surface, the shock position is well captured by the simulations. Considering the middle stations (see Figure 6.8),  $C_P$  distributions agree well despite that the leading suction peaks are slightly over-predicted. At most outboard stations (see Figure 6.9), a mild shock is found at the vicinity of the leading edge on the lower surfaces and the  $C_P$  is well represented. The use of thin aerofoils in conjunction with a moderate taper tip shape tend to limit the compressibility effects in the tip region, encountered at this flight condition at high advance ratio.



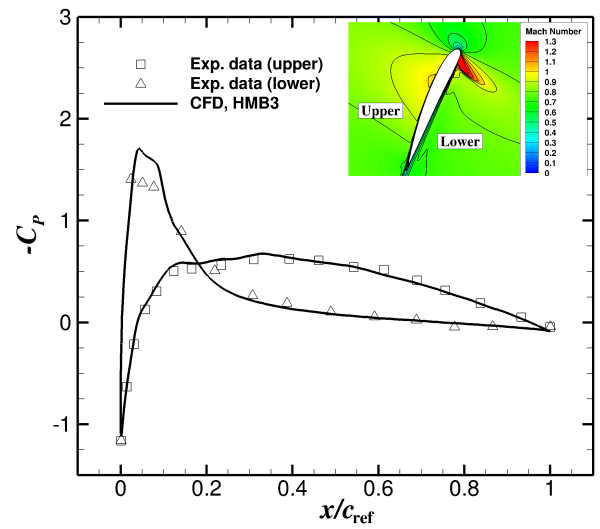
(a) Radial stations.



(b)  $r/R = 0.351$ .

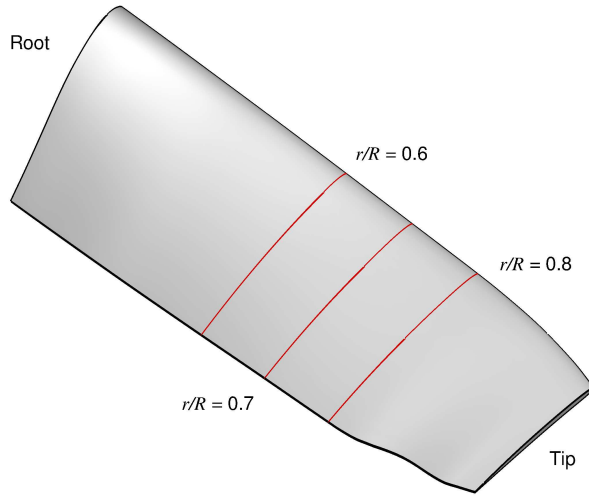


(c)  $r/R = 0.423$ .

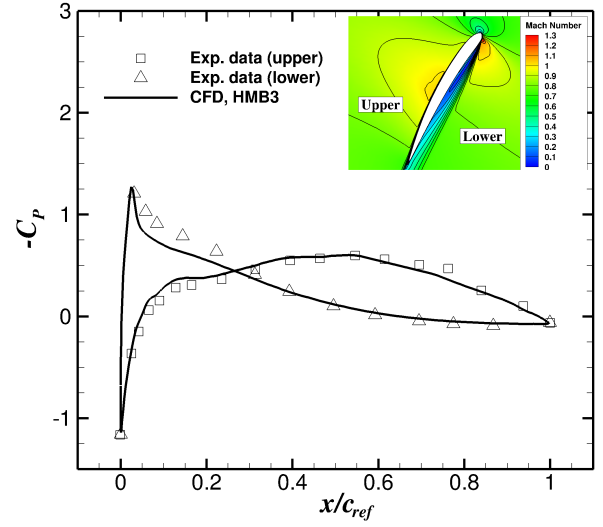


(d)  $r/R = 0.495$ .

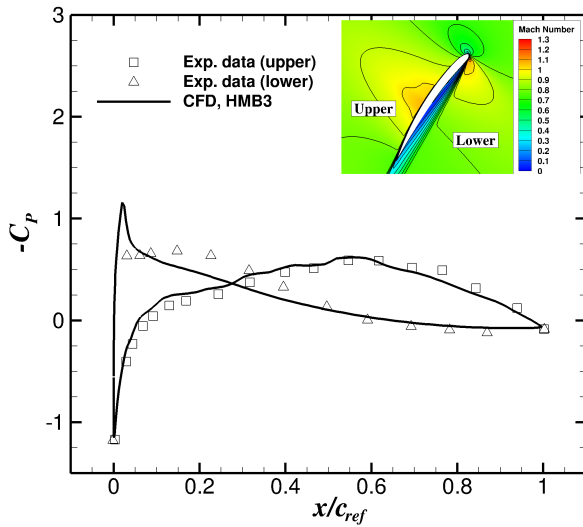
Figure 6.7:  $C_p$  profile comparisons between experimental data [72] and HMB3 at radial stations  $r/R = 0.351, 0.423$ , and  $0.495$ . Contours of Mach number is also shown in the figures.



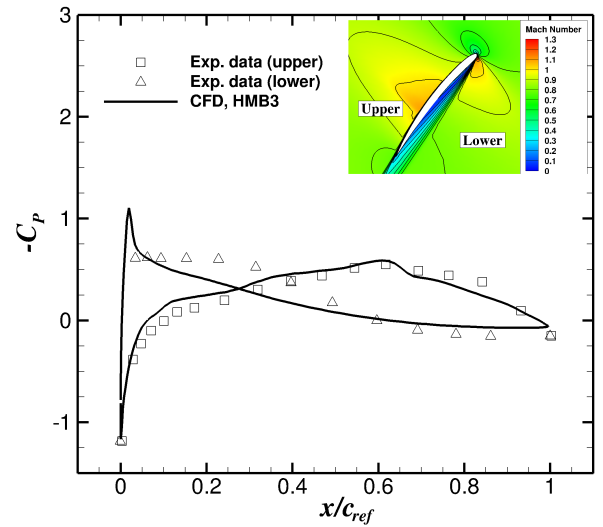
(a) Radial stations.



(b)  $r/R = 0.6$ .

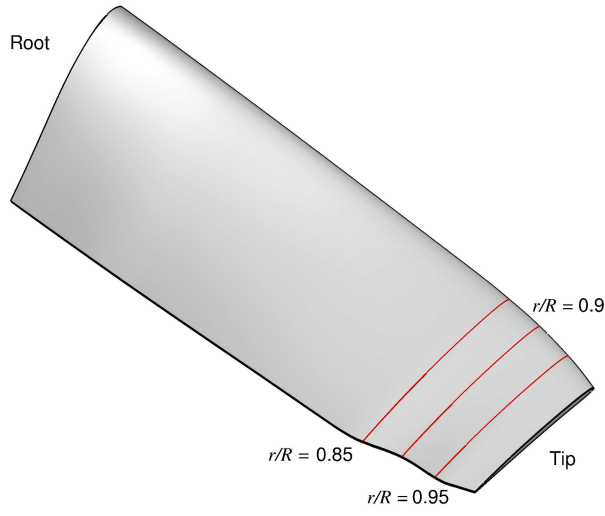


(c)  $r/R = 0.7$ .

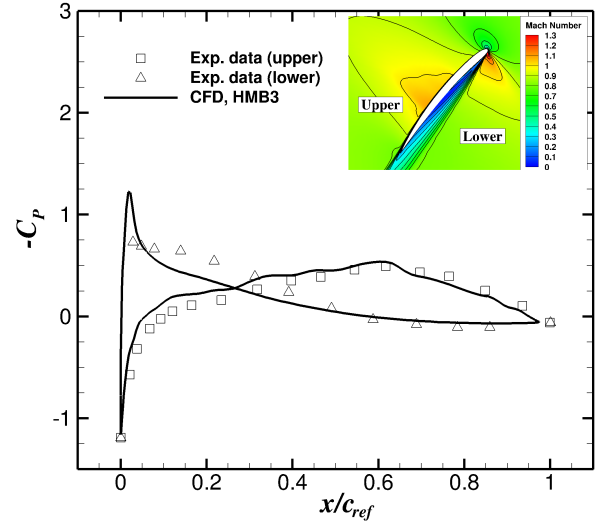


(d)  $r/R = 0.8$ .

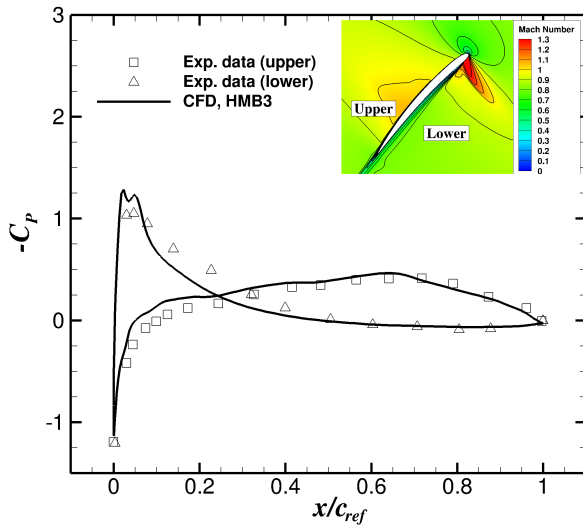
Figure 6.8:  $C_p$  profile comparisons between experimental data [72] and HMB3 at radial stations  $r/R = 0.6, 0.7$ , and  $0.8$ . Contours of Mach number is also shown in the figures.



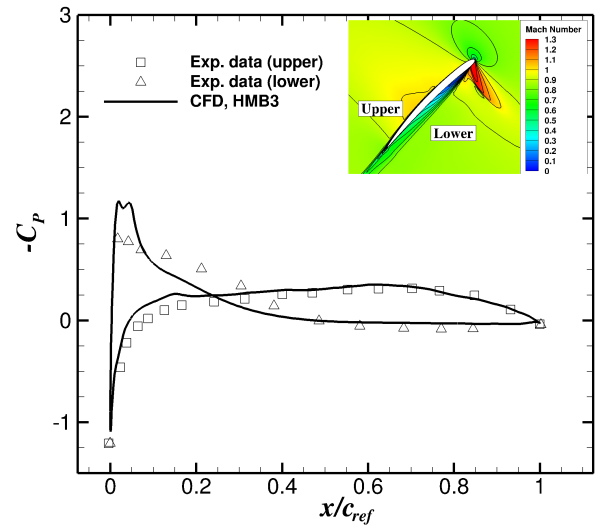
(a) Radial stations.



(b)  $r/R = 0.85$ .



(c)  $r/R = 0.9$ .



(d)  $r/R = 0.95$ .

Figure 6.9:  $C_p$  profile comparisons between experimental data [72] and HMB3 at radial stations  $r/R = 0.85, 0.9$ , and  $0.95$ . Contours of Mach number is also shown in the figures.

# Chapter 7

## Validation of HMB for Tiltrotor Blades

The objective of this chapter is to validate the employed CFD method for flows relevant to tiltrotor blades before moving into complete tiltrotor configurations and tiltrotor blade optimisations. The XV-15 tiltrotor blades are simulated in hover and propeller modes for a range of design points and compared with experimental data. An aeroacoustic study is also included in the tip-path-plane of the rotor. Finally, the impact of a fully-turbulent  $k-\omega$  SST and transitional  $k-\omega$  SST- $\gamma$  models on the predicted figure of merit is also shown at collective angles of  $3^\circ$  and  $10^\circ$ . The ability of those models in predicting the experimental skin friction distribution [88] on the blade surface is also discussed.

### 7.1 Aerodynamic and Aeroacoustic Study

#### 7.1.1 XV-15 Rotor Geometry

The three-bladed XV-15 rotor geometry was generated based on the full-scale wind tunnel model tested by Betzina in the NASA Ames 80- by 120- foot wind tunnel facility [87]. NACA 6-series five-digit aerofoil sections comprise the rotor blade, and its identity and radial location along the rotor blade is reported in Table 7.1.

---

Part of this work is published in A. Jimenez-Garcia *et al.*, Tiltrotor CFD Part I - Validation, The Aeronautical Journal, 121 (1239), 2017, 577-610, doi: 10.1017/aer.2017.17



Table 7.1: Radial location of the XV-15 rotor blade aerofoils [84].

$r/R$	Aerofoil
0.09	NACA 64-935
0.17	NACA 64-528
0.51	NACA 64-118
0.80	NACA 64-(1.5)12
1.00	NACA 64-208

The main geometric characteristics of the XV-15 rotor blades [87] are summarised in Table 7.2. It is interesting to note that unlike conventional helicopter blades, tiltrotor blades are characterised by high twist and solidity, along with a small rotor radius.

Table 7.2: Geometric properties of the full-scale XV-15 rotor [87].

Parameter	Value
Number of blades, $N_b$	3
Rotor radius, $R$	3.81 m (150 in)
Reference blade chord, $c_{\text{ref}}$	0.355 m (14 in)
Aspect ratio, $R/c_{\text{ref}}$	10.71
Rotor solidity, $\sigma$	0.089
Non-linear twist, $\Theta$	$-40.25^\circ$

A detailed sketch of the XV-15 blade planform and the blade radial twist, and chord distributions is shown in Figure 7.1. The rotor blade chord is held constant, and extends at almost 80% of the rotor blade. The blade root, however, was not modelled due to the lack of information on the cuff geometry in the literature.

### 7.1.2 XV-15 Rotor Mesh

A mesh generated using the chimera technique was used for the aerodynamic study of the XV-15 rotor. It includes a cylindrical off-body mesh used as background, and a body-fitted mesh for the blade. The use of an overset grid method allowed for the blade pitch angle to be changed by rotating the body-fitted mesh. Because the XV-15 rotor was numerically evaluated in hover and propeller modes (axial flight), only a third of the computational domain was meshed, assuming periodic conditions for the flowfield in the azimuthal direction (not applicable to stall condition).

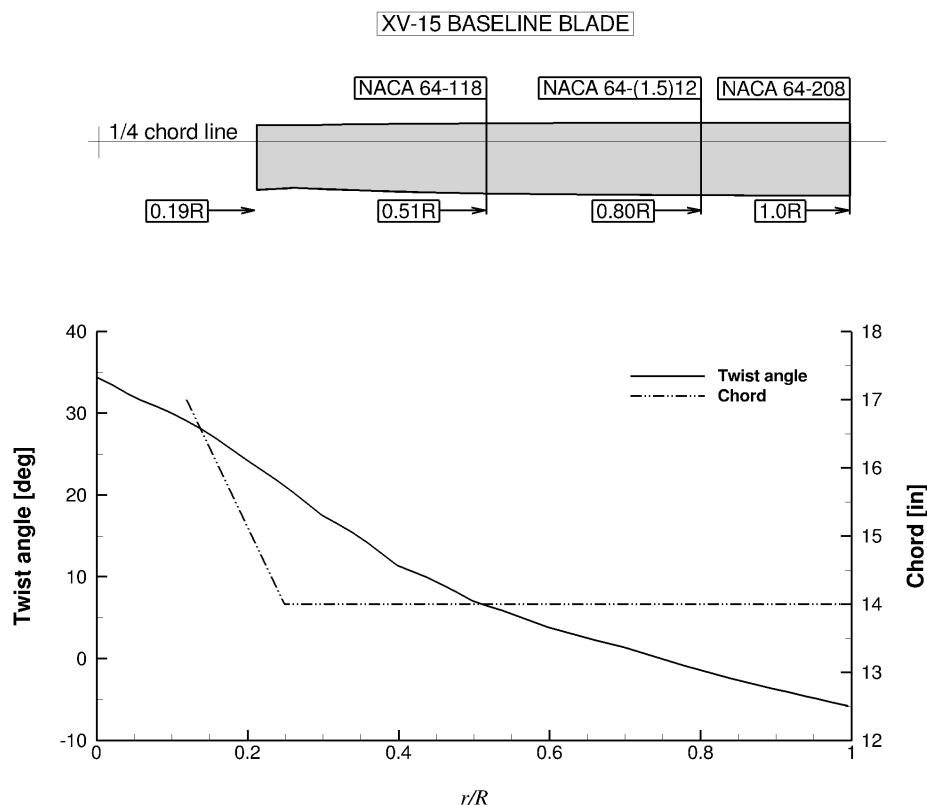
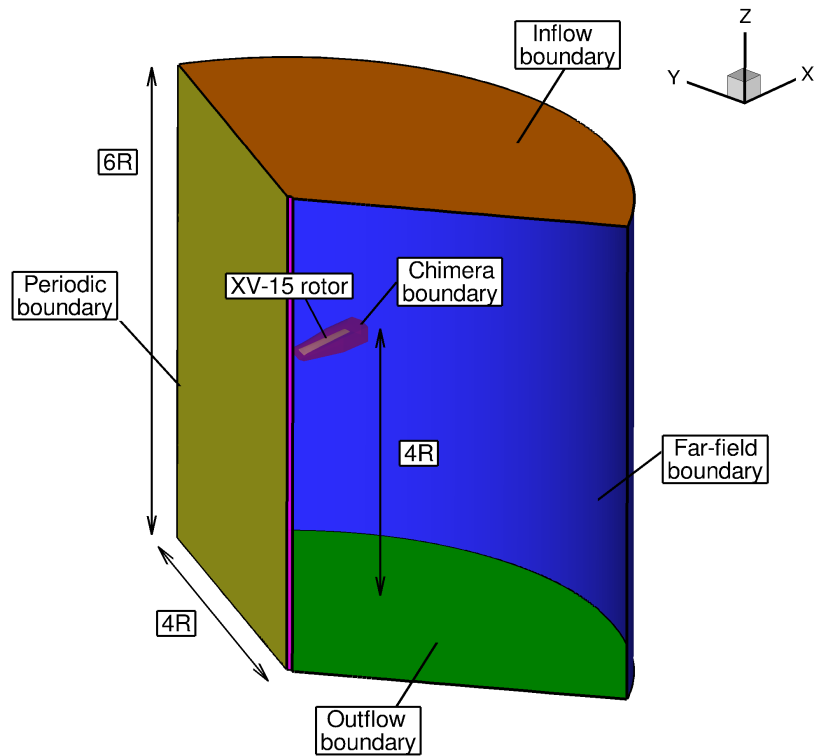


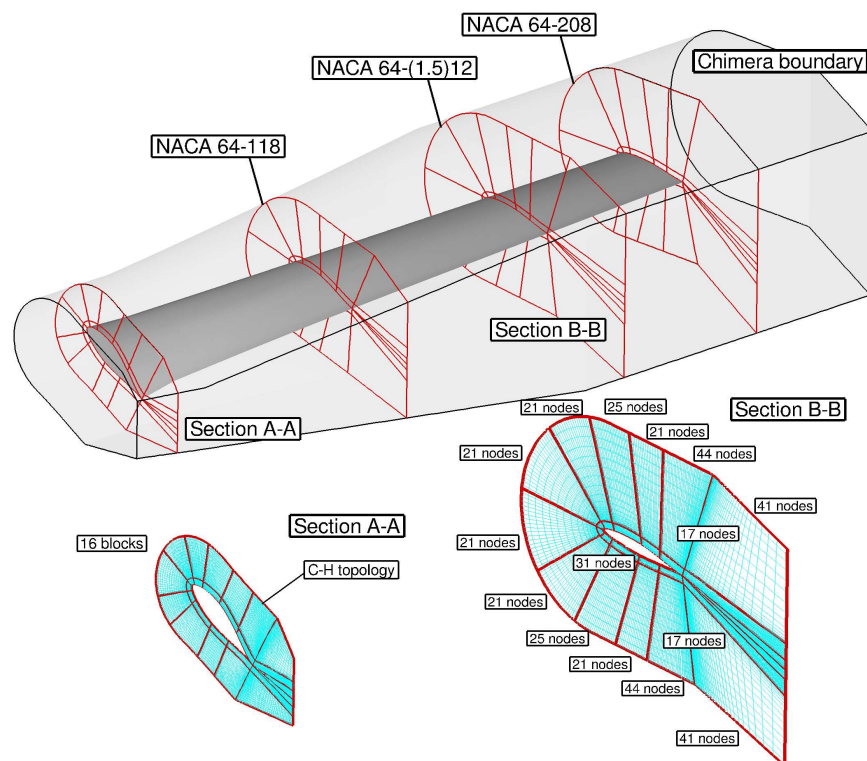
Figure 7.1: Planform of the XV-15 rotor blade (top) and twist and chord distributions [250] (bottom).

A view of the computational domain, along with the employed boundary conditions is given in Figure 7.2 (a). Farfield boundaries were extended to  $2R$  (above rotor) and  $4R$  (below rotor and in the radial direction) from the rotor plane, which assures a solution independent of the boundary location. Furthermore, an ideal rotor hub was modelled and approximated as a cylinder, extending from inflow to outflow with a radius of  $0.05R$ .

A C-topology was selected for the leading edge of the blade, while an H-topology was employed at the trailing edge. This configuration permits an optimal resolution of the boundary layer due to the orthogonality of the cells around the surface blade (Figure 7.2 (b)). The height of the first layer of mesh points above the blade surface was set to  $1.0 \times 10^{-5} c_{\text{ref}}$ , which leads to  $y^+$  less than 1.0 all over the blade. Regarding the chordwise and spanwise directions of the blade, 264 and 132 mesh points were used, while the blunt trailing-edge was modelled with 42 mesh points.



(a) Computational domain.



(b) XV-15 rotor mesh.

Figure 7.2: Computational domain and boundary conditions employed (top) and detailed view of the XV-15 rotor mesh (bottom).

To guarantee a mesh independent solution, two computational domains were built. Table 7.3 lists the grids used and shows the breakdown of cells per blade. The coarse and medium grids have 6.2 and 9.6 million cells per blade (equivalent to 18.6 and 28.8 million cells for three blades), with the same grid resolution for the body-fitted mesh (3.6 million cells). The background mesh, however, was refined at the wake and near-body regions, increasing the grid size from 2.6 to 6 million cells.

Table 7.3: Meshing parameters for the XV-15 rotor mesh.

	<b>Coarse Mesh</b>	<b>Medium Mesh</b>
Background mesh size (cells)	2.6 million	6.0 million
Blade mesh size (cells)	3.6 million	3.6 million
Overall mesh size (cells)	6.2 million	9.6 million
Height of the first layer of mesh points	$1.0 \times 10^{-5} c_{\text{ref}}$	$1.0 \times 10^{-5} c_{\text{ref}}$

### 7.1.3 Test Conditions and Computations

Table 7.4 summarises the employed conditions and the computations performed in hover and propeller modes. For hover, the blade-tip Mach number was set to 0.69, and four blade pitch angles were considered, covering to low, medium, and high disk loadings. The Reynolds number, based on the reference blade chord of 14 inches and on the tip speed, was  $4.95 \times 10^6$ . The cruise condition was modelled at 0 ft (ISA+0°), with a blade-tip Mach number of 0.54 and advance ratio  $\mu = V_\infty/V_{\text{tip}}$  of 0.337. The Reynolds number for this case was  $4.50 \times 10^6$ , again based on the reference blade chord and rotor tip speed (with no account for the advance velocity).

Table 7.4: Flow conditions for the full-scale XV-15 tiltrotor blade.

	<b>Helicopter Mode</b>	<b>Aeroplane Mode</b>
Blade-tip Mach number, $M_{\text{tip}}$	0.69	0.54
Reynolds number, $Re$	$4.95 \times 10^6$	$4.50 \times 10^6$
Blade pitch angle, $\theta_{75}$	3°, 5°, 10°, 13°	26°, 27°, 28°, 28.8°
Grid	Coarse and Medium	Coarse and Medium
Turbulence model	$k-\omega$ SST	$k-\omega$ SST

All flow solutions were computed solving the RANS equations, coupled with Menter's  $k-$

$\omega$  SST turbulence model [191]. The flow equations were integrated with the implicit dual-time stepping method of HMB, using a pseudo-time CFL equal to 4 for the helicopter and 2 for the aeroplane modes.

### 7.1.4 Helicopter Mode

The effect of the mesh density on the figure of merit, and torque coefficient  $C_Q$  as functions of the thrust coefficient  $C_T$  are shown in Figure 7.3. Experimental data of the full-scale XV-15 rotor is also shown, carried out by Felker *et al.* [84] at Outdoor Aeronautic Research Facility (OARF), and by Light [86] and Betzina [87] at the NASA 80- by 120-foot wind tunnel. The majority of works on performance analysis of rotor blades do not model the hub and blade root, mainly due to the complexity of mesh generation and lack of detailed geometry. In this regard, experiments were corrected for the hub and the experimental apparatus tares. Vertical lines labelled as empty (4,574 kg,  $C_T = 0.0073$ ) and maximum gross (6,000 kg,  $C_T = 0.0096$ ) weight, define the hover range of the XV-15 helicopter rotor [73]. Momentum-based estimates of the figure of merit are also included, using Equation 7.1, where an induced power factor  $k_i$  of 1.1 and an overall profile drag coefficient  $C_{DO}$  of 0.01 were used.

$$\text{FoM} = \frac{C_T^{3/2} / \sqrt{2}}{\left( \sigma \frac{C_{D0}}{8} + k_i \frac{C_T^{3/2}}{\sqrt{2}} \right)}. \quad (7.1)$$

Using the obtained CFD results, a polynomial fit was computed and shown with solid lines and squares (coarse grid) or triangles (medium grid). Considering the sets of experiments, good agreement was found between them, with a maximum discrepancy of 4.11% in the figure of merit. The reason for this disagreement (4 counts of FoM) may be partly due to the variations in experimental setups and conditions between the different facilities. CFD results present an excellent agreement with the test data of Betzina[87] for all blade pitch angles. It is found that the effect of the grid size on the overall performance is negligible at low thrust, with a small influence at high thrust.

Predicted and measured [84, 86, 87] peak figure of merit is reported in Table 7.5. Experiments performed by Felker show a higher FoM (2 counts) if compared with the experiments by Light and Betzina. A large recirculation zone was reported in the  $80 \times 120 \text{ ft}^2$  test section of

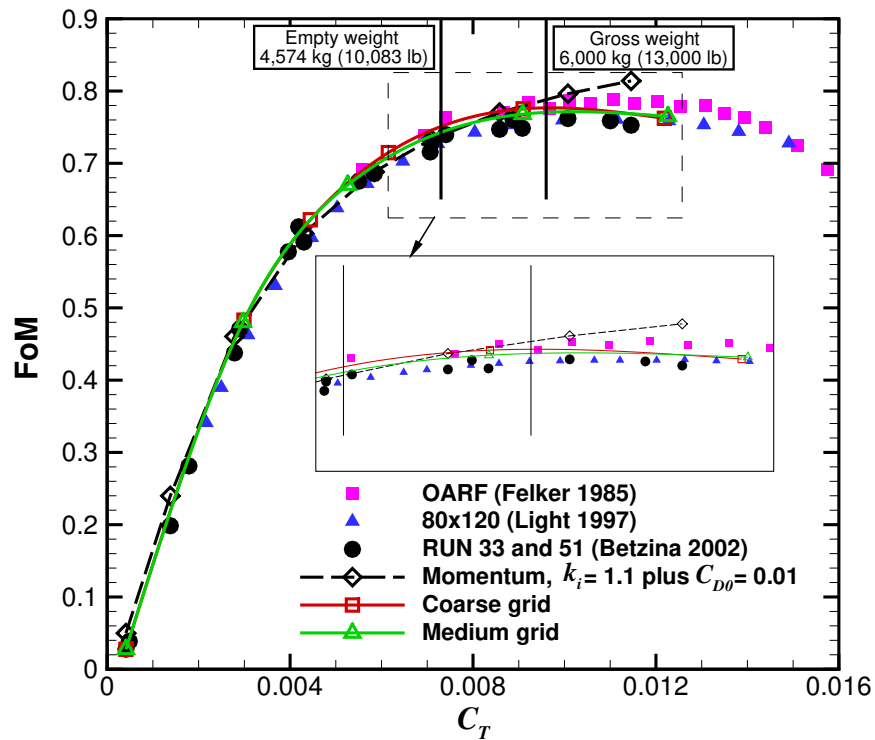
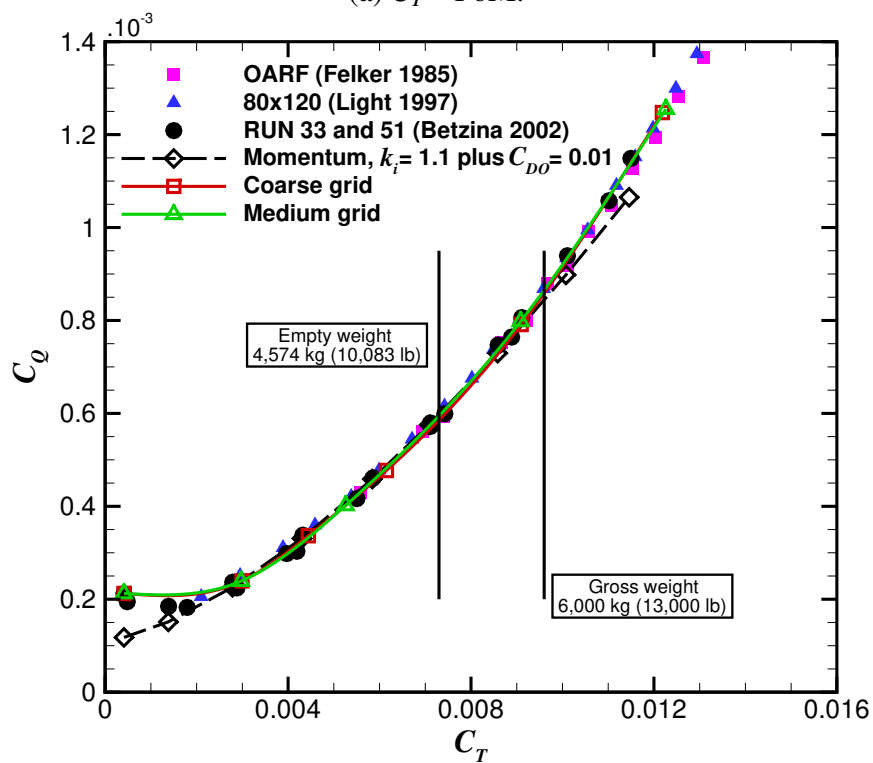

 (a)  $C_T$  - FoM.

 (b)  $C_T$  -  $C_Q$ .

Figure 7.3: Effect of the mesh density on the figure of merit (top) and torque coefficient (bottom) for the full-scale XV-15 rotor.

NASA by Felker, which may be the reason of this disagreement. Predictions with the medium grid indicate good correlation with the experiments (0.91% respect to Betzina and Light, and 2.53% respect to Felker). These results show that the present method is able to capture the overall performance of tiltrotors. To assess if all flow physics is accurately modelled, more detailed experimental data is needed (flow visualisations, surface pressure and skin friction coefficients, etc.)

Table 7.5: Predicted and experimental peak FoM for the full-scale XV-15 rotor.

	Experiments			CFD	
	Felker [84]	Light [86]	Betzina [87]	Coarse grid	Medium grid
FoM	0.788	0.761	0.761	0.776	0.768

In terms of the turbulence model employed, it seems that the fully turbulent flow assumption captures the trend of FoM and torque coefficient (Figure 7.3 (b)). Similar conclusions were drawn in previous work by Kaul *et al.* [94], Yoon *et al.* [98], and Sheng *et al.* [99], where fully turbulent flows were successfully employed. Comparison between the predicted and measured [88] FoM at a blade pitch angle of  $10^\circ$  is reported in Table 7.6. The predictions obtained on the medium grid indicate good correlation with the experiments (0.8 counts of FoM), which highlights the ability of this grid density in accurately predicting the FoM at a modest CPU time.

Table 7.6: Predicted and experimental [88] figure of merit at blade pitch angle of  $10^\circ$ .

Case	FoM	$\Delta\text{FoM} [\%]$
Coarse grid	0.775	1.97%
Medium grid	0.768	1.05%
Experiment	(0.760) [98]	-

## Surface Pressure Predictions

Due to the lack of experimental surface pressure measurements, a comparison between HMB3 and CFD data published by Kaul *et al.* [95] using the OVERFLOW2 solver is shown in Figure 7.4. Three radial stations are considered ( $r/R = 0.72, 0.83$ , and  $0.94$ ) at a collective angle of  $10^\circ$ . The surface pressure coefficient is computed based on the local velocity at each radial station:

$$C_P = \frac{P - P_\infty}{1/2\rho_\infty(\Omega r)^2}. \quad (7.2)$$

CFD results using HMB correspond to the coarse grid (18.6 million cells for the three blades) where the  $k-\omega$  SST turbulence model [191] was employed. Kaul's results were obtained with a grid size of 35 million cells using the Spalart-Allmaras turbulence model [97]. Despite a small variation on the predicted peak  $C_p$ , a fair agreement is found for all radial stations. Regarding the radial stations  $r/R = 0.72$  and  $r/R = 0.83$ , it is clear that the suction peak does not exceed the critical  $C_p^*$  values, while the most outboard section ( $r/R = 0.94$ ) reaches sonic conditions.

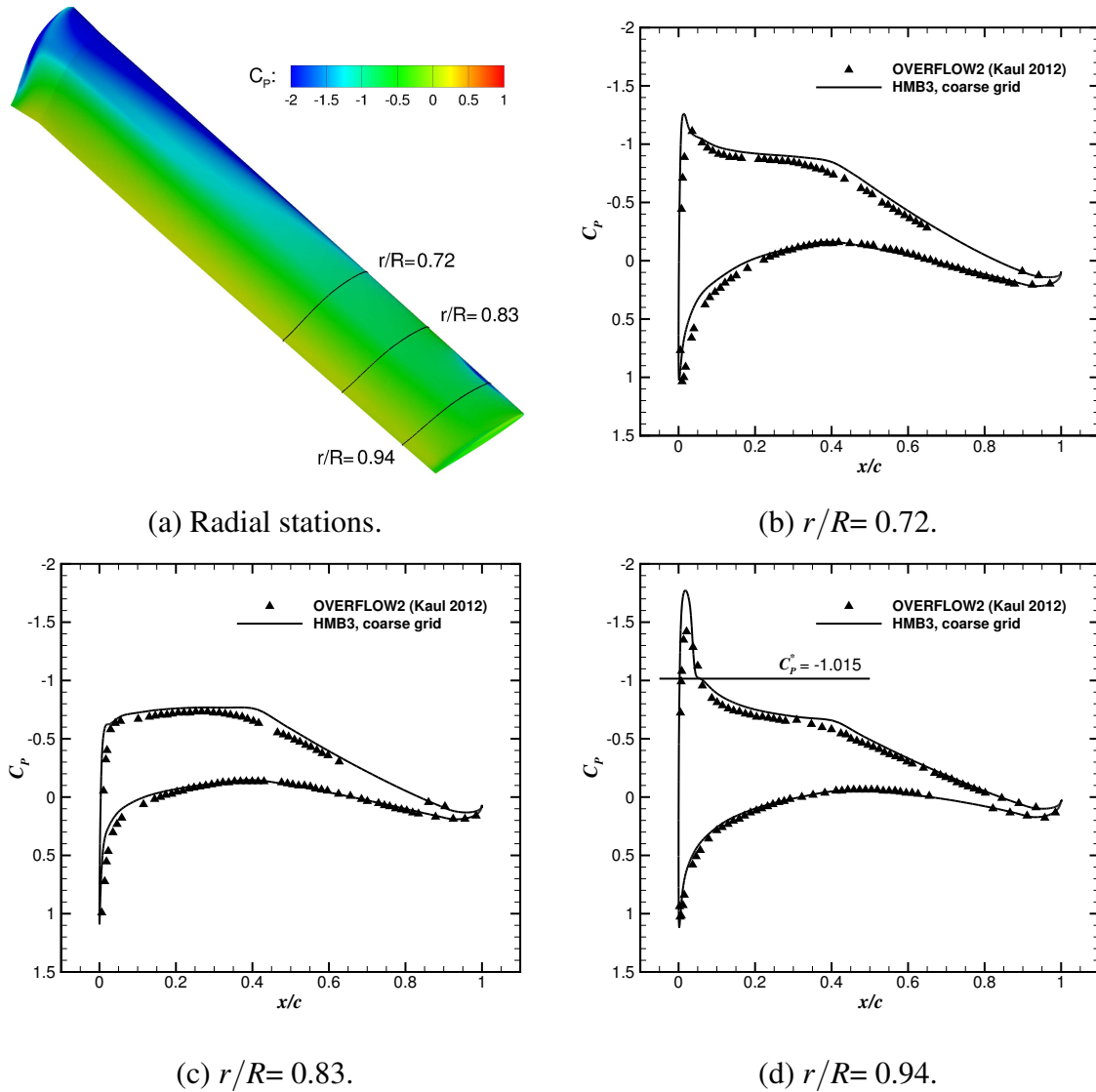
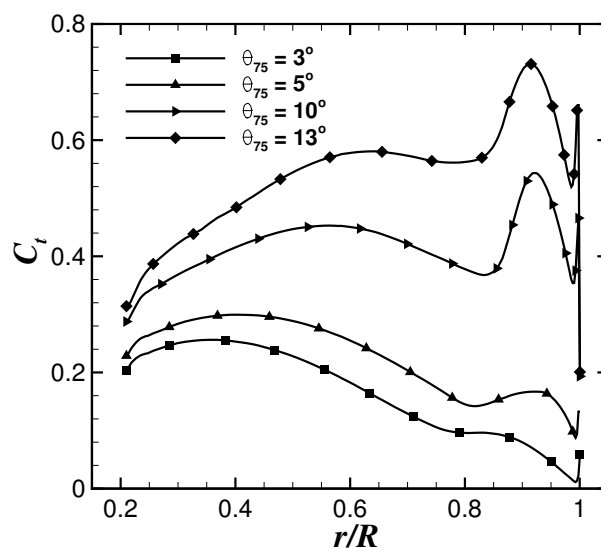


Figure 7.4: Comparison of predicted surface pressure coefficient between HMB3 using the coarse grid and OVERFLOW2 from Kaul *et al.* [95].

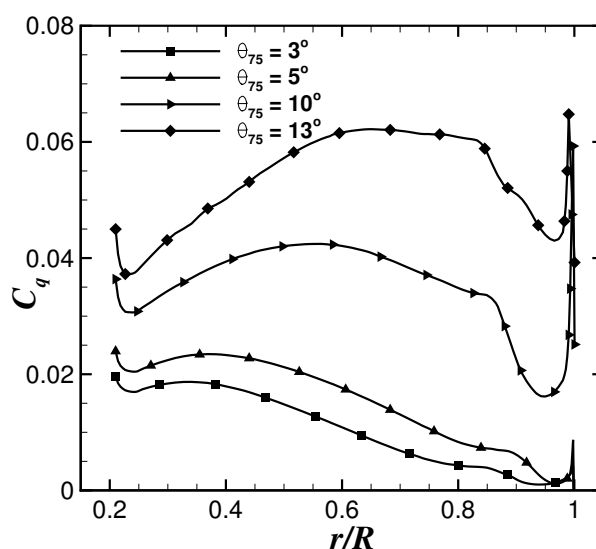


### Sectional Blade Loads

Figure 7.5 shows the distribution of sectional thrust and torque coefficients along the rotor radius for blade pitch angles from  $3^\circ$  to  $13^\circ$ . The influence of the tip vortex on the tip region (from 90%  $R$  to 100%  $R$ ) is visible in terms of the loading and torque coefficients. It is interesting to note that the torque coefficient is significantly decreased in the tip region ( $r/R > 0.90$ ) as a consequence of the change on the planform due to the twist and aerofoil sections.



(a) Blade sectional thrust coefficient.



(b) Blade sectional torque coefficient.

Figure 7.5: Blade sectional thrust coefficient (top) and torque coefficient (bottom) for the full-scale XV-15 rotor in helicopter mode.

### Aeroacoustic Analysis

The HFWH code is used here to predict the mid and farfield noise on the full-scale XV-15 main rotor. As introduced earlier, this method uses the Farassat 1A formulation (also known as retarded-time formulation) of the original FW-H equation [207]. This acoustic code has been previously employed for three-dimensional rotor hover predictions such the S-76 rotor (see Jimenez-Garcia and Barakos [9]), showing good correlation with the theory [209, 210].

A comparison with theory is also presented here in terms of total noise predictions. Analytical solutions are based on the work of Gopalan *et al.* [209, 210] and have been successfully employed in the helicopter community [208]. The key idea is to convert the FW-H integral equations to explicit algebraic expressions. Figure 7.6 shows a comparison of the theoretical and numerical total noise in dB, as a function of the radial distance at the rotor-disk plane. Three blade pitch angles were selected for this study ( $\theta_{75} = 7^\circ, 10^\circ, 13^\circ$ ), covering medium and high thrust, using the coarse grid. The results show a fair agreement between theory and the predicted total noise for all blade pitch angles, although small differences were found at radial distances lower than  $2R$ . In fact, these findings support the idea that this theory is only valid at radial distances above  $3R$ .

Table 7.7 shows the effect of the blade pitch angle when increased from  $7^\circ$  to  $10^\circ$  and  $13^\circ$  degrees on the thrust coefficient, FoM, and total noise. It is clearly seen that the thrust coefficient linearly increases with the collective, whilst the FoM presents a drop of almost 2%. As expected, the sound pressure level (SPL) correlates in a linear fashion with the collective.

Table 7.7: Effect of the collective pitch angle on the thrust coefficient, FoM, and total noise in SPL for the full-scale XV-15 rotor.

Collective	$\Delta C_T$	$\Delta \text{FoM}$	$\Delta \text{SPL}$
$7^\circ$	-	-	-
$10^\circ$	4.78%	8.47%	4.28%
$13^\circ$	9.67%	6.64%	8.36%

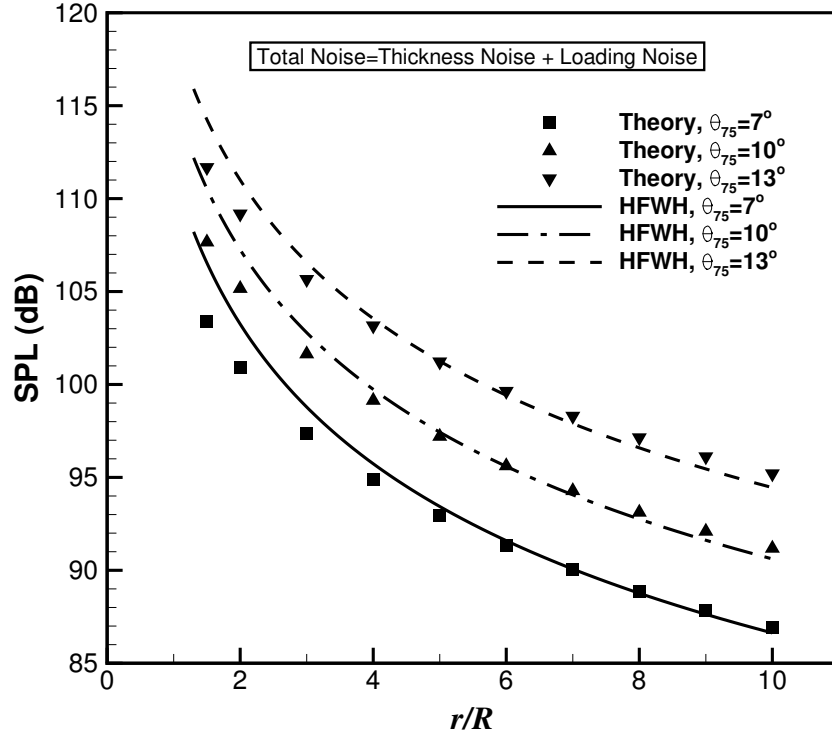


Figure 7.6: Total noise in dB as function of the normalised radial distance  $r/R$  at the tip-path-plane of the full-scale XV-15 rotor.

### 7.1.5 Aeroplane Mode

Like for hover simulations, only a third of the computational domain was meshed, modelling this case as steady-state problem with periodic conditions for the flow in the azimuthal direction. Simulations were performed at advance ratio  $\mu = 0.337$ , blade pitch angles of  $26^\circ, 27^\circ, 28^\circ$  and  $28.8^\circ$ , and blade-tip Mach number of 0.54 (see Table 7.4). In aeroplane mode, the rotor efficiency is indicated by the propeller propulsive efficiency, which is the ratio between the useful power output of the propeller and the absorbed power:

$$\eta = \frac{C_T V_\infty}{C_Q V_{\text{tip}}}. \quad (7.3)$$

Figure 7.7 compares the total load predictions with the available experimental data [82] (represented by square symbols), where the propeller efficiency  $\eta$  and torque coefficient are given as function of the thrust coefficient. The experimental data reported here, were performed on a propeller test rig in the NASA 40- by 80- foot Wind Tunnel [82], and are the only available published

data for the XV-15 in aeroplane mode. HMB results with the coarse grid show an under-predicted propulsive propeller efficiency for all thrust coefficient, with a maximum discrepancy of 4.5%. However, results with the medium grid provide are in good agreement with the experimental data.

### Sectional Blade Loads

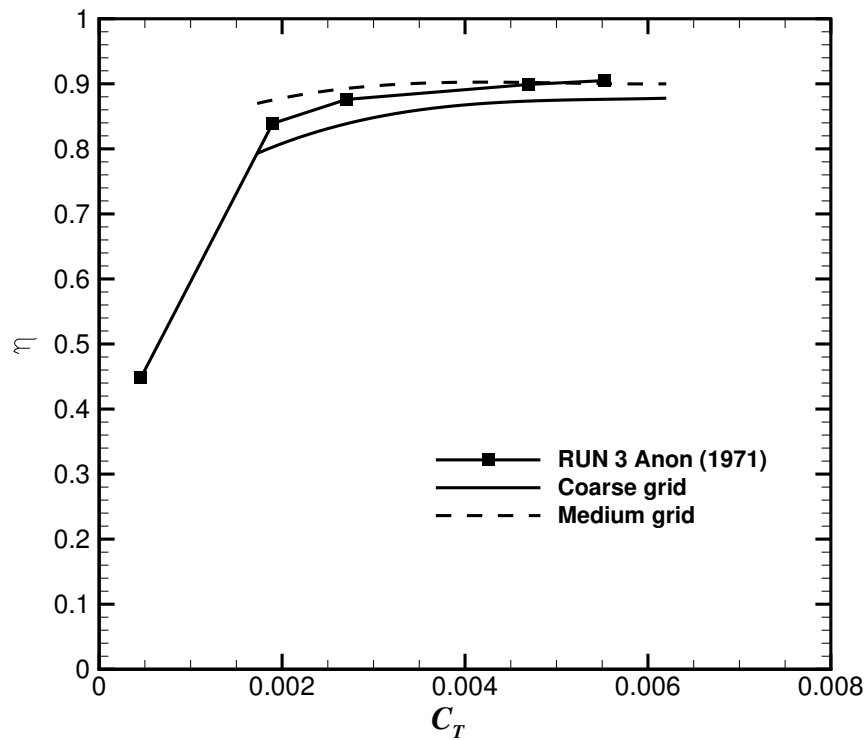
Propeller radial loading distributions are shown in Figure 7.8 for the sectional thrust and torque coefficients. For this case, results obtained with the coarse grid were used. At low blade pitch angles ( $\theta_{75} = 26^\circ$ ), a negative loading is observed inboards up to 40%  $R$ . In fact, this part of the propeller is acting as a windmill (power is absorbed from the flow) mainly due to the negative AoA seen by those aerofoils. Consequently, this leads to low propeller efficiency for this cruise condition. For high collective angles ( $\theta_{75} = 28^\circ$  and  $28.8^\circ$ ), however, both inner and outer parts act as a propeller, providing high efficiency.

### Surface Pressure Predictions

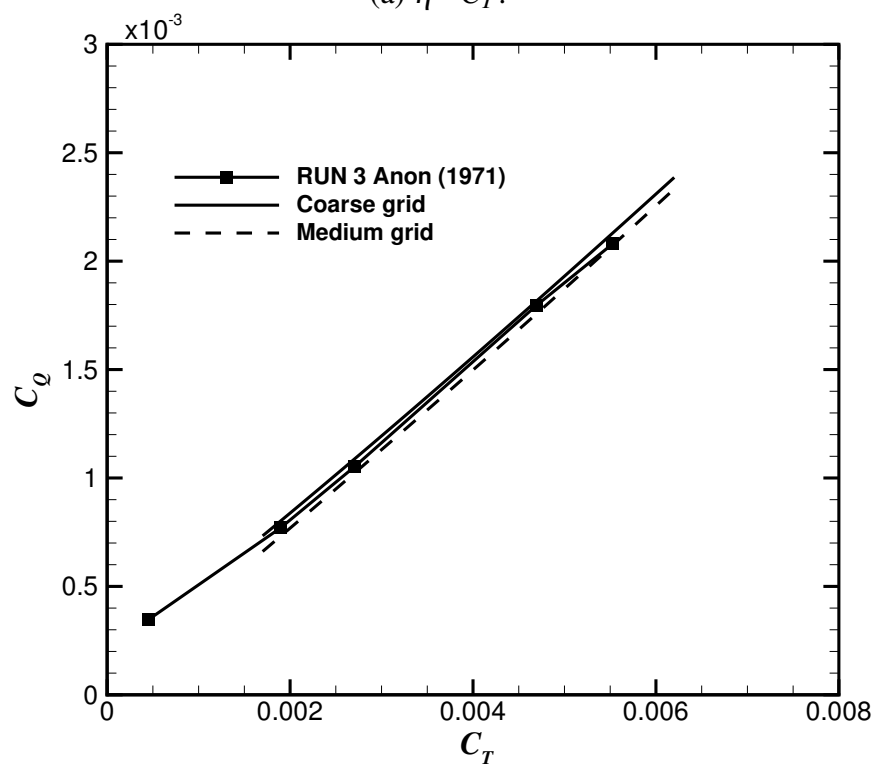
Figure 7.9 shows pressure coefficient contours for the XV-15 upper blade at the computed advance ratio, where the  $C_P$  is computed based on the local velocity. Results at low thrust coefficient confirm the idea that the inboard part of the rotor is off-loaded. As the collective pitch angle increases, contours of  $C_P$  at outboard part of the blade indicate a more uniform propeller load distributions.

### Flowfield Details

Flowfield visualisation of the rotor wake for the full-scale XV-15 rotor blade in propeller mode using the  $\tilde{Q}$ -criterion is given in Figure 7.10. Contours of  $C_P$  are also included. Despite that a coarse grid was used as background (2.6 million cells), the wake development shows a well-preserved first and second passage of the vortex. Moreover, the strong interaction between the blade and the vortex typically encountered in hovering rotors, is not present here. In fact, the rapid downstream convection of the rotor wake at  $M_\infty=0.182$ , results in a much less complex wake.

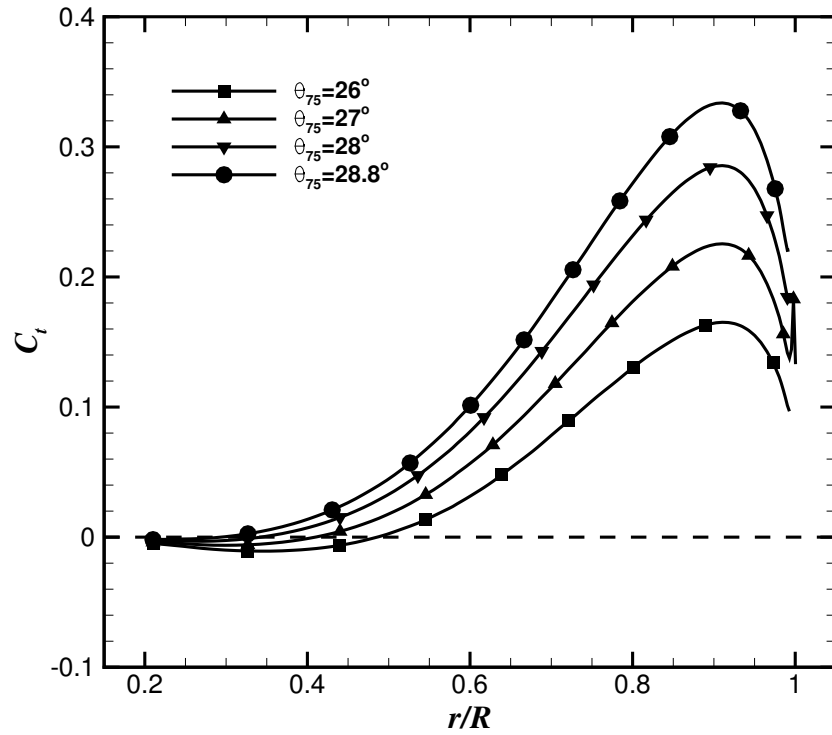


(a)  $\eta - C_T$ .

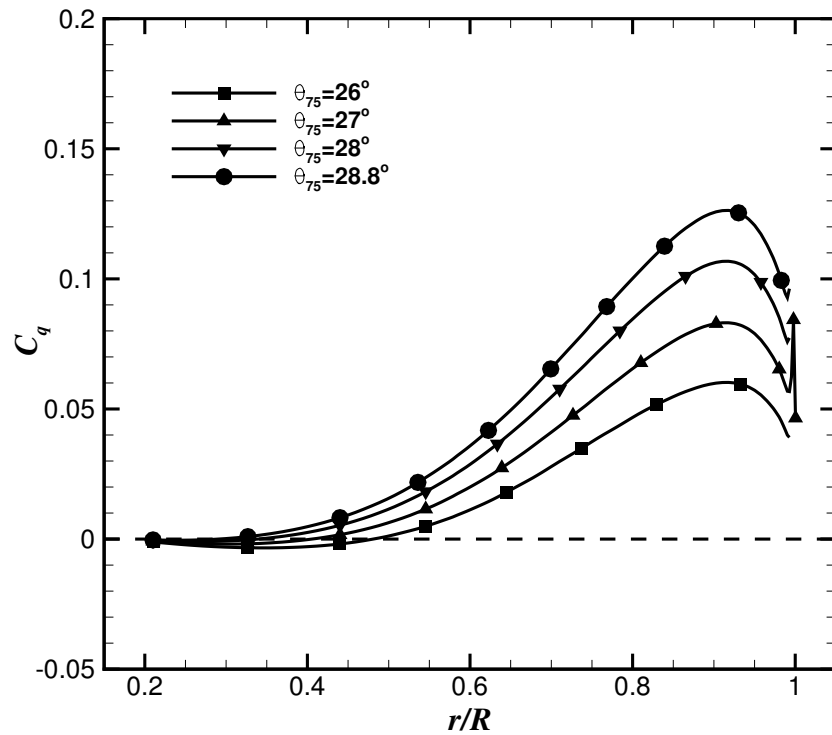


(b)  $C_Q - C_T$ .

Figure 7.7: Propulsive propeller efficiency and torque coefficient as function of the thrust coefficient for the XV-15 rotor blade in propeller mode configuration.

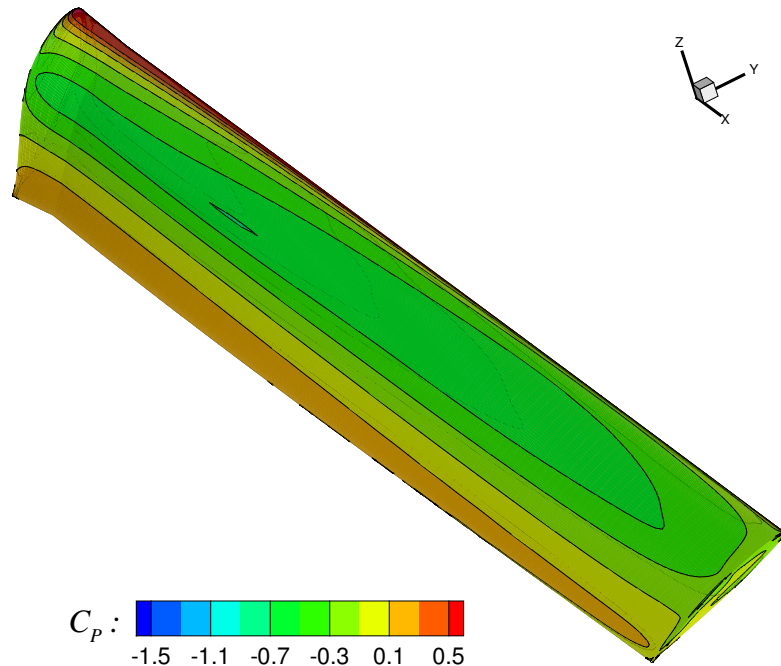


(a) Blade sectional thrust coefficient.

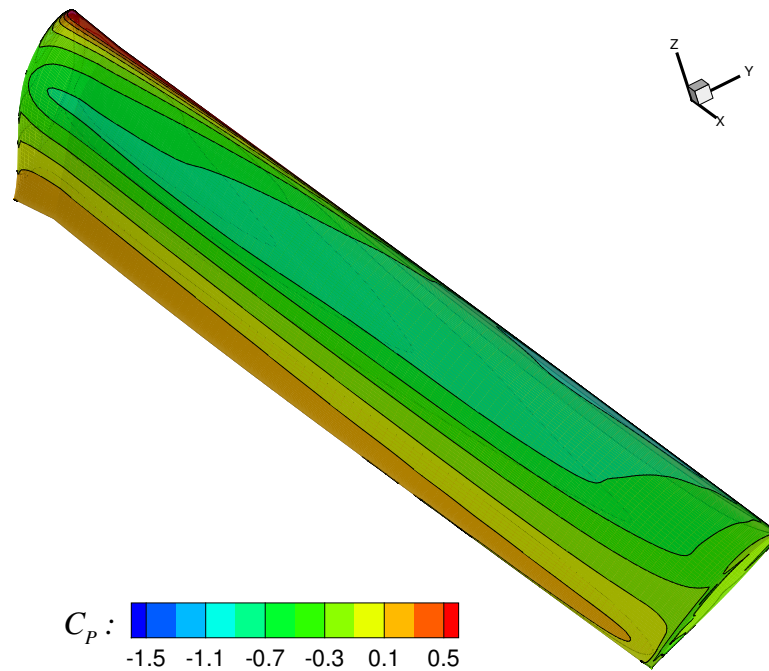


(b) Blade sectional torque coefficient.

Figure 7.8: Blade sectional thrust coefficient (top) and torque coefficient (bottom) for the full-scale XV-15 rotor in aeroplane mode.

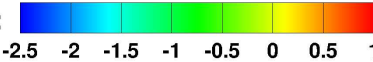


(a)  $\theta_{75} = 26^\circ$ .

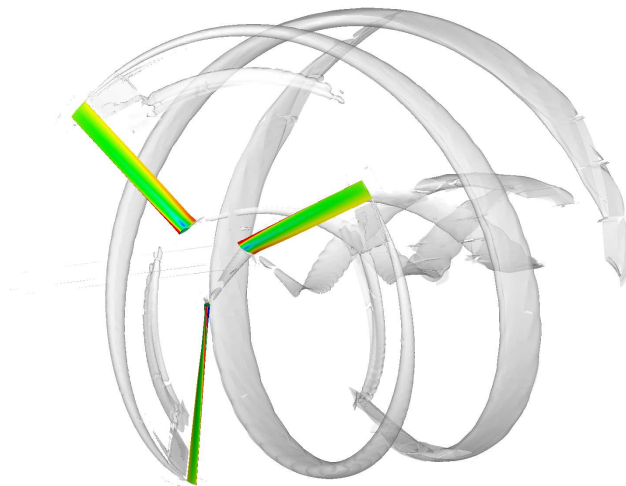


(b)  $\theta_{75} = 28.8^\circ$ .

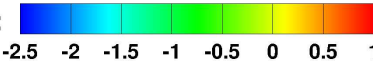
Figure 7.9: Contours of surface pressure coefficient on the XV-15 rotor blade.

$$C_p = (\mathbf{P} - \mathbf{P}_\infty) / (1/2 \rho_\infty V_{loc}^2):$$


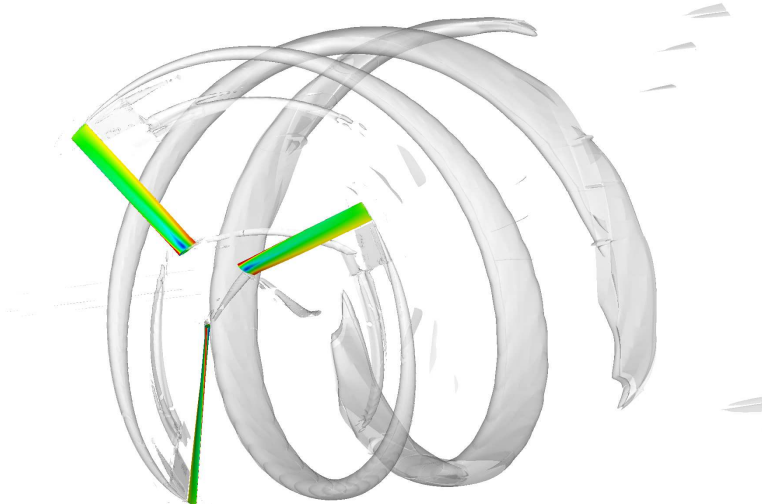
-2.5 -2 -1.5 -1 -0.5 0 0.5 1



(a)  $\theta_{75} = 26^\circ$ .

$$C_p = (\mathbf{P} - \mathbf{P}_\infty) / (1/2 \rho_\infty V_{loc}^2):$$


-2.5 -2 -1.5 -1 -0.5 0 0.5 1



(b)  $\theta_{75} = 28.8^\circ$ .

Figure 7.10: Wake visualisation of the propeller wake using  $\tilde{Q}$ -criterion shaded by contours of  $C_p$  at blade pitch angle of  $\theta_{75} = 26^\circ$  (top) and  $\theta_{75} = 28.8^\circ$  (bottom).

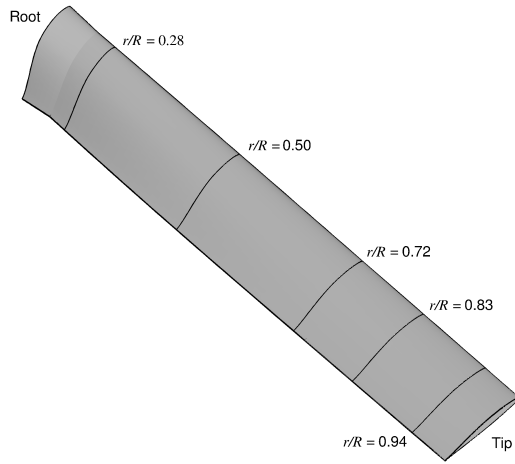


## 7.2 Effect of the Turbulence Model

In this study, transition effects, based on the  $k-\omega$  SST- $\gamma$  transition model [194] are investigated. The predicted skin friction coefficient is compared with measurements by Wadcock *et al.* [88]. Moreover, a comparison with the solution obtained with the fully-turbulent  $k-\omega$  SST model is presented. For this case, a matched grid is used, with 10.2 million cells per blade.

Figures 7.11 and 7.12 show the computed skin friction coefficient  $C_f$  compared with the available experimental data of Wadcock *et al.* [88] for blade pitch angles of  $3^\circ$  and  $10^\circ$  at radial stations of  $r/R=0.28, 0.5, 0.72, 0.83$ , and  $0.94$ . At low disk loading (Figure 7.11), the experiment shows transition for all stations at about 50% of the chord. It seems that the present transition model is able to capture the onset and length of the natural transition with discrepancies found only at the inboard station  $r/R=0.28$ . As expected, results obtained with the fully-turbulent model show no transition. Moreover, the values of skin friction coefficient are under and over-predicted in the laminar and turbulent flow regions. Considering the  $C_f$  at blade pitch angle of  $10^\circ$  (Figure 7.12), the experimental  $C_f$  presents a similar pattern as seen for the lower collective pitch angles. However, the onset of transition is shifted towards the leading edge, with a fully-turbulent flow region observed at the outboard station  $r/R=0.94$ . Results corresponding to the transition model accurately predicted the onset location and length of transition. This physical phenomenon is not captured by the turbulent flow solution. The surface skin friction coefficient of both turbulence models is shown in Figure 7.13, where the laminar-turbulent region can be only identified for the  $k-\omega$  SST- $\gamma$  model.

Once the distribution of skin friction coefficient was analysed, the impact of the turbulence model on the hover performance of the XV-15 blade was investigated. Table 7.8 reports the predicted  $C_T$ ,  $C_Q$ , and FoM using the fully-turbulent  $k-\omega$  SST and transition model  $k-\omega$  SST- $\gamma$  at two disk loading conditions. It is shown that results are mildly sensitive to the turbulence model employed, with a higher figure of merit predicted by the transition model.



(a) Radial stations.

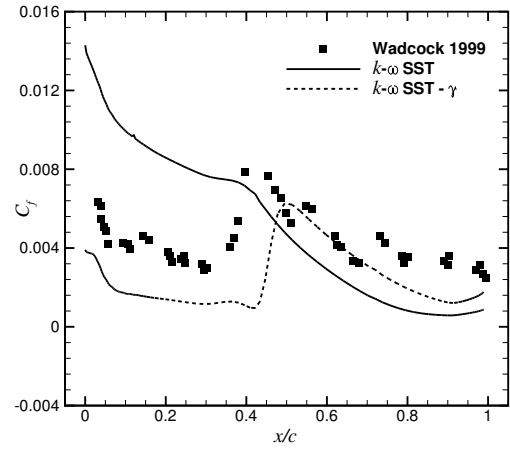
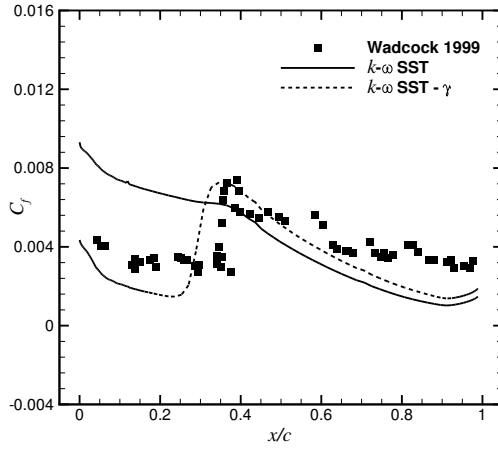
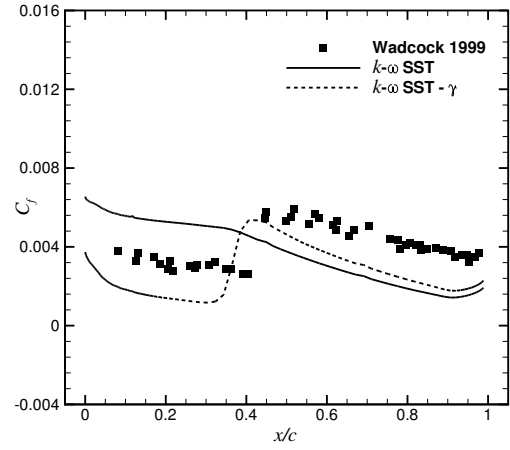
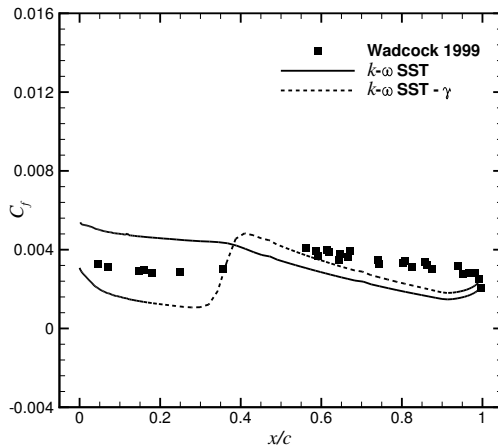
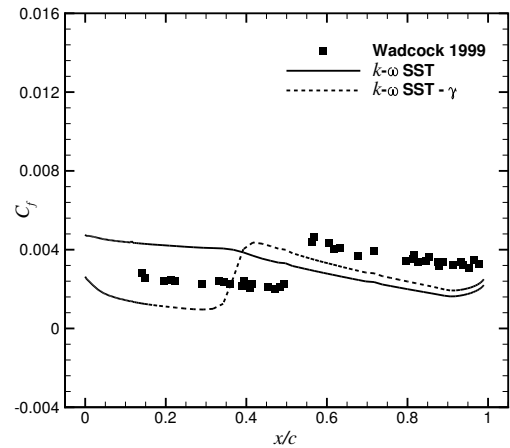
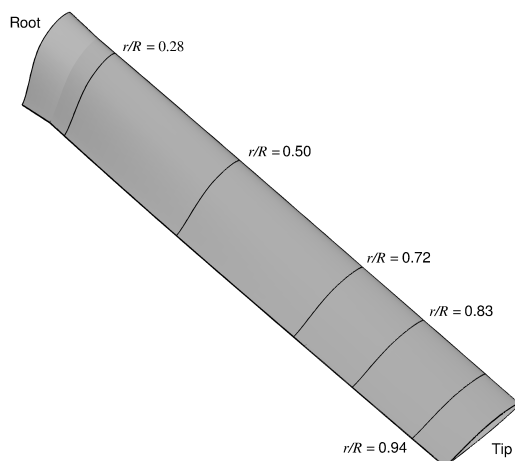

 (b)  $r/R = 0.28$ .

 (c)  $r/R = 0.5$ .

 (d)  $r/R = 0.72$ .

 (e)  $r/R = 0.83$ .

 (f)  $r/R = 0.94$ .

Figure 7.11: Comparison between the computed skin friction coefficient using fully turbulent and transitional solutions with the experimental data of Wadcock *et al.* [88]. Conditions employed:  $M_{\text{tip}} = 0.69$ ,  $Re = 4.95 \times 10^6$ , and  $\theta_{75} = 3^\circ$ .



(a) Radial stations.

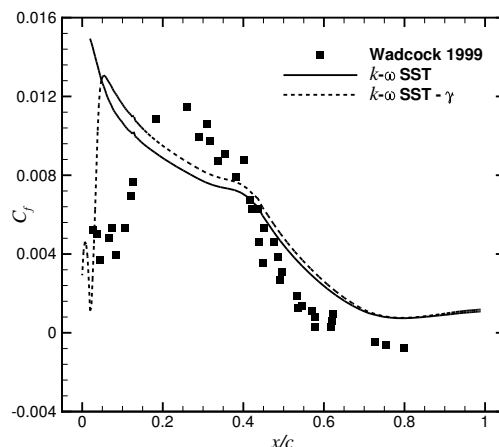
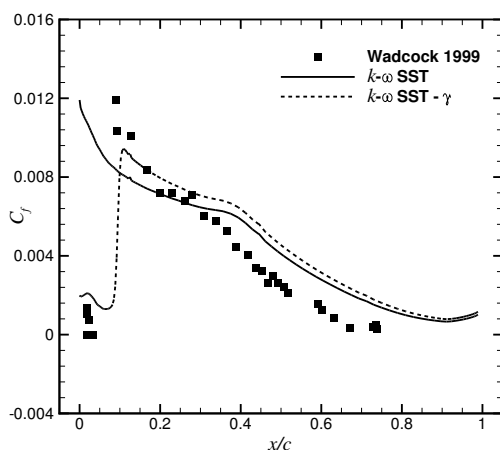
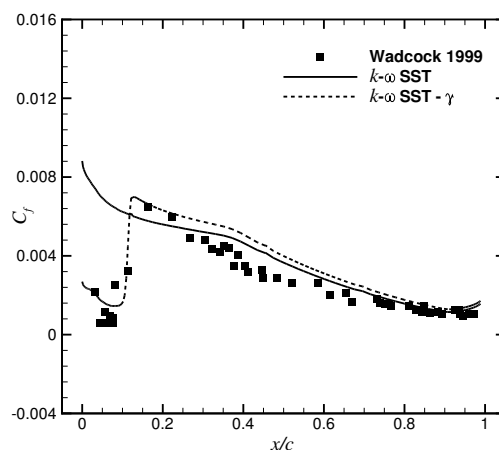
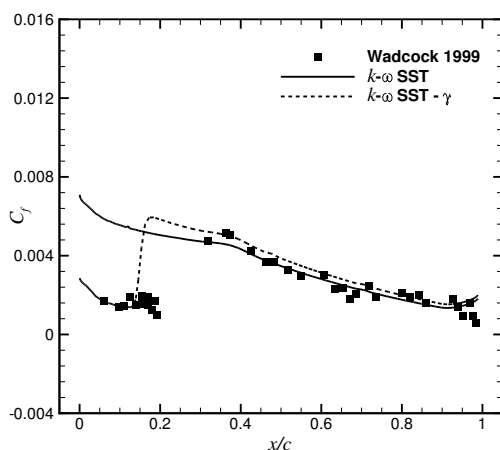
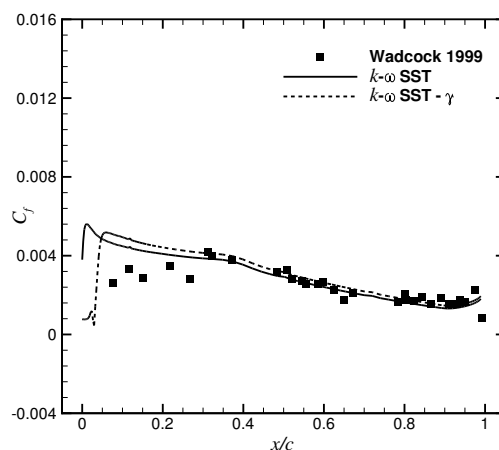

 (b)  $r/R = 0.28$ .

 (c)  $r/R = 0.5$ .

 (d)  $r/R = 0.72$ .

 (e)  $r/R = 0.83$ .

 (f)  $r/R = 0.94$ .

Figure 7.12: Comparison between the computed skin friction coefficient using fully turbulent and transitional solutions with the experimental data of Wadcock *et al.* [88]. Conditions employed:  $M_{\text{tip}} = 0.69$ ,  $Re = 4.95 \times 10^6$ , and  $\theta_{75} = 10^\circ$ .

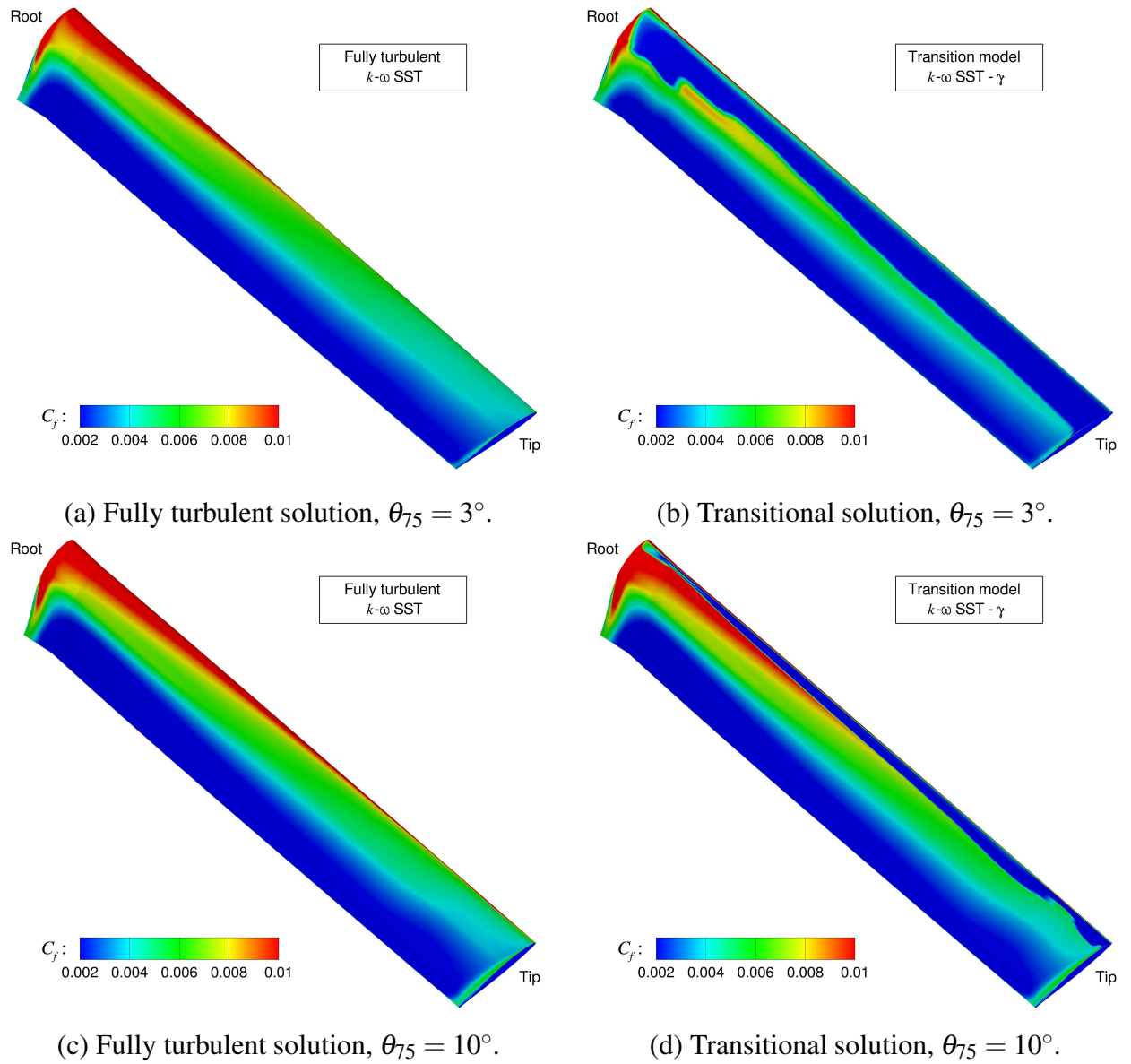


Figure 7.13: Surface skin friction coefficient for the fully turbulent and transition cases.

Table 7.8: Comparison of predicted  $C_T$ ,  $C_Q$ , and FoM at  $3^\circ$  and  $10^\circ$  collective angles between the fully-turbulent  $k-\omega$  SST and transitional  $k-\omega$  SST- $\gamma$ . Conditions employed:  $M_{\text{tip}} = 0.69$  and  $Re = 4.95 \times 10^6$ .

	$C_T$	$C_Q$	FoM
FT $3^\circ$	0.00293	0.000249	0.450
TM $3^\circ$	0.00297	0.000223	0.512
FT $10^\circ$	0.00906	0.000807	0.756
TM $10^\circ$	0.00909	0.000803	0.763

FT=Fully-Turbulent; TM=Transitional-Model.

### 7.3 Summary of Findings

The main conclusions of this chapter are:

- The method was able to capture the performance in the different modes for the XV-15 tiltrotor blade; hover and propeller.
- The transition onset and distribution of skin friction are well predicted and, for this case, were found to have a mild effect on the overall figure of merit.
- The employed grid of 6.2 and 9.6 million cells show reasonable mesh convergence and yield results with modest CPU time of 17.1 CPU hours.
- The wake of the highly loaded tiltrotor blades convects fast away from the rotor giving weaker interaction with the blade.

# Chapter 8

## Validation of HMB for Complete Tiltrotors

The aim of this chapter is to assess the capability of the present CFD method in predicting airloads on complete tiltrotors at different flight configurations. In this regard, three representative flight configurations of the ERICA tiltrotor were selected, corresponding to aeroplane, transition corridor, and helicopter modes.

### 8.1 Aerodynamic Models

Two aerodynamic methods are employed to model the rotor blades. The higher fidelity method includes the geometry of the blades in the computational domain and it will be referred to as fully resolved blade (FRB). This methodology provides a full representation of the wake and detailed information of the source of unsteadiness of the flow. Furthermore, the boundary layers on the blades are resolved, so this method provides the best load estimates. The other aerodynamic models are actuator disks (AD) [10], which simulate the effect of the rotor blades by creating a pressure jump across an infinitesimally thin disk. These methods are useful in predicting average loads on the fuselage.

The two actuator disk models employed here are described below. The first model is a

---

This work is published in A. Jimenez-Garcia *et al.*, Numerical Simulations on the ERICA Tiltrotor, Aerospace Science and Technology, 64 (1), 2017, 171–191, doi: 10.1016/j.ast.2017.01.023.

uniform rotor actuator disk (URAD) in loading while the second model allows for variable disk loading as function of the rotor radius (NURAD, Non-Uniform Rotor Actuator Disk).

As previously introduced, the actuator disk simulates the effect of the rotor blades by creating a pressure difference on a single plane. For the case of uniform rotor actuator disk, the pressure jump in non-dimensional form is:

$$\Delta P^* = \frac{T}{\rho_\infty V_\infty^2 S_{\text{rot}}}, \quad (8.1)$$

where the thrust coefficient is defined as  $C_T = \frac{T}{\rho_\infty V_{\text{tip}}^2 S_{\text{rot}}}$  with  $S_{\text{rot}}$  being the rotor disk area.

The non-uniform rotor actuator disk calculates the pressure jump across the disk plane based on Shaidakov's method [198]. This approach results in a non-uniform pressure distribution and as a function of radial position along the blade ( $r$ ) and blade azimuth  $\Psi$ . The model is based on the following equation:

$$\Delta P^* = P_0 + P_{1S} \sin(\Psi) + P_{2C} \cos(2\Psi), \quad (8.2)$$

where the coefficients  $P_0$ ,  $P_{1S}$  and  $P_{2C}$  depend on rotor radius and solidity, rotor attitude, advance ratio, thrust coefficient, lift coefficient slope, and freestream velocity. The model is detailed in [198, 199].

Figure 8.1 shows an overview of the relative position of the actuator disk for the ERICA tiltrotor for the transition corridor (top) and for the helicopter mode configurations (bottom).

## 8.2 ERICA Tiltrotor Mesh

The chimera method was employed to ease the generation of structured multi-block grids. For all configurations, self-contained component grids for the main fuselage and the nacelle-tiltable wing were built, while four ADYN blades were embedded in the nacelle mesh component. To enable the relative motion between nacelle and tiltable wing, as well as, tiltable and fixed wings, independently generated overlapping grids were used, employing a 4mm gap between them. Likewise, a gap between the blade root and spinner for the full blade representation was allowed. A Cartesian

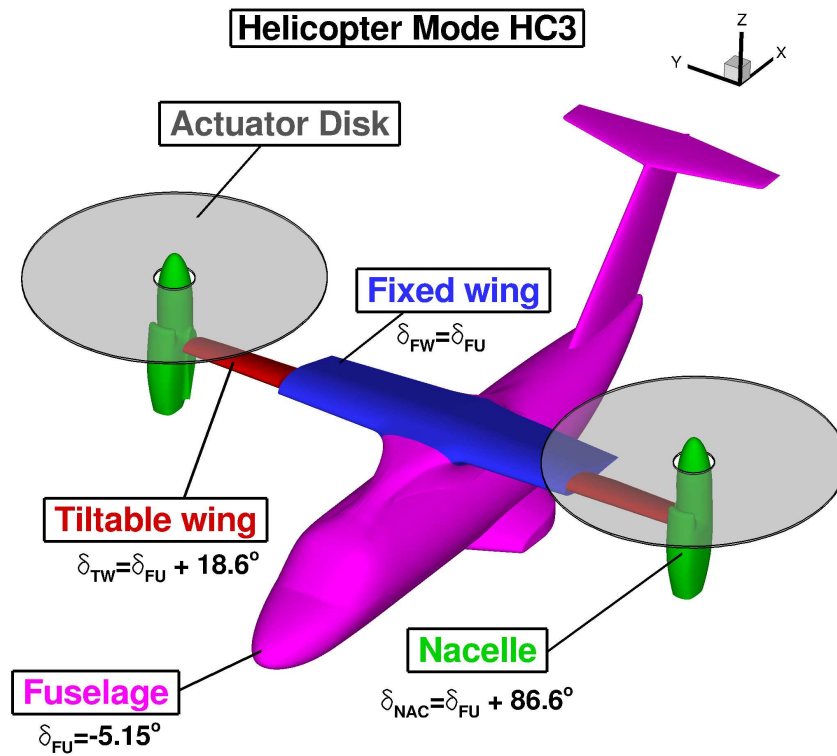
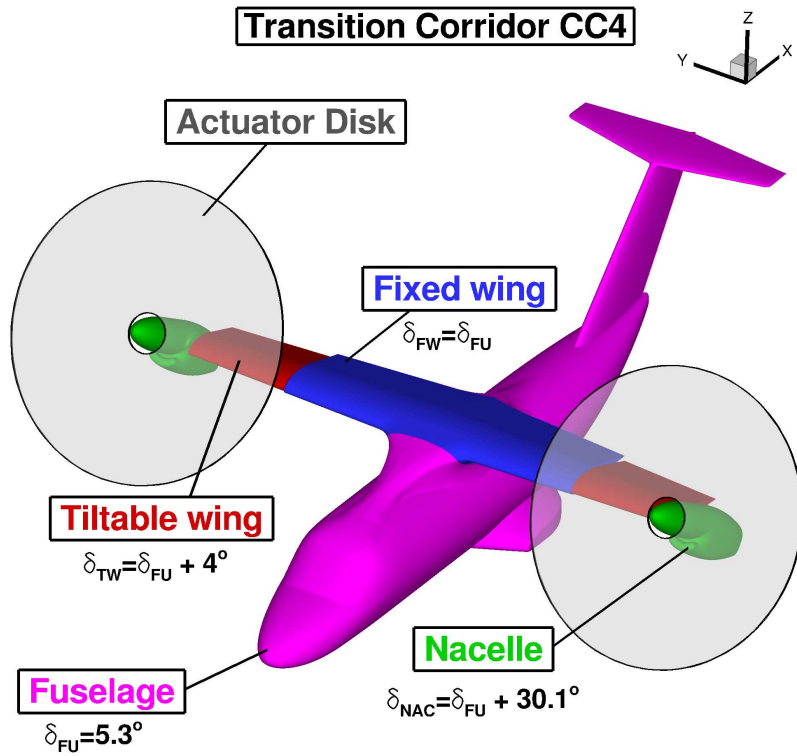


Figure 8.1: Set-up of the transition corridor (top) and helicopter mode (bottom) configurations with the rotor actuator disk.



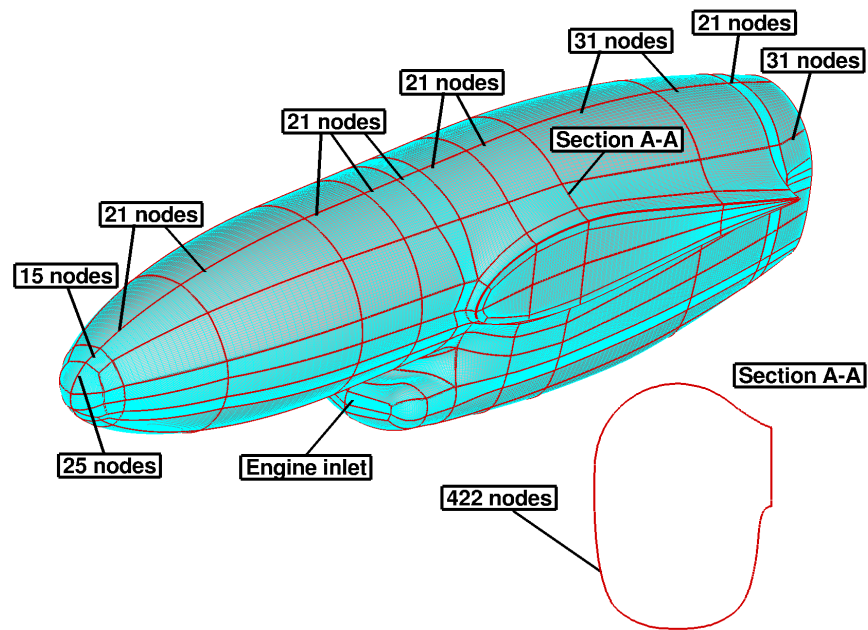
off-body mesh was used as the background to capture the convection of the tip vortex generated by the blades. Table 8.1 compares the mesh size used here for CFD computation. For the actuator disk method, a reduction of the mesh size of about 20% and 18% for the aeroplane and transition corridor/helicopter modes is achieved.

Table 8.1: ERICA model-scale component mesh sizes, given as million of nodes.

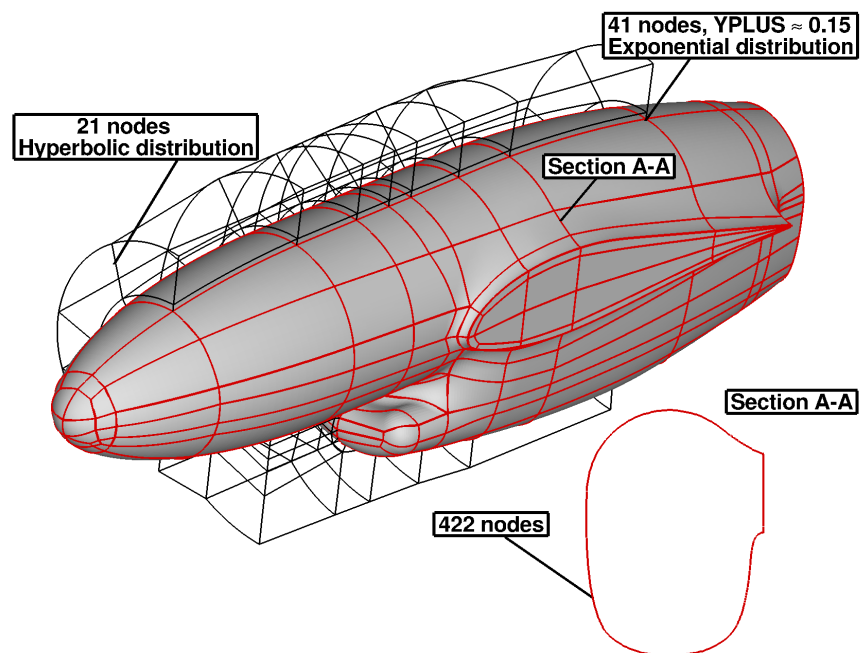
<b>Components</b>	<b>Aeroplane Mode</b>	<b>Transition Corridor</b>	<b>Helicopter Mode</b>
Fuselage and fixed wing	9.9	9.9	9.9
Tilttable wing	-	3.6	3.6
Nacelle	30.3	10.9	10.9
Rotor blades (x4)	11.4	11.4	11.4
Wind tunnel	4.6	27.6	27.6
<b>Total</b>	<b>56.2</b>	<b>63.4</b>	<b>63.4</b>

Figure 8.2 shows a detailed view of the surface mesh and the multi-block topology of the ERICA's nacelle. To match the wind tunnel model [91, 92], the engine inlet was treated as solid. In the longitudinal direction of the nacelle, 270 mesh points are used, while 422 points are used around the nacelle. In the wall normal direction (see Figure 8.2 (b)) 41 points are used. That mesh spacing corresponds to a  $y^+$  of approximately 0.15. A C-topology around the leading edge of the connection with the tilttable wing was chosen, whilst an O-topology was used at the nose and rear parts of the nacelle. Figure 8.3 shows a view of the surface and body-fitted mesh around the fuselage. An O multi-block topology was built at the front and rear parts of the fuselage, whereas a C-H multi-block topology was generated around the wing and horizontal stabiliser (see Figure 8.3 (b)). In the chordwise direction around the fixed wing, 310 points are used, with 138 around the horizontal stabiliser. The distribution of points normal to the fixed wing and fuselage, follow exponential law with the first point located at  $4 \times 10^{-6}$  of the reference length ( $L_{\text{ref}}$ ), leading to a  $y^+$  of approximately 0.15.

The multi-block overset arrangement of the ERICA tiltrotor for the case of the aeroplane mode is shown in Figure 8.4. Farfield and symmetry boundary conditions were applied at the background level, while chimera boundaries were used at the nacelle, blades, and fuselage components. The wind tunnel model support was not modelled.

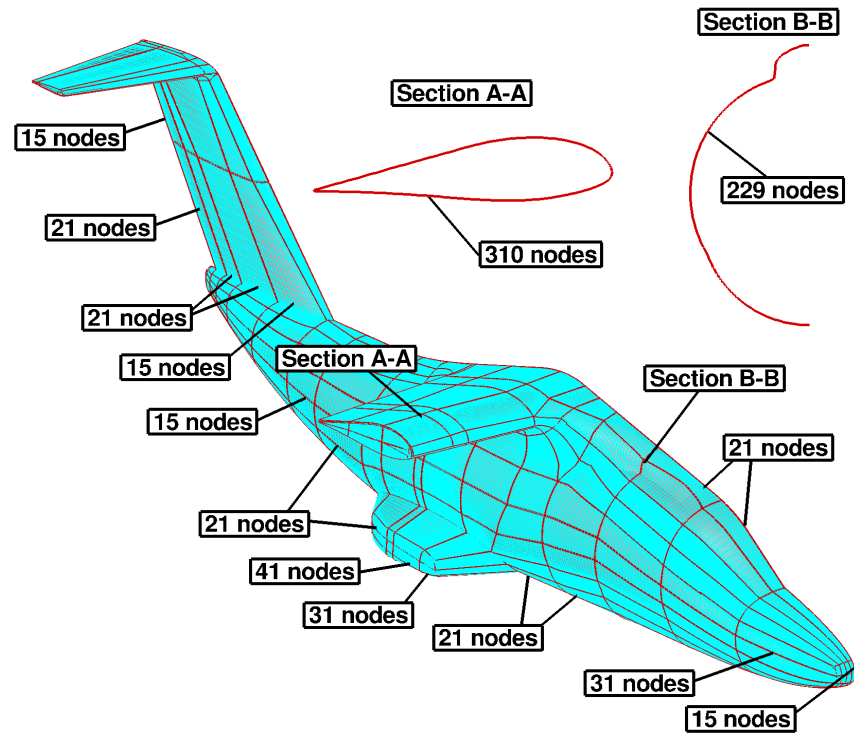


(a) Surface mesh.

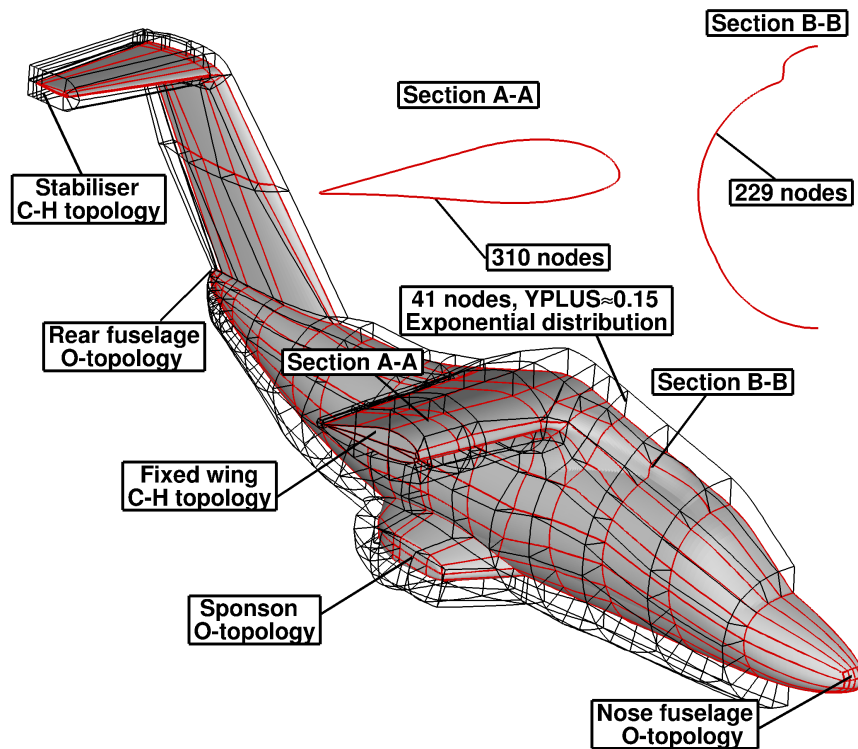


(b) Multi-block topology.

Figure 8.2: ERICA's nacelle structured mesh domain, topology, and surface mesh detail.

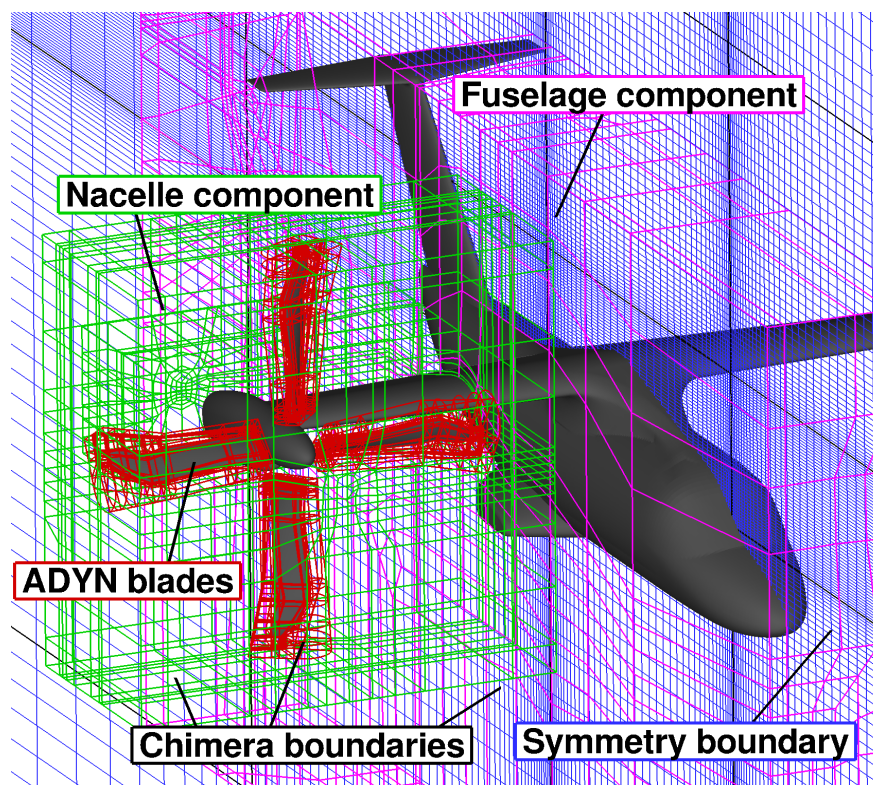


(a) Surface mesh.

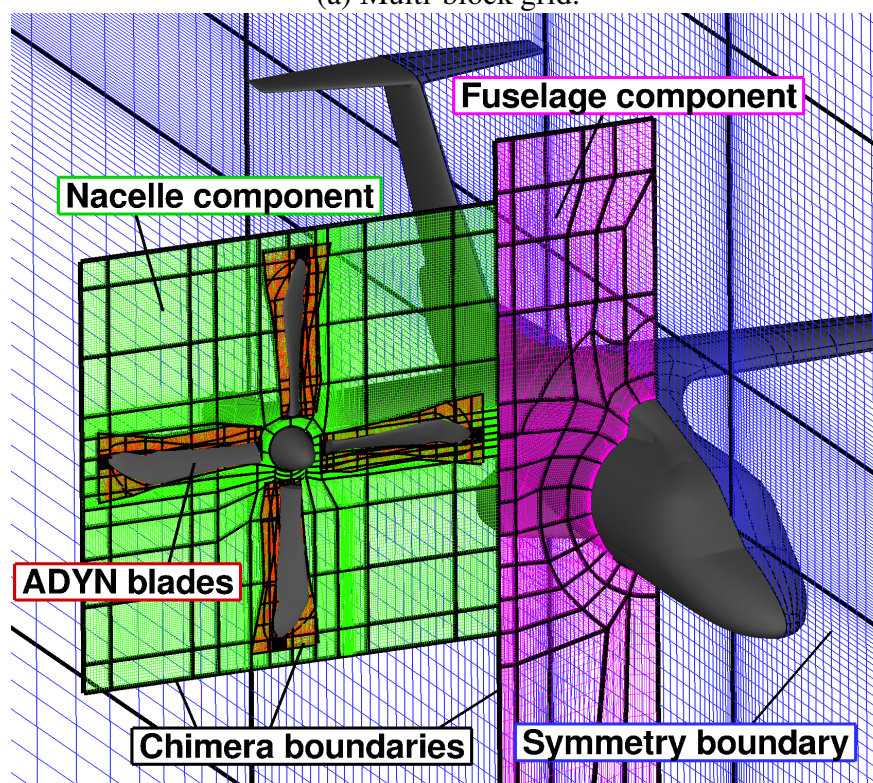


(b) Multi-block topology.

Figure 8.3: ERICA's fuselage structured mesh domain, topology, and surface mesh detail.



(a) Multi-block grid.



(b) Cross section of the multi-block grid.

Figure 8.4: Details of the multi-block overset arrangement of the ERICA tiltrotor in aeroplane mode configuration. Blue line=background component; purple line=fuselage component; green line=nacelle component; grey line=blade component.

Table 8.2 summarises the conditions for each computed case. The first configuration is labelled as AC1 (aeroplane configuration), and refers to a very low speed aeroplane-mode flight at  $M_\infty = 0.168$  and a large aircraft AoA of  $\delta_{FU} = 10.02$  degrees. Neither the nacelles nor the tiltable wings were tilted with respect to the fuselage ( $\delta_{FU} = \delta_{NAC} = \delta_{TW}$ ). The second case corresponds to a typical transition corridor configuration with a moderate AoA of 5.30 degrees, labelled as CC4. Unlike the AC1, the nacelle was significant rotated with respect to the fuselage ( $\delta_{NAC} = \delta_{FU} + 30.1$ ), while a small rotation of the tiltable wing ( $\delta_{TW} = \delta_{FU} + 4.0$ ) was allowed. Finally, a helicopter configuration labelled as HC3 was selected for computation. This configuration HC3 is characterised for a moderate forward speed ( $M_\infty = 0.104$ ) with an aircraft AoA of -5.15 degrees and the nacelles tilted by 86.6 degrees with respect to the fuselage. The Reynolds numbers, based on the reference length  $L_{ref}$  and on the freestream velocity  $V_\infty$ , were  $1.70 \times 10^6$  and  $1.16 \times 10^6$  for the AC1/CC4 and HC3 cases respectively. Figure 8.5 shows the different test conditions employed here, and the nacelle pitch angle as function of the freestream Mach number.

Table 8.2: Test conditions for the selected cases [251, 252].

Parameters	Aeroplane Mode AC1	Transition Corridor CC4	Helicopter Mode HC3
$M_\infty$	0.168	0.168	0.104
$M_{tip}$	0.470	0.603	0.560
$\mu = M_\infty / M_{tip}$	0.357	0.278	0.185
$Re_{ref}$	$1.70 \times 10^6$	$1.70 \times 10^6$	$1.16 \times 10^6$
$\delta_{FU}$ [deg]	10.02°	5.30°	-5.15°
$\delta_{NAC}$ [deg]	10.02°	35.40°	81.45°
$\delta_{TW}$ [deg]	10.02°	9.30°	13.45°
RPM blade rotor	2,130	2,730	2,490
$\theta_{75}$ [deg]	27.36°	16.6°	9.0°

AC1=Aeroplane Mode; CC4=Transition Corridor; HC3=Helicopter Mode.

### 8.3 Test Conditions and Computations

Table 8.3 summarises the cases performed for the ERICA tiltrotor. For the aeroplane configuration AC1, several cases were computed. The rotor blades were represented by means of a uniform



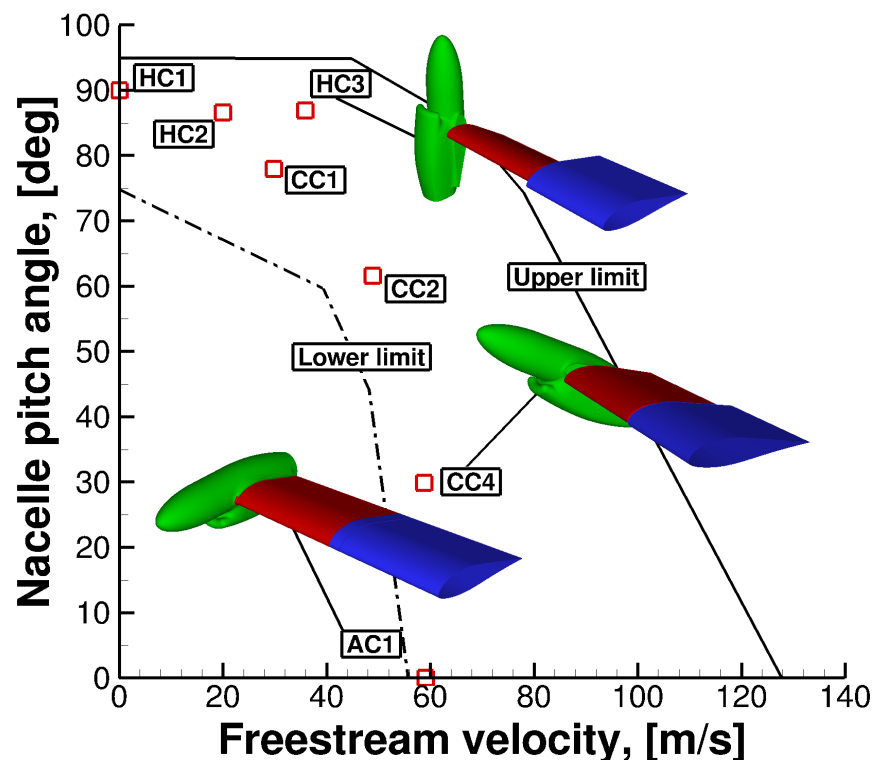


Figure 8.5: Trimmed test conditions for the ERICA tiltrotor reported by Bruin *et al.* [251]. AC1 (Aeroplane configuration), CC4 (Transition Corridor), and HC3 (Helicopter configuration) were selected for numerical computations.

rotor actuator disk (case #1), non-uniform rotor actuator disk (case #2), and fully resolved blade (case #3). To quantify the effect of the aerodynamic interference between the rotor and wing of the ERICA, case #4 was also computed which did not include any rotor. For all cases, a half model of the aircraft was included in the computational domain, employing symmetry boundary conditions. The complete aircraft was simulated using a uniform rotor actuator disk (case #6), with the aim to investigate the effect of the symmetry boundary conditions on the top fuselage centre-line. The transition corridor configuration was also computed using a uniform rotor actuator disk (case #6) and fully resolved blades (case #7). The helicopter case HC3 was computed using a steady-state flow approach with the rotor blades modelled via a uniform actuator disk (case #8). Unsteady Reynolds Averaged Navier-Stokes computations were used for the cases with fully resolved blades, and steady RANS was used for cases with actuator disk models.

All flow solutions were computed by solving the RANS/URANS equations, coupled with

Table 8.3: Computational cases for the 1:5 model-scale ERICA tiltrotor.

ID Case	Configuration	St/Uns	Methodology	Semi/Full Span
#1	AC1	Steady	URAD	S-S
#2	AC1	Steady	NURAD	S-S
#3	AC1	Unsteady	FRB	S-S
#4	AC1	Steady	Free	S-S
#5	AC1	Steady	URAD	F-S
#6	CC4	Steady	URAD	S-S
#7	CC4	Unsteady	FRB	S-S
#8	HC3	Steady	URAD	S-S

St=Steady; Uns=Unsteady; URAD=Uniform Rotor Actuator Disk; NURAD=Non-Uniform Rotor Actuator Disk; FRB=Fully Resolved Blade; Free=Neither Rotor Actuator Disk nor Propeller; S-S=Semi-Span; F-S=Full-Span.

Wilcox's  $k-\omega$  turbulence model [190]. This was based only on experience and the reputation of this model for stability. The flow equations were integrated with the implicit dual-time stepping method of HMB, using a pseudo-time CFL equal to 4 for the RANS cases. For the URANS cases, the selected time step corresponded to half a degree of rotor revolution.

## 8.4 Results and Discussion

To assess the capability of the present CFD method in accurately predicting tiltrotor flows, twenty one cross-sections were selected for  $C_p$  profile comparisons between CFD and experiments [91, 92] (see Table 8.4). Two sections were selected on the top and bottom symmetry planes of the fuselage (labelled with SYM-TOP and SYM-BOT respectively), four sections on the fixed wing (labelled with FW), three on the tiltable wing (labelled with TW) which define the zone of aerodynamic interaction between the tiltable wing and the blades, four on the nacelle (labelled with NA), and eight on the fuselage (labelled with FU). Figure 8.6 shows the position of the selected sections on the ERICA tiltrotor for the aeroplane mode AC1.

Considering the AC1 configuration, the surface  $C_p$  was analysed for the FRB, URAD, and NURAD approaches. The first goal was to evaluate the ability of the aerodynamic methods in producing adequate estimates of the loads at the aerodynamic interaction zone behind the blades.

The second goal was to investigate if results of the AD provide good agreement with test data for the fuselage loads. Total loads on the ERICA tiltrotor and visualisation of the flowfield using iso-surfaces of the  $\tilde{Q}$ -criterion are also presented for the FRB approach. Finally, results for the transition corridor and helicopter mode configurations are compared through  $C_p$  distribution on the selected stations with the experimental data.

Table 8.4: Nomenclature of the stations selected for  $C_p$  profile comparisons.

Nomenclature	Description
SYM-TOP	Fuselage symmetry plane (top), station $y=0$ mm.
SYM-BOT	Fuselage symmetry plane (bottom), station $y=0$ mm.
FW-A	Fixed wing, station $y=280$ mm.
FW-B	Fixed wing, station $y=490$ mm.
FW-C	Fixed wing, station $y=700$ mm.
FW-D	Fixed wing, station $y=805$ mm.
TW-A	Tiltable wing, station $y=855$ mm.
TW-B	Tiltable wing, station $y=955$ mm.
TW-C	Tiltable wing, station $y=1117.5$ mm.
NA-A	Nacelle (top), $y=1500$ mm.
NA-B	Nacelle (bottom), $y=1500$ mm.
NA-C	Nacelle (central), $x=1560$ mm.
NA-D	Nacelle (rear), $x=1860$ mm.
FU-A	Fuselage, station $x=260$ mm.
FU-B	Fuselage, station $x=535$ mm.
FU-C	Fuselage, station $x=810$ mm.
FU-D	Fuselage, station $x=1163$ mm.
FU-E	Fuselage, station $x=1470$ mm.
FU-F	Fuselage, station $x=1810$ mm.
FU-G	Fuselage, station $x=2460$ mm.
FU-H	Fuselage, station $x=2760$ mm.

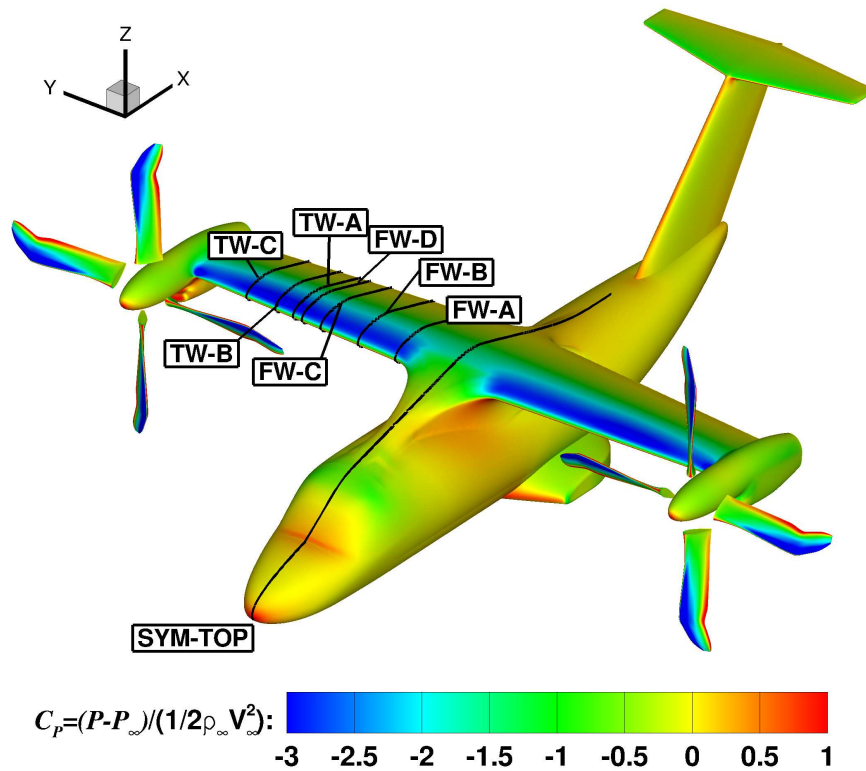
BOT=Bottom; FU=Fuselage; FW=Fixed Wing; NA=Nacelle; TW=Tiltable Wing; SYM=Symmetry.

### 8.4.1 Aeroplane Mode AC1

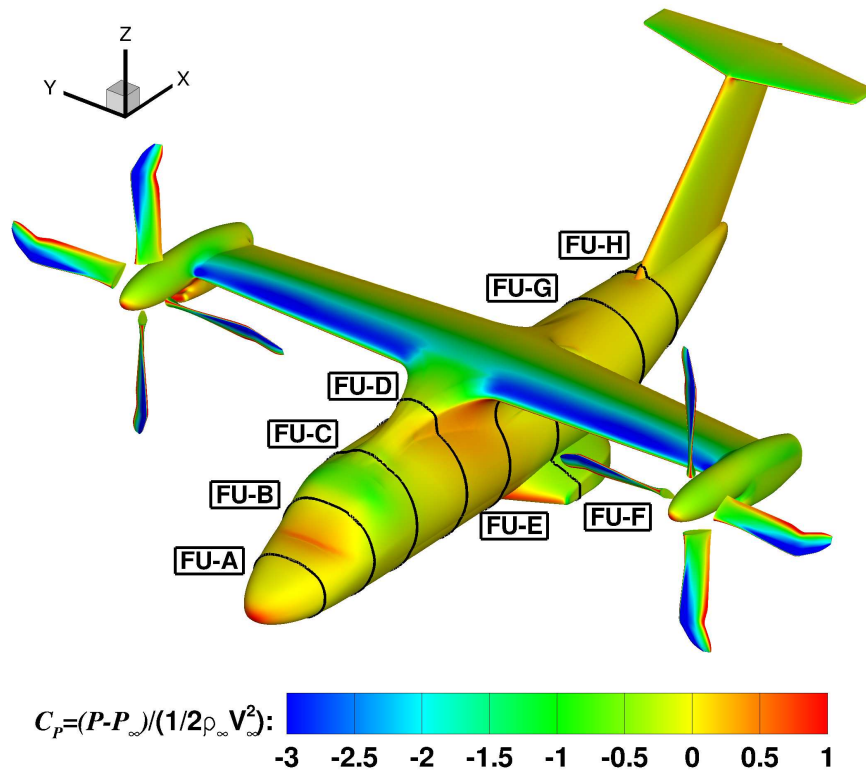
#### Surface Pressure Predictions

$C_p$  profile comparisons between CFD and experiments [91, 92] on the fuselage, fixed and tiltable wings of the ERICA tiltrotor are given in Figures 8.7 and 8.8. They correspond to the top fuselage centre-line and inner, middle, and outer tiltable and fixed wing sections. The CFD results were





(a) Sections on the fixed and tiltable wings.



(b) Sections on the fuselage.

Figure 8.6: Cross-sections selected for comparisons between CFD and experiments [92, 91] on the fixed and tiltable wings, and fuselage of the ERICA tiltrotor for the aeroplane mode configuration.

not averaged in phase, like the test data, which could lead to a source of error in the comparison. For the FRB cases,  $C_P$  values were averaged over the last computed rotor revolution instead of time-averaging. Regarding the  $C_P$  profile at the centre-line of the fuselage (Figure 8.7 (a)), a zone of recirculation is seen by both sets of experiments (Modane and DNW experiments are denoted by squares and triangles, respectively) represented by a pressure plateau after the wing leading edge suction peak. The HMB predictions (URAD=green line, NURAD=blue line, FRB=red line) overestimate the suction peak ( $C_{P \text{ URAD}} = 1.70$ ;  $C_{P \text{ NURAD}} = 1.70$ ;  $C_{P \text{ FRB}} = 1.66$ ;  $C_{P \text{ DNW}} = 1.25$ ;  $C_{P \text{ ONERA}} = 1.18$ ) and do not capture the region of recirculation. This can be due to a failure of the employed turbulence model, wind tunnel effects, and lack of the exact trim conditions employed during the wind tunnel tests. By contrast, the CFD results at the front and rear part of the fuselage are in close agreement with the experimental data. Considering the inner fixed wing section (Figure 8.7 (b)), experiments suggest that this region is separated due to the presence of a plateau on the  $C_P$  data. CFD predictions slightly overestimate the suction peak and the pressure plateau is not well reproduced. This is consistent with the flowfield predicted in Figure 8.7 (a).

In the middle and outer fixed wing sections (Figures 8.7 (c) and (d)), wind tunnel experiments and CFD are in good agreement, with small differences of 9% for the suction peak. Results show good agreement with the experiment at all stations, even if the trailing edge pressure plateau is slightly under-estimated. Regarding the zone of aerodynamic interaction located near the tiltable wing sections (Figure 8.8), good agreement between CFD and experimental results is observed. Moreover, results of the CFD with the actuator disk produced adequate estimates of the  $C_P$  profile with a small discrepancy of 1.59% on the suction peak between both approaches. As can be seen, negligible differences were found between the URAD and NURAD results for all stations. Note that the differences between the two sets of experiments are always larger than the differences between FRB and AD results.

Using the URAD loads as a reference, the effects of using half or complete aircraft geometries with or without rotor modes can be assessed in terms of pressure distributions, in Figures 8.9 and 8.10. For all stations, numerical simulations for the whole aircraft (referred to as URAD F-S) have a negligible impact on the  $C_P$  if compared with predictions using symmetry (referred to as

URAD). Regarding the effect of the prop rotor on the loads, it can be observed that the centre-line of the fuselage and the fixed-wing regions are weakly influenced by the wake-body interaction (solution without rotor is referred to as Free). The tiltable wing regions, however, are strongly affected by the rotor wake, thus giving rise to a larger increase in the normal ( $C_n$ ) and tangential ( $C_t$ ) coefficients (see Figures 8.10 (c) and (d)).

Figure 8.11 shows  $C_P$  profile comparisons on the nacelle, corresponding to the top and bottom centre lines, and its central and rear sections (see Figure 8.11 (a)). Considering the top and bottom centre-line sections (Figures 8.11 (b)-(c)), a noticeable scatter of  $C_P$  is observed for both sets of experiments. The CFD results captured the trend of the averaged experimental  $C_P$  at both sections, where the results with the actuator disk provided slightly higher  $C_P$  values compared to the fully resolved blades. Finally, for the middle and rear part of the nacelle (Figures 8.11 (d)-(e)), good agreement is seen between CFD and experiments.

Figures 8.12 and 8.13 present  $C_P$  comparisons on the ERICA fuselage at eight cross-sections. All CFD curves are close to the experimental data. Better agreement is obtained at the front of the fuselage (see Figures 8.12 (a)-(d)), where the flowfield is attached. The HMB solution captures well all features shown by the experiments. Even for stations located behind the fixed wing (see Figures 8.13 (a)-(d)), the agreement is still fair near the sponsons and the fin of the model. It is noticeable that discrepancies appear not to be present when the actuator disk approaches were employed, which encourages the use of this approach in predicting loads on the fuselage.

The effect of the model support on the ERICA tiltrotor results was also assessed using the average  $C_P$  distribution on the bottom part of the fuselage in Figure 8.14. The model of the DNW-LLF was supported via a ventral sting set-up at the rear part of the fuselage, whilst a straight sting was set-up in the ONERA model. As shown in Figure 8.14, the effect of the model support on the fuselage is stronger for the DNW-LLF, and is less pronounced for the ONERA setup. From a numerical point of view, HMB predictions compare well with the experimental data of ONERA, where the support is straight. This is consistent with the fact that the model support was not modelled in the computational domain. Furthermore, no discrepancies were found between FRB and AD results, which suggests that this zone is not influenced by details of the rotor blades.

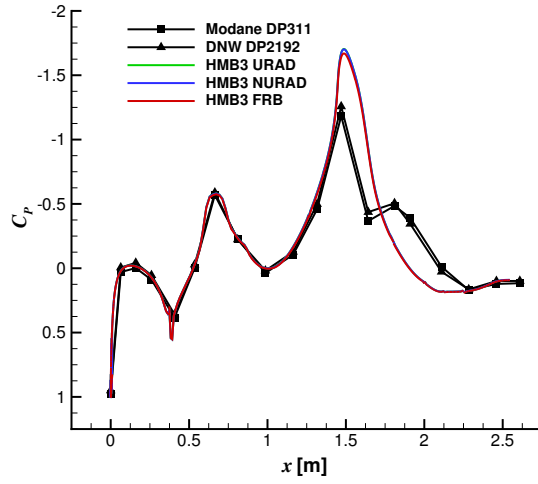
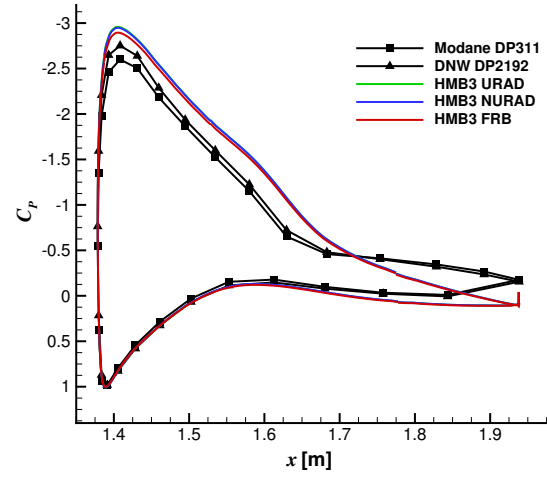
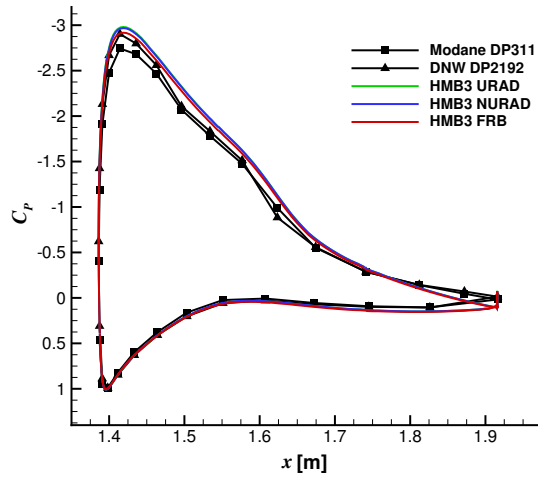
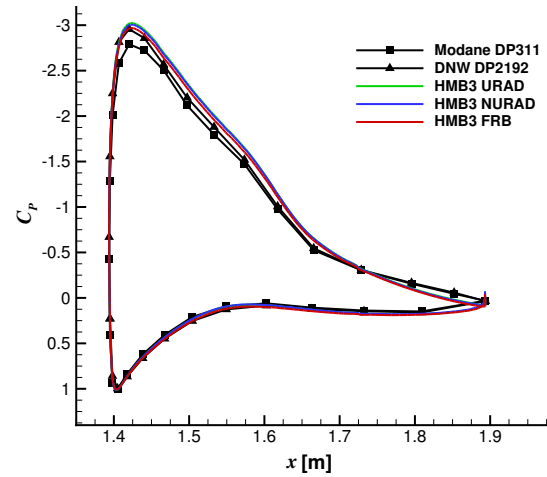

 (a) SYM-TOP, section  $y=0$  mm.

 (b) FW-A, section  $y=280$  mm.

 (c) FW-B, section  $y=490$  mm.

 (d) FW-C, section  $y=700$  mm.

Figure 8.7:  $C_p$  profile comparisons between CFD and experiments [92, 91] on the fixed and tiltable wings of the ERICA tiltrotor for the aeroplane mode configuration AC1 (sections SYM-TOP, FW-A, FW-B, and FW-C).

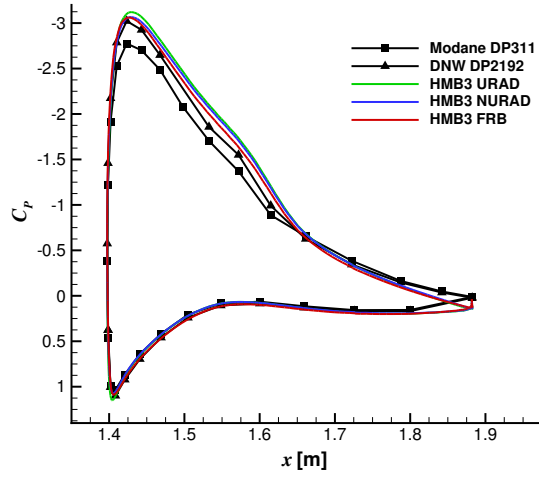
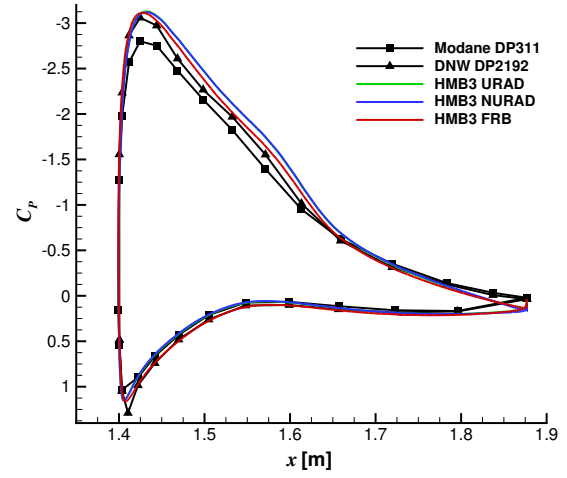
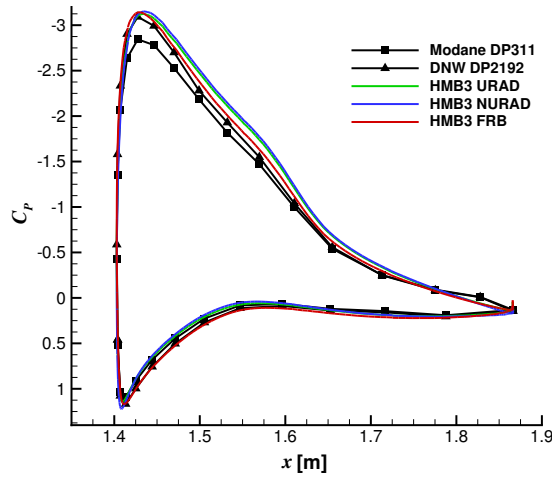
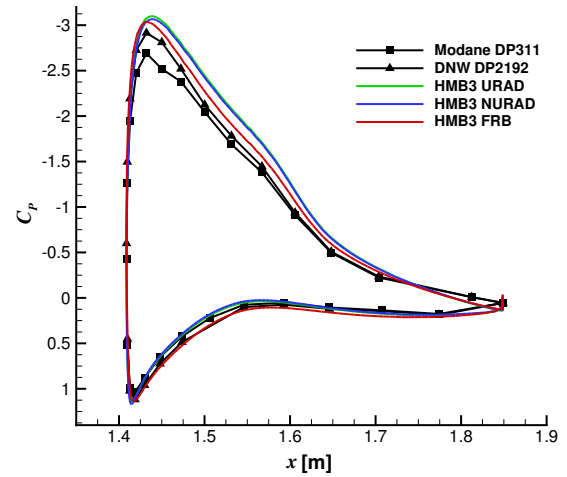

 (a) FW-D, section  $y=805$  mm.

 (b) TW-A, section  $y=855$  mm.

 (c) TW-B, section  $y=995$  mm.

 (d) TW-C, section  $y=1117$  mm.

Figure 8.8:  $C_p$  profile comparisons between CFD and experiments [92, 91] on the fixed and tiltable wings of the ERICA tiltrotor for the aeroplane mode configuration AC1 (sections FW-D, TW-A, TW-B, and TW-C).

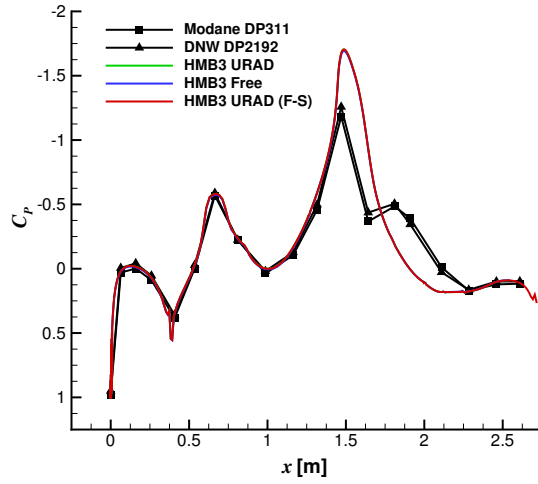
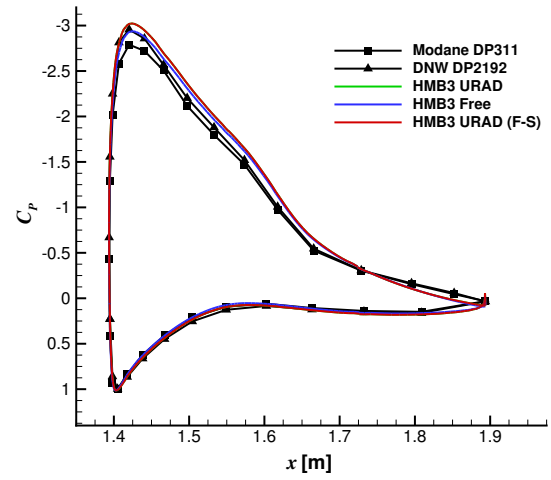
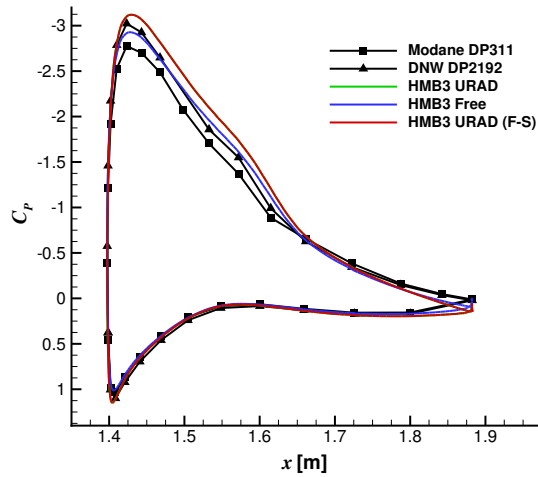
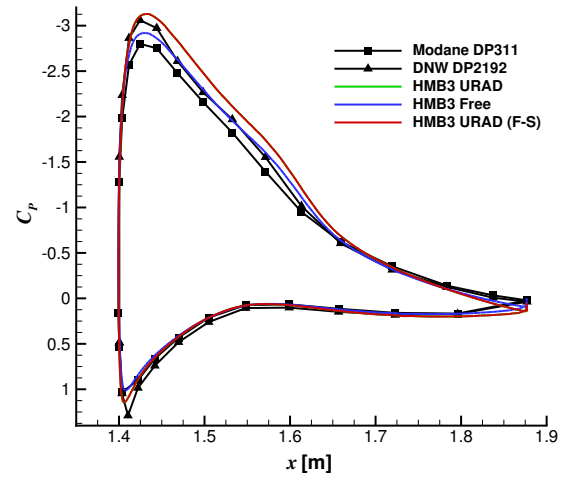

 (a) SYM-TOP, section  $y=0$  mm.

 (b) FW-C, section  $y=700$  mm.

 (c) FW-D, section  $y=805$  mm.

 (d) TW-A, section  $y=855$  mm.

Figure 8.9:  $C_p$  profile comparisons between CFD and experiments [92, 91] on the fixed and tiltable wings of the ERICA tiltrotor for the aeroplane mode configuration AC1. Results correspond to half or complete aircraft geometries with or without rotor (sections SYM-TOP, FW-C, FW-D, and TW-A).

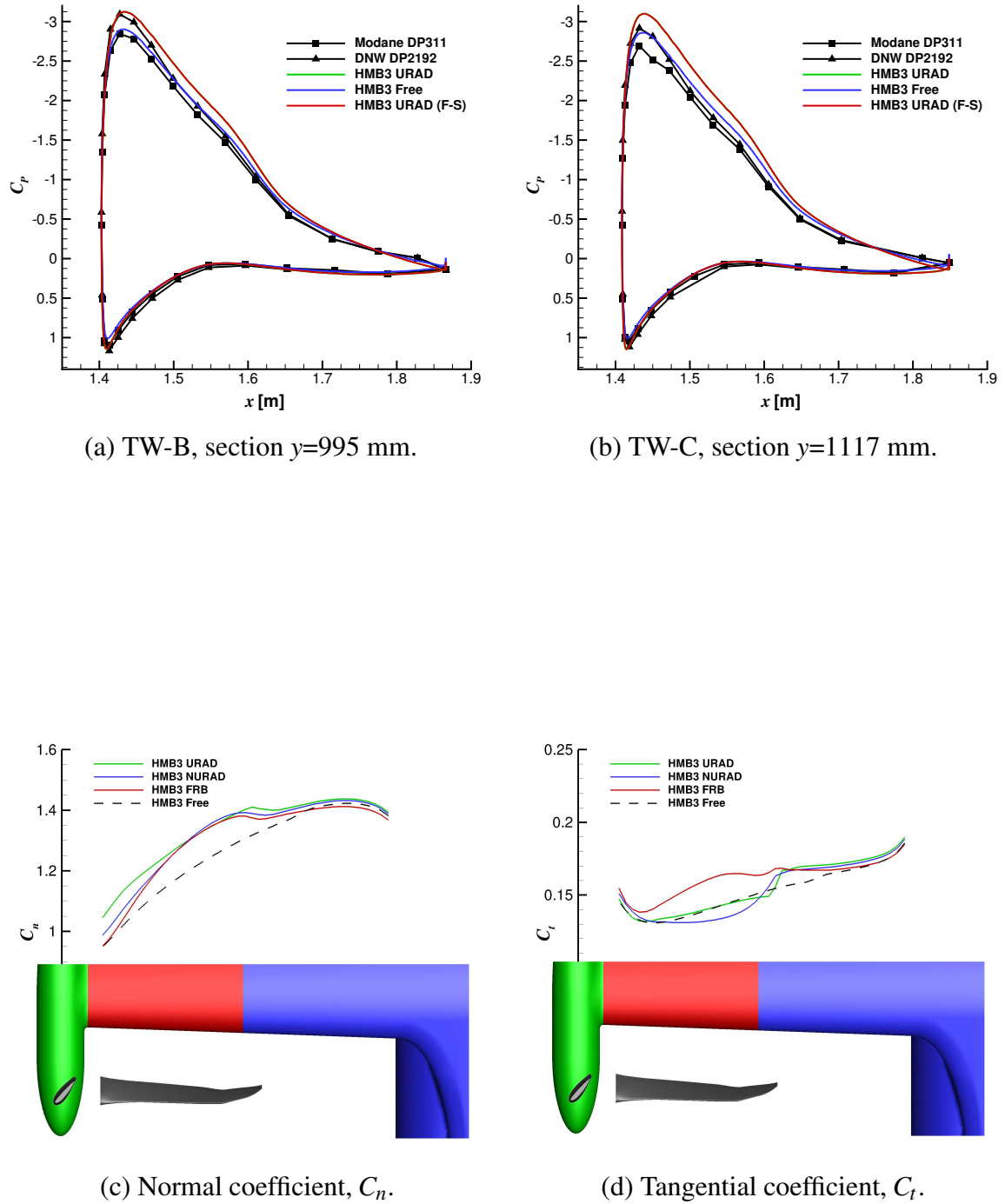
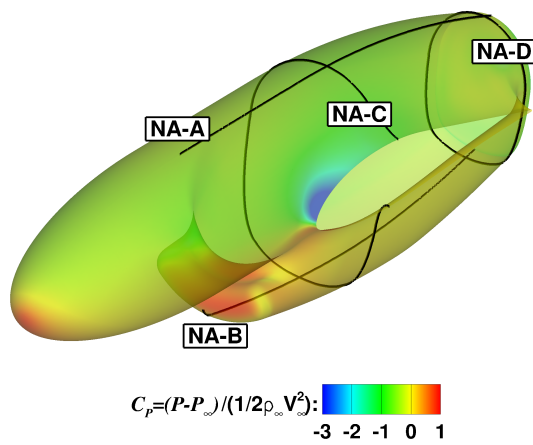


Figure 8.10:  $C_p$  profile comparisons between CFD and experiments [92, 91] on the fixed and tiltable wings of the ERICA tiltrotor for the aeroplane mode configuration AC1. Results correspond to half or complete aircraft geometries with or without rotor (sections TW-B and TW-C).



(a) Location of the cross-sections.

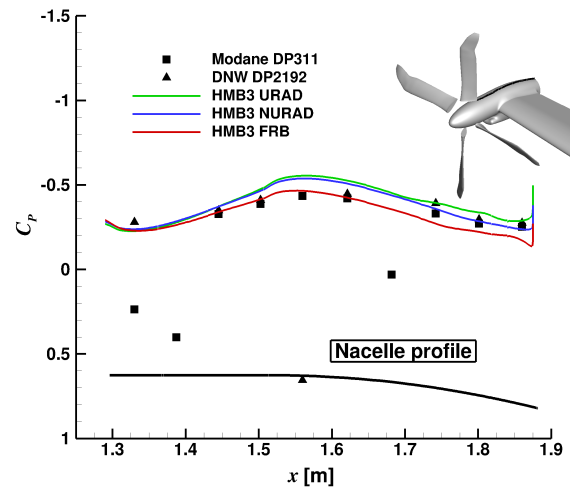
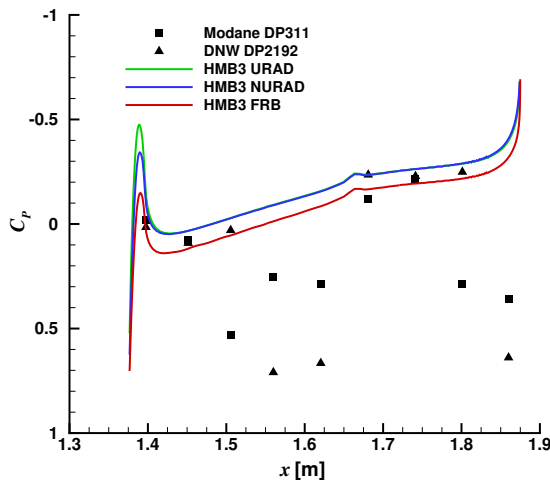
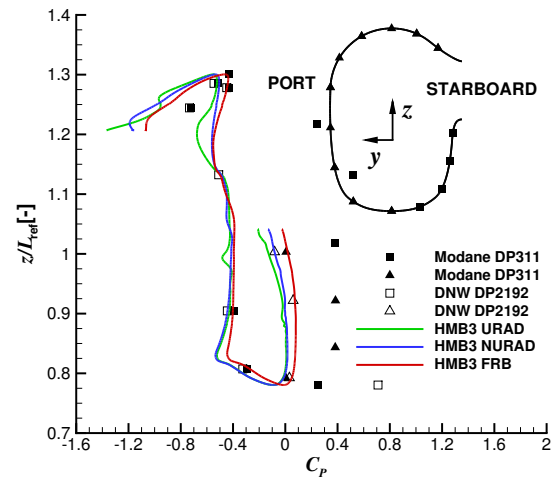
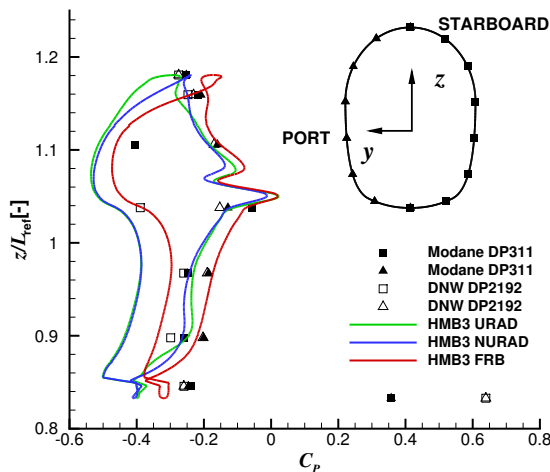

 (b) NA-A, section  $y=1500$  mm.

 (c) NA-B, section  $y=1500$  mm.

 (d) NA-C, section  $x=1560$  mm.

 (e) NA-D, section  $x=1860$  mm.

 Figure 8.11:  $C_p$  profile comparisons between CFD and experiments [92, 91] on the nacelle of the ERICA tiltrotor for the aeroplane mode configuration AC1.



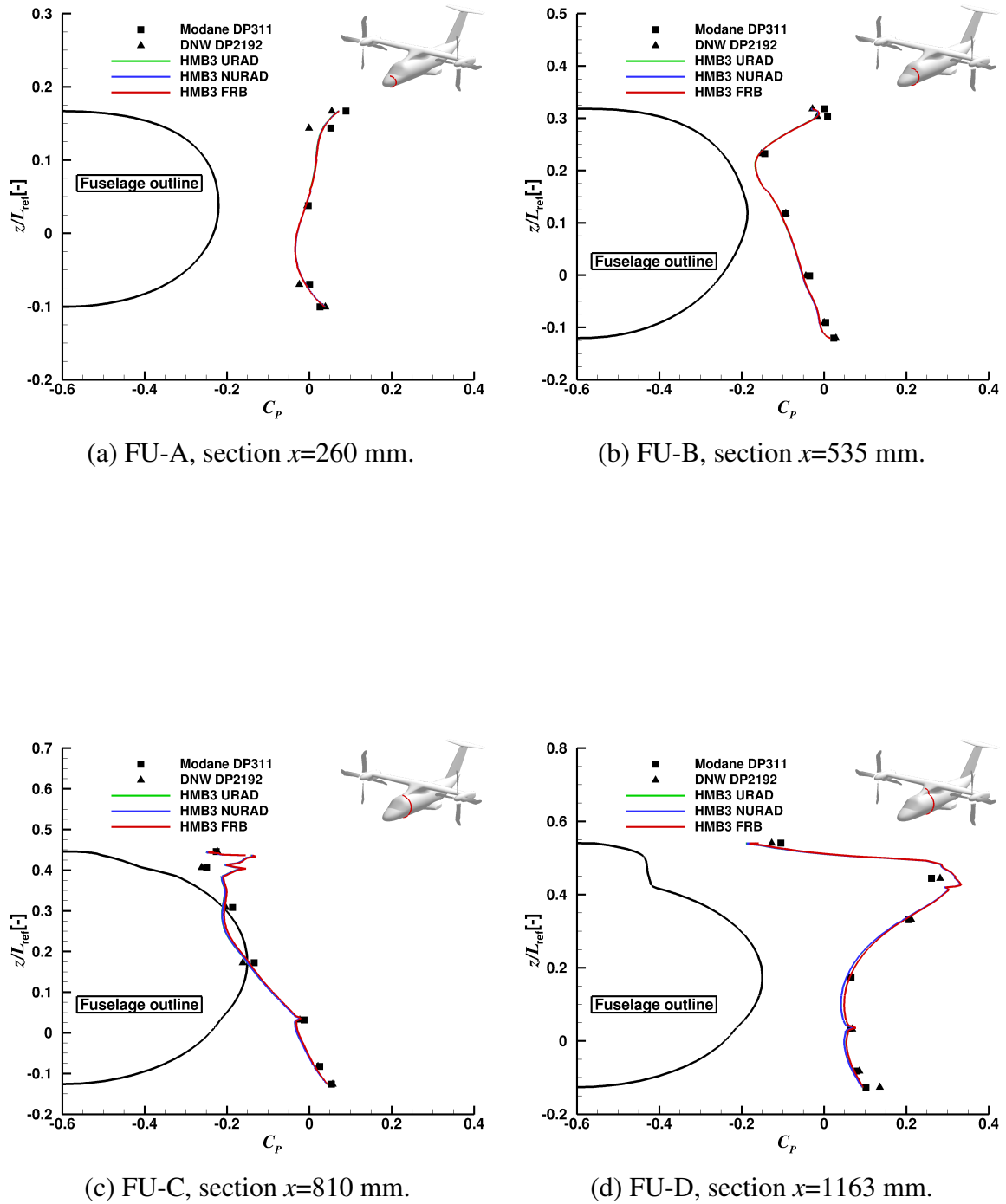


Figure 8.12:  $C_p$  profile comparisons between CFD and experiments [92, 91] on the fuselage of the ERICA tiltrotor for the aeroplane mode configuration AC1 (sections FU-A, FU-B, FU-C, and FU-D).

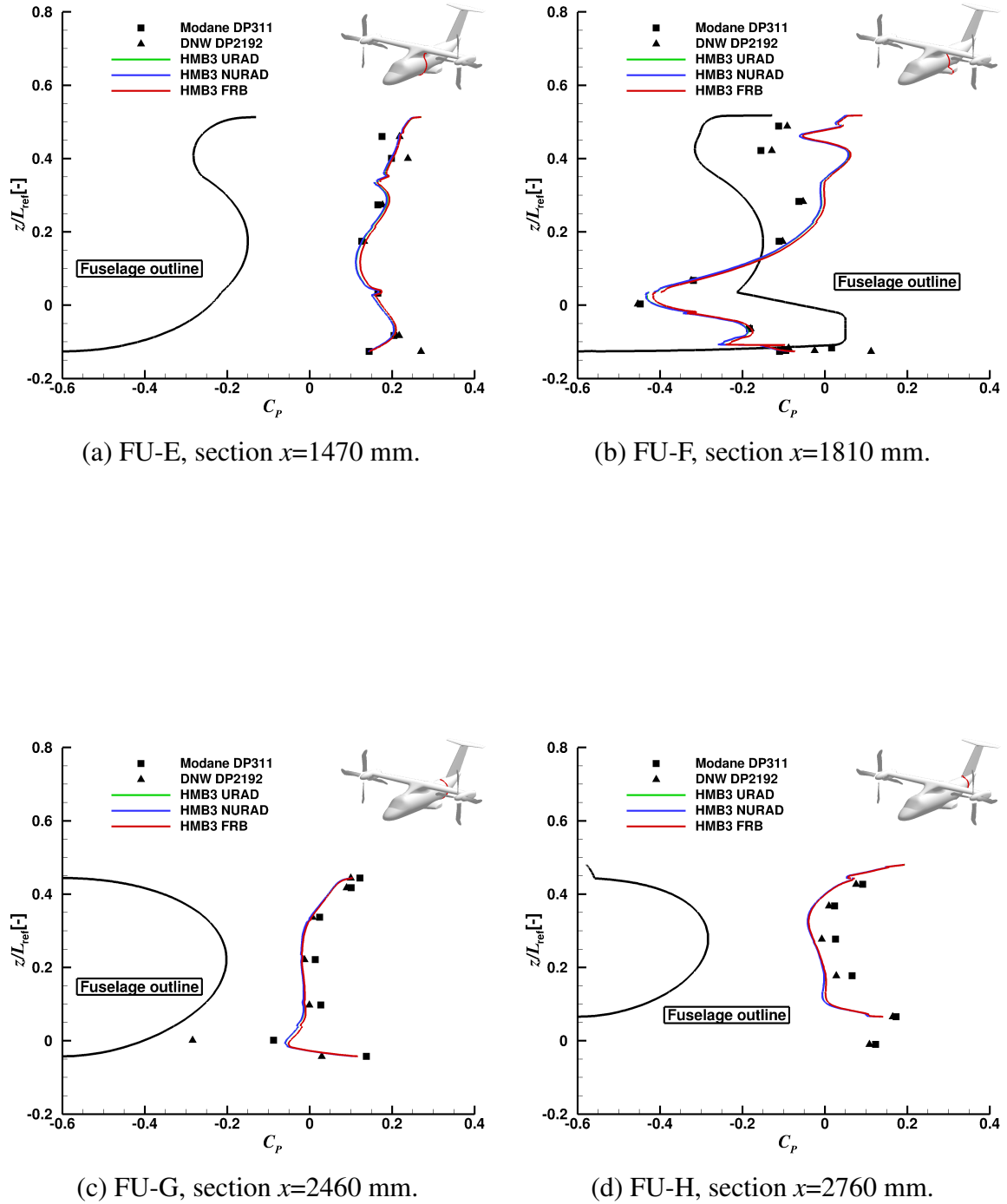


Figure 8.13:  $C_p$  profile comparisons between CFD and experiments [92, 91] on the fuselage of the ERICA tiltrotor for the aeroplane mode configuration AC1 (sections FU-E, FU-F, FU-G, and FU-H).

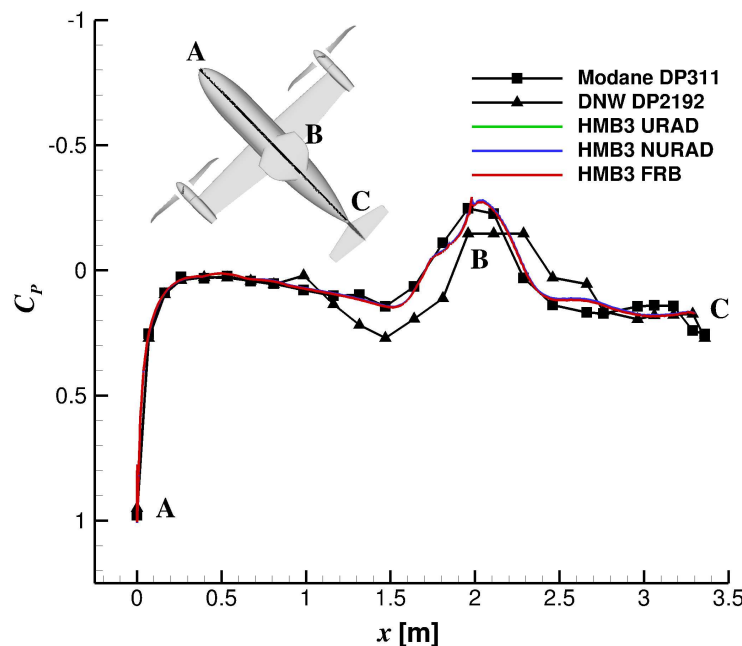


Figure 8.14:  $C_p$  profile comparisons between CFD and experiments [92, 91] on the bottom part of the fuselage of the ERICA tiltrotor for the aeroplane mode configuration AC1.

## Load Distributions

In this section, the integrated loads generated on the nacelle, tiltable wing, and the rest of the fuselage with the fixed wing are analysed for the aeroplane configuration with the fully resolved blade approach. Lift ( $C_L$ ) and drag ( $C_D$ ) coefficients on the tiltable wing as function of the main rotor azimuth  $\Psi$  are shown in Figure 8.15 (a). The  $C_D$  and  $C_L$  coefficients are represented by squares and triangles, respectively, while their averaged values are represented with solid lines. As can be seen, the 4/rev. blade passage effect on the tiltable wing is well captured, with fluctuation values of 5.14% and 23.8% for the lift and drag, respectively. Previous work [93], reported fluctuations of lift and drag between 5%-7% and 20%-30% depending on the employed CFD code and mesh.

Likewise, the history of the loads on the nacelle is given in Figure 8.15 (b), which reveals the 4/rev. blade passage effect for both aerodynamic coefficients. The lift and drag fluctuations are 6.86% and 2.5%, respectively, which suggests that the nacelle has a milder unsteady behaviour than the tiltable wing. The fuselage and fixed wing lift and drag coefficients are presented in Figure 8.15 (c), which also shows a 4/rev. signal due to the blade passage. The results show small

fluctuations of drag (5.64%) and lift (2.17%) coefficients.

Finally, the lift and drag coefficients of the complete ERICA tiltrotor are compared with the experimental data. Table 8.5 shows a breakdown of the total averaged lift and drag coefficient for each component. A discrepancy of 15.51% and 33.9% for the lift and drag coefficients is found. Results reported in Decours *et al.* [93] also found a discrepancy on lift about 15%, and no drag values were reported. The NICETRIP experimental data is relatively new and not well explored by researchers. It is therefore likely that corrections should be applied to the experimental data.

Table 8.5: Averaged lift and drag coefficient comparisons between CFD and experiments [92, 91] for the ERICA tiltrotor.

Component	HMB3		Wind tunnel	
	$C_L$	$C_D$	$C_L$	$C_D$
Tiltable wing	0.244	0.012	-	-
Nacelle	0.039	0.017	-	-
Fuselage	0.432	0.041	-	-
Rotor	0.073	-	-	-
<b>Total</b>	<b>0.789</b>	<b>0.071</b>	<b>0.683</b>	<b>0.053</b>

### Flowfield Details

Visualisation of the flowfield of the ERICA tiltrotor using the  $\tilde{Q}$ -criterion [206] coloured by Mach number is presented in Figure 8.16 (a) for the fully resolved blade and the uniform rotor actuator disk approaches. Regarding the FRB approach, the wake behind the rotor disk is preserved for more than one rotor diameter downstream thanks to the refined mesh employed in this region (Figure 8.17). This informative plot shows the interaction of the rotor wake with the nacelle and tiltable wings. From these iso-surfaces it can be seen that the rotor wake does not directly interact with the fuselage and the fixed part of the wings. Iso-surface contours of  $\tilde{Q}$ -criterion are shown from the CFD simulations using the uniform rotor actuator disk in Figure 8.16 (b), revealing that the detailed wake characteristics cannot be easily identified with this method.

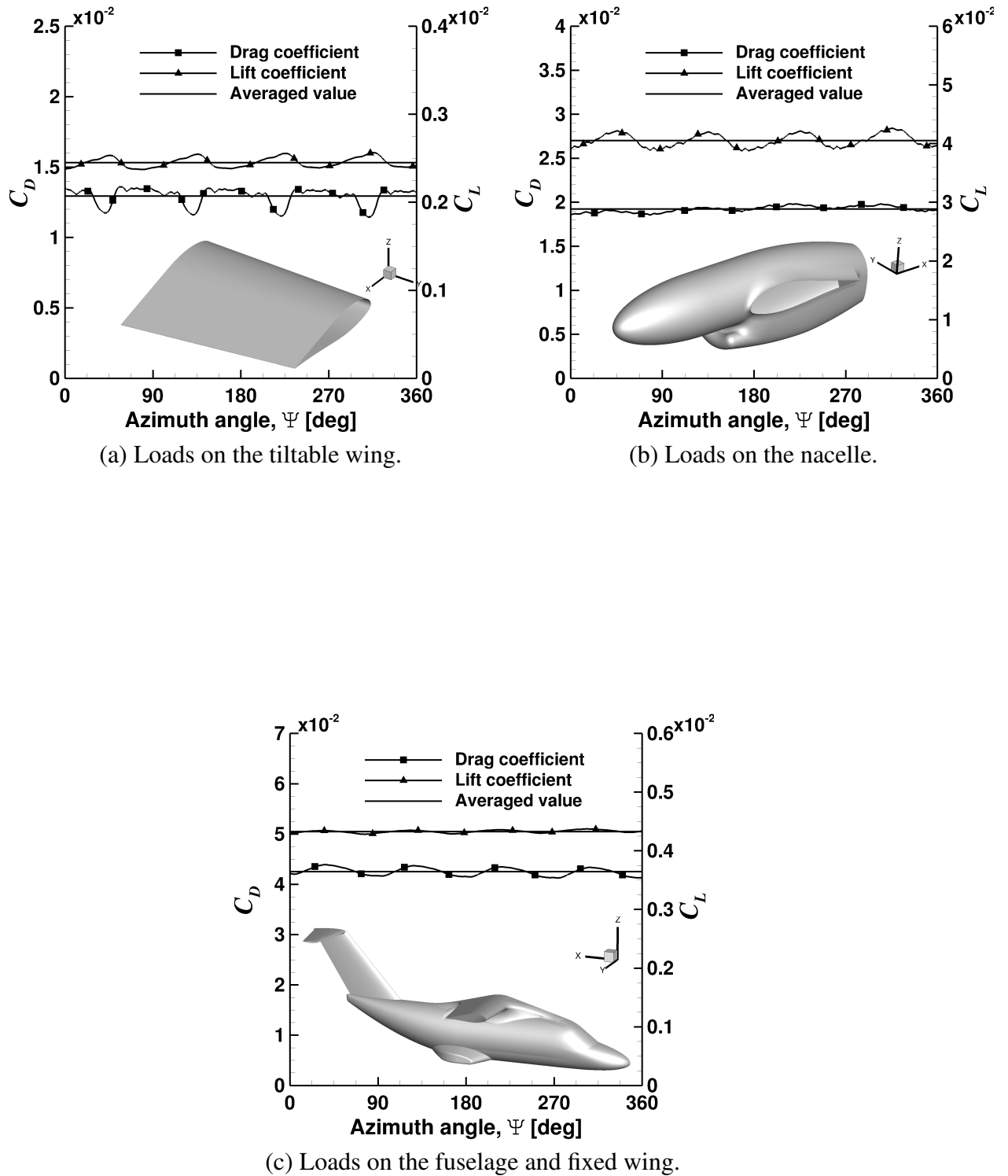
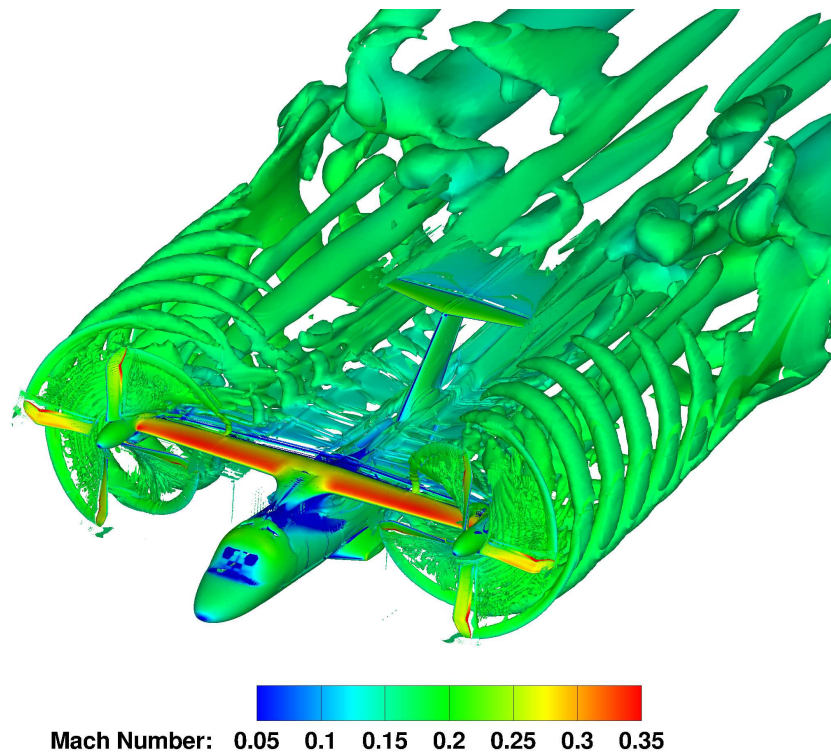
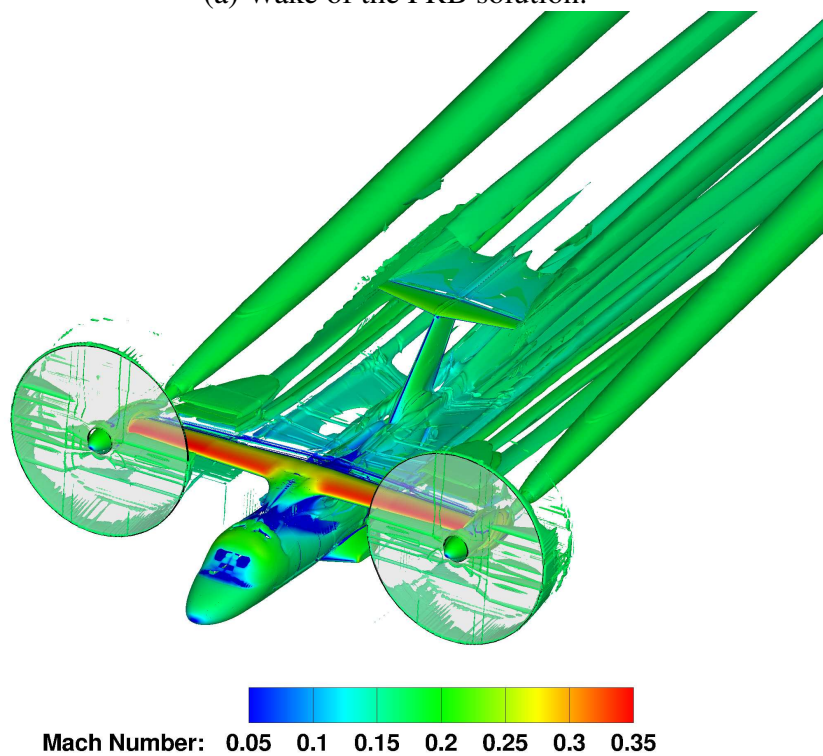


Figure 8.15: History of the lift and drag coefficients in the tiltable wing, nacelle, and fuselage and fixed wing of the ERICA tiltrotor.



(a) Wake of the FRB solution.



(b) Wake of the URAD solution.

Figure 8.16: Wake-visualisation of the ERICA tiltrotor in aeroplane mode configuration using  $\tilde{Q}$ -criterion ( $\tilde{Q}=0.075$ ) shaded by contour of Mach numbers. Results with the FRB (top) and URAD (bottom).



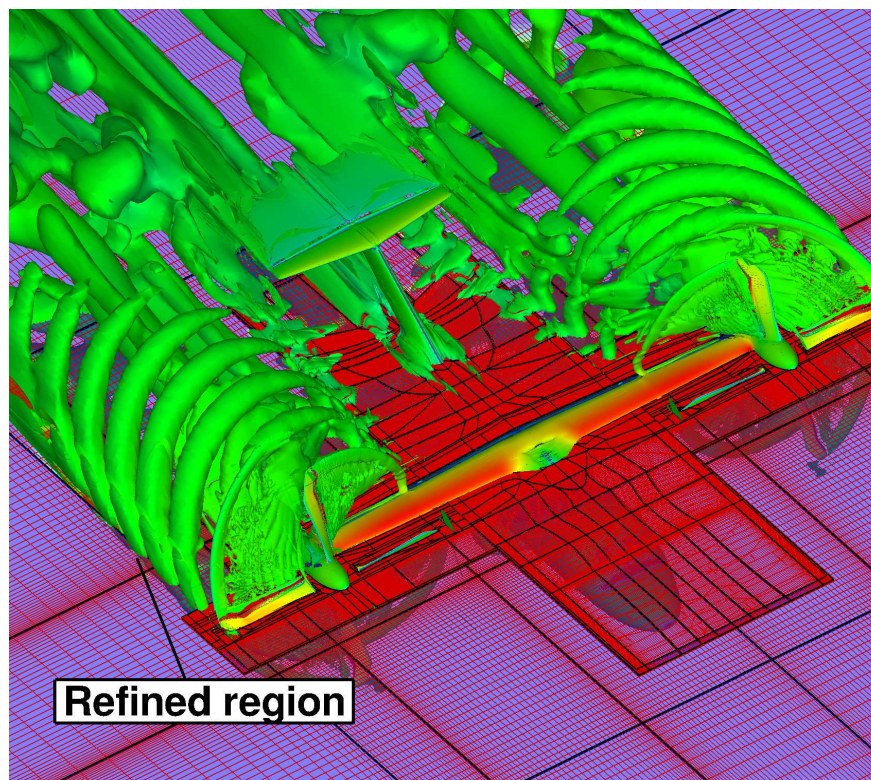
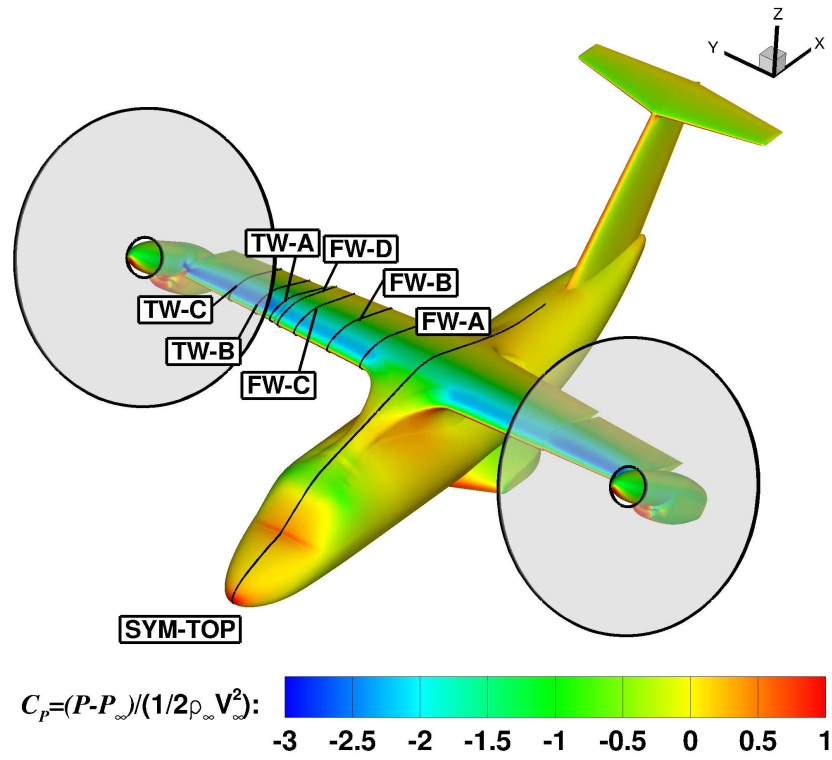


Figure 8.17: Detailed view of the refined mesh employed for the aeroplane mode configuration with the fully resolved blade.

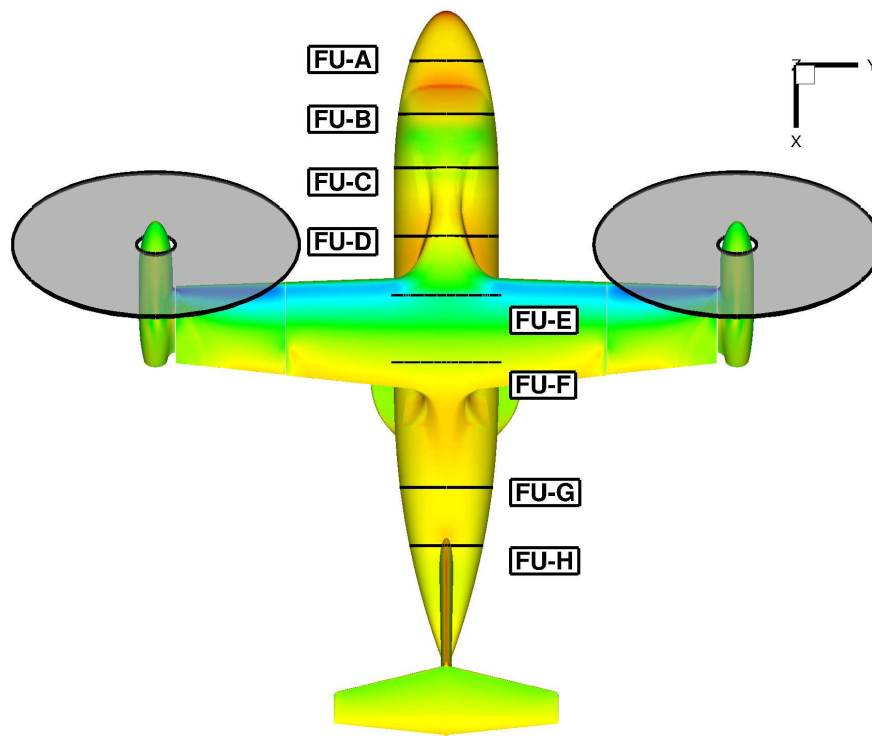
## 8.4.2 Transition Corridor CC4

### Surface Pressure Predictions

The CC4 case corresponds to a typical tiltrotor corridor configuration with a moderate AoA of 5.30 degrees. The tiltable wing and nacelle angles were 4 and 30.1 degrees, respectively, relative to the aircraft axis. Like for the AC1 case, profile comparisons of  $C_p$  between CFD and experiment were assessed on the fuselage, fixed and tiltable wings of the ERICA tiltrotor (see Figure 8.18). Considering the AC1 results, no significant differences were found between the URAD and NURAD results. This supports the idea of using the simplest aerodynamic model (URAD) here to compare with the FRB approach.



(a) Sections on the fixed and tiltable wings.



(b) Sections on the fuselage.

Figure 8.18: Cross-sections selected for comparisons between CFD and experiments [92, 91] on the fixed and tiltable wings, and fuselage of the ERICA tiltrotor for the transition corridor configuration.



Considering the pressure coefficient at the centre-line of the fuselage (Figure 8.19 (a)), the experiments suggest the absence of flow separation mainly due to a reduction of the angle of attack by almost 5 degrees. Results are in fair agreement with both experiments, where the suction peak is slightly over-estimated ( $C_{P \text{ URAD}} = 1.56$ ;  $C_{P \text{ FRB}} = 1.53$ ;  $C_{P \text{ DNW}} = 1.49$ ;  $C_{P \text{ ONERA}} = 1.39$ ). In the inner fixed wing (see Figure 8.19 (b)), a discrepancy on the suction peak is presented by both sets of experiments (21% higher for DNW than Modane). It is interesting to note that no pressure plateau is present at the experiments, which supports the idea of absence of flow separation. From a numerical point of view, the CFD results compare well with the experimental data of DNW and, where the pressure plateau is well reproduced. The same analysis can be done for the middle and outer fixed wing (Figures 8.19 (c) and (d)). Furthermore, small differences are found between the FRB and URAD approaches, which a maximum discrepancy of the suction peak of 1.29%.

Figure 8.20 shows  $C_p$  comparisons within the aerodynamic interaction zone. The experiments present a different behaviour of the pressure plateau near at the trailing edge, where the DNW measurements suggest that the flow is not attached (see Figure 8.20 (d)). The agreement between experiments and CFD results are still fair and minor discrepancies appear to be present when the actuator disk approach was employed. Despite that use of the actuator disk model, CFD predictions are in close agreement with the DNW experiment, which highlights the capability of this low-fidelity approach in predicting averaged wing loads.

Finally, a quantitative assessment of  $C_p$  profile comparisons on the ERICA fuselage is done, considering eight cross-sections (Figures 8.21 and 8.22). Despite that a minor discrepancy is found between experiments in the middle of the wing (see Figure 8.22 (a)), a good agreement can be seen between the two wind tunnel measurements. Like for the AC1 case, the uniform actuator disk can cope with the loads on the fuselage, where a fair agreement has been obtained.

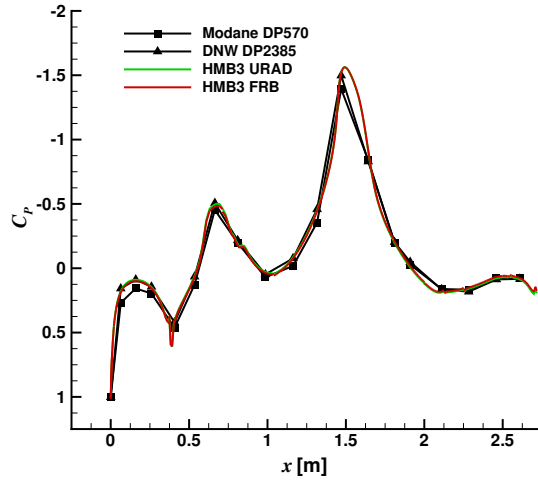
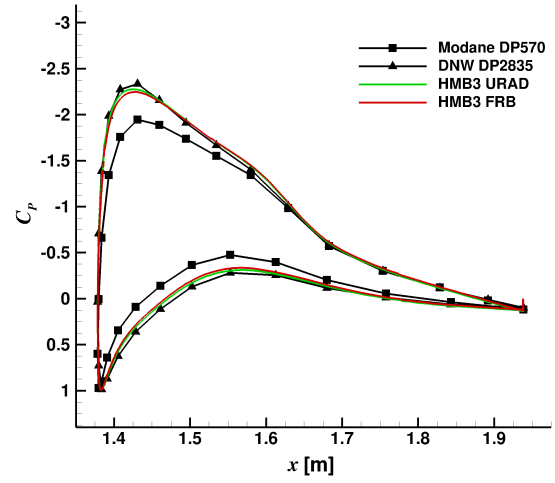
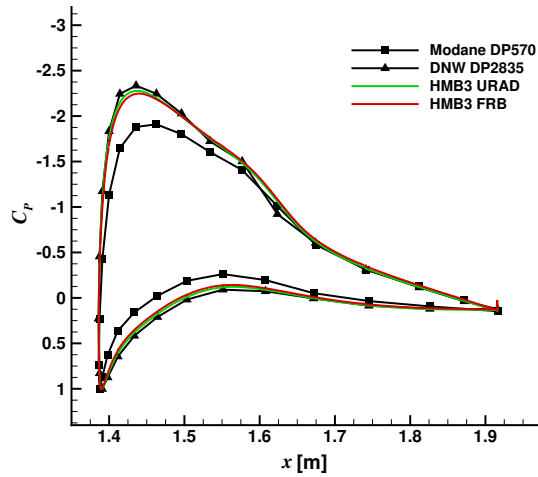
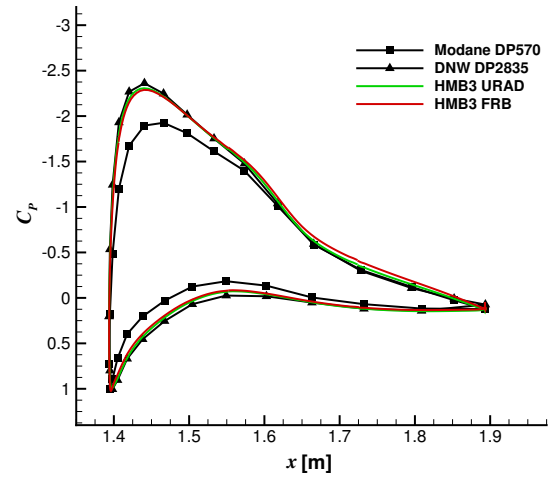

 (a) SYM-TOP, section  $y=0$  mm.

 (b) FW-A, section  $y=280$  mm.

 (c) FW-B, section  $y=490$  mm.

 (d) FW-C, section  $y=700$  mm.

Figure 8.19:  $C_p$  profile comparisons between CFD and experiments [92, 91] on the fixed and tiltable wings of the ERICA tiltrotor for the transition corridor configuration (sections SYM-TOP, FW-A, FW-B, and FW-C).

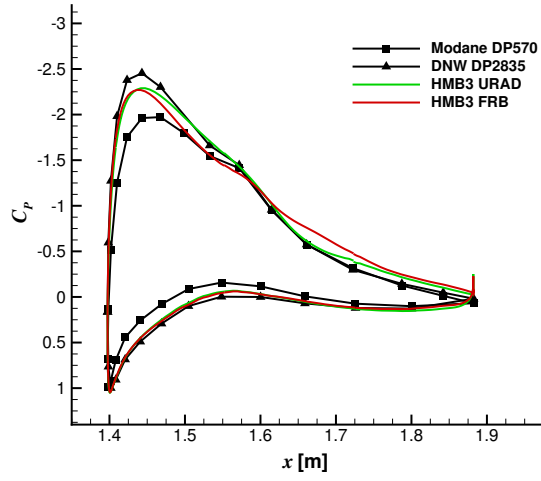
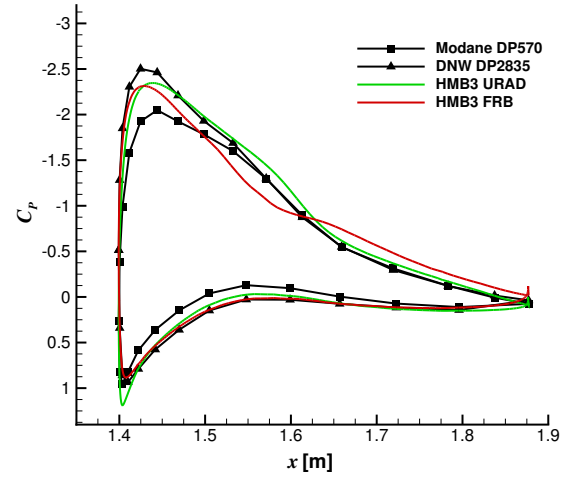
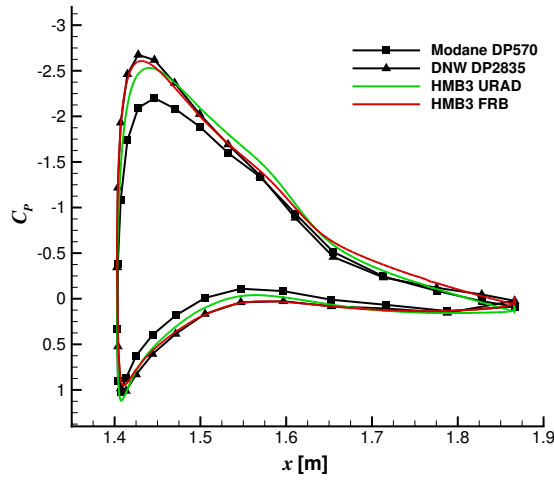
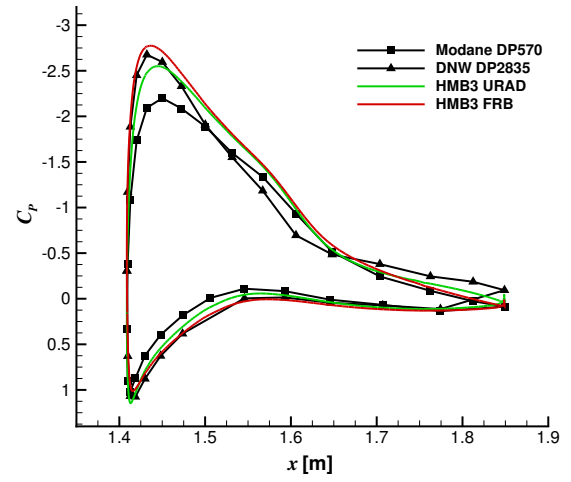

 (a) FW-D, section  $y=805$  mm.

 (b) TW-A, section  $y=855$  mm.

 (c) TW-B, section  $y=995$  mm.

 (d) TW-C, section  $y=1117$  mm.

Figure 8.20:  $C_p$  profile comparisons between CFD and experiments [92, 91] on the fixed and tiltable wings of the ERICA tiltrotor for the transition corridor configuration (sections FW-D, TW-A, TW-B, and TW-C).

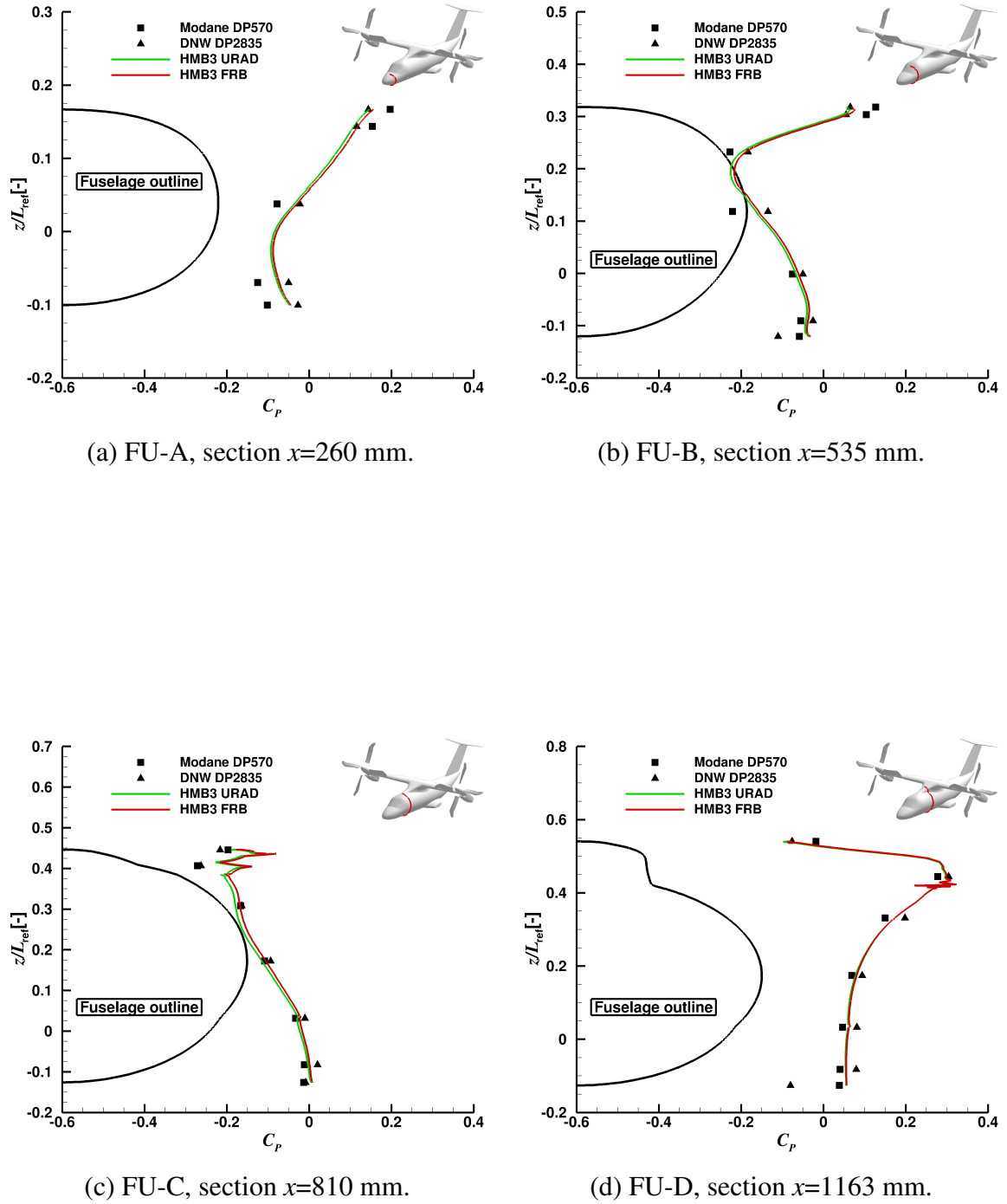


Figure 8.21:  $C_p$  profile comparisons between CFD and experiments [92, 91] on the fuselage of the ERICA tiltrotor for the transition corridor configuration (sections FU-A, FU-B, FU-C, and FU-D).

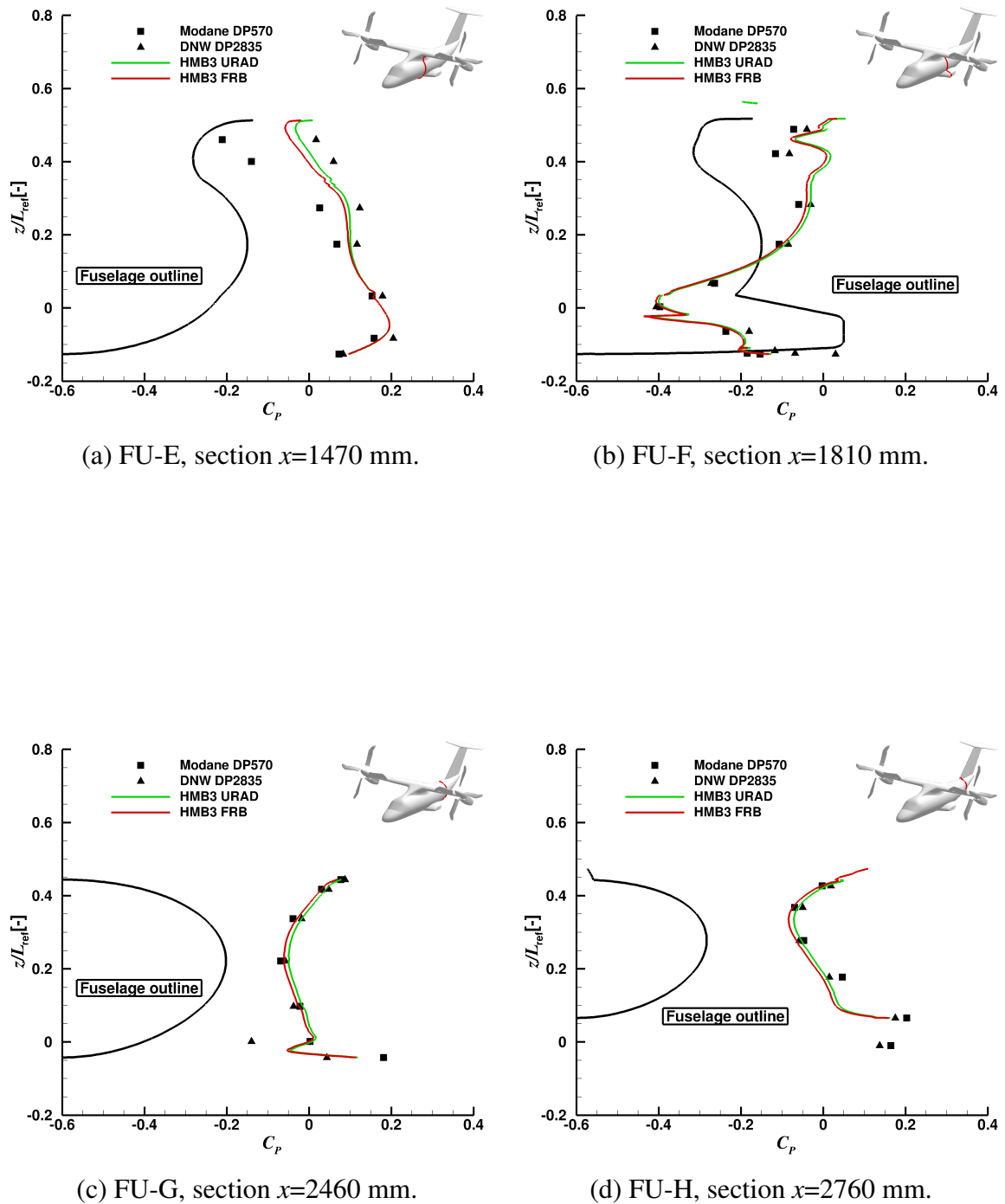


Figure 8.22:  $C_p$  profile comparisons between CFD and experiments [92, 91] on the fuselage of the ERICA tiltrotor for the transition corridor configuration (sections FU-E, FU-F, FU-G, and FU-H).

### Flowfield and Aerodynamic Comparison Between AC1 and CC4

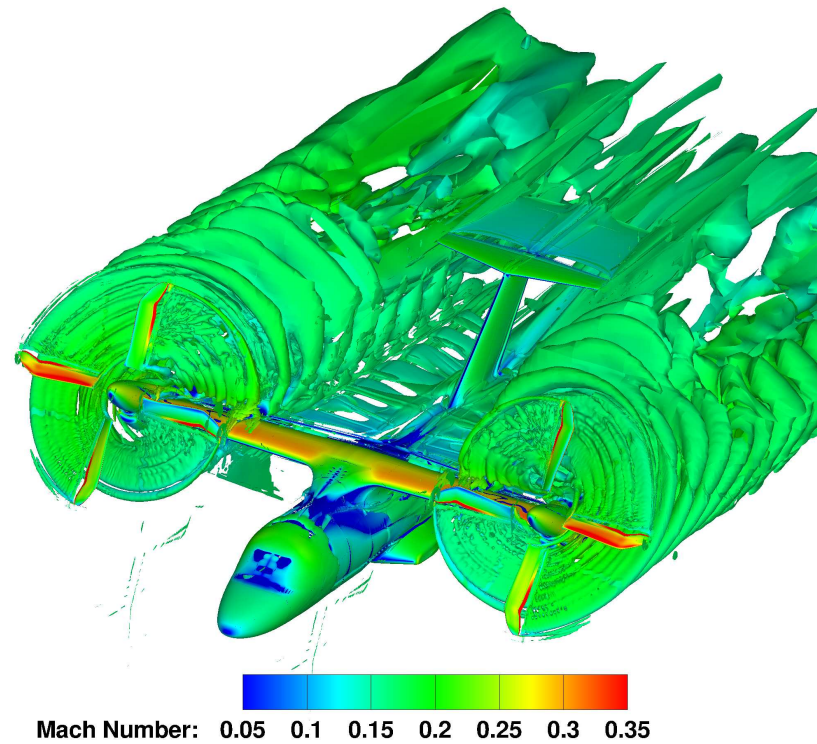
The flowfield around the ERICA tiltrotor using iso-surface is presented in Figure 8.23 for the FRB and URAD solutions using  $\tilde{Q}$ -criteria. Considering the FRB approach (Figure 8.23 (a)), a more complex wake is developed behind the rotor disk if compared with the AC1 wake due to the stronger wake/wing interaction for the CC4 configuration.

Figures 8.24 and 8.25 shows a comparison of the aeroplane and transition corridor modes for the surface pressure distributions at stations located on the fixed and tiltable wings of the ERICA tiltrotor. The DNW experimental data was selected for both modes. The freestream Mach number was kept constant ( $M_\infty = 0.168$ ), so the changes observed on the experimental and predicted peak of  $C_p$  are mainly due to the difference in the AoA and the rotor/wing interaction. The CFD and test data agree fairly well, at all stations, and the CFD captures the same difference between AC1 and CC4 as measured in the wind tunnel. This is an encouraging result regarding the use of CFD for these very complex flow cases.

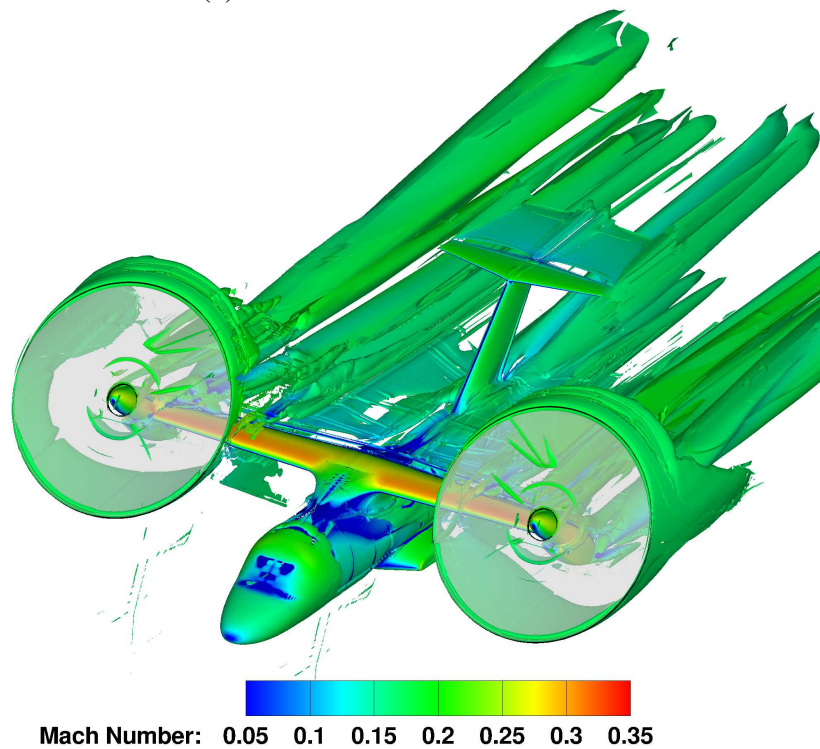
### 8.4.3 Helicopter Mode HC3

#### Surface Pressure Predictions

Numerical simulations of a helicopter configuration (nacelles tilted by 86.6 degrees) labelled as HC3 is also carried out. This configuration is characterised for a moderate forward speed ( $M_\infty = 0.104$ ) with an aircraft angle of attack of -5.15 degrees (see Figure 8.5). Like the previous cases, profile comparisons of  $C_p$  between CFD and experiment were assessed on the fuselage, fixed and tiltable wing of the ERICA tiltrotor (see Figure 8.26) where a URAD approach was used. Unlike the AC1 and CC4 configurations where experiments in DNW and ONERA was available, the HC3 test was only carried out in the DNW wind tunnel.



(a) Wake of the FRB solution.



(b) Wake of the URAD solution.

Figure 8.23: Wake-visualisation of the ERICA tiltrotor in transition corridor configuration using  $\tilde{Q}$ -criterion ( $\tilde{Q}=0.075$ ) shaded by contour of Mach numbers. Results with the FRB (top) and URAD (bottom).

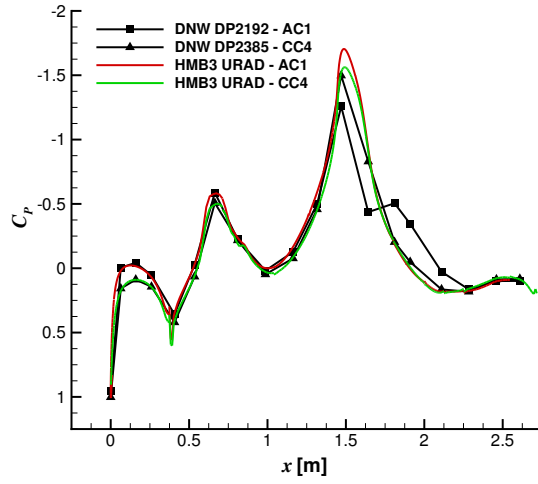
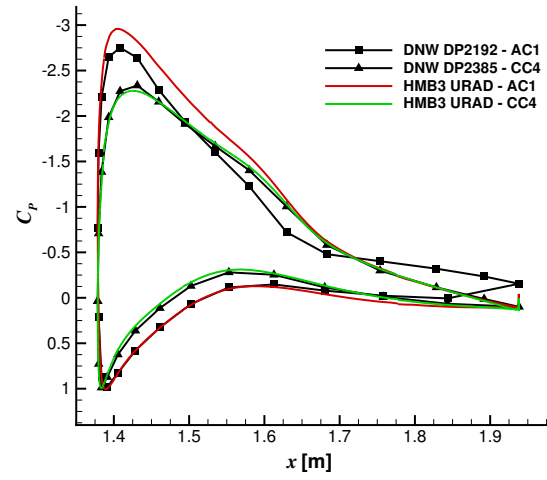
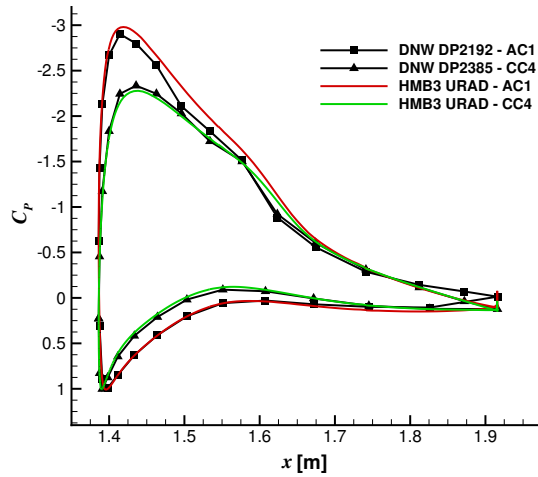
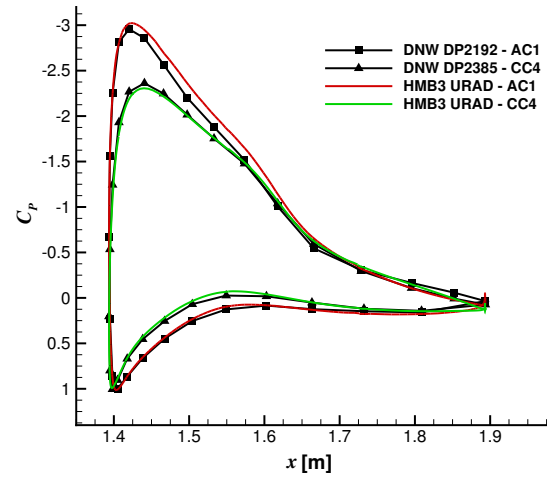

 (a) SYM-TOP, section  $y=0$  mm.

 (b) FW-A, section  $y=280$  mm.

 (c) FW-B, section  $y=490$  mm.

 (d) FW-C, section  $y=700$  mm.

Figure 8.24:  $C_p$  profile comparisons between CFD and experiments [91] on the fixed and tiltable wings of the ERICA tiltrotor for the aeroplane and transition corridor configurations (sections SYM-TOP, FW-A, FW-B, and FW-C).



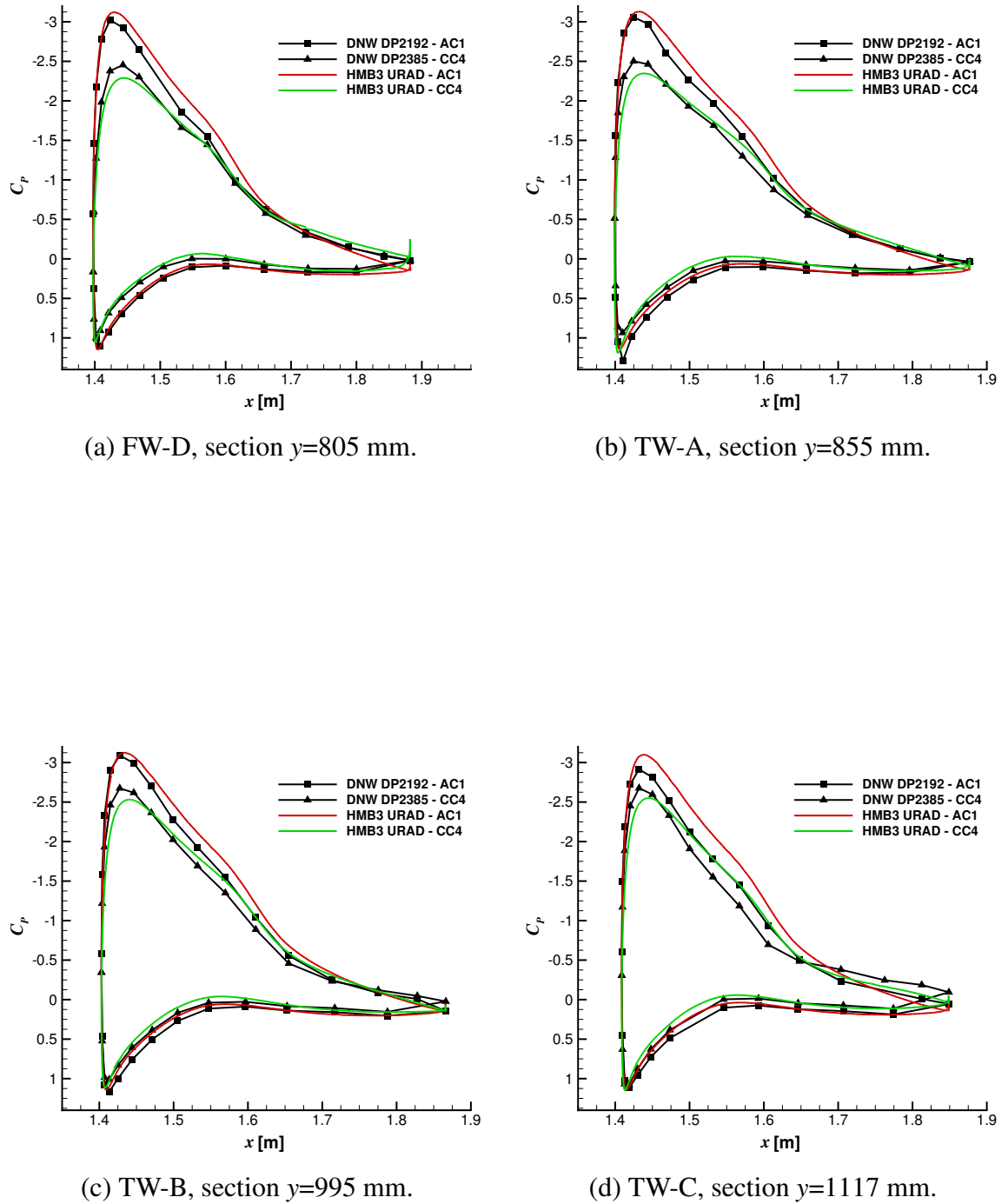
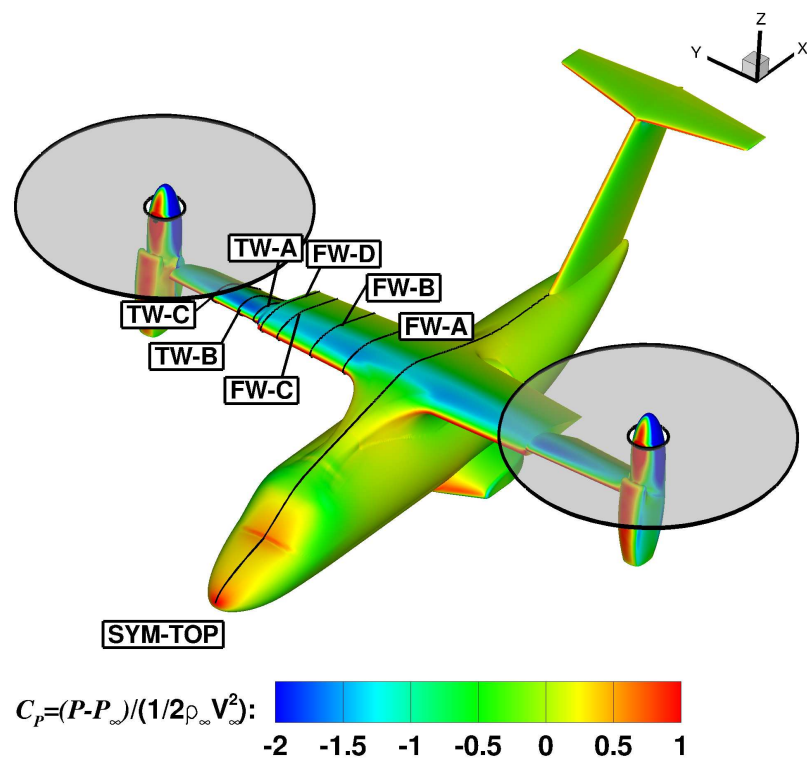
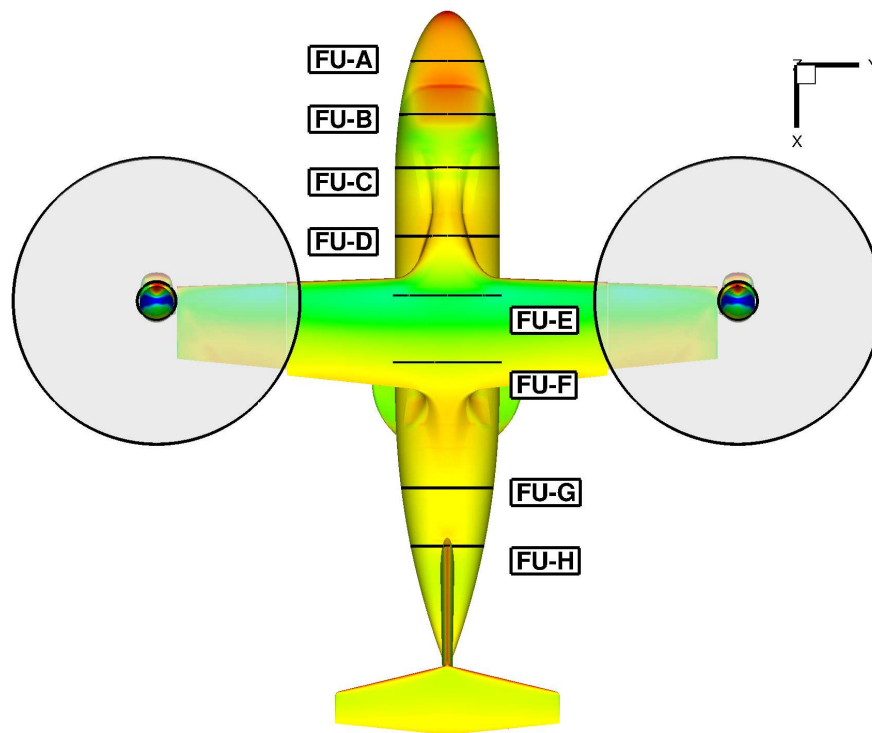


Figure 8.25:  $C_p$  profile comparisons between CFD and experiments [91] on the fixed and tiltable wings of the ERICA tiltrotor for the aeroplane and transition corridor configurations (sections FW-D, TW-A, TW-B, and TW-C).



(a) Sections on the fixed and tiltable wings.



(b) Sections on the fuselage.

Figure 8.26: Cross-sections selected for comparisons between CFD and experiment [91] on the fixed and tiltable wings, and fuselage of the ERICA tiltrotor for the helicopter configuration.

Considering the pressure coefficient at the centre-line of the fuselage (Figure 8.27 (a)), the DNW experiments suggest absence of flow separation. The CFD results are in a good agreement with experiments, and the suction peak is well represented ( $C_{P\text{ HMB}} = 1.28$ ;  $C_{P\text{ DNW}} = 1.26$ ) with a small discrepancy of 1.58%. The same analysis can be done for the inner fixed wing (see Figure 8.27 (b)), where the suction peak and pressure plateau at the trailing edge are well captured. It is noticeable that discrepancies appear to be present, when sections on the fixed wing (Figures 8.27 (c) and (d)) are analysed. In fact, the CFD predictions reveal an under-predicted suction peak compared to the experiment, even if the pressure plateau distribution is well captured. The same behaviour was found in the aerodynamic interaction zone (Figure 8.28). It can be seen that experiments seem to predict separated flow at the further station on the tiltable wing (Figure 8.28 (d)). The CFD predictions did not capture this the region of recirculation. To conclude, the performance analysis of the ERICA tiltrotor for the HC3 configuration, a comparison of  $C_P$  profile have also been performed, considering eight cross-sections on the fuselage (Figures 8.29 and 8.30). As can be seen, all CFD curves are in close agreement with the experiments. This agreement is still fair for stations located behind the fixed wing and near the sponsons (Figure 8.30 (b)).

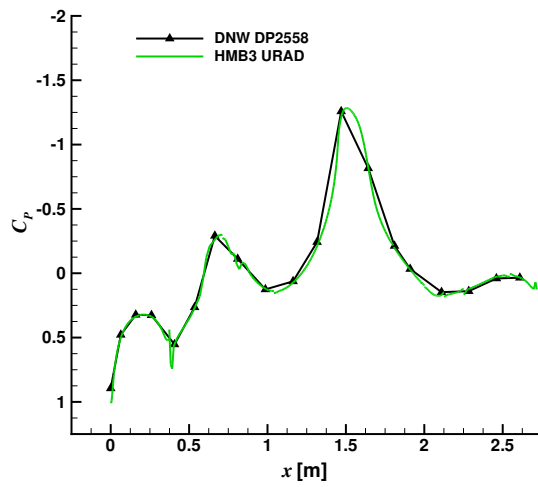
## 8.5 Summary of Findings

This work demonstrated the capability of the HMB CFD to predict tiltrotor flows. The 1:5 model-scale ERICA tiltrotor was considered for validation, where three flight configurations (aeroplane, transition corridor, and helicopter) were selected. The main conclusions are:

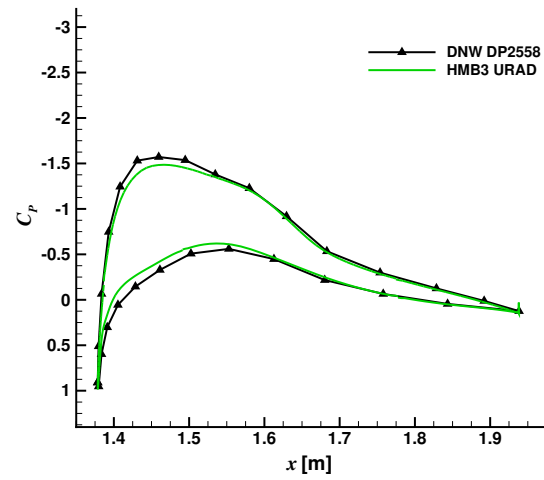
- For the AC1 case, the aerodynamic interactions in the region of the nacelle and tiltable wing were captured by the FRB results, and the CFD with URAD and NURAD models also produced adequate estimates of the wing loads. The effect of the model support was also investigated and it was found that sting-mounted cases was less intrusive. The overall lift and drag of the vehicle were not, however, captured accurately.
- For the CC4 case,  $C_P$  comparisons between CFD and experiments showed good agree-

ment for all stations investigated with small discrepancies between FRB and URAD results.

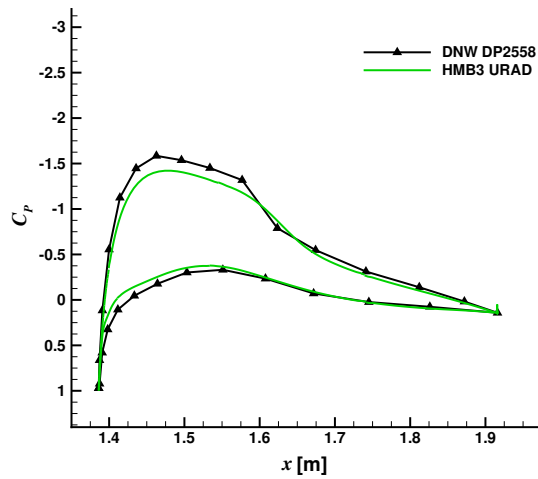
- Regarding the HC3 case, CFD results under-estimated the distribution of surface pressure coefficient at the aerodynamic interaction zone. The reason of this discrepancy may be due to lack of exact trimmed conditions.
- The integrated loads agree less well between CFD and tests than the surface  $C_p$  distributions. The data of ERICA is new and corrections may be necessary.



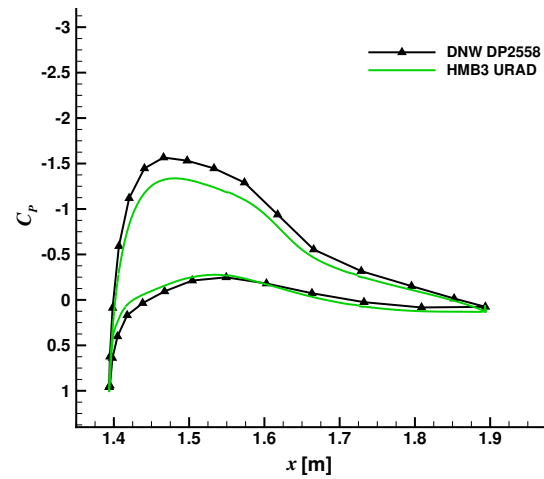
(a) SYM-TOP, section  $y=0$  mm.



(b) FW-A, section  $y=280$  mm.



(c) FW-B, section  $y=490$  mm.



(d) FW-C, section  $y=700$  mm.

Figure 8.27:  $C_p$  profile comparisons between CFD and experiment [91] on the fixed and tiltable wings of the ERICA tiltrotor for the helicopter configuration (stations SYM-TOP, FW-A, FW-B, and FW-C).

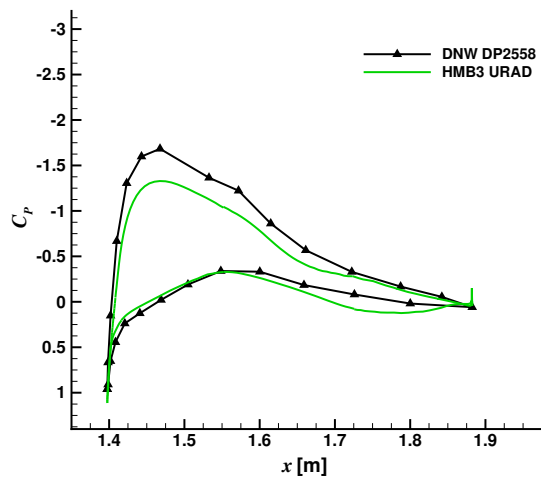
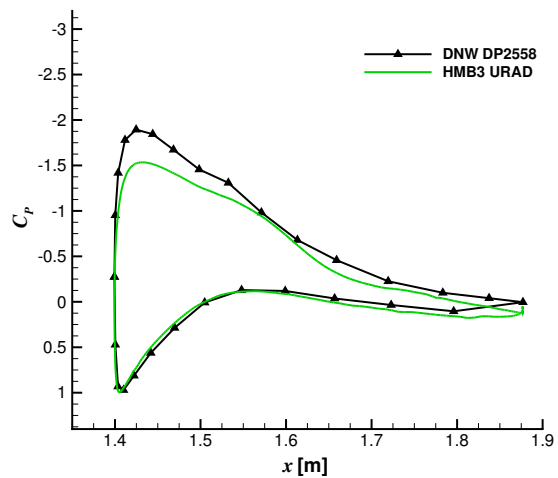
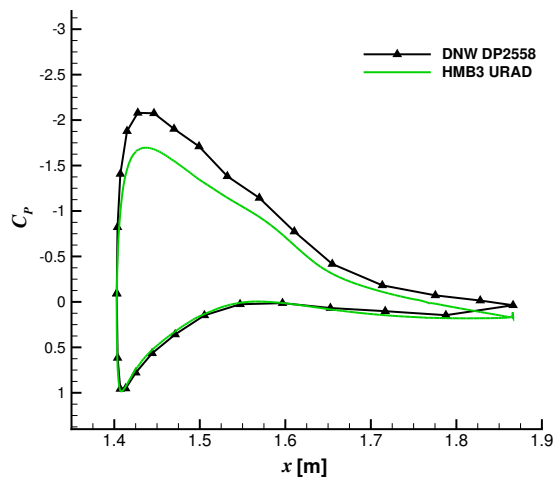
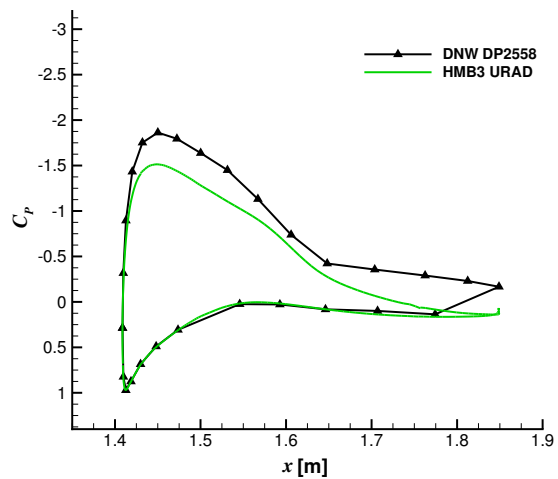

 (a) FW-D, section  $y=805$  mm.

 (b) TW-A, section  $y=855$  mm.

 (c) TW-B, section  $y=995$  mm.

 (d) TW-C, section  $y=1117$  mm.

 Figure 8.28:  $C_p$  profile comparisons between CFD and experiment [91] on the fixed and tiltable wings of the ERICA tiltrotor for the helicopter configuration (sections FW-D, TW-A, TW-B, and TW-C).

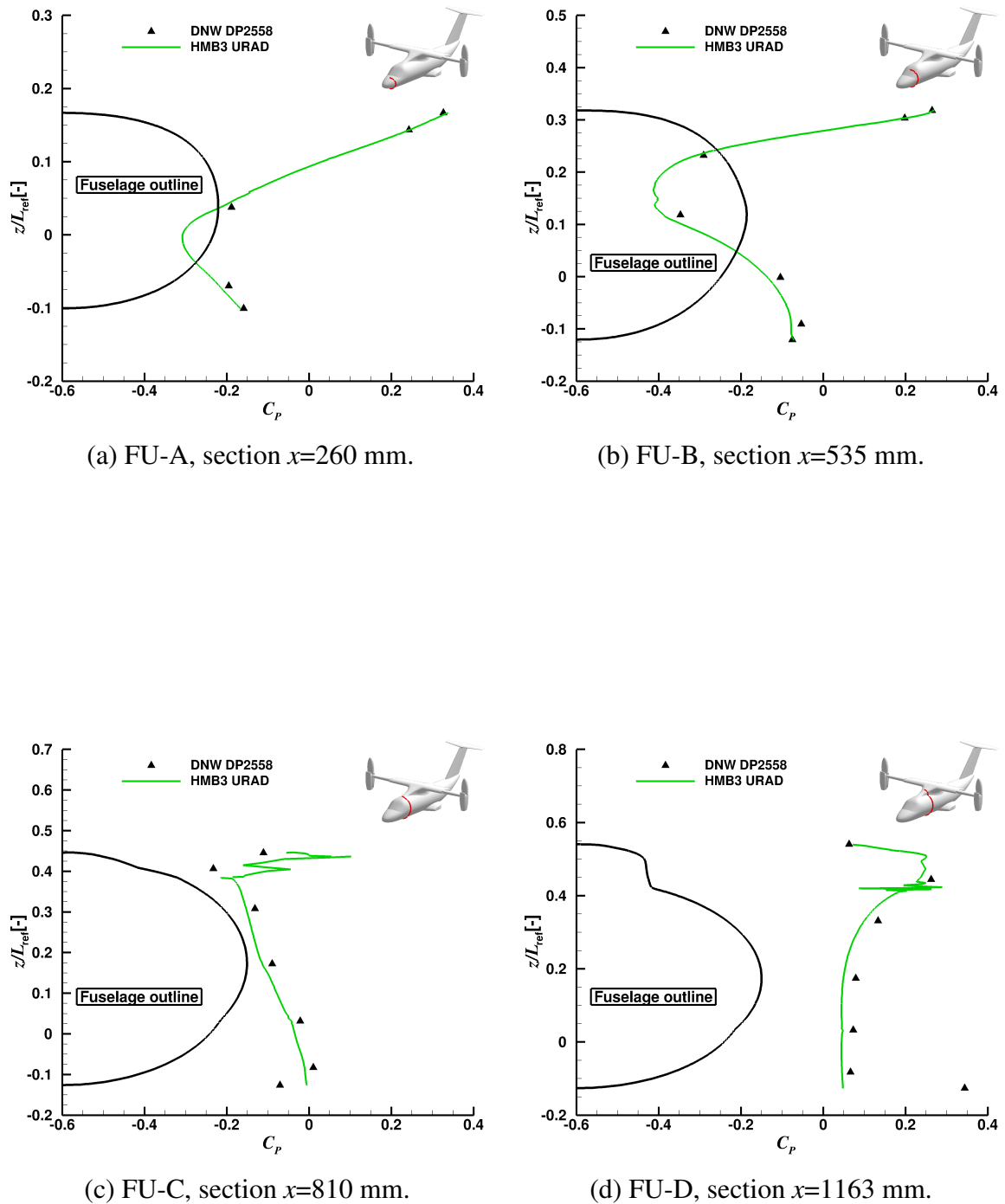


Figure 8.29:  $C_p$  profile comparisons between CFD and experiment [91] on the fuselage of the ERICA tiltrotor for the helicopter configuration (stations FU-A, FU-B, FU-C, and FU-D).

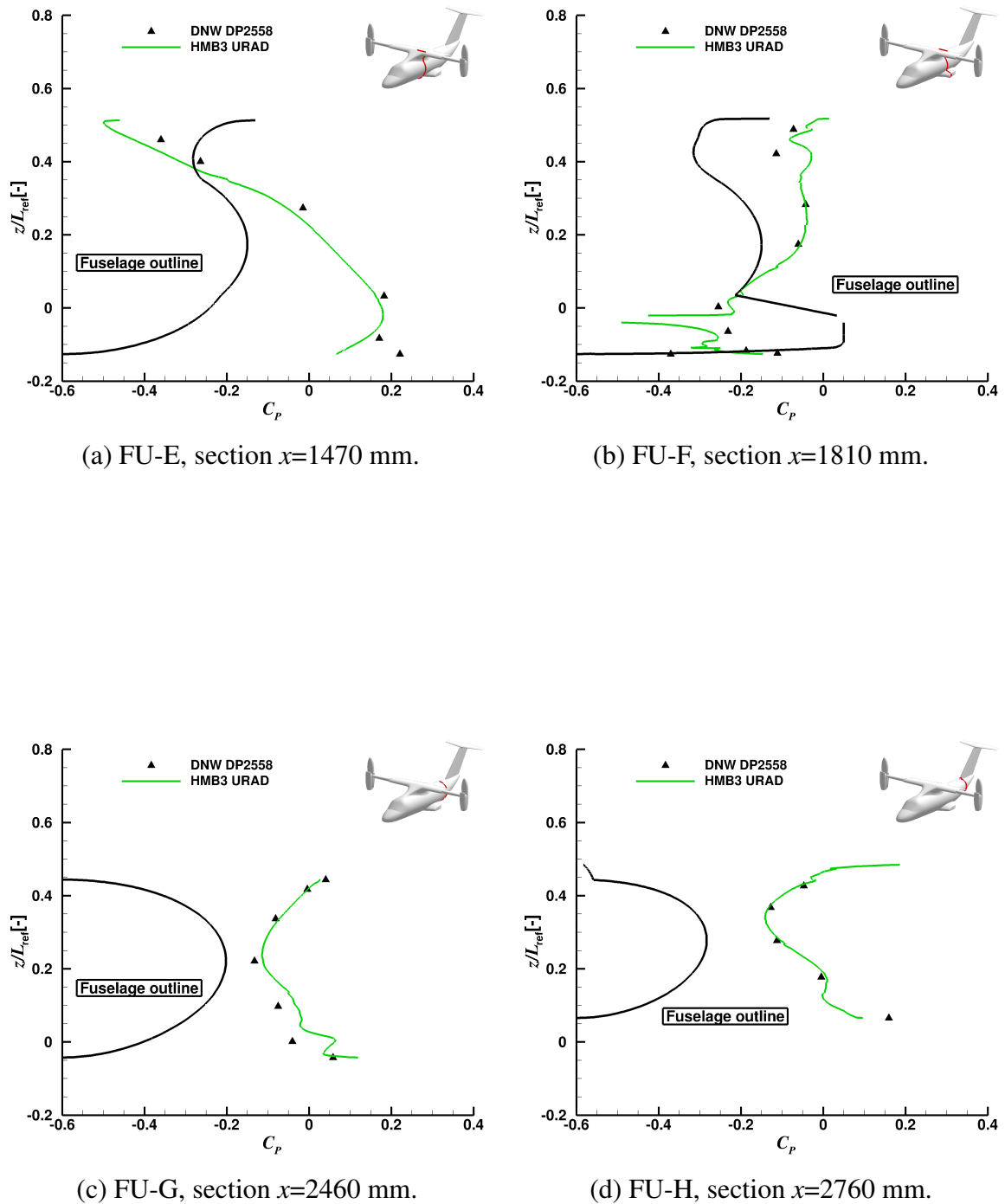


Figure 8.30:  $C_p$  profile comparisons between CFD and experiment [91] on the fuselage of the ERICA tiltrotor for the helicopter configuration (stations FU-E, FU-F, FU-G, FU-H).



## Chapter 9

# Aerodynamic Optimisation of Tiltrotor Blades

### 9.1 Introduction

The aerodynamic design of tiltrotor blades is a challenging task, requiring the best compromise in performance between hover and propeller modes [115, 116]. In hover, the blade aerodynamics is characterised by strong interactions with the rotor wake, resulting in a significant effect on the induced and total drag [17]. The propeller mode, on the other hand, is dominated by strong compressibility effects, especially at high advance ratio, resulting in a prominent contribution of the profile and wave drag components [117]. As a consequence, to accurately capture the effect of the blade shape on the optimal rotor design, the use of high-fidelity flow models is required. Unlike for helicopter and propeller blades, the aerodynamic optimisation of tiltrotor blades has not been the subject of considerable research. The present work analyses the contribution of the main blade shape parameters to the optimal performance of the tiltrotor using high-fidelity computational fluid

---

This work is published in A. Jimenez-Garcia *et al.*, Tiltrotor CFD Part II - Aerodynamic Optimisation of Tiltrotor Blades, The Aeronautical Journal, 121 (1239), 2017, 611-636, doi: 10.1017/aer.2017.21

dynamics. It also demonstrates the use of gradient-based optimisation and the discrete adjoint for the efficient design of tiltrotor blades.

Aerodynamic optimisation needs large computational resources, since each design point requires the solution of the Navier-Stokes equations. The choice of the optimisation algorithm is therefore crucial. The optimisation algorithms can be classified in gradient-based or gradient-free methods. Gradient-based methods usually require a limited number of flow evaluations [118], and this makes them particularly attractive for complex aerodynamic optimisation problems. They need, however, the computation of flow derivatives with respect to the design variables, which can be an expensive task, unless the adjoint method is used. Also, gradient-based methods are local in nature, and they do not guarantee to find the global optimum. On the other hand, gradient-free methods are simpler to implement, because they do not require flow derivatives, and some of them ensure to reach the global optimum. Nevertheless, they typically need two to three orders of magnitude more objective function evaluations than gradient-based methods [119]. Gradient-free methods are therefore effective only when coupled with low-fidelity, or reduced-order models, for which the evaluation of functionals depending upon the flow solution is cheap. It can be stated that gradient-free methods are more appropriate to the preliminary design of the aircraft, while gradient-based methods, coupled with high-fidelity flow models, may be used at more advanced stages of the design process.

For a tiltrotor, its blades must be designed to efficiently work both in helicopter and aeroplane modes. This makes their design particularly challenging, because the aerodynamic characteristics of helicopter and propeller blades are significantly different, and the optimal values of the main shape parameters (*e.g.* twist and chord distributions, sweep, anhedral, etc.) can be different in the two cases. So, tiltrotor blade design requires the solution of a multi-objective optimisation problem, where the objective functions are suitable measures of the performance at selected flight conditions in both helicopter and aeroplane modes. A multi-objective optimisation of the ER-ATO blade in conjunction with a gradient based-optimiser was put forward by Leon *et al.* [131], seeking to maximise the figure of merit in hover and minimise the rotor power in forward flight. Wilke [132] applied single and multi-objective techniques for the variable-fidelity optimisation of

a helicopter rotor. Single optimisations of hover and forward flight blades showed a detriment in performance when used in opposite flight conditions. However, the shape obtained with the multi-objective optimisation technique was a compromised design of both antagonistic objectives. To reduce the computational cost, the multi-objective optimisation can be reduced to a single-objective optimisation by considering the weighted sum of the objective functions at each flight condition. Higher weights are assigned to flight conditions that cover the most part of the typical tiltrotor mission. This strategy is usually referred to as “multi-point” optimisation.

In this chapter, we perform both single and multi-point optimisations of the XV-15 tiltrotor blade with different sets of design variables, to provide a breakdown of the impact that different geometrical features have on the optimal design. This approach can give engineers more insight in tiltrotor blade design. The employed optimisation framework is based on the Least-Square Sequential Quadratic Programming (SLSQP) algorithm [205], coupled with the HMB3 CFD solver and to a discrete adjoint method with full accounting of the Menter’s  $k-\omega$  SST turbulence model coupling terms. The linear system for the adjoint variable is solved using a Flexible Generalised Minimum Residual solver with Deflated Restarting (FGMRES-DR) nested with GMRES-DR as a pre-conditioner [203]. To reduce the computational cost, we solved the hover and propeller flows by casting the equations as a steady-state problem in a noninertial reference frame. Rigid rotor blades were considered in this study, based upon the good agreement obtained with the experiments as shown in chapter 7. Results are presented for a range of design points, which include medium and high thrust hovering flight conditions, and a high axial ratio propeller condition.

The structure of this chapter is as follows: section 9.2 describes the optimisation framework, the objective and constraint functions, and the blade shape parametrisation technique. Section 9.3 presents the numerical results. At first, single-point optimisation results are shown, to investigate the effect of the twist and chord/sweep distributions on the helicopter and aeroplane modes tiltrotor performance. Then, multi-point optimisation results are presented. Finally, conclusions are drawn in section 9.4.

## 9.2 Optimisation Framework

### 9.2.1 Objective and Constraint Functions

The objective functions for the tiltrotor blade optimisation should be suitable measures of the performance in helicopter and aeroplane modes. For the helicopter mode, the FoM is used as an indicator of the rotor efficiency, because it represents the ratio between the ideal absorbed power in hover predicted by momentum theory and the actual absorbed power:

$$\text{FoM} = \frac{C_T^{3/2}}{\sqrt{2}C_Q}. \quad (9.1)$$

In aeroplane mode, on the other hand, we use the propeller propulsive efficiency, which is the ratio of the useful power output of the propeller to the absorbed power:

$$\eta = \frac{C_T V_\infty}{C_Q V_{\text{tip}}}. \quad (9.2)$$

After the preliminary sizing of the tiltrotor, the rotor thrust in hover and a cruise conditions are typically fixed. Therefore, the optimisation should not alter these values, and a constraint on the thrust must be imposed. It follows that the problem of maximising the FoM in helicopter mode and the propeller propulsive efficiency in aeroplane mode can be seen as a minimisation problem for the torque coefficient in either cases. The single-point design problem then reads:

$$\begin{cases} \text{Minimise } I = \frac{C_Q}{\bar{C}_Q} \text{ subject to} \\ C_T = \bar{C}_T \end{cases} \quad (9.3)$$

Note that the torque coefficient  $C_Q$  is normalised by the baseline rotor torque coefficient  $\bar{C}_Q$ , so that the cost function  $I$  is  $O(1)$ . The quantity  $\bar{C}_T$  denotes the thrust coefficient of the baseline rotor.

For the multi-point optimisation of the tiltrotor, a composite objective function  $I_{\text{mp}}$  is constructed as a weighted sum of the cost functions associated to  $N$  selected flight conditions, representing both helicopter and aeroplane operational modes:

$$I_{\text{mp}} = \sum_{i=1}^N w_i \frac{C_{Q,i}}{\bar{C}_{Q,i}}, \quad (9.4)$$

where  $w_i$ ,  $i = 1, \dots, N$  represent the weighting factors, which are chosen so that

$$\sum_{i=1}^N w_i = 1. \quad (9.5)$$

The multi-point design problem is then stated as follows:

$$\begin{cases} \text{Minimise } I_{\text{mp}} \text{ subject to} \\ C_{T,i} = \bar{C}_{T,i}, \quad i = 1, \dots, N \end{cases} \quad (9.6)$$

Any number  $N$  of flight conditions can be considered for the multi-point optimisation. For instance, it is possible to include low and high disk loading cases in hover, and low and high speed cases for the aeroplane mode. However, in the present work we consider only the case  $N = 2$ , with one hovering and one aeroplane mode condition. The objective function is then written as:

$$I_{\text{mp}} = w_{\text{hm}} \frac{C_{Q,\text{hm}}}{\bar{C}_{Q,\text{hm}}} + w_{\text{am}} \frac{C_{Q,\text{am}}}{\bar{C}_{Q,\text{am}}}, \quad (9.7)$$

where the subscript “hm” refers to the helicopter mode and the subscript “am” refers to the aeroplane mode.

### 9.2.2 Optimisation Tools Chain

An economic way to obtain the flow gradients with CFD is the adjoint method, which reduces the cost of evaluating derivatives of the objective function with respect to the design variables to about the cost of the base flow solution, regardless of the number of design variables. The underlying idea is to write explicitly the cost function  $I$  in terms of the flow variables  $\mathbf{W}$  and of the design variables  $\boldsymbol{\alpha}$ , that is,  $I = I(\mathbf{W}(\boldsymbol{\alpha}), \boldsymbol{\alpha})$ . The flow variables are subject to satisfy the fluid dynamics governing equations (*e.g.* the Reynolds Averaged Navier–Stokes equations) written in compact form as:

$$\mathbf{R}(\mathbf{W}(\boldsymbol{\alpha}), \boldsymbol{\alpha}) = 0. \quad (9.8)$$

Formally, taking the derivative of  $I$  with respect to  $\boldsymbol{\alpha}$  we obtain:

$$\frac{dI}{d\boldsymbol{\alpha}} = \frac{\partial I}{\partial \boldsymbol{\alpha}} + \frac{\partial I}{\partial \mathbf{W}} \frac{\partial \mathbf{W}}{\partial \boldsymbol{\alpha}}. \quad (9.9)$$

By introducing the adjoint variable  $\boldsymbol{\lambda}$  as the solution of the following linear system:

$$\left(\frac{\partial \mathbf{R}}{\partial \mathbf{W}}\right)^T \boldsymbol{\lambda} = -\left(\frac{\partial I}{\partial \mathbf{W}}\right)^T, \quad (9.10)$$

equation (9.9) can be rewritten as:

$$\frac{dI}{d\boldsymbol{\alpha}} = \frac{\partial I}{\partial \boldsymbol{\alpha}} + \boldsymbol{\lambda}^T \frac{\partial \mathbf{R}}{\partial \boldsymbol{\alpha}}, \quad (9.11)$$

which is known as the *dual* form of the sensitivity equation. The computation of the derivatives of the functional  $I$  is reduced to the solution of the linear sensitivity problem (9.10)-(9.11). The computational cost scales with the number of outputs, since the right-hand side of the linear system (9.10) depends on  $I$ , but it is independent of the input parameters. The linear system (9.10) is usually hard to compute, since the Jacobian matrix  $\partial \mathbf{R} / \partial \mathbf{W}$  is characterised by high stiffness, and the solution time can be comparable to that of the base flow.

The HMB3 flow solver embeds two methods for solving the linear system (9.10). The first is an implicit, fixed-point iteration scheme [204], while the second is a nested FGMRES-DR/GMRES-DR Krylov-subspace method [203]. Both adjoint solvers can be interfaced to a gradient based optimiser to efficiently solve a design problem, which amounts in minimising an objective function  $I$  (*e.g.* drag, power, etc.), possibly subject to constraints (*e.g.* fixed lift, fixed thrust, etc.). In the current implementation, the optimisation problem is solved using a Least-Square Sequential Quadratic Programming algorithm [205].

The design optimisation procedure is described in Figure 9.1, and can be summarised as follows.

- 1 The flow around the aerodynamic surface  $S$  to be optimised (*e.g.* aerofoil, blade, etc.) is solved. For the first iteration, this solution represents the baseline flow solution.
- 2 The objective function  $I$  and the constraints  $g_j$ ,  $j \in \{1, \dots, m\}$ ,  $h_k$ ,  $k \in \{1, \dots, p\}$ , are evaluated from the flow solution.
- 3 The adjoint problem is solved to compute the gradients  $dI/d\boldsymbol{\alpha}$ ,  $dg_j/d\boldsymbol{\alpha}$ ,  $j \in \{1, \dots, m\}$ ,  $dh_k/d\boldsymbol{\alpha}$ ,  $k \in \{1, \dots, p\}$ .

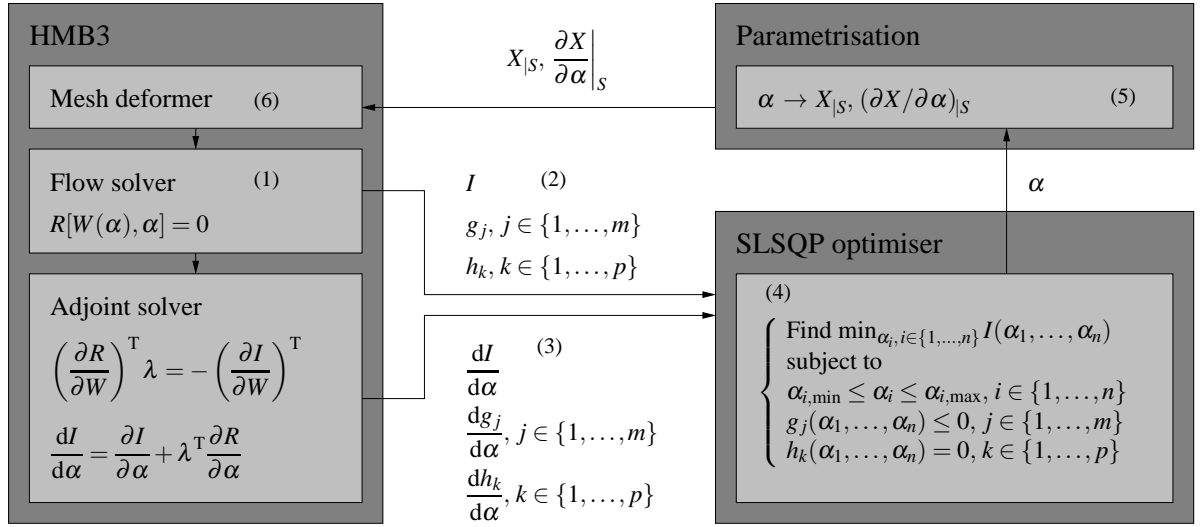


Figure 9.1: Flow chart of the optimisation process. Steps of the method are shown in brackets ().

- 4 The cost functional, the constraints and their gradients are fed to the gradient based optimiser, which produces a new set of design variables  $\alpha$ , corresponding to a design candidate in the search direction.
- 5 Based on the new values of the design variables  $\alpha$ , the point vector  $X|_S$  describing the surface  $S$  is updated, as well as the derivatives of these points with respect to the design variables  $(\partial X / \partial \alpha)|_S$ .
- 6 A mesh deformation algorithm, based on Inverse Distance Weighting (IDW) [203], computes the new volume mesh points positions  $X$ , and the derivatives  $\partial X / \partial \alpha$ . A new surface  $S$  is generated to close the cycle.

Steps 1–6 are repeated for several design cycles until convergence criteria are met. These criteria include checks on the objective function gradient module, and checks on the variation of the design variables and of the objective function between successive cycles of the optimisation process.

### 9.2.3 Parametrisation Technique

The parametrisation technique used here allows for variations of the blade twist, chord and sweep distributions (see Figure 9.2). The shape of the blade sections, coning and collective pitch angles, however, were not accounted for in this work. The twist parametrisation considers the perturbation of the blade sectional angle of attack with respect to the baseline blade. This twist perturbation  $\Delta\Theta$  is expressed in terms of a Bernstein polynomial expansion, due to its simplicity and the smoothness of the resulting design space:

$$\Delta\Theta(\hat{r}) = \sum_{m=0}^n \alpha_m K_{m,n} \hat{r}^m (1 - \hat{r})^{n-m} \quad (9.12)$$

where  $\hat{r}$  is the nondimensional coordinate along the blade span, which has value 0 at the rotation axis, and 1 at the blade tip. The symbol  $K_{m,n}$  denotes the binomial coefficient, which is defined as:

$$K_{m,n} = \binom{n}{m} = \frac{n!}{m!(n-m)!}. \quad (9.13)$$

The polynomial expansion coefficients  $\alpha_m$ ,  $m = 0, \dots, n$ , represent the design variables for the twist. In all the presented cases, seven design variables were used to represent the twist perturbation ( $\alpha_0, \dots, \alpha_6$ ). The values of the design variables for the twist perturbation are limited to the range  $\pm 5^\circ$ .

Two design variables,  $\alpha_7$  and  $\alpha_8$ , were used to describe the variation of the blade chord. The former represents the relative variation of the blade chord between  $\hat{r} = 0.25$  and  $\hat{r} = 0.80$ . The latter is the relative chord variation at the tip, and a parabolic shape is imposed between  $\hat{r} = 0.8$  and  $\hat{r} = 1$ . The blade root chord, at  $\hat{r} = 0.2$ , is kept fixed, and the chord variation is interpolated linearly between  $\hat{r} = 0.2$  and  $\hat{r} = 0.25$ . The design variable  $\alpha_7$  is limited to  $1 \pm 15\%$ , while  $\alpha_8$  can vary in the range  $1 \pm 50\%$ .

Finally, one design variable  $\alpha_9$  is used to control the blade sweep distribution between  $\hat{r} = 0.8$  and  $\hat{r} = 1$ . Its value represents the sweep at  $\hat{r} = 1$ , and a parabolic sweep distribution is imposed in the range  $[0.8, 1]$ . The value of the design variable  $\alpha_9$  is limited to  $[-0.5c, 0.15c]$ , where a positive number denotes a shift of the blade section in the direction pointing from trailing



to leading edge. Table 9.1 lists the design variables  $\alpha$  along with their baseline and boundary values.

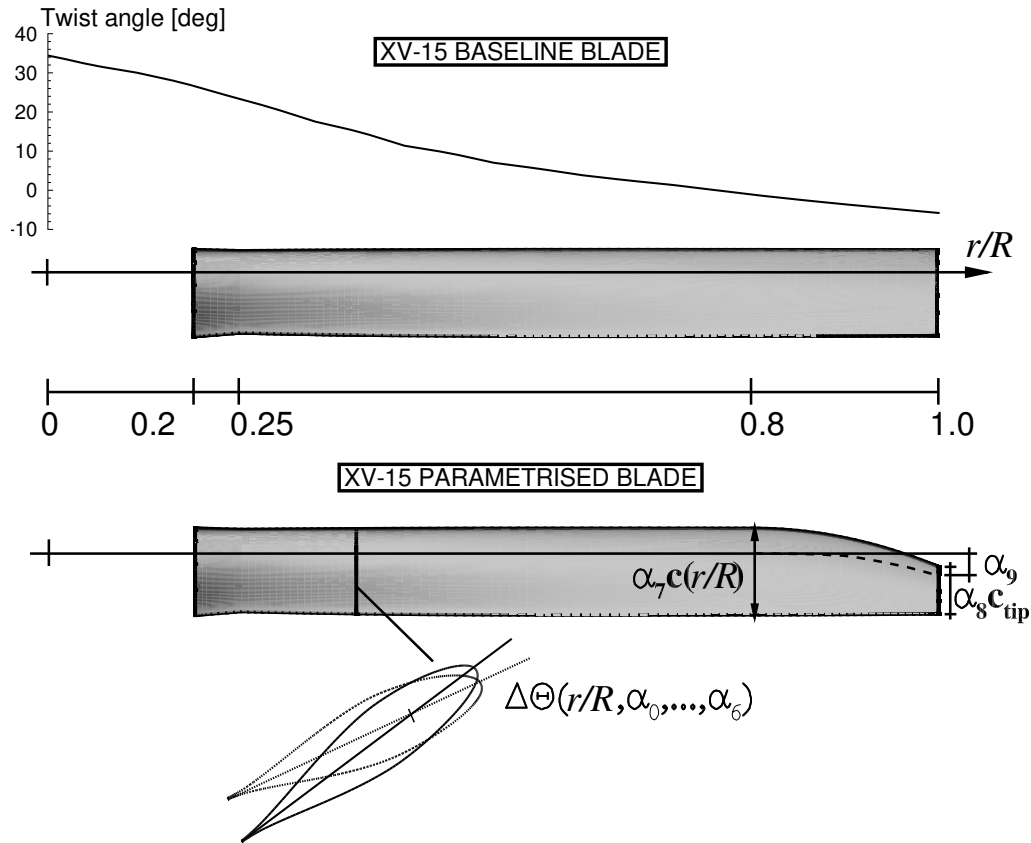


Figure 9.2: Schematic view of the twist, chord, and sweep parametrisation for the XV-15 tiltrotor blade.

Table 9.1: Design variables along with their baseline and boundary values employed to describe the variation of the blade twist, chord, and sweep distributions.

Design variable	Parameter	Baseline value	Boundaries
$\alpha_0$	Twist	$0^\circ$	$\pm 5^\circ$
$\alpha_1$	Twist	$0^\circ$	$\pm 5^\circ$
$\alpha_2$	Twist	$0^\circ$	$\pm 5^\circ$
$\alpha_3$	Twist	$0^\circ$	$\pm 5^\circ$
$\alpha_4$	Twist	$0^\circ$	$\pm 5^\circ$
$\alpha_5$	Twist	$0^\circ$	$\pm 5^\circ$
$\alpha_6$	Twist	$0^\circ$	$\pm 5^\circ$
$\alpha_7$	Chord	$1.0c$	$\pm 0.15c$
$\alpha_8$	Chord	$1.0c$	$\pm 0.50c$
$\alpha_9$	Sweep	$0c$	$[-0.5c, 0.15c]$

## 9.3 Results and Discussion

The performance of the XV-15 rotor can be adequately captured by the employed HMB3 solver as demonstrated in chapter 7 of this thesis.

### 9.3.1 Ideal Twist Using Blade Element Theory

Blade element theory [10] refers to an aerodynamic loading distribution for minimum induced power (which ignores profile and wake losses), and demonstrates an “ideal” rotor blade twist of the form:

$$\Theta_{\text{twist}}^{\text{IP}} = \Theta_{\text{nom}} \left( \frac{1}{r/R} - 4/3 \right). \quad (9.14)$$

A range of these distributions (herein referred as “ideal” twist for convenience) is shown in Figure 9.3 as function of the nominal twist  $\Theta_{\text{nom}}$ . However, these ideal distributions generate impractical inboard values and so a minor modification can be made (herein referred as modified “ideal” twist). Blade element theory evaluations reveal that such approximations have a negligible effect on the hover and propeller performance for low and moderate twist, whilst at the higher twist values prevent excessive local incidences at the inboard blade sections. Consequently, efficient inboard aerofoils can be designed for these reduced incidence ranges, and in reality the result is higher performance than what would be achieved with the unmodified theoretical ideal distribution. The linear inboard approximation is therefore confirmed as reasonable.

Blade element theory evaluations for the rotor performance of these twist distributions, reveal a conflicting requirement between the hover and propeller design conditions; there will exist an optimum ideal twist distribution for a tiltrotor blade in hovering conditions and a different, much higher, twist distribution for the most efficient operation in propeller mode. For a tiltrotor aircraft, it is difficult to imagine any scenario where one of these distributions would completely “win” over the other and therefore it would seem logical for a rotor designer to seek some compromise which would provide an acceptable performance trade between these two distinct aircraft operating conditions.

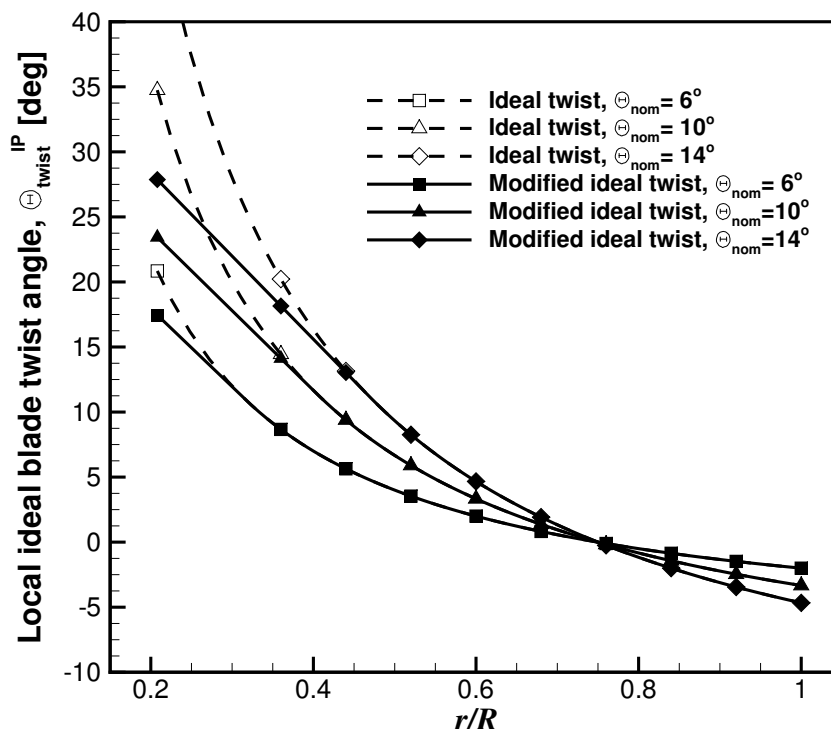


Figure 9.3: Modified “ideal” twist distributions for minimum power with a linear inboard approximation.

An optimum concept distribution can be derived which combines the best inboard distribution for hover conditions (labelled with modified ideal twist  $\Theta_{nom} = 12^\circ$  in Figure 9.4) with an increased outboard (and overall) blade twist which provides the propeller efficiency (labelled with modified ideal twist  $\Theta_{nom} = 24^\circ$  in Figure 9.4). The extent to which the outboard blade is twisted will depend on the required aircraft cruise speeds and the trade-off with hover performance. In reality, the increased outboard twist is often beneficial for the hover case since it off-loads the blade tip, postponing flow separation and stall that are not accounted for in the basic theory.

The theory is based on the idea of a minimum induced power which forms the majority of the total power consumption for a tiltrotor blade in hover with very high disk loading and so the overall rotor performance is very sensitive to the twist distribution (i.e. big returns for relatively small twist variations). Despite that BET does not resolve the blade tip vortex, the combined twist distribution is a good starting point. However, for an actual design, further refinements would of course follow, for example to accommodate design choices for the:

- Tip region (based on detailed simulations and tip shape selection).
- Root region (based on the imposed constraints from blade structural design).
- Secondary performance requirements (autorotation, acoustics).

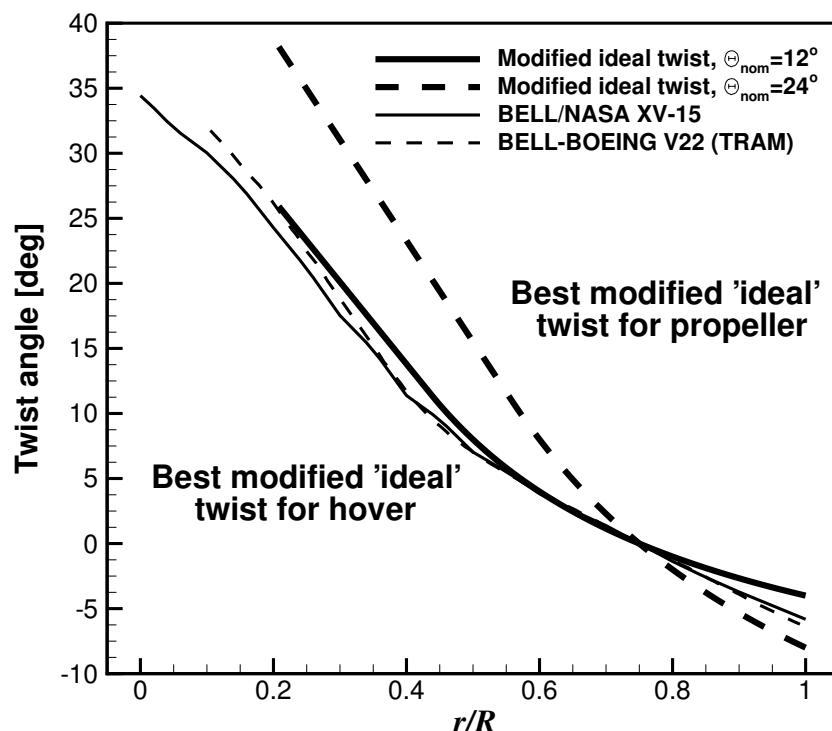


Figure 9.4: The conflicting tiltrotor blade twist requirements for efficient operation in two distinct flight modes and comparison with two successful tiltrotor blade designs [253, 250].

In addition, the aerofoil family, their radial distribution and the blade planform (which have been fixed for the purposes of this discussion) will also have a major influence on the final performance.

In Figure 9.4, the aforementioned twist distribution combining the inboard (based on hover) and outboard (based on propeller) twists, is compared with two successful tiltrotor blade designs of the Bell-Boeing V-22 (TRAM) and Bell/NASA XV-15 and the similarities are clear for the inboard distributions (probably set for best hover performance) and with the outboard twist apparently set for whichever propeller conditions were important for the specific aircraft operating conditions.

### 9.3.2 XV-15 Blade Mesh

A mesh generated using the chimera technique was used for the design study of the XV-15 rotor, and was composed of a periodic background mesh and a component mesh for the blade. The use of an overset grid method allowed to employ the same mesh for the helicopter and the aeroplane modes, since the blade pitch angle could be easily changed by rotating the chimera component mesh containing the blade. This mesh was used in the chapter 7 of this thesis to analyse the aerodynamic performance of the XV-15 rotor. It was found that, despite the relatively small size (6.2 million cells per blade), there was a good correlation between the experiments and the CFD predictions. For this reason, the same mesh was also employed for the aerodynamic optimisation study.

Table 9.2 shows a breakdown of the number of cells (per blade) used for the background mesh, and for the body-fitted mesh around the XV-15 rotor blade. A more detailed description of the computational domain, boundary conditions, and meshing parameters can be found in chapter 7.

Table 9.2: Meshing parameters for the XV-15 mesh rotor blade.

Background mesh size (cells)	2.6 million
Blade mesh size (cells)	3.6 million
Overall mesh size (cells)	6.2 million
Height of first mesh layer at blade surface	$1.0 \times 10^{-5} c_{\text{ref}}$

### 9.3.3 Design Cases

Representative flight conditions in hover and propeller modes were selected from the available literature on the XV-15 [73]. For the hover mode, the blade-tip Mach number was set to 0.69, and two blade pitch angles were considered,  $7^\circ$  and  $10^\circ$ , corresponding to a medium and a high disk loading, respectively. The Reynolds number, based on the reference blade chord of 14 inches and on the tip speed, was  $4.95 \times 10^6$ . Cruise condition was modelled at 20,000 ft (ISA+0°), with a tip Mach number of 0.60, axial ratio 0.759 and pitch angle of  $47^\circ$ . The Reynolds number for this case

was  $2.2 \times 10^6$ , again based on the reference blade chord and rotor tip speed (with no account for the axial velocity).

All flow solutions were computed by solving the RANS equations, coupled with Menter's  $k-\omega$  SST turbulence model [191]. The flow equations were integrated with the implicit dual-time stepping method of HMB3, using a pseudo-time CFL equal to 4 for the helicopter mode computations, and equal to 2 for the aeroplane mode. The linear system (9.10) for the adjoint variable was solved by means of the nested Krylov-base solver FGMRES-DR(300,100)-GMRES(40), where the number of inner GMRES iterations was limited to 40. Typically, 2500 outer iterations were necessary to drop the residual by 6 orders of magnitude (as found to be necessary in previous works [204]) for the hover adjoint solutions, while about 300 iterations were necessary to reach the same convergence level for the aeroplane mode adjoint solutions.

Table 9.3: Design cases considered in the aerodynamic optimisation study.

Design case	$\theta_{75, \text{hm}}$	$\theta_{75, \text{am}}$	Twist	Chord	Sweep	$w_{\text{hm}}$	$w_{\text{am}}$
HM1	$7^\circ$	-	✓			1	0
HM2	$10^\circ$	-	✓			1	0
HM3	$10^\circ$	-	✓	✓	✓	1	0
AM1	-	$47^\circ$	✓			0	1
AM2	-	$47^\circ$	✓	✓	✓	0	1
MP1	$10^\circ$	$47^\circ$	✓			1/2	1/2
MP2	$10^\circ$	$47^\circ$	✓			1/3	2/3
MP3	$10^\circ$	$47^\circ$	✓	✓	✓	1/3	2/3

Table 9.3 lists the design cases considered for the aerodynamic optimisation of the XV-15 tiltrotor blade, along with the employed design variables (twist, chord, and sweep) and the objective function weights for the case of multi-point optimisation ( $w_{\text{hm}}$  for the helicopter mode, and  $w_{\text{am}}$  for the aeroplane mode). Cases HM1 and HM2 evaluate the impact of the twist distribution on the hovering performance, while HM3 the potential contribution of the chord and sweep. Likewise, cases AM1 and AM2 show the effect of twist, combined with that of chord and sweep, on the propeller performance. The possibility of selecting a twist distribution that is optimal for both hover and aeroplane modes is investigated through the multi-point design cases MP1 and MP2. The two cases differ only in the selection of the weights associated to the two operational conditions in

the composite objective function. Finally, for case MP3 of Table 9.3, the effect of the chord and sweep is accounted for in the multi-point optimisation.

### 9.3.4 Helicopter Mode

The single-point design cases for the helicopter mode are discussed here. Table 9.4 compares the performance of the baseline XV-15 blade at  $\theta_{75} = 7^\circ$  and  $\theta_{75} = 10^\circ$ , with the results of the single-point optimisations of the blade. The optimal twist distribution was computed for both collective angles (cases HM1 and HM2), while for the collective angle  $\theta_{75} = 10^\circ$  only, the optimal chord and sweep distributions were also determined (case HM3).

Table 9.4: Results of single-point design cases for the helicopter mode.

Design case	Helicopter Mode			
	$C_T$	$C_Q$	FoM	$\Delta\text{FoM} [\%]$
Baseline, $\theta_{75} = 7^\circ$	0.00614	0.000477	0.714	-
HM1	0.00614	0.000462	0.736	3.081
Baseline, $\theta_{75} = 10^\circ$	0.00909	0.000791	0.775	-
HM2	0.00909	0.000775	0.790	1.988
HM3	0.00909	0.000774	0.791	2.046

Cases HM1 and HM2 converged in about 9 design cycles and resulted in an increase of the FoM of 3.081% and 1.988% at the respective design conditions. The optimal twist distributions for the two cases are shown in Figure 9.5, where the baseline, ideal, and modified twist curves are also reported for comparison. The overall similarity between theory-based ideal twist distributions, confirms the validity of the optimisation process in independently generating a realistic tiltrotor blade twist distribution. The local variations near the blade tip are most likely due to the fact that only CFD simulations can capture the behaviour of the blade tip 3D effects and the wake induced effects near 80%  $R$ . The baseline blade follows closely the ideal distributions for  $r/R$  between 0.4 and 0.8. It has, however, a linear twist in the inboard region, and a slightly off-loaded tip with respect to the ideal. For both HM1 and HM2 cases, the optimal twist has the same linear behaviour as the baseline at the inboard region ( $r/R < 0.4$ ), but the optimal twist value is lower. The main differences are instead observed outboard. Also, the optimal blades present a more pronounced

off-loading at the tip, for  $r/R > 0.9$ , and an increased loading in the region between  $r/R = 0.6$  and  $r/R = 0.9$ , which is necessary to satisfy the fixed thrust constraint.

To better understand the mechanism that leads to the optimal design, we use as a measure of the contribution of each blade section to the overall rotor efficiency the ratio  $C_t/C_q$ , where  $C_t(\hat{r}) = dC_T/d\hat{r}$  is the local contribution to the thrust, and  $C_q(\hat{r}) = dC_T/d\hat{r}$  the local contribution to the torque. Figure 9.6 shows the  $C_t/C_q$  curve for the baseline blade and for the optimal design HM2. The off-loading of the tip allowed all blade sections for  $r/R > 0.85$  to work more efficiently, locally providing a contribution to the overall thrust with lower absorbed power penalty.

The modification of the twist distribution in the tip region also impacts on the tip vortex generation. Figure 9.7 reports the contours of the vorticity vector magnitude in a plane behind the blade, for both the baseline and the optimal design HM2. It is evident that the tip vortex for the optimal design is weaker, and also the trajectory has been altered. The effect of the tip can also be observed on the induced velocity distribution near the tip path plane, which is shown in Figure 9.8. The induced velocity at the rotor plane was obtained and averaged using the CFD velocity field at several upstream and downstream locations. Further information about the employed method can be found in [254].

A consequence of the tip optimisation is that the blade now has a very mild shock at the tip region, while the baseline blade had a rather strong shock, as confirmed by Figure 9.9, that shows the Mach number distribution at  $r/R = 0.95$ .

The performances of the optimal blade designs HM1 and HM2 were assessed over a whole range of collective angles. For both cases, the FoM curves are compared to that of the baseline blade in Figure 9.10. As expected, the blade optimised at  $7^\circ$  collective performs better at low values of the thrust coefficient, while the blade optimised at  $10^\circ$  is more efficient at higher disk loadings. It is interesting to note that the optimised blades perform better than the baseline not only at the design points, but over the whole range of considered thrust coefficient values.



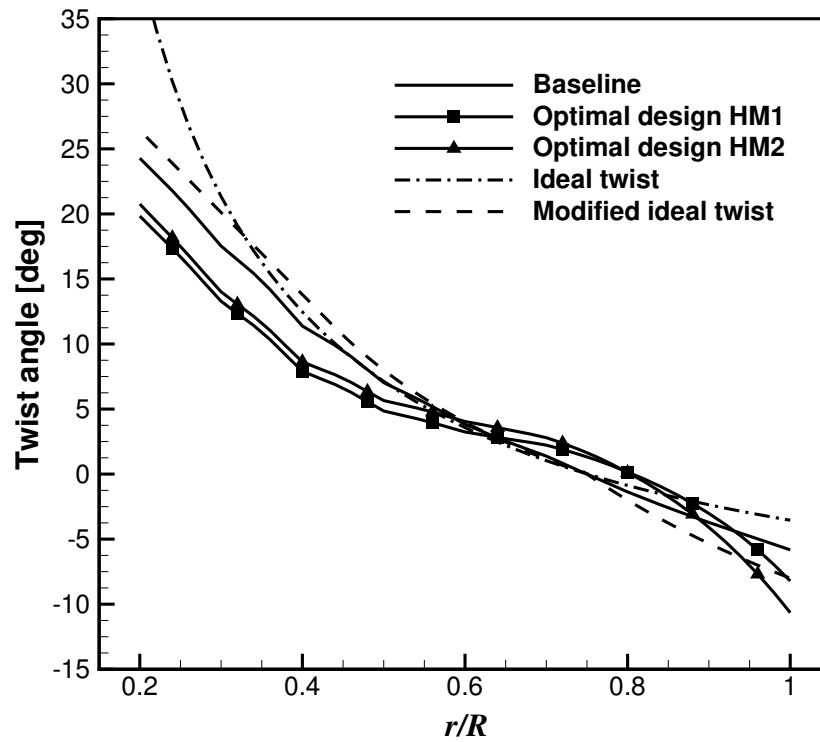


Figure 9.5: Plot of baseline, ideal, and optimal blade twist distributions.

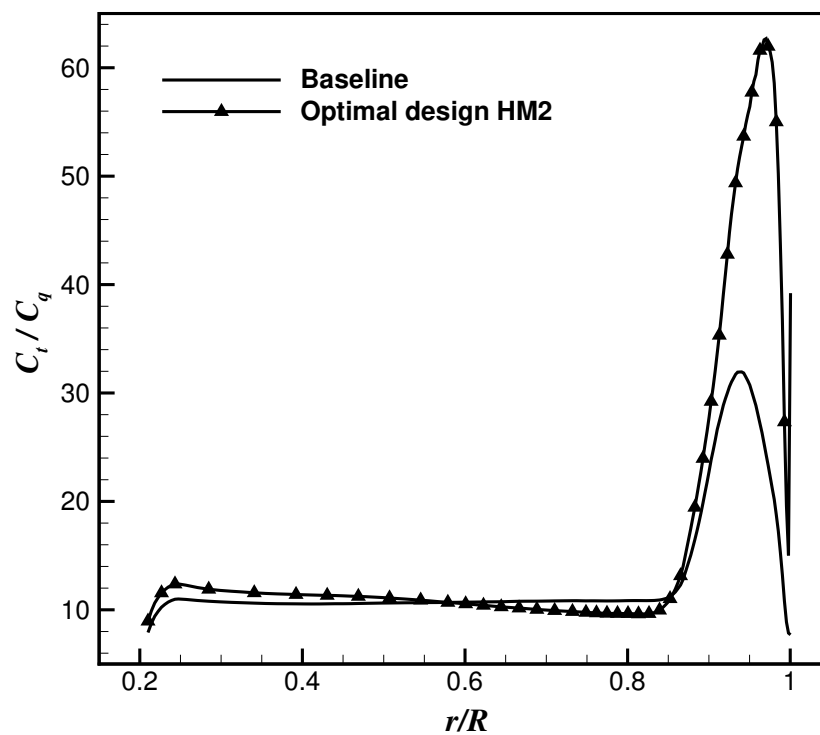


Figure 9.6:  $C_t/C_q$  curve for the baseline blade and optimal design case HM2.

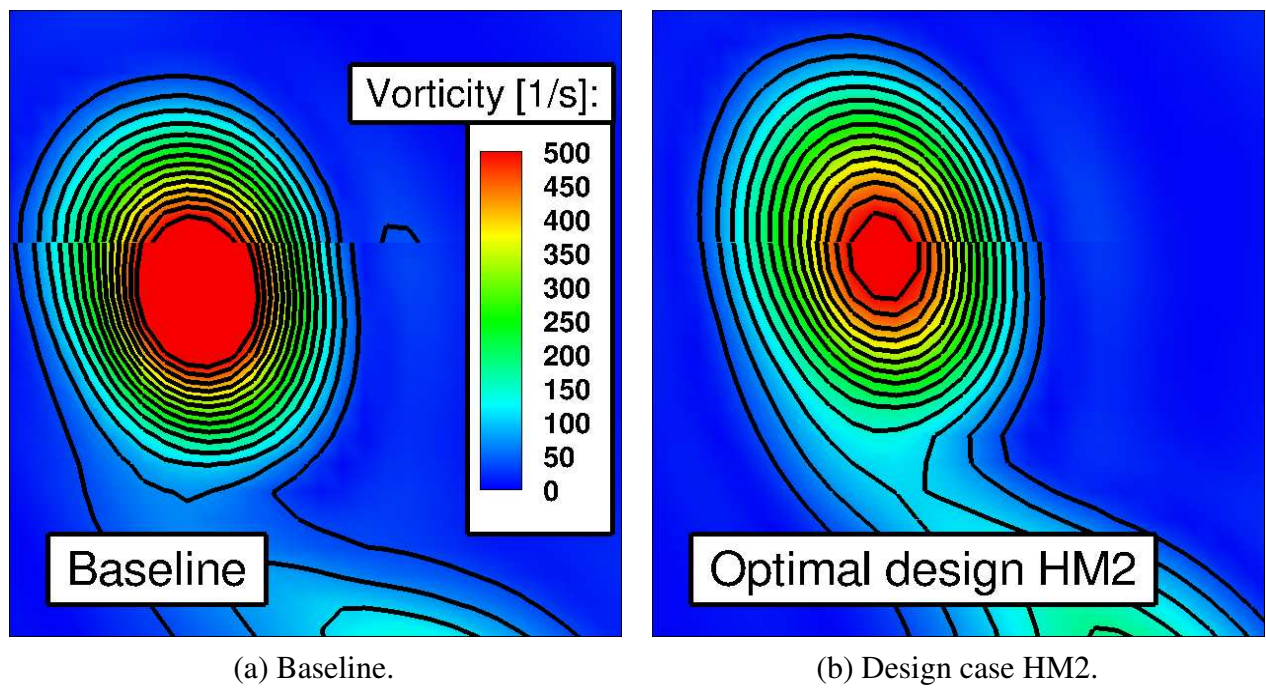


Figure 9.7: Vorticity contours of the blade-tip vortex for baseline blade and design case HM2

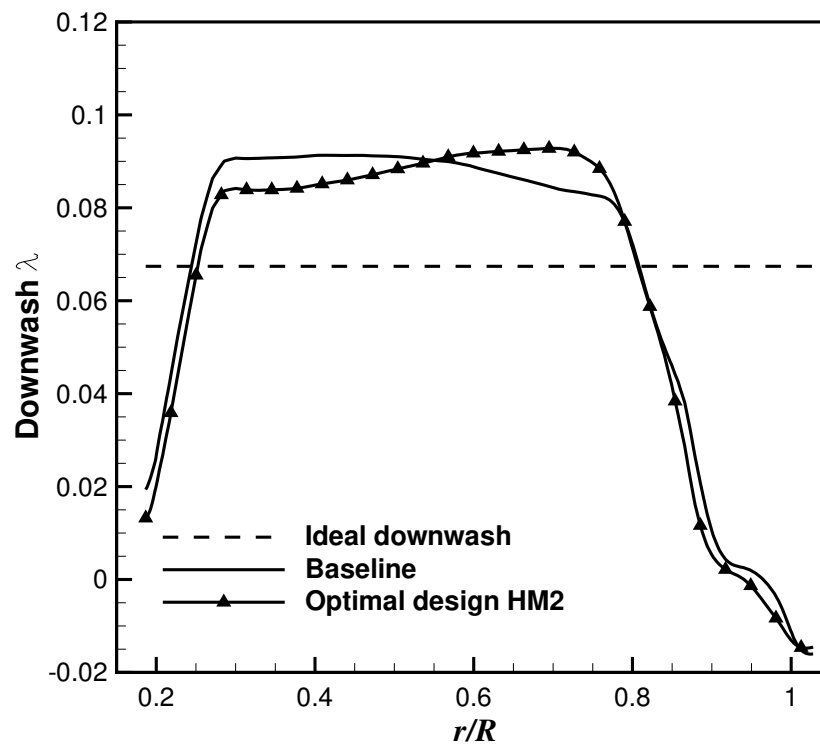


Figure 9.8: Comparison between ideal, baseline, and optimal induced velocity distribution.

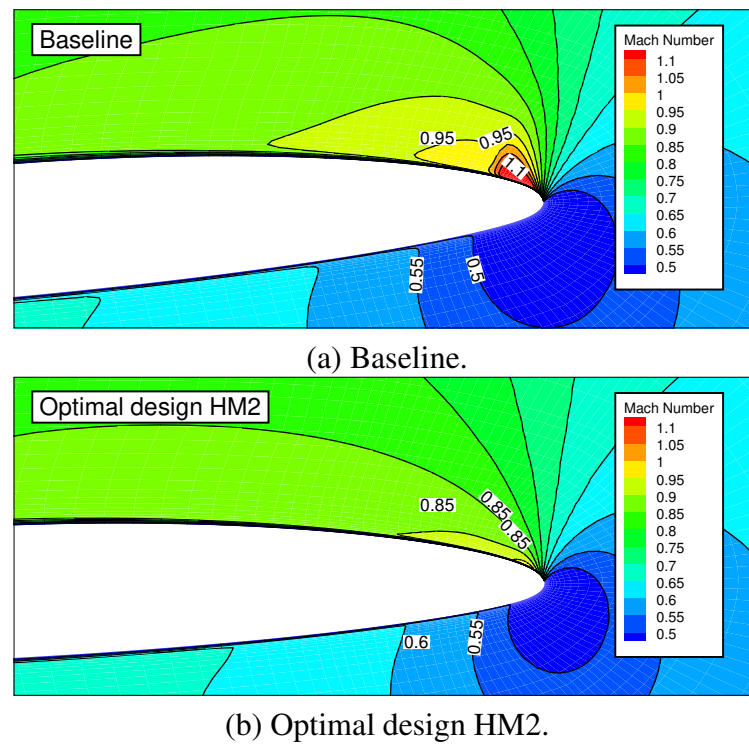


Figure 9.9: Contours of Mach number at blade section  $r/R = 0.95$  for the baseline blade (top) and design case HM2 (bottom).

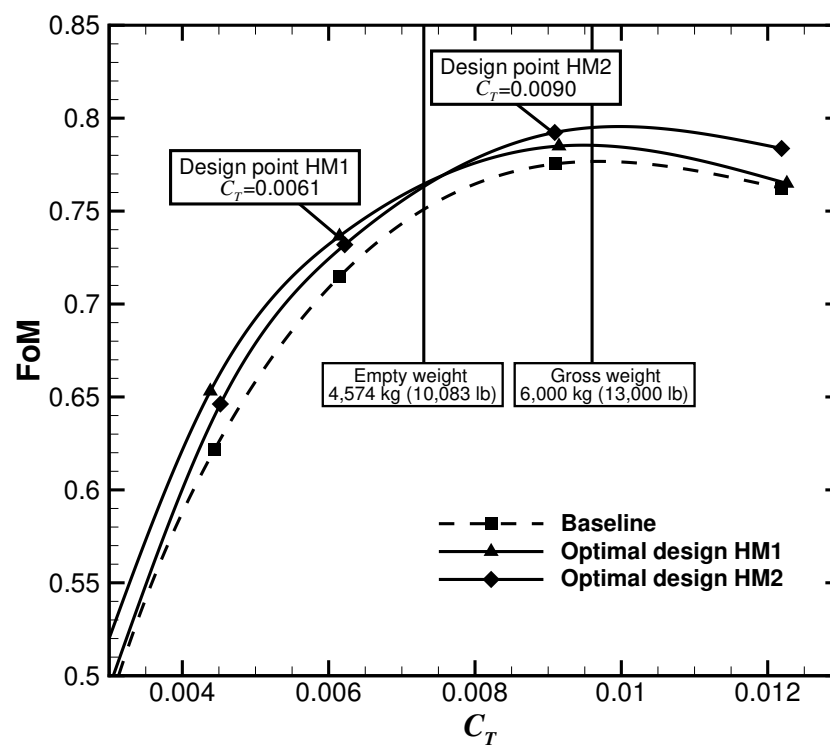


Figure 9.10: Figure of merit of the baseline and optimal designs HM1 and HM2.

The design case HM3 includes the chord and sweep distributions in the blade parametrisation. It converged after 19 design cycles, and the resulting optimal blade is characterised by a reduction of the blade chord by 1.3% for  $r/R < 0.8$ , and by 4.6% at the tip. The rotor FoM is 2.046% higher than the baseline, showing a very limited benefit with respect to the pure twist optimisation, which suggests that the chord and the sweep play a secondary role in the hovering rotor performance. Figure 9.11 shows the comparison of the twist distribution of the baseline and of the optimal design cases HM2 and HM3. The design case HM3 presents higher AoA at the inboard part of the blade, up to  $r/R = 0.7$ , with small differences observed outboard.

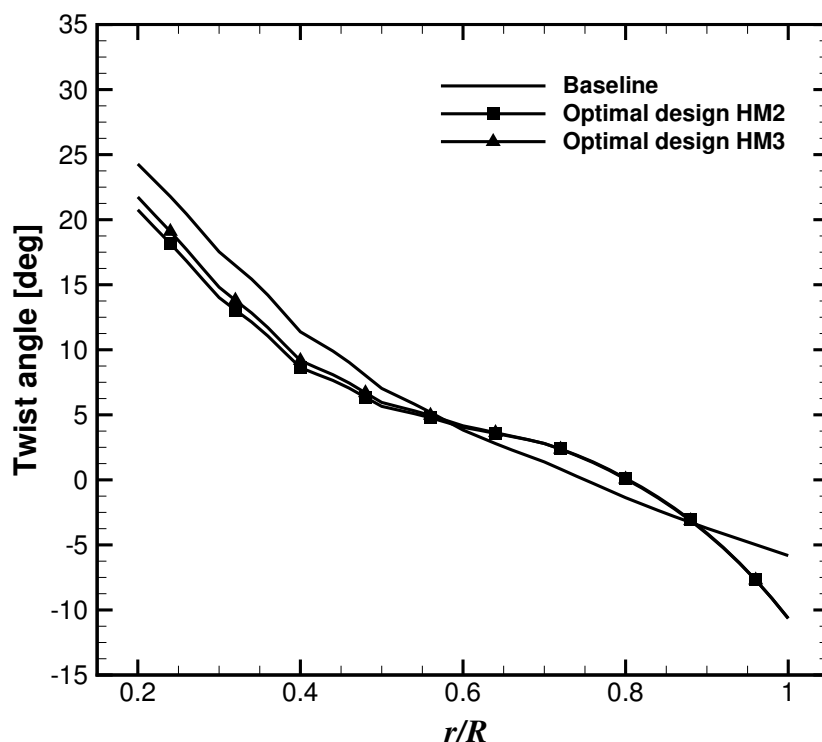


Figure 9.11: Plot of baseline and optimal blade twist distributions.

### 9.3.5 Aeroplane Mode

Like for the helicopter mode, single-point optimisation cases were initially performed considering only twist, whereas chord and sweep distributions were added at a second stage. Table 9.5 reports a comparison between the performance of the baseline XV-15 blade at  $\theta_{75} = 47^\circ$  and  $\mu = 0.759$ ,

and the results from single-point optimisations.

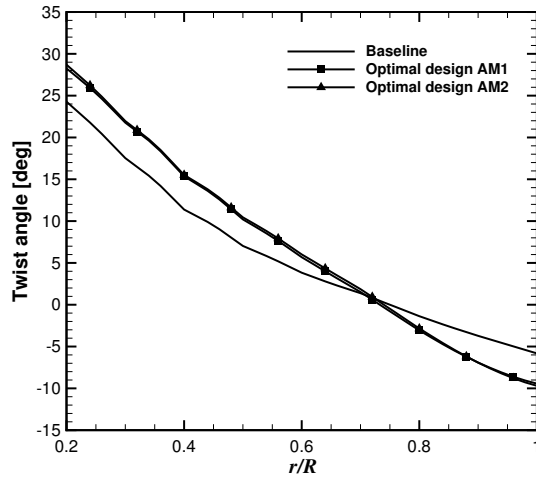
Table 9.5: Results of single-point design cases for the aeroplane mode.

Design case	Aeroplane Mode			
	$C_T$	$C_Q$	$\eta$	$\Delta\eta$ [%]
Baseline $\theta_{75} = 47^\circ$	0.00292	0.00270	0.819	-
AM1	0.00294	0.00256	0.873	6.593
AM2	0.00292	0.00249	0.886	8.180

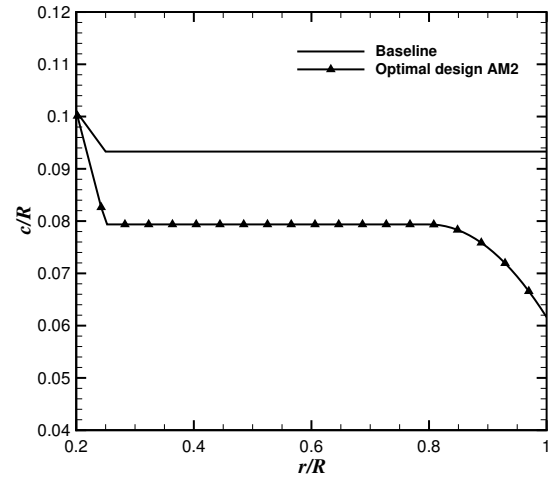
The optimisation of the blade twist distribution AM1 increases the propeller propulsive efficiency of the rotor by 6.593%. The inclusion of the chord and sweep in the parametrisation (design case AM2) allows for a further improvements, with a performance increase of 8.180% over the baseline. In aeroplane mode, in fact, the rotor torque is dominated by transonic compressibility effects, which can be influenced by altering the chord and by modifying the local normal Mach number through a swept tip. Both optimisation cases converged in about 30 design cycles.

The optimal twist for the two cases is plotted in Figure 9.12 (a), and the baseline twist distribution is superimposed. Despite a small difference near the blade root, the two distributions are very similar. Unlike helicopter mode, the optimal twist for the aeroplane mode is approximatively linear over all the blade span. Compared to the baseline, the optimal distribution presents higher AoA at the inboard part of the blade, up to  $r/R = 0.7$ , and lower AoA outboard. The large increase of the AoA at the blade root is due to the fact that the baseline blade is working as a windmill at the selected cruise condition, as shown by Figure 9.13, which displays the distribution of  $C_t$  and  $C_q$  over the blade span.

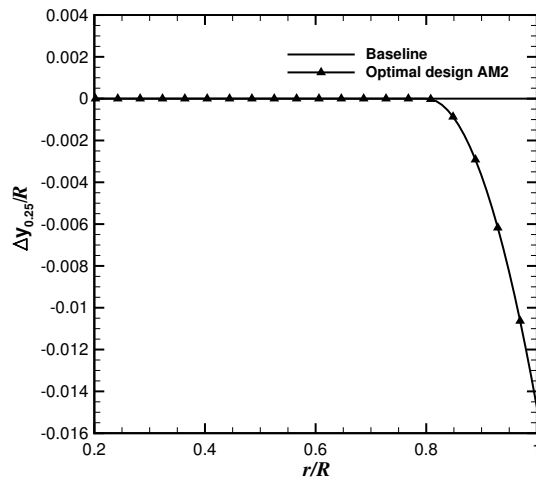
Figure 9.12 shows the twist, chord and sweep distributions of the optimal blade for design case AM2. The figure also contains a comparison between the baseline and the optimal blade shapes. A reduction of the blade chord of about 15% is found by the optimiser. The chord is further reduced at the tip, where it is 34% less than the baseline, to create a swept tip shape (see Figure 9.12 (b)). This shape modification, together with a backward shift of the quarter chord line introduced by the sweep design variable (see Figure 9.12 (c)) tend to limit compressibility effects, and reduce the wave drag as observed in Figure 9.14.



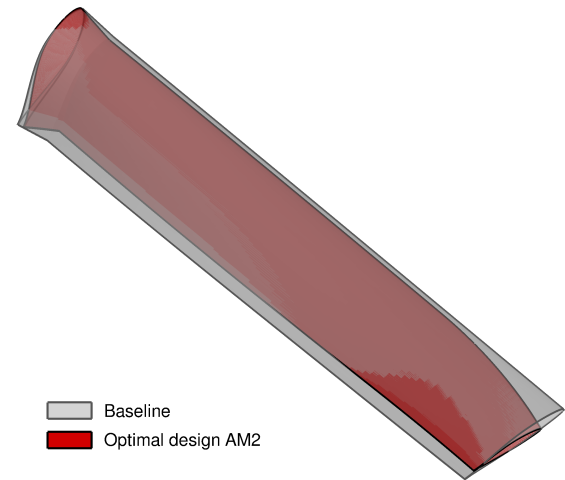
(a) Twist distribution.



(b) Chord distribution.

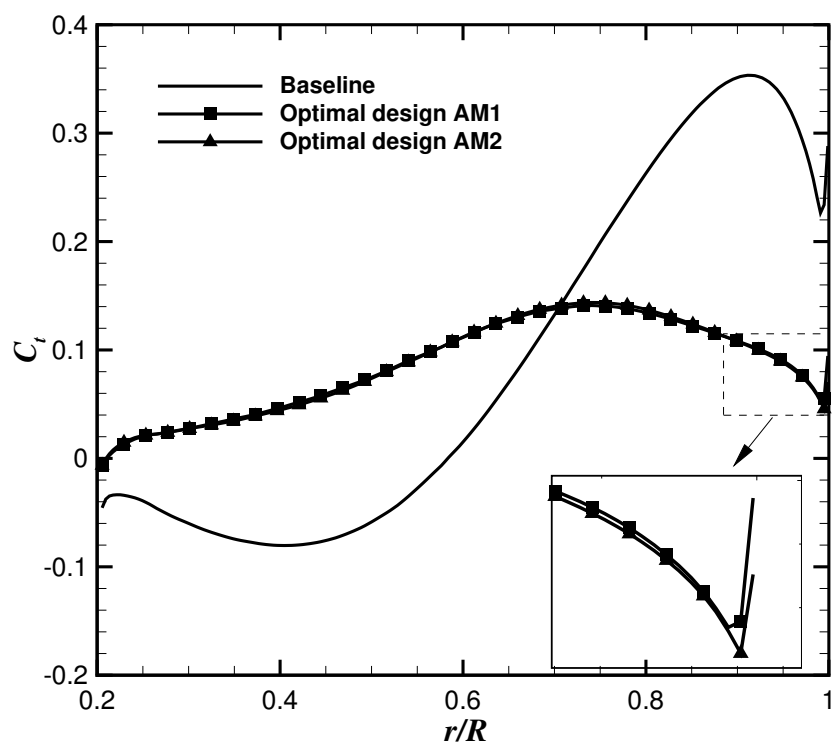


(c) Sweep distribution.

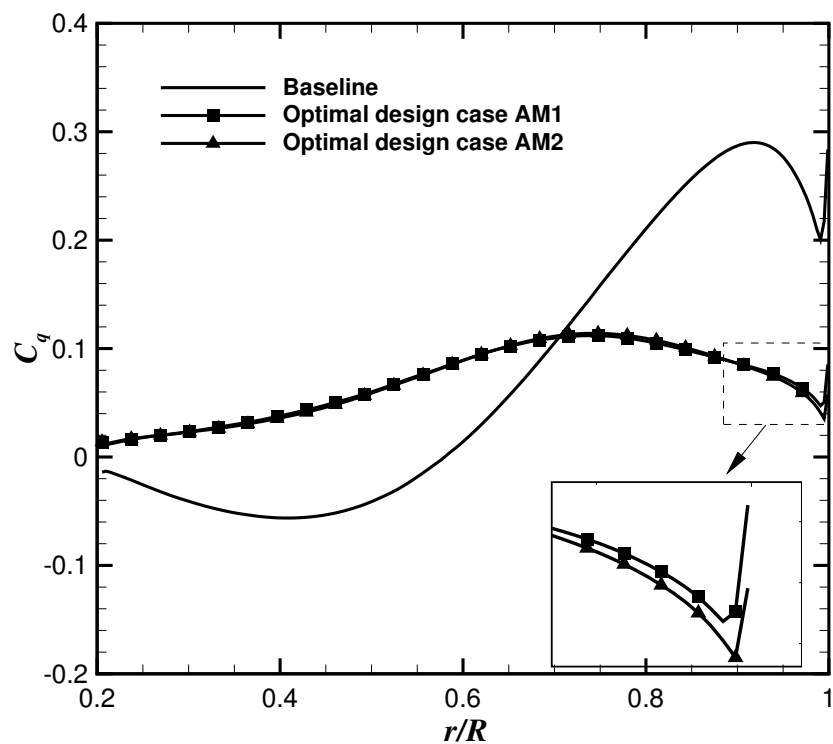


(d) Blade shape.

Figure 9.12: Comparison of (a) twist, (b) chord, (c) sweep distributions, and (d) blade shape between baseline and design case AM2.



(a) Blade sectional thrust coefficient.



(b) Blade sectional torque coefficient.

Figure 9.13: Blade sectional thrust coefficient (top) and torque coefficient (bottom) for the baseline blade and design cases AM1 and AM2.

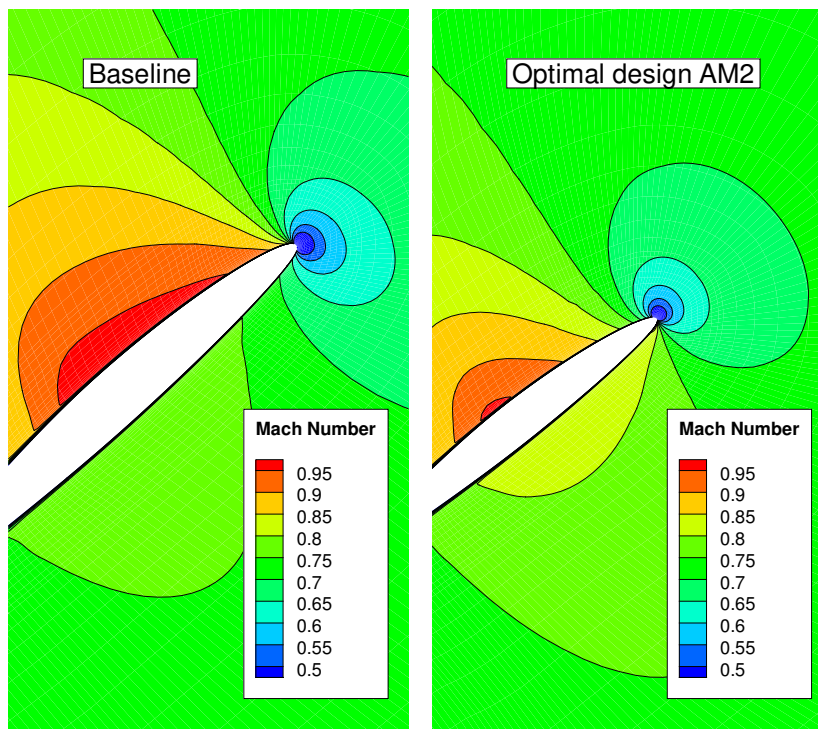


Figure 9.14: Contours of Mach number at blade section  $r/R = 0.95$  for the baseline blade and design case HM2.

### 9.3.6 Multi-Point Optimisation

Results of the multi-point optimisations are now presented, where a composite objective function is used to weigh the performance indices of the helicopter and aeroplane mode conditions (see Eq. (9.7)). Three cases were considered: two pure twist optimisations which differ in the weight selection (cases MP1 and MP2), and a case with the same weights as MP2, but which includes the optimisation of the chord and sweep. Case MP1 has equal weights for the helicopter and aeroplane modes ( $w_{hm} = 1/2$  and  $w_{am} = 1/2$ ), while cases MP2 and MP3 weigh more the cruise condition ( $w_{hm} = 1/3$  and  $w_{am} = 2/3$ ).

Table 9.6 reports the optimised values of the thrust and torque coefficients, FoM, and propeller propulsive efficiency, along with their relative changes over the baseline values. The single-point optimisations are also shown for comparison. The pure twist optimisations (MP1 and MP2) result in a FoM increment of 0.645% for both cases, while the propeller propulsive efficiency in-



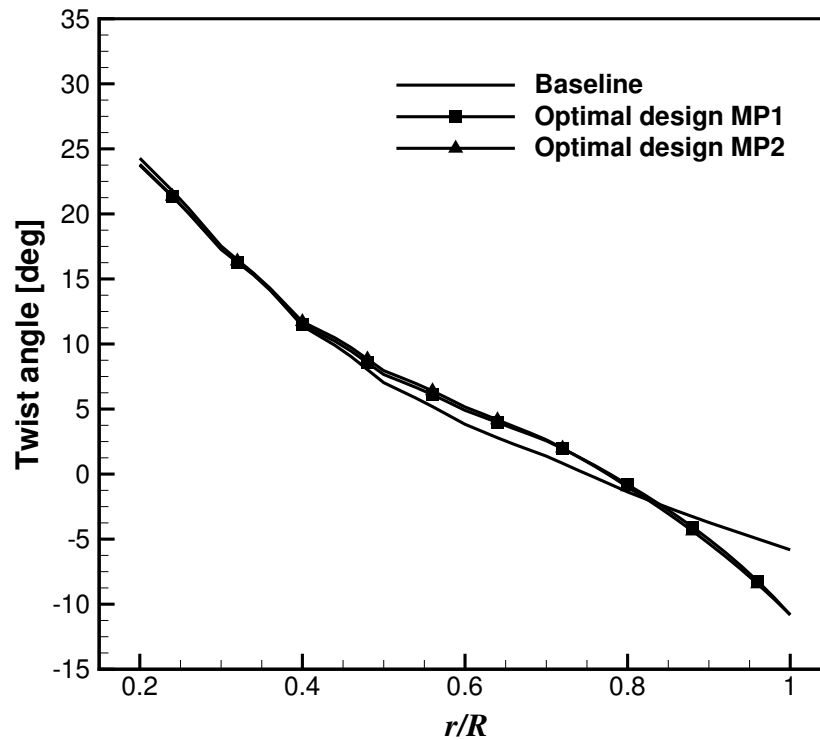
creases by 2.197% when the operational modes are weighted equally, and by 2.686% when the cruise condition is weighted more. All three optimisation cases took about 10 design cycles to reach a converged solution.

Table 9.6: Results of single and multi-point design cases.

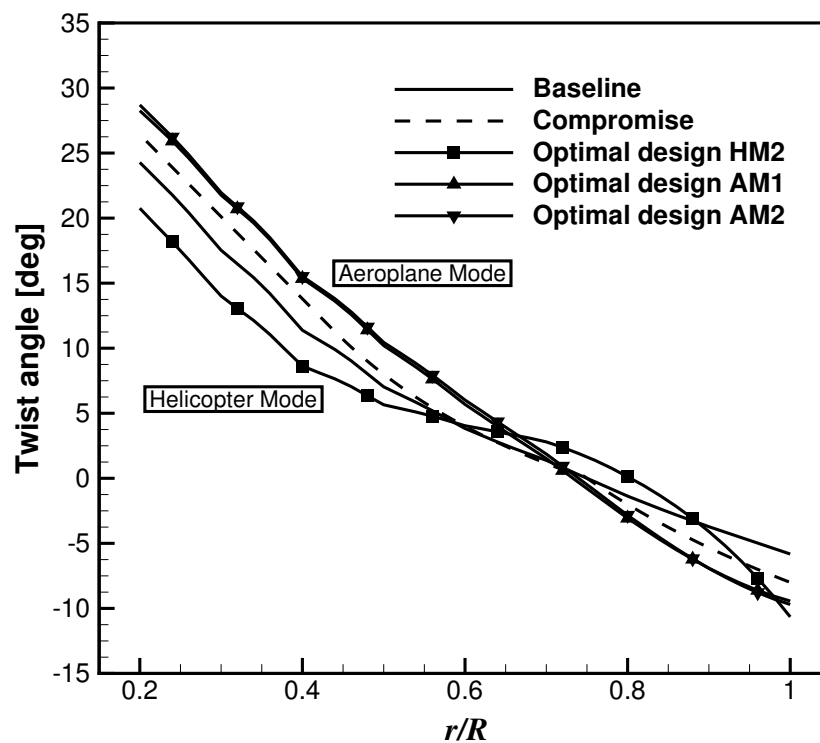
Case	Helicopter Mode				Aeroplane Mode			
	$C_T$	$C_Q$	FoM	$\Delta\text{FoM} [\%]$	$C_T$	$C_Q$	$\eta$	$\Delta\eta [\%]$
Baseline	0.00909	0.000791	0.775	-	0.00292	0.00270	0.819	-
HM2	0.00909	0.000775	0.790	1.988	-	-	-	-
HM3	0.00909	0.000774	0.791	2.046	-	-	-	-
AM1	-	-	-	-	0.00294	0.00256	0.873	6.593
AM2	-	-	-	-	0.00292	0.00249	0.886	8.180
MP1	0.00909	0.000786	0.780	0.645	0.00292	0.00265	0.837	2.197
MP2	0.00910	0.000786	0.780	0.645	0.00292	0.00263	0.841	2.686
MP3	0.00907	0.000790	0.772	-0.387	0.00292	0.00257	0.860	4.945

Figure 9.15 (a) shows the comparison of the twist distribution of the baseline and of the optimal design cases MP1 and MP2. The two multi-point results are very similar, almost identical at the resolution used for the plot. The multi-point results should be compared to the helicopter and aeroplane mode single-point optimal designs, which are reported in Figure 9.15 (b). At the inboard sections, for  $r/R < 0.6$ , the multi-point optimal twist curve lies halfway between the helicopter and aeroplane mode curves. At the tip region, it has a nonlinear behaviour similar to the helicopter mode optimal solution, but less pronounced.

The design case MP3 includes the chord and sweep distributions in the blade parametrisation, and the resulting optimal blade has 0.387% lower FoM and 4.945% higher propeller propulsive efficiency than the baseline. Compared to the pure twist optimisation there is a significant benefit, because of the increase of the aeroplane mode performance, with only a small penalty on the helicopter mode. Figure 9.16 shows a comparison of the twist, chord, sweep distributions between the optimal blade for the design cases HM3, AM2, and MP3. The figure also contains a comparison between the baseline and the optimal blade shape MP3. The multi-point optimised blade has a swept tip, where the chord has been reduced by about 5%. This value is similar to that obtained for the single-point helicopter mode optimisation, but lower than the optimal for the



(a) Multi-point design cases.



(b) Single-point design cases.

Figure 9.15: Comparison of baseline and optimal blades twist distributions for the multi-point cases (top) and for the single-point cases (bottom).

aeroplane mode. Nevertheless, it is sufficient to limit the compressibility effects at the tip region encountered in aeroplane mode at high advance ratio.

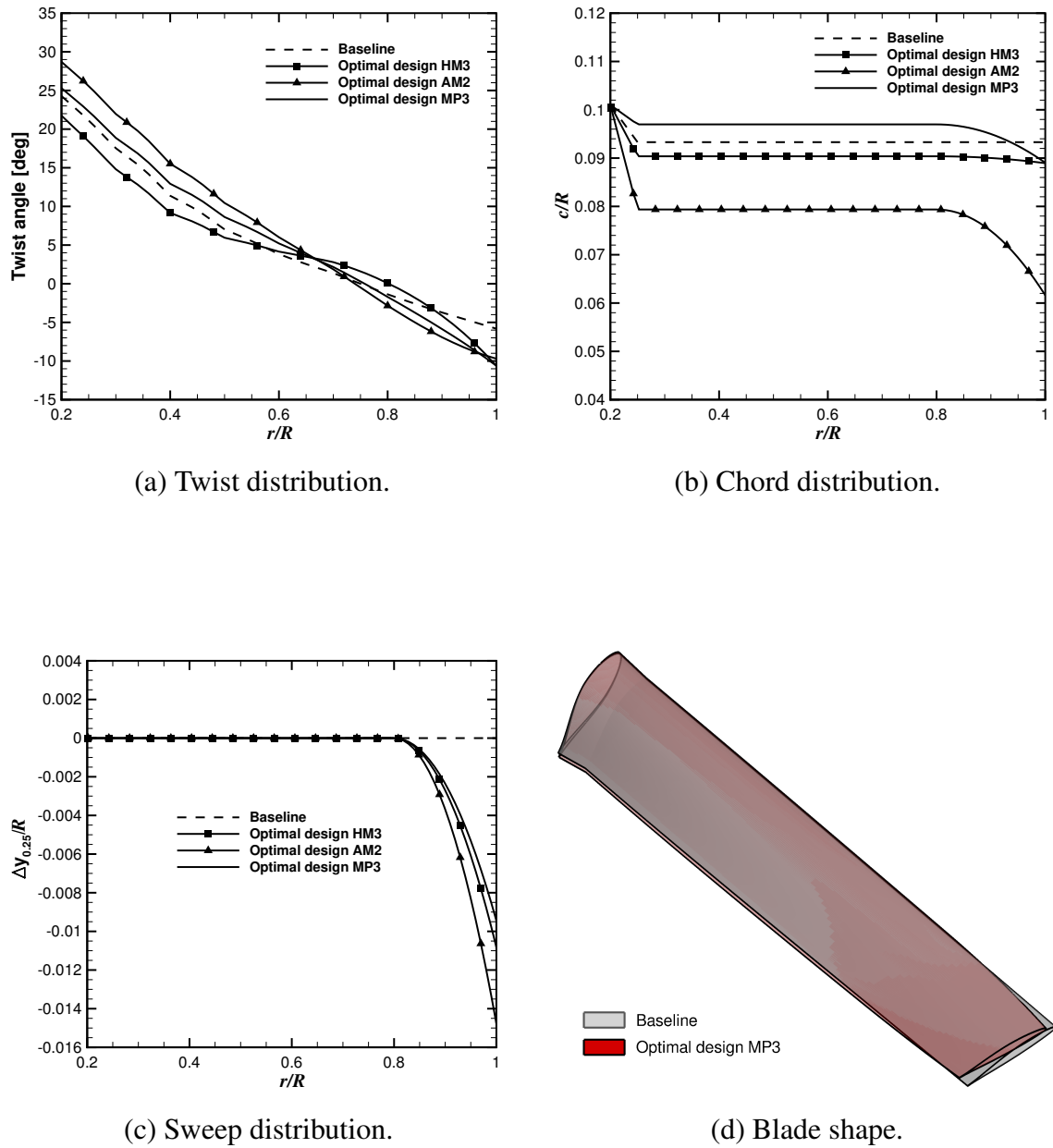


Figure 9.16: Comparison of (a) twist, (b) chord, (c) sweep distributions, and (d) blade shape between baseline and design cases HM3, AM2, and MP3.

Figure 9.17 shows the improvements of FoM and  $\eta$  for all HM, AM, and MP design cases. Note that for the single-point optimisation cases, values of 1 were set for the opposite flight condition. This plot is not a complete Pareto front, but highlights the contradicting objective functions which a tiltrotor blade has to satisfy. Nevertheless, trade-off blade designs can be obtained using a multi-point optimisation strategy.

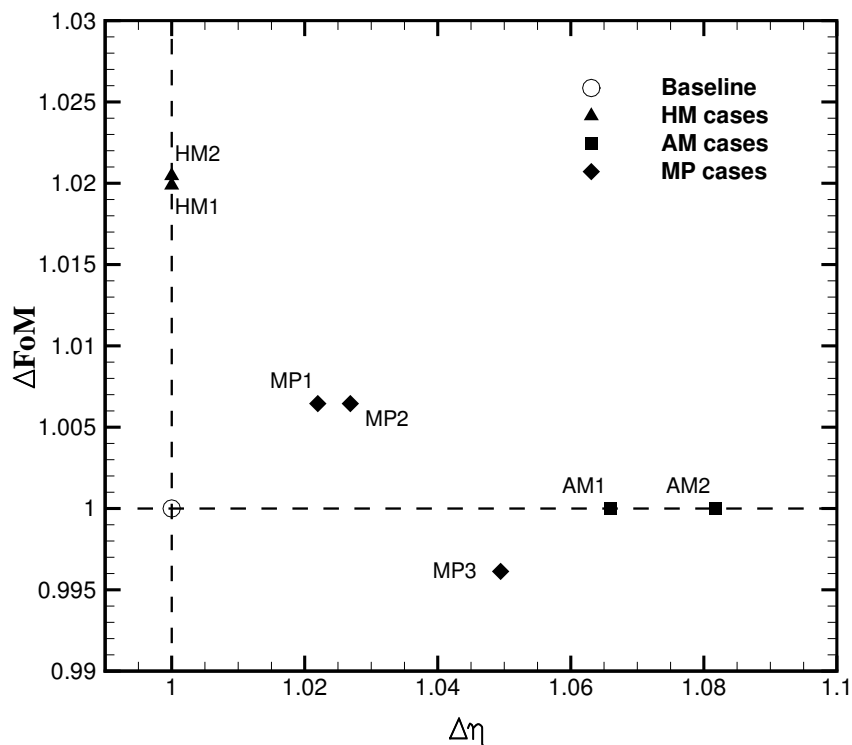


Figure 9.17: Improvements of the optimal design cases HM, AM, and MP for  $\eta$  (x-axis) and FoM (y-axis).

## 9.4 Summary of Findings

This work demonstrated an aerodynamic optimisation method applied to tiltrotor blades. Both single and multi-point problems were solved, to investigate the effect of several blade geometrical features on the optimal performance. The main conclusions are:

- Adequate parametrisation of the blade shape can be obtained using ten design variables. This includes twist, chord, and tip shapes.

- Single-point optimisations of the twist distribution resulted in a 1.99% increase of the FoM, and a 6.59% increase of the propeller propulsive efficiency at the selected design conditions.
- The inclusion of the chord and sweep resulted in a limited improvement for the helicopter mode performance, while it allowed an 8.18% increase of the propeller propulsive efficiency over the baseline, thanks to reduction of the adverse compressibility effects at the blade tip.
- Results of the multi-point optimisations showed that, either for the pure twist case and for the case including the chord and sweep, a compromise blade shape can be obtained. The blade with optimal twist, chord and sweep increased the propeller propulsive efficiency by 4.95%, with only a small penalty on the hovering rotor performance.
- In all of the presented cases, the accuracy of the adjoint gradients resulted in a small number of flow evaluations for obtaining the optimal solution, indicating that gradient-based optimisation is a viable tool for modern tiltrotor design. A typical computation with the single-point optimisation required 19 design cycles for helicopter and 30 for the aeroplane mode. Regarding the multi-point optimisation, 10 design cycles were required. This is in agreement with data published in the literature [115].

## Chapter 10

# Validation of High-Order Methods in the HMB CFD Solver

This chapter aims to validate the high-order scheme of chapter 4 through a variety of test problems. The first part is devoted to the application of the scheme to Euler's equations to study the aerodynamic interaction between a vortex and a NACA-0012 aerofoil (blade-vortex interaction). The new scheme is then applied to steady, transonic, turbulent flow over the RAE2822 aerofoil, where the capability of the scheme in preserving accuracy for non-smooth solutions is investigated.

The second part concerns the application of the new scheme to three-dimensional steady and unsteady flows around the 7AD, S-76, and XV-15 blades in hover, and the UH-60A rotor in forward flight. Finally, an assessment of the effect of the spatial accuracy on the airloads and wake of the ERICA tiltrotor is carried out. Table 10.1 lists the test cases used in the validation of the present high-order scheme.

### 10.1 Blade-Vortex Interaction

The aerodynamic interaction between a vortex and a NACA-0012 aerofoil (BVI) is studied in this section. BVI has been widely investigated in the past through theoretical research and experiments [255]. Numerical simulation of the BVI has been attempted using different methods, such as

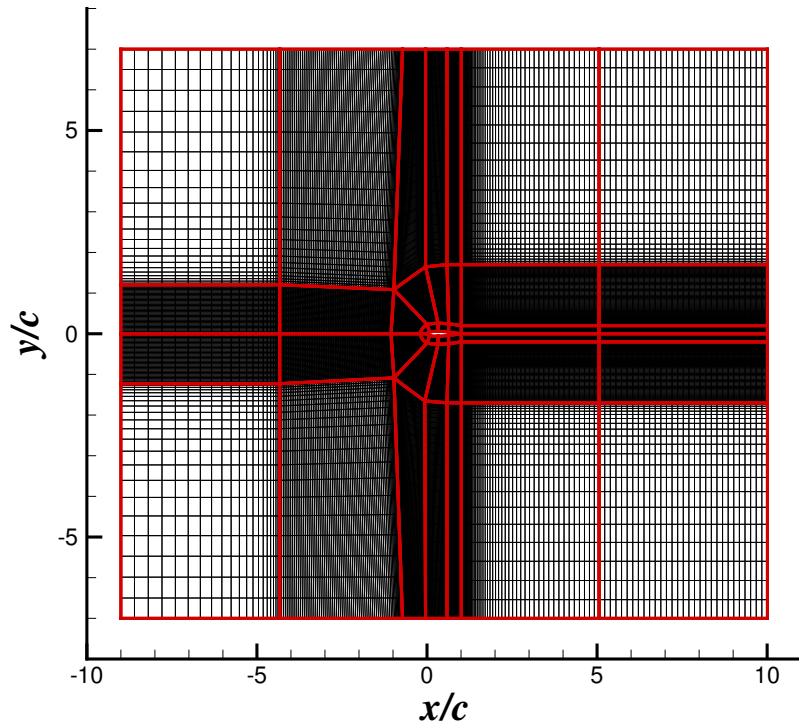
Table 10.1: List of test cases used in the validation of high-order methods.

Test Case	Equations	Steady/Unsteady
BVI	Euler (2D)	Unsteady
RAE2822 aerofoil	Navier-Stokes (2D)	Steady
7AD rotor	Euler (3D)	Steady
S-76 rotor	Navier-Stokes (3D)	Steady
JORP propeller	Navier-Stokes (3D)	Steady
XV-15 tiltrotor	Navier-Stokes (3D)	Steady
UH-60A	Navier-Stokes (3D)	Unsteady
ERICA tiltrotor	Navier-Stokes (3D)	Unsteady

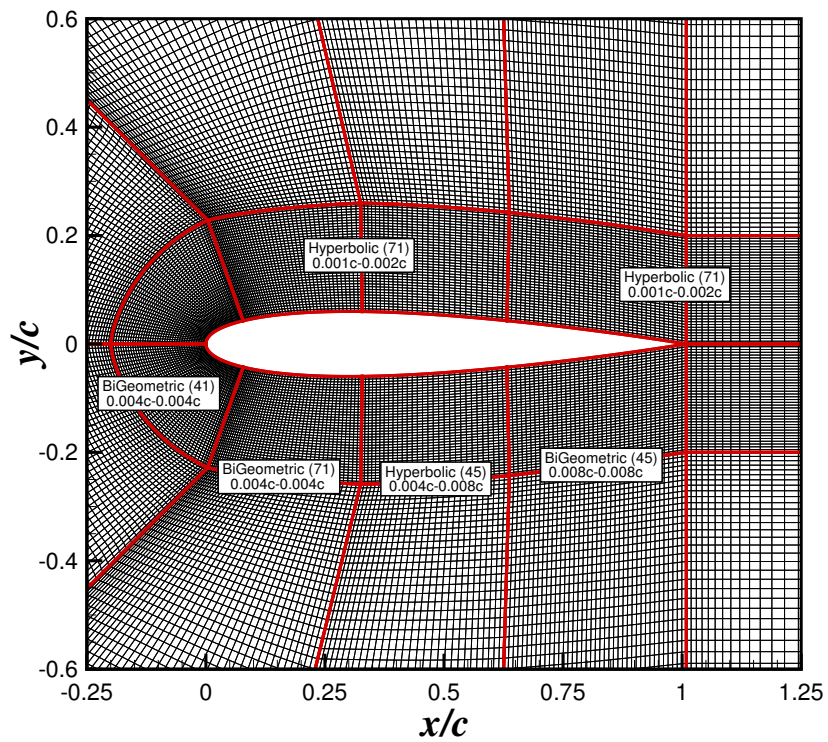
the indicial method [256], the cloud-in-cell method [257], or full potential methods [258]. Neither the non-linearities of the flow associated to compressibility effects, nor to rotational flow predictions are taken into account by these approaches, which may lead to errors in the predictions of blade-vortex problems. Computational Fluid Dynamics in the form of unsteady Reynolds-averaged Navier-Stokes with the use of high-order spatial schemes, represents an alternative to those methods due to its ability to well-preserved vortices. Indeed, the vortex shape and strength are crucial for simulating BVI, and can be preserved using high-order schemes [259].

The test case presented here concerns the aerodynamic interaction between a vortex and a NACA-0012 aerofoil at freestream Mach number  $M_\infty = 0.57$ , which is referred to as Case 1 in the experiments carried out by Lee and Bershader [260]. Surface pressure coefficient on the upper and lower sides of the blade were measured. Considering the set-up of the initial condition, a Scully-vortex with a non-dimensionalised vortex strength  $\hat{\Gamma} = -0.283$  and core radius  $R_c = 0.018c$  was introduced in the flowfield,  $1.5c$  ahead the aerofoil.

The computational domain and the multi-block topology employed are shown in Figures 10.1 (a) and (b), respectively. The grid is composed by 42 blocks with a total size of 70,000 cells. To capture the blade-vortex interaction, the mesh is refined close to the aerofoil surface and along the path travelled by the convected vortex. The RK4 scheme was used to march the solution in time, and MUSCL-2 and MUSCL-4 schemes were used. No-slip wall and free-stream conditions were applied on the aerofoil surface and on the outer boundaries, respectively.



(a) Computational domain.



(b) Multi-block topology.

Figure 10.1: Computational domain and multi-block topology of the 2D grid used for the simulation of the head-on BVI, NACA-0012 aerofoil.



Comparisons of the time histories of the predicted and experimental surface pressure coefficients are given in Figure 10.2. Probes on the upper and lower sides of the aerofoil surface were considered, corresponding to  $x/c = 0.02, 0.05, \text{ and } 0.10$ . Regarding the probes located at the upper surface (see Figures 10.2 (a),(c), and (e)), results obtained with the MUSCL-4 scheme show a higher resolution of the suction peak  $C_p$  if compared with standard MUSCL solutions. The low dissipation of the present high-order schemes gives a much better representation of the blade-vortex interaction. Comparisons of the  $C_p$  on the lower side (see Figures 10.2 (b),(d), and (f)) also support this idea, where the small features of the flowfield were only well-captured by the MUSCL-4 scheme.

## 10.2 Turbulent Flow over the RAE2822 Aerofoil

The application of the MUSCL-4 scheme to the steady, transonic, turbulent flow over the RAE2822 aerofoil is presented here. This case is designed to give information on how the shock limiter works with the new high-order scheme. In this regard, results are compared with available experimental data in terms of  $C_p$ . The case considered here corresponds to Case 6 in Cook *et al.* [261], where the Mach and Reynolds numbers were set to 0.731 and 6.5 million (based on the mean aerodynamic chord) with an AoA of  $2.51^\circ$ . For this particular case, the Mach number and AoA were corrected by Tatsumi *et al.* [262] to account for wind tunnel effects. The flow solutions were computed solving the RANS equations, coupled with the Menter's  $k-\omega$  SST turbulence model [191].

A C-H mesh topology was employed with the outer boundaries were located 50 chord lengths away from the aerofoil. The mesh had 371 nodes on the aerofoil surface along with 91 points in the normal direction following an exponential distribution (the mesh wall distance was  $4 \times 10^{-6} c_{\text{ref}}$ ), which resulted in a grid size of 93,000 cells.

The numerical solutions were obtained using MUSCL-2 and MUSCL-4 schemes, and the RK4 scheme is used to march the solution in time to steady state. Figure 10.3 (a) shows contours of pressure around the transonic RAE2822 aerofoil. The shock on the upper surface of the aerofoil is visible. Figure 10.3 (b) shows a comparison of  $C_p$  between the MUSCL-4 scheme and exper-

iments [261] on the aerofoil surface. Despite small discrepancies found in the predicted suction peak, an excellent agreement is observed between the numerical simulation and the experimental data, where the position of the shock is well captured.

### 10.3 7AD Helicopter Blade

The flow around the 7AD four-bladed main rotor is solved to demonstrate the performance of the MUSCL-4 scheme for a three-dimensional flow and for a coarse mesh with the Euler equations. In fact, the lack of a natural dissipation mechanism for the Euler equations (such as viscosity in the Navier-Stokes equations) makes it easier to analyse the impact of the numerical dissipation associated to spatial discretisation in preserving the vortex core. Simulations using the MUSCL-2 are also undertaken for comparison.

The 7AD main rotor consists of four blades of aspect ratio ( $R/c$ ) of 15. The blades use aerofoils of the OA2XX series of 9% thickness. The 7AD model rotor blade had 2.1 m radius, 0.14 m chord, linear twist distribution, and was equipped with anhedral tips with parabolic taper [113].

Experiments were conducted at the DNW wind tunnel within the European project HELISHAPE [263]. The hover conditions considered here refer to the test case of the HELISHAPE project [263], which employs blade-tip Mach number  $M_{\text{tip}} = 0.66$ , blade pitch angle of 7.5 degrees and  $C_T/\sigma = 0.076$ .

As the 7AD is a four-bladed rotor, only a quarter of the domain was meshed, assuming periodic conditions for the flow in the azimuthal direction. Outer boundaries were located  $2R$  (above) and  $4R$  (below) away of the blade tip, while the mesh extended by 3 radii in the radial direction. A C-topology around the leading edge of the blade was selected, whereas an H-topology was employed at the trailing edge of the blade, resulting in a coarse mesh with dimensions of 1 million nodes per blade. The domain was decided based on previous experience [6].

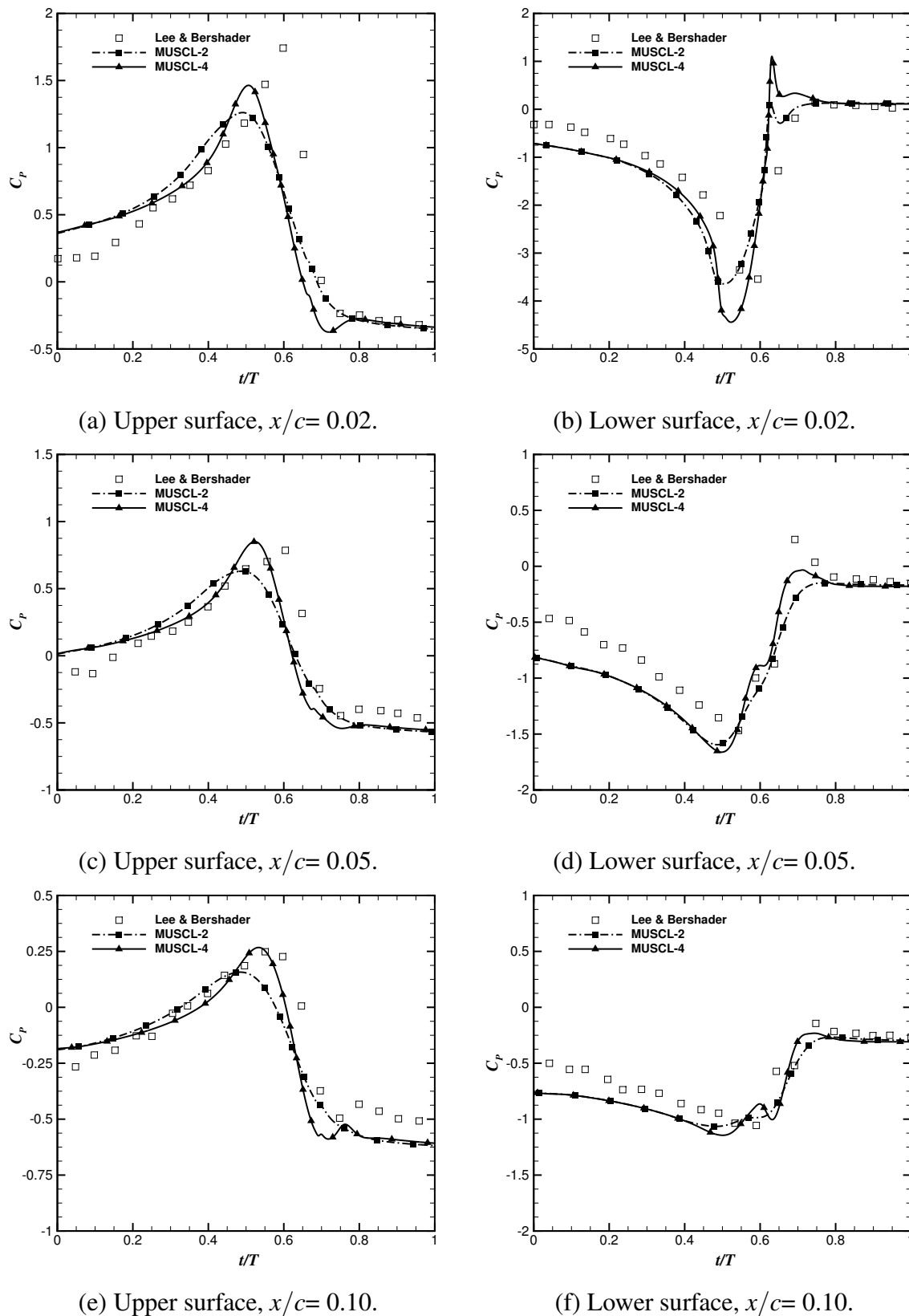
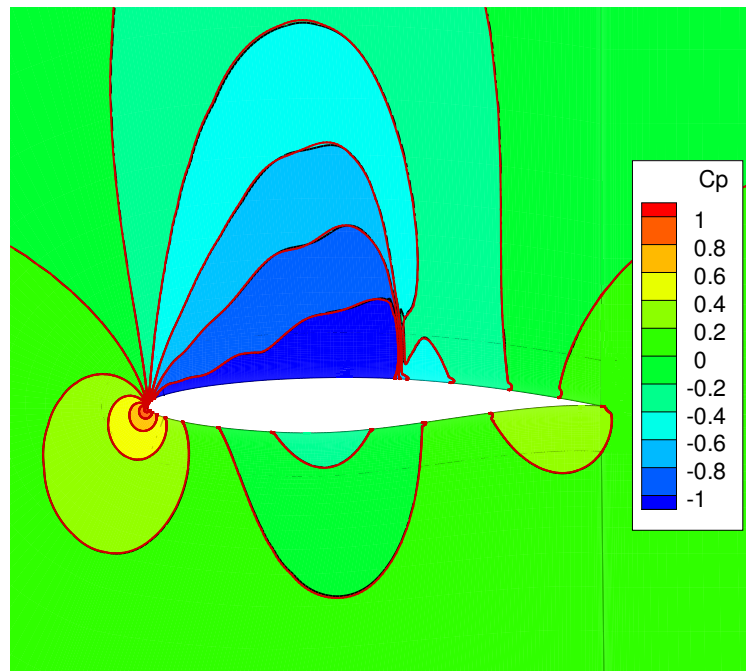
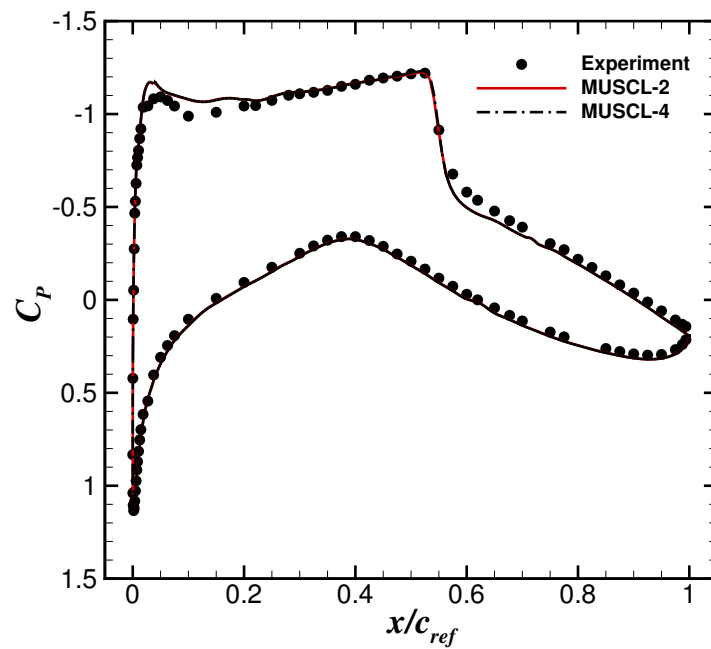


Figure 10.2: Influence of the high spatial accurately numerical schemes on the time history of the surface pressure coefficient. Head-on BVI problem, NACA-0012 aerofoil, inviscid calculations,  $M_\infty=0.5$ , Scully-model with  $\hat{\Gamma} = -0.283$  and  $R_c = 0.018$ .



(a) Pressure contours.



(b)  $C_p$  profile.

Figure 10.3: (a) Contours of pressure and (b)  $C_p$  profile comparison between CFD and experiments [261] around the RAE2822 aerofoil. Red and black lines correspond to MUSCL-2 and MUSCL-4 solutions, respectively.

Figure 10.4 shows comparisons of  $C_P$  profiles between CFD and experiment [263] at radial stations  $r/R = 0.5, 0.7$ , and  $0.915$  for MUSCL-2 and MUSCL-4 schemes. At inboard stations ( $r/R = 0.5$  and  $0.7$ ) both schemes are in close agreement with the experiments with negligible differences between them. At the most outboard station ( $r/R = 0.915$ ), however, the effect of the scheme becomes noticeable on the prediction of the suction peak. Table 10.2 reports the predicted suction peak  $C_P$  for both schemes as well as the experimental one for the most outboard stations. Especially, for  $r/R = 0.915$ , MUSCL-4 appears to agree better with test data even if there is scatter between measurements obtained on each of the four blades as can be seen by the test data where four symbols are present at each  $x/c_{\text{ref}}$  station.

Table 10.2: Predictions and experimental suction peak  $C_P$  for the full-scale 7AD rotor.

$r/R$	Experiment	CFD	
		MUSCL-2 (% change)	MUSCL-4 (% change)
0.915	-1.47	-1.75 (19.04)	-1.58 (7.48)
0.975	-1.20	-1.82 (51.66)	-1.70 (41.66)

Figure 10.5 shows the wake visualisation of the 7AD rotor using iso-surfaces of  $\tilde{Q}$ -criterion. The capability of both schemes in preserving the helical tip vortex in the wake can thus be assessed. It is observed that the MUSCL-2 scheme can only resolve the first vortex passage (wake age of  $90\pi$  radians). The MUSCL-4 scheme shows a completely preservation of the first and second vortex passage (wake age of  $180\pi$  radians).

Figure 10.6 shows the vorticity field near the tip vortex and the vortex of the preceding blade generated by the hovering 7AD rotor in azimuthal planes located behind the blade. The visualisations highlight the ability of the present high-order scheme to capture and preserve the wake vortices. For instance, vorticity values of the tip vortex core computed with MUSCL-2 presents a reduction of the core vorticity by almost 20% with respect to the MUSCL-4 results.

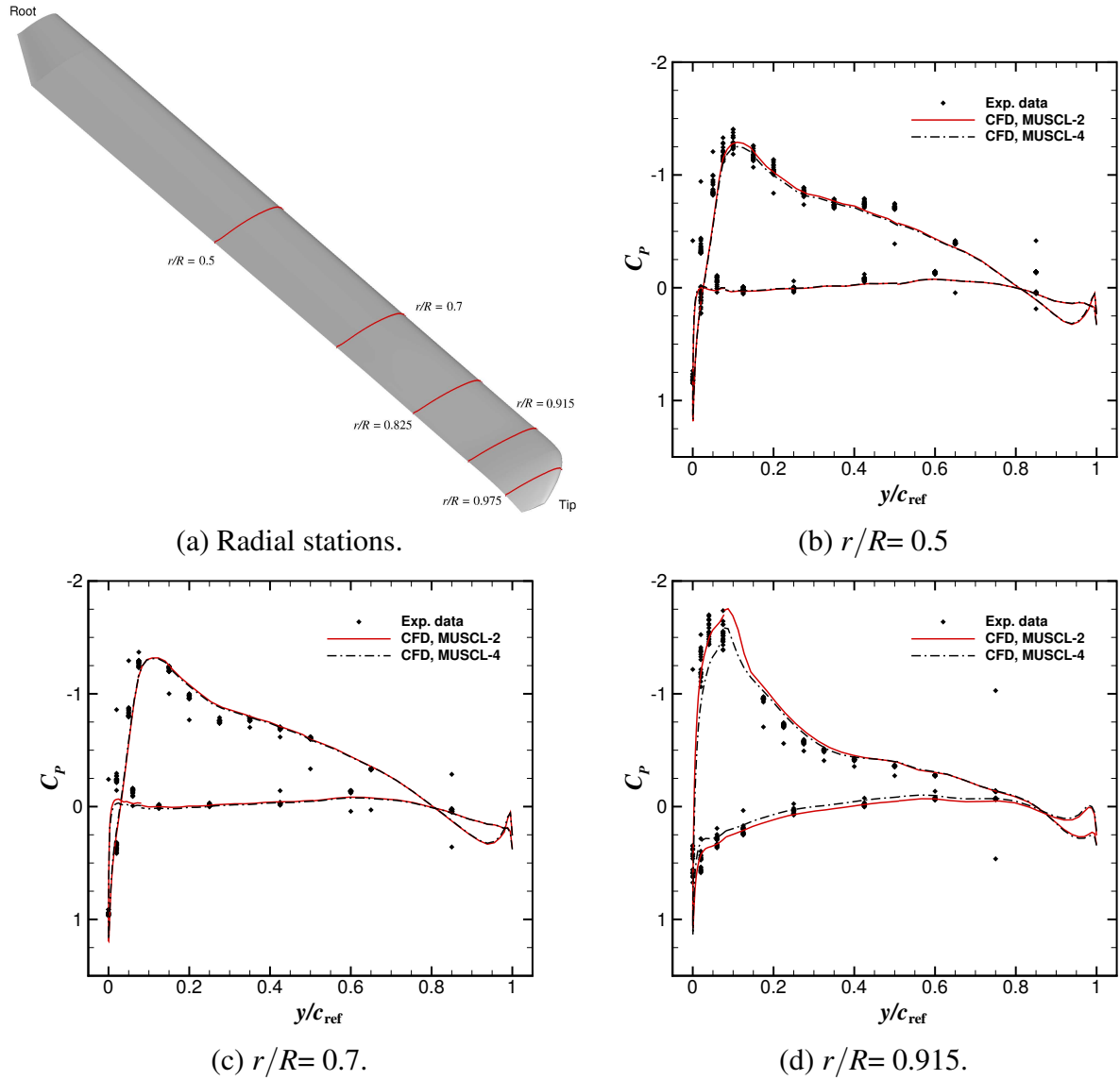
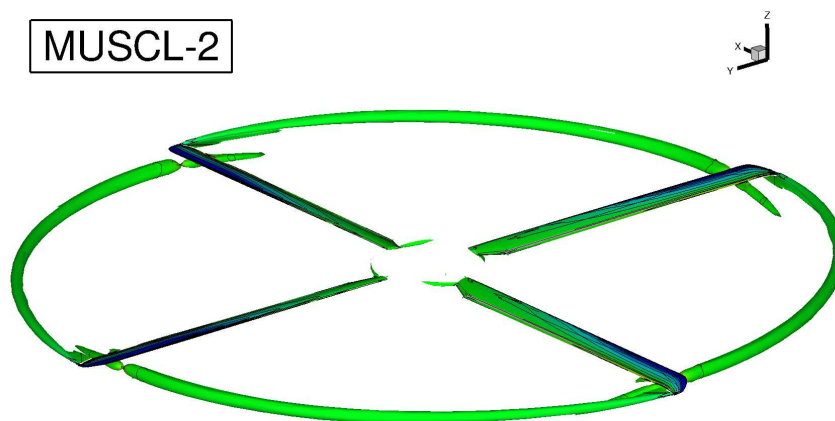
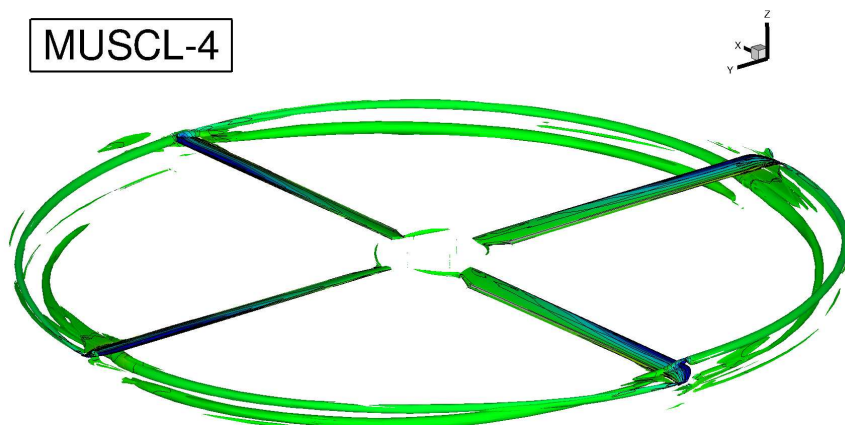


Figure 10.4:  $C_p$  profile comparisons between experiment [263] and MUSCL-2 and MUSCL-4 schemes for the full-scale 7AD rotor.



(a) Wake flow using MUSCL-2 scheme.



(b) Wake flow using MUSCL-4 scheme.

Figure 10.5: Wake flowfield for the 7AD rotor using  $\tilde{Q}$ -criterion ( $\tilde{Q} = 0.05$ ) obtained with MUSCL-2 (top) and MUSCL-4 (bottom) schemes.

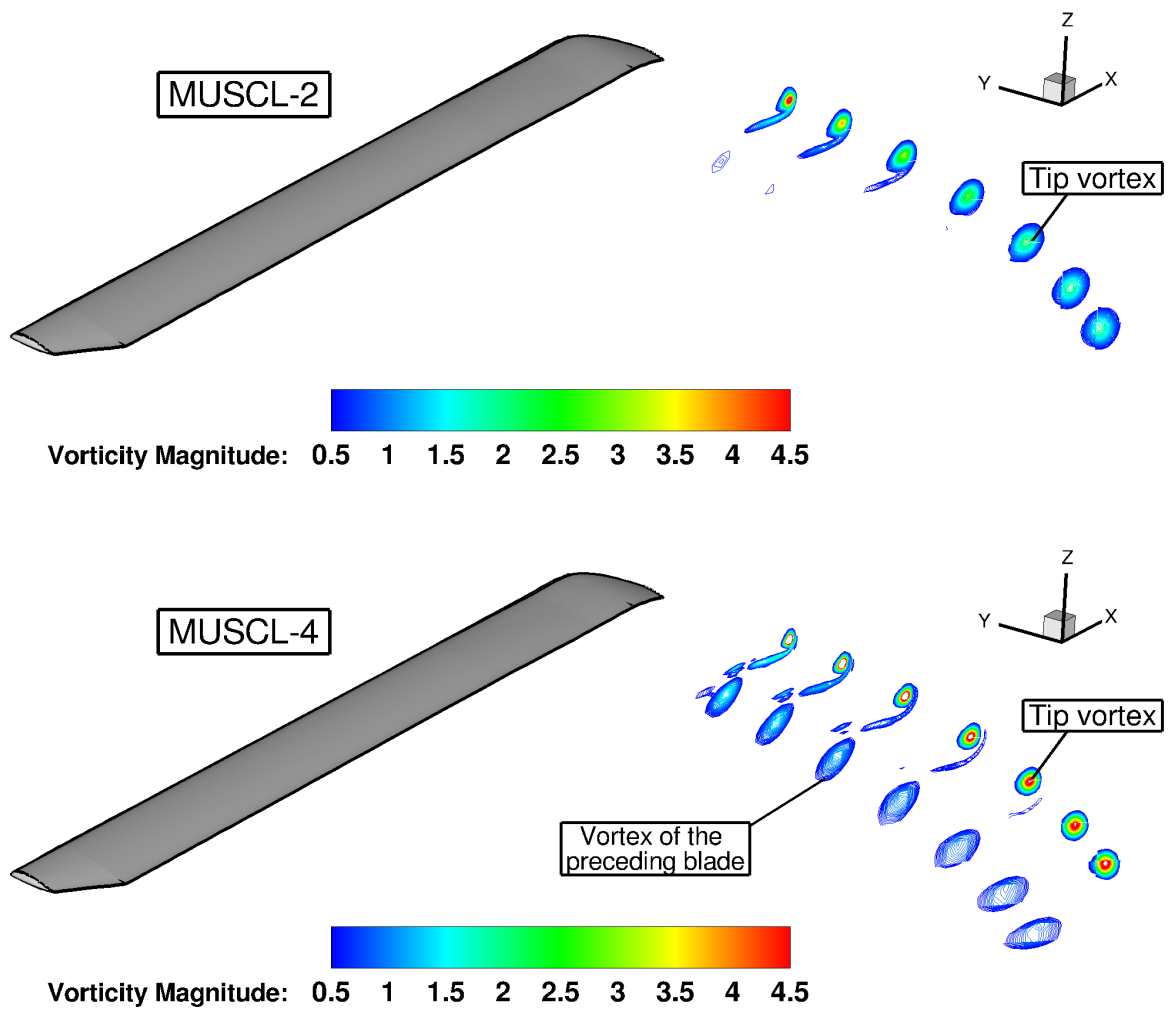


Figure 10.6: Vorticity field of the 7AD hovering rotor using MUSCL-2 (top) and MUSCL-4 (bottom) schemes.



## 10.4 S-76 Helicopter Blade

In this section, the flow around the 1/4.71 scale S-76 rotor blade, in hover, is computed using the MUSCL-2 and MUSCL-4 schemes. Due to the public availability of the case, and data sets with various tip shapes, the AIAA Applied Aerodynamics Rotor Simulations Working Group [31, 226, 264] was established in 2014 to evaluate the current state-of-the-art in hover prediction using different CFD solvers and methods for the same blade geometry. Therefore, this blade has been extensively studied [50, 52, 45, 57, 202] and represent a unique benchmark for the validation of MUSCL-4 scheme on hovering helicopter rotors.

The four-bladed S-76 model rotor, of 1/4.71 scale, has  $-10^\circ$  of non-linear twist, and three aerofoil sections comprise its planform: the SC-1013-R8 is used from the root of the blade up to  $18.9\% R$ , the SC-1095-R8 aerofoil is used from  $40\% R$  to  $80\% R$ , and the SC-1095 aerofoil is used from  $84\% R$  to the tip. For this study, the planform of the S-76 model rotor with  $60\%$  taper and  $35^\circ$  swept tip is selected at a scale of 1/4.71. The main characteristics of the model rotor blades are summarised in Table 10.3.

Table 10.3: Geometric properties of the 1/4.71 scale S-76 rotor [33].

Parameter	Value
Number of blades, $N_b$	4
Rotor radius, $R$	56.04 inches
Reference blade chord, $c_{\text{ref}}$	3.1 inches
Aspect ratio, $R/c_{\text{ref}}$	18.07
Rotor solidity, $\sigma$	0.0704
Non-linear twist, $\Theta$	$-10^\circ$

The blade-tip Mach number was set to 0.65 and three blade collective angles were considered, corresponding to low, medium, and high thrust. The Reynolds number, based on the reference blade chord of 3.1 inches and on the tip speed, was  $1.18 \times 10^6$ . All flow solutions were computed by solving the RANS equations, coupled with Menter's  $k-\omega$  SST turbulence model [191]. The flow equations were integrated with the implicit dual-time stepping method of HMB.

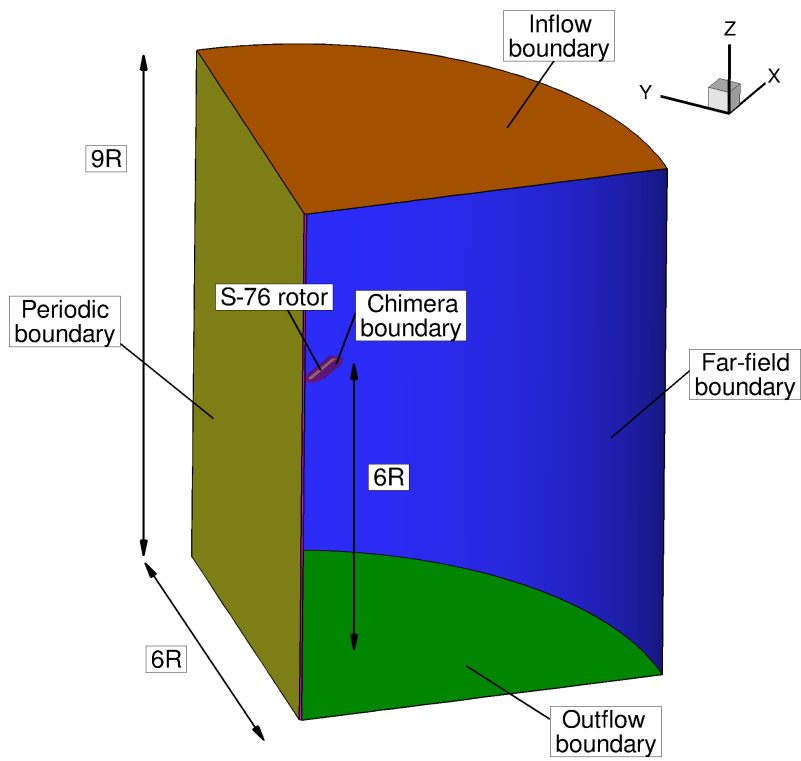
A mesh generated using the chimera technique was used for the design study of the S-76 rotor, composed of a periodic background mesh and a component mesh for the blade (see Figure

10.7 (a)). As the S-76 is a four-bladed rotor, only a quarter of the domain was meshed. A C-topology around the leading edge of the blade was selected, whereas an H-topology was employed at the trailing edge of the blade (see Figure 10.7 (b)). Coarse and medium grids were built. Table 10.4 shows a breakdown of the number of cells (per blade) used for the background mesh, and for the body-fitted mesh around the S-76 rotor blade. Because the number of cells of the foreground mesh is sufficient to accurately capture the loads on the blade, the second-order scheme is used in this level, while MUSCL-4 scheme is activated only on the background level.

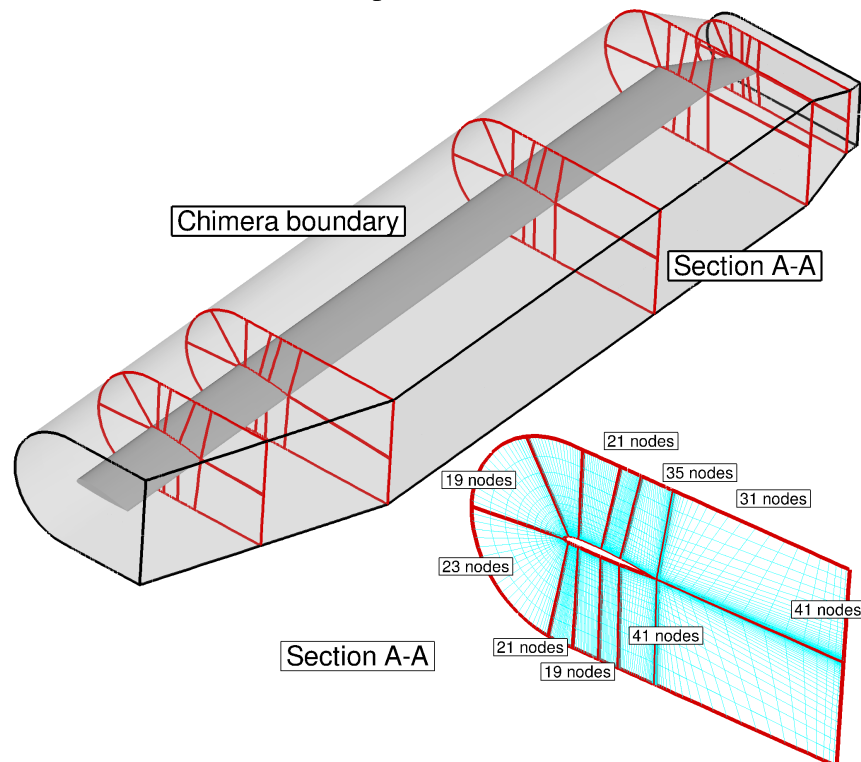
Table 10.4: Mesh size in million cells for the S-76 rotor mesh.

	<b>Coarse Mesh</b>	<b>Medium Mesh</b>
Background mesh size	2 million	3.5 million
Blade mesh size	3 million	4 million
Overall mesh size	5 million	7.5 million
Wall distance	$1.0 \times 10^{-5} c_{\text{ref}}$	$1.0 \times 10^{-5} c_{\text{ref}}$

The effect of the spatial discretisation accuracy on the figure of merit and torque coefficient as a function of the blade loading coefficient  $C_T/\sigma$  are shown in Figures 10.8 (a) and (b), respectively. Vertical lines labelled as empty (3,177 kg,  $C_T/\sigma = 0.06$ ) and maximum gross (5,307 kg,  $C_T/\sigma = 0.1$ ) weight, define the hover range of the S-76 helicopter rotor. CFD solutions were obtained with the MUSCL-2 and MUSCL-4 schemes using a coarse (red and black lines, respectively) and medium grids (green solid lines with deltas and pink cross, respectively). The test data of Balch and Lombardi [33] are represented by opened squares. The ability to resolve the vortex structure at the background level is key for accurate predictions of the loading on the blade. Hence, half million cells were added to the new background mesh (see Table 10.4). Consequently, the medium mesh shows a better agreement at low, medium, and high thrust coefficients with the test data of Balch and Lombardi [33]. Results obtained with the MUSCL-4 scheme and the coarse mesh show very good agreement with the experimental data and with the MUSCL-2 scheme with the medium grid.



(a) Computational domain.



(b) S-76 rotor mesh.

Figure 10.7: Computational domain and boundary conditions employed (top) and detailed view of the body-fitted S-76 rotor mesh (bottom).

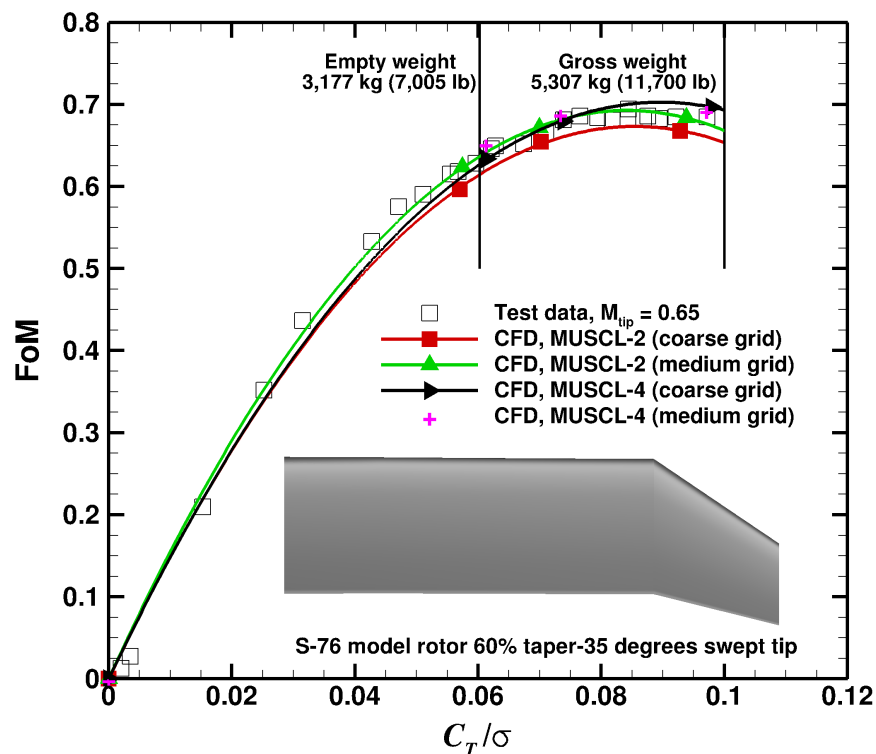
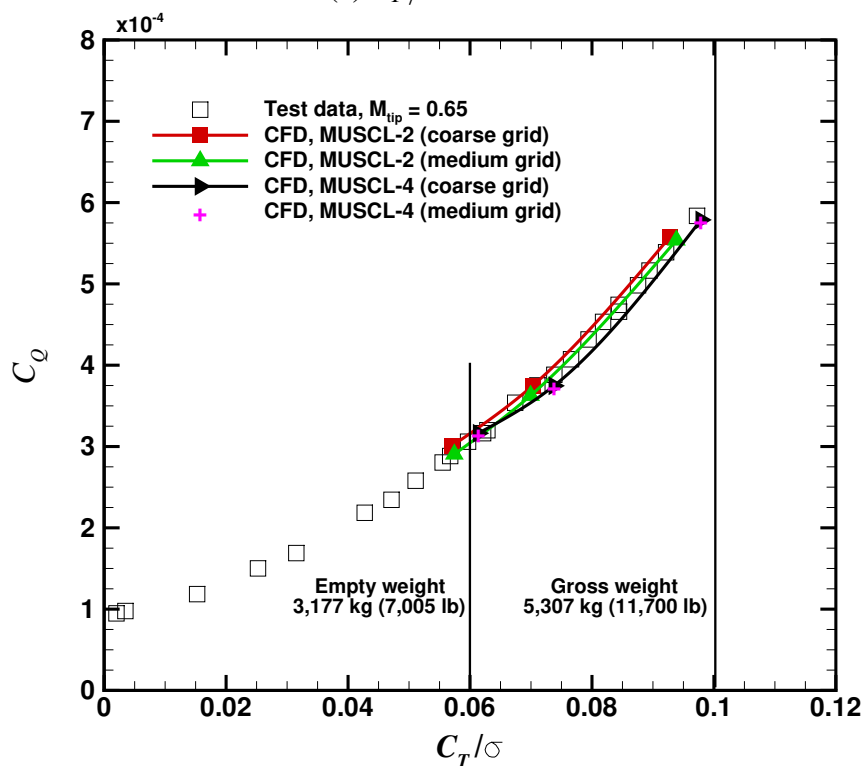

 (a)  $C_T/\sigma$  - FoM.

 (b)  $C_T/\sigma$  -  $C_Q$ .

Figure 10.8: Effect of the MUSCL-2 and MUSCL-4 schemes on the figure of merit (top) and torque coefficient (bottom) for the 1/4.71 scale S-76 rotor blade.

### 10.4.1 CPU and Memory Overheads

Table 10.5 reports the computational run-time in work units per implicit iteration for the S-76 rotor blade when MUSCL-2 and MUSCL-4 schemes are used on the coarse and medium grids, respectively (see Table 10.4). Solutions were computed on 8 cores of the high performance cluster of Glasgow University Jupiter, comprised of Intel Xeon E5620 processors. For both meshes, a CPU overhead of about 22% is found. Implicit iterations were used, so the time required to compute the pre-conditioner matrix and resolve the linear system (when using the same number of Conjugate Gradient steps) should be similar for both schemes. So, the extra CPU time required by MUSCL-4 scheme is shared across five main tasks: computing cell centre values for the first and second derivatives using Green-Gauss's method, exchanging data between processors for the first and second derivatives, and computing the new left and right states (high-order correction terms). Regarding the coarse mesh, CPU overheads of 0.5% and 0.95% are reported to compute first and second derivatives, showing a small penalty. Halo data exchanges require, however, 1.5% and 4.2% for the first and second derivatives, respectively. For this case, penalties of 8.25% and 5.6% need to be paid when computing the new residual Jacobian matrix with the high-order correction terms, and resolve the linear systems, respectively. CPU overheads of 0.6% (first derivate), 1.16% (second derivate), 1.66% (data exchange first derivate), and 5.23% (data exchange second derivate) were reported for the medium mesh. The run-time associated to the computation of the first and second derivatives does not show a strong dependency on either the mesh size and the parallel process, while the halo data exchange for the first and second derivatives seems to be more affected. This is due to the fact that the parallelisation technique used for the halo data exchange of both derivatives follows the same logic as the standard HMB adopts for exchanging the solution vector. Instead of sharing between processors a single vector of 9 variables  $(\frac{\partial F}{\partial x}, \frac{\partial F}{\partial y}, \frac{\partial F}{\partial z}, \frac{\partial^2 F}{\partial x^2}, \frac{\partial^2 F}{\partial y^2}, \frac{\partial^2 F}{\partial z^2}, \frac{\partial^2 F}{\partial x \partial y}, \frac{\partial^2 F}{\partial x \partial z}, \frac{\partial^2 F}{\partial y \partial z})$ , each variable is sent individually. This should be a priority for future work, so CPU overhead can be drastically dropped when massive meshes are used.

If a two equation turbulence model is used, MUSCL-4 provides a memory overhead of 23%. Its breakdown is as follows:  $3 \times 7$  and  $6 \times 7$  double precision numbers per cell are needed for

the first and second derivatives, respectively, and 18 extra for the distance vectors, resulting in 81 double precision numbers. This value needs to be added to the 350 doubles of the standard HMB, resulting in the aforementioned 23% of memory overhead (see chapter 4).

Table 10.5: Computational run-time for the S-76 rotor blade with MUSCL-2 and MUSCL-4 schemes on the coarse and medium meshes.

<b>Mesh</b>	<b>Scheme</b>	<b>CPU work units/iteration</b>
Coarse Mesh	MUSCL-2	1
	MUSCL-4	1.21 (21%)
Medium Mesh	MUSCL-2	1
	MUSCL-4	1.22 (22%)

The computational efficiency of the MUSCL-4 schemes can also be demonstrated. For this case, the MUSCL-4 scheme is more expensive than the MUSCL-2 scheme on the same grid ( $\sim 22\%$ ). When comparing solutions, however, with similar errors, the MUSCL-4 scheme is less expensive. As discussed before, MUSCL-2 on the medium mesh provides similar blade loads as MUSCL-4 on the coarse mesh (see Figure 10.8). However, MUSCL-4 on the coarse mesh is 14.7% less expensive than MUSCL-2 on the medium mesh.

## 10.5 JORP Propeller Blade

To evaluate the high-order method in accurately predicting airloads for modern propeller blades at high cruise speed, the JORP propeller blade is considered [72]. A single row of six blades were built with an unswept planform in conjunction with a minimum interference spinner. The blades comprise two different aerofoils from the ARA-D/A family located at 60%  $R$  and 95%  $R$ . Those sections are a modified version of the original ARA-D family for high efficiency, especially at high speed. The rotor radius has 0.457 m and the reference chord at 70%  $R$  0.1143 m, leading to an aspect ratio of 4. The chord distribution is reduced from its reference value of 0.1143 m to 0.089 m at the tip, resulting in a moderate taper of 78%.

Like the S-76, a mesh using the chimera technique was used for the JORP rotor, composed

of a periodic background mesh, where MUSCL-4 was activated, and a component mesh for the blade (MUSCL-2 scheme was activated). Table 10.6 shows the number of cells (per blade) used for the background (6.3 M), and the foreground (3.1 M) meshes.

Table 10.6: Mesh size in million cells for the JORP rotor mesh.

	<b>Medium Mesh</b>
Background mesh size	6.3 million
Blade mesh size	3.1 million
Overall mesh size	9.4 million
Wall distance	$1.0 \times 10^{-5} c_{\text{ref}}$

Table 10.7 shows the conditions employed for the axial flight. The cruise condition was modelled at 0 ft (ISA+0°), with a blade-tip Mach number of 0.529 and advance ratio 1.309. The Reynolds number for this case was  $1.163 \times 10^6$ , based on the reference blade chord and rotor tip speed (with no account for the advance velocity). The blade pitch angle  $\theta_{70}$  was set to 60° degrees.

Table 10.7: Flow conditions for the propeller blade.

<b>Parameter</b>	<b>Value</b>
Blade-tip Mach number, $M_{\text{tip}}$	0.54
Freestream Mach number, $M_{\infty}$	0.69
Advance ratio, $\mu$	1.309
Reynolds number, $Re$	$1.163 \times 10^6$
Blade pitch angle, $\theta_{70}$	60°

All flow solutions were computed by solving the RANS equations, coupled with Menter’s  $k-\omega$  SST turbulence model [191]. The flow equations were integrated with the implicit dual-time stepping method of HMB, using a pseudo-time CFL equal to 3. Typically, 40,000 iterations were necessary to drop the residual by almost 6 orders of magnitude for the flow solutions  $(\rho, u, v, w, P)$ . As discussed earlier in chapter 4, in 1D the approximation of the derivate at the cell-centre is 4th-order accurate, with no mechanism of dissipation. Moreover, a low dissipation  $\delta$  can be introduced to reduce spurious oscillation and at the same time maintain the high-order accuracy when  $k_2$  is set to  $-\frac{4}{3} + \delta$ , where a value of  $\delta = 1 \times 10^{-4}$  is used. This allows us to use MUSCL-4 without a lower-order solution to initiate the flow, keeping the robustness of the standard HMB solver as shown in Figure 10.9.

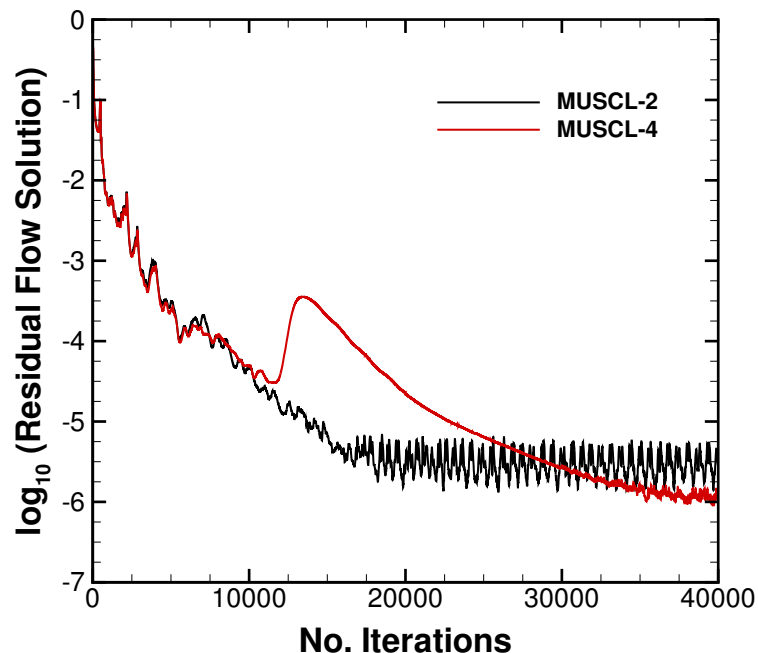


Figure 10.9: Residual of the flow solution of the JORP propeller blade as function of the number of iterations for the MUSCL-2 and MUSCL-4 schemes.

Figure 10.10 shows  $C_p$  profile comparisons between experimental data [72] and HMB at the radial stations  $r/R = 0.6$  and  $0.9$ . CFD results obtained with both schemes provide a good resolution of the airloads of the propeller blade for this demanding flight condition, and they are almost identical between the two methods. The use of thin aerofoil in conjunction with a moderate taper tip shape tend to limit the compressibility effects at the tip region encountered in this flight condition at high advance ratio.

Figure 10.11 shows iso-surfaces of  $\tilde{Q}$ -criteria obtained from the MUSCL-2 (top) and MUSCL-4 (bottom) solutions. It is clear that the helical vortex filaments trail from the tip-blade are preserved much better when the MUSCL-4 scheme is used. The same is seen for the blade root vortices.

### 10.5.1 CPU and Memory Overheads

Table 10.8 reports the computational run-time in work units per implicit iteration for the JORP propeller blade when MUSCL-2 and MUSCL-4 schemes are used on the same grids, respectively.



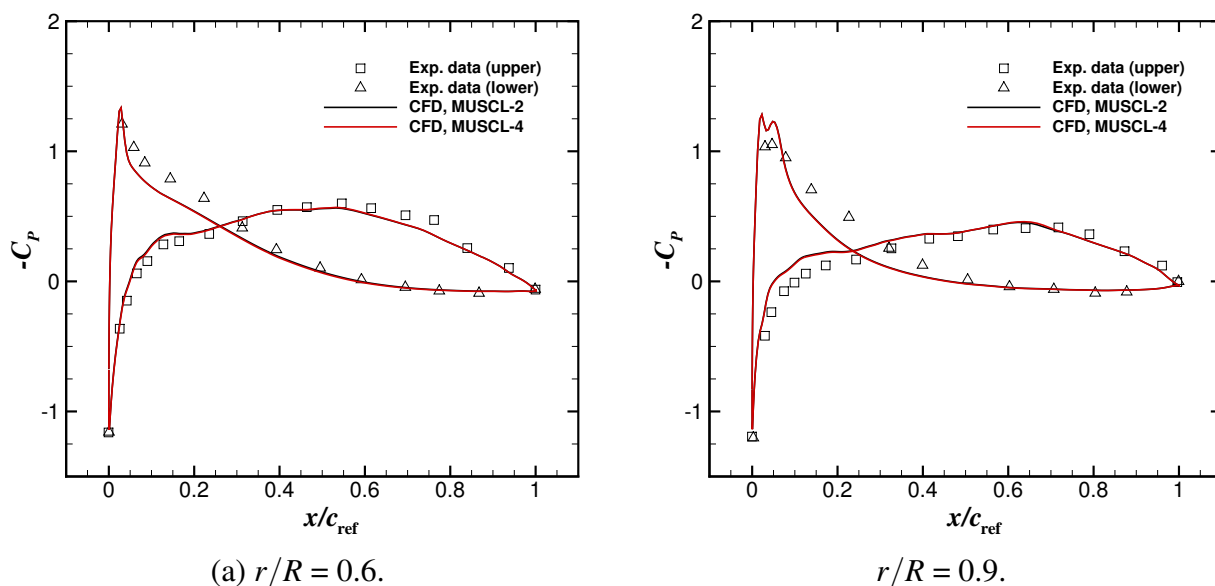
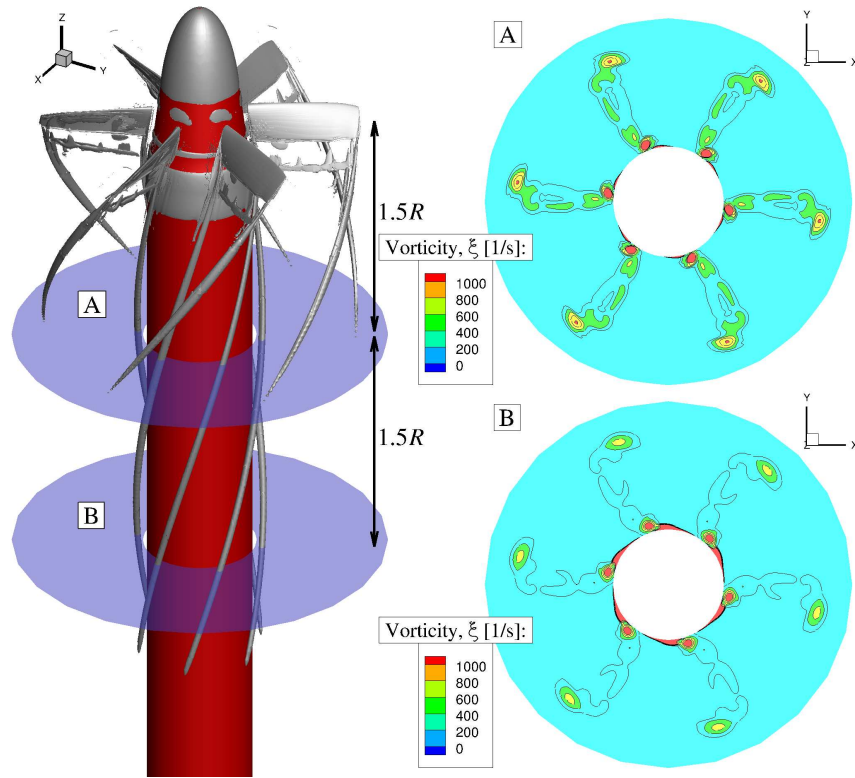


Figure 10.10:  $C_p$  profile comparisons between experimental data [72] and MUSCL-2 and MUSCL-4 schemes for the JORP propeller blade at radial stations  $r/R = 0.6$  (left) and  $0.9$  (right).

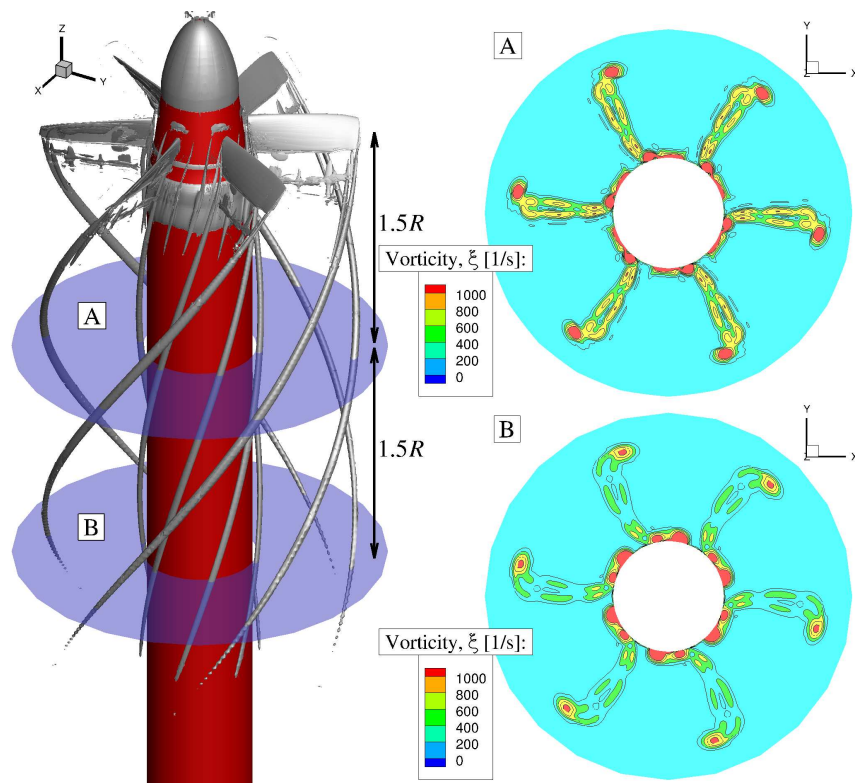
Solutions were computed on 8 cores of the high performance cluster of Glasgow University Jupiter, comprised of Intel Xeon E5620 processors. This case shows a smaller penalty compared to the S-76, with a CPU overhead of about 13%. CPU overheads of 0.7% and 1.3% are reported to compute first and second derivatives. Halo data exchanges require 1.6% and 4.17% for the first and second derivatives, respectively. Computing the new residual Jacobian matrix with the high-order correction terms and resolving the linear systems add 4.1% and 1.3% CPU overheads, respectively. Like the S-76, a memory overhead of 23% is added when the MUSCL-4 scheme is used. Nevertheless, solutions obtained with MUSCL-4 provide better wake resolution with a small penalty on CPU and memory for this medium mesh of 9 million cells.

Table 10.8: Computational run-time for the JORP propeller blade with MUSCL-2 and MUSCL-4 schemes.

Mesh	Scheme	CPU work units/iteration
Medium Mesh	MUSCL-2	1
	MUSCL-4	1.13 (13%)



(a) Wake flow using MUSCL-2 scheme.



(b) Wake flow using MUSCL-4 scheme.

Figure 10.11: Wake flowfield for the JORP propeller blade using  $\tilde{Q}$ -criterion ( $\tilde{Q} = 0.1$ ) obtained with MUSCL-2 (top) and MUSCL-4 (bottom) schemes.

## 10.6 XV-15 Tiltrotor Blade

This section demonstrates the performance of the MUSCL-4 scheme with the chimera technique for a three-dimensional tiltrotor flow. This highly loaded rotor can produce strong wakes. The resolution of which may benefit from a higher-order scheme.

The flow around the three-bladed hovering XV-15 rotor [87] is solved in steady-state by casting the equations in a noninertial reference frame. The MUSCL-4 scheme is compared with the scheme MUSCL-2 in terms of integrated airloads (FoM,  $C_T$ , and  $C_Q$ ), visualisation of the wake flow features, and wake structure (radial and vertical displacements of the vortex). All flow solutions were computed using the RANS equations and Menter's  $k-\omega$  SST turbulence model [191]. The flow equations were integrated with the implicit dual-time stepping method of HMB.

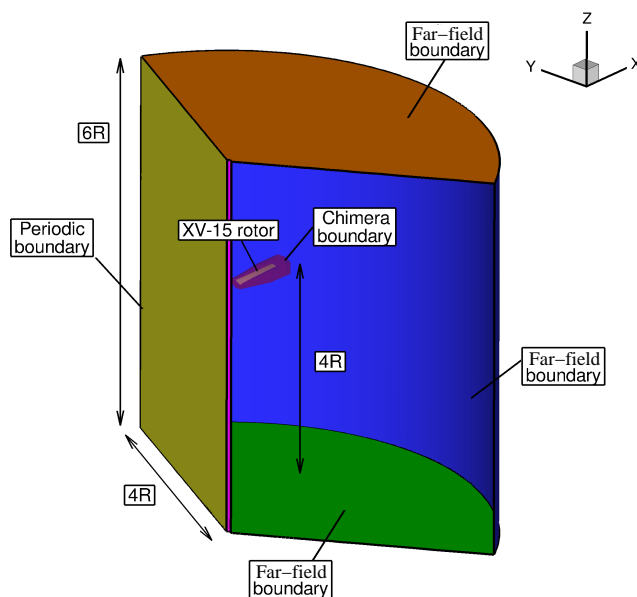
The three-bladed XV-15 rotor geometry comprises NACA 6-series five-digit aerofoil sections, and its main geometric characteristics [87] are summarised in Table 10.9. Regarding the test conditions, the blade-tip Mach number was set to 0.69, and five blade pitch angles were considered ( $\theta_{75} = 3^\circ, 5^\circ, 7^\circ, 10^\circ$ , and  $13^\circ$ ), corresponding to low, medium, and high disk loadings. The Reynolds number, based on the reference blade chord of 14 inches and on the tip speed, was  $4.95 \times 10^6$ .

Table 10.9: Geometric properties of the full-scale XV-15 rotor [87].

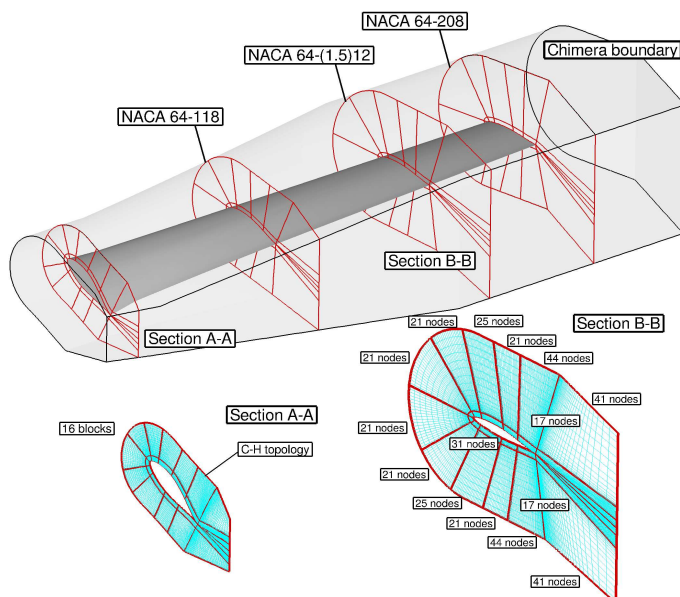
Parameter	Value
Number of blades, $N_b$	3
Rotor radius, $R$	150 inches
Reference blade chord, $c_{\text{ref}}$	14 inches
Aspect ratio, $R/c_{\text{ref}}$	10.71
Rotor solidity, $\sigma$	0.089
Non-linear twist, $\Theta$	$-40.25^\circ$

The computational domain was composed by a cylindrical off-body mesh used as a background (Figure 10.12 (a)), and a body-fitted mesh for the blade with a C-H topology (Figure 10.12 (b)). Table 10.10 lists the grids used and the breakdown of cells per blade. Coarse and medium meshes have 6.2 and 9.6 million cells per blade (equivalent to 18.6 and 28.8 million cells for three blades), with the same grid resolution for the body-fitted mesh (3.6 million cells). The background

mesh, however, was refined at the wake and near-body regions, increasing the grid size from 2.6 to 6 million cells. Solutions were obtained with the MUSCL-2 scheme using the coarse and medium grids, whilst the MUSCL-4 was only employed with the coarse grid. Like all cases using chimera, MUSCL-2 and MUSCL-4 schemes were activated at the foreground and background levels, respectively.



(a) Computational domain.



(b) XV-15 rotor mesh.

Figure 10.12: Computational domain and boundary conditions employed (top) and detailed view of the body-fitted XV-15 rotor mesh (bottom).

Table 10.10: Mesh size in million cells for the XV-15 rotor mesh.

	Coarse Mesh	Medium Mesh
Background mesh size	2.6 million	6.0 million
Blade mesh size	3.6 million	3.6 million
Overall mesh size	6.2 million	9.6 million
Wall distance	$1.0 \times 10^{-5} c_{\text{ref}}$	$1.0 \times 10^{-5} c_{\text{ref}}$

Regarding the stability of MUSCL-4 scheme, Figure 10.13 shows the residual of the flow solution ( $\rho, u, v, w, P$ ) corresponding to the XV-15 tiltrotor blade with the coarse mesh as function of the number of iterations for the MUSCL-2 and MUSCL-4 schemes. A similar behaviour was found between both schemes, without any sign of lack of stability for the MUSCL-4 scheme. This support the idea that with the introduction of low dissipation  $\delta$ , the robustness of the standard HMB solver is maintained when high-order schemes are used.

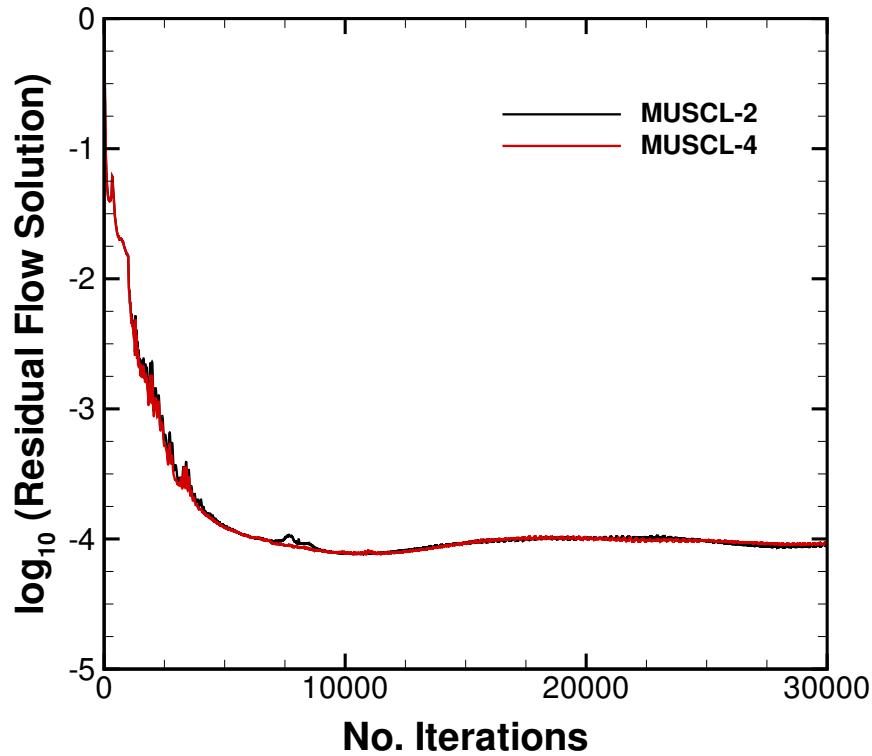


Figure 10.13: Residual of the flow solution of the XV-15 tiltrotor blade (coarse mesh) as function of the number of iterations for the MUSCL-2 and MUSCL-4 schemes.

Figure 10.14 shows the influence of the MUSCL-2 and MUSCL-4 schemes on the predicted figure of merit and torque coefficient for the full-scale XV-15 rotor. Experimental data is also

shown, carried out by Felker *et al.* [84] at OARF, and by Light [86] and Betzina [87] at the NASA 80×120ft wind tunnel. Vertical lines labelled as empty (4,574 kg,  $C_T = 0.0073$ ) and maximum gross (6,000 kg,  $C_T = 0.0096$ ) weight, define the hover range of the XV-15 in helicopter mode [73]. Momentum-based estimates of the figure of merit are also included, where an induced power factor  $k_i$  of 1.1 and overall profile drag coefficient  $C_{DO}$  of 0.01 were used. Polynomial fit curves were computed using the obtained CFD results and shown with solid lines and squares (MUSCL-2 with a coarse grid), deltas (MUSCL-2 with a medium grid), and triangles (MUSCL-4 with a coarse grid). The CFD results obtained with the MUSCL-2 scheme present are in good agreement with the test data of Betzina [87] for all blade pitch angles. Moreover, the grid size has a mild effect on the overall performance at low thrust, and a small influence at high thrust. Regarding the results obtained with the MUSCL-4 scheme, good agreement was obtained, when compared to the MUSCL-2 scheme, and using a medium grid, with the experimental data of Betzina.

To assess the ability of the MUSCL-4 scheme to accurately predict the loads when a coarse mesh is employed, a comparison between predicted and measured [88, 98] FoM at a blade pitch angle of  $10^\circ$  is reported in Table 10.11. Predictions with the MUSCL-2 scheme using the coarse and medium grids show good correlation with experiments (1.5 and 0.8 counts of FoM differences, respectively). Results obtained with the MUSCL-4 scheme on a coarse grid present a small discrepancy of 0.5 counts of FoM, which highlights the benefit of using higher-order numerical scheme in accurately predicting integrated airloads.

Table 10.11: Predicted and experimental [88, 98] figure of merit at blade pitch angle of  $10^\circ$ .

Case	FoM	Difference [absolute]	Difference [%]
Experiment	0.760	-	-
MUSCL-2 coarse grid	0.775	0.015	1.97%
MUSCL-2 medium grid	0.768	0.008	1.05%
MUSCL-4 coarse grid	0.765	0.005	0.65%

Despite that the lower-order numerical scheme is sufficient to predict the loads over the blades [170], it did not preserve the near-blade and wake flow features. In hover, to ensure realistic predictions of the wake-induced effects and therefore induced-drag, the radial and vertical

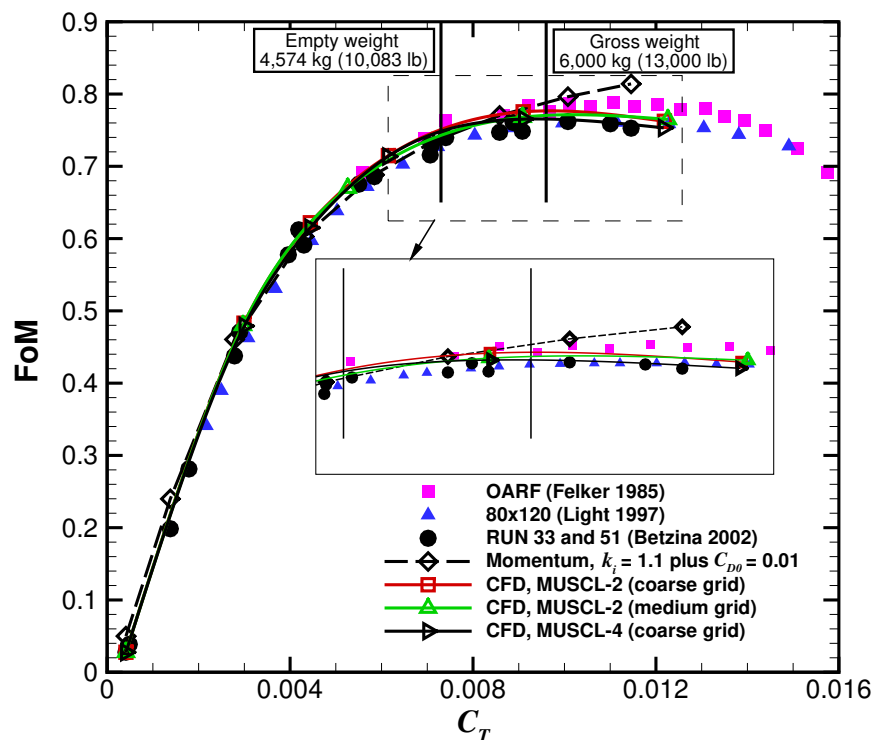
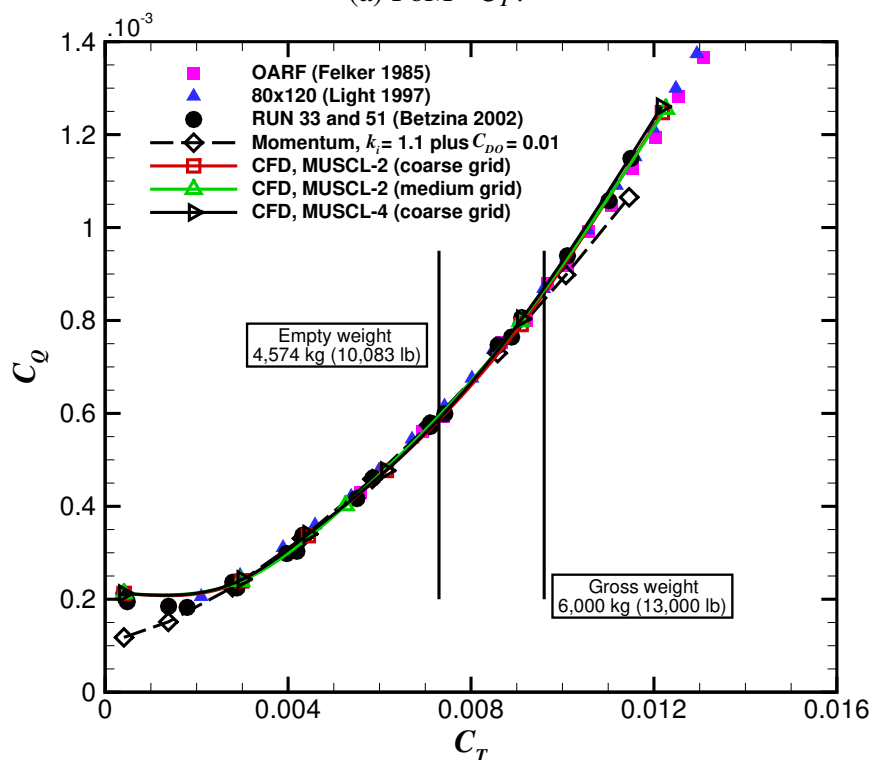

 (a) FoM -  $C_T$ .

 (b)  $C_T$  -  $C_Q$ .

Figure 10.14: Effect of the MUSCL-2 and MUSCL-4 schemes on the figure of merit (top) and torque coefficient (bottom) for the full-scale XV-15 rotor.

displacements of the vortex core should be resolved, at least for the first and second wake passages.

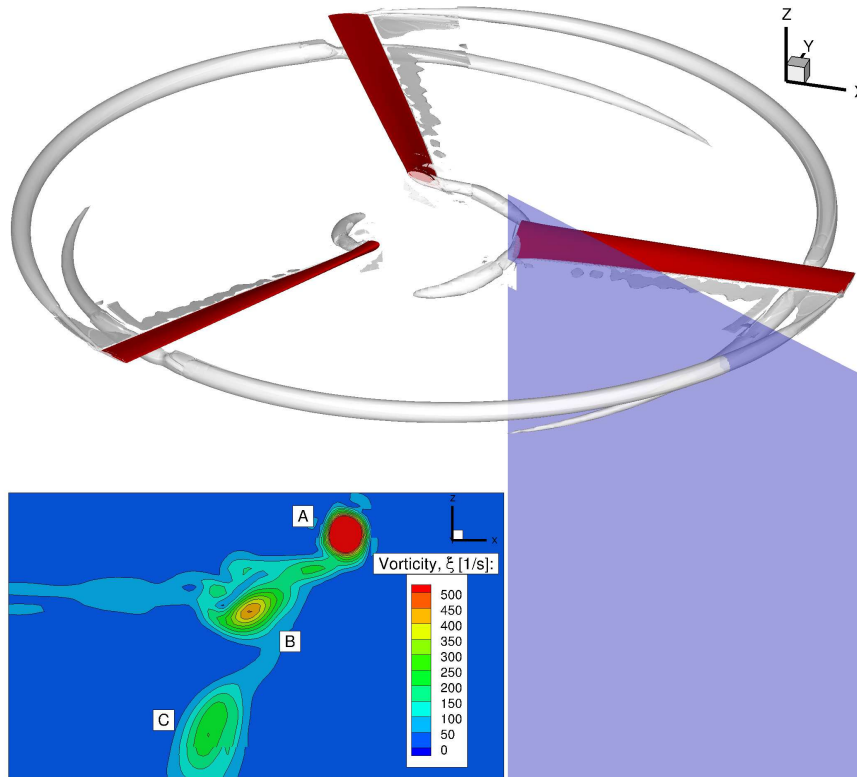
Figure 10.15 shows the wake flowfield for the full-scale XV-15 rotor using iso-surfaces of  $\tilde{Q}$ -criterion obtained with MUSCL-2 (a) and MUSCL-4 (b) with the same coarse grid of Table 10.10. It should be mentioned that, a blade pitch angle of  $10^\circ$  degrees was selected for the comparison. It is observed that the MUSCL-4 scheme preserves better the helical vortex filaments that trail from each of the blade tips, and the wake sheets trailed along the trailing edge of the blade when compared to the MUSCL-2 solution. Therefore, the lower dissipation of the MUSCL-4 scheme results in an improved preservation of the rotor wake structures. In this regard, if the MUSCL-2 is employed, the vorticity of the vortex cores (computed using the local vorticity maximum criterion) is significantly dissipated at a wake age of  $2\pi/3$  (or  $\Psi=120^\circ$ ) (first blade passage in Figure 10.16) when compared to MUSCL-4 results. Likewise, at wake ages of  $4\pi/3$  (second blade passage) and  $2\pi$  (third blade passage) a reduction of vorticity by 42.8% and 45.2% is observed when MUSCL-2 is employed.

Figure 10.17 shows a comparison of the radial (a) and vertical (b) displacements of the tip vortices, as functions of the wake age (in degrees), with the prescribed wake-models of Kocurek and Tangler [20] and Landgrebe [19]. Like for the previous plots, the MUSCL-2 and MUSCL-4 schemes with the coarse grid at blade pitch angle of  $10^\circ$  degrees were selected for comparison. It is seen that the radial displacement is less sensitive to changes on the prescribed wake-models than the vertical displacement. Until the first passage (wake age of  $120^\circ$ ), a slow convection of the tip vortices is seen in vertical displacement ( $-z/R$ ), which compares very well with Landgrebe model. The MUSCL-2 scheme showed a higher dissipation rate.

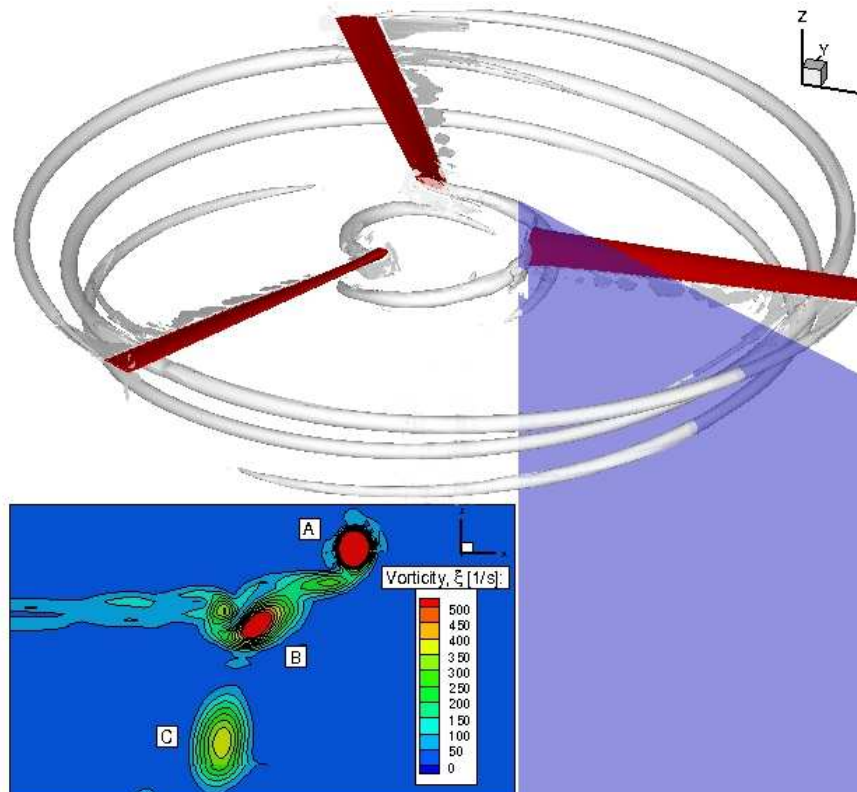
### 10.6.1 CPU and Memory Overheads

As dicussed earlier, solutions obtained with the MUSCL-4 scheme on the coarse grid show better predicted loads and rotor wake structures. Table 10.12 reports the relative computational run-time in work units per implicit iteration for the XV-15 tiltrotor blade when MUSCL-2 and MUSCL-4 schemes are used on the coarse grid. Solutions were computed on 8 cores of the high performance





(a) Wake flow using MUSCL-2 scheme.



(b) Wake flow using MUSCL-4 scheme.

Figure 10.15: Wake flowfield for the full-scale XV-15 rotor using  $\tilde{Q}$ -criterion ( $\tilde{Q}=0.05$ ). Results with the MUSCL-2 (top) and MUSCL-4 (bottom) schemes. Vortex A has wake age of  $\Psi=30^\circ$ .

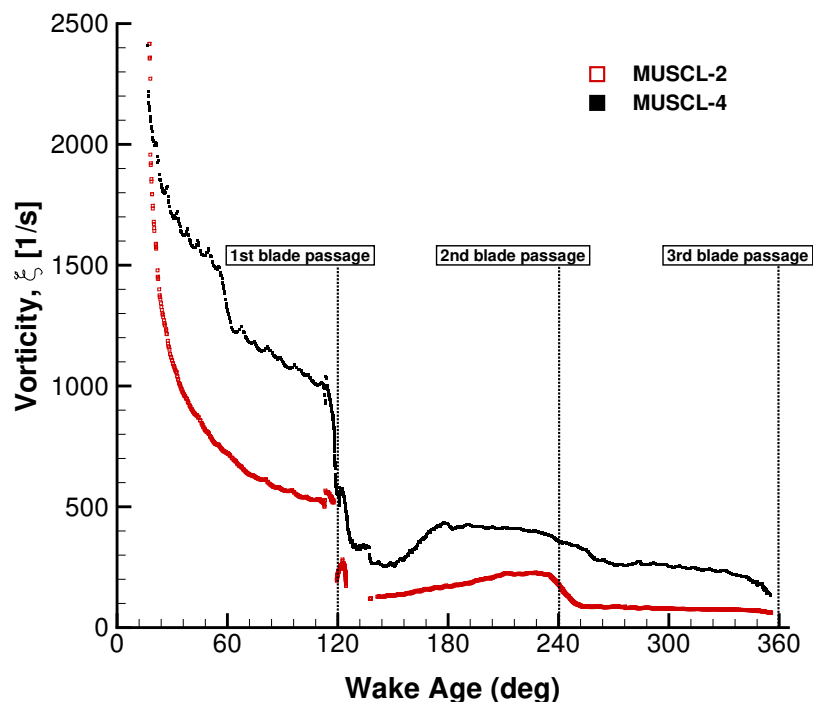


Figure 10.16: Vorticity of the vortex cores as function of the wake age in degrees obtained with the MUSCL-2 and MUSCL-4 schemes on the coarse grid.

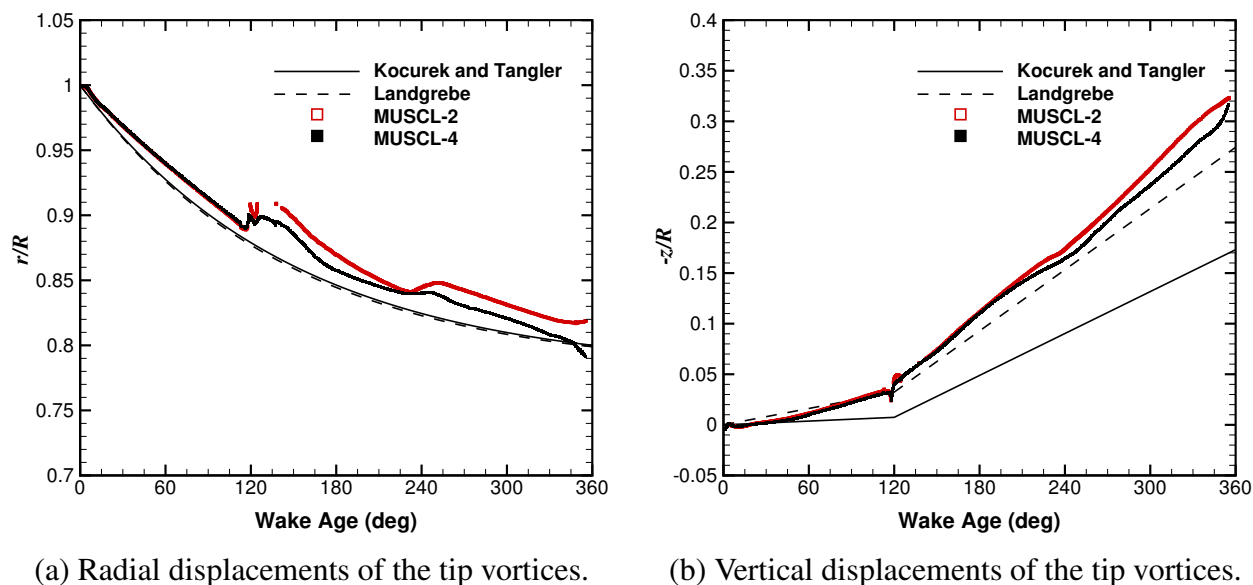


Figure 10.17: Comparison between the radial (left) and vertical (right) tip vortex displacements computed with the MUSCL-2 and MUSCL-4 schemes.

cluster of Glasgow University Jupiter, comprised of Intel Xeon E5620 processors. This case shows similar CPU overheads compared to the S-76 and JORP blades, with a penalty of about 16%. CPU overheads of 0.5% and 0.95% are reported to compute first and second derivatives. Halo data

exchanges require 1.71% and 4.4% for the first and second derivatives, respectively, and 6.4% and 2% for computing the new residual Jacobian matrix with the high-order correction terms and solve the linear system. Like the previous cases, a memory overhead of 23% is paid when the MUSCL-4 scheme is used.

Table 10.12: Computational run-time for the XV-15 tiltrotor blade with MUSCL-2 and MUSCL-4 schemes on the coarse mesh.

Mesh	Scheme	CPU work units/iteration
Coarse Mesh	MUSCL-2	1
	MUSCL-4	1.16 (16%)

## 10.7 UH-60A Rotor in Forward Flight

To validate the present high-order scheme for a three-dimensional unsteady flow with overset and moving grids, the UH-60A rotor in forward flight was considered. The UH-60A is a four-bladed rotor made of two aerofoil profiles; the SC-1095 and SC-1095R [227]. The planform of the UH-60A rotor features a  $20^\circ$  swept tip which covers 6% of the blade's radius, with a  $-16^\circ$  of non-linear twist. The main geometric characteristics of the UH-60A blade [33, 265, 266] are summarised in Table 10.13.

Table 10.13: Geometric properties of the UH-60A rotor [33, 265, 266].

Parameter	Value
Number of blades, $N_b$	4
Rotor radius, $R$	321.96 inches
Reference blade chord, $c_{\text{ref}}$	20.76 inches
Aspect ratio, $R/c_{\text{ref}}$	15.5
Rotor solidity, $\sigma$	0.0821
Non-linear twist, $\Theta$	$-16^\circ$

The multi-block structured grid for the full rotor has a total of 39.3 million cells with 2,064 blocks, with 31.1 and 8.2 million cells for the background and body-fitted grids, respectively. A hub was also included in the computational domain and modelled as a generic ellipsoidal surface.

The case selected for validation corresponds to the UH-60A main rotor at high-speed forward flight. Flight test data corresponding to this demanding configuration (flight C8534) was acquired by the U.S. Army/NASA UH-60A Airloads Program [267]. The rotor advance ratio was  $\mu = 0.368$ , and the freestream Mach number to 0.236. To meet the target thrust coefficient  $C_T/\sigma = 0.08$  while having zero roll and pitching moments, a matrix trimming method is used in HMB [6], which uses the blade element theory to compute the sensitivity matrix of loads to control angles. The flow solutions corresponding to MUSCL-2 and MUSCL-4 schemes were computed by solving the URANS equations, coupled with Menter's  $k-\omega$  SST turbulence model [191]. The time step corresponds to 0.25 deg in the azimuthal direction and was based on the experience gained with previous rotor computations in forward flight [174]. The trim state is specified in Table 10.14 and the comparison of the blade normal force and pitch moment (mean removed) at three radial stations is show in Figure 10.18. Good agreement is found between experimental and predicted load with similar trends between MUSCL-2 and MUSCL-4 results.

Table 10.14: Trim state for the UH-60A forward flight case using MUSCL-2 and MUSCL-4 schemes.

Parameter	Value	
	MUSCL-2	MUSCL-4
$\mu$	0.368	0.368
$M_{\text{tip}}$	0.648	0.648
$\theta_{\text{shaft}}$	7.30°	7.30°
$\theta_0$	12.13°	11.97°
$\theta_{1s}$	8.58°	8.35°
$\theta_{1c}$	−2.27°	−2.17°
$\beta_0$	3.43°	3.43°
$\beta_{1s}$	−1.0°	−1.0°
$\beta_{1c}$	−0.70°	−0.70°

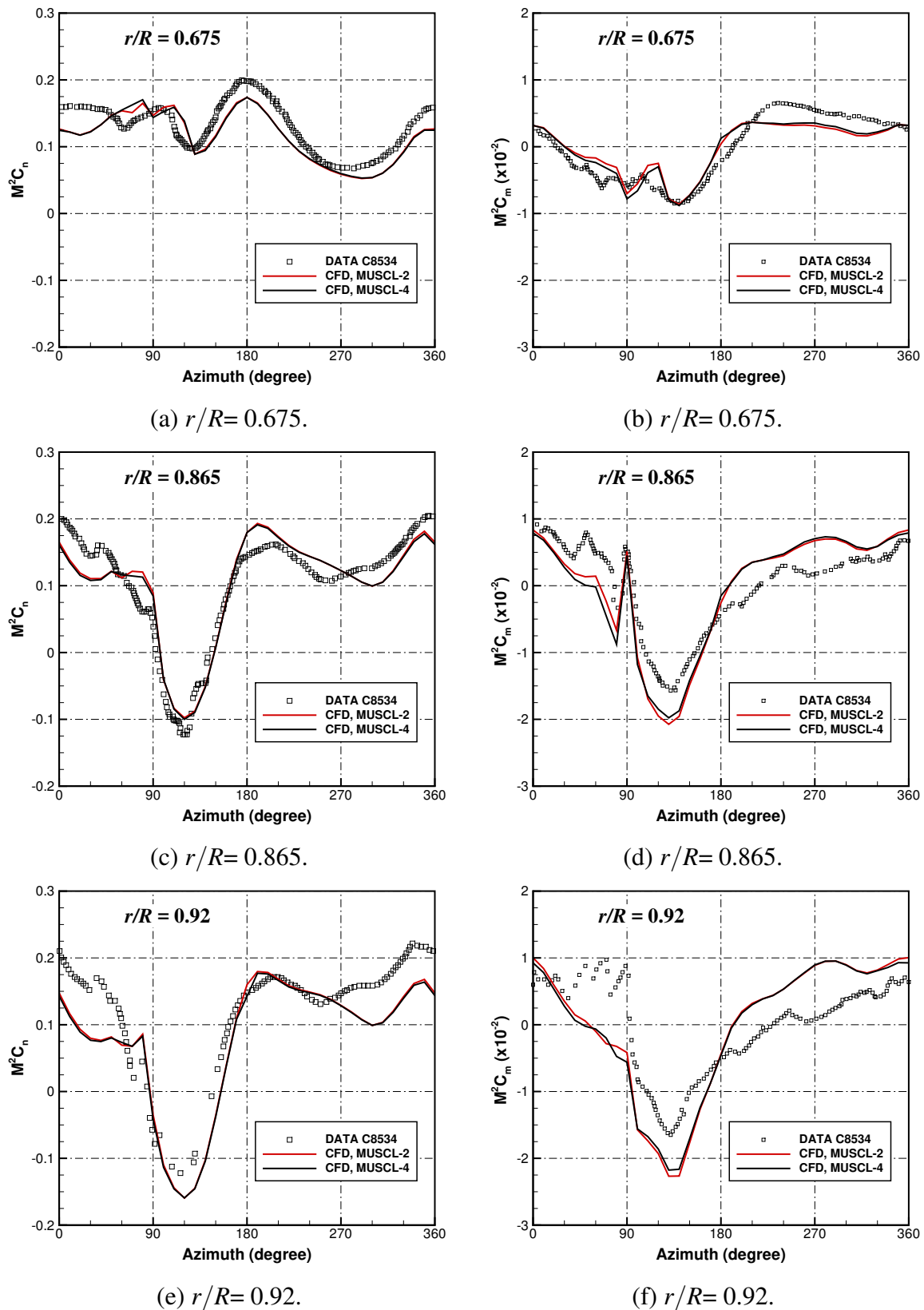


Figure 10.18: Comparison between experimental data and predictions using MUSCL-2 and MUSCL-4 schemes for the UH-60A blade normal force and pitching moment (mean removed) at advance ratio ( $\mu = 0.368$ ) at three radial stations.

Figures 10.19 and 10.20 show vorticity contours at the planes  $x/R=0.5$  and 1, respectively, of the blade 1 ( $\Psi=0$ ) for the MUSCL-2 and MUSCL-4 schemes. Results with MUSCL-4 show a higher resolution of the rotor wake structures at the advancing and retreating sides when compared to the MUSCL-2. In fact, the vortex C ( $\Psi=270^\circ$ ) computed with MUSCL-2 in Figures 10.19 and 10.20 shows a reduction of the core maximum vorticity by almost 20% compared to the MUSCL-4 results (see Table 10.15).

Table 10.15: Comparison of core maximum vorticity for the UH-60A forward flight case using MUSCL-2 and MUSCL-4 schemes.

Plane	Value	
	MUSCL-2	MUSCL-4
$x/R=0.5$ , Vortex C	342.2 rad/s	403.4 rad/s
$x/R=1$ , Vortex C	68.46 rad/s	85.2 rad/s

Visualisation of the flowfield of the UH-60A rotor using the  $\tilde{Q}$ -criterion [206] is presented in Figure 10.21 for the MUSCL-2 and MUSCL-4 approaches. The wake obtained with MUSCL-4 solution is preserved for much longer than the one obtained with MUSCL-2. Figure 10.22 shows vorticity contours at the plane  $x/R=2$  (dashed lines in Figure 10.21), which highlights the capacity of the MUSCL-4 scheme in preserving the vortex cores and rotor wake structures (A, and B in Figure 10.22).

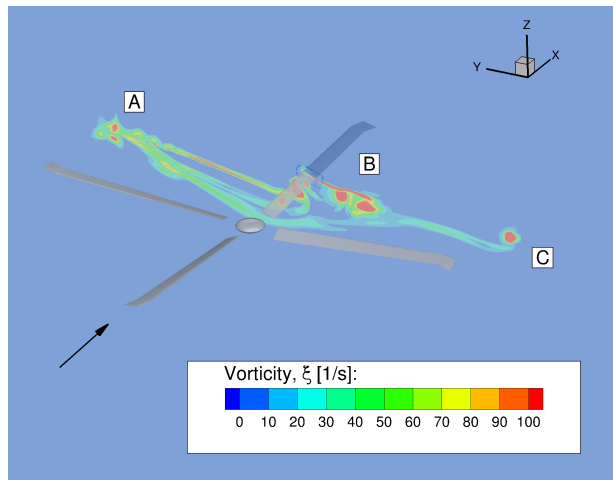
### 10.7.1 CPU and Memory Overheads

Table 10.16 reports the computational run-time in work units per implicit iteration for the UH-60A rotor in forward flight when MUSCL-2 and MUSCL-4 schemes are used on the same grid. The multi-block structured grid for this case has a total of 39.3 million cells with 2,064 blocks, with 31.1 and 8.2 million cells for the background and body-fitted grids, respectively. Due to the large mesh, this case needs to be computed using parallel executions, so solutions were computed on 48 cores of the high performance cluster of Glasgow University Jupiter. For the S-76, JORP propeller, and XV-15 blades, results with MUSCL-4 show CPU penalties of 22%, 13%, and 16%, respectively, where the computational cost associated with the halo data of the first and second

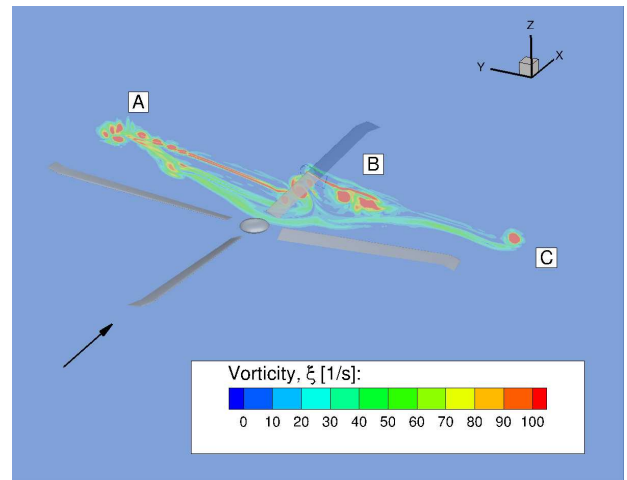
derivatives is less than 5%. This is not the case when larger meshes are used, mainly due to the poor parallelisation of both exchanges, so a CPU overheads of about 130% is added when MUSCL-4 is used for the UH-60A rotor in forward flight. CPU overheads of 0.69% and 1.52% are reported to compute first and second derivatives and 39.95% and 79.98% for halo data exchanges for the first and second derivatives, respectively. This calls for some improvement on the parallelisation of the scheme in order to obtain CPU overheads of the order of the medium grids. Regarding the memory overhead, of 23% is added when MUSCL-4 scheme is used.

Table 10.16: Computational run-time for the UH-60A rotor in forward flight with MUSCL-2 and MUSCL-4 schemes on the same mesh.

<b>Mesh</b>	<b>Scheme</b>	<b>CPU work units/iteration</b>
Fine Mesh	MUSCL-2	1
	MUSCL-4	2.3 (130%)

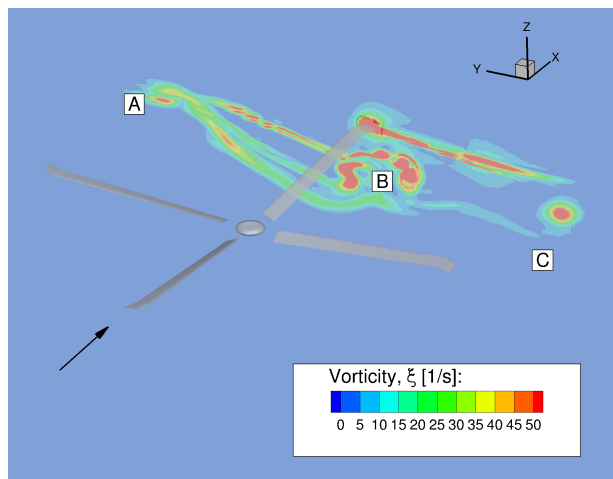


(a) MUSCL-2 scheme.

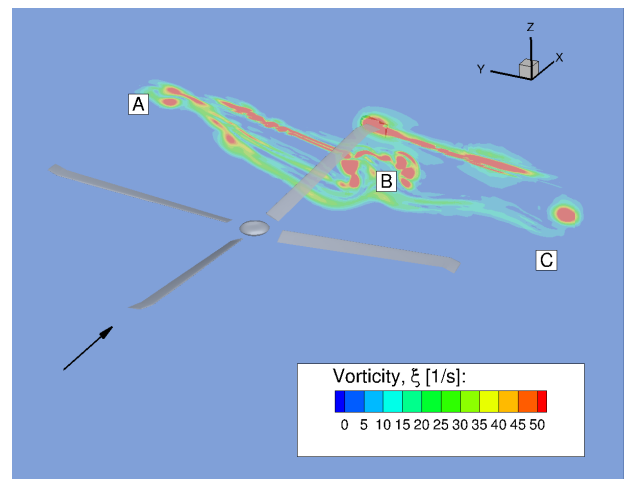


(b) MUSCL-4 scheme.

Figure 10.19: Vorticity contours at the plane  $x/R = 0.5$  of the blade 1 ( $\Psi = 0$ ) for the MUSCL-2 and MUSCL-4 schemes.



(a) MUSCL-2 scheme.



(b) MUSCL-4 scheme.

Figure 10.20: Vorticity contours at the plane  $x/R = 1$  of the blade 1 ( $\Psi = 0$ ) for the MUSCL-2 and MUSCL-4 schemes.



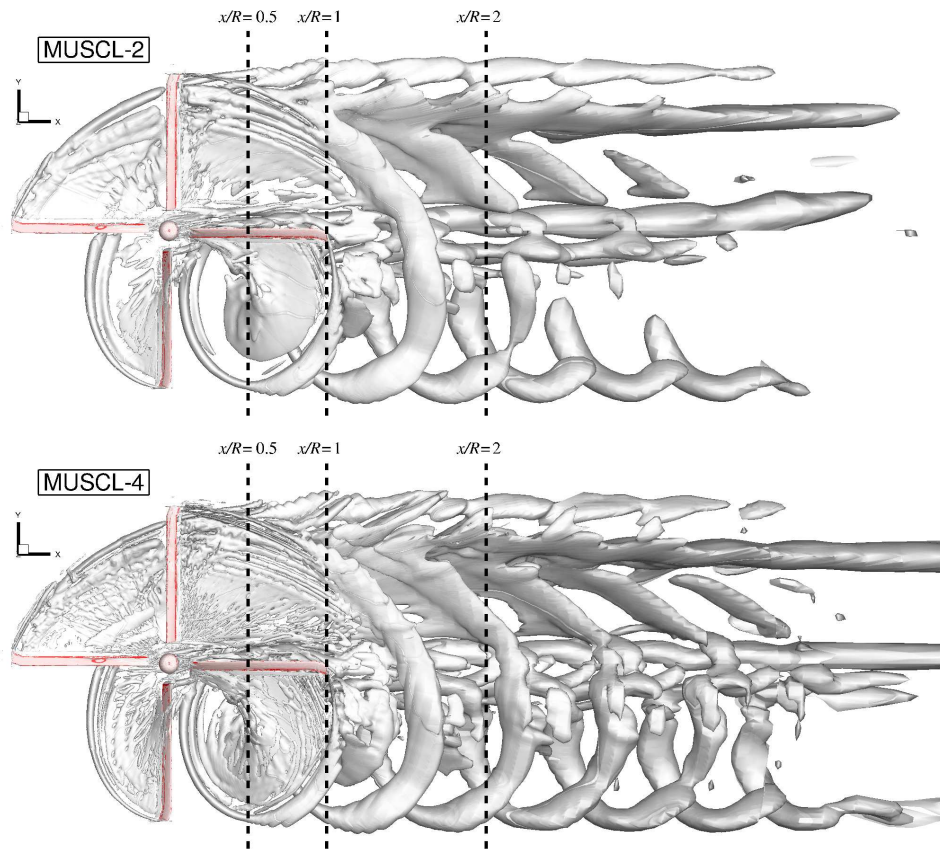
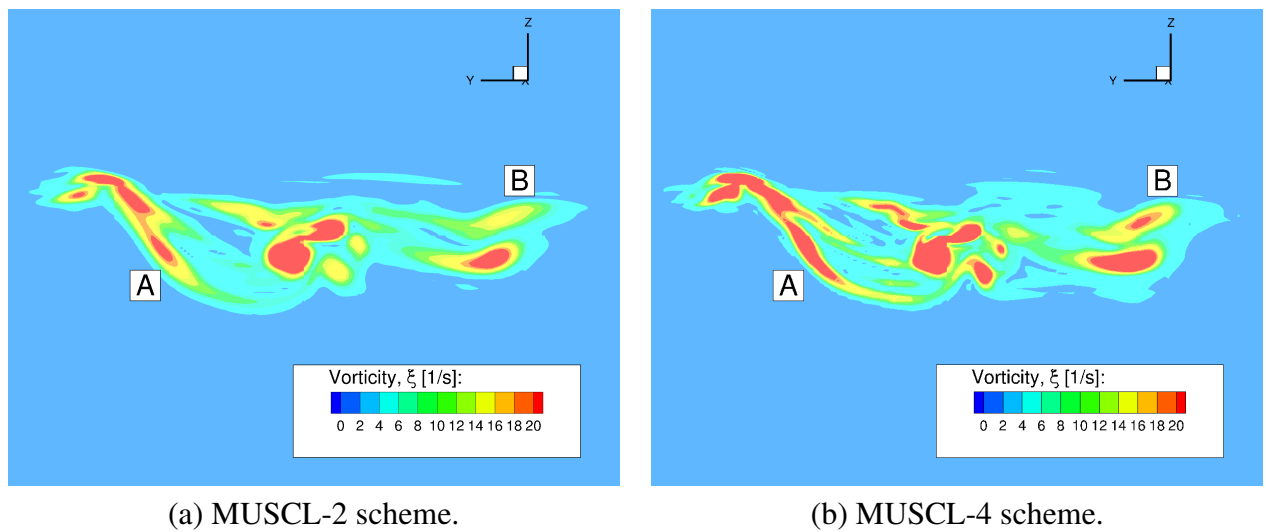


Figure 10.21: Wake-visualisation of the UH-60A rotor in forward flight using  $\tilde{Q}$ -criterion ( $\tilde{Q}=0.0007$ ). Results with the MUSCL-2 (top) and MUSCL-4 (bottom) schemes.



(a) MUSCL-2 scheme.

(b) MUSCL-4 scheme.

Figure 10.22: Vorticity contours at the plane  $x/R = 2$  of the blade 1 ( $\Psi = 0$ ) for the MUSCL-2 and MUSCL-4 schemes.

## 10.8 Complete Tiltrotor Computation

To demonstrate that the current scheme can deliver on complex cases, a complete tiltrotor is simulated. Numerical simulations of the ERICA tiltrotor using the MUSCL-2 and MUSCL-4 schemes were performed and are presented here.

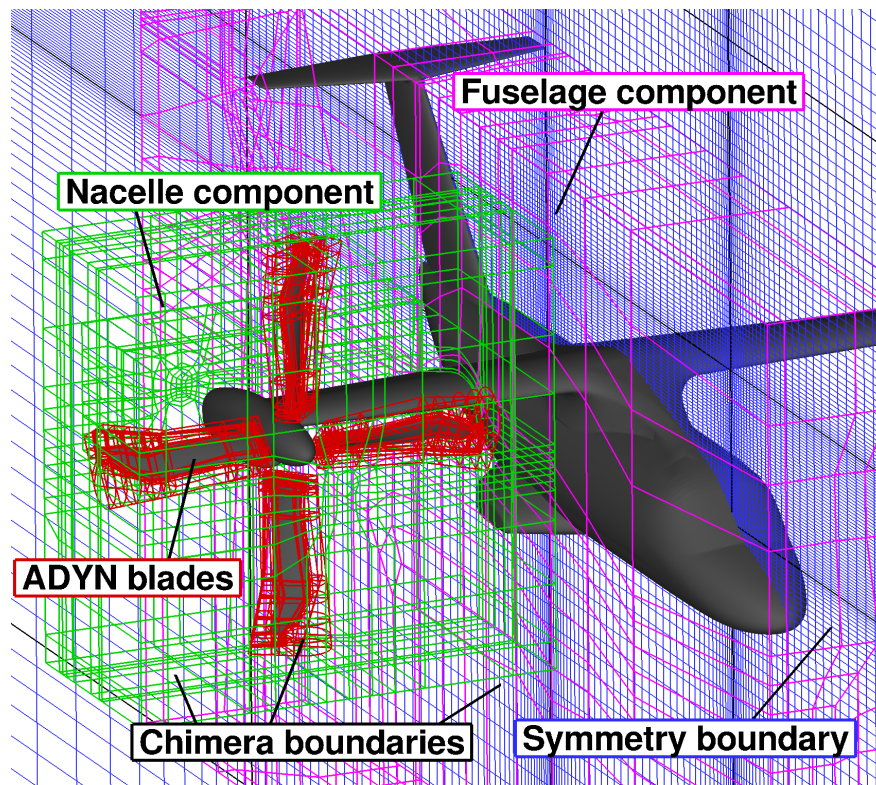
The chimera method was employed to ease the generation of the different structured multi-block grids. Self-contained component grids for the main fuselage and the nacelle-tiltable wing were built, while four ADYN blades were embedded in the nacelle mesh component. A Cartesian off-body mesh was used as the background to capture the convection of the tip vortex generated by the blades. Table 10.17 compares the mesh size used here for CFD computation. The multi-block overset arrangement of the ERICA tiltrotor for the aeroplane mode is shown in Figure 10.23.

Table 10.17: ERICA model-scale component mesh sizes, given as million nodes.

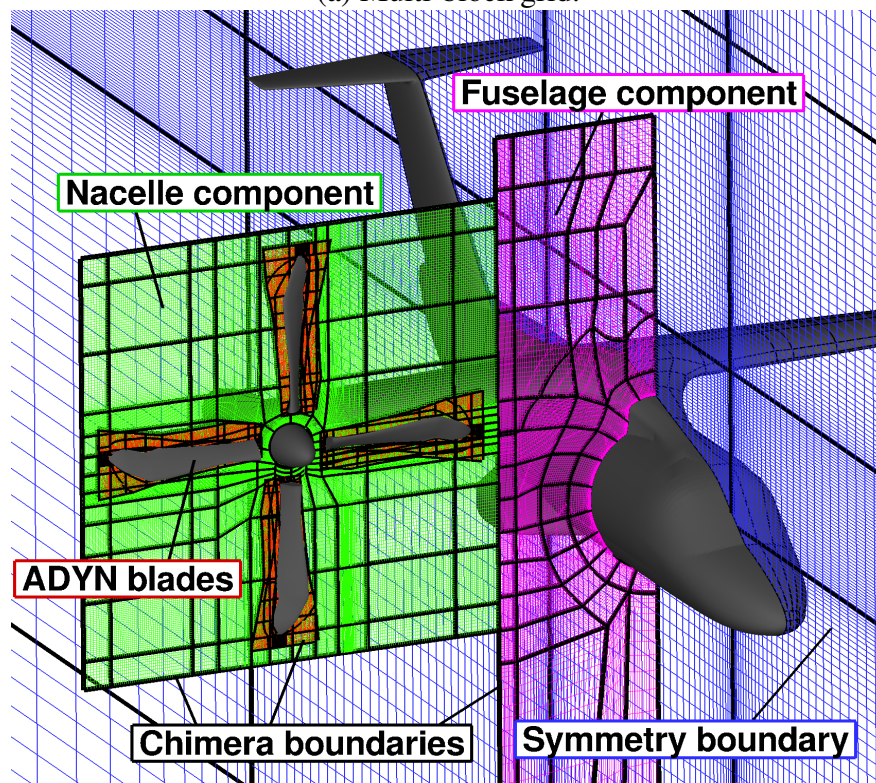
Components	Aeroplane Mode
Fuselage and fixed wing	9.9
Nacelle and tiltable wing	30.3
Rotor blades (x4)	11.4
Wind tunnel	4.6
<b>Total</b>	<b>56.2</b>

Table 10.18 summarises the test conditions employed for computations. The aeroplane mode is labelled as AC1 (aeroplane configuration), and refers to a very low speed aeroplane-mode  $M_\infty = 0.168$ , along with a large aircraft AoA of  $\delta_{FU} = 10.02$  degrees. Neither the nacelles nor the tiltable wings were tilted with respect to the fuselage ( $\delta_{FU} = \delta_{NAC} = \delta_{TW}$ ). The Reynolds numbers, based on the reference length  $L_{ref}$  and on the freestream velocity  $V_\infty$ , was  $1.70 \times 10^6$ .

Eight cross-sections were selected for  $C_p$  profile comparisons between CFD and experiments [91, 92] (see Table 10.19). One section was selected on the top symmetry plane of the fuselage (labelled with SYM-TOP), one section on the fixed wing (labelled with FW), two on the tiltable wing (labelled with TW) which define the zone of aerodynamic interaction between the tiltable wing and the blades, and four on the fuselage (labelled with FU).



(a) Multi-block grid.



(b) Cross section of the multi-block grid.

Figure 10.23: Details of the multi-block overset arrangement of the ERICA tiltrotor in aeroplane mode configuration. Blue line=background component; purple line=fuselage component; green line=nacelle component; grey line=blade component.

Table 10.18: Test conditions for the aeroplane mode AC1 [251, 252].

Parameters	Aeroplane Mode AC1
$M_\infty$	0.168
$M_{\text{tip}}$	0.470
$\mu = M_\infty/M_{\text{tip}}$	0.357
$Re_{\text{ref}}$	$1.70 \times 10^6$
$\delta_{\text{FU}}$ [deg]	$10.02^\circ$
$\delta_{\text{NAC}}$ [deg]	$10.02^\circ$
$\delta_{\text{TW}}$ [deg]	$10.02^\circ$
RPM blade rotor	2,130
$\theta_{75}$ [deg]	$27.36^\circ$

Table 10.19: Nomenclature of the stations selected for  $C_p$  profile comparisons.

Nomenclature	Description
SYM-TOP	Fuselage symmetry plane (top), station $y=0$ mm.
FW-A	Fixed wing, station $y=490$ mm.
TW-A	Tiltable wing, station $y=855$ mm.
TW-B	Tiltable wing, station $y=1117.5$ mm.
FU-A	Fuselage, station $x=260$ mm.
FU-B	Fuselage, station $x=1163$ mm.
FU-C	Fuselage, station $x=1810$ mm.
FU-D	Fuselage, station $x=2760$ mm.

FU=Fuselage; FW=Fixed Wing; TW=Tiltable Wing; SYM=Symmetry.

$C_p$  profile comparisons between CFD and experiments [91, 92] on the fuselage, fixed and tiltable wings of the ERICA tiltrotor are given in Figure 10.24. They correspond to the top fuselage centre-line and inner, middle, and outer tiltable and fixed wing sections. The CFD results were not averaged in phase, like the test data, which could lead to a source of error in the comparison. Regarding the  $C_p$  profile at the centre-line of the fuselage (Figure 10.24 (a)), a zone of recirculation is seen by both sets of experiments (Modane and DNW experiments are denoted by squares and triangles, respectively) represented by a pressure plateau after the wing leading edge suction peak. The HMB predictions (MUSCL-2=red line, MUSCL-4=green line) overestimate the suction peak and do not capture the region of recirculation. This can be due to a failure of the employed turbulence model, wind tunnel effects, and lack of the exact trim conditions employed during the wind tunnel tests.

In the middle fixed and tiltable wing sections (Figures 10.24 (c) and 10.24 (d)), wind tunnel experiments show a good agreement to each other, with small differences of 9% for the suction peak. Note that the differences between the two sets of experiments were always larger than the differences between the MUSCL-2 and MUSCL-4 results.

Figure 10.25 presents  $C_p$  comparisons on the ERICA fuselage at four cross-sections. As can be seen, all CFD curves are close to the experimental data. Better agreement is obtained at the front of the fuselage, where the flowfield is attached. Both solutions appear to capture well all features shown the experiments. Even for stations located behind the fixed wing, the agreement is still fair near the sponsons and the fin of the model.

Regarding the MUSCL-2 solution, the wake behind the rotor disk (see Figure 10.26 (a)) is preserved for more than one rotor diameter downstream. This informative plot shows the interaction of the rotor wake with the nacelle and tiltable wings. From these iso-surfaces it can be seen that the rotor wake does not directly interact with the fuselage and the fixed part of the wings. Iso-surface contours of  $\tilde{Q}$ -criterion are shown from the CFD simulations using the MUSCL-4 scheme in Figure 10.26 (b), which reveals that detailed wake characteristics can be easily identified when using high-order schemes.

### 10.8.1 CPU and Memory Overheads

Table 10.20 reports the computational run-time in work units per implicit iteration for the ERICA tiltrotor when MUSCL-2 and MUSCL-4 schemes are used on the same grid. Solutions were computed on 48 cores of the cluster Jupiter. Like the UH-60 in forward flight, a large penalty is paid when the halo data of the first and second derivatives are exchanged for parallel execution. So, this case shows a CPU overhead of about 144%. CPU overheads of 0.13% and 0.26% are reported to compute first and second derivatives, showing a small penalty of 0.39%. However, halo data exchanges require 48.2% and 96.31% for the first and second derivatives, respectively. Despite that the results obtained with MUSCL-4 are promising showing the ability of the scheme in preserving the wake much better, a more efficient parallelisation of the halo data need is needed.

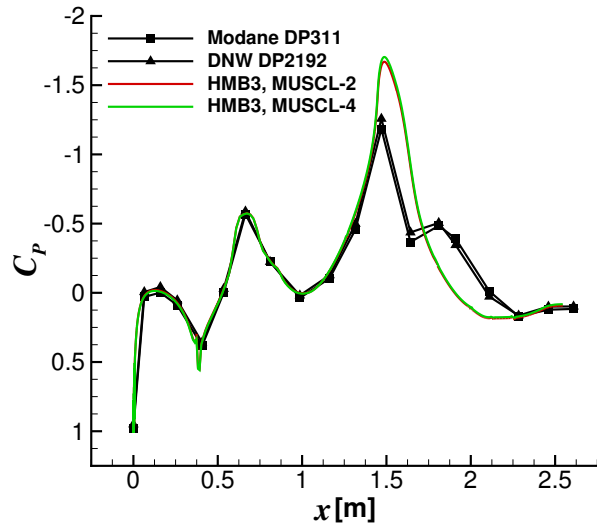
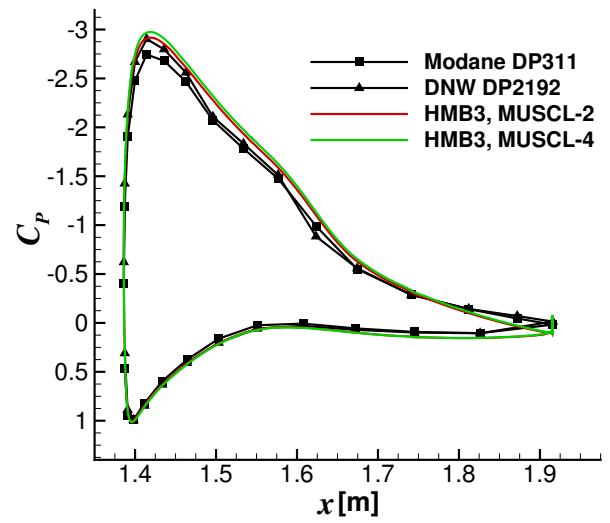
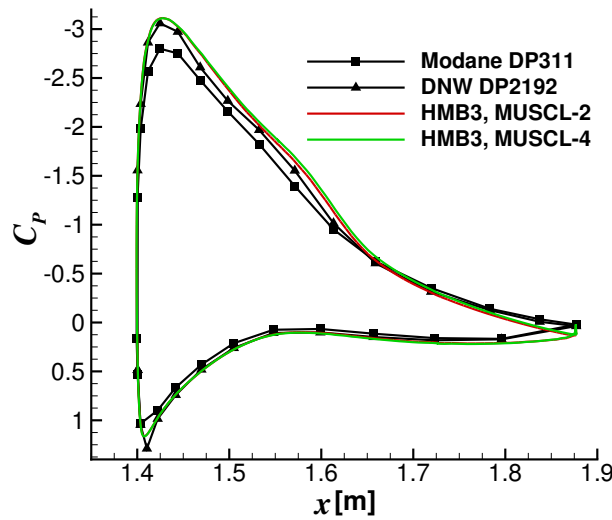
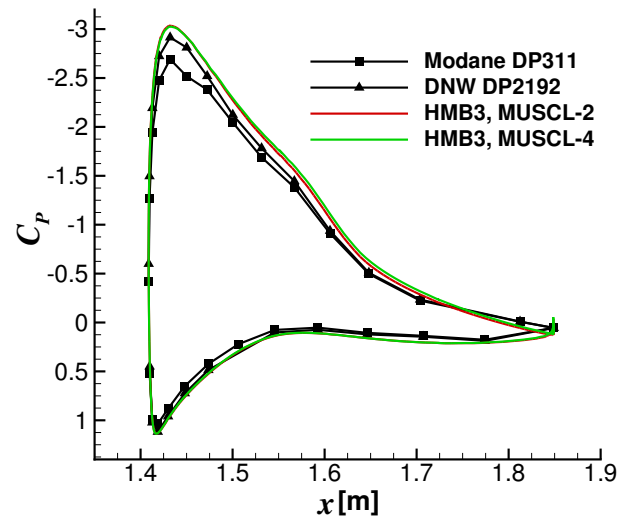

 (a) SYM-TOP, section  $y=0$  mm.

 (b) FW-A, section  $y=490$  mm.

 (c) TW-A, section  $y=855$  mm.

 (d) TW-B, section  $y=1117.5$  mm.

 Figure 10.24:  $C_p$  profile comparisons between CFD and experiments [92, 91] on the fixed and tiltable wings of the ERICA tiltrotor for the aeroplane mode configuration AC1.



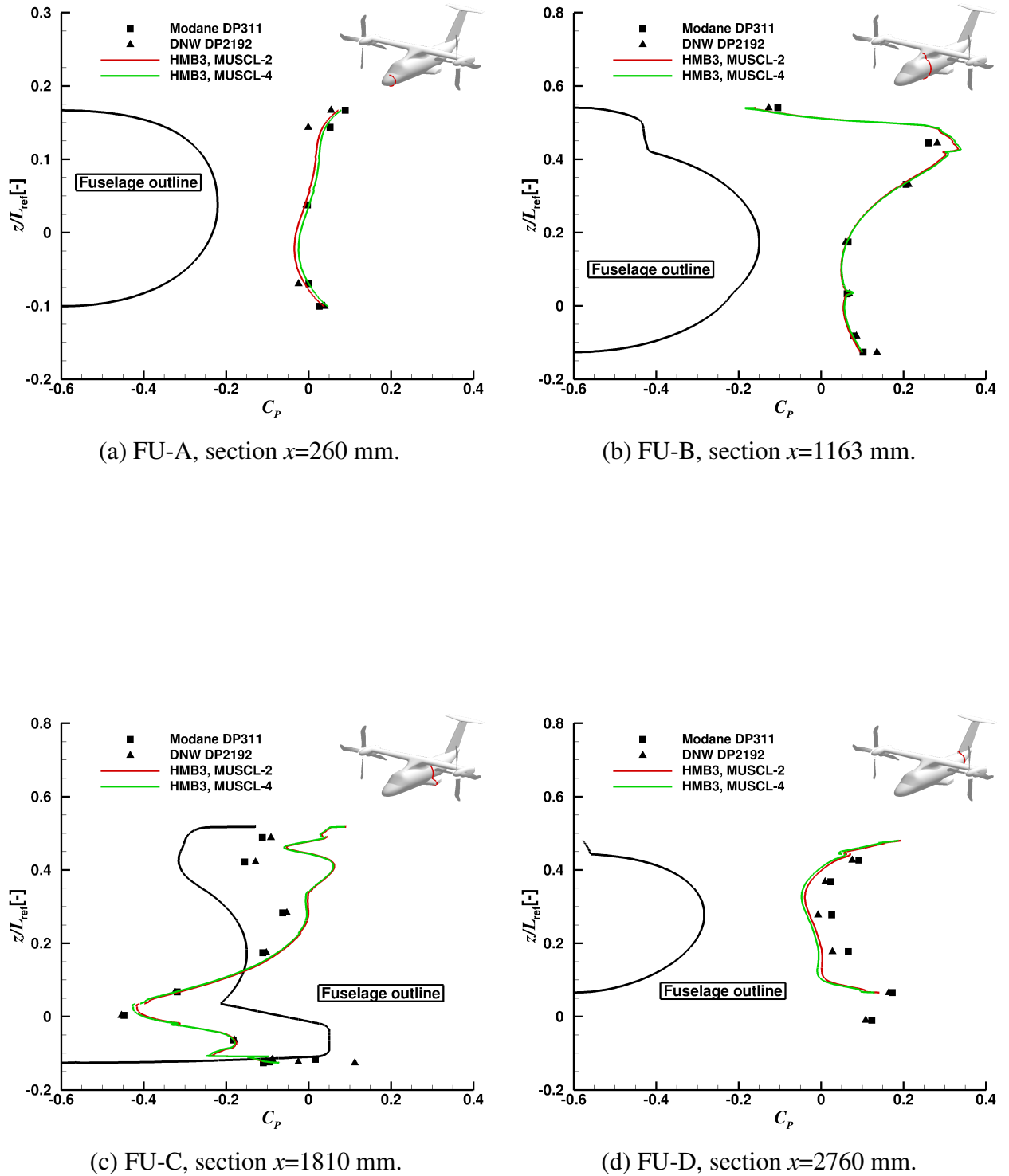
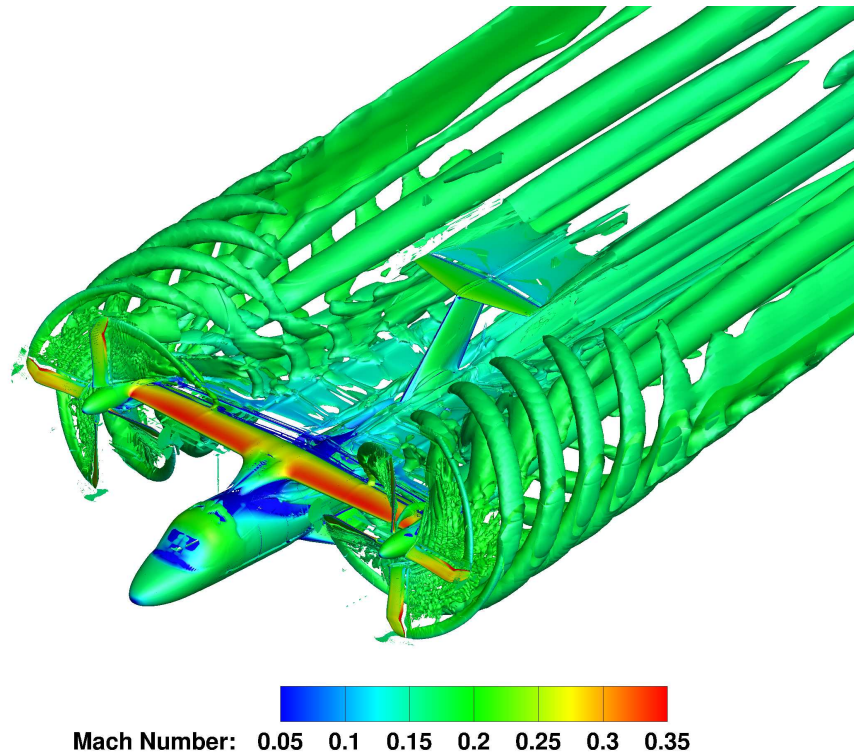
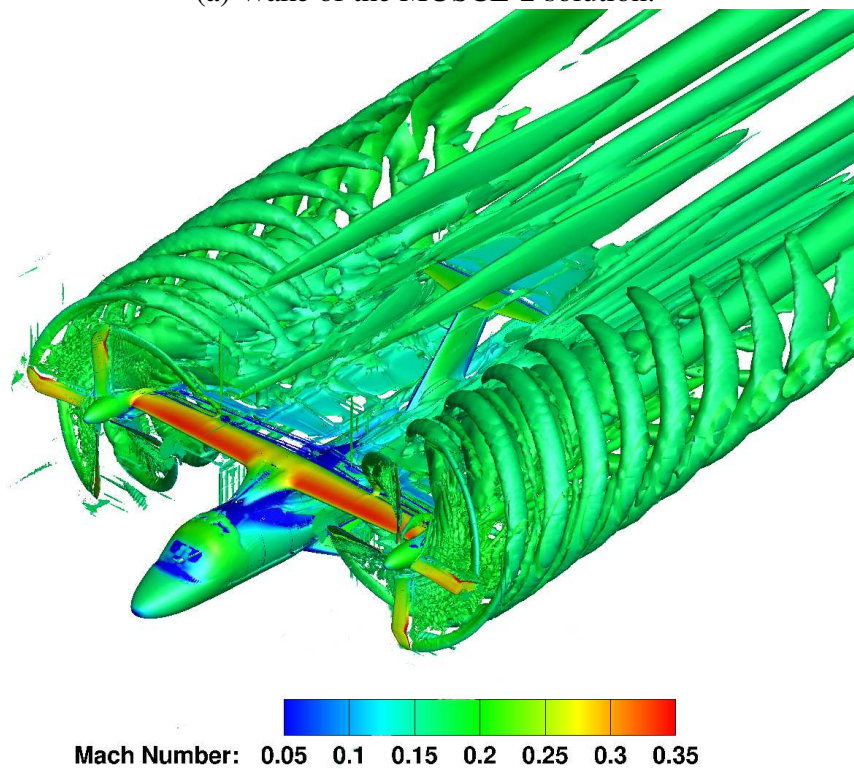


Figure 10.25:  $C_p$  profile comparisons between CFD and experiments [92, 91] on the fuselage of the ERICA tiltrotor for the aeroplane mode configuration AC1.



(a) Wake of the MUSCL-2 solution.



(b) Wake of the MUSCL-4 solution.

Figure 10.26: Wake-visualisation of the ERICA tiltrotor in aeroplane mode configuration using  $\tilde{Q}$ -criterion ( $\tilde{Q}=0.007$ ) shaded by contour of Mach numbers. Results with the MUSCL-2 (top) and MUSCL-4 (bottom) schemes.



Table 10.20: Computational run-time for the ERICA tiltrotor with MUSCL-2 and MUSCL-4 schemes on the same mesh.

Mesh	Scheme	CPU
		work units/iteration
Fine Mesh	MUSCL-2	1
	MUSCL-4	2.44 (144%)

## 10.9 Summary of Findings

The implementation of a high-order finite-volume scheme in the HMB CFD solver was evaluated. The scheme showed a higher level of accuracy when compared to the standard MUSCL, and 4th-order accuracy was achieved on Cartesian grids. Furthermore, the significantly higher spectral resolution (dispersion and dissipation) of the new scheme was demonstrated for several flows. Two- and three-dimensional test cases were considered. Results of the steady flow around the 7AD, S-76, JORP propeller, and XV-15 blades showed a better wake and higher resolution of the vortical structures compared to the standard MUSCL solution, with a small CPU and memory overhead. The method was also demonstrated for three-dimensional unsteady flows using overset and moving grid computations for the UH-60A rotor in forward flight and the ERICA tiltrotor in aeroplane mode. The computational expense associated with the parallelisation of the halo data exchange between processors for the first and second derivatives makes this scheme less efficient for larger meshes (above 50 million cells). Nevertheless, the method showed promising results in capturing and preserving the rotor wake along with a small penalty in terms of CPU and memory when compared to the MUSCL-2 scheme for medium grid sizes (up to 10 million cells). Similar penalties can be obtained for larger grids with improvements of the parallelisation process.

# Chapter 11

## Conclusions and Future Work

### 11.1 Summary and Conclusions

The present thesis investigated some aspects of helicopters, propellers, and tiltrotors using Computational Fluid Dynamics based on the Unsteady Reynolds Averaged Navier-Stokes (URANS) equations. Firstly, the acoustic solver BENP of Leonardo Helicopters was integrated with the HMB3 solver, and a description of the inputs required was presented. An implementation of an efficient, high-order, finite-volume scheme (up to 4th-order of spatial accuracy) in the HMB CFD solver was later introduced.

The second part of this thesis shows the ability of HMB3 CFD methods to accurately predict hover performance of rotors with modest computer resources. Three well-studied blades, the B0-105, S-76, and PSP main rotor blades, were used and results are compared with experimental data. Likewise, performance analyses of the JORP propeller and XV-15 tiltrotor blades were presented, aiming to validate the employed CFD method for such flows.

The third part of this thesis was devoted to numerical simulations of complete tiltrotor aircraft. The aim of this section was to assess the capability of the present CFD method for predicting airloads on the tiltrotor at different flight configurations. In this regard, three representative flight configurations of the ERICA tiltrotor were selected, corresponding to aeroplane, transition corridor, and helicopter modes, thus covering most modes of tiltrotor flight.

Aerodynamic optimisation of tiltrotor blades with high-fidelity computational fluid dynamics was also carried out. This research showed how the main blade shape parameters influence the optimal performance of the tiltrotor in helicopter and aeroplane modes, and how a compromise blade shape can increase the overall tiltrotor performance. Finally, the underlying high-order method is demonstrated for a variety of problems, including two- and three-dimensional test cases are presented.

The main conclusions of the thesis are:

- For axial flight, a second-order accurate CFD method using steady-state computations and nine million cells per blade was enough to predict rotor performance at low and high disk loadings. This was the case for the investigated helicopter, propeller, and tiltrotor blades.
- Transition affected the distribution of the skin friction coefficient on the blade but not so much the overall performance of the blade. This is the case since most power required in hover is due to the induced flow. If more laminarity on the blades is obtained, then this may have a stronger effect on the overall performance of the blade.
- The acoustics predicted with the HFWH aeroacoustic code agreed with theory for the rotor tip-path plane where thickness noise dominates. At the same thrust coefficient, anhedral tips showed a reduction of the total noise due to the blade being off-loaded near the anhedral part. More work is needed to validate the acoustics at other directions where loading noise is dominant.
- For complete tiltrotors, the surface pressure coefficient was well predicted, but this is not the same for the lift and drag coefficients. For all cases studied, the aerodynamic interactions in the region of the nacelle and tiltable wing were captured by the fully resolved blade results, and the CFD with uniform and non-uniform rotor actuator disk models also produced adequate estimates of the wing loads. Computations with resolved blades are nevertheless necessary if all flow details must be accurately cap-

tured. In aeroplane mode, the region of recirculation at the centre-line of the fuselage is not well reproduced. Most CFD solvers in Europe did not capture this phenomenon either and this can be due to a failure of the employed turbulence model, wind tunnel effects, and lack of information about the exact trimmed conditions used during tunnel tests. Nevertheless, the overset grid method was found to be a good tool for easing mesh generation for such cases.

- Optimisation of the XV-15 blade showed that single-point optimisations of the twist distribution resulted in 1.99% increase of the FoM, and a 6.59% increase in propeller propulsive efficiency at the selected design conditions. The inclusion of optimal chord and sweep resulted in limited improvements for the helicopter mode performance, but it allowed an 8.18% increase of the propeller propulsive efficiency over the baseline, thanks to reduction of the adverse compressibility effects at the blade tip. Results of the multi-point optimisations for the pure twist case and for the case with optimal chord and sweep showed that a compromise blade shape can be obtained. Nevertheless, multi-point optimisations are mandatory for tiltrotor blades due to the completely different aerodynamic characteristics of aeroplane and helicopter modes. Overall, gradient-based optimisation is a useful and efficient tool for modern tiltrotor design.
- For the investigated helicopter, propeller, and tiltrotor blades, high-order spatial discretisation substantially improved the resolution of the wake and of the vortical structures when compared to the second order method, but did not affect blade loads in a significant way. For medium-size grids, MUSCL-4 solutions add CPU and memory overheads of 22% and 23%, respectively. CPU overhead increases to 100% for grids of more than 50 million cells due to additional data exchange necessary for this scheme.

## 11.2 Future Work

Based on the current thesis and the aforementioned conclusions, the following future steps are suggested:

- Unsteady hover computations combined with transition turbulence models, blade deformation, and high-order spatial discretisation need to be performed in OGE and IGE conditions for helicopter, propeller, and tiltrotor blades. The effect of the quadrupole terms of the HFWH aeroacoustic code should also be evaluated at high blade-tip Mach numbers.
- The effect of transition needs to be assessed for the XV-15 tiltrotor in propeller mode.
- Unsteady pressure is needed to assess the capability of the present CFD method in predicting the acoustics and performance on the ERICA tiltrotor at different flight configurations.
- The blade sections and the blade anhedral tip need to be included in the optimisation of tiltrotor blades.
- More work on computations and measurements is needed to compare CFD predictions with detailed wake data to completely validate the present high-order CFD method.
- For fine grids, the halo data exchanges for the first and second derivatives need to be optimised to lower CPU overheads for the investigated MUSCL-4 scheme.
- Data from tests at full-scale for blades or complete vehicles would be useful to enhance the level of confidence in CFD tools.

# Bibliography

- [1] “Web of Knowledge,” <http://www.webofknowledge.com>, Accessed: 16th February 2017.
- [2] “Scopus,” <http://www.scopus.com>, Accessed: 16th February 2017.
- [3] “NASA Technical Report Server,” <http://www.sti.nasa.gov>, Accessed: 16th February 2017.
- [4] “American Institute of Aeronautics and Astronautics,” <http://www.aiaa.org>, Accessed: 16th February 2017.
- [5] Srinivasan, G. R., Raghavan, V., and Duque, E. P. N., “Flowfield Analysis of Modern Helicopter Rotors in Hover by Navier-Stokes Method,” *International Technical Specialists Meeting, Rotorcraft Acoustics and Rotor Fluid Dynamics*, Philadelphia, Pennsylvania, USA, 1991, pp. 1–18.
- [6] Steijl, R., Barakos, G. N., and Badcock, K., “A Framework for CFD Analysis of Helicopter Rotors in Hover and Forward Flight,” *International Journal for Numerical Methods in Fluids*, Vol. 51, No. 8, 2006, pp. 819–847, doi: 10.1002/fld.1086.
- [7] Chaderjian, N. M. and Ahmad, J. U., “Navier-Stokes Assessment of Test Facility Effects on Hover Performance,” *Proceedings of the 71st American Helicopter Society, Annual Forum*, Virginia Beach, Virginia, USA, AHS-71-2015-048, 2015, pp. 1–24.
- [8] Sheng, C., Wang, J., and Zhao, Q., “Improved Rotor Hover Predictions Using Advanced Turbulence Modeling,” *Journal of Aircraft*, Vol. 53, No. 5, 2016, pp. 1549–1560, doi: 10.2514/1.C033512.
- [9] Jimenez-Garcia, A. and Barakos, G. N., “CFD Analysis of Hover Performance of Rotors at Full-and Model-Scale Conditions,” *The Aeronautical Journal*, Vol. 120, No. 1231, 2016, pp. 1386–1424, doi: 10.1017/aer.2016.58.
- [10] Leishman, J. G., *Principles of Helicopter Aerodynamics*, Cambridge University Press, 2006.
- [11] Jimenez-Garcia, A. and Barakos, G. N., “Accurate Predictions of Rotor Hover Performance at Low and High Disc Loadings,” *Journal of Aircraft*, Advance online publication, 2017, doi: 10.2514/1.C034144.
- [12] Yamauchi, G. K. and Young, L. A., “A Status of NASA Rotorcraft Research,” NASA TP–215369, Sept. 2009.

- [13] Gray, R. B., "On the Motion of the Helical Vortex Shed From a Single Bladed Hovering Model Rotor and its Application to the Calculation of the Spanwise Aerodynamic Loading," Princeton University Aero. Engineering Department, Report No. 313, Sept. 1955.
- [14] Gray, R. B., "Vortex Modeling for Rotor Aerodynamics - The 1991 Alexander A. Nikolsky Lecture," *Journal of the American Helicopter Society*, Vol. 37, No. 1, 1992, pp. 3–14, doi: 10.4050/JAHS.37.3.
- [15] Young, L. A., "Vortex Core Size in the Rotor Near-Wake," NASA TM–212275, June 2003.
- [16] Landgrebe, A. J., "An Analytical and Experimental Investigation of Helicopter Rotor Hover Performance and Wake Geometry Characteristics," USAAMRDL TR–71-24, June 1971.
- [17] Johnson, W., *Helicopter Theory*, Princeton University Press, New Jersey, 1980.
- [18] Brocklehurst, A. and Barakos, G. N., "Evaluating Tail Rotor Tip Shapes using Computational Fluid Dynamics," *Proceedings of the 52nd Aerospace Sciences Meeting*, National Harbor, Maryland, USA, AIAA-2014-0043, 2014, pp. 1–44.
- [19] Landgrebe, A. J., "The Wake Geometry of a Hovering Rotor and its Influence on Rotor Performance," *Journal of the American Helicopter Society*, Vol. 17, No. 4, 1972, pp. 3–15, doi: 10.4050/JAHS.17.3.
- [20] Kocurek, J. D. and Tangler, J. L., "A Prescribed Wake Lifting Surface Hover Performance Analysis," *Journal of the American Helicopter Society*, Vol. 22, No. 1, 1977, pp. 24–35, doi: 10.4050/JAHS.22.24.
- [21] Mohd, N. A. R. N., *Numerical Modelling of Flow Field near Helicopter Rotors using Hybrid Navier-Stokes & Free Wake Methods*, Ph.D. thesis, University of Liverpool, UK, Sept. 2011.
- [22] Jenney, D. S., Olson, J. R., and Landgrebe, A. J., "A Reassessmemt of Rotor Hovering Performance Prediction Methods," *Journal of the American Helicopter Society*, Vol. 13, No. 2, 1968, pp. 1–26, doi: 10.4050/JAHS.13.1.
- [23] Egolf, T. A. and Landgrebe, A. J., "Helicopter Rotor Wake Geometry and Its Influence in Forward Flight, Volume I - Generalized Wake Geometry and Wake Effect on Rotor Airloads and Performance," NASA CR–3726, Oct. 1983.
- [24] Landgrebe, A. J., "An Analytical Method for Predicting Rotor Wake Geometry," *Journal of the American Helicopter Society*, Vol. 14, No. 4, 1969, pp. 20–32, doi: 10.4050/JAHS.14.20.
- [25] Clark, D. R. and Leiper, A. C., "The Free Wake Analysis, A Method for the Prediction of Helicopter Rotor Hovering Performance," *Journal of the American Helicopter Society*, Vol. 15, No. 1, 1970, pp. 3–11, doi: 10.4050/JAHS.15.3.
- [26] Scully, M. P., *Computation of Helicopter Rotor Wake Geometry and its influence on Rotor Harmonic Airloads*, Ph.D. thesis, Massachusetts Institute of Technology, USA, Sept. 1975.
- [27] Bliss, D. B., Teske, M. E., and Quackenbush, T. R., "A New Methodology for Free Wake Analysis using Curved Vortex Elements," NASA CR–3958, Dec. 1987.

- [28] Quackenbush, T. R., Wachspress, D. A., and Bliss, D. B., “New Free-Wake Analysis of Rotorcraft Hover Performance using Influence Coefficients,” *Journal of Aircraft*, Vol. 26, No. 12, 1989, pp. 1090–1097, doi: 10.2514/3.45885.
- [29] Strawn, R. C., Caradonna, F. X., and Duque, E. P. N., “30 Years of Rotorcraft Computational Fluid Dynamics Research and Development,” *Journal of the American Helicopter Society*, Vol. 51, No. 1, 2006, pp. 5–21, doi: 10.4050/1.3092875.
- [30] Verley, S., “Torque Analysis Based on the CFD ”Far-Field” Philosophy for Rotors in Hover,” *Proceeding of the 46th Applied Aerodynamics Symposium*, 3AF, Orleans, France, 2011, pp. 1–13.
- [31] Hariharan, N., Egolf, A., and Sankar, L., “Simulation of Rotor in Hover: Current State and Challenges,” *Proceedings of the 52nd Aerospace Sciences Meeting*, National Harbor, Maryland, USA, AIAA-2014-0041, 2014, pp. 1–28.
- [32] Hariharan, N., Steffen, M., Wissink, A., and Potsdam, M., “Tip Vortex Field Resolution using and Adaptive Dual-Mesh Computational Paradigm,” *Proceedings of the 49th Aerospace Sciences Meeting*, Orlando, Florida, USA, AIAA-2011-1108, 2011, pp. 1–16.
- [33] Balch, D. T. and Lombardi, J., “Experimental Study of Main Rotor Tip Geometry and Tail Rotor Interactions in Hover. Vol I - Text and Figures,” NASA CR–177336, Feb. 1985.
- [34] Balch, D. T. and Lombardi, J., “Experimental Study of Main Rotor Tip Geometry and Tail Rotor Interactions in Hover. Vol II - Run Log and Tabulated Data Progress Report,” NASA CR–177336, Feb. 1985.
- [35] Shinoda, P. M., “Performance Results from a Test of an S-76 Rotor in the NASA Ames 80-by 120- Foot Wind Tunnel,” *Proceedings of the 11th Applied Aerodynamics Conference*, Monterey, California, USA, AIAA-93-3414, 1993, pp. 126–144.
- [36] Shinoda, P. M., “Full-Scale S-76 Rotor Performance and Loads at Low Speeds in the NASA Ames 80-by 120-Foot Wind Tunnel,” NASA TM–110379, April 1996.
- [37] Balch, D. T., Saccullo, A., and Sheehy, T. W., “Experimental Study of Main Rotor/Tail Rotor/Airframe Interactions in Hover - Volume I,” NASA CR–166485, June 1983.
- [38] Balch, D. T., “Experimental Study of Main Rotor/Tail Rotor/Airframe Interactions in Hover,” *Journal of the American Helicopter Society*, Vol. 30, No. 2, 1985, pp. 49–56, doi: 10.4050/JAHS.30.49.
- [39] Johnson, W., “Performance and Loads Data From a Wind Tunnel Test of a Full-Scale Rotor With Four Blade Tip Planforms,” NASA TM–81229, Sept. 1980.
- [40] Jepson, D., Moffitt, R., Hilzinger, K., and Bissell, J., “Analysis and Correlation of Test Data from and Advanced Technology Rotor System,” NASA CR–3714, Aug. 1983.
- [41] Swanson, A. A., “Application of the Shadowgraph Flow Visualisation Technique to a Full-Scale Helicopter Rotor in Hover and Forward Flight,” *Proceedings of the 11th Applied Aerodynamics Conference*, Monterey, California, USA, AIAA-93-3411, 1993, pp. 1–15.



- [42] “AIAA Applied Aero Rotorcraft Working Group,” [https://info.aiaa.org/tac/ASG/APATC/Web%20Pages/RotorSim-DG\\_Info.aspx](https://info.aiaa.org/tac/ASG/APATC/Web%20Pages/RotorSim-DG_Info.aspx), Accessed: 5th April 2017.
- [43] Kim, J. W., Sankar, L. N., Marpu, R., Egolf, T. A., and Hariharan, N., “Assessment of Plan-form Effects on Rotor Hover Performance,” *Proceedings of the 53rd Aerospace Sciences Meeting*, Kissimmee, Florida, USA, AIAA-2015-1716, 2015, pp. 1–12.
- [44] Jung, M. K., Hwang, J. Y., and Kwon, O. J., “Assessment of Rotor Aerodynamic Performances in Hover Using an Unstructured Mixed Mesh Method,” *Proceedings of the 52nd Aerospace Sciences Meeting*, National Harbor, Maryland, USA, AIAA-2014-0042, 2014, pp. 1–20.
- [45] Sheng, C., Zhao, Q., and Wang, J., “S-76 Rotor Hover Prediction using U<sup>2</sup>NCLE Solver,” *Proceedings of the 52nd Aerospace Sciences Meeting*, National Harbor, Maryland, USA, AIAA-2014-004, 2014, pp. 1–19.
- [46] Sheng, C. and Narramore, J. C., “Computational Simulation and Analysis of Bell Boeing Quad Tiltrotor Aero Interaction,” *Journal of the American Helicopter Society*, Vol. 54, No. 4, 2009, pp. 1–15, doi: 10.4050/JAHS.54.042002.
- [47] Langtry, R. B., *A Correlation-Based Transition Model using Local Variables for Unstructured Parallelized CFD codes*, Ph.D. thesis, University of Stuttgart, Germany, May 2006.
- [48] Langtry, R. B. and Menter, F. R., “Correlation-Based Transition Modeling for Unstructured Parallelized Computational Fluid Dynamics Codes,” *AIAA Journal*, Vol. 47, No. 12, 2010, pp. 2894–2906, doi: 10.2514/1.42362.
- [49] Spalart, P. R., Deck, S., Sur, M. L., Squires, K. D., Strelets, M., and Travin, A., “A New Version of Detached-Eddy Simulation, Resistant to Ambiguous Grid Densities,” *Theoretical and Computational Fluid Dynamics*, Vol. 20, No. 3, 2006, pp. 181–195, doi: 10.1007/s00162-006-0015-0.
- [50] Baeder, J. D., Medida, S., and Kalra, T. S., “OVERTURNS Simulations of S-76 Rotor in Hover,” *Proceedings of the 52nd Aerospace Sciences Meeting*, National Harbor, Maryland, USA, AIAA-2014-0045, 2014, pp. 1–11.
- [51] Srinivasan, G. R. and Baeder, J. D., “TURNS: A Free-Wake Euler/Navier-Stokes Numerical Method for Helicopter Rotors,” *Journal of Aircraft*, Vol. 31, No. 5, 1993, pp. 959–962, doi: 10.2514/3.49036.
- [52] Jain, R. K. and Potsdam, M. A., “Hover Predictions on the Sikorsky S-76 Rotor using Helios,” *Proceedings of the 52nd Aerospace Sciences Meeting*, National Harbor, Maryland, USA, AIAA-2014-0207, 2014, pp. 1–22.
- [53] Wissink, A., Jayaraman, B., Datta, A., Sitaraman, J., Potsdam, M., Kamkar, S., Mavriplis, D., Yang, Z., Jain, R., Lim, J., and Strawn, R., “Capability Enhancements in Version 3 of the Helios High-Fidelity Rotorcraft Simulation Code,” *Proceedings of the 50th Aerospace Sciences Meeting*, Nashville, Tennessee, USA, AIAA-2012-0713, 2012, pp. 1–21.

- [54] Nichols, R. H. and Buning, P. G., "OVERFLOW User's Manual, Version 2.2," NASA Langley Research Center, Hampton, VA, Aug. 2010.
- [55] Jain, R., "Hover Predictions for the S-76 Rotor with Tip Shape Variation using CREATE-AV Helios," *Proceedings of the 53rd Aerospace Sciences Meeting*, Kissimmee, Florida, USA, AIAA-2015-1244, 2015, pp. 1–29.
- [56] Tadghighi, H., "Helios Simulation of Rotors in Hover: The Boeing Company," *Proceedings of the 52nd Aerospace Sciences Meeting*, National Harbor, Maryland, USA, AIAA-2014-0209, 2014, pp. 1–9.
- [57] Narducci, R., "OVERFLOW Simulation of Rotors in Hover: The Boeing Company," *Proceedings of the 52nd Aerospace Sciences Meeting*, National Harbor, Maryland, USA, AIAA-2014-0208, 2014, pp. 1–9.
- [58] Rajmohan, N., Sankar, L. N., and Costello, M., "Effect of Inflow Model on Coupling between Aeromechanics and Flight Mechanics," *Proceedings of the 49th Aerospace Sciences Meeting*, Orlando, Florida, USA, AIAA-2011-1192, 2011, pp. 1–11.
- [59] Marpu, R. P., Sankar, L. N., Egolf, T. A., and Hariharan, N., "Analysis of Rotor in Hover using Hybrid Methodology," *Proceedings of the 52nd Aerospace Sciences Meeting*, National Harbor, Maryland, USA, AIAA-2014-0210, 2014, pp. 1–12.
- [60] Choi, J. Y., Summers, M., and Corrigan, J. J., "Validation of CHARM Wake Methodology for Computation of Loads and Vibrations," *Proceedings of 65th American Helicopter Society, Annual Forum*, Grapevine, Texas, USA, AHS-65-2009-143, 2009, pp. 1–12.
- [61] Brown, R. E. and Line, A. J., "Efficient High-Resolution Wake Modeling using the Vorticity Transport Equation," *AIAA Journal*, Vol. 43, No. 7, 2005, pp. 1434–1443, doi: 10.2514/1.13679.
- [62] Whitehouse, G. R., Wachspress, D. A., and Quackenbush, T. R., "Predicting the Influence of Blade Tip Shape on Hovering Rotor Performance with Comprehensive Analyses," *Proceedings of the 53rd Aerospace Sciences Meeting*, Kissimmee, Florida, USA, AIAA-2015-1248, 2015, pp. 1–12.
- [63] Anusonti-Inthra, P., "The effects of Turbulence Modelings on CFD Simulations of S76 Hovering Rotor," *Proceedings of the 53rd Aerospace Sciences Meeting*, Kissimmee, Florida, USA, AIAA-2015-1245, 2015, pp. 1–14.
- [64] "ANSYS Fluent," <http://www.ansys.com/Products/Fluids/ANSYS-Fluent>, Accessed: 5th April 2017.
- [65] Liu, Z., Kim, J., Sankar, L., Hariharan, N., and Egolf, T. A., "High Order Evaluation of S-76 in Hover," *Proceedings of the 53rd Aerospace Sciences Meeting*, Kissimmee, Florida, USA, AIAA-2015-1714, 2015, pp. 1–9.
- [66] Srinivasan, G. R., Baeder, J. D., Obayashi, S., and McCroskey, W. J., "Flow-Field of a Lifting Rotor in Hover: A Navier-Stokes Simulation," *AIAA Journal*, Vol. 30, No. 10, 1992, pp. 2371–2378, doi: 10.2514/3.11236.

- [67] Usta, E., *Application of a Symmetric Total Variation Diminishing Scheme to Aerodynamics of Rotors*, Ph.D. thesis, Georgia Institute of Technology, USA, Aug. 2002.
- [68] Min, B. Y. and Sankar, L. N., “Hybrid Navier-Stokes/Free-Wake Method for Modeling of Blade-Vortex Interactions,” *Journal of Aircraft*, Vol. 47, No. 3, 2010, pp. 975–982, doi: 10.2514/1.46550.
- [69] Min, B. Y. and Wake, B., “Analysis of a Hovering Rotor using UT-GENCAS: A Modified Hybrid Navier-Stokes/Free-Wake Method,” *Proceedings of the 53rd Aerospace Sciences Meeting*, Kissimmee, Florida, USA, AIAA-2015-1247, 2015, pp. 1–15.
- [70] Abras, J. N. and Hariharan, N., “Comparison of CFD Hover Predictions on the S-76 Rotor,” *Proceedings of the 53rd Aerospace Sciences Meeting*, Kissimmee, Florida, USA, AIAA-2015-1711, 2015, pp. 1–11.
- [71] Wachspress, D. A., Quackenbush, T. R., and Boschitsch, A. H., “First-Principles Free-Vortex Wake Analysis for Helicopters and Tiltrotors,” *Proceedings of the 59th American Helicopter Society, Annual Forum*, Phoenix, Arizona, USA, AHS-59-2003-047, 2003, pp. 1–24.
- [72] Scrase, N. and Maina, M., “The Evaluation of Propeller Aero-Acoustic Design Methods by Means of Scaled-Model Testing Employing Pressure Tapped Blades and Spinner,” *Proceeding of the 19th Congress of the International Council of the Aeronautical Sciences*, Anaheim, California, USA, ICAS-94-6.1.2, 1994, pp. 183–195.
- [73] Maisel, M. D., Giulianetti, D. J., and Dugan, D. C., “The History of the XV-15 Tilt Rotor Research Aircraft: From Concept to Flight,” NASA SP-2000-4517, Feb. 2000.
- [74] Felker, F. F. and Light, J. S., “Rotor/Wing Aerodynamic Interactions in Hover,” NASA-TM-88255, May 1986.
- [75] Potsdam, M. A., Schaller, D. F., Rajagopalan, R. G., and Silva, M. J., “Tilt Rotor Aeromechanics Phenomena in Low Speed Flight,” *Proceedings of the 4th Decennial Specialist’s Conference on Aeromechanics*, San Francisco, California, USA, AHS-40-2004-023, 2004, pp. 1–13.
- [76] Bridgeman, J. O., Cummings, A., Narramore, J. C., and Kisor, R., “Analysis of V-22 Rotor Blade Performance Enhancements for Improved Payload,” *Proceedings of the 64th American Helicopter Society, Annual Forum*, Montreal, Canada, AHS-64-2008-312, 2008, pp. 1–12.
- [77] “Development of an Advanced Rotor for Tilt-rotor,” <http://www.transport-research.info/project/development-advanced-rotor-tilt-rotor>, last visited date: 29/09/2016.
- [78] A. Visingardi, W. Khier, J. D., “The Blind-Test Activity of TILTAERO Project for the Numerical Aerodynamic Investigation of a Tilt Rotor,” *Proceedings of the European Congress on Computational Methods in Applied Sciences and Engineering*, ECCOMAS, Jyväskylä, Finland, 2004, pp. 1–20.

- [79] Beaumier, P., Decours, J., and Lefebvre, T., “Aerodynamic and Aero-acoustic Design of Modern Tilt-rotors: The ONERA Experience,” *Proceedings of the 26th International Congress of the Aeronautical Sciences*, ICAS, Anchorage, Alaska, 2008, pp. 1–11.
- [80] Decours, J. and Lefebvre, T., “Navier-Stokes Computations Applied to Tilt-Rotors,” *Proceedings of the 33rd European Rotorcraft Forum*, Kazan, Russia, ERF-2007-13, 2007, pp. 1–18.
- [81] Nannoni, F., Giancamilli, G., and Cicale, M., “ERICA: The European Advanced Tiltrotor,” *Proceeding of the 27th European Rotorcraft Forum*, Moscow, Russia, ERF-2001-055, 2001, pp. 1–15.
- [82] Anon, “Advancement of Proprotor Technology Task II - Wind Tunnel Results,” NASA CR-114363, Sept. 1971.
- [83] Weiberg, J. A. and Maisel, M. D., “Wind-Tunnel Tests of the XV-15 Tilt Rotor Aircraft,” NASA TM-81177, April 1980.
- [84] Felker, F. F., Betzina, M. D., and Signor, D. B., “Performance and Loads Data from a Hover Test of a Full-Scale XV-15 Rotor,” NASA TM-86833, Sept. 1985.
- [85] Bartie, K., Alexander, H., McVeigh, M., Mon, S. L., and Bishop, H., “Hover Performance Tests of Baseline Meter and Advanced Technology Blade (ATB) Rotor Systems for the XV-15 Tilt Rotor Aircraft,” NASA CR-114626, Oct. 1986.
- [86] Light, J. S., “Results from an XV-15 Rotor Test in the National Full-Scale Aerodynamics Complex,” *Proceedings of the 53rd American Helicopter Society, Annual Forum*, AHS, Virginia Beach, Virginia, USA, 1997.
- [87] Betzina, M. D., “Rotor Performance of an Isolated Full-Scale XV-15 Tiltrotor in Helicopter Mode,” *Proceedings of 58th American Helicopter Society, Annual Forum*, Montreal, Canada, AHS-58-2002-008, 2002, pp. 1–12.
- [88] Wadcock, A. J., Yamauchi, G. K., and Driver, D. M., “Skin Friction Measurements on a Hovering Full-Scale Tilt Rotor,” *Journal American Helicopter Society*, Vol. 44, No. 4, 1999, pp. 312–319, doi: 10.4050/JAHS.44.312.
- [89] “NICETRIP - Novel Innovative Competitive Effective Tilt Rotor Integrated Project: NICETRIP website,” <http://www.transport-research.info/project/novel-innovative-competitive-effective-tilt-rotor-integrated-project>, last visited date: 29/09/2016.
- [90] Alli, P., Nannoni, F., and Cicalé, M., “ERICA: The European Tiltrotor Design and Critical Technology Projects,” *AIAA/ICAS, International Air and Space Symposium and Exposition: The Next 100 Years*, Dayton, Ohio, USA, 2005.
- [91] Philipsen, I. and Heinrich, S., “Test Report on Measurements on the NICETRIP Large-Scale Powered Model in DNW-LLF,” Project Number 2410.1338, Aug. 2013.
- [92] Lebrun, F., “NICETRIP test - ERICA 1/5th Scale Powered Model in the Test Section No.2 - 45m<sup>2</sup> of S1MA Wind Tunnel,” Test Report Number PV 1/17648 DSMA, June 2014.

- [93] Decours, J., Beaumier, P., Khier, W., Kneisch, T., Valentini, M., and Vigeveno, L., “Experimental Validation of Tilt-Rotor Aerodynamic Predictions,” *Proceeding of the 40th European Rotorcraft Forum*, Southampton, UK, ERF-2014-097, 2014, pp. 1–12.
- [94] Kaul, U. K. and Ahmad, J., “Skin Friction Predictions Over a Hovering Tilt-Rotor Blade Using OVERFLOW2,” *Proceedings of the 29th Applied Aerodynamics Conference*, Honolulu, Hawaii, USA, AIAA-2011-3186, 2011, pp. 1–19.
- [95] Kaul, U. K., “Effect of Inflow Boundary Conditions on Hovering Tilt-Rotor Flows,” *Proceedings of the 7th International Conference on Computational Fluid Dynamics*, ICCFD7, Big Island, Hawaii, USA, 2012, pp. 1–19.
- [96] Kaul, U. K. and Ahmad, J., “Skin-Friction Predictions on a Hovering Tilt-Rotor Blade,” *Journal of Aircraft*, Vol. 49, No. 6, 2012, pp. 1726–1738, doi: 10.2514/1.C031401.
- [97] Spalart, P. R. and Allmaras, S., “A One-Equation Turbulence Model for Aerodynamic Flows,” *La Recherche Aéronautique*, Vol. 1, No. 1, 1994, pp. 5–21.
- [98] Yoon, S., Pulliam, T. H., and Chaderjian, N. M., “Simulations of XV-15 Rotor Flows in Hover Using OVERFLOW,” *Proceedings of the 50th AHS Aeromechanics Specialists*, AHS, San Francisco, California, USA, 2014, pp. 1–11.
- [99] Sheng, C. and Zhao, Q., “Investigations of XV-15 Rotor Hover Performance and Flow Field Using U2NCLE and HELIOS Codes,” *Proceedings of the 54th Aerospace Sciences Meeting*, San Diego, California, USA, AIAA-2016-303, 2016, pp. 1–18.
- [100] Sheng, C. and Zhao, Q., “Assessment of Transition Models in Predicting Skin Frictions and Flow Field of a Full-Scale Tilt Rotor in Hover,” *Proceedings of 72nd American Helicopter Society, Annual Forum*, West Palm Beach, Florida, USA, AHS-72-2016, 2016, pp. 1–20.
- [101] Gates, S., “Aerodynamic Analysis of Tiltrotors in Hovering and Propeller Modes Using Advanced Navier-Stokes Computations,” *Proceedings of the 39th European Rotorcraft Forum*, Moscow, Russia, ERF-2013-561, 2013, pp. 1–26.
- [102] Massaro, A. and D’Andrea, A., “Multi-Point Aerodynamic Optimization by Means of Memetic Algorithm for Design of Advanced Tiltrotor Blades,” *Proceedings of the 39th European Rotorcraft Forum*, Moscow, Russia, ERF-2013-1278, 2013, pp. 1–14.
- [103] D’Andrea, A., “Development of a Multi-Processor Unstructured Panel Code coupled with a CVC Free Wake Model for Advanced Analysis of Rotorcraft and Tiltrotors,” *Proceedings of the 64th American Helicopter Society, Annual Forum*, Montreal, Canada, AHS-64-2008-120, 2008, pp. 1–19.
- [104] Guntupalli, K., Novak, L. A., and Rajagopalan, R. G., “RotCFD: An Integrated Design Environment for Rotorcraft,” *Proceedings of the AHS Technical Meeting on Aeromechanics Design for Vertical Lift*, AHS, San Francisco, California, USA, 2016, pp. 1–18.
- [105] Koning, W. J. F., Acree, C. W., and Rajagopalan, G., “Using RotCFD to Predict Isolated XV-15 Rotor Performance,” *Proceedings of the AHS Technical Meeting on Aeromechanics Design for Vertical Lift*, AHS, San Francisco, California, USA, 2016, pp. 1–15.

- [106] Corrigan, J. J. and Schillings, J. J., “Empirical Model for Stall Delay Due to Rotation,” *Proceedings of the AHS Aeromechanics Specialists Conference*, AHS, San Francisco, California, USA, 1994, pp. 1–15.
- [107] Johnson, W., “CAMRAD II Comprehensive Analytical Model of Rotorcraft Aerodynamics and Dynamics,” Johnson Aeronautics, Palo Alto, 2005.
- [108] Johnson, W., “An Assessment of the Capability To Calculate Tilting Prop-Rotor Aircraft Performance, Loads, and Stability,” NASA TP-2291, March 1984.
- [109] “Turbulence Modelling Resource, Langley Research Center,” <http://turbmodels.larc.nasa.gov>, Accessed: 6th April 2017.
- [110] Fox, E., “BVWT 0468 - 0.15 Scale V-22 High Angle of Attack Wind Tunnel Test Report,” Boeing Document Number 901-909-665, Feb. 2000.
- [111] Abras, J. and Narducci, R., “Analysis of CFD Modeling Techniques over the MV-22 Tiltrotor,” *Proceedings of the 66th Annual Forum*, Phoenix, Arizona, USA, AHS-66-2010-037, 2010, pp. 1–11.
- [112] Cambier, L., Heib, S., and Plot, S., “The Onera elsA CFD software: input from research and feedback from industry,” *Mechanics and Industry - Cambridge Journals*, Vol. 14, No. 3, 2013, pp. 159–174, doi: 10.1051/meca/2013056.
- [113] Biava, M., *RANS Computations of Rotor/Fuselage Unsteady Interactional Aerodynamics*, Ph.D. thesis, Dipartimento di Ingegneria Aerospaziale, Politecnico di Milano, Milano, Italy, 2007.
- [114] Kroll, N., Eisfeld, B., and Bleecke, H., “The Navier-Stokes Code FLOWer,” *Notes on Numerical Fluid Mechanics, Vieweg, Braunschweig*, Vol. 71, 1999, pp. 58–71.
- [115] Jones, W. T., Nielsen, E. J., Lee-Rausch, E. M., and Acree, C. W., “Multi-point Adjoint-Based Design of Tilt-Rotors in a Noninertial Reference Frame,” *Proceedings of the 10th AIAA Multidisciplinary Design Optimization Conference*, National Harbor, Maryland, USA, AIAA-2014-0290, 2014, pp. 1–18.
- [116] Droandi, G. and Gibertini, G., “Aerodynamic Shape Optimisation of a Proprotor and its Validation by Means of CFD and Experiments,” *Aeronautical Journal*, Vol. 119, No. 1220, 2015, pp. 1223–1250, doi: 10.1017/S0001924000011222.
- [117] McCormick, B. W., *Aerodynamics Aeronautics and Flight Mechanics*, Wiley, New York, 1979.
- [118] Lyu, Z., Xu, Z., and Martins, J. R. R. A., “Benchmarking Optimization Algorithms for Wing Aerodynamic Design Optimization,” *8th International Conference on Computational Fluid Dynamics*, Chengdu, China, ICCFD8-2014-0203, 2014, pp. 1–18.
- [119] Zingg, D. W., Nemec, M., and Pulliam, T. H., “A Comparative Evaluation of Genetic and Gradient-Based Algorithms Applied to Aerodynamic Optimization,” *European Journal of Computational Mechanics*, Vol. 17, No. 1, 2008, pp. 103–126, doi: 10.3166/remn.17.103-126.

- [120] Walsh, J., Bingham, G., and Riley, M., “Optimization Methods Applied to the Aerodynamic Design of Helicopter Rotor Blades,” *Proceedings of the 26th AIAA/ASME/ASCE/AHS Structures, Structural Dynamics and Materials Conference*, Orlando, Florida, USA, AIAA-1985-0644, 1985, pp. 1–9.
- [121] Zibi, J., Defresne, G., and Costes, M., “A Numerical Procedure for Aerodynamic Optimization of Helicopter Rotor Blades,” *Proceedings of the 18th European Rotorcraft Forum*, Avignon, France, ERF-1992-B20, 1992, pp. 1–13.
- [122] Pape, A. L. and Beaumier, P., “Numerical Optimization of Helicopter Rotor Aerodynamic Performance in Hover,” *Aerospace Science and Technology*, Vol. 9, No. 3, 2005, pp. 191–201, doi: 10.1016/j.ast.2004.09.004.
- [123] Choi, S., Potsdam, M., Lee, K., Iaccarino, G., and Alonso, J. J., “Helicopter Rotor Design Using a Time-Spectral and Adjoint-Based Method,” *AIAA Journal*, Vol. 51, No. 2, 2008, pp. 412–423, doi: 10.2514/6.2008-5810.
- [124] Dumont, A., Pape, A. L., Peter, J., and Huberson, S., “Aerodynamic Shape Optimization of Hovering Rotors Using a Discrete Adjoint of the Reynolds-Averaged Navier-Stokes Equations,” *Journal of the American Helicopter Society*, Vol. 56, No. 3, 2011, pp. 1–11, doi: 10.4050/JAHS.56.032002.
- [125] Schwabacher, M., Ellman, T., and Hirsh, H., “Learning to Set Up Numerical Optimisations of Engineering Designs,” *Artificial Intelligence for Engineering Design, Analysis and Manufacturing Journal*, Vol. 12, No. 2, 1998, pp. 173–192, doi: 10.1017/S0890060498122084.
- [126] Chen, C. and Lee, H., “An Efficient Gradient Forecasting Search Method Utilising the Discrete Difference Equation Prediction Model,” *Applied Intelligence Journal*, Vol. 16, No. 2, 2002, pp. 43–58, doi: 10.1023/A:1012817410590.
- [127] Imiela, M., “High-Fidelity Optimization Framework for Helicopter Rotors,” *Aerospace Science and Technology*, Vol. 23, No. 1, 2011, pp. 2–16, doi: 10.1016/j.ast.2011.12.011.
- [128] Johnson, C. S. and Barakos, G. N., “Optimising Aspects of Rotor Blades in Forward Flight,” *Proceedings of the 49th Aerospace Sciences Meeting Including the New Horizons Forum and Aerospace Exposition*, Orlando, Florida, USA, AIAA-2011-1194, 2011, pp. 1–28.
- [129] Cho, J. and Lee, S.-C., “Propeller Blade Shape Optimization For Efficiency Improvement,” *Computer and Fluids*, Vol. 27, No. 3, 1998, pp. 407–419, doi: 10.1016/S0045-7930(97)00035-2.
- [130] Marinus, B. G., Roger, M., and der Braembussche, R. A. V., “Aeroacoustic and Aerodynamic Optimization of Aircraft Propeller Blades,” *Proceedings of the 16th AIAA/CEAS Aeroacoustic Conference*, Stockholm, Sweden, AIAA-2010-3850, 2010, pp. 1–17.
- [131] Leon, E. R., Pape, A. L., Desideri, J. A., Alfano, D., and Costes, M., “Concurrent Aerodynamic Optimization of Rotor Blades Using a Nash Game Method,” *Proceedings of the 69th American Helicopter Society, Annual Forum*, Phoenix, Arizona, USA, AHS-69-2013-168, 2013, pp. 1–24.

- [132] Wilke, G., “Applying Multi-Objective Variable-Fidelity Optimization Techniques to Industrial Scale Rotors: Blade Designs for CleanSky,” *Proceedings of the 41st European Rotorcraft Forum*, Munich, Germany, ERF-2015-38, pp. 1–14.
- [133] Droandi, G. and Gibertini, G., “Aerodynamic Blade Design with Multi-Objective Optimization for Tiltrotor Aircraft,” *Aircraft Engineering and Aerospace Technology*, Vol. 87, No. 1, 2013, pp. 19–29, doi: 10.1108/AEAT-01-2013-0005.
- [134] Booth, E. R., McCluer, M., and Tadghighi, H., “Acoustic Characteristics of an Isolated Tiltrotor Model in the DNW,” *Journal of the American Helicopter Society*, Vol. 46, No. 1, 1999, pp. 72–80, doi: 10.4050/JAHS.46.72.
- [135] Anderson, W. K. and Bonhaus, D. L., “An Implicit Upwind Algorithm for Computing Turbulent Flows on Unstructured Grids,” *Computers and Fluids*, Vol. 23, No. 1, 1994, pp. 1–21, doi: 10.1016/0045-7930(94)90023-X.
- [136] Nielsen, E. J., *Aerodynamic Design Sensitivities on an Unstructured Mesh Using the Navier-Stokes Equations and a Discrete Adjoint Formulation*, Ph.D. thesis, Virginia Polytechnic Institute and State University, USA, Dec. 1998.
- [137] Brentner, K. S. and Farassat, F., “Modeling Aerodynamically Generated Sound of Helicopter Rotors,” *Progress in Aerospace Sciences*, Vol. 39, No. 2, 2003.
- [138] Deming, A. F., “Noise from Propellers with Symmetrical Sections at Zero Blade Angle,” NACA TN–605, July 1937.
- [139] Deming, A. F., “Noise from Propellers with Symmetrical Sections at Zero Blade Angle, II,” NACA TN–679, Dec. 1938.
- [140] Gutin, L., “On the Sound Field of a Rotating Propeller,” NACA TM–1195, Oct. 1948.
- [141] Garrick, I. E. and Watkins, C. E., “A Theoretical Study of the Effect of Forward Speed on the Free-Space Sound-Pressure Field around Propellers,” NACA TN–3018, Oct. 1953.
- [142] Lowson, M. V., “The Sound Field for Singularities in Motion,” *Proceedings of the Royal Society of London. Series A, Mathematical and Physical Sciences*, Vol. 286, No. 1407, 1965, pp. 559–572, doi: 10.1098/rspa.1965.0164.
- [143] Wright, S. E., “Sound Radiation from a Lifting Rotor Generated by Asymmetric Disc Loading,” *Journal of Sound and Vibration*, Vol. 9, No. 2, 1969, pp. 223–240, doi: 10.1016/0022-460X(69)90029-7.
- [144] Lighthill, M. J., “On Sound Generated Aerodynamically. I. General Theory,” *Proceedings of the Royal Society of London. Series A, Mathematical and Physical Sciences*, Vol. 221, No. 1107, 1952, pp. 564–587, doi: 10.1098/rspa.1952.0060.
- [145] Brentner, K. S., Lyrantzis, A., and Koutsavdis, E. K., “A Comparison of Computational Aeroacoustic Prediction Methods for Transonic Rotor Noise,” *Proceedings of 52nd American Helicopter Society, Annual Forum*, Washington, D.C., USA, AHS-52-1996, 1996, pp. 1–12.



- [146] Liu, Y., Anusonti-Inthra, P., and Diskin, B., “Development and Validation of a Multidisciplinary Tool for Accurate and Efficient Rotorcraft Noise Prediction,” NASA CR–2011-217057, Feb. 2011.
- [147] Wang, Z. J., Fidkowski, K., Abgrall, R., Bassi, F., Caraeni, D., Cary, A., Deconinck, H., Hartmann, R., Hillewaert, K., Huynh, H. T., Kroll, N., May, G., Persson, P.-O., van Leer, B., and Visbal, M., “High-Order CFD Methods: Current Status and Perspective,” *International Journal for Numerical Methods in Fluids*, Vol. 72, No. 8, 2013, pp. 811–845, doi: 0.1002/fld.3767.
- [148] Kroll, N., Bieler, H., Deconinck, H., Couaillier, V., van der Ven, H., and Sorensen, K., “ADIGMA - a European Initiative on the Development of Adaptive Higher-Order Variational Methods for Aerospace Applications,” *Notes on Numerical Fluid Mechanics and Multidisciplinary Design*, Vol. 113, 2010.
- [149] Gottlieb, S. and Orszag, A., *Numerical Analysis of Spectral Methods: Theory and Applications*, SIAM: Philadelphia, 1977.
- [150] Godunov, S. K., “A Finite-Difference Method for the Numerical Computation of Discontinuous Solutions of the Equations of Fluid Dynamics,” *Matematicheski Sbornik*, Vol. 47, No. 3, 1959, pp. 271–306.
- [151] Lele, S. K., “Compact Finite Difference Schemes with Spectral-like Resolution,” *Journal of Computational Physics*, Vol. 103, No. 1, 1992, pp. 16–42, doi: 10.1016/0021-9991(92)90324-R.
- [152] Liu, X., Osher, S., and Chan, T., “Weighted Essentially Non-Oscillatory Schemes,” *Journal of Computational Physics*, Vol. 115, No. 1, 1994, pp. 200–212, doi: 10.1006/jcph.1994.1187.
- [153] Barth, T. and Frederickson, P., “High-order Solution of the Euler Equations on Unstructured Grids Using Quadratic Reconstruction,” *AIAA Journal*, Vol. 90, No. 13, 1990, doi: 10.2514/6.1990-13.
- [154] Nogueira, X., Colominas, I., Cueto-Felgueroso, L., Khelladi, S., Navarrina, F., and Casteleiro, M., “Resolution of Computational Aeroacoustics Problems on Unstructured Grids with a Higher-Order Finite Volume Scheme,” *Journal of Computational and Applied Mathematics*, Vol. 234, No. 7, 2010, pp. 2089–2097, doi: 10.1016/j.cam.2009.08.067.
- [155] Yang, H. Q., Chen, Z. J., Przekwas, A., and Dudley, J., “A High-Order CFD Method Using Successive Differentiation,” *Journal of Computational Physics*, Vol. 281, No. 1, 2015, pp. 690–707, doi: 10.1016/j.jcp.2014.10.046.
- [156] Yang, H. Q. and Harris, R. E., “Vertex-Centered, High-order Schemes for Turbulent Flows,” *Proceedings of the 54th Aerospace Sciences Meeting*, San Diego, California, USA, AIAA-2016-1098, 2016, pp. 1–24.
- [157] Tam, C. K. W. and Webb, J. C., “Dispersion-Relation-Preserving Finite Difference Schemes for Computational Acoustics,” *Journal of Computational Physics*, Vol. 107, No. 2, 1993, pp. 262–281, doi: 10.1006/jcph.1993.1142.

- [158] Visbal, M. R. and Gaitonde, D. V., “High-Order Accurate Methods for Complex Unsteady Subsonic Flows,” *AIAA Journal*, Vol. 37, No. 10, 1999, pp. 1231–1239, doi: 10.2514/2.591.
- [159] McCorquodale, P., Dorr, M. R., Hittinger, J. A. F., and Colella, P., “A High-Order Finite-Volume Methods for Hyperbolic Conservation Laws on Mapped Multiblock Grids,” *Journal of Computational Physics*, Vol. 288, No. C, 2015, pp. 181–195, doi: 10.1016/j.jcp.2015.01.006.
- [160] Colella, P., Dorr, M. R., Hittinger, J. A. F., and Martin, D. F., “High-Order, Finite-Volume Methods in Mapped Coordinates,” *Journal of Computational Physics*, Vol. 230, No. 8, 2011, pp. 2952–2976, doi: 10.1016/j.jcp.2010.12.044.
- [161] Ekaterinaris, J. A., “High-order accurate, low numerical diffusion methods for aerodynamics,” *Progress in Aerospace Sciences*, Vol. 41, No. 1, 2005, pp. 192–300, doi: 10.1016/j.paerosci.2005.03.003.
- [162] Calhoun, D. A., Helzel, C., and Leveque, R. J., “Logically Rectangular Grids and Finite Volume Methods for PDEs in Circular and Spherical Domains,” *SIAM Rev.*, Vol. 50, No. 4, 2008, pp. 723–752, doi: 10.1137/060664094.
- [163] Harten, A., Engquist, B., Osher, S., and Chakravarthy, S., “Uniformly High Order Essentially Non-Oscillatory Schemes, III,” *Journal Computational Physics*, Vol. 131, No. 1, 1997, pp. 3–47, doi: 10.1006/jcph.1996.5632.
- [164] Shu, C.-W. and Osher, S., “Efficient Implementation of Essentially Non-Oscillatory Shock Capturing Schemes,” *Journal Computational Physics*, Vol. 77, No. 2, 1988, pp. 439–471, doi: 10.1016/0021-9991(88)90177-5.
- [165] Shu, C.-W. and Osher, S., “Efficient Implementation of Essentially Non-Oscillatory Shock Capturing Schemes, II,” *Journal Computational Physics*, Vol. 83, No. 1, 1989, pp. 32–78, doi: 10.1016/0021-9991(89)90222-2.
- [166] Jiang, G. and Shu, C.-W., “Efficient Implementation of Weighted ENO Schemes,” *Journal of Computational Physics*, Vol. 126, No. 1, 1996, pp. 202–228, doi: 10.1006/jcph.1996.0130.
- [167] Balsara, D. and Shu, C.-W., “Monotonicity Preserving Weighted Essentially Non-Oscillatory Schmes with Increasingly High Order of Accuracy,” *Journal Computational Physics*, Vol. 160, No. 2, 2000, pp. 405–452, doi: 10.1006/jcph.2000.6443.
- [168] Levy, D., Puppo, G., and Russo, G., “Central WENO Schemes for Hyperbolic Systmes of Conservation Laws,” *Mathematical Modelling and Numerical Analysis*, Vol. 33, No. 3, 1999, pp. 547–571, doi: 10.1051/m2an:1999152.
- [169] Levy, D., Puppo, G., and Russo, G., “Central WENO Schemes for Hyperbolic Systmes of Conservation Laws,” *SIAM Journal on Scientific Computing*, Vol. 22, No. 2, 2000, pp. 656–672, doi: 10.1137/S1064827599359461.
- [170] Ghosh, D., *Compact-Reconstruction Weighted Essentially Non-Oscillatory Schemes for Hyperbolic Conservation Laws*, Ph.D. thesis, University of Maryland, United States, Jan. 2013.

- [171] Shu, C.-W., “Essentially Non-Oscillatory and Weighted Essentially Non-Oscillatory Schemes for Hyperbolic Conservation Laws, in Advanced Numerical Approximation of Nonlinear Hyperbolic Equations,” *Lecture Notes in Mathematics*, Springer, Vol. 1697, No. 1, 1998, pp. 325–432, doi: 10.1007/BFb0096355.
- [172] Barakos, G., Steijl, R., Badcock, K., and Brocklehurst, A., “Development of CFD Capability for Full Helicopter Engineering Analysis,” *Proceedings of the 31st European Rotorcraft Forum*, ERF, Florence, Italy, 2005, pp. 1–15.
- [173] Lawson, S. J., Steijl, R., Woodgate, M., and Barakos, G. N., “High performance computing for challenging problems in computational fluid dynamics,” *Progress in Aerospace Sciences*, Vol. 52, 2012, pp. 19–29, doi: 10.1016/j.paerosci.2012.03.004.
- [174] Steijl, R. and Barakos, G. N., “Sliding mesh algorithm for CFD analysis of helicopter rotor-fuselage aerodynamics,” *International Journal for Numerical Methods in Fluids*, Vol. 58, No. 5, 2008, pp. 527–549, doi: 10.1002/d.1757.
- [175] Hirt, C. W., Amsten, A. A., and Cook, J. L., “An Arbitrary Lagrangian-Eulerian Computing Method for All Flow Speeds,” *Journal of Computational Physics*, Vol. 14, No. 3, 1974, pp. 227–253, doi: 10.1006/jcph.1997.5702.
- [176] Osher, S. and Chakravarthy, S., “Upwind Schemes and Boundary Conditions with Applications to Euler Equations in General Geometries,” *Journal of Computational Physics*, Vol. 50, No. 3, 1983, pp. 447–481, doi: 10.1016/0021-9991(83)90106-7.
- [177] Roe, P. L., “Approximate Riemann Solvers, Parameter Vectors, and Difference Schemes,” *Journal of Computational Physics*, Vol. 43, No. 2, 1981, pp. 357–372, doi: 10.1016/0021-9991(81)90128-5.
- [178] van Leer, B., “Towards the Ultimate Conservative Difference Scheme. V. A Second-Order Sequel to Godunov’s Method,” *Journal of Computational Physics*, Vol. 32, No. 1, 1979, pp. 101–136, doi: 10.1016/0021-9991(79)90145-1.
- [179] van Albada, G. D., van Leer, B., and Roberts, W. W., “A Comparative Study of Computational Methods in Cosmic Gas Dynamics,” *Astronomy and Astrophysics*, Vol. 108, No. 1, 1982, pp. 76–84.
- [180] Axelsson, O., *Iterative Solution Methods*, Cambridge University Press, 1994.
- [181] van Leer, B., “Towards the Ultimate Conservative Difference Scheme. IV. A New Approach to Numerical Convention,” *Journal of Computational Physics*, Vol. 23, No. 1, 1977, pp. 276–299, doi: 10.1016/0021-9991(77)90095-X.
- [182] Mavriplis, D. J., “Revisiting the Least-Squares Procedure for Gradient Reconstruction on Unstructured Meshes,” *Proceedings of the 16th Computational Fluid Dynamics Conference*, Orlando, Florida, USA, AIAA-2003-3986, 2003, pp. 1–13.
- [183] Lax, P. D., *Hyperbolic Systems of Conservation Laws and the Mathematical Theory of Shock Waves*, Philadelphia: SIAM Publications, 1973.

- [184] Reynolds, O., “On the dynamical theory of turbulent incompressible viscous fluids and the determination of the criterion,” *Phil. Trans. R. Soc. London*, Vol. A 186, 1894, pp. 123–161.
- [185] Pope, S. B., *Turbulent Flows*, Cambridge University Press, 2000.
- [186] Chassaing, P., *Turbulence en Mecanique des Fluides*, Editions Cepadues, 2005.
- [187] Jimenez-Garcia, A. and Barakos, G. N., “Numerical Simulations on the ERICA Tiltrotor,” *Aerospace Science and Technology*, Vol. 64, No. 1, 2017, pp. 171–191, doi: 10.1016/j.ast.2017.01.023.
- [188] Gatski, T. B. and Bonnet, J. P., *Compressibility, Turbulence and High Speed Flow*, Elsevier, Amsterdam, 2009.
- [189] White, F. M., *Viscous Fluid Flow*, McGraw Hill, New York, 1974.
- [190] Wilcox, D. C., “Multiscale Model for Turbulent Flows,” *AIAA Journal*, Vol. 26, No. 11, 1988, pp. 1311–1320, doi: 10.2514/3.10042.
- [191] Menter, F. R., “Two-Equation Eddy-Viscosity Turbulence Models for Engineering Applications,” *AIAA Journal*, Vol. 32, No. 8, 1994, pp. 1598–1605, doi: 10.2514/3.12149.
- [192] Wilcox, D., “Simulation of Transition with a Two-Equation Turbulence Model,” *AIAA journal*, Vol. 32, No. 2, 1994, pp. 247–255, doi: 10.2514/3.59994.
- [193] Menter, F., Langtry, R., Rikhi, R., Suzen, S., Huang, P., and Volker, S., “A Correlation-Based Transition Model Using Local Variables - Part I: Model Formulation,” *Journal of Turbomachinery*, Vol. 128, No. 3, 2006, pp. 1598–1605, doi: 10.1115/1.2184352.
- [194] Menter, F. R., Smirnov, P. E., Liu, T., and Avancha, R., “A One-Equation Local Correlation-Based Transition Model,” *Flow Turbulence Combust*, Vol. 95, No. 4, 2015, pp. 583–619, doi: 10.1007/s10494-015-9622-4.
- [195] Michel, R., “Etude de la Transition sur les Profils D’Aile, Etablissement d’un Critere de Determination du Point de Transition et Calcul de la Trainee de Profil Incompressible,” Technical report 1/1578a, 1951.
- [196] Cebeci, T. and Smith, A. M. O., *Analysis of Turbulent Boundary Layers*, Applied Mathematics and Mechanics. Academic Press, 1974.
- [197] Michel, R., “Determination du Point de Transition et Calcul de la Trainee des Profiles D’Ailes en Incompressible,” Onera, 1952.
- [198] Shaidakov, V. I., “Disc Vortex Theory of the Main Rotor with the Constant Load over a Disc,” *Proektirovanie vertoletov (Helicopter Design)*, Moscow: MAI, Vol. 381, 1976.
- [199] Crozon, C., *Coupling Flight Mechanics and CFD Numerical Simulation of Shipborne Rotors*, Ph.D. thesis, University of Liverpool, UK, June 2015.
- [200] Jarkowski, M., Woodgate, M., Barakos, G. N., and Rokicki, J., “Towards Consistent Hybrid Overset Mesh Methods for Rotorcraft CFD,” *International Journal for Numerical Methods in Fluids*, Vol. 74, No. 8, 2014, pp. 543–576, doi: 10.1002/fld.3861.

- [201] Dehaeze, F. and Barakos, G. N., “Aeroelastic CFD Computations for Rotor Flows,” *Proceedings of the 37th European Rotorcraft Forum*, ERF, Vergiate and Gallarate, Italy, 2011, pp. 1–20.
- [202] Jimenez-Garcia, A. and Barakos, G. N., “Hover Predictions on the S-76 Rotor using HMB2,” *Proceedings of the 53rd Aerospace Sciences Meeting*, Kissimmee, Florida, USA, AIAA-2015-1712, 2015, pp. 1–34.
- [203] Biava, M. and Barakos, G. N., “Optimisation of Ducted Propellers for Hybrid Air Vehicles Using High-Fidelity CFD,” *The Aeronautical Journal*, Vol. 120, No. 1232, 2016, pp. 1632–1657, doi: 10.1017/aer.2016.78.
- [204] Biava, M., Woodgate, M., and Barakos, G. N., “Fully Implicit Discrete Adjoint Methods for Rotorcraft Applications,” *AIAA Journal*, Vol. 54, No. 2, 2015, pp. 735–749, doi: 10.2514/1.J054006.
- [205] Kraft, D., “Algorithm 733: TOMP-Fortran Modules for Optimal Control Calculations,” *ACM Transactions on Mathematical Software*, Vol. 20, No. 3, 1994, pp. 262–281.
- [206] Jeong, J. and Hussain, F., “On the Identification of a Vortex,” *Journal of Fluid Mechanics*, Vol. 285, No. 1, 2015, pp. 69–94, doi: 10.1017/S0022112095000462.
- [207] Ffowcs-Williams, J. E. and Hawkings, D. L., “Sound Generation by Turbulence and Surfaces in Arbitrary Motion,” *Proceedings of the Royal Society of London. Series A, Mathematical and Physical Sciences*, Vol. 264, No. 1151, 1969, pp. 321–342, doi: 10.1098/rsta.1969.0031.
- [208] Kusyumov, A. N., Mikhailov, S. A., Garipova, L. I., Batrakov, A. S., and Barakos, G. N., “Prediction of Helicopter Rotor Noise in Hover,” *Proceedings of the EPJ Web of Conferences*, EDP Sciences, Český Krumlov Czech Republic, 2014, pp. 1–5.
- [209] Gopalan, G. and Shmitz, F. H., “Far-Field Near-In Plane Harmonic Main Rotor Helicopter Impulsive Noise Reduction Possibilities,” *Proceedings of the 64th American Helicopter Society, Annual Forum*, AHS, Montreal, Canada, 2008, pp. 1–22.
- [210] Gopalan, G. and Shmitz, F. H., “Understanding Far Field Near-In-Plane High Speed Harmonic Helicopter Rotor Noise in Hover: Governing Parameters and Active Acoustic Control Possibilities,” *Proceedings of the AHS Specialists Conference on Aeromechanics*, AHS, San Francisco, California, USA, 2008, pp. 1–23.
- [211] Ponza, R., “Flying Helicopters Acoustic Impact Assessment: Towards a More Realistic Simulation Methodology,” *Proceedings of the European Congress on Computational Methods in Applied Sciences and Engineering*, ECCOMAS, Jyväskylä, Finland, 2004, pp. 1–11.
- [212] Quackenbush, T. R., Wachspress, D. A., and Boschitsch, A. H., “Rotor Aerodynamic Loads Computation Using a Constant Vorticity Contour Free Wake Model,” *Journal of Aircraft*, Vol. 32, No. 5, 1995, pp. 911–920, doi: 10.2514/3.46818.
- [213] Johnson, W., *Camrad/JA - A Comprehensive Analytical Model of Rotorcraft Aerodynamics and Dynamics - Volume II: User’s Manual*, Johnson Aeronautics, 1988.

- [214] Tuinstra, M. and Gerales, C. D., *HELicopter Environmental Noise Analysis (HELENA) Software Tool*, NLR-CR-2010-346, 2010.
- [215] Melone, S. and D'Andrea, A., "Helicopter Main Rotor - Tail Rotor Interactional Aerodynamics and Related Effects on the On-Ground Noise Footprint," *Proceeding of the 37th European Rotorcraft Forum*, ERF, Vergiate and Gallarate, Italy, 2011, pp. 1–11.
- [216] Jimenez-Garcia, A., *D4.5 Aeroacoustic Method, HiperTilt Project*, Technology Strategy Board (TSB), 2015.
- [217] Burg, C. O. E., "Higher Order Variable Extrapolation For Unstructured Finite Volume RANS Flow Solvers," *Proceedings of the Seventieth AIAA Computational Fluid Dynamics Conference*, AIAA, Toronto, Ontario, 2005, pp. 1–17.
- [218] Anderson, W. K., Thomas, J. L., and van Leer, B., "Comparison of Finite Volume Flux Vector Splittings for the Euler Equations," *AIAA Journal*, Vol. 24, No. 9, 1986, pp. 1453–1460, doi: 10.2514/3.9465.
- [219] McCorquodale, P. and Colella, P., "A High-Order Finite-Volume Method for Conservation Laws on Locally Refined Grids," *Communications in Applied Mathematics and Computational Science*, Vol. 6, No. 1, 2011, pp. 1–25, doi: 10.2140/camcos.2011.6.1.
- [220] Barakos, G. N. and Johnson, C. S., "Acoustic Comparison of Propellers," *International Journal of Aeroacoustics*, Vol. 15, No. 6, 2016, pp. 575–594, doi: 10.1177/1475472X16659214.
- [221] Steijl, R., Woodgate, M., and Barakos, G. N., "CFD Requirements for Efficient Smart-Rotor Analysis," *Proceedings of the 35th European Rotorcraft Forum*, ERF, Hamburg, Germany, 2009, pp. 1–11.
- [222] Shu, C. W., "Essentially non-Oscillatory and weighted essentially non-Oscillatory schemes for hyperbolic conservation laws," ICASE Report 97-65, 1997.
- [223] Rohardt, C. H., "Flow Visualisation on a Helicopter Rotor in Hover Using Acenaphthne," *Proceeding of the 13th European Rotorcraft Forum*, Arles, France, ERF-1987-62, 1987, pp. 1–22.
- [224] Ridhwan, N. A., *Numerical Modelling of Flow Field near Helicopter Rotors using Hybrid Navier-Stokes & Free Wake methods*, Ph.D. thesis, University of Liverpool, UK, Sept. 2011.
- [225] Heister, C. C., Raddatz, J., and Klein, A., "Accurate Numerical Flow Simulation of Hovering Rotors using Different Transition Prediction Methods," *Proceeding of the 36th European Rotorcraft Forum*, Paris, France, ERF-2010-111, 2010, pp. 1–12.
- [226] Hariharan, N., Egolf, A., and Sankar, R. N. L., "Helicopter Rotor Aerodynamic Modeling in Hover: AIAA Standardized Hover Evaluations," *Proceedings of the 53rd Aerospace Sciences Meeting*, Kissimmee, Florida, USA, AIAA-2015-1242, 2015, pp. 1–34.
- [227] Bousman, W. G., "Aerodynamic Characteristics of SC1095 and SC1094R8 Airfoils," NASA TP-2003-212265, Dec. 2003.

- [228] Brocklehurst, A., *High Resolution Method for the Aerodynamic Design of Helicopter Rotors*, Ph.D. thesis, University of Liverpool, UK, June 2013.
- [229] Brocklehurst, A. and Barakos, G. N., “A Review of Helicopter Rotor Blade Tip Shapes,” *Progress in Aerospace Sciences*, Vol. 56, No. 1, 2013, pp. 35–74, doi: 10.1016/j.paerosci.2012.06.003.
- [230] Makofski, R. A., “Charts for Estimating the Hovering Endurance of a Helicopter,” NACA TN–3810, Langley Aeronautical Laboratory, Oct. 1956.
- [231] Anon, “Sikorsky S-76C++ Helicopter,” S-76C++ Executive Transport Technical Information S76-084, Feb. 2009.
- [232] Stroub, R. H., Rabbott, J. P., and Niebanck, C. F., “Rotor Blade Tip Shape Effects on Performance and Control Loads From Full-Scale Wind Tunnel Testing,” *Journal of the American Helicopter Society*, Vol. 24, No. 5, 1979, pp. 28–35, doi: 10.4050/JAHS.24.28.
- [233] Balch, D. T., “Correlation of Full-Scale Wind Tunnel Test Data with Model Rotor Test Data and Theory for a Modern Helicopter Main Rotor,” *Journal of the American Helicopter Society*, Vol. 24, No. 4, 1979, pp. 45–50, doi: 10.4050/JAHS.24.45.
- [234] Dehaeze, F., “Aeroelastic Simulations of Hovering Rotors,” TN11-004-Aeroelastic Coupling Hover, CFD Lab, University of Glasgow, March 2011.
- [235] Hamade, K. S. and Kufeld, R. M., “Modal analysis of UH-60A instrumented rotor blades,” NASA TR–4239, Aug. 1990.
- [236] Monico, M. R., *Reduced Weight Rotor Blades as a Result of Flap-Bending Torsion Coupling*, Ph.D. thesis, Rensselaer Polytechnic Institute, Hartford, Connecticut, USA, Aug. 2013.
- [237] Singleton, J. D. and Yeager, W. T., “Important Scaling Parameters for Testing Model-Scale Helicopter Rotors,” *Journal of Aircraft*, Vol. 37, No. 3, 2000, pp. 396–402, doi: 10.2514/2.2639.
- [238] Yamauchi, G. K. and Johnson, W., “Trends of Reynolds Number Effects on Two-Dimensional Airfoil Characteristics for Helicopter Rotor Analyses,” NASA TM–84363, April 1983.
- [239] Wong, O. D., Noonan, K. W., Watkins, A. N., Jenkins, L. N., and Yao, C. S., “Non-Intrusive Measurements of a Four-Bladed Rotor in Hover - A First Look,” *Proceedings of the American Helicopter Society Aeromechanics Specialists*, AHS, San Francisco, California, USA, 2010, pp. 1–11.
- [240] Wong, O. D., Watkins, A. N., Goodman, K. Z., Crafton, J., Forlines, A., Goss, L., Gregory, J. W., and Juliano, T. J., “Blade Tip Pressure Measurements using Pressure Sensitive Paint,” *Proceedings of the 68th American Helicopter Society, Annual Forum*, Fort Worth, Texas, USA, AHS-2012-000233, 2012, pp. 1–14.

- [241] Watkins, A. N., Leighty, B. D., Lipford, W. E., Goodman, K. Z., Crafton, J., and Gregory, J. W., "Measuring Surface Pressures on Rotor Blades Using Pressure-Sensitive Paint," *AIAA Journal*, Vol. 54, No. 1, 2016, pp. 206–215, doi: 10.2514/1.J054191.
- [242] Overmeyer, A. D. and Martin, P. B., "Measured Boundary Layer Transition and Rotor Hover Performance at Model Scale," *Proceedings of the 55th Aerospace Sciences Meeting*, Grapevine, Texas, USA, AIAA-2017-1872, 2017, pp. 1–36.
- [243] Noonan, K. W., "Aerodynamic Characteristics of Two Rotorcraft Airfoils Designed for Application to the Inboard Region of a Main Rotor Blade," NASA TP-3009, U.S. Army Aviation Systems Command, TR-90-B-005, July 1990.
- [244] Noonan, K. W., "Aerodynamic Characteristics of Two Rotorcraft Airfoils Designed for Application to the Inboard Region of a Main Rotor Blade," NASA TM-4264, U.S. Army Aviation Systems Command, TR-91-B-003, May 1991.
- [245] Wong, T.-C., "Application of CREATE<sup>TM</sup>-AV Helios in an Engineering Environment: Hover Prediction Assessment," *Proceedings of the 55th Aerospace Sciences Meeting*, Grapevine, Texas, USA, AIAA-2017-1667, 2017, pp. 1–26.
- [246] Vieira, B. A. O., Kinzel, M. P., and Maughmer, M. D., "CFD Hover Predictions Including Boundary-Layer Transition," *Proceedings of the 55th Aerospace Sciences Meeting*, Grapevine, Texas, USA, AIAA-2017-1665, 2017, pp. 1–16.
- [247] Jain, R., "CFD Performance and Turbulence Transition Predictions on an Installed Model-scale Rotor in Hover," *Proceedings of the 55th Aerospace Sciences Meeting*, Grapevine, Texas, USA, AIAA-2017-1871, 2017, pp. 1–29.
- [248] Coder, J. G., "OVERFLOW Rotor Hover Simulations Using Advanced Turbulence and Transition Modeling," *Proceedings of the 55th Aerospace Sciences Meeting*, Grapevine, Texas, USA, AIAA-2017-1432, 2017, pp. 1–19.
- [249] Maynard, J. D. and Murphy, M. P., "Pressure Distributions on the Blade Sections of the NACA 10-(3)(066)-033 Propeller under Operating Conditions." NACA-RM-L9L12, Jan. 1950.
- [250] Acree, C., "Rotor Design Options for Improving XV-15 Whirl-Flutter Stability Margins," NASA TP-2004-212262, March 2004.
- [251] Bruin, A. and Schneider, O., "A Discussion of Measured Static and Dynamic Rotor Loads During Testing of the ERICA Tilt-Wing Rotorcraft Configuration in DNW-LLF Wind Tunnel," *Proceeding of the 40th European Rotorcraft Forum*, Southampton, UK, ERF-2014-5C, 2014, pp. 1–15.
- [252] Vigeveno, L., Beaumier, P., Decours, J., Khier, W., Kneisch, T., and Vitagliano, P., "Tilt-Rotor Aerodynamics Activities During the NICETRIP Project," *Proceeding of the 40th European Rotorcraft Forum*, Southampton, UK, ERF-2014-16A, 2014, pp. 1–14.
- [253] Johnson, W., "Calculation of the Aerodynamic Behavior of the Tilt Rotor Aeroacoustic Model (TRAM) in the DNW," *Proceedings of the 57th American Helicopter Society, Annual Forum*, Washington, D.C., USA, AHS-57-2001-35, 2001, pp. 1–37.



- [254] Guntur, S. and Sorensen, N., “An Evaluation of Several Methods of Determining the Local Angle of Attack on Wind Turbine Blades,” *Proceeding of the Science of Making Torque from Wind 2012*, Oldenburg, Germany, 2012, pp. 1–11.
- [255] Lent, H. M., Meier, G. E. A., Muller, K. J., Obermeier, F., Schievelbush, U., and Shurmann, O., “Mechanisms of Transonic Blade-Vortex Interaction Noise,” *Journal of Aircraft*, Vol. 30, No. 1, 1993, pp. 88–93, doi: 10.2514/3.10776.
- [256] Beddoes, T., “Unsteady Aerodynamics Application to Helicopter Noise and Vibration Sources,” Technical Report, Westland Helicopter Ltd, Yeovil, Somerset BA202YB, UK, 1990.
- [257] Lewis, R. I., *Vortex Element Methods for Fluid Dynamic Analysis of Engineering Systems*, Chapter 8, Cambridge University Press, 1991.
- [258] Caradonna, F., Kitaplioglu, C., McCluer, M., Baeder, J., Leishman, J. G., Berezin, C., Visintainer, J., Bridgeman, J., Burley, C., Epstein, R., Lyrintzis, A., Koutsavdis, E., Rahier, G., Delrieux, Y., Rule, J., and Bliss, D., “Methods of the Prediction of Blade-Vortex Interaction Noise,” *Journal of the American Helicopter Society*, Vol. 45, No. 4, 2000, pp. 303–317, doi: 10.4050/JAHS.45.303.
- [259] Hall, C. M., *High-Order Accurate Simulations of Wake and Tip Vortex Flowfield*, Ph.D. thesis, The Pennsylvania State University, USA, Dec. 1998.
- [260] Lee, S. and Bershader, D., “Head-on parallel blade-vortex interaction,” *AIAA Journal*, Vol. 32, No. 1, 1994, pp. 16–22, doi: 10.2514/3.11945.
- [261] Cook, P. H., McDonald, M. A., and Firmin, M. C. P., “Aerofoil RAE 2822 - Pressure Distributions, and Boundary Layer and Wake Measurements,” Experimental Data Base for Computer Program Assessment, AGARD Report AR 138, 1979.
- [262] Tatsumi, S., Martinelli, L., and Jameson, A., “A new high resolution scheme for compressible flows past airfoil,” *Proceedings of the 33rd Aerospace Sciences Meeting*, Reno, Nevada, USA, AIAA-1995-0466, 1995, pp. 1–16.
- [263] Schultz, K.-J., Splettstoesser, W., Junker, B., Wagner, W., Schoell, E., Arnould, G., Mercker, E., Pengel, K., and Fertis, D., “A Parametric Wind Tunnel Test on Rotorcraft Aerodynamics and Aeroacoustics (HELISHAPE) - Test Documentation and Representative Results,” *Proceedings of the 22nd European Rotorcraft Forum*, ERF, Brighton, UK, 1996.
- [264] Hariharan, N., Narducci, R., Reed, E., and Egolf, T. A., “Helicopter Aerodynamic Modeling of Rotor with Tip-Shape Variations: AIAA Standardized Hover Evaluations,” *Proceedings of the 54th Aerospace Sciences Meeting*, San Diego, California, USA, AIAA-2016-0031, 2016, pp. 1–42.
- [265] Shinoda, P. M., Yeo, H., and Norman, T. R., “Rotor Performance of a UH-60 Rotor System in the NASA Ames 80- by 120-Foot Wind Tunnel,” *Proceedings of 58th American Helicopter Society, Annual Forum*, AHS, Montreal, Canada, 2002, pp. 1–18.

## BIBLIOGRAPHY

---

- [266] Dindar, M., Shephard, M. S., Flaherty, J. E., and Jansen, K., “Adaptive CFD analysis for rotorcraft aerodynamics,” *Computer Methods in Applied Mechanics and Engineering*, Vol. 189, No. 1, 2000, pp. 1055–1076, doi: 10.1016/S0045-7825(99)00368-0.
- [267] Kufeld, R., Balough, D., Cross, J., Studebaker, K., and Jennison, C., “Flight Testing the UH-60A Airloads Aircraft,” *Proceedings of 50th American Helicopter Society, Annual Forum*, Alexandria, Virginia, USA, AHS-50-1994-044, 1994, pp. 1–22.

# Appendix A

## Matlab Program for the Theoretical Noise

```
1 function Theoretical_Noise (n)
2
3 %%%%%%%%%%%%%%%%%%%%%%%%%%%%%%%%%%%%%%%%%%%%%%%%%%%%%%%%%%%%%%%%%%%%%%%%%
4 %%%%%%%%%%%%%%%%%%%%%%%%%%%%%%%%%%%%%%%%%%%%%%%%%%%%%%%%%%%%%%%%%%%%%%%%%
5 rho = 1.225; % air density in kg/m^3 %
6 ao = 340.30; % sound speed in m/s %
7 R = 1.4234; % rotor radius in m %
8 rh = n*R; % observer distance from rotor hub in m %
9 Ae = 0.06588*(3.092*0.0254)^2; % aerofoil cross sectional area in m^2 (75%R) %
10 A = pi*R^2; % rotor disk area in m^2 %
11 Mh = 0.65; % tip Mach number %
12 Nb = 4; % number of blades %
13 omega = Mh*ao/R; % rotor rotational speed rad/s %
14 CT_s = 0.06; % blade loading coefficient (US) %
15 sigma = 0.07043; % rotor solidity %
16 T=(CT_s*sigma)*rho*A*(Mh*ao)^2; % rotor thrust in Newton %
17 %%%%%%%%%%%%%%%%%%%%%%%%%%%%%%%%%%%%%%%%%%%%%%%%%%%%%%%%%%%%%%%%%%%%%%%%%
18 %%%%%%%%%%%%%%%%%%%%%%%%%%%%%%%%%%%%%%%%%%%%%%%%%%%%%%%%%%%%%%%%%%%%%%%%%
19
20
21 Fh=R/rh;
22 Fe=Ae/A;
23 Ft=1/(60*sqrt(2)*Nb)*(T/(rho*(ao^2)*A))^(1.5);
24
25 psi=linspace(0,2*pi,180);
26
27
28 for i=1:length(psi)
29
30 %Thickness noise%
31 a(i)=-(3-Mh*sin(psi(i)))*sin(psi(i))/(1-Mh*sin(psi(i)))^3;
32
33
34 b(i)=Mh*cos(psi(i))^2/(10*(1-Mh*sin(psi(i)))^4);
35
36
37 c(i)=50+39*Mh^2-45*Mh*sin(psi(i))-11*(Mh^2)*sin(psi(i))^2+12*(Mh^3)*sin(psi(i))-18*(Mh^3)*sin(psi(i))^3;
38
39 Tm(i)=(Mh^3)/12*(a(i)+b(i)*c(i));
40
41
42 PT(i)=rho*(ao^2)/2*Fh*Fe*Tm(i);
43 %Thickness noise&
44
45
46 %Loading noise%
47 d(i)=60+30*(Mh^2)*cos(psi(i))^2-120*Mh*sin(psi(i));
48
49 e(i)=-30*(Mh^3)*sin(psi(i))*cos(psi(i))^2+80*(Mh^2)*sin(psi(i))^2;
50
51
52 f(i)=9*(Mh^4)*(sin(psi(i))^2)*(cos(psi(i))^2)-20*(Mh^3)*sin(psi(i))^3;
53
54
55 Lm(i)=cos(psi(i))*((1-Mh*sin(psi(i)))^(-3))*(d(i)+e(i)+f(i));
56
57
58 PL(i)=rho*(ao^2)/2*Fh*Ft*Lm(i);
59
60 t(i)=(psi(i)+Mh*(cos(psi(i))-1))/omega;
61
62 end
63
64
65 Thickness=[t*omega*180/pi; PT]';
66 Loading =[t*omega*180/pi; PL]';
67 Total =[t*omega*180/pi; (PT+PL)]';
```

## APPENDIX A. MATLAB PROGRAM FOR THE THEORETICAL NOISE

---

```
68
69 save PT.dat Thickness -ascii
70 save PL.dat Loading -ascii
71 save PTL.dat Total -ascii
```